

**Homo- and Heteronuclear Transition Metal Complexes Supported by
Multinucleating Ligands**

Thesis by
Sandy Suseno

In Partial Fulfillment of the Requirements
for the Degree of Doctor of Philosophy

CALIFORNIA INSTITUTE OF TECHNOLOGY
Division of Chemistry and Chemical Engineering
Pasadena, California
2015
(Defended on October 29, 2014)

*To Mom and Dad,
my older sister, Jessica,
and my younger sisters, Clarinta and Valencia*

“Don’t spend time beating on a wall,
hoping to transform it into a door.” –Coco Chanel

ACKNOWLEDGEMENTS

The several years that I have spent at Caltech will always be a bittersweet memory that I will never forget in my entire life. From the rigorous research to the people I have met, there is this substantial influence and knowledge gained over the years that overrides my old beliefs and transform me into someone else I never thought I would become, for the better I hope. There is a long list of individuals whom I'd like to acknowledge who have truly changed me, challenged me, and inspired me to become who I am today. I hope that I'm not missing anyone as I write these acknowledgements.

The first person that comes to mind is indeed my advisor, Theodor Agapie. I knew Theo before he "officially" started his research lab at Caltech. As an undergraduate who worked with him in the Marletta lab, I learned about all the biochemistry techniques I know today from Theo. Thank you for being patient when I spilled almost all the lysed cells in an attempt to pour it into the homogenizer. Theo then offered for me to join his group at Caltech to work on a bioinorganic project, challenging me to work on many other projects afterwards: organometallic chemistry, metal-ion fluorescent probes, synthetic inorganic chemistry, and heterogeneous material chemistry. Through Theo's rigorous training and all my projects, successes, and failures, I believe I've learned to become a wiser and stronger woman, ready to take on the world with my knowledge. Thank you for continuously pushing me in my graduate school years and supporting me in my future career.

I would also like to thank my other thesis committee members, Jonas Peters, John Bercaw, and Doug Rees, for all of the insightful comments, ideas, and annual constructive criticisms to inspire me to always think about my chemistry from a different perspective. I learn to *not* worry about the little details, but always set the target to the BIGGER picture. I also really appreciate all the support and suggestions you offered regarding my future career plans.

Not only my thesis committee, others in the Caltech chemistry family have often extended their help and willingness to discuss my research. I'd like to thank Harry Gray, Jay Winkler, and Jay Labinger, who have provided me useful suggestions on my research. Bruce Brunschwig was an important individual who has let me borrow his oxygen-sensing probe and amazingly maintained the MMRC for users. Nate Lewis

allowed me to borrow one of his lab's powerful potentiostats and his group for helpful discussions regarding materials science.

I'd like to thank my family: mom, dad, Jessica, Clarinta, and Valencia. Thank you for all the love and support whenever the graduate study 'slump' got the best of me. Just simply hearing your voices over the phone was so emotionally lifting that kept me moving forward towards my dreams. Thank you for all the little troubles as well, to distract me from my bigger problems. Special thanks to my older sister, Jessica, who has taken care of me since February 1999. Being in the U.S. without our parents was not the most emotionally privileged way to grow up, but we had each other, and I always know that you got my back. Thank you for being there all my life and through all the ups and downs, you have shown me courage and set great examples to the naive me. Don't worry, I also got your back... *always*.

My best friends, Whitney, Joan, and Kyle were always there throughout my entire graduate study. To Whitney, who is a best friend of mine since middle school, you were one of my first friends in the U.S., and I cherish all the times we spent and all the travelling we did together. Thank you for your lifetime support through all my problems, and I can only hope that I'm also reciprocating your care. To Joan, who is my spontaneous best friend, thank you for telling me all of your secret crushes since 9th grade and being my best hot-pot buddy anytime I was having a bad/good day. You deserve the best from everyone! To Kyle, who has been the closest friend and colleague to me throughout the latter 3.5 years of graduate school: your Horak style and attitude have always kept me laughing and puzzled. I truly appreciate your affection and consideration, always trying your best to cheer me up whenever I needed strength. As a mentor, I am proud to have trained you to become an expert at synthetic inorganic chemistry. Thank you for being such a good listener and a fast learner, and for being someone I can depend on. Let's keep up the good work in years ahead.

In the Agapie lab, I have had the privilege to work with the most hard-working group of graduate students in the entire campus. Davide Lionetti has always been a good friend that I can rely on and learn from. Honestly, in my first year, I never thought I would end up having fun dinners and cracking jokes with you, the cool, bearded Italian dude who never eats pineapple (no problem, I don't like it too). I am

glad to be acquainted with such a considerate, trustworthy person who always fails to say no to Ernie's on Wednesdays and Golden Deli with Kyle and I. Emily Tsui has always been a friend, a mentor, and an inspiration. I am glad to learn so much from you. With your attitude and knowledge, I have no doubt that one day I can come to your research group meeting and happily ask your future students random questions. Madalyn Radlauer has always provided me with courage and smiles. Maddy's cheerfulness was so contagious and uplifting, it's hard not to smile back (I tried). Maddy's diligence is impeccable, I only wish to achieve such greatness. Thanks for keeping us safe, safety officer Maddy! Paul Kelley was my partner in crime, bioinorganic buddy in the bio-room. No one else in the Agapie lab understood how it felt to only get 3% protein expression yield from a 9-liter *E. coli* culture. Paul's sense of humor has always been so crazy that I am grateful I came to understand his jokes and forget all my troubles. Sibó Lin was the chill guy who never raised his voice at anyone. Thanks for being my passionate kick-boxing buddy and passing on the false belief that if you don't pay for the food, it's calorie-free! Steven Chao, despite our brief 1.5 years overlap, I appreciate your warm welcome on my first day at Caltech by impulsively stating, "So.. you are the Berkeley lady?"

Jacob Kanady, as the other student in the same year with Davide and I, has provided me with Daft Punk music and positivity. Thank you for being open-minded and stubborn at the same time. One day I will challenge you on spicy food eating contest! Everyone loves Guy, or so I say. Thank you for being the eternal icebreaker, and being so patient with everyone. You're doing a marvelous job keeping us safe, too! One day I will visit "Guy's garage" and get a discount. Justin Henthorn a.k.a. the bear (and Kate), thank you for providing the Wii at every party and for all the helpful suggestions in chemistry. I'd like to thank Joshua Buss for generally being really nice and adorable while working hard. Thank you for sharing glovebox 2 with me for a while and keeping it up before the raging tide. To Dave Herbert, thank you for teaching me everything I know about how to solve my own structures. Thank you for all the lessons and the insights that inspire me to work more efficiently. I'd also like to thank Po-Heng for all his humility and willingness to help everyone. You owe me a treat in Taiwan, too!

For Marcus Low and Siti Riduan, there's this strange bond between us that reads, "Southeast Asia." One day I will visit both of you in Singapore so prepare yourselves! Jessica, keep up the good work but don't stay up too late in lab. I wish you all the best in your chemistry! HB, thank you for taking over the cobalt project, I hope one day you'll get the dangler with the asymmetric ligand. To all the post-docs in the Agapie group, Graham de Ruiter, Zhiji Han, Gyeongshin Choi, and Aimee Bryan, work hard and don't let the pressure get to you. Good luck with your future careers!

I'd like to extend my gratitude for those outside the Agapie group. James Blakemore and Charles McCrory were the ones who taught me electrochemistry on heterogeneous material. Wesley Sattler and Aaron Sattler were always willing to give their useful insights into my research projects, offer their help, and extend their kindness. I'd like to thank Mike Grodick, Tom Teets, Dave Leitch, Ian Tonks, Rachel Klett, Taylor Lenton, Jonathan Rittle, and Henry Fong for the friendliness and all the help. To all of our collaborators, Rosalie Tran, Junko Yano, Ruchira Chatterjee, Luo Lu, R. David Britt, Jens Kaiser, Kurtis Carsch, and Bill Goddard, thank you for the hard work and contribution for the great stories.

For all the staff members at Caltech who have made a difference: I'd like to especially thank Larry Henling. Without him, my Chapters 2-4 would have never been finished. Thank you for helping me mount my SURF quality crystals in the middle of the night, for the cookies, and also the calendars! I truly appreciate Larry and Michael K. Takase's efforts in keeping up the small molecule crystallography lab. Agnes has done a tremendous job keeping the graduate students on track. Thank you for caring and all the planning you've done for all of us! Others in the CCE who have also been instrumental for me are Rick Gerhart for always helping me fix my broken glassware (Schlenk line too), Anne Penney for helping me with administrative matters, Steve Gould for keeping track of our orders, Tom Dunn and Jeff Groseth for repairing our electronics, and Joe Drew for always being so helpful. The custodian on our floor, Jose, has always been so kind to all of us, and I enjoy our little daily conversation.

I only hope that I did not forget anyone, but for everyone else, thank you for making my Caltech experience a memorable one. I feel honored to be part of a big Caltech family, surrounded by people who truly care about others.

PREFACE

Parts of this thesis have been adapted from published articles co-written by the author and articles that are currently in preparation.

The following articles were reproduced in part with permission from the American Chemical Society:

“Intramolecular Arene C–H and C–P Functionalization by Nickel(II) and Palladium(II)” Sandy Suseno and Theodor Agapie. *Organometallics*, **2013**, 32, 3161-3164.

“Trinuclear Nickel Complexes with Metal–Arene Interactions Supported by Tris- and Bis(phosphinoaryl)benzene Frameworks” Sandy Suseno, Kyle T. Horak, and Theodor Agapie. *Organometallics*, **2013**, 32, 6883-6886

RESPECTIVE CONTRIBUTIONS

Parts of the work described in this thesis, in particular in Chapter 4-5, are the result of collaborative effort. Specific notes are included for compounds synthesized by others and spectroscopic characterizations performed by our collaborators.

The precursor of the multimetallic tetra-oxido clusters, the $[\text{CaMn}_3\text{O}_4]$ cubane cluster (**10-Ca**) was first synthesized by Dr. Jacob S. Kanady. The other heterometallic Mn tetraoxido and dioxido clusters with redox-*inactive* metals were developed by Dr. Emily Y. Tsui and Dr. Po-Heng Lin. Their compounds serve as additional comparison to the clusters synthesized and studied by the author. In Chapter 4, the O atom transfer studies of the heterometallic cubane clusters and the dioxido clusters were run in collaboration with Dr. Emily Y. Tsui.

In Chapter 4, the X-ray absorption spectroscopy studies were performed by Dr. Rosalie Tran, Dr. Ruchira Chatterjee, and Dr. Junko Yano. Dr. Jens Kaiser assisted in the dispersive difference Fourier transform (anomalous diffraction) studies on the heterometallic cluster. The Mössbauer studies were performed by Jonathan Rittle. The EPR studies were performed by Luo Lu and Prof. R. David Britt.

In Chapter 5, the X-ray absorption spectroscopy studies were performed by Dr. Rosalie Tran and Dr. Junko Yano. The rotating disk voltammetry experiments ran at the Joint Center for Artificial Photosynthesis (JCAP) were performed in collaboration with Dr. Charles C. McCrory.

ABSTRACT

This dissertation is mainly divided into two sub-parts: organometallic and bioinorganic/materials projects. The approach for the projects involves the use of two different multinucleating ligands to synthesize mono- and multinuclear complexes. Chapter 2 describes the synthesis of a multinucleating tris(phosphinoaryl)benzene ligand used to support mono-nickel and palladium complexes. The isolated mononuclear complexes were observed to undergo intramolecular arene C–H to C–P functionalization. The transformation was studied by nuclear magnetic resonance spectroscopy and X-ray crystallography, and represents a rare type of C–H functionalization mechanism, facilitated by the interactions of the group 10 metal with the arene π -system.

Chapter 3 describes the construction of multinickel complexes supported by the same triphosphine ligand from Chapter 2. This chapter shows how the central arene in the ligand's triarylbenzene framework can interact with dinickel and trinickel moieties in various binding modes. X-ray diffraction studies indicated that all compounds display strong metal–arene interactions. A cofacial triangulo nickel(0) complex supported by this ligand scaffold was also isolated and characterized. This chapter demonstrates the use of an arene as versatile ligand design element for small molecular clusters.

Chapter 4 presents the syntheses of a series of discrete mixed transition metal Mn oxido clusters and their characterization. The synthesis of these oxide clusters displaying two types of transition metals were targeted for systematic metal composition-property studies relevant to mixed transition metal oxides employed in electrocatalysis. A series of heterometallic trimanganese tetraoxido cubanes capped with

a redox-active metal $[\text{MMn}_3\text{O}_4]$ ($\text{M} = \text{Fe}, \text{Co}, \text{Ni}, \text{Cu}$) was synthesized starting from a $[\text{CaMn}_3\text{O}_4]$ precursor and structurally characterized by X-ray crystallography and anomalous diffraction to conclusively determine that M is incorporated at a single position in the cluster. The electrochemical properties of these complexes were studied via cyclic voltammetry. The redox chemistry of the series of complexes was investigated by the addition of a reductant and oxidant. X-ray absorption and electron paramagnetic resonance spectroscopies were also employed to evaluate the product of the oxidation/reduction reaction to determine the site of electron transfer given the presence of two types of redox-active metals. Additional studies on oxygen atom transfer reactivities of $[\text{MMn}_3\text{O}_4]$ and $[\text{MMn}_3\text{O}_2]$ series were performed to investigate the effect of the heterometal M in the reaction rates.

Chapter 5 focuses on the use of $[\text{CoMn}_3\text{O}_4]$ and $[\text{NiMn}_3\text{O}_4]$ cubane complexes discussed in Chapter 4 as precursors to heterogeneous oxygen evolution reaction (OER) electrocatalysts. These well-defined complexes were dropcasted on electrodes with/without heat treatment, and the OER activities of the resulting films were evaluated. Multiple spectroscopic techniques were performed on the surface of the electrocatalysts to gain insight into the structure-function relationships based on the heterometallic composition. Depending on film preparation, the Co-Mn-oxide was found to change metal composition during catalysis, while the Ni-Mn oxide maintained the NiMn_3 ratio. These studies represent the use of discrete heterometallic-oxide clusters as precursors for heterogeneous water oxidation catalysts.

Appendix A describes the ongoing effort to synthesize a series of heteromultimetallic $[\text{MMn}_3\text{X}]$ clusters ($\text{X} = \text{O}, \text{S}, \text{F}$). Complexes such as $[\text{ZnMn}_3\text{O}]$, $[\text{CoMn}_3\text{O}]$, $[\text{Mn}_3\text{S}]$, and $[\text{Mn}_4\text{F}]$ have been synthesized and structurally characterized. An

amino-bis-oxime ligand (PRABO) has been installed on the $[\text{ZnMn}_3\text{O}]$ cluster. Upon the addition of O_2 , the desymmetrized $[\text{ZnMn}_3\text{O}]$ cluster only underwent an outer-sphere, one-electron oxidation. Efforts to build and manipulate other heterometallic $[\text{MMn}_3\text{X}]$ clusters are still ongoing, targeting O_2 binding and reduction. Appendix B summarizes the multiple synthetic approaches to build a $[\text{Co}_4\text{O}_4]$ -cubane complex relevant to heterogeneous OER electrocatalysis. Starting with the tricobalt cluster $[\text{LCo}_3(\text{O}_2\text{CR})_3]$ and treatment various strong oxidants that can serve as oxygen atom source in the presence Co^{2+} salt only yielded tricobalt mono-oxo complexes. Appendix C presents the efforts to model the H-cluster framework of $[\text{FeFe}]$ -hydrogenase by incorporating a synthetic diiron complex onto a protein-supported or a synthetic ligand-supported $[\text{Fe}_4\text{S}_4]$ -cluster. The mutant ferredoxin with a $[\text{Fe}_4\text{S}_4]$ -cluster and triscarbene ligand have been characterized by multiple spectroscopic techniques. The reconstruction of an H-cluster mimic has not yet been achieved, due to the difficulty of obtaining crystallographic evidence and the ambiguity of the EPR results.

TABLE OF CONTENTS

Dedication	iii
Acknowledgements	iv
Preface	viii
Respective contributions	ix
Abstract	x
Table of Contents	xiii
Chapter 1	1
General Introduction: Heterometallic effects on electron transfer and reactivity of synthetic multinuclear complexes	
Chapter 2	55
Intramolecular C–H to C–P Functionalization Mediated by Ni(II) and Pd(II)	
Abstract	56
Introduction	57
Results and Discussion	58
Conclusions	67
Experimental Section	68
References	87
Chapter 3	91
Trinuclear Nickel Complexes with Metal–Arene Interactions Supported by Tris(phosphinoaryl)benzene Framework	
Abstract	92
Introduction	93
Results and Discussion	94
Conclusions	102
Experimental Section	102
References	109
Chapter 4	112
Synthesis and Characterization of a Series of Mixed Transition Metal Manganese-Oxido Cubanes and Their Oxygen Atom Transfer Reactivity	
Abstract	113
Introduction	114
Results and Discussion	117
Conclusions	156
Experimental Section	157
References	176

Chapter 5	179
Molecular Mixed–Metal Manganese Oxido Cubanes as Precursors to Heterogeneous Oxygen Evolution Catalysts	
Abstract	180
Introduction	181
Results and Discussion	183
Conclusions	195
Experimental Section	197
References	211
Appendix A	214
Synthesis of Heterometallic [MMn ₃ X] Clusters (X = N, O, F, S) for O ₂ Activation	
Abstract	215
Introduction	216
Results and Discussion	218
Conclusions	232
Experimental Section	233
References	240
Appendix B	242
Synthesis of [Co ₃ O]-Clusters as Preliminary Routes to Build [Co ₄ O ₄] Cubane	
Abstract	243
Introduction	244
Results and Discussion	245
Conclusions	260
Experimental Section	262
References	267
Appendix C	269
Modeling [FeFe] Hydrogenase: Incorporation of Synthetic Di-iron Complex to Bioengineered and Synthetic [4Fe4S]-Clusters	
Abstract	270
Introduction	271
Results and Discussion	275
Conclusions	300
Experimental Section	302
References	308

Appendix D	309
NMR Spectra	
Chapter 2	310
Chapter 3	326
Chapter 4	330
Chapter 5	n/a
Appendix A	334
Appendix B	337
Appendix C	340

CHAPTER 1

General Introduction

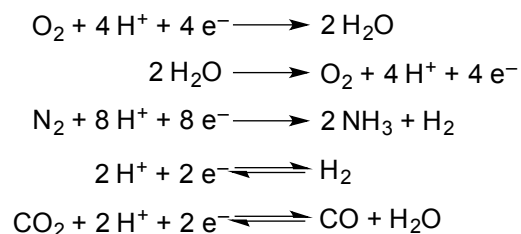
The text for this chapter was reproduced in part from:

Lionetti, D.; Suseno, S.; Agapie, T. *Review manuscript in preparation*

Introduction

The increasing global energy consumption is arguably the one of the most important concerns in the 21st century, especially with growing population and economy. As technology advances to improve our lives, we are facing a number of challenges in energy production and habits of energy consumption. Theoretically speaking, the energy demand can still be met by means of fossil fuel, however, the finite nature of fossil fuel and the increasing production of CO₂ as a greenhouse gas have led us to substantially reconsider the values of renewable resources. While the deleterious effects of the extensive use of fossil fuels over the last two and a half centuries are still being evaluated worldwide, the significance in investing research efforts into the development of alternative, renewable energy resources has finally been realized. This energy conversion issue has fuelled research efforts towards the design and development of efficient solar fuels and fuel cells.

Scheme 1. Several transformations relevant to energy conversion research



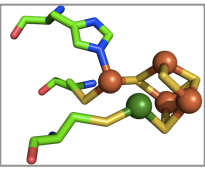
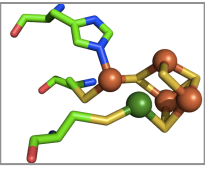
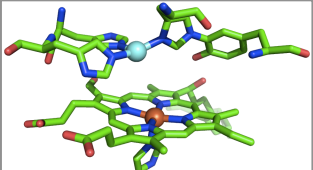
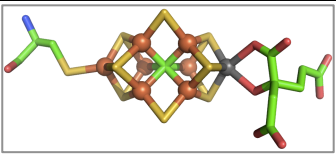
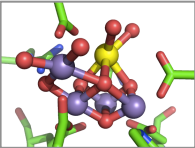
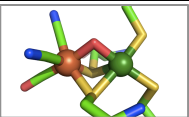
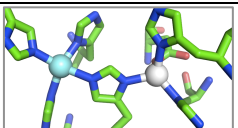
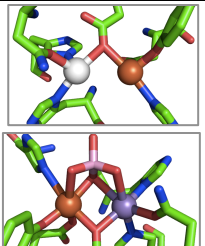
The science behind renewable energy is concerned with a handful of chemical transformations outlined in Scheme 1. These conversions appear simple, involving small diatomic or triatomic molecules; however, these transformations necessitate the activation of inert small molecules, which require multiple electron and proton transfer steps to proceed, rendering them substantially more challenging. Achieving such goals

will require the rational design of a suitable catalyst to perform the desired reactions at useful rates and avoid the formation of reactive intermediate products that may result in unproductive pathways.

Considerable efforts have been made to design catalysts, both homo- and heterogeneous in nature, capable of performing these efficiently, as well as to study the mechanisms by which they occur.¹ Many of these efforts have chosen Nature as a source of inspiration for the design of chemical systems that can effect small molecule transformations, as many organisms have evolved to take advantage of these enzymatic transformations to generate their source of energy. Many of the key insights into the mechanism of these reactions, as well as into the design elements that are crucial to the development of viable catalysts, have originated from the study of the natural systems via discrete model systems.

In Nature, all reactions in Scheme 1 are performed by enzymatic active sites that contain metal cofactors.² Many of these cofactors are multimetallic, heteronuclear active sites. This discovery is of particular significance in light of the numerous heterogeneous materials of multiple different metallic elements capable of carrying out these transformations. The main advantage of utilizing multiple metal centers to effect these conversions is the ability to divide the redox reaction requirements among several redox-active metal centers. However, the evolutionary reasons for *heterometallic* active sites are less clear due to a limited understanding of the effects of the interactions between metal centers in heteronuclear complexes.

Table 1. Enzymes with heterometallic active sites and catalyzed reactions.

Enzyme (abbreviation, <i>PDB</i> ^a <i>code</i>)	Active site ^b	Metals	Transformations	Ref.
Anaerobic Carbon Monoxide Dehydrogenase (CODH, <i>1SU8</i>)		Fe ₄ Ni	$\text{CO}_2 + 2\text{H}^+ + 2\text{e}^- \rightleftharpoons \text{CO} + \text{H}_2\text{O}$	3
Anaerobic Carbon Monoxide Dehydrogenase (CODH, <i>1SU8</i>)		Fe ₄ Ni	$\text{CO}_2 + 2\text{H}^+ + 2\text{e}^- \rightleftharpoons \text{CO} + \text{H}_2\text{O}$	3
Cytochrome <i>c</i> Oxidase (CcO, <i>1V54</i>)		FeCu	$\text{O}_2 + 4\text{H}^+ + 4\text{e}^- \longrightarrow 2\text{H}_2\text{O}$	4
Nitrogenase (<i>3U7Q</i>)		Fe ₇ Mo	$\text{N}_2 + 8\text{H}^+ + 8\text{e}^- \longrightarrow 2\text{NH}_3 + \text{H}_2$	5
Photosystem II (PSII, <i>3ARC</i>)		Mn ₄ Ca	$2\text{H}_2\text{O} \longrightarrow \text{O}_2 + 4\text{H}^+ + 4\text{e}^-$	6
Ni-Fe Hydrogenase (<i>1YRQ</i>)		NiFe	$2\text{H}^+ + 2\text{e}^- \rightleftharpoons \text{H}_2$	7
Superoxide Dismutase (SOD, <i>2SOD</i>)		CuZn	$\text{O}_2^- + 2\text{H}^+ + \text{e}^- \longrightarrow \text{H}_2\text{O}_2$ $\text{O}_2^- \longrightarrow \text{O}_2 + \text{e}^-$	8
Purple Acid Phosphatases (Fe, Zn-PAP, <i>1KBP</i> Fe, Mn-PAP, <i>1XZW</i>)		FeZn, FeMn	$\text{ROPO}_3^{2-} + \text{H}_2\text{O} \longrightarrow \text{ROH} + \text{PO}_3(\text{OH})^{2-}$	9

^aEntry code from the RCSB Protein Data Bank. ^bActive sites rendered from crystallographic data with the PyMol. Green = C; red = O; blue = N; mustard = S; orange = Fe; forest green = Ni; cyan = Cu; grey = Mo; yellow = Ca; violet = Mn; white = Zn; pink = P

The enzymes that have been structurally characterized to contain heterometallic cofactors are listed in Table 1, together with their active site structure and the reaction(s) they catalyze (FeMn-ribonucleotide reductase [Fe, Mn-RNR], which has been proposed to contain a Fe-Mn active site based on reconstitution and activity studies,³ is excluded). Many of these enzymatic transformations are relevant to energy conversion, such as oxygen reduction and hydrogen oxidation for fuel cell development, water oxidation and proton reduction for the water splitting reaction, CO₂ fixation for greenhouse gas capture, and nitrogen fixation to supplement the energy-intensive Haber-Bosch process. The metals included in these active sites are also varied: all first row transition metals from manganese to zinc are represented, together with calcium (an alkaline earth metal) and molybdenum (second row transition metal). This diversity is a result of the different environmental constraints experienced by different organisms, and it showcases the potential for inexpensive, abundant first row transition metals for use in homogeneous catalysis relevant to energy conversion.

On the other hand, heterogeneous mixed metal oxides have gained significant attention over the last decade for their role as electrocatalysts in electrochemical energy conversion processes, such as oxygen evolution reaction (OER)⁴ and oxygen reduction reaction (ORR),^{4c,4e,5} that are central to the development of solar electrolytic water splitting devices^{1f,6} and fuel cells.^{5b} Heterometallic oxides are also relevant for the advancement of electrochemical energy storage in the form of lithium-ion batteries, electrochemical capacitors, and metal-O₂ batteries.^{5b,7} Unfortunately, the wide spread commercialization of these technologies is hampered by their high production costs and low efficiency. Therefore, development and rational design of new materials that can

lower the cost, increase the efficiency, and improve the durability of these devices may result in the viability of global commercialization and usage.

In the materials currently developed and studied by many scientists, the role of the heterometallic components is not yet elucidated. There are some examples of heterometallic Mn oxide birnessites OER electrocatalysts displaying structural resemblance to Nature's oxygen evolving complex (OEC) of photosystem II (Figure 1).^{4f,4g} Analyzing the simpler synthetic small molecule models of Nature's heterometallic enzymes and their electrochemical activities may provide some insight into useful chemical compositions and their synergetic effects that contribute to the mixed metal oxides' high catalytic activity or capacitance. Looking into the difference in oxidation states or valencies of the metal centers in the synthetic system will also be relevant for determining electron transfer properties of the materials for the design of desirable electrochemical behavior of electrocatalysts for fuel cells or metal-O₂ batteries.

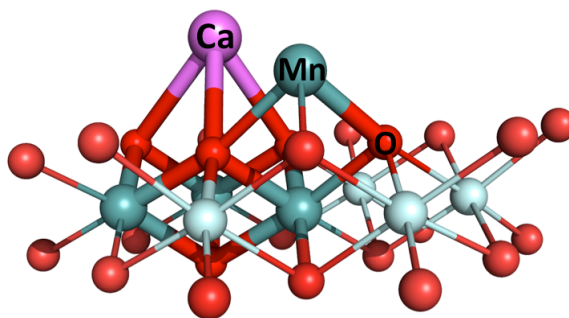


Figure 1. Schematic drawing of one proposed structure of calcium-doped manganese oxide (birnessite) material.^{4f,8}

At this point, it is clear that heteromultimetallic complexes are capable of facilitating desirable reactivity when appropriately and optimally constructed. Interest in better understanding the interactions of multiple different metal centers in a single

complex has led to numerous studies on synthetic heteromultimetallic complexes. The reported synthetic complexes discussed in this chapter will provide an overview of discrete first-row, mixed transition metal complexes that display intriguing reactivity or electron transfer properties, with a focus on specific bridging ligand sets related to those in the enzymes' active sites. The scope of this chapter focuses on redox-active heteromultimetallic complexes that do *not* display metal-metal bonds. Electrochemical studies on these systems, if available, will be examined against the pK_a of the heterometal to determine if there is any apparent Lewis acid effect.. The discussion on the reported systems will be divided by the ligand scaffolds used, highlighting the various ligand designs to construct these small multimetallic clusters.

1.1 Bridging phenolates

Neves and co-workers reported the synthesis of novel isostructural series of bimetallic $[\text{Fe}^{\text{III}}\text{M}^{\text{II}}(\text{BPBPMP})(\mu\text{-OAc})_2]^+$ (**1.1-M**; M = Fe, Mn, Co, Ni, Cu, Zn) as a synthetic biomimetic catalytic system for purple acid phosphatases (Figure 2).⁹ The Fe^{III} center is coordinated by the pyridine and phenolate arms, while the varied M^{2+} center is bound to the other two pyridine moieties on the other side of the ligand. They determined the electrochemical properties of the series by cyclic voltammetry to reveal the redox processes of the complexes. The values for the cathodic $\text{Fe}^{\text{III}}/\text{Fe}^{\text{II}}$ redox couple (vs. Fc/Fc^+) of the complexes are as follows: $\text{Fe}^{\text{III}}\text{Fe}^{\text{II}}$ (-0.89 V), $\text{Fe}^{\text{III}}\text{Mn}^{\text{II}}$ (-0.87 V), $\text{Fe}^{\text{III}}\text{Co}^{\text{II}}$ (-0.97 V), $\text{Fe}^{\text{III}}\text{Ni}^{\text{II}}$ (-0.94 V), $\text{Fe}^{\text{III}}\text{Cu}^{\text{II}}$ (-1 V), and $\text{Fe}^{\text{III}}\text{Zn}^{\text{II}}$ (-0.91 V). As observed, the maximum $\Delta E_{1/2}$ across the series is only ~ 0.13 V, indicative of only a slight difference in potential range between complexes. From the cyclic voltammetry

studies on these bimetallic complexes, one may deduce that the observed similarity between reduction potentials is most likely due to the overall clusters' charge.

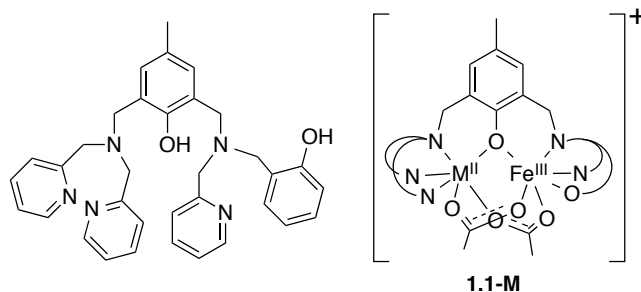


Figure 2. Phenolate ligand (left) and the bimetallic complex $[\text{Fe}^{\text{III}}\text{M}^{\text{II}}(\text{BPBPMP})(\mu\text{-OAc})_2]^+$ (right).

A similar ligand scaffold has also been used by Ulstrup and co-workers where the ligand arm with a phenolate and a pyridine moiety shown in Figure 2 has been modified to a bis-pyridine moiety (Figure 3).¹⁰ A series of mixed-valent iron and mixed-metal complexes of the phenolate hinged dinucleating ligand, $[\text{Fe}^{\text{III}}\text{M}^{\text{II}}(\text{bpbp})(\mu\text{-OAc})_2]^{2+}$ (**1.2-M**, M = Fe, Co, Ni, Cu, Zn), have been prepared and characterized. Via cyclic voltammetry studies, all heterometallic complexes exhibit a single reversible one-electron wave corresponding to the $\text{Fe}^{\text{III}}/\text{Fe}^{\text{II}}$ couple. Similarly to the systems reported by Neves and co-workers above, the low potential $E_{1/2}$ of the $\text{Fe}^{\text{III}}/\text{Fe}^{\text{II}}$ couple depends only insignificantly on the nature of the second metal (−0.33 V for FeFe, −0.35 V for FeCo, −0.39 V for FeNi, −0.31 V for FeCu, and −0.33 V for FeZn). This suggests that the interaction between the two centers is still dominated by the overall charge rather than by the nature of the heterometal.

On a different report, Ulstrup and co-workers analysed the electrochemical properties of a slightly different series of bimetallic complexes using the same

binucleating ligand bpbp^- .¹¹ The only difference is that instead of bis- μ -acetato ligands bridging the two metal centers in **1.2-M**, the Fe center is bound by two terminal fluoride ions and M is coordinated to one or two aquo terminal ligands (**1.3-M** and **1.4-M** in Figure 4). The fluoride ligands are derived from the hydrolysis of tetrafluoroborate.

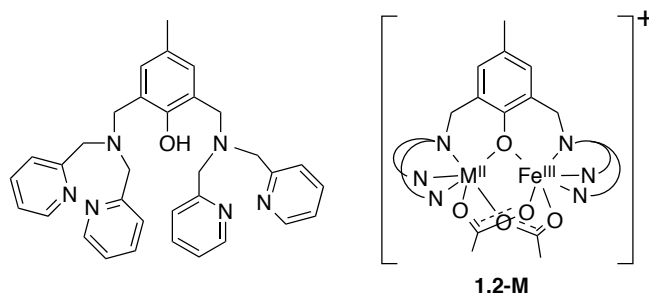


Figure 3. The bpbp^- ligand used (left) to support bimetallic complexes (right).

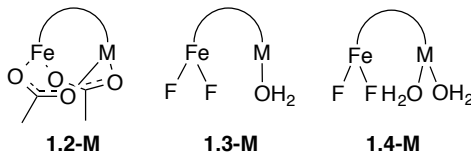


Figure 4. Core structures based on $[\text{Fe}^{\text{III}}(\text{bpbp})\text{M}^{\text{II}}]^{2+}$: bridging bis- μ -acetato ligands (**1.2-M**) and difluoro(aqua) structures (**1.3-M** and **1.4-M**); the phenolate-hinged dinucleating ligand bpbp^- is represented by curved lines.

The electrochemical properties of **1.3-M** and **1.4-M** are compared to the analogous series that contain the bridging acetate groups (**1.2-M**) discussed above. Electrochemical results indicate that the Fe^{III} ions in the bis-fluoride complexes are stabilized by ~ 300 mV more negative compared to the bis- μ -acetate complex **1.2-M**. This result is expected given the higher negative charge around the Fe^{III} when two fluoride ions are coordinated. The similarity of the reduction potential with maximum $\Delta E_{1/2}$ across the series is only ~ 0.07 V, supporting the previous claim that the charges on the complexes are the dominant cause of the resulting redox properties.

1.2 Binucleating bisphenolate amine/imine macrocyclic ligand

A binucleating macrocyclic ligand that contains 6- and 4-coordination sites was prepared by Bosnich and co-workers to support homo- and heterobimetallic complexes **1.5-M₁M₂** (Figure 5).¹² The ligand was designed as binucleating to fully encapsulate one metal (M₁) but still allow the other metal (M₂) to bind to reducible substrates (e.g., dioxygen). The desired reactivity involves the encapsulated metal functioning to transfer electrons to the neighboring metal as well as to provide a defined structural framework for selectivity in catalytic reactions. M₁ would be coordinatively saturated in a hexadentate site, whereas M₂ is either in a square-planar or square pyramidal site to allow for substrate binding.

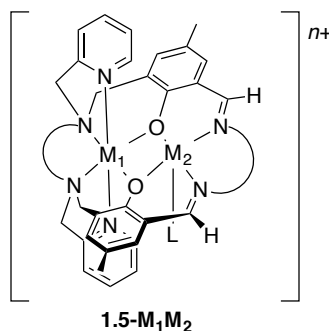


Figure 5. Heterobimetallic cyclim/cypim complexes **1.5-M₁M₂**.

A desired reactivity, for example, would be interaction of O₂ with the open-site metal (M₂) that can lead to either the oxidation of M₂ only and the formation of a superoxide species or the oxidation of both metals to form a peroxide ligand. With appropriate metal and ligand combinations, it may be possible to induce 4-electron reduction of dioxygen to obtain oxo complexes. The synthesized complexes of the type [M₁(cyclim)M₂](PF₆) (**1.5-M₁M₂**; M₁M₂ = ZnZn, Mn^{II}Zn, ZnMn^{II}, Mn^{II}Mn^{II}, Co^{II}Co^{II}) were inert to O₂ in the solid state but displayed variable reactivity in acetonitrile

solution. Exposure of **1.5-MnMn** solution to air yielded the mixed-valence complex $[\text{Mn}^{\text{II}}(\text{cyclim})(\mu\text{-Cl})\text{Mn}^{\text{III}}\text{Cl}](\text{PF}_6)$. The same Mn(II)/Mn(III) complex can be prepared by the addition of one equivalent or excess $[\text{FeCp}]^+$ in the presence of Cl^- ions, which suggests that the oxidation state of the closed site Mn(II) is more difficult after the open site Mn(II) has been oxidized to Mn(III).

Bosnich and co-workers have also synthesized a series of heterobimetallic complexes using a chiral version of the binucleating ligand bearing six- and four-coordinate sites (*S,S*-cypim).¹²⁻¹³ Among the heterobimetallic complexes prepared were (1) complexes derived from Co(III) in the *closed* site and the metals Zn(II), Cu(II), Ni(II), Co(II), Mn(II), and V(III) in the *open* site, (2) complexes with Cu(II) in the open-site and Zn(II), Cu(II), Ni(II), Co(II), and Mn(II) in the *closed* site, and (3) complexes derived from Fe(II) in the closed side and V(III) in the open site. The heterobimetallic complexes were prepared in order to systematically investigate the cooperative physical and electrochemical properties of a given metal in a specific site when the metal in the other site is varied. Such information is important in assessing the feasibility of employing the reducing power of contiguous metals in the oxidative addition of reactants to the open-site metal and the potential for tuning the reactivity of the open-site metal in these complexes by varying the closed-site metal.

In order to assess the cooperative effects of one metal on the redox couple of another, cyclic voltammetry was used to measure the formal potentials ($E_{1/2}$) of the invariant metal. While the Cu(II)/Cu(I) couple for the $\text{Mn}^{\text{II}}\text{Cu}^{\text{II}}$ complex has irreversible character in the CV, the $\text{Co}^{\text{II}}\text{Cu}^{\text{II}}/\text{Co}^{\text{II}}\text{Cu}^{\text{I}}$ couple was found at -0.54 V (vs. Fc/Fc^+), $\text{Ni}^{\text{II}}\text{Cu}^{\text{II}}/\text{Ni}^{\text{II}}\text{Cu}^{\text{I}}$ at -0.72 V, $\text{Cu}^{\text{II}}\text{Cu}^{\text{II}}/\text{Cu}^{\text{II}}\text{Cu}^{\text{I}}$ at -0.72 V, and $\text{ZnCu}^{\text{II}}/\text{ZnCu}^{\text{I}}$ at -0.92

V.^{13a} The complexes exhibit considerable variation at the closed-site metal ion where the $E_{1/2}$ ($\text{Cu}^{\text{II/I}}$) range from -0.54 V to -0.92 V. From this study, Bosnich and co-workers proposed that the origins of the observed variations in the $\text{Cu}(\text{II})/\text{Cu}(\text{I})$ couples of the S,S -cypim complexes may arise from structural differences, from metal-metal communication, or from both. It is not clear that possible structural variations of the ligand from one complex to another away from planarity could lead to such a large range of potentials. It is probable that both structural and electronic interactions effect the observed differences. Looking at the Lewis acidities of the varied M^{2+} of the $\text{M}(\text{II})\text{Cu}(\text{II})$ complexes, the $\text{p}K_{\text{a}}$ window of the $\text{M}(\text{aqua})^{2+}$ ions (~ 0.5 $\text{p}K_{\text{a}}$ unit) is too small to provide useful insights into the redox tunability of the system by the heterometal.

When the invariant metal at the closed-site is $\text{Co}(\text{III})$,^{13e} the cyclic voltammetry studies of the $[\text{Co}^{\text{III}}(S,S\text{-cypim})\text{M}^{\text{II}}\text{Cl}]^{2+}$ (**1.5-CoM₂**) series show $E_{1/2}$ ($\text{Co}^{\text{III/II}}$) (vs. Fc/Fc^+) for $\text{Co}^{\text{III}}\text{Mn}^{\text{II}}/\text{Co}^{\text{II}}\text{Mn}^{\text{II}}$ at -0.32 V, $\text{Co}^{\text{III}}\text{Co}^{\text{II}}/\text{Co}^{\text{II}}\text{Co}^{\text{II}}$ at -0.38 V, $\text{Co}^{\text{III}}\text{Ni}^{\text{II}}/\text{Co}^{\text{II}}\text{Ni}^{\text{II}}$ at -0.37 V, and $\text{Co}^{\text{III}}\text{Zn}/\text{Co}^{\text{II}}\text{Zn}$ at -0.43 V. For the series of $[\text{Co}^{\text{III}}(S,S\text{-cypim})\text{M}^{\text{II}}]^{3+}$ with no chloride ligand on M, the $E_{1/2}$ ($\text{Co}^{\text{III/II}}$) (vs. Fc/Fc^+) for $\text{Co}^{\text{III}}\text{Mn}^{\text{II}}/\text{Co}^{\text{II}}\text{Mn}^{\text{II}}$ is at -0.36 V, $\text{Co}^{\text{III}}\text{Co}^{\text{II}}/\text{Co}^{\text{II}}\text{Co}^{\text{II}}$ at -0.33 V, $\text{Co}^{\text{III}}\text{Ni}^{\text{II}}/\text{Co}^{\text{II}}\text{Ni}^{\text{II}}$ at -0.38 V, $\text{Co}^{\text{III}}\text{Cu}^{\text{II}}/\text{Co}^{\text{II}}\text{Cu}^{\text{II}}$ at -0.27 V, and $\text{Co}^{\text{III}}\text{Zn}/\text{Co}^{\text{II}}\text{Zn}$ at -0.44 V. In these two series, the closed-site $\text{Co}(\text{III})$ center should only have slight structural differences between complexes, therefore the redox potentials corresponding to $\text{Co}^{\text{III/II}}$ couple can be traced primarily to metal-metal interactions within a particular charge type. The cause of the redox variations observed for the $[\text{Co}^{\text{III}}(S,S\text{-cypim})\text{M}^{\text{II}}\text{Cl}]^{2+}$ and the $[\text{Co}^{\text{III}}(S,S\text{-cypim})\text{M}^{\text{II}}]^{3+}$ series is still not clear since the potential differences within each series and

the similarity between the two series cannot be simply explained by the overall charge of the complexes, structural changes, or Lewis acidity effects of the heterometal.

Bosnich *et al.* reported that when one of the metals in a dicobalt (II) complexes was oxidized, the other metal was deactivated to oxidation despite the fact that either site was capable of supporting the higher Co(III) oxidation state.^{13d} They also demonstrated that this mutual deactivation is *not* metal dependent, because they studied the oxidation of an iron(II)-vanadium(III) and cobalt(II)-vanadium(III) systems using an oxo-transfer reagent.^{13f} Reaction of the Fe(II)-V(III) complex with the oxo transfer reagent led to the initial formation of a vanadium(V) oxo species, which was expected to give a Fe^{III}-V^{IV}O complex if the Fe^{II} in the closed site is readily oxidizable. Instead, intramolecular electron transfer does not occur, rather an unknown intermolecular electron transfer process appears to take place to yield the thermodynamically stable Fe^{II}-V^{IV}O complex. This behavior also extends to the analogous Co^{II}-V^{III} complex as well.

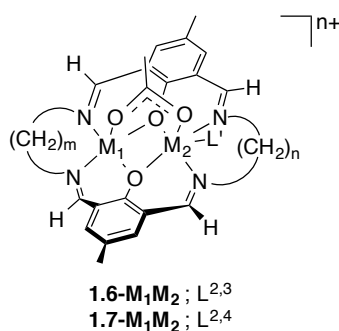


Figure 6. Bimetallic complexes supported by bisphenoxide-based macrocyclic ligand ($\text{L}^{m,n}$)²⁻ ($m = 2$, $n = 3$ or 4 ; $\text{L}' = \text{DMF}$).

Okawa and co-workers have utilized slightly different macrocyclic bisphenoxide bis-imine ligands with varying methylene linker ($(\text{CH}_2)_x$) to support bimetallic

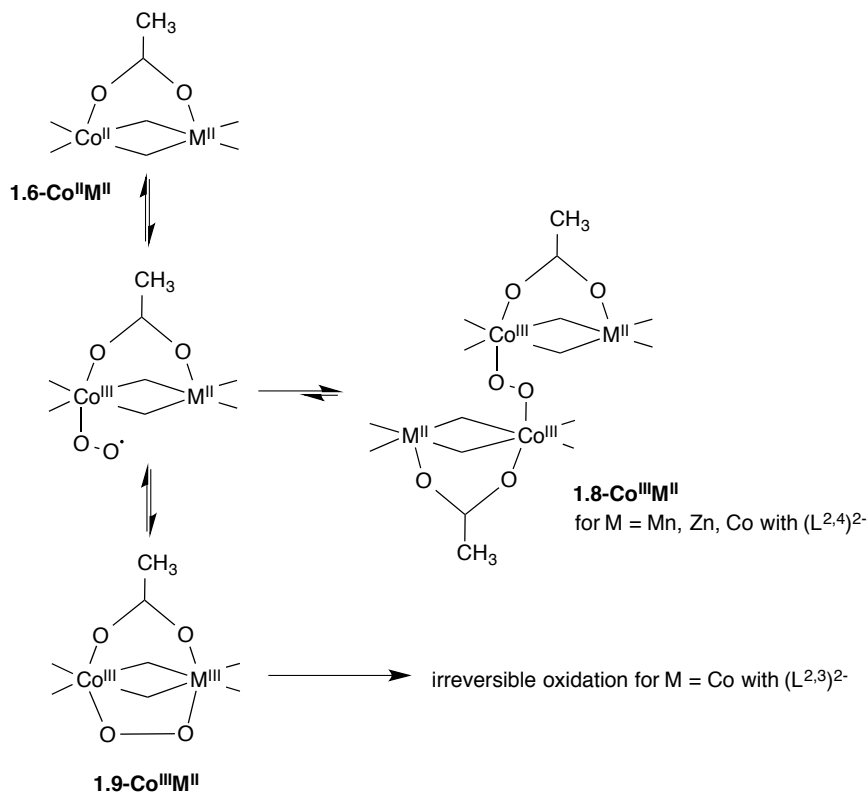
complexes (Figure 6). They have synthesized a few series of homo- and heterobimetallic complexes, **1.6-** and **1.7-M₁M₂**, supported by (L^{2,3})²⁻ and (L^{2,4})²⁻ respectively where M₁ = Co^{II} and M₂ = Mn^{II}, Co^{II}, Zn^{II}.¹⁴ Because Co(salen) complexes are known for their reactivity toward small molecules such as O₂ and NO, the dinuclear Co^{II}M^{II} with Co^{II} in the salen-like (m = 2) metal binding site of the macrocycles are of great interest regarding the neighboring M^{II} effect upon incorporation and activation of O₂ at the Co(salen) center.

Consistent with the other bisphenoxide-supported bimetallic systems by Bosnich and co-workers, the complexes reported by Okawa and co-workers, **1.6-** and **1.7-Co^{II}M₂**, display similar electrochemical properties analysed by cyclic voltammetry. The complexes resemble each other in redox behavior and show an irreversible or quasi-reversible couple at -0.3 V (vs. Ag/Ag⁺) that is assigned to Co^{II/III} oxidation and a reversible couple at ~ -1.3 V attributed to the Co^{II/I} reduction. The varied M does not display redox activity within the potential sweep window of the CV. In this case, the similar redox properties of the homo- and heterobimetallic complexes are evidence of the dominant electronic effect on the reduction potentials of the systems. Other analogous systems with varied M²⁺ and slightly different bisphenoxide ligands have also been reported by Okawa *et al.*, and display similar trends in electrochemical properties in terms of a small range (~100 mV) of redox behavior difference in the CV.¹⁵

A notable feature in the report by Okawa and co-workers is the reactivity of the complexes with dioxygen.¹⁴ Oxygenation of the complexes was studied by means of electronic spectral and NMR techniques. The ESR spectrum for the oxygenated solution of [CoMn(L^{2,3})(AcO)]⁺ (**1.6-Co^{II}Mn^{II}**) was consistent with isolated Mn^{II}

species. The result indicates that the oxygenated species is a peroxo dimer $[\{\text{Co}^{\text{III}}\text{Mn}^{\text{II}}(\text{L}^{2,3})(\text{AcO})\}_2(\text{O}_2^{2-})]^{2+}$ (**1.8-Co^{III}Mn^{II}**) with an *intermolecular* $\text{Co}^{\text{III}}\text{-O-O-Co}^{\text{III}}$ linkage (Scheme 2). A similar ESR spectrum was obtained for the oxygenation of **1.7-Co^{II}Mn^{II}**, indicative of an analogous peroxo species formed. The formation of the peroxo dimer **1.8-Co^{III}Zn^{II}** for the oxygenation of **1.6-** and **1.7-Co^{II}Zn** was detected via NMR studies, consistent with the inability of the redox-inert Zn^{II} to be involved in the two-electron reduction of dioxygen.

Scheme 2. Oxygenation and oxidation behavior of **1.6-** and **1.7-Co^{II}Co^{II}**



The oxygenation of **1.7-Co^{II}Co^{II}** suggests the formation of a similar peroxo dimer species **1.8-Co^{III}Co^{II}** (Scheme 2). On the contrary, complex **1.6-Co^{II}Co^{II}** is highly sensitive to dioxygen. Soon after oxygenation, the formation of **1.9-Co^{III}Co^{II}** was

observed, indicative that the intermediate complex is oxidized by a mechanism differing from the peroxo dimer formation discussed above. Okawa *et al.* proposed the formation of *intramolecular* peroxo species where the peroxo bridges over the CoCo core at the open face based on the possibility of obtaining the species by analyzing the crystal structure of the starting material. Oxygenation of **1.7-Co^{II}Co^{II}** behaves differently compared to the analogous complex, **1.6-Co^{II}Co^{II}**, supported by the (L^{2,3})²⁻ and does not form the intramolecular peroxo complex due to the coordination geometry on the Co^{II} site being too large to accommodate low-spin Co^{III}. This study indicates that the reactivity of the Co^{II}M^{II} complexes toward dioxygen at the Co(salen) center is influenced by the neighboring M^{II} ion and the Co^{II}M^{II} core structure. Other analogous series of complexes reported by Okawa and coworkers show similar oxygenation behaviors to the one discussed above.¹⁶

In contrast, the Ni^{II}Mn^{II} and the Cu^{II}Mn^{II} analogous complexes do not display catalase-like function.^{15a} One noticeable difference between the homodinuclear Mn^{II}Mn^{II} complexes and the heterodinuclear M^{II}Mn^{II} (M = Ni, Cu) is the Mn^{II/III} oxidation potential. The Mn^{II/III} oxidation occurs at ~ +0.3 V (vs. SCE) for Mn^{II}Mn^{II} complexes whereas this occurs at a higher potential in the heterodinuclear (+0.9 – 1.1 V) complexes. Okawa and co-workers proposed that no catalase-like activity was observed for the Ni^{II}Mn^{II} and Cu^{II}Mn^{II} complexes due to the high Mn^{II/III} oxidation potential, which cannot be achieved by H₂O₂.

1.3 Bisphenoxy-carbamoyl bridging ligand

A different bisphenoxy-type ligand was used to support heterobimetallic complexes employing the carbamoyl moiety to support one of the metal centers.

Tuchagues and co-workers reported that dipotassium *N,N'*-1,2-diphenylbis (2-carbamoyl-phenolato) cuprate(II), $K_2[CuL]$, reacts with $M(OAc)_2$ ($M = Co, Ni, Zn$) and 2,2'-bipyridine to yield the heterobimetallic complexes $[CuLM(bpy)_2]$ complexes (**1.10-MCu**, Figure 7).¹⁷ In this work, cyclic voltammetry studies were done to analyze the redox processes occurring on both metal centers. Focusing our attention to the oxidation potential of the invariant metal Cu, the $E_{1/2}$ ($Cu^{II/III}$) vs. Fc/Fc^+ for the **1.10-NiCu** complex is at -0.22 V, **1.10-CoCu** at -0.19 V, and **1.10-ZnCu** at -0.144 V. Given the small range of the potential difference across the series with variation of M, perhaps the electrostatic effects in this case are the primary explanation behind the similar redox properties of the complexes.

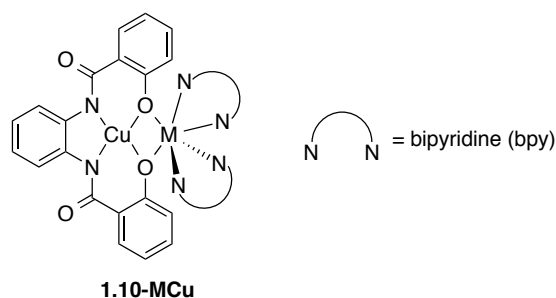


Figure 7. Di- μ -phenoxo-bridged dinuclear $[CuLM(bpy)_2]$ complexes.

1.4 Pyridine bis-(carbamoyl-tetrazole) ligand to generate mono-oxo trinuclear complex

Complexes $[Fe^{III}_2M^{II}OL_3]$ (**1.11-Fe₂M**; $M = Fe, Co, Ni, Cu$) have been synthesized by Cannon and co-workers (Figure 8) in which L^{2-} is a pentadentate ligand designed to coordinate all three metal atoms in the central cluster.¹⁸ This series of complexes is one of the few reported heterotrinuclear mixed transition metal complexes containing one or more oxido bridges. Cannon and co-workers studied the series electrochemically and determined the facile electron transfer involving the couples

$\text{Fe}^{\text{III}}_3/\text{Fe}^{\text{III}}_2\text{Fe}^{\text{II}}$ and $\text{Fe}^{\text{III}}_2\text{Co}^{\text{III}}/\text{Fe}^{\text{III}}_2\text{Co}^{\text{II}}$, and also $\text{Fe}^{\text{III}}_2\text{M}^{\text{II}}/\text{Fe}^{\text{III}}\text{Fe}^{\text{II}}\text{M}^{\text{II}}$, ($\text{M} = \text{Fe}, \text{Co}, \text{Ni}, \text{Cu}$). The retained structures for the oxidized and reduced forms of the complexes with minimal ligand rearrangement accompanying the electron transfers have allowed the systematic study of how the heterometal affects the redox properties of the cluster.

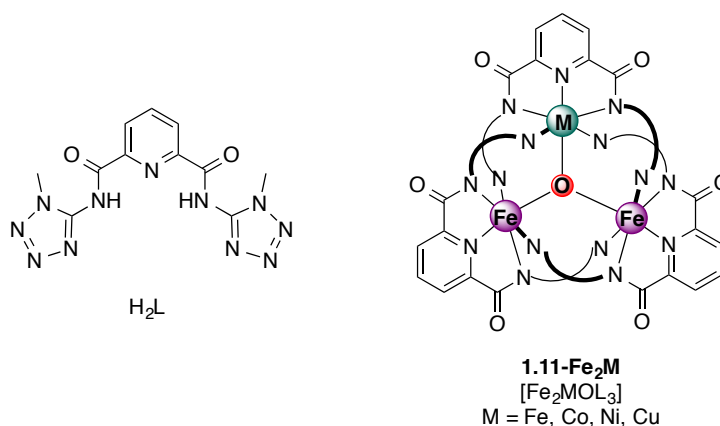


Figure 8. Pentadentate ligand H_2L (left) and the corresponding heterotrinnuclear mono-oxo clusters, **1.11-Fe₂M**, supported by L_3 (right).

The CV of **1.11-Fe₂Fe** (vs. Fc/Fc^+) shows three distinct one-electron processes: a reversible oxidation at +0.085 V, a reversible reduction at -0.64 V, and a quasi-reversible reduction at -1.23 V. **1.11-Fe₂Co** displays three similar processes at -0.035 V, -0.66 V, and -1.31 V respectively. The oxidation of **1.11-Fe₂Co** is assigned as an electron transfer at the cobalt center supported by comparisons of $\text{Co}^{\text{III}/\text{II}}$ and $\text{Fe}^{\text{III}/\text{II}}$ potentials for a series of mononuclear complexes. The **1.11-Fe₂Ni** complex shows reversible and quasi-reversible reduction at -0.73 V and at -1.43 V, respectively, and **1.11-Fe₂Cu** at -0.55 V and -1.22 V, respectively.

All four complexes show reversible reduction that is assigned to the $\text{Fe}^{\text{III}}_2\text{M}^{\text{II}}/\text{Fe}^{\text{III}}\text{Fe}^{\text{II}}\text{M}^{\text{II}}$ couple. Comparing the redox potentials of the **1.11-Fe₂M** series where $\text{M} = \text{Fe}$ at -0.64 V, Co at -0.66 V, Ni at -0.73 V, and Cu at -0.55 V, the $\Delta E_{1/2}$ is

substantial (up to 180 mV difference). Given the similarities between the ionic radii of these four M^{2+} , one would expect the reversible reduction potential across all four complexes to be close to one another if one only considers the electrostatic effect of the clusters on the redox properties. This is not the case, however, with this unique series of μ_3 -oxo-bridged trinuclear clusters, since the first reduction event occurs at significantly shifted potentials across the series. Looking at the pK_a of each M^{2+} aquo species, the Lewis acidity of the heterometal appears to also play a role in modulating the redox potential of the system. A linear correlation can be observed through the plot of $E_{1/2}$ ($Fe^{III}M^{II}/Fe^{III}Fe^{II}M^{II}$ couple) vs. Lewis acidity (as the pK_a of the $M(aqua)^{2+}$ ion) displayed in Figure 9. The linear fit shows a slope of ~ 0.08 V/ pK_a unit. This slope is similar to that of the $[Fe_3MO(OH)]$ series (~ 0.07 V/ pK_a unit)¹⁹ that is discussed later in this chapter. This intriguing similarity can be attributed to the fact that both systems are Fe-based with differences of nuclearities and ligand environments, but this proposed idea has not yet been proven.

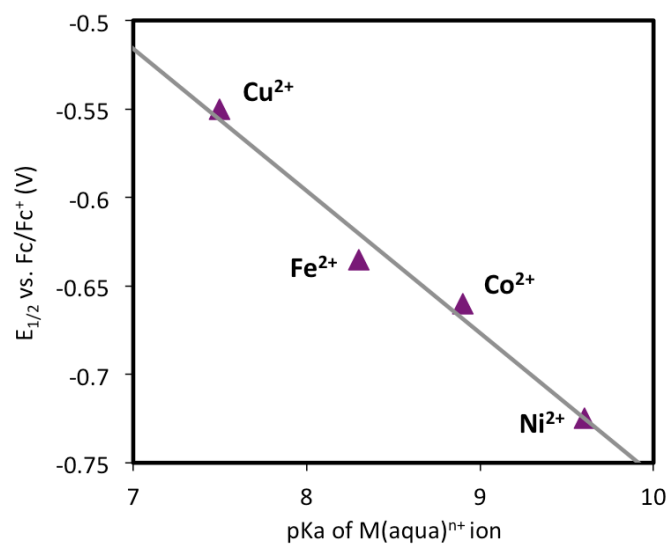


Figure 9. Plot of redox potential vs. Lewis acidity for **1.11- Fe_2M**

1.5 Heterobimetallic porphyrins as mimics of cytochrome c oxidase (CcO)

Cytochrome c oxidase (CcO), which catalyzes four electron reduction of O₂ to water, has been characterized by protein X-ray crystallography to consist of a high-spin heme group (with proximal histidine) and a copper ion ligated by three histidine situated on the distal side. Several research groups have focused in the synthesis and reactivity of CcO small molecule models. Naruta and coworkers reported the reaction of O₂ with tetraphenylporphyrin (TPP)-Fe^{II}-linked tris(2-pyridylmethyl) amine (TPA)-Cu^I dinuclear complexes and the formation of peroxo-bridged dinuclear species Fe-O₂-Cu by X-ray crystallography (**1.12-FeCu**, Figure 10a).²⁰ The only crystallographically characterized Fe-O₂-Cu moiety has a $\mu\text{-}\eta^2\text{:}\eta^1$ coordination mode where both oxygen atoms of the peroxo ligand bind to Fe while only one oxygen binds to Cu.

Karlin and co-workers, on the other hand, have studied synthetic models of CcO using Fe or Co heme with Cu or Co ion on the distal non-heme coordination environment (**1.13-M_AM_B**, Figure 10b).²¹ Reaction of **1.13-Fe^{II}Cu^I** with O₂ at low temperature yield the spectroscopically characterized first superoxo-Fe^{III} complex with subsequent formation of the peroxo-bridged [Fe^{III}-(O₂²⁻)-Cu^{II}]⁺ (either $\mu\text{-}\eta^2\text{:}\eta^1$ or $\mu\text{-}\eta^2\text{:}\eta^2$ peroxo depending on the tetradentate or tridentate ligand supporting the Cu^{II}, respectively).^{21f} Allowing the reaction with O₂ to warm to room temperature results in the formation of a μ -oxo bimetallic [Fe^{III}-(O²⁻)-Cu^{II}]⁺ complex that was crystallographically characterized.^{21a,21b,21d} Karlin *et al.* compared in their studies the reactions of porphyrinate-Fe^{II} with O₂ and **1.13-Fe^{II}Cu^I** with O₂ by looking at the rate constants and activation parameters for the formation of (porphyrinate)-Fe^{III}(O₂)

(superoxo-Fe^{III}) complex.^{21d} Essentially the result of the studies shows that the (ligand)-Cu^I complex has no effect on the formation of the superoxo-Fe^{III} complex.

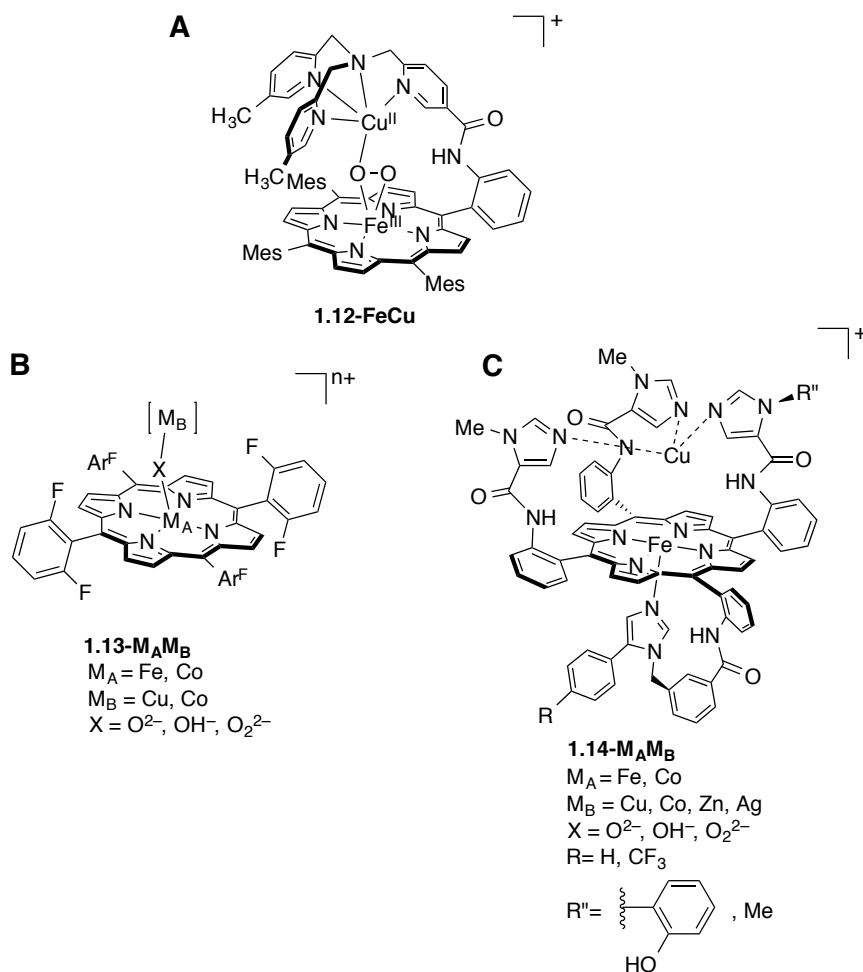


Figure 10. Synthetic models of cytochrome *c* oxidase.

On the other hand, varying M_A from Fe to Co and M_B from Cu to Co shows different reactivity towards O₂.^{21e} Unexpectedly, the reaction of **1.13-Fe^{II}Co^{II}** with O₂ does not lead to a stable μ-peroxo [Fe^{III}-(O₂²⁻)-Co^{III}] species that could be spectroscopically characterized, whereby if formed, the product decomposed rapidly into Fe^{III}-OH complex. Looking at the O₂ chemistry of **1.13-Co^{II}Co^{II}**, a dicobalt μ-peroxo complex [Co^{III}-(O₂²⁻)-Co^{III}]²⁺ forms at low temperature reversibly upon

oxygenation/deoxygenation. The (porphyrinate)-Co^{II} complex by itself is unreactive towards O₂ in the absence of a base. The (ligand)-Co^{II} reacts with O₂ first to form the metastable [Co^{III}-(O₂⁻)]²⁺, then further reacts with the (porphyrinate)-Co^{II} to make the μ -peroxo dicobalt complex.

Functional models related to CcO that can catalyze the 4-electron reduction of O₂ to H₂O have been achieved by Collman and co-workers (**1.14-M_AM_B**, Figure 10c).²² The main difference between Collman's model from Karlin's and Naruta's is the presence of an axial imidazole moiety covalently attached to the proximal face of the porphyrin. **1.14-Co^{II}Cu^I** strongly binds O₂ in 1:1 stoichiometry as bridging peroxide (evidenced by ¹⁸O₂ IR and mass spectrometry) that upon quantitative reduction with four equivalents of cobaltocene (CoCp₂) cleanly regenerates the deoxygenated starting complex.^{22a} The strong binding of O₂ to **1.14-Co^{II}Cu^I** was demonstrated by the lack of displacement of bound O₂ under continuous purge with pure argon, in contrast to the Cu-free compound that displays reversible O₂ binding. This difference shows that Cu plays a crucial role in O₂ binding. A separate experiment involving the use of a Co-Cu complex lacking the appended imidazole ligand only exhibited 2e⁻ reduction of O₂ to H₂O₂.

A series of porphyrinate-Co^{II} models of CcO have also been synthesized with redox-active, oxyphilic Cu^I or redox-stable, non-oxyphilic metals (Ag, Zn) coordinated in the distal superstructure (the tris-imidazole pickets).²³ Unexpectedly, Co superoxide was found to be the end product for all these porphyrin complexes. These model compounds present examples where two metals that readily react with O₂, placed at a favorable intermetallic distance, result in a metal-superoxide product rather than a

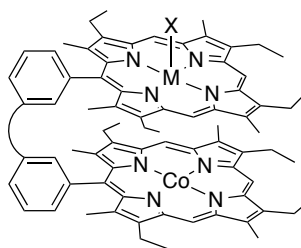
metal-metal μ -peroxo or μ -oxo/hydroxo like the ones reported by Karlin and co-workers discussed earlier. For **1.14-Co^{II}Cu^I** and **1.14-Co^{II}Zn^{II}**, H-bonding of the O₂ unit to the picket-amide-NH is indicated by H/D EPR experiments. Negligible reversibility of O₂ binding is observed for all bimetallic porphyrins compared to the Co-only porphyrin that show reversible dioxygen binding. The authors proposed that a tight distal cavity, H-bonding, and electrostatic effects strongly influence the dioxygen affinity and the stabilization of bound superoxide.

Collman and co-workers also reported **1.14-Fe^{II}Cu^I** as a functional analogue of CcO.^{22b-d} Based on this system, they propose that under rapid electron flux, Cu bound to the distal imidazoles does not affect the kinetics of the catalysts by comparing the $E_{1/2}$ at ~100 mV vs. NHE for both **1.14-Fe^{II}Cu^I** and Cu-free catalysts or the stability, which is consistent with the hypothesis that Cu in CcO only acts as electron storage. However, from their electrocatalytic reactivity studies and comparing **1.14-Fe^{II}Cu^I** catalyst to the Cu-free catalyst, Cu suppresses the superoxide releasing autoxidation once O₂ binds. Cu also accelerates O₂ binding and minimizes the O–O bond homolysis in H₂O₂ reduction. A more recent report by Collman and co-workers on **1.14-Fe^{II}M** system (M = Cu, Zn) shows that the presence of distal metal has an effect on the redox potential of the heme.²⁴ The potential of the heme shifts from +87 mV for a Fe-only species to +123 mV with distal Cu^I and +96 V with distal Zn. The rates of O₂ binding are markedly affected by the presence of a distal metal, but are surprisingly unaffected when Cu is replaced by Zn. O₂ binding rates are also independent of the redox potential of the iron porphyrins, but dependent on the distal porphyrin structure.

1.6 Pacman assemblies (bisporphyrins and corrole/porphyrin ligands)

In the scope of this introduction chapter, we will focus on heterometallic Pacman assemblies. A review on the homodinuclear original Pacman complexes and their reactivities is covered elsewhere.²⁵

Co(II)–M– bisporphyrins



1.15-CoM

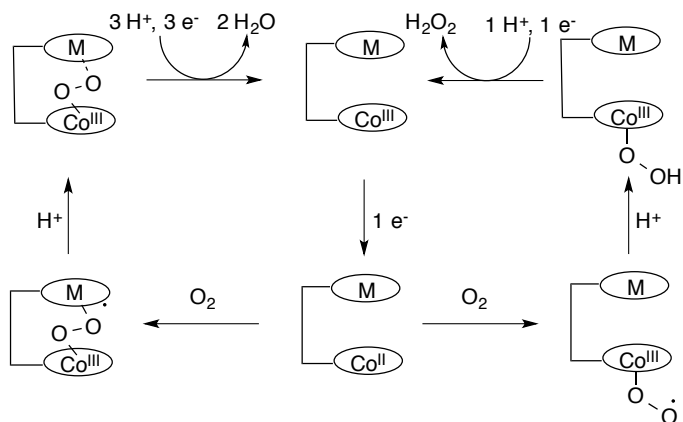
M-X = TiO, Ga(OAc), Ga(OH),
InCl, Lu(acac), Sc(OH), Al(OR)

Figure 11. Heterobimetallic cofacial diporphyrin (DP)CoMX complexes.

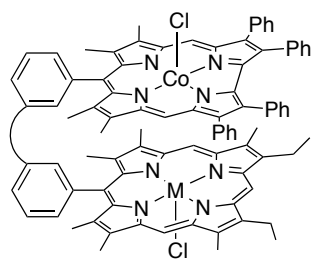
Guilard and co-workers reported the first example of a four-electron reduction of dioxygen, under acidic conditions, mediated by heterometallic complexes with one Co^{II} center for dioxygen binding and another metal with a strong Lewis acid character using a bisporphyrin Pacman ligand (**1.15-CoM**, Figure 11).²⁶ The catalytic activity of each heterobimetallic complex is compared to that of the known four-electron catalyst, bisporphyrin- Co_2 (**1.15-CoCo**), that reduces O_2 to H_2O .²⁷ The reactivity was studied using adsorption of the complexes onto a highly oriented edge plane graphite rotating electrode (EPGE) and analysing the reduction wave of dioxygen in acidic aqueous media. The reduction current for the known **1.15-CoCo** catalyst begins to increase at about +0.8 V vs. NHE and plateau around +0.5–0.6 V. Looking at the CV of the complex, the reduction of O_2 is strictly related to the redox behavior of the catalyst that

matches the redox event assigned to the $\text{Co}_2^{\text{III/II}}$ couple. It was proposed that dioxygen binds to **1.15-Co^{III}Co^{II}** through Co^{II} and that a Lewis acidic center (Co^{III}) is necessary. Compared to **1.15-CoCo**, the mono-cobalt–monoporphyrin precursor is a two-electron catalyst. A few of the heterobimetallic Pacman complexes, such as **1.15-CoFe**, **1.15-CoMn**, **1.15-CoIn**, **1.15-CoTi**, **1.15-CoAl**, and **1.15-CoGa**, were found to reduce dioxygen at potentials close to the Co–monoporphyrin at +0.55 V, corresponding to a two-electron mechanism. On the other hand, **1.15-CoLu** and **1.15-CoSc** display dioxygen reduction at +0.7 V (100 mV more negative compared to **1.15-CoCo** and 300 mV more positive than the Co–monoporphyrin).

While **1.15-CoCo** selectively reduces O_2 by 4 electrons down to H_2O , **1.15-CoLu** and **1.15-CoSc** display some production of H_2O_2 in addition to water that was detected at the ring electrode upon dioxygen reduction. The apparent number of electrons transferred per dioxygen molecule for **1.15-CoLu** and **1.15-CoSc** is 3.7 electrons. The authors proposed that there might be two possible pathways for the catalytic reduction of dioxygen presented in Scheme 3. From this study, bimetallic complexes are required for four-electron reduction of dioxygen, and the metal–metal distance must be suitable to allow for a cooperative effect of the two centers. The choice of the metal turns out to be a determining factor as effective catalysis were obtained when the heterometal is Co^{III} , Lu^{III} , or Sc^{III} . It is still unclear how the Lewis acidities of the heterometals M play a role in the observed activity. For example, Co^{3+} and Mn^{3+} both have similar Lewis acidities (measured as pK_a of $(\text{M aqua})^{\text{n}+}$ ion) and so do Sc^{3+} and Al^{3+} . However, when $\text{M} = \text{Co}^{3+}$, Sc^{3+} , 4-electron reduction of O_2 was observed, while only 2-electron process occurred with $\text{M} = \text{Mn}^{3+}$, Al^{3+} .

Scheme 3. Proposed pathways of dioxygen reduction by Pacman complex (DP)CoMX

Co(IV) corroles – M (porphyrin)

**1.16-CoM(L)**

M = Mn, Fe, Co

L = (

L = B (biphenylene),
A (anthracene), X (xanthene),
O (dibenzofuran)

Figure 12. Homo- and heterobimetallic complexes of bridged porphyrin–Co^{IV} corrole dyads.

Heterobimetallic complexes of cobalt(IV) porphyrin-corrrole dyads **1.16-CoM(L)** (M = Mn, Fe, Co) have been synthesized by Kadish and co-workers (Figure 12).²⁸ The bridge L between the porphyrin and corrole moiety is biphenylene (B), anthracene (A), 9,9-dimethylxanthene (X), or dibenzofuran (O). Studying the cyclic voltammetry of the series of complexes, the anodic oxidation peak potential assigned for the Co^{IV}Cl/Co^{III}

ranges between +0.20 and +0.07 V and varies with the type of metal ion and type of spacer in the complexes with the latter displaying a more dominant effect (Table 2).

Table 2. Half-wave potentials of $\text{Co}^{\text{IV}}\text{Cl}/\text{Co}^{\text{III}}$ for **1.16-CoM(L)**

Entry	Compound	$\text{Co}^{\text{IV}}\text{Cl}/\text{Co}^{\text{III}}$ potential (V vs. SCE)
1	1.16-CoFe(O)	+0.15
2	1.16-CoFe(A)	+0.14
3	1.16-CoFe(B)	+0.07
4	1.16-CoMn(O)	+0.18
5	1.16-CoMn(A)	+0.22
6	1.16-CoMn(B)	+0.10

The reactivity of these series of complexes as catalysts for the electroreduction of O_2 were studied and compared to the dicobalt porphyrin-corrole analog **1.16-CoCo(L)** and to the monometallic corrole Co or porphyrin Co complex.²⁹ In the case of **1.16-CoM(L)**, the $E_{1/2}$ values for the electrocatalytic reduction of O_2 are close to the $E_{1/2}$ values for the $\text{Co}(\text{IV})/\text{Co}(\text{III})$ process of monocorrole-Co complex in the absence of O_2 . The average $E_{1/2}$ value for the electroreduction of O_2 by **1.16-CoCo(L)** is +0.45 V (vs. NHE) while the other heterobimetallic complexes show an average $E_{1/2}$ of +0.34 V.³⁰ The latter value is close to the $E_{1/2}$ for the electroreduction of O_2 using the monocorrole-Co complex (+0.38 V).³¹ **1.16-CoCo(L)** performs electroreduction of O_2 at much more positive potentials that are close to the $E_{1/2}$ of +0.43 V for the activity of the analogous cobalt monoporphyrin. Kadish *et al.* proposed that the results provide strong evidence that the first step in the electrocatalysis with **1.16-CoCo(L)** is initiated by a reduction of the porphyrin and not the corrole unit of the dyad, since the $\text{Co}^{\text{IV}}/\text{Co}^{\text{III}}$ corrole redox process occurs at significantly more negative half-wave potentials ($E_{1/2} =$

+0.38 V). The large difference in O₂ reduction potentials ($\Delta E_{1/2} \sim 110$ mV) observed between **1.16-CoCo(L)**, **1.16-CoM(L)**, and the corrole-cobalt indicates that the cobalt(II) porphyrin unit of **1.16-CoCo(L)** catalyzes the electroreduction of O₂, whereas the cobalt corrole unit remains catalytically inactive towards O₂. Another difference in reactivity observed through rotating disk voltammetry is the O₂ reduction products being full 4-electron reduction to H₂O or 2-electron reduction to H₂O₂. For the homometallic **1.16-CoCo(L)**, the average number of electron transferred to reduce O₂ ranges from 3.5 to 3.7 electrons while for the monometallic Co-corrole and **1.16-CoM(L)** are on average 2.7 electrons. The fact that all of the experimentally determined electron transferred are larger than 2.0 for the **1.16-Co** and **1.16-CoM(L)** complexes requires that a portion of the O₂ be reduced by 4 electrons to H₂O, since Co(III) corroles are generally weak catalysts for the reduction of H₂O₂. The introduction of a second Co in the **1.16-CoCo(L)** results in significantly higher selectivity toward the four-electron reduction of O₂ than the **1.16-CoM(L)** systems.

1.7 Terpyridine-porphyrin Pacman

Nocera and co-workers have reported the preparation of a hetero-Pacman scaffold that was crystallographically isolated as a bis(terpyridine)-iron unit bridged by a xanthene backbone to two zinc porphyrin units (**1.17-Zn₂Fe**, Figure 12).³² The trinuclear compound was studied by cyclic voltammetry and compared to their mononuclear counterparts with the redox potentials ($E_{1/2}$) displayed in Table 3.

As expected, the redox events of Zn(TMP) and the mono Zn(Pacman) complex are very similar with one reduction wave around -2.0 V and two oxidation waves at ~ +0.3 and +0.7 V, assigned as porphyrin-based redox. On the other hand, **1.17-Zn₂Fe**

complex displays the initial porphyrin-based oxidation event at +0.47 V, considerably shifted compared to the initial oxidation event for Zn(TMP) and the mono Zn(Pacman) complexes at $\sim +0.3$ V. The second oxidation event at +0.80 V is irreversible and consists of an overlap of the second porphyrin oxidation and the $\text{Fe}^{\text{II/III}}$ couple. The three reduction events were tentatively assigned to the two one-electron terpyridine-based reductions (at -1.49 and -1.78 V) and a porphyrin-centered reduction at -2.05 V; these three reduction potentials are in good agreement with those found for the mononuclear counterparts (Table 3). The redox properties are a result of the summation of the individual subunits of the hetero-Pacman assembly. However, for **1.17-Zn₂Fe**, an interaction between the terpyridine and porphyrin subunits in the double-oxidized excited state was demonstrated.

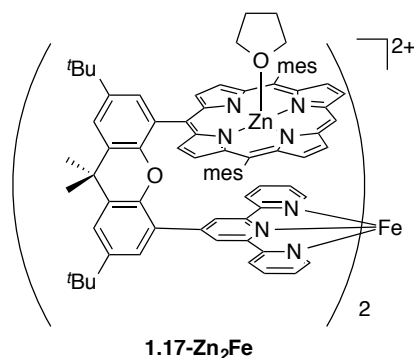


Figure 12. Trinuclear Pacman with two Zn-porphyrin and bis(terpyridine)-Fe moieties.

Table 3. Electrochemical properties of Pacman complexes compared to Zn(TMP) and $[\text{Fe}(\text{terpy})_2]^{2+}$

Entry	Compound	$E_{1/2}$ vs. Fc/Fc^+ (V)				
1	Zn(TMP)	-2.04			+0.33	+0.70
2	Mono Zn(Pacman)	-2.02			+0.30	+0.68
3	1.17-Zn₂Fe	-2.05	-1.78	-1.49	+0.47	+0.80
4	$[\text{Fe}(\text{terpy})_2]^{2+}$		-1.66	-1.48		+0.89

1.8 Multinucleating 1,4,7-tris(4-*tert*-butyl-2-mercaptobenzyl)-1,4,7-triazacyclo nonane ligand

Wieghardt and co-worker reported the synthesis of $[\text{LFeMFeL}]^{n+}$ ($\text{M} = \text{Cr}, \text{Co}, \text{Fe}$) series of complexes (**1.18-M**, Figure 13) supported by the trianionic ligand 1,4,7-tris(4-*tert*-butyl-2-mercaptobenzyl)-1,4,7-triazacyclo nonane.³³ All compounds contain linear trinuclear cations with an $\text{N}_3\text{Fe}(\mu\text{-SR})_3\text{M}(\mu\text{-SR})_3\text{FeN}_3$ core structure. The electron transfer property of the series is represented by the cyclic voltammetry study done on the complexes.

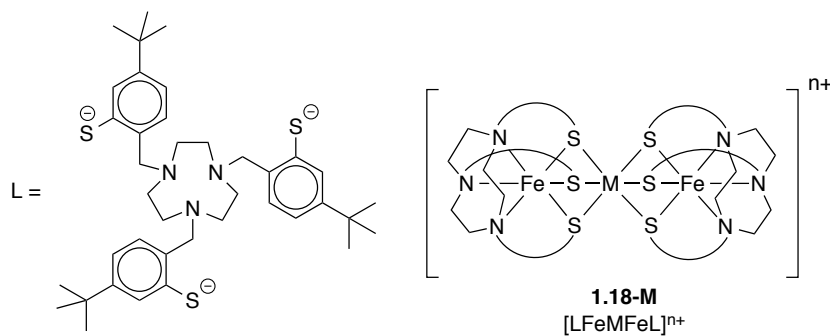


Figure 13. Trianionic ligand L (left) and schematic structure of **1.18-M** (right).

The CVs of all trinuclear complexes display (within the potential range +1.5 to –1.3 V vs. Fc/Fc^+) up to three reversible one-electron transfer waves. These processes correspond to the couples $[\text{LFeMFeL}]^{(n+1)/n+}$, i.e., 4+/3+, 3+/2+, and 2+/1+. The redox event that is reversible across all three complexes ($\text{M} = \text{Cr}, \text{Co}, \text{Fe}$) is the $[\text{LFeMFeL}]^{3+/2+}$ couple. The reduction potentials ($E_{1/2}$) of the $[\text{LFeMFeL}]^{3+/2+}$ couple for the series are –0.23 V for Cr, –0.23 V for Co, and –0.14 V for Fe. The dicationic and tricationic species of $[\text{LFeMFeL}]^{3+/2+}$ of all three complexes are reported to be stable in solution and chemically accessible. Looking at the XAS data of $[\text{LFeCrFeL}]^{1+/2+/3+}$, the Fe K-edge measurements shift significantly over the different oxidation states of cluster while the Cr K-edge shows no change in the local oxidation

state.³³ Therefore, irrespective of the overall oxidation level in the $[\text{LFeCrFeL}]^{n+}$ series, the Cr oxidation state is invariably 3+. The same observation goes for the $[\text{LFeCoFeL}]^{n+}$ series, where it was concluded that the oxidation state of the Co remains 3+. For the $[\text{LFeFeFeL}]^{3+/2+}$ series, Mössbauer and UV-Vis spectroscopies data suggest that upon one electron reduction, the excess electron is delocalized over all three Fe centers.

For the comparison purpose of this chapter, we will assume that the reduction is localized and occurs on one of the terminal Fe centers to yield the $[\text{LFe}^{\text{III}}\text{Fe}^{\text{III}}\text{Fe}^{\text{II}}\text{L}]^{3+}/[\text{LFe}^{\text{III}}\text{Fe}^{\text{III}}\text{Fe}^{\text{II}}\text{L}]^{2+}$ couple or on the central Fe metal to yield the $[\text{LFe}^{\text{III}}\text{Fe}^{\text{III}}\text{Fe}^{\text{III}}\text{L}]^{3+}/[\text{LFe}^{\text{III}}\text{Fe}^{\text{II}}\text{Fe}^{\text{III}}\text{L}]^{2+}$ couple. In this case of mixed-transition metal series bridged by thiophenolate ligands, the redox event occurs on the terminal Fe for $M = \text{Cr}, \text{Co}$. Based on the CV discussed above, the observed reduction potential value seems unaffected by the Lewis acidity of the M^{3+} heteroatom and only influenced by the electrostatic interactions between the metal centers. Meanwhile, the central Fe oxidation state is obscured due to the delocalization of the excess electron, therefore convoluting the more complete analysis of M effect on the overall cluster redox properties.

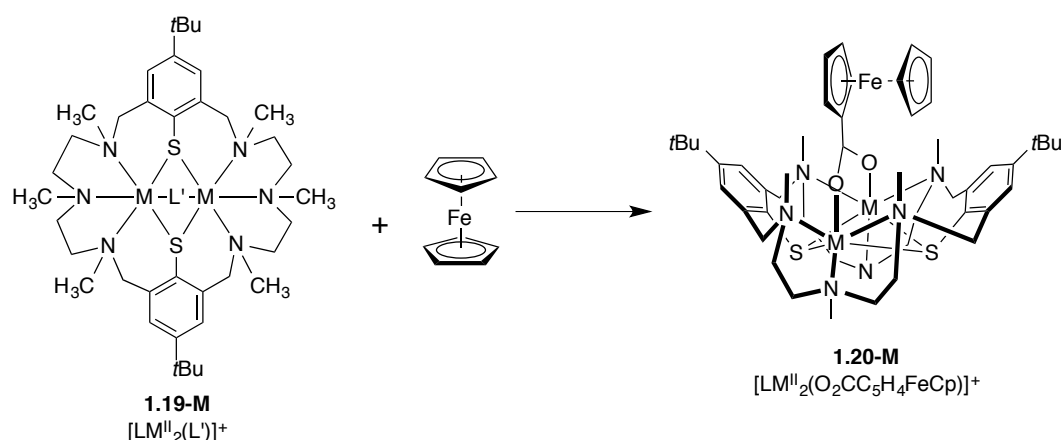
1.9 Macrocyclic hexaazadithiophenolate ligand

A series of novel trinuclear complexes composed of dinuclear LM_2 units (**1.19-M**; $M = \text{Co}, \text{Ni}, \text{Zn}$; $L = 24\text{-membered macrocyclic hexaazadithiophenolate ligand}$) have been reported by Kersting and co-workers and prepared by substitution reactions from labile $[\text{LM}^{\text{II}}\text{L}']^+$ precursors ($L' = \text{Cl}, \text{OAc}$) and ferrocenecarboxylate anion in methanol (Scheme 4).³⁴

The presence of a redox-active ferrocene unit in close proximity to the $[\text{LM}_2]^{2+}$ group suggests that electron transfer events may influence one another owing to the

short distance ($\sim 5.6 \text{ \AA}$) and the bridging carboxylate between the redox centers. Electrochemical studies reveal significant anodic potential shifts for the oxidation potential of the ferrocenyl moieties upon complexation and the magnitude of the potential shift appears to correlate with the charge of the LM_2 subunits. The CV of the **1.20-Zn** complex shows one reversible redox event at $+0.54 \text{ V vs. SCE}$ that is assigned to the oxidation of the ferrocene moiety. The complexation of $[\text{CpFe}(\text{C}_5\text{H}_4\text{COO})]^-$ causes an anodic potential shift of 90 mV in the reversible redox wave of the ferrocene moiety. It is assumed that this potential shift results from the electrostatic repulsion (Coulombic) effect between the two Zn^{2+} ions bonded by the macrocycle and the positively charged ferrocenium moiety. Therefore, the complexation of $[\text{CpFe}(\text{C}_5\text{H}_4\text{COO})]^-$ by the positively charged $[\text{LZn}_2]^{2+}$ unit makes the ferrocenyl group more difficult to oxidize. This is qualitatively explained in terms of destabilizing electrostatic interactions between the M^{2+} ions of the LM_2 unit and the proximate ferrocenium fragment.

Scheme 4. Preparation of $[\text{LM}^{\text{II}}_2(\text{O}_2\text{CC}_5\text{H}_4\text{FeCp})]^+$; $\text{M} = \text{Co, Ni, Zn, L}' = \text{Cl, OAc}$



In the presence of redox active $[\text{LCo}^{\text{II}}_2]^{2+}$ unit in **1.20-Co**, the first two reversible oxidation events occur on the Co centers sequentially from $\text{Co}^{\text{II}}\text{Co}^{\text{II}} \rightarrow$

$\text{Co}^{\text{II}}\text{Co}^{\text{III}}$ followed by from $\text{Co}^{\text{II}}\text{Co}^{\text{III}} \rightarrow \text{Co}^{\text{III}}\text{Co}^{\text{III}}$ as indicated by the absence of characteristic absorption maxima at 388 and 467 nm of the ferrocenium ion. The oxidation of the ferrocenyl unit in **1.20-Co** at +0.81 V vs. SCE shows significantly larger potential shift than in **1.20-Zn** ($\Delta E = +0.27$ V). This larger potential shift can still be attributed to the higher positive charge of the $[\text{LCo}^{\text{III}}_2]^{5+}$ fragment to which the ferrocenyl unit is attached.

The third complex reported by Kersting and co-workers was **1.20-Ni**. The CV of **1.20-Ni** reveals two electrochemically reversible redox waves, which are tentatively assigned to a metal-centered $\text{Ni}^{\text{II}}\text{Ni}^{\text{II}} \rightarrow \text{Ni}^{\text{III}}\text{Ni}^{\text{II}}$ oxidation ($E = +0.55$ V vs. SCE) followed by the oxidation of the ferrocenyl group at +0.74 V vs. SCE. The observed anodic shift ($\Delta E = 0.20$ V) again supports the finding that the electron transfer events of the ferrocenyl moiety and the binuclear subunit influence one another through electrostatic effect. This is explained by the fact that the oxidation potential shift of the ferrocenyl unit is not as pronounced compared to that of the **1.20-Co** system. Since Co and Ni atomic radii are not too different from one another, perhaps there is additional Lewis acidity effect from the metal ion M^{n+} in addition to the electrostatic effect on the redox properties observed on the ferrocenyl unit. Unfortunately this claim cannot be proven without the reversible second oxidation of $\text{Ni}^{\text{III}}\text{Ni}^{\text{II}} \rightarrow \text{Ni}^{\text{III}}_2$ in the **1.20-Ni** system.

1.10 N,N'-dimethyl-3,7-diazanonane-1,9-dithiolato supporting [NiFe] hydrogenase model

Synthetic analogues of heterobimetallic [NiFe]-hydrogenase have been reported that are either homobimetallic or heterobimetallic complexes.³⁵ In this section, we will discuss the three notable heterobimetallic, functional structural models of the enzyme.

Reported first by Ogo and co-workers is the [NiRu] aqua complex **1.21** (Figure 14a) capable of cleaving H_2 heterolytically to generate H^+ in aqueous solution.³⁶ In this complex, the H_2O ligand is proposed to accommodate the water solubility of the complex as well as act as a base to release H_3O^+ .

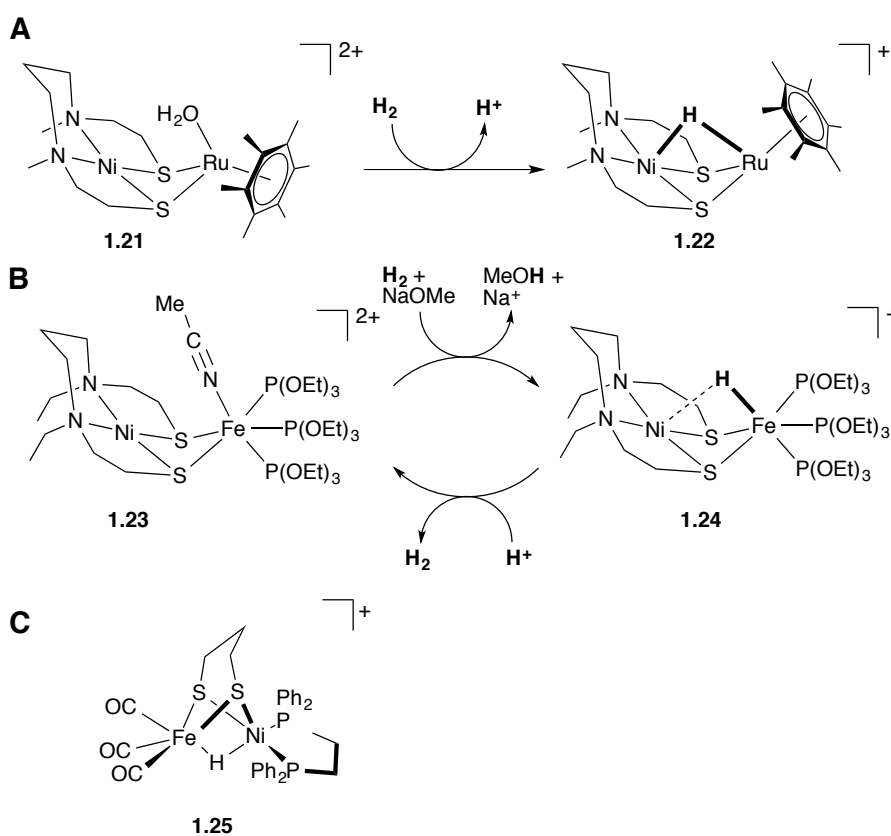


Figure 14. Functional synthetic analogues of [NiFe]-hydrogenase.

Ogo and co-workers later reported a different synthetic model of the [NiFe]-hydrogenase using a [NiFe] complex **1.23** (Figure 14b).³⁷ Complex **1.23** uses NaOMe as base instead of H_2O and heterolytically cleaves H_2 in organic solvent (MeCN/MeOH mixture). Unlike the [NiRu] model **1.22** that can only perform the electron transfer, complex **1.24** can perform both hydride and electron transfers, in common with the enzyme. An additional difference is that complex **1.22** exchanges bound H^+ for solution

D^+ (hydride ligand is protic), while the hydride ligand of **1.24** is hydrotic and reacts with H^+ to produce H_2 .

Rauchfuss and co-workers have also reported a functional [NiFe] synthetic model of the enzyme (**1.25**, Figure 14c).³⁸ However, in contrast to the reactivity of complex **1.24** in heterolytic cleavage of H_2 , complex **1.25** is an active catalyst for proton reduction to H_2 . The catalytic current for proton reduction was observed at -1.37 V vs. Fc/Fc^+ . They propose that the catalytic cycle commences with reduction of the hydride in **1.25** followed by protonation to generate dihydrogen.

1.11 Dicarboxamido-dithiolato ligand

Structural models of the bimetallic subunit at the A-cluster of acetyl coenzyme A synthase/CO dehydrogenase (ACS/CODH) have been developed by Mascharak and co-workers.³⁹ The bimetallic site contains a square planar $Ni(II)_d$ site (distal to the $[Fe_4S_4]$ -cubane) while the other metal center, designated as the proximal metal (M_p), is now proposed to be Ni ion. Studies done by Mascharak et al. focus on using the $Ni(II)_d$ synthons depicted in Figure 15 to construct [NiCu] and [NiNi] dinuclear analogs and to look at their reactivity with CO. Treatment of **1.26** with $[Cu(neo)-Cl]$ (neo = 2,9-dimethyl-1,10-phenanthroline) afforded the dinuclear $[Ni(II)Cu(I)]$ complex bridged by the thiolato-S donors in **1.26-M**. The CV of the **1.26-Cu** complex does not exhibit any reduction wave up to -1.8 V vs. SCE, consistent with the $Ni(II)$ center being resistant to reduction. No reactivity with CO was observed as well for **1.26-Cu**. To make the [NiNi] model, **1.26** was reacted with $[Ni(terpy)Cl_2]$ and **1.27** with $[Ni(dppe)Cl_2]$. Both [NiNi] models (**1.26-Ni** and **1.27-Ni**) can be reduced chemically by one electron and subsequently react with CO to yield a bimetallic structure with a terminal $Ni(I)-CO$

adduct (studied by IR spectroscopy). The Ni_p mimic in these models only binds CO in the reduced (Ni^{I}) state while the Ni_d center shows no affinity toward CO under similar reducing conditions. Consistent with the metal identities in the active site of ACS/CODH, the reduced $[\text{NiNi}]$ models in these studies are the reactive species toward CO addition.

Analogous trimetallic $[\text{Ni-Cu-Ni}]$ and $[\text{Ni-Ni-Ni}]$ complexes ($\text{Ni}_d\text{-M}_p\text{-Ni}_d$) using synthons **1.26** and **1.27** have also been synthesized.^{39b,40} Similar reactivity profile to the binuclear analogues was observed for both complexes where only the reduced Ni–Ni–Ni complex affords the CO-adduct upon treatment with CO.

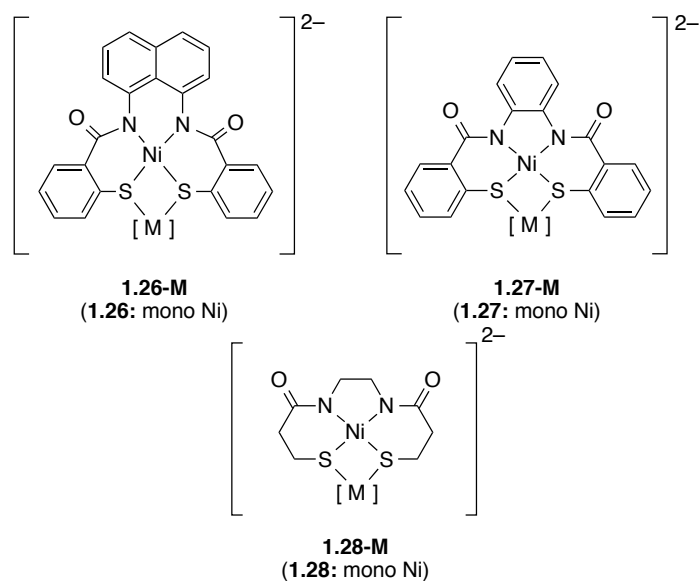


Figure 15. $\text{Ni}(\text{II})_d$ synthons for the bimetallic subunit ($\text{M} = \text{Ni}, \text{Cu}$).

Rauchfuss and co-workers have also done studies on the structural analogues of the bimetallic reaction center in ACS/CODH using **1.28** as the $\text{Ni}(\text{II})_d$ synthon (Figure 15).⁴¹ Reaction of **1.28** with $[\text{Cu}(\text{MeCN})_4](\text{PF}_6)$ in the presence of P^tPr_3 yields the bimetallic $[\text{Ni}(\text{II})\text{Cu}(\text{I})]$ complex (**1.28-Cu**) with a trigonal planar Cu center. The CV of

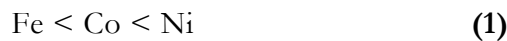
the **1.28-Cu** features an irreversible oxidation at low potential +0.18 V vs. Ag/AgCl attributed to the Ni^{II/III} couple. No reactivity with CO was observed with the **1.28-Cu**. Treatment of **1.28** with Ni(cod)₂ (cod = bis-cyclooctadiene) at low temperature followed by addition of CO resulted in the binuclear species with two terminal CO's on the Ni(0) center. This result is again consistent with the crystal structure of the ACS/CODH active site.

1.12 Multinucleating 1,3,5-tris((4,6-dimethyl-3-mercaptophenyl)thio)-2,4,6-tris(*p*-tolylthio)benzene

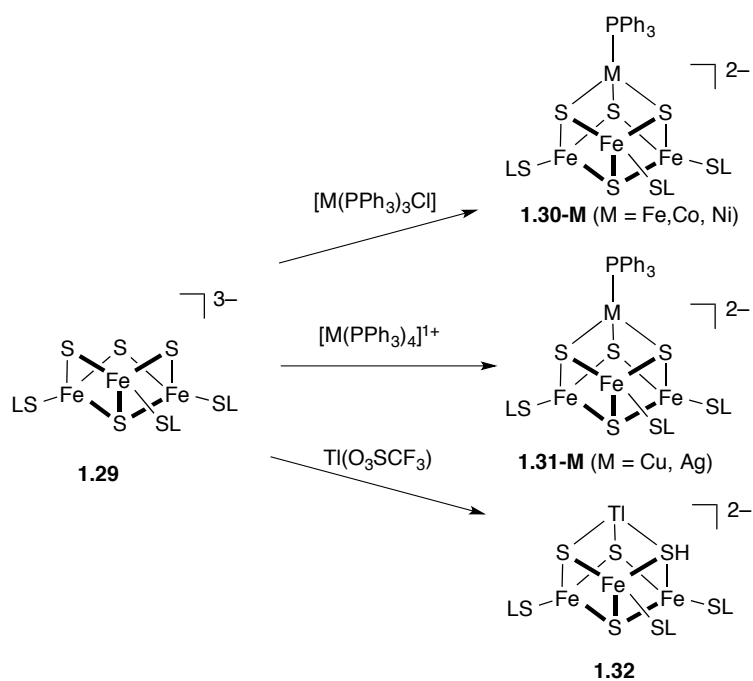
The frequent occurrence of [Fe₃S₄(SCys)₃] cluster moiety in proteins has prompted extensive studies on its chemical and biology properties. The cluster is known to sustain two reactions: (i) electron transfer and (ii) heterometal ion incorporation. Holm and co-workers have pioneered the controlled synthesis of heterometallic [MFe₃S₄(LS₃)L'] (LS₃ = 1,3,5-tris((4,6-dimethyl-3-mercaptophenyl)thio)-2,4,6-tris(*p*-tolylthio)benzene; L' = Ph₃P) clusters⁴² where M have been varied from Co, Ni, Cu, Ag, and Tl (Scheme 5). The work involves the stoichiometric reaction of cuboidal [Fe₃S₄] (**1.29**) as a *cluster ligand*. The [MFe₃S₄(LS₃)(SMet)]-clusters (M = Fe, Co, Ni; SMet = mesitylenethiolate) or **1.30-M** have been synthesized to include [Fe₄S₄(LS₃)] in the series, albeit with a different terminal ligand bound to the apical Fe metal.

The influence of heterometal on the redox potentials of protein-bound clusters is difficult to discern because of the possible differences in terminal ligation, local protein charge, and other environmental effects. With the synthetic clusters prepared by Holm and co-workers, a more systematic comparison of cluster redox potentials can be made as a function of the heterometal through cyclic voltammetry studies. Based on the cyclic voltammetry studies on the heterometallic clusters *without* the multinucleating

ligand support $[\text{MFe}_3\text{S}_4(\text{SR}_4)]^{2-/3-}$ ($\text{R} = \text{Et}, \text{Mes}$) and $[(\text{Smes})\text{MFe}_3\text{S}_4(\text{LS}_3)]^{2-/3-}$ couples (not pictured),⁴³ the potential order (1) was established.



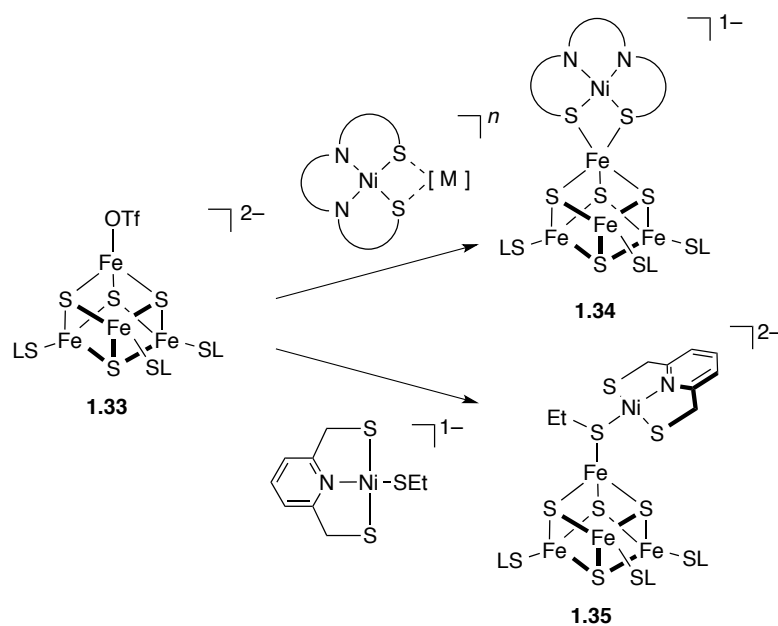
Scheme 5. Preparation of $[\text{MFe}_3\text{S}_4(\text{LS}_3)]$



When the results for all $[(\text{Ph}_3\text{P})\text{MFe}_3\text{S}_4(\text{LS}_3)]^{2-/3-}$ couples in **1.30-M**, **1.31-M**, and **1.32** are considered, the potential order (2) was observed where iron is tentatively placed in the latter series on the basis of its position in order (1) due to the lack of synthesis of $[\text{Fe}_4\text{S}_4]$ -cluster with identical ligation system measurement of $[\text{Fe}_4\text{S}_4]^{1+/0}$ redox steps. The orders (1) and (2) are formulated on the basis of invariant ligation (except for $\text{M} = \text{Tl}$ in **1.32** where there is no terminal ligation on Tl) and cluster net charge, conditions which require equality of core charge in redox couples. These studies can be considered to represent the intrinsic effect of heterometals on $[\text{MFe}_3\text{S}_4]$ redox potentials. The available

evidence suggests that the primary electron density change occurs within the $[\text{Fe}_3\text{S}_4]$ core rather than at M in both synthetic and protein-bound clusters.⁴² The potentials represent the perturbations placed on the $[\text{Fe}_3\text{S}_4]^{0/-1}$ and (unknown) $[\text{Fe}_3\text{S}_4]^{-1/-2}$ potentials by metal incorporation.

Scheme 6. Construction of $[\text{Fe}_4\text{S}_4]^{2+}-(\mu_2\text{-SR})-\text{Ni}^{\text{II}}$ as an A-cluster analogue of CODH/ACS enzyme



Another notable advantage of using the 3:1 site-differentiated clusters $[\text{Fe}_4\text{S}_4(\text{LS}_3)\text{L}']^{2-}$ (**1.33**, $\text{L}' = \text{OTf}, \text{SEt}$) is the capability of the cluster to bridge to another metal complex (Scheme 6). Described in the study by Holm and co-workers⁴⁴ is the synthesis of a heterobimetallic A-cluster analogue of carbon monoxide dehydrogenase/acetylcoenzyme A synthase (CODH/ACS) (Scheme 6). This work exemplifies the possibility of having two intramolecular S-bridges to the $[\text{Fe}_4\text{S}_4]$ -cluster using a cis-planar $\text{Ni}^{\text{II}}-\text{S}_2\text{N}_2$ complex to generate **1.34** while a single unsupported bridge

is also achievable yet less robust in **1.35**. Reaction with the bimetallic $\text{Ni}^{\text{II}}\text{M}-\text{S}_2\text{N}_2$ complex still yield **1.34** without incorporating M into the overall complex.

1.13 *Tris(alkoxy)-hexapyridyl triarylbenzene framework*

The design of model complexes of polynuclear heterometallic clusters such as the oxygen-evolving complex (OEC) presents synthetic inorganic chemists with many challenges. The difficulty of precisely constructing such an intricate complex has forced researchers to rely heavily on self-assembly for preparation of Mn/Ca oxido clusters. This synthetic approach has not been without some successes, as Christou and co-workers were able to isolate a carboxylate-supported $[\text{Mn}_3\text{Ca}_2\text{O}_4]$ complex (**1.36**, Figure 16) containing a $[\text{Mn}_3\text{CaO}_4]$ cubane-like moiety analogous to one observed in the OEC.⁴⁵ In this model, the fourth, ‘dangler’ Mn center in the OEC is absent, and its position is instead occupied by a second Ca atom. Complex **1.36** is a reasonable structural model of the cubane subsite of the OEC, corroborated by multiple spectroscopic studies.

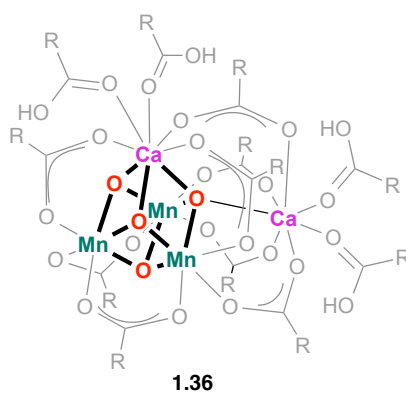


Figure 16. $\text{Mn}_3\text{Ca}_2\text{O}_4$ complex isolated by Christou and co-workers.

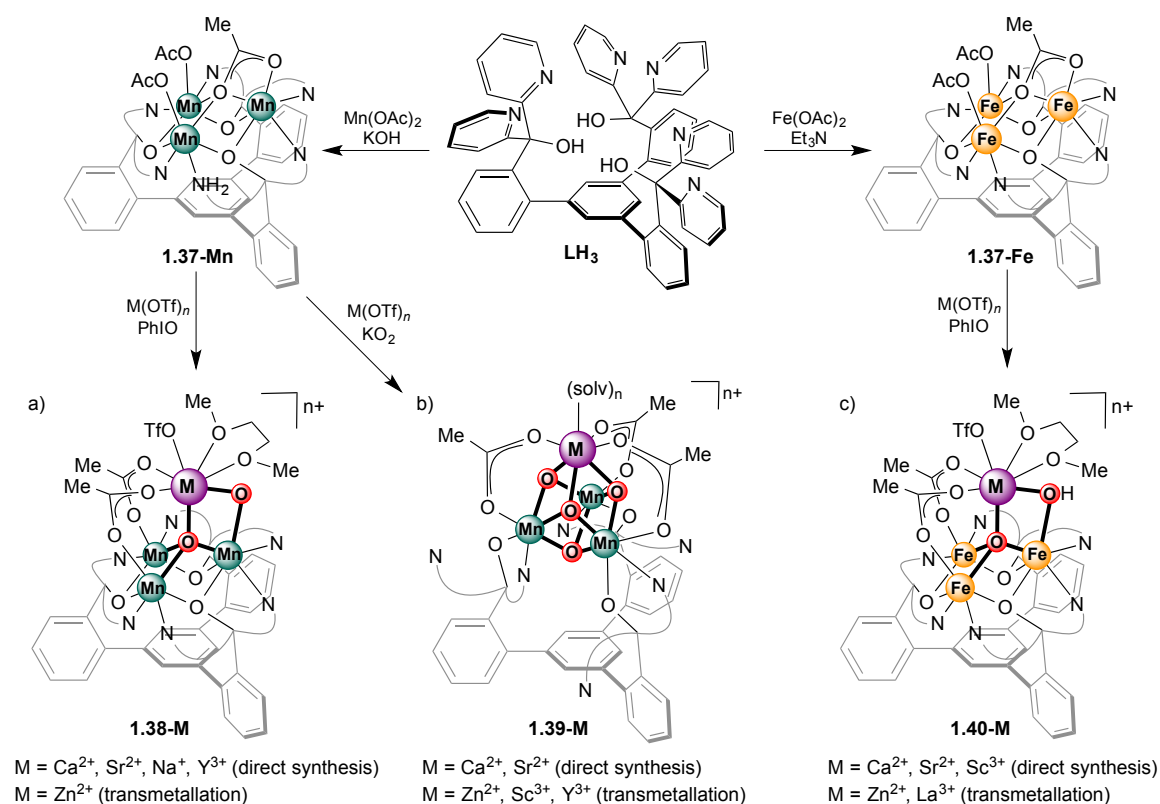
Although **1.36** is a reasonable structural model of the cubane subsite of the OEC, the potential for modification to the structure of the complex is limited due to

the self-assembly process utilized in its synthesis. Rational design of ligand scaffolds capable of supporting clusters may allow for more precise alterations to obtain desired novel structures. The same site-differentiation approach utilized by Holm for iron-sulfur clusters can be useful to isolate oxido clusters with specific compositions. Implementation of just such a strategy using a multinucleating ligand has allowed our group to provide a Mn_3Ca model of the cubane subsite of the OEC and to substitute the Ca center for a variety of redox-active and redox-inactive metals (**1.39-M**, Scheme 7). The same ligand scaffold has been used to study related dioxido complexes (**1.38-M**) and Fe_3 -based oxido/hydroxide complexes (**1.40-M**). The three resulting series represent one of the first systematic studies of the effects of Lewis acidity over a broad range of values on electron-transfer properties.

A triarylbenzene framework bearing three alkoxide and six pyridine donors (**H₃L**) can support homotrimetallic complexes of first-row transition metals (**1.37-M**)⁴⁶ that serve as precursors for preparation of tetrametallic metal-oxido clusters. Synthesis of a higher-nuclearity species is usually achieved via treatment with an oxidant/O-atom source in the presence of a salt of the desired additional metal. Access to related complexes for which this synthetic route is not viable is achieved via transmetallation from the preformed cluster of a less Lewis acidic metal. Modification of reaction conditions allows isolation of clusters displaying differences in ligand coordination mode and displaying varying oxygen-atom incorporation and valence. Treatment of the **1.37-Mn** with iodosobenzene (PhIO) in the presence of $\text{Ca}(\text{OTf})_2$, $\text{Sr}(\text{OTf})_2$, $\text{Na}(\text{OTf})$, or $\text{Y}(\text{OTf})_3$ led to isolation of **1.38-M** (Scheme 4); an analogous Zn complex was obtained via transmetallation from the Ca cluster.⁴⁷ These isostructural complexes

display the same multidentate ligand binding mode as in their trimetallic precursor. One of the two oxido moieties bridges across all four metal center, while the other bridges one of the Mn centers to the redox inactive metal. The apical metal coordination sphere is completed by two acetate ligands and, depending on its identity, a triflate anion and/or a bound solvent molecule. In two cases (Sr^{2+} , Na^+), the clusters were isolated as dimers. The transfer of two O-atoms to the cluster is accompanied by a concurrent four-electron oxidation resulting in a $\text{Mn}^{\text{III}}_2\text{Mn}^{\text{IV}}$ complex.

Scheme 7. Preparation of tetrametallic clusters supported by hexapyridyl ligand: (a) dioxido clusters, (b) tetraoxido clusters, (c) oxido/hydroxido clusters.



The Lewis acidity of the redox-inactive metal directly influences the electronics of the cluster, as displayed in the shift in redox potential across the series of

compounds. The $E_{1/2}$ for the $\text{Mn}^{\text{III}}_2\text{Mn}^{\text{IV}}/\text{Mn}^{\text{III}}_3$ couple in these species are listed in Table 4, and range from -0.30 V vs. Fc^+/Fc for Na^+ to $+0.42$ V for Y^{3+} . These values correlate linearly with Lewis acidity measured by the $\text{p}K_a$ method, and their broad range of Lewis acidities allows for a more accurate quantitative interpretation of the trend, which shows that a shift in one $\text{p}K_a$ unit corresponds to a potential shift of ~ 0.1 V. Redox-tuning of clusters by Lewis acids supports the hypothesis that this is a potential role of redox-inactive metals in both natural systems (e.g., PSII) and heterogeneous materials (e.g., birnessites).

Table 4. Redox potential of Mn-dioxido, Mn-tetraoxido, and Fe-oxido-hydroxido complexes. ^a $E_{1/2}$ in V vs. Fc^+/Fc . ^b $\text{p}K_a$ of $\text{M}(\text{aqua})^{n+}$ complex⁴⁸

Entry	M	1.38-M ^a	1.39-M ^a	1.40-M ^a	$\text{p}K_a^b$
1	Na^+	-0.305	-	-	14.8
2	Sr^{2+}	-0.072	-0.944	-0.49	13.2
3	Ca^{2+}	-0.071	-0.94	-0.48	12.6
4	Zn^{2+}	-0.163	-0.628	-0.20	9.3
5	La^{3+}	-	-0.487	-0.08	9.06
6	Nd^{3+}	-	-0.435	-	8.43
7	Gd^{3+}	-	-0.432	-	8.35
8	Eu^{3+}	-	-0.429	-	8.31
9	Tb^{3+}	-	-0.408	-	8.16
10	Dy^{3+}	-	-0.413	-	8.1
11	Y^{3+}	+0.419	-0.428	-	8.04
12	Yb^{3+}	-	-0.381	-	7.92
13	Sc^{3+}	-	-0.246	+0.07	4.79
14	Mn^{3+}	-	+0.29	-	0.1

A separate series of complexes is obtained via a slight modification of the conditions used to isolate the dioxido cluster. Treatment of the same **1.37-Mn** precursor in the presence of Ca^{2+} or Sr^{2+} with potassium superoxide in place of iodosobenzene leads to formation of *tetraoxido* clusters **1.39-Ca/Sr** displaying a $[\text{Mn}_3\text{MO}_4]$ cubane structural motif, with the redox-inactive metal situated at the apical position.⁴⁹ The incorporation of four oxido ligands causes the multidentate ligand to change binding mode to one in which the alkoxide donors are terminal, rather than bridging, and one of the pyridines on each ligand arm is unbound. Acetate ligands bridge each face of the cubane core. The Mn centers in the **1.39-M** for $\text{M} = \text{Ca}, \text{Sr}, \text{Zn}, \text{Y}, \text{Sc}, \text{Ln}$ are all in the Mn^{IV} oxidation state. Related clusters are accessible via transmetallation from the Ca^{2+} complex with a variety of alkali, alkaline earth, and transition metal salts.⁵⁰ Furthermore, the analogous all-Mn cubane complex **1.39-Mn** can be isolated by treatment of the **1.37-Mn** with permanganate, which supplies all oxidizing, oxygen-atom, and Mn equivalents required.^{49a} In this case, the cluster is isolated in the $\text{Mn}^{\text{III}}_2\text{Mn}^{\text{IV}}_2$ oxidation state. Similarly to what is observed for the **1.38-M** clusters, the electronics of **1.39-M** are markedly affected by the Lewis acidity of the apical metal. The redox potentials for the $\text{Mn}^{\text{III}}\text{Mn}^{\text{IV}}_2/\text{Mn}^{\text{IV}}_3$ couple in these complexes are listed in Table 4, and shift from -0.944 V for Sr^{2+} to $+0.29$ V for Mn^{3+} . These values once again correlate linearly with Lewis acidity ($\text{p}K_{\text{a}}$ method, Figure 17). Interestingly, the linear fit shows a similar slope to that for the dioxido cluster series (~ 0.10 V/ $\text{p}K_{\text{a}}$ unit).

The third series of heterometallic clusters supported by this multidentate ligand is built on the **1.37-Fe** complex analogous to the **1.37-Mn** species mentioned above. Under similar conditions to those used to isolate the **1.38-M**, use of the Fe^{II} precursor

allows access to structurally analogous oxo-hydroxo **1.40-M** clusters ($M = \text{Ca}^{2+}, \text{Sr}^{2+}$). Observation of a hydroxo-bridged cluster is presumably a result of the instability of the $[\text{Fe}^{\text{IV}}\text{-O}]$ species that would result from four-electron oxidation of the Fe^{II}_3 complex by iodosobenzene, whereas in the case of Mn the +4 oxidation state is more stable and the dioxo complex is isolated. Therefore, if at any point during the reaction any $[\text{Fe}^{\text{IV}}\text{-O}]$ species is formed, it may be sufficiently oxidizing to abstract an H-atom (likely from solvent). The assignment of the μ_2 -bridge as a hydroxo moiety is suggested by charge balance in the solid-state structure (three counteranions are present) and by the bond metrics of the Fe–O(H) bond (too long for a $\text{Fe}^{\text{III}}\text{-O}$ bond based on literature examples), concurrent with Fe oxidation state assignment via Mössbauer spectroscopy.

Under analogous reaction conditions using $\text{Sc}(\text{OTf})_3$ in place of $\text{Ca}(\text{OTf})_2$, the Sc^{3+} cluster is isolated, albeit in the one-electron reduced $\text{Fe}^{\text{II}}_2\text{Fe}^{\text{II}}$ oxidation state. The Sc^{3+} complex is expected to be a stronger oxidant, and *in situ* reduction by starting Fe^{II}_3 complex likely occurs. Transmetallation from the Ca complex yields the Zn^{2+} and La^{3+} clusters, to give a five-complex series with redox-inactive metals spanning nine pK_a units. Three of the clusters have been characterized in the $\text{Fe}^{\text{II}}_2\text{Fe}^{\text{III}}$ state – the Sc^{3+} , Ca^{2+} , and La^{3+} complexes, the latter two via chemical reduction with cobaltocene ($E_{1/2} = -1.34 \text{ V vs. Fc}^+/\text{Fc}$). The Fe oxidation states are confirmed by Mössbauer spectroscopy.

Crystallographic characterization reveals that the one-electron reduction event occurs at one of the two Fe centers that are *not* bound to the hydroxide bridge. This observation is intriguing, as it implies that H-atom abstraction from one of these reduced complexes would proceed via transfer of the hydroxide proton concurrent with

the electron transfer from a Fe center not directly bound to the source of the proton, and only few reports have described this type of H-atom transfer reactivity. As with the other two series, $\text{Fe}_3\text{MO}(\text{OH})$ complexes experience a shift in redox potential upon changes in the Lewis acidity of the apical metal, with the $\text{Fe}^{\text{III}}_3/\text{Fe}^{\text{III}}_2\text{Fe}^{\text{II}}$ couple moving from -0.49 V vs. Fc^+/Fc for $\text{Ca}^{2+}/\text{Sr}^{2+}$ to $+0.70$ for Sc^{3+} . All potentials for **1.40-M** are listed in Table 4. As before, $E_{1/2}$ values correlate linearly with $\text{p}K_a$ of the metal aquo complexes, however, the slope of the linear fit for the **1.40-M** complexes is different (0.07 V/ $\text{p}K_a$ unit) from that of either **1.38-** and **1.39-M** series. The change from oxido to hydroxido ligands may engender a change in the communication between the redox-inactive metal and the redox-active centers. It is also possible that the difference in slope is simply due to the change in redox center from Mn to Fe.

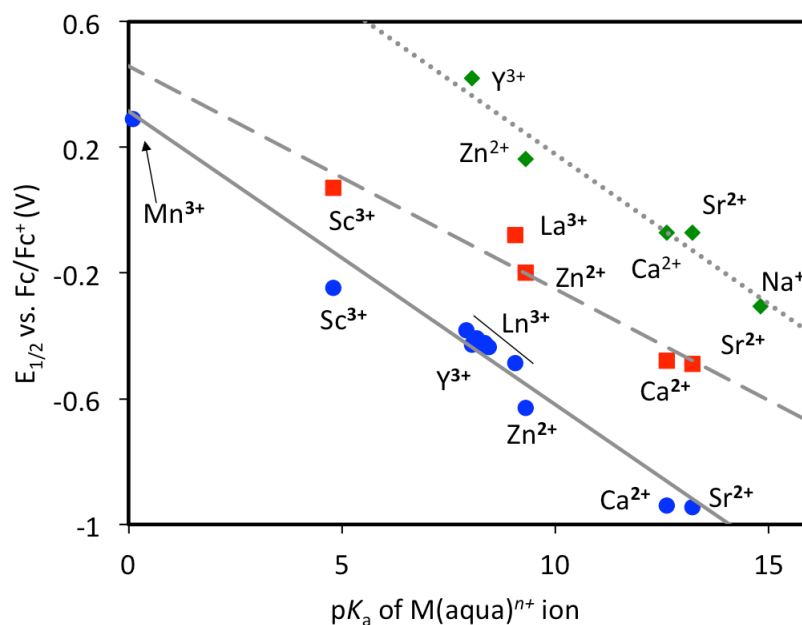


Figure 17. Plots of redox potential vs. Lewis acidity for **1.39-M** (blue), **1.38-M** (green), and **1.40-M** clusters (red) supported by the tris(arylbenzene) framework. Ln = La, Nd, Eu, Gd, Tb, Dy, Yb, Y.

Summary

Despite the challenging nature to rationally synthesize heteromultimetallic clusters, a number of discrete first-row, mixed transition metal series of complexes supported by specific bridging ligands have been reported and studied electronically via cyclic voltammetry. Heterobimetallic complexes with bridging phenolates in the ligand backbone display small $\Delta E_{1/2} < 0.15$ V, indicative of the dominant effect of the overall cluster charge on the electronic properties. On the other hand, mixed-metal clusters supported by bridging bisphenolates exhibit larger $\Delta E_{1/2} \sim 0.38$ V on the non-varied metal center despite the similarity in Lewis acidities of the heterometal (with ~ 0.5 pK_a unit window of the M(aqua)²⁺ ions); in this case, both structural variations and electronic interactions of the complexes may play a role in the redox properties of the systems. Slight ligand variation that leads to minimal structural change in the complex may also lead to different reactivity with O₂ for a dicobalt system, stressing the importance of ligand design to achieve the desired reactivity.

A series of complexes supported by bisphenoxy-carbamoyl bridging ligand also shows minimal change in the redox potential as studied by the CV, indicative of the primary electrostatic effect on the clusters' electronic properties. Other designs of ligands that include mono- and bis-porphyrins and corrole/porphyrin ligands show variable reactivities for O₂ reduction (4-electron vs. 2-electron) that result from either ligand design or the heterometal effect. Heteromultimetallic complexes supported by multinucleating macrocyclic ligands that include a triazacyclo nonane framework do not display Lewis acidity effect on their reduction potentials. A more direct correlation

between the reduction potentials of series of clusters and the Lewis acidities of the heterometals is observed for complexes bridged by oxido and sulfido ligands, suggesting the tunability of the redox potentials of the clusters.

From the reported systems summarized in this chapter, it is evident that ligand design plays a key role in the observed the electronic properties as well as the resulting reactivity toward small molecules. Of particular interest are the special cases of heterometallic complexes with more specialized oxido and sulfido bridging ligands that display Lewis acidity effect on the redox properties. Therefore, rationally designing a ligand that can support multinuclear oxido or sulfido clusters with the ability to systematically vary the heterometal will be beneficial to further our understanding of the electron transfer mechanism in the heteromultimetallic clusters found in nature's enzymes.

2.1 This work

Building multinuclear clusters using multidentate ligands to activate small molecules or to model the active sites in biological and heterogeneous catalysts for O₂ evolution still represents a significant synthetic challenge. Ligand design is crucial to facilitate multiple metal centers of different types, metals lability, and cluster geometry. This dissertation describes two different multinucleating ligand: a trisphosphine ligand (**1a**) and a tris(alkoxy)-hexapyridyl ligand (**H₃L**), both hinged on a rigid 1,3,5-triarylbenzene framework. The initial goal of using these multinucleating ligands is to construct heterometallic multinuclear clusters designed for small molecules activation.

Chapter 2 describes the synthesis of a tris(phosphinoaryl)benzene ligand used to support mono-nickel and palladium complexes. Despite the multidentate nature of the trisphosphine ligand, under the specific reaction conditions, only mononuclear Ni or Pd complexes were isolated. In this case, two phosphine arms coordinated to the metal center, while the third phosphine was found to form a C–P bond with dearomatization of the central arene. Deprotonation effected the rearomatization of the central ring and metal reduction from M(II) to M(0). This represents an overall C–H to a C–P bond transformation of an unactivated arene. Chapter 3 describes the construction of multinickel complexes supported by the same trisphosphine ligand from Chapter 2. Di- and trinuclear metal complexes supported by a triphosphine ligand display diverse metal-arene binding modes, demonstrating the use of an arene as versatile ligand design element for small molecular clusters.

Chapter 4 presents the syntheses of a series of discrete mixed *redox-active* transition metal [MMn₃O₄] clusters (M = Fe, Co, Ni, Cu) supported by **H₃L** and their characterization. The synthesis of these oxide clusters displaying two types of transition metals were targeted for systematic metal composition-property studies relevant to mixed transition metal oxides employed in electrocatalysis. The electrochemical properties of these complexes were studied via cyclic voltammetry, and the redox chemistry of the series of complexes was investigated to determine the site of electron transfer given the presence of two types of redox-active transition metals. Studies on oxygen atom transfer reactivities of [MMn₃O₄] and [MMn₃O₂] series were performed to investigate the effect of the heterometal M in the reaction rates.

Chapter 5 focuses on the use of $[\text{CoMn}_3\text{O}_4]$ and $[\text{NiMn}_3\text{O}_4]$ cluster complexes discussed in Chapter 4 as precursors to heterogeneous oxygen evolution reaction (OER) electrocatalysts. The electrolysis of these complexes as films on electrodes was evaluated for OER activity in basic media. Systematic structure-function relationships of these heterogeneous electrocatalysts based on the heterometallic composition can be analyzed against the previous structural characterizations of the small molecule complexes, other heterometallic oxides, and the OEC in PSII. This study suggests that, depending on film preparation, the Co-Mn-oxide was found to change metal composition during catalysis, while the Ni-Mn oxide maintained the NiMn_3 ratio.

These studies serve to further our fundamental understanding of how complicated multimetallic clusters found in nature are structurally relevant and specifically tuned to achieve their catalytic activity. By using certain ligands that were specifically designed to support multinuclear complexes, we can learn some lessons from these studies that will lead in the advancements of future catalyst designs.

References

- (a) Cheng, F. Y.; Chen, J. *Chem. Soc. Rev.* **2012**, *41*, 2172. (b) Malavasi, L.; Fisher, C. A. J.; Islam, M. S. *Chem. Soc. Rev.* **2010**, *39*, 4370. (c) Du, P. W.; Eisenberg, R. *Energy Environ. Sci.* **2012**, *5*, 6012. (d) Kondratenko, E. V.; Mul, G.; Baltrusaitis, J.; Larrazabal, G. O.; Perez-Ramirez, J. *Energy Environ. Sci.* **2013**, *6*, 3112. (e) Pagliaro, M.; Konstandopoulos, A. G.; Ciriminna, R.; Palmisano, G. *Energy Environ. Sci.* **2010**, *3*, 279. (f) Lewis, N. S.; Nocera, D. G. *Proc. Natl. Acad. Sci. USA* **2006**, *103*, 15729.
- Bertini, I. *Biological inorganic chemistry : structure and reactivity*; University Science Books: Sausalito, Calif., 2007.
- Jiang, W.; Yun, D.; Saleh, L.; Barr, E. W.; Xing, G.; Hoffart, L. M.; Maslak, M. A.; Krebs, C.; Bollinger, J. M. *Science* **2007**, *316*, 1188.

- 4 (a) Smith, R. D. L.; Prevot, M. S.; Fagan, R. D.; Trudel, S.; Berlinguette, C. P. *J. Am. Chem. Soc.* **2013**, *135*, 11580. (b) Smith, R. D. L.; Prevot, M. S.; Fagan, R. D.; Zhang, Z. P.; Sedach, P. A.; Siu, M. K. J.; Trudel, S.; Berlinguette, C. P. *Science* **2013**, *340*, 60. (c) Liang, Y. Y.; Wang, H. L.; Zhou, J. G.; Li, Y. G.; Wang, J.; Regier, T.; Dai, H. J. *J. Am. Chem. Soc.* **2012**, *134*, 3517. (d) Trotochaud, L.; Ranney, J. K.; Williams, K. N.; Boettcher, S. W. *J. Am. Chem. Soc.* **2012**, *134*, 17253. (e) Yuan, C.; Wu, H. B.; Xie, Y.; Lou, X. W. D. *Angew. Chem. Int. Ed.* **2014**, *53*, 1488. (f) Zaharieva, I.; Najafpour, M. M.; Wiechen, M.; Haumann, M.; Kurz, P.; Dau, H. *Energy Environ. Sci.* **2011**, *4*, 2400. (g) Wiechen, M.; Zaharieva, I.; Dau, H.; Kurz, P. *Chem. Sci.* **2012**, *3*, 2330. (h) Merrill, M. D.; Dougherty, R. C. *J. Phys. Chem. C.* **2008**, *112*, 3655. (i) McCrory, C. C. L.; Jung, S. H.; Peters, J. C.; Jaramillo, T. F. *J. Am. Chem. Soc.* **2013**, *135*, 16977.
- 5 (a) Ding, K. Q. *Int. J. Electrochem. Sci.* **2010**, *5*, 72. (b) Suntivich, J.; Gasteiger, H. A.; Yabuuchi, N.; Nakanishi, H.; Goodenough, J. B.; Shao-Horn, Y. *Nature Chem.* **2011**, *3*, 546.
- 6 Gray, H. B. *Nature Chem.* **2009**, *1*, 112.
- 7 (a) Armand, M.; Tarascon, J. M. *Nature* **2008**, *451*, 652. (b) Goodenough, J. B.; Kim, Y. *Chem. Mater.* **2010**, *22*, 587. (c) Hassoun, J.; Lee, K. S.; Sun, Y. K.; Scrosati, B. *J. Am. Chem. Soc.* **2011**, *133*, 3139. (d) Wang, H. L.; Liang, Y. Y.; Gong, M.; Li, Y. G.; Chang, W.; Mefford, T.; Zhou, J. G.; Wang, J.; Regier, T.; Wei, F.; Dai, H. J. *Nature Commun.* **2012**, *3*. (e) Wang, Z.-L.; Xu, D.; Xu, J.-J.; Zhang, X.-B. *Chem. Soc. Rev.* **2014**, *43*, 7746.
- 8 Tsui, E. Y.; Kanady, J. S.; Agapie, T. *Inorg. Chem.* **2013**, *52*, 13833.
- 9 (a) Karsten, P.; Neves, A.; Bortoluzzi, A. J.; Lanznaster, M.; Drago, V. *Inorg. Chem.* **2002**, *41*, 4624. (b) Lanznaster, M.; Neves, A.; Bortoluzzi, A. J.; Szpoganicz, B.; Schwingel, E. *Inorg. Chem.* **2002**, *41*, 5641. (c) Batista, S. C.; Neves, A.; Bortoluzzi, A. J.; Vencato, I.; Peralta, R. A.; Szpoganicz, B.; Aires, V. V. E.; Terenzi, H.; Severino, P. C. *Inorg. Chem. Commun.* **2003**, *6*, 1161. (d) Lanznaster, M.; Neves, A.; Bortoluzzi, A. J.; Aires, V. V. E.; Szpoganicz, B.; Terenzi, H.; Severino, P. C.; Fuller, J. M.; Drew, S. C.; Gahan, L. R.; Hanson, G. R.; Riley, M. J.; Schenk, G. J. *Biol. Inorg. Chem.* **2005**, *10*, 319. (e) Schenk, G.; Peralta, R. A.; Batista, S. C.; Bortoluzzi, A. J.; Szpoganicz, B.; Dick, A. K.; Herrald, P.; Hanson, G. R.; Szilagy, R. K.; Riley, M. J.; Gahan, L. R.; Neves, A. J. *Biol. Inorg. Chem.* **2008**, *13*, 139. (f) Xavier, F. R.; Neves, A.; Casellato, A.; Peralta, R. A.; Bortoluzzi, A. J.; Szpoganicz, B.; Severino, P. C.; Terenzi, H.; Tomkowicz, Z.; Ostrovsky, S.; Haase, W.; Ozarowski, A.; Krzystek, J.; Telser, J.; Schenk, G.; Gahan, L. R. *Inorg. Chem.* **2009**, *48*, 7905.

- 10 Ghiladi, M.; McKenzie, C. J.; Meier, A.; Powell, A. K.; Ulstrup, J.; Wocadlo, S. *J. Chem. Soc. Dalton Trans.* **1997**, 4011.
- 11 Ghiladi, M.; Jensen, K. B.; Jiang, J. Z.; McKenzie, C. J.; Morup, S.; Sotofte, I.; Ulstrup, J. *J. Chem. Soc. Dalton Trans.* **1999**, 2675.
- 12 Fraser, C.; Johnston, L.; Rheingold, A. L.; Haggerty, B. S.; Williams, G. K.; Whelan, J.; Bosnich, B. *Inorg. Chem.* **1992**, *31*, 1835.
- 13 (a) Fraser, C.; Bosnich, B. *Inorg. Chem.* **1994**, *33*, 338. (b) Mccollum, D. G.; Fraser, C.; Ostrander, R.; Rheingold, A. L.; Bosnich, B. *Inorg. Chem.* **1994**, *33*, 2383. (c) Mccollum, D. G.; Hall, L.; White, C.; Ostrander, R.; Rheingold, A. L.; Whelan, J.; Bosnich, B. *Inorg. Chem.* **1994**, *33*, 924. (d) McCollum, D. G.; Yap, G. P. A.; Rheingold, A. L.; Bosnich, B. *J. Am. Chem. Soc.* **1996**, *118*, 1365. (e) Fraser, C.; Ostrander, R.; Rheingold, A. L.; White, C.; Bosnich, B. *Inorg. Chem.* **1994**, *33*, 324. (f) McCollum, D. G.; Yap, G. P. A.; LiableSands, L.; Rheingold, A. L.; Bosnich, B. *Inorg. Chem.* **1997**, *36*, 2230.
- 14 Kita, S.; Furutachi, H.; Okawa, H. *Inorg. Chem.* **1999**, *38*, 4038.
- 15 (a) Wada, H.; Aono, T.; Motoda, K. I.; Ohba, M.; Matsumoto, N.; Okawa, H. *Inorg. Chim. Acta* **1996**, *246*, 13. (b) Furutachi, H.; Okawa, H. *Inorg. Chem.* **1997**, *36*, 3911.
- 16 Furutachi, H.; Fujinami, S.; Suzuki, M.; Okawa, H. *J. Chem. Soc. Dalton Trans.* **1999**, 2197.
- 17 Sunatsuki, Y.; Matsuo, T.; Nakamura, M.; Kai, F.; Matsumoto, N.; Tuchagues, J. P. *Bull. Chem. Soc. Jpn.* **1998**, *71*, 2611.
- 18 Stadler, C.; Daub, J.; Kohler, J.; Saalfrank, R. W.; Coropceanu, V.; Schunemann, V.; Ober, C.; Trautwein, A. X.; Parker, S. F.; Poyraz, M.; Inomata, T.; Cannon, R. D. *J. Chem. Soc. Dalton Trans.* **2001**, 3373.
- 19 Herbert, D. E.; Lionetti, D.; Rittle, J.; Agapie, T. *J. Am. Chem. Soc.* **2013**, *135*, 19075.
- 20 Chishiro, T.; Shimazaki, Y.; Tani, F.; Tachi, Y.; Naruta, Y.; Karasawa, S.; Hayami, S.; Maeda, Y. *Angew. Chem. Int. Ed.* **2003**, *42*, 2788.
- 21 (a) Nanthakumar, A.; Fox, S.; Murthy, N. N.; Karlin, K. D.; Ravi, N.; Huynh, B. H.; Orosz, R. D.; Day, E. P.; Hagen, K. S.; Blackburn, N. J. *J. Am. Chem. Soc.* **1993**, *115*, 8513. (b) Karlin, K. D.; Nanthakumar, A.; Fox, S.; Murthy, N. N.; Ravi, N.; Huynh, B. H.; Orosz, R. D.; Day, E. P. *J. Am. Chem. Soc.* **1994**, *116*, 4753. (c) Ju, T. D.; Ghiladi, R. A.; Lee, D. H.; van Strijdonck, G. P. F.; Woods, A. S.; Cotter, R. J.; Young, V. G.; Karlin, K. D. *Inorg. Chem.* **1999**, *38*, 2244. (d) Kim, E.; Helton, M. E.; Wasser, I. M.; Karlin, K. D.; Lu, S.; Huang, H. W.; Moenne-Loccoz, P.; Incarvito, C. D.; Rheingold, A. L.; Honecker, M.; Kaderli, S.; Zuberbuhler, A. D. *Proc. Natl. Acad. Sci. USA* **2003**, *100*, 3623. (e) Chufan, E. E.; Verani, C.

- N.; Puiu, S. C.; Rentschler, E.; Schatzschneider, U.; Incarvito, C.; Rheingold, A. L.; Karlin, K. D. *Inorg. Chem.* **2007**, *46*, 3017. (f) Halime, Z.; Kieber-Emmons, M. T.; Qayyum, M. F.; Mondal, B.; Gandhi, T.; Puiu, S. C.; Chufan, E. E.; Sarjeant, A. A. N.; Hodgson, K. O.; Hedman, B.; Solomon, E. I.; Karlin, K. D. *Inorg. Chem.* **2010**, *49*, 3629.
- 22 (a) Collman, J. P.; Fu, L.; Herrmann, P. C.; Zhang, X. M. *Science* **1997**, *275*, 949. (b) Boulatov, R.; Collman, J. P.; Shiryaeva, I. M.; Sunderland, C. J. *J. Am. Chem. Soc.* **2002**, *124*, 11923. (c) Collman, J. P.; Devaraj, N. K.; Decreau, R. A.; Yang, Y.; Yan, Y. L.; Ebina, W.; Eberspacher, T. A.; Chidsey, C. E. D. *Science* **2007**, *315*, 1565. (d) Collman, J. P.; Ghosh, S.; Dey, A.; Decreau, R. A.; Yang, Y. *J. Am. Chem. Soc.* **2009**, *131*, 5034.
- 23 Collman, J. P.; Berg, K. E.; Sunderland, C. J.; Aukauloo, A.; Vance, M. A.; Solomon, E. I. *Inorg. Chem.* **2002**, *41*, 6583.
- 24 Collman, J. P.; Decreau, R. A.; Dey, A.; Yang, Y. *Proc. Natl. Acad. Sci. USA* **2009**, *106*, 4101.
- 25 Rosenthal, J.; Nocera, D. G. *Accounts. Chem. Res.* **2007**, *40*, 543.
- 26 Guilard, R.; Brandes, S.; Tardieux, C.; Tabard, A.; Lher, M.; Miry, C.; Gouerec, P.; Knop, Y.; Collman, J. P. *J. Am. Chem. Soc.* **1995**, *117*, 11721.
- 27 Collman, J. P.; Denisevich, P.; Konai, Y.; Marrocco, M.; Koval, C.; Anson, F. C. *J. Am. Chem. Soc.* **1980**, *102*, 6027.
- 28 Guilard, R.; Burdet, F.; Barbe, J. M.; Gros, C. P.; Espinosa, E.; Shao, J. G.; Ou, Z. P.; Zhan, R. Q.; Kadish, K. M. *Inorg. Chem.* **2005**, *44*, 3972.
- 29 Kadish, K. M.; Fremond, L.; Burdet, F.; Barbe, J. M.; Gros, C. P.; Guilard, R. *J. Inorg. Biochem.* **2006**, *100*, 858.
- 30 Kadish, K. M.; Fremond, L.; Ou, Z. P.; Shao, J. G.; Shi, C. N.; Anson, F. C.; Burdet, F.; Gros, C. P.; Barbe, J. M.; Guilard, R. *J. Am. Chem. Soc.* **2005**, *127*, 5625.
- 31 Kadish, K. M.; Shao, J. G.; Ou, Z. P.; Fremond, L.; Zhan, R. Q.; Burdet, F.; Barbe, J. M.; Gros, C. P.; Guilard, R. *Inorg. Chem.* **2005**, *44*, 6744.
- 32 Schwalbe, M.; Metzinger, R.; Teets, T. S.; Nocera, D. G. *Chem. Eur. J.* **2012**, *18*, 15449.
- 33 Glaser, T.; Beissel, T.; Bill, E.; Weyhermuller, T.; Schunemann, V.; Meyer-Klaucke, W.; Trautwein, A. X.; Wieghardt, K. *J. Am. Chem. Soc.* **1999**, *121*, 2193.
- 34 Lozan, V.; Buchholz, A.; Plass, W.; Kersting, B. *Chem. Eur. J.* **2007**, *13*, 7305.
- 35 Ogo, S. *Chem. Commun.* **2009**, 3317.
- 36 Ogo, S.; Kabe, R.; Uehara, K.; Kure, B.; Nishimura, T.; Menon, S. C.; Harada, R.; Fukuzumi, S.; Higuchi, Y.; Ohhara, T.; Tamada, T.; Kuroki, R. *Science* **2007**, *316*, 585.

- 37 Ogo, S.; Ichikawa, K.; Kishima, T.; Matsumoto, T.; Nakai, H.; Kusaka, K.; Ohhara, T. *Science* **2013**, *339*, 682.
- 38 Barton, B. E.; Whaley, C. M.; Rauchfuss, T. B.; Gray, D. L. *J. Am. Chem. Soc.* **2009**, *131*, 6942.
- 39 (a) Harrop, T. C.; Olmstead, M. M.; Mascharak, P. K. *J. Am. Chem. Soc.* **2004**, *126*, 14714. (b) Harrop, T. C.; Olmstead, M. M.; Mascharak, P. K. *Inorg. Chem.* **2006**, *45*, 3424.
- 40 Harrop, T. C.; Olmstead, M. M.; Mascharak, P. K. *Chem. Commun.* **2004**, 1744.
- 41 Linck, R. C.; Spahn, C. W.; Rauchfuss, T. B.; Wilson, S. R. *J. Am. Chem. Soc.* **2003**, *125*, 8700.
- 42 Zhou, J.; Raebiger, J. W.; Crawford, C. A.; Holm, R. H. *J. Am. Chem. Soc.* **1997**, *119*, 6242.
- 43 Zhou, J.; Scott, M. J.; Hu, Z. G.; Peng, G.; Munck, E.; Holm, R. H. *J. Am. Chem. Soc.* **1992**, *114*, 10843.
- 44 Rao, P. V.; Bhaduri, S.; Jiang, J. F.; Hong, D.; Holm, R. H. *J. Am. Chem. Soc.* **2005**, *127*, 1933.
- 45 Mukherjee, S.; Stull, J. A.; Yano, J.; Stamatatos, T. C.; Pringouri, K.; Stich, T. A.; Abboud, K. A.; Britt, R. D.; Yachandra, V. K.; Christou, G. *Proc. Natl. Acad. Sci. USA* **2012**, *109*, 2257.
- 46 (a) Tsui, E. Y.; Kanady, J. S.; Day, M. W.; Agapie, T. *Chem. Commun.* **2011**, *47*, 4189. (b) Tsui, E. Y.; Day, M. W.; Agapie, T. *Angew. Chem. Int. Ed.* **2011**, *50*, 1668.
- 47 Tsui, E. Y.; Tran, R.; Yano, J.; Agapie, T. *Nature Chem.* **2013**, *5*, 293.
- 48 Perrin, D. D.; International Union of Pure and Applied Chemistry. Commission on Equilibrium Data. *Ionisation constants of inorganic acids and bases in aqueous solution*; 2nd ed.; Pergamon Press: Oxford Oxfordshire ; New York, 1982.
- 49 (a) Kanady, J. S.; Tsui, E. Y.; Day, M. W.; Agapie, T. *Science* **2011**, *333*, 733. (b) Tsui, E. Y.; Agapie, T. *Proc. Natl. Acad. Sci. USA* **2013**, *110*, 10084.
- 50 Kanady, J. S.; Mendoza-Cortes, J. L.; Tsui, E. Y.; Nielsen, R. J.; Goddard, W. A.; Agapie, T. *J. Am. Chem. Soc.* **2013**, *135*, 1073.

CHAPTER 2

INTRAMOLECULAR ARENE C–H TO C–P FUNCTIONALIZATION MEDIATED BY Ni(II)
AND Pd(II)

Published in part as:
Suseno, S.; Agapie, T. *Organometallics* **2013**, *32*, 3161-3164

ABSTRACT

A trisphosphine ligand with a triarylbenzene backbone was employed to support mono-nickel(II) and palladium(II) complexes. Two phosphine arms coordinated to the metal center, while the third phosphine was found to form a C–P bond with dearomatization of the central arene. Deprotonation effected the rearomatization of the central ring and metal reduction from M(II) to M(0). The overall conversion corresponds to a functionalization of an unactivated arene C–H bond to a C–P bond. This transformation represents a rare type of C–H functionalization mechanism, facilitated by the interactions of the group 10 metal with the arene π -system. This conversion is reminiscent of and expands the scope of recently reported intramolecular rearrangements of biaryl phosphine ligands common in group 10 catalysis.

INTRODUCTION

The functionalization of C-H bonds catalyzed by transition metals has been an active field of research due to the potential applications in fine and commodity chemical synthesis, and petrochemical conversion.¹ Many metal-facilitated C-H functionalizations involve direct metal coordination or attack on the C-H moiety. This can take several forms: coordination of the C-H bond prior to oxidative addition, σ -bond metathesis, 1,2-addition, electrophilic aromatic metallation, or radical cleavage.^{1a,1b,2} The oxidative addition mechanism as a common mode of C-H functionalization is shown in Figure 1a. For the functionalization of the C-H bonds of aromatic compounds, an alternative, extensively studied mechanism involves Cr and Mn η^6 -arene complexes that are susceptible to nucleophilic attack (Figure 1b).³ Subsequent oxidation leads to the rearomatization and release of functionalized arene. Arene elaboration upon strong binding of metals to part of the aromatic π -system has also been reported.⁴ The latter two strategies for C-H functionalization require harsh conditions for metal removal due to strong metal-arene interactions.

Development of conceptually related chemistry with group 10 metals is appealing given the weaker metal-arene interactions and potential for metal removal under mild conditions conducive to catalyst turnover. Intramolecular C-H to C-C conversion has been recently reported for palladium coordinated biphenyl phosphines.⁵ C-C bond formation with dearomatization was also observed for a nickel biphenyl phosphine complex.⁶ The common property of these species is interaction of the metal center with arene, leading to activation toward attack of the π -system. Herein, we

present a rare example of C–H to C–P conversion with a new type of mechanism for C–H functionalization based on group 10 metal activation of an arene π -system (Figure 1c).

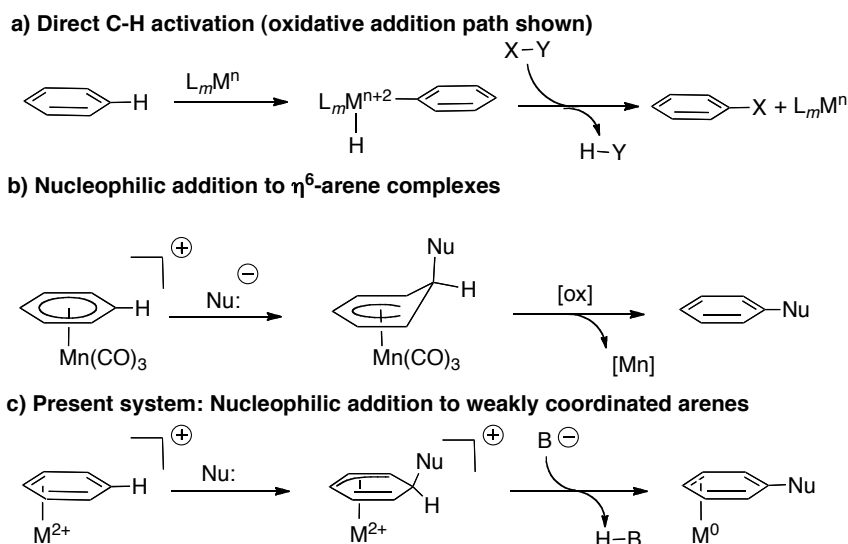
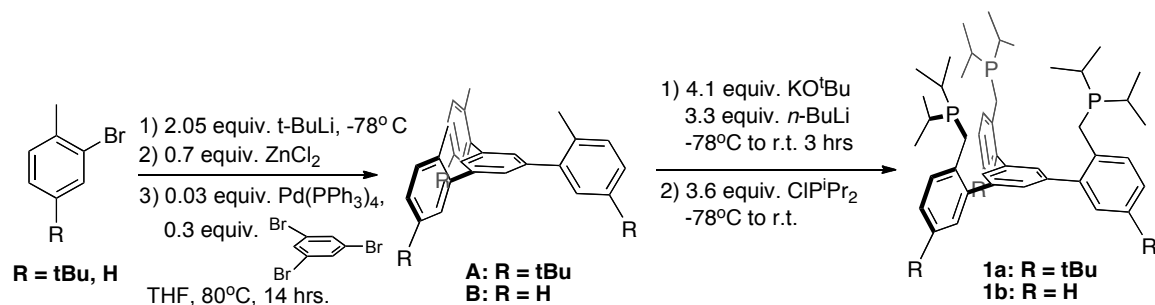


Figure 1. Mechanisms of C-H activation.

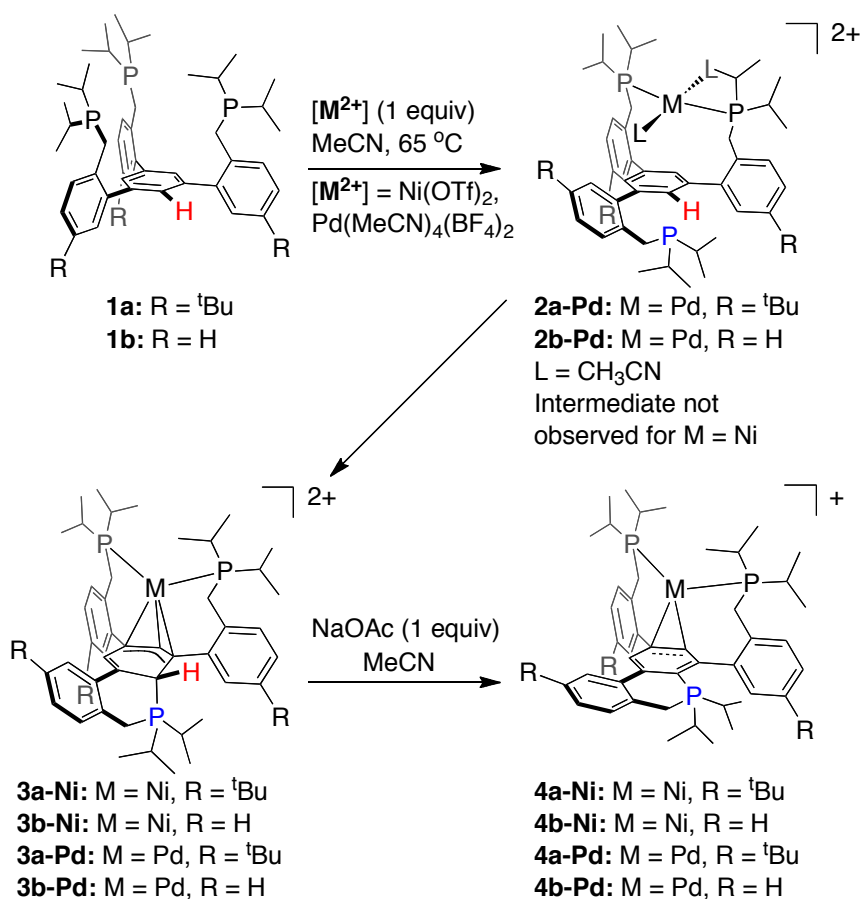
RESULTS AND DISCUSSION

2.1 Ligand synthesis

We have developed a family of bis- and trisphosphine ligands with terphenyl or triphenylbenzene linkers respectively, that support Ni complexes exhibiting metal-arene interactions.⁷ To further explore the reactivity profile of such late metal-arene coordination complexes, we synthesized a modified trisphosphine **1a/b** (Scheme 1). Compounds **1a/b** contain an extra methylene group between the triarylbenzene core and the phosphine moieties, which renders the framework more flexible compared to the related trisphosphine ligand^{7c} with the phosphorus atoms directly bound to the outer aryl groups.

Scheme 1. Synthesis of Ligands **1a** and **1b**

2.2 Synthesis and structure of mono-nickel and palladium complexes

Scheme 2. Synthesis of metal complexes and intramolecular C–H to C–P conversion

Treatment of **1a/b** with one equivalent of $\text{Pd}(\text{MeCN})_4(\text{BF}_4)_2$ (MeCN = acetonitrile) led to the formation of transient species, **2a/b-Pd** (Scheme 2) monitored by nuclear magnetic resonance (NMR) spectroscopy. **2a/b-Pd** has not been structurally

characterized yet while **2a/b-Ni** formation was not observed by NMR spectroscopy. The ^{31}P NMR spectrum of **2b-Pd** displays two peaks at 13.6 and 39.9 ppm in a 1:2 ratio (Figure 2). A separate attempt to serve as evidence of the formation of **2b-Pd** was done by using an analogous bisphosphine ligand **1c**. The reaction of $\text{Pd}(\text{MeCN})_4(\text{BF}_4)_2$ with **1c** formed the species **2c-Pd** (Scheme 3) with a ^{31}P NMR signal at 39.7 ppm (Figure 3).⁸ The XRD study of **2c-Pd** shows a square planar Pd complex ligated by two phosphine arms and two acetonitrile ligands (Figure 4).

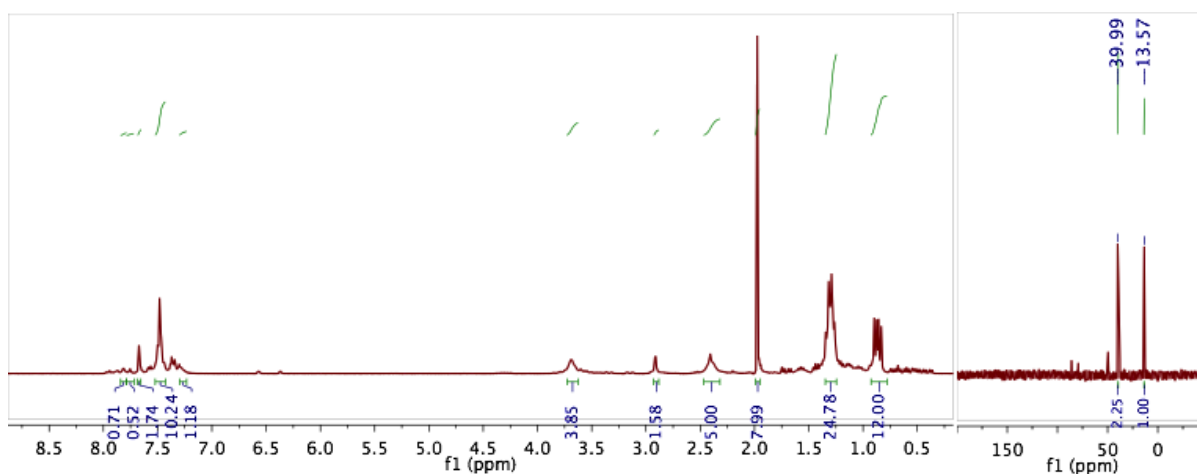
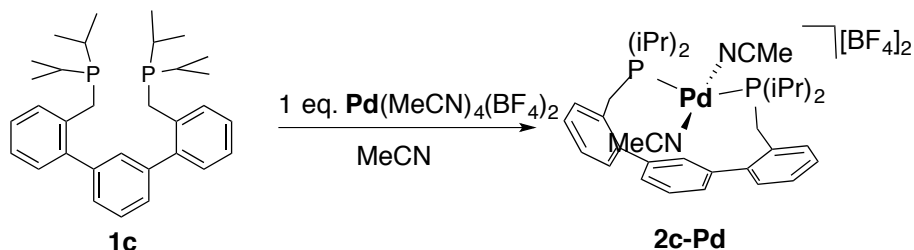


Figure 2. ^1H (left; 300 MHz, CD_3CN) and ^{31}P (right; 121 MHz, CD_3CN) NMR spectra of **2b-Pd**. *Note:* the smaller impurity peaks correspond to the concurrent formation of **3b-Pd**.

Scheme 3. Synthesis of **2c-Pd**



other hand, within 2 hours at room temperature, **2a/b-Pd** converted to new complexes **3a/b-Pd**, each with three peaks in the ^{31}P NMR spectrum. The ^1H NMR spectra of **3a/b-Pd** exhibit peaks in the olefinic region around 4.2 ppm.

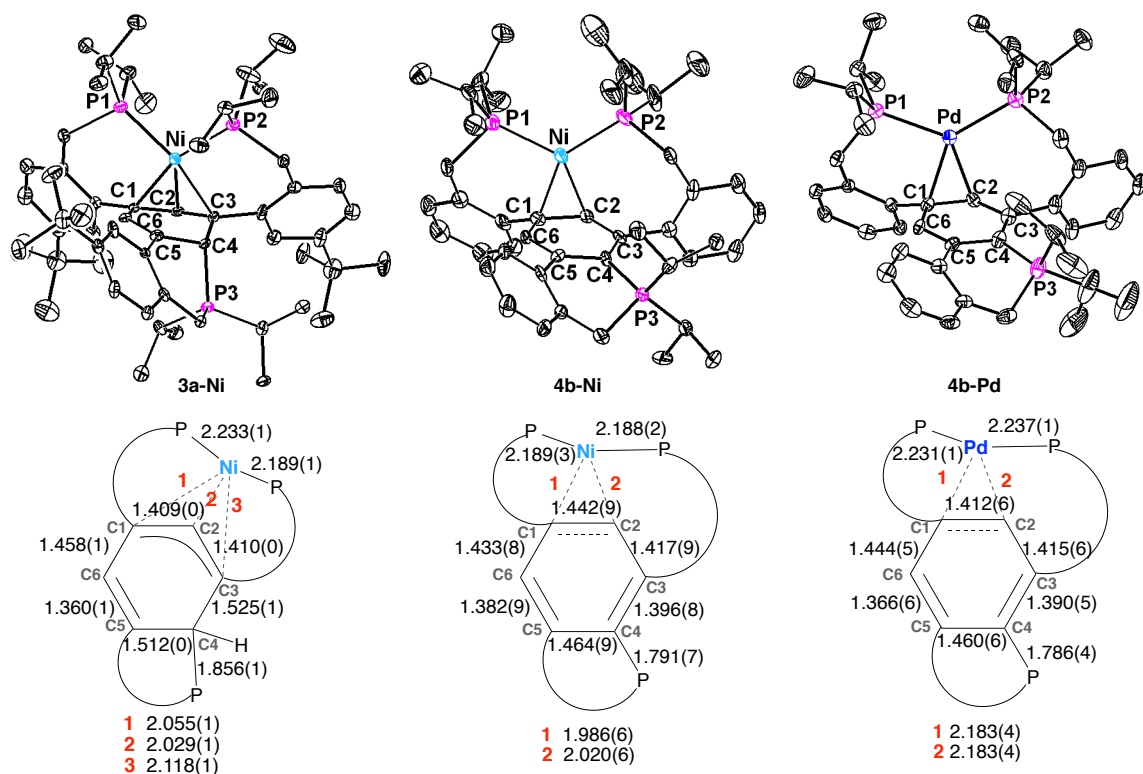


Figure 5. Solid-state structures (top) and selected C–C, Ni–C, and M–P bond distances (Å, bottom) of **3a-Ni** (left), **4b-Ni** (center), and **4b-Pd** (right). Hydrogen atoms and anions are omitted for clarity

Treatment of **1a/b** with one equivalent of $\text{Ni}(\text{OTf})_2$ ($\text{OTf} =$ trifluoromethanesulfonate) generated complexes **3-Ni** (Scheme 2) that possess ^1H NMR features similar to **3-Pd**. A single crystal X-ray diffraction (XRD) study of **3a-Ni** revealed a C_1 Ni^{II} complex (Figure 5). The Ni center is coordinated to two phosphine arms (with P(1)–Ni–P(2) wide bite angle of 253°)⁹ and presents short contacts (2.029(1)–2.118(1) Å) with three carbons of the central ring (Figure 5), consistent with an allyl-like

bonding.¹⁰ Most interestingly, one phosphine arm is now bonded to a carbon of the central ring. The sum of CCC and PCC angles ($\sim 329^\circ$) at C4 suggests an sp^3 carbon.

2D NMR spectroscopy experiments (Figures 6-8) allowed for identification of the signal at 3.8-4.2 ppm for **3a-Ni** as the proton on the central ring sp^3 carbon. Two of the central ring C–C bonds are longer than 1.55 Å, consistent with dearomatization. Additionally, the C5–C6 distance is shorter (1.360(1) Å), indicating an increased double bond character. Overall, these data suggest the formation of a phosphonium moiety. X-ray quality single crystals of **3-Pd** have not been obtained to date, but the NMR spectra are consistent with the analogous, structurally characterized **3-Ni**.

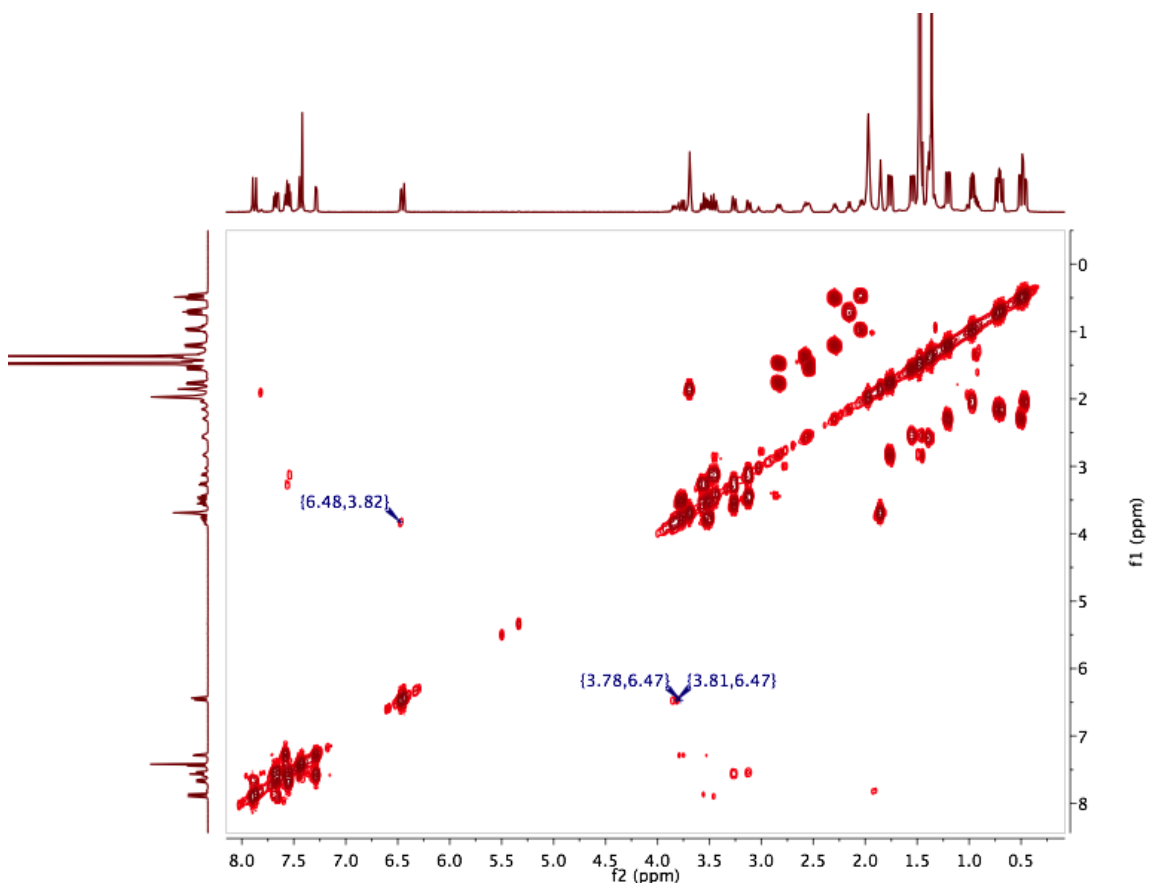


Figure 6. ^1H – ^1H gCOSY(600 MHz, CD_3CN) spectrum of **3a-Ni**. The labeled peaks are the central-ring proton correlations

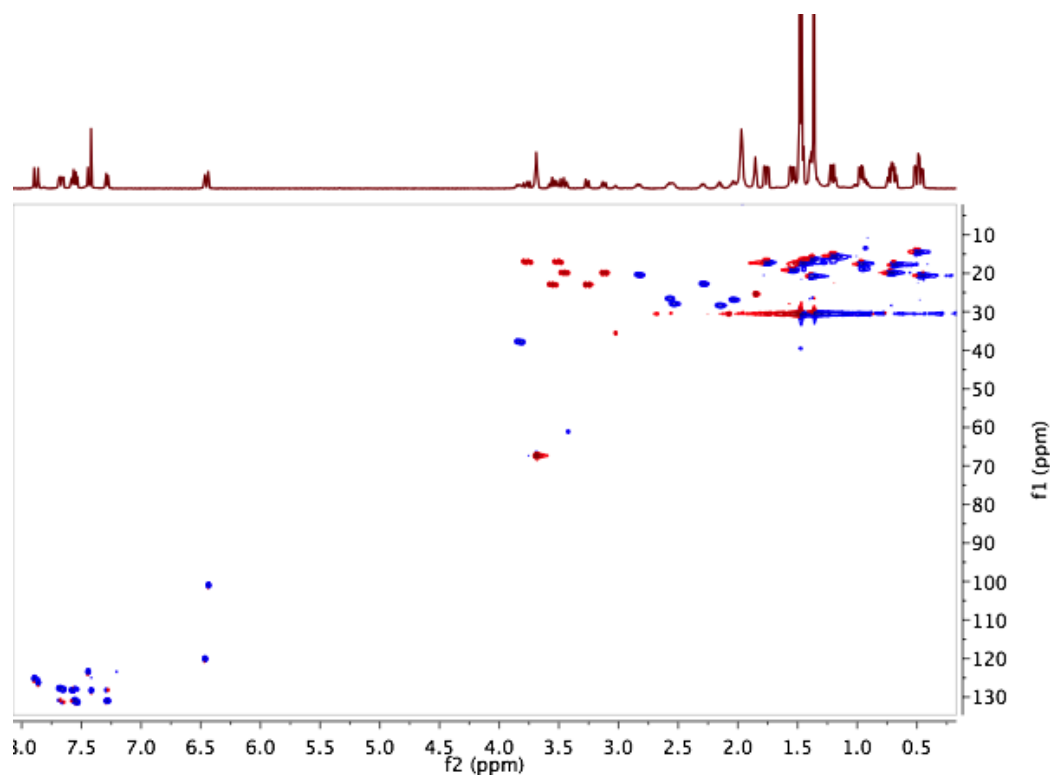


Figure 7. ^1H - ^{13}C gHSQC (600 MHz, CD_3CN) spectrum of **3a-Ni**

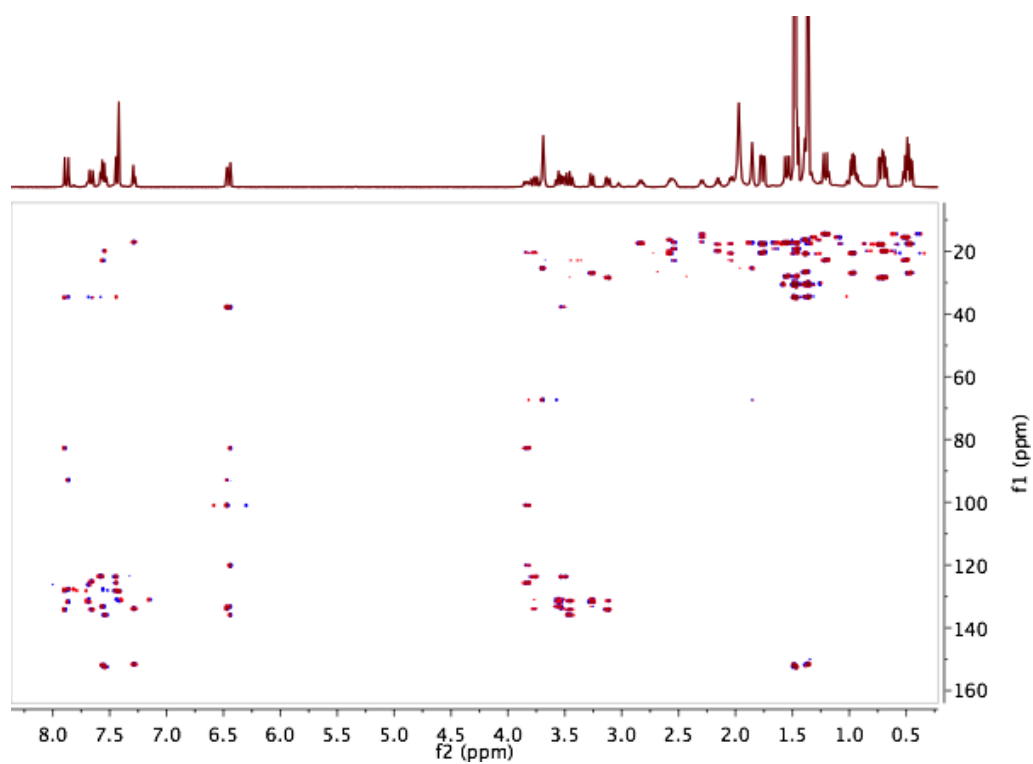


Figure 8. ^1H - ^{13}C gHMBC (600 MHz, CD_3CN) spectrum of **3a-Ni**

The dearomatization of the ring in compounds **3-Ni/Pd** is stabilized by the strong metal-allyl interaction. Although metal arene interactions were not observed in the precursors **2-Pd**, we propose that they are transient and activate the arene sufficiently for nucleophilic attack by the phosphine. Interactions of group 10 metal(II) centers with arenes have been observed by crystallography, in particular for biaryl phosphines.¹¹ Recent reports of arene activation with C–C bond formation occur in intramolecular fashion as well. A Pd-facilitated reaction was proposed to occur via the insertion of an arene olefin moiety into a metal-aryl bond, as supported by the *syn* stereochemistry of the product.^{5a,5b} In the present case, the pendant, free phosphine attacks the ring *anti* with respect to the metal center, indicating that nucleophile coordination to the metal is not a prerequisite for attack on the ring. Hence, this provides an alternate mechanistic path for ring functionalization with heteroatom-based reagents, with potential for the development of intermolecular versions.

Treatment of compounds **3-Ni/Pd** with sodium acetate led to clean formation of new species. The ¹H NMR spectra suggest deprotonation at the central ring *ip*³ position and rearomatization to generate **4-Ni/Pd** (Scheme 2). XRD studies of **4b-Ni/Pd** revealed a planar, aromatic central ring, in which the sum of CCC and PCC angles at C4 is 359° (Figure 5). The C–C distances of the central ring for **4b-Ni/Pd**, between 1.363(6) to 1.460(6) Å, depart slightly from aromaticity (Figure 5). This is due to the metal binding to one of the olefin moieties of the central arene, leading to partial localization of single and double bonds in the ring for which short and long C–C distances alternate.^{7d} The Ni–C (1.986(6) and 2.020(6) Å) and Pd–C (2.183(4) Å)

distances are consistent with M^0 oxidation state.^{7a,12} Hence, deprotonation leads to formal metal reduction from M^{II} to M^0 .

The transition-metal mediated nucleophilic addition to arene double bond followed by deprotonation is effectively a C–H bond functionalization that leads to C–P bond formation in this case. To our knowledge, this is the first example of such a mechanism mediated by Ni^{II} and Pd^{II} without involving the formation of σ -complex or strong metal arene bonds (Scheme 2). Previously reported transition-metal-mediated dearomatization reactions via nucleophilic attack have been limited to d^6 -complexes such as $(\eta^6\text{-arene})Cr(CO)_3$ and $[(\eta^6\text{-arene})Mn(CO)_3]^+$.^{3,13} Rearomatization of the arene requires the presence of an anionic leaving group or stoichiometric chemical oxidation and metal loss, which has hindered the development of catalytic versions (Figure 1).^{3a-c,3i} Our system is similar to the aforementioned such that the electrophilic, metal-coordinated arene moiety is susceptible to nucleophilic attack (Scheme 2). However, rearomatization to give the functionalized arene, with metal reduction, can be achieved by facile deprotonation due to the accessible M^0/M^{II} two electron couple for group 10 metals. Additionally, group 10 metals display only weak metal-arene interactions that, although strong enough to allow for nucleophilic attack, are susceptible to arene exchange with potential for the development of catalytic versions of arene C–H functionalization.¹⁴

CONCLUSIONS

In summary, we have demonstrated a rare example of arene C–H functionalization mediated by Ni^{II} and Pd^{II} in an intramolecular fashion on a tris(phosphinoaryl)benzene framework. The Ni^{II} and Pd^{II} centers have been shown to promote nucleophilic attack on the central arene to yield a phosphonium moiety and dearomatization facilitated by the metal-allyl interaction. Deprotonation at the sp³ carbon of these M^{II}-allyl complexes with base results in rearomatization and formal two-electron reduction of the metal center. The mechanism consistent with the present transformation has several attractive features stemming from the utilization of group 10 metals: activation of arene by weak metal-arene interactions, nucleophilic attack without metal coordination to nucleophile, and a facile M⁰/M^{II} redox couple. With the current conceptual demonstration, future studies include the development of intermolecular and catalytic versions of this transformation using various nucleophiles.

EXPERIMENTAL SECTION

General considerations

Unless otherwise specified, all air- and moisture-sensitive compounds were manipulated using glovebox or using standard Schlenk line techniques with an N₂ atmosphere. Anhydrous tetrahydrofuran (THF) was purchased from Aldrich in 18 L Pure-Pac™ containers. Anhydrous acetonitrile, benzene, dichloromethane, diethyl ether, and THF were purified by sparging with nitrogen for 15 minutes and then passing under nitrogen pressure through a column of activated A2 alumina (Zapp's). Acetonitrile-*d*₃ and chloroform-*d*₁, were purchased from Cambridge Isotopes, dried over calcium hydride, and vacuum transferred prior to use. Benzene-*d*₆ was also purchased from Cambridge Isotope Laboratories, Inc., dried over sodium/benzophenone ketyl, and vacuum transferred prior to use. Unless indicated otherwise, all commercial chemicals were used as received. Pd(PPh₃)₄, Ni(OTf)₂, and Pd(MeCN)₄(BF₄)₂ were purchased from Strem. 1,3,5-tribromobenzene, ZnCl₂, potassium *tert*-butoxide, ^tBuLi, and ⁿBuLi were purchased from Alfa Aesar. Chlorodiisopropylphosphine was purchased from Acros Organics. 2-bromotoluene and 1,3-dibromobenzene were purchased from Sigma-Aldrich. 2-bromo-4-(*tert*-butyl)-toluene was synthesized according to literature procedure.¹⁵ ¹H, ¹³C, and ³¹P NMR spectra were recorded on Varian Mercury 300 MHz or Varian INOVA-500 or 600 MHz spectrometers at room temperature. Chemical shifts for ¹H and ¹³C NMR data are reported with respect to internal deuterated solvent.¹⁶ ³¹P NMR chemical shifts are reported with respect to the deuterated solvent used to lock the instrument. Elemental analyses were performed by Complete Analysis Laboratories, Inc., Parsippany, NJ and Robertson Microlit Laboratories, Ledgewood, NJ.

Synthesis of A (R = tBu)

To an oven-dried Schlenk tube fitted with a screw-in Teflon stopper was added 2-bromo-4-(*tert*-butyl)-toluene (4.87 g, 21.5 mmol) and 73 mL THF under nitrogen. The solution was cooled to -78°C and then ^tBuLi solution (1.7M in pentane, 26 mL, 44.2 mmol) was added via syringe or canula transferred under nitrogen atmosphere. The solution was stirred at -78°C for one hour. ZnCl₂ (2.05 g, 15.1 mmol) was then added as solid to the mixture under positive pressure of N₂, then the mixture was allowed to warm to room temperature and stirred for 2 h. A solution of tribromobenzene (2.03 g, 6.45 mmol) in dry, degassed THF (30 mL) was prepared in an inert atmosphere glovebox and canula transferred under N₂ to the Zn-complex solution. Pd(PPh₃)₄ (1.24 g, 1.08 mmol) was then added as solid into the mixture under nitrogen. The reaction mixture was heated to 85°C and stirred for 14 h. The product formation was checked by GC-MS. Cooled reaction mixture to room temperature, and then water (20 mL) was added. Volatiles were removed via rotary evaporation. The mixture was extracted with CH₂Cl₂ (three times). The combined organic fraction was dried over MgSO₄, filtered, and dried under vacuum. Recrystallization from CH₂Cl₂/MeOH afforded the clean product as white solid in 79% yield (2.63 g, 5.09 mmol). ¹H NMR (300 MHz, CDCl₃) δ 7.37 (d, *J*= 2.1 Hz, 3H, aryl-*H*), 7.34 (s, 3H, aryl-*H*), 7.33 (s, 3H, aryl-*H*), 7.31 (d, *J*= 2.2 Hz, 3H, aryl-*H*), 2.36 (s, 9H, CH₃), 1.33 (s, 27H, *tert*-butyl-*H*) ppm. ¹³C NMR (126 MHz, CDCl₃) δ 148.95 (s), 141.98 (s), 141.45 (s), 132.60 (s), 130.34 (s), 128.83 (s), 127.27 (s), 124.46 (s), 34.61 (s), 31.61 (s), 20.34 (s) ppm. MS (*m/z*): calcd, 516.3756 (M⁺); 516.3739 (FAB-MS, M⁺).

Synthesis of B (R = H)

Analogous protocol to the synthesis of **A** using 2-bromotoluene as the starting reagent to make **B** in 77% yield. The NMR spectra of the product match those of literature.¹⁷

Synthesis of 1b (R = H)

The synthesis of **1b** was adapted and modified from an analogous literature procedure.¹⁸

Potassium *tert*-butoxide (5.10 g, 45.5 mmol) was added under N₂ to an oven-dried Schlenk tube fitted with a screw-in Teflon stopper. THF (140 mL) was then added to the Schlenk tube under nitrogen. The solution was cooled to -78°C. ⁿBuLi solution (2.5 M in hexane, 14.4 mL, 36.1 mmol) was added slowly via syringe under N₂ over 15 min. The mixture was stirred at -78°C for 20 min. A solution of **A** (3.84 g, 11.0 mmol) in dry, degassed THF (20 mL) was canula transferred slowly to the cold super base solution under nitrogen. The resulting solution turned blue then purple after all of **A** had been added. The mixture was stirred at -78°C for 40 min, then allowed to warm to room temperature and stirred for 2 h. Upon stirring for 2 hr at r.t., the homogeneous solution became a heterogeneous suspension with wine-red color precipitate. The suspension was cooled to -78°C, then chlorodiisopropylphosphine (6.3 mL, 39.6 mmol) was added via syringe to the reaction mixture under dinitrogen atmosphere. The reaction mixture turned clear yellow-brown color after all of the chlorodiisopropylphosphine was added. The mixture was allowed to warm to r.t. and stirred overnight. The solvent was removed *in vacuo*. Degassed Et₂O and saturated citric acid solution were added to the residue. The aqueous fraction was discarded, and the organic layer was washed two more times with degassed water. The organic fraction was collected, dried over MgSO₄, and filtered. Removal of solvent under vacuum gave light yellow solid residue. The

residue was washed with CH₃CN three times to give the clean product **1** as white solid in 76% yield (5.8 g, 8.3 mmol).

¹H NMR (500 MHz, C₆D₆) δ 7.67 (dd, 3H, aryl-*H*), 7.54 (s, 3H, central aryl-*H*), 7.44 (dd, 3H, aryl-*H*), 7.13-7.21 (m, 6H, aryl-*H*), 2.91 (s, 6H, CH₂), 1.61 (m, 6H, CH(CH₃)₂), 0.91 (dd, 36H, CH(CH₃)₂) ppm. ³¹P NMR (121 MHz, C₆D₆) δ 11.37 ppm. ¹³C NMR (126 MHz, C₆D₆) δ 142.40 (d, *J* = 3.4 Hz), 142.14 (s), 138.04 (d, *J* = 8.1 Hz), 131.17 (d, *J* = 11.4 Hz), 130.79 (s), 130.22 (s), 127.67 (s), 125.91 (d, *J* = 2.1 Hz), 27.65 (s), 27.47 (s), 23.82 (d, *J* = 16.8 Hz), 19.74 (dd, *J* = 13.0, 6.6 Hz) ppm. MS (*m/z*): calcd, 696.4143 (M⁺); 697.4254 (FAB-MS, M+H).

Synthesis of **1a** (R = *t*Bu)

Similar protocol to synthesize **1b** was carried out to make **1a** in 70% yield.

¹H NMR (300 MHz, C₆D₆) δ 7.69 (s, 3H, aryl-*H*), 7.67 (dd, 3H, aryl-*H*), 7.60 (d, 3H, aryl-*H*), 7.32 (dd, 3H, aryl-*H*), 3.02 (s, 6H, CH₂), 1.65 (m, 6H, CH(CH₃)₂), 1.28 (s, 27H, *tert*-butyl-*H*), 0.99 (dd, 36H, CH(CH₃)₂) ppm. ³¹P NMR (121 MHz, C₆D₆) δ 10.78 ppm. ¹³C NMR (126 MHz, C₆D₆) δ 148.52 (d, *J* = 2.1 Hz), 142.70 (s), 142.22 (d, *J* = 3.3 Hz), 134.88 (d, *J* = 8.0 Hz), 130.89 (d, *J* = 10.9 Hz), 130.33 (s), 124.77 (s), 34.54 (s), 31.61 (s), 27.32 (s), 27.15 (s), 23.81 (d, *J* = 16.9 Hz), 19.86 (dd, *J* = 23.3, 13.1 Hz) ppm. MS (*m/z*): calcd, 864.6021 (M⁺); 865.6099 (FAB-MS, M+H).

Synthesis of **2b-Pd**

1b (100 mg, 0.144 mmol) was transferred into an oven-dried J. Young NMR tube. A solution of Pd(MeCN)₄(BF₄)₂ (64 mg, 0.144 mmol) in CD₃CN (1 mL) was added to the J. Young tube. The J. Young tube was sealed with the fitted Teflon cap, and the mixture

was allowed to react for 2 h at room temperature where everything became homogeneous yellow solution. ^1H and ^{31}P NMR spectra were taken immediately after 2 h where the product was beginning to convert to **3b-Pd**. **2b-Pd** could not be isolated cleanly without further conversion to **3b-Pd**, thus, the NMR spectra collected contained peaks that correspond to the minor **3b-Pd** species in the mixture. NMR peak assignments were done in comparison to **3b-Pd** and the similar Pd-complex supported by diphosphine ligand variant **2c-Pd**. ^1H NMR (300 MHz, CD_3CN) δ 7.81 (b, 1H, aryl-*H*), 7.75 (s, 1H, aryl-*H*), 7.67 (app d, $J = 1.3$ Hz, 2H, aryl-*H*), 7.52 – 7.42 (m, 10H, aryl-*H*), 7.28 (m, 1H, aryl-*H*), 3.69 (b, 4H, unbound phosphine arm CH_2), 2.91 (s, 2H, unbound phosphine arm CH_2), 2.46 – 2.31 (m, 6H, *CH*), 1.98 (s, 6H, CH_3CN), 1.30 (app dd, $J = 15.9, 8.1$ Hz, 24H, bound phosphine arm $\text{CH}(\text{CH}_3)_2$), 0.86 (app dd, $J = 12.2, 7.1$ Hz, 12H, unbound phosphine arm $\text{CH}(\text{CH}_3)_2$) ppm. ^{31}P NMR (121 MHz, CD_3CN) δ 39.99 (s, 2P), 13.57 (s, 1P) ppm. ^{13}C NMR (126 MHz, CD_3CN) δ 143.95 (s), 142.78 (s), 142.21 (s), 141.10 (s), 132.96 (s), 132.65 (s), 131.68 (s), 131.35 (s), 131.04 (s), 130.86 (s), 130.42 (s), 129.93 (s), 129.74 (s), 129.43 (s), 128.93 (s), 126.90 (s), 28.60 (s), 28.07 – 27.00 (m), 23.86 (d, $J = 15.6$ Hz), 19.63 (d, $J = 11.3$ Hz), 19.31 (s), 18.88 (s) ppm.

Synthesis of **1c**

Similar procedure to make **1b** was carried out to synthesize **1c** using 1,3-dibromobenzene as the starting reagent.^{8a,8c} The number of equivalents of reagents was adjusted to synthesize the diphosphine ligand variant. The product was isolated as pale yellow oil in 80% yield. ^1H NMR (300 MHz, C_6D_6) δ 7.61 (app d, $J = 7.7$ Hz, 1H), 7.45 (app t, $J = 1.6$ Hz, 1H), 7.34 – 7.21 (m, 5H), 7.17 – 7.01 (m, 5H), 2.85 (d, $J = 1.7$ Hz, 2H), 1.50 (dtd, $J = 14.1, 7.0, 1.5$ Hz, 4H), 0.90 – 0.80 (dd, $J = 12.4, 7.1$ Hz, 24H) ppm.

^{31}P NMR (121 MHz, C_6D_6) δ 11.64 (s) ppm. ^{13}C NMR (126 MHz, C_6D_6) δ 142.47 (d, J = 3.4 Hz), 142.37 (s), 137.98 (d, J = 8.3 Hz), 131.89 (s), 131.08 (d, J = 11.4 Hz), 130.71 (d, J = 2.6 Hz), 128.67 (d, J = 1.9 Hz), 127.96 (s), 127.62 (s), 125.91 (d, J = 2.2 Hz), 27.41 (d, J = 22.1 Hz), 23.73 (d, J = 16.8 Hz), 19.67 (dd, J = 13.1, 9.4 Hz) ppm. MS (m/z): calcd, 490.2918 (M+); 490.2922 (FAB-MS, M+H).

Synthesis of 2c-Pd

1c (1 g, 2.04 mmol) and $\text{Pd}(\text{MeCN})_4(\text{BF}_4)_2$ (906 mg, 2.04 mmol) were suspended in MeCN (80 mL). The reaction mixture was stirred at r.t. for 16 h or monitored by ^{31}P NMR spectroscopy. Solvent was removed under vacuum, and the residue was washed with CH_2Cl_2 to give the clean insoluble product as pale yellow solid in 65% yield (1.13g, 1.33 mmol). The product can be recrystallized from acetonitrile/toluene solution mixture. ^1H NMR (300 MHz, CD_3CN) δ 7.72 (s, 1H, aryl-*H*), 7.69 – 7.66 (m, 1H, aryl-*H*), 7.60 (app d, J = 1.5 Hz, 1H, aryl-*H*), 7.58 (br s, 1H, aryl-*H*), 7.50 – 7.39 (m, 8H, aryl-*H*), 3.63 (s, 4H, CH_2), 2.40 – 2.26 (m, 4H, $\text{CH}(\text{CH}_3)_2$), 1.95 (s, theoretical 6H, CH_3CN), 1.31 – 1.14 (m, 24H, $\text{CH}(\text{CH}_3)_2$) ppm. ^{31}P NMR (121 MHz, CD_3CN) δ 39.70 (s) ppm. ^{13}C NMR (126 MHz, CD_3CN) δ 143.12 (s), 142.53 (s), 132.86 (t, J = 2.4 Hz), 132.41 (s), 130.86 (t, J = 2.9 Hz), 130.83 (s), 130.21 (s), 129.64 (s), 129.36 (s), 129.30 (s), 28.17 (app t, J = 9.0 Hz), 26.75 (s), 19.07 (d, J = 22.3 Hz) ppm. Anal. Calcd. for: $\text{C}_{36}\text{H}_{50}\text{B}_2\text{F}_8\text{N}_2\text{P}_2\text{Pd}$ (**2c-Pd**) (%): C, 50.70; H, 5.91; N, 3.28. Anal. Calcd. for: $\text{C}_{38}\text{H}_{53}\text{B}_2\text{F}_8\text{N}_3\text{P}_2\text{Pd}$ (**2c-Pd MeCN**) (%): C, 51.06; H, 5.98; N, 4.70. Found: C, 51.06; H, 5.76; N, 4.72.

Synthesis of 3a-Ni

A solution of **1a** (500 mg, 0.72 mmol) in THF (10 mL) and a suspension of $\text{Ni}(\text{OTf})_2$ (513 mg, 1.44 mmol) in CH_3CN (20 mL) were added to an oven-dried Schlenk tube

fitted with a screw-in Teflon stopper. The mixture was heated to 65°C for 40 h where the color of the solution turned red-orange. The solvent was removed under vacuum. The dried residue was washed with Et₂O to remove unreacted ligand. The rest of the residue was resuspended in minimal amount of CH₃CN and filtered. Et₂O was added carefully to the solution to precipitate out light purple solid. The light purple solid (possibly some nickel salts) was filtered off and discarded. The remaining filtrate was further concentrated *in vacuo*, and Et₂O was added to the concentrated solution to precipitate/crystallize out the product cleanly as red-orange crystalline solid in 51% yield (450 mg, 0.37 mmol).

¹H NMR (300 MHz, CD₃CN) δ 7.85 (d, *J* = 1.8 Hz, 1H, side aryl-*H*), 7.82 (d, *J* = 1.9 Hz, 1H, side aryl-*H*), 7.63 (d, *J* = 1.8 Hz, 1H, side aryl-*H*), 7.62 (d, *J* = 1.8 Hz, 1H, side aryl-*H*), 7.48-7.54 (m, 3H, side aryl-*H*), 7.40 (s, 1H, side aryl-*H*), 7.24 (app d, *J* = 8.1 Hz, 1H, side aryl-*H*), 6.42 (app d, *J* = 3.4 Hz, 1H, central ring-*H*), 6.39 (s, 1H, central ring-*H*), 3.86 – 3.66 (m, 2H, central ring sp³-*H* and CH₂), 3.57 – 3.43 (m, 2H, CH₂), 3.39 (d, *J* = 15.2 Hz, 1H, CH₂), 3.21 (d, *J* = 15.3 Hz, 1H, CH₂), 3.09 (dd, *J* = 15.4, 3.6 Hz, 1H, CH₂), 2.85 – 2.69 (m, 1H, CH), 2.58 – 2.43 (m, 2H, CH), 2.30 – 2.18 (m, 1H, CH), 2.17 – 2.03 (m, 1H, CH), 2.04 – 1.94 (m, 1H, CH), 1.69 (dd, *J* = 15.3, 8.1 Hz, 3H, CH₃), 1.50 (dd, *J* = 15.8, 7.1 Hz, 3H, CH₃), 1.45 – 1.27 (m, 12H, CH₃), 1.44 (s, 9H, *tert*-butyl-CH₃), 1.42 (s, 9H, *tert*-butyl-CH₃), 1.32 (s, 9H, *tert*-butyl-CH₃), 1.16 (app dd, *J* = 17.6, 7.1 Hz, 3H, CH₃), 0.92 (app dd, *J* = 12.4, 6.8 Hz, 3H, CH₃), 0.66 (app ddd, *J* = 14.7, 11.7, 7.0 Hz, 6H, CH₃), 0.51 – 0.35 (m, 6H, CH₃) ppm. ³¹P NMR (121 MHz, CD₃CN) δ 73.99 (dd, *J* = 14.0, 5.1 Hz), 63.76 (dd, *J* = 45.3, 5.1 Hz), 31.44 (dd, *J* = 45.2, 14.0 Hz) ppm. ¹³C NMR (126 MHz, CD₃CN) δ 152.77 (s), 152.20 (s), 151.93 (s), 136.18 (s), 134.47 (s), 134.21 (s), 133.48 (s), 132.01 (s), 131.67 (s), 131.36 (s), 131.26 (s), 131.21 – 131.05 (m),

128.62 (s), 128.43 (d, $J = 18.0$ Hz), 127.99 (s), 126.56 (s), 125.49 (s), 123.98 (s), 123.71 (s), 120.35 (s), 101.24 (s), 93.20 (s), 82.99 (s), 67.62 (s), 38.01 (d, $J = 16.9$ Hz), 34.97 (s), 34.81 (s), 30.87 (s), 30.76 (s), 30.60 (s), 28.61 (d, $J = 22.0$ Hz), 28.16 (d, $J = 21.3$ Hz), 27.14 (d, $J = 18.5$ Hz), 26.79 (d, $J = 21.5$ Hz), 25.61 (s), 23.25 (s), 23.11 (s), 22.87 (s), 20.98 (s), 20.83 (s), 20.48 (s), 20.13 (s), 20.02 (s), 19.40 (s), 18.00 (s), 17.80 (s), 17.47 (s), 17.12 (s), 16.55 (s), 15.75 (s), 14.70 (s) ppm. Anal. Calcd. for: $C_{59}H_{87}F_6NiO_6P_3S_2$ (%): C, 57.99; H, 7.18. Found: C, 57.84; H, 7.03. λ_{max} (CH₃CN, nm), ϵ (M⁻¹cm⁻¹): 502, 1.61×10^3 ; 427, 2.89×10^3 ; 359, 7.84×10^3 ; 291, 1.28×10^3 .

Synthesis of 3b-Ni

3b-Ni was synthesized in 60% yield using an analogous protocol to make **3a-Ni**.

¹H NMR (300 MHz, CD₃CN) δ 7.96 (m, 1H, aryl-*H*), 7.88 (m, 1H, aryl-*H*), 7.53-7.58 (m, 8H, aryl-*H*), 7.42 (app d, $J = 6.3$ Hz, 1H, aryl-*H*), 7.38 (app d, $J = 4.6$ Hz, 1H, aryl-*H*), 7.30 (app d, $J = 7.4$ Hz, 1H), 6.43 (app d, $J = 3.2$ Hz, 1H, central aryl-*H*), 6.24 (s, 1H, central aryl-*H*), 3.87 (ddd, $J = 25.4, 14.4, 8.5$ Hz, 2H, central ring sp³-*H*, CH₂), 3.50 (ddd, $J = 20.7, 14.8, 10.0$ Hz, 3H, CH₂), 3.27 (d, $J = 14.8$ Hz, 1H, CH₂), 3.17 (dd, $J = 15.4, 4.2$ Hz, 1H, CH₂), 2.73 (m, 1H, CH), 2.50 (m, 2H, CH), 2.39 (m, 1H, CH), 2.11 (m, 1H, CH), 1.99 (m, 1H, CH), 1.72 (dd, $J = 17.2, 7.2$ Hz, 3H, CH₃), 1.52 – 1.27 (m, 15H, CH₃), 1.17 (dd, $J = 17.7, 7.1$ Hz, 3H, CH₃), 0.89 (dd, $J = 12.2, 5.5$ Hz, 3H, CH₃), 0.71 – 0.58 (m, 6H, CH₃), 0.51 (dd, $J = 18.3, 7.0$ Hz, 3H, CH₃), 0.35 (dd, $J = 17.0, 7.4$ Hz, 3H, CH₃) ppm. ³¹P NMR (121 MHz, CD₃CN) δ 75.69 (dd, $J = 14.0, 4.7$ Hz), 63.92 (dd, $J = 43.7, 4.8$ Hz), 31.74 (dd, $J = 43.6, 14.0$ Hz) ppm. ¹³C NMR (126 MHz, CD₃CN) δ 137.86 (s), 137.08 (s), 135.42 (s), 134.75 (d, $J = 4.3$ Hz), 134.54 (d, $J = 5.9$ Hz), 131.88 (d, $J = 7.9$ Hz), 131.75 (s), 131.62 (d, $J = 5.7$ Hz), 131.38 (s), 131.11 (s), 131.01 (s),

130.14 (s), 129.90 (s), 129.24 (s), 129.11 (s), 127.48 (s), 127.17 (d, $J = 6.8$ Hz), 126.36 (d, $J = 11.6$ Hz), 123.03 (s), 121.42 (s), 120.48 (s), 101.87 (s), 92.93 (d, $J = 9.3$ Hz), 82.75 (s), 38.16 (d, $J = 22.9$ Hz), 29.03 (d, $J = 22.1$ Hz), 28.47 (d, $J = 21.4$ Hz), 27.33 (d, $J = 18.4$ Hz), 27.00 (d, $J = 21.6$ Hz), 23.99 (d, $J = 18.5$ Hz), 22.67 (s), 21.36 (d, $J = 5.6$ Hz), 20.98 (d, $J = 4.1$ Hz), 20.81 (d, $J = 21.8$ Hz), 20.41 (d, $J = 38.3$ Hz), 20.36 (s), 19.51 (s), 18.28 (s), 18.08 (d, $J = 3.4$ Hz), 17.99 (d, $J = 5.0$ Hz), 17.84 (s), 17.74 (d, $J = 4.4$ Hz), 16.90 (d, $J = 6.5$ Hz), 16.29 (d, $J = 4.3$ Hz), 15.08 (d, $J = 3.1$ Hz) ppm.

Synthesis of 3a-Pd

A solution of Pd(MeCN)₄(BF₄)₂ (25.7 mg, 0.0578 mmol) in CH₃CN (5 mL) was added to **1a** (50 mg, 0.0578 mmol). The resulting suspension was stirred and heated to 55°C for 4 h, when the mixture became homogeneous yellow. The solvent was removed *in vacuo* to give the product as a yellow solid analytically clean by ³¹P NMR spectroscopy. Attempts to grow X-ray quality single crystals have been unsuccessful to date. This material was utilized in the subsequent step without further purification.

¹H NMR (300 MHz, CD₃CN) δ 7.80 (s, 1H, aryl-*H*), 7.77 (d, $J = 1.6$ Hz, 1H, aryl-*H*), 7.61 – 7.55 (m, 4H, aryl-*H*), 7.49 (d, $J = 8.1$ Hz, 1H, aryl-*H*), 7.25 (d, $J = 8.2$ Hz, 1H aryl-*H*), 7.22 (d, $J = 1.7$ Hz, 1H, aryl-*H*), 6.54 (app d, $J = 3.5$ Hz, 1H, central ring-*H*), 6.50 (app d, $J = 1.3$ Hz, 1H, central ring-*H*), 4.19 (m, 1H, central ring sp³-*H*), 3.62-3.75 (m, 2H, CH₂), 3.46-3.57 (m, 2H, CH₂), 3.29 (d, $J = 14.6$ Hz, 1H, CH₂), 3.05 (dd, $J = 14.8, 3.2$ Hz, 1H, CH₂), 2.89 (m, 1H, CH), 2.51 (m, 2H, CH), 2.30 (m, 1H, CH), 2.16 (m, 1H, CH), 2.04 (m, 1H, CH), 1.69 (dd, $J = 17.0, 7.2$ Hz, 3H, CH₃), 1.41 (s, 9H, *tert*-butyl CH₃), 1.40 (s, 9H, *tert*-butyl CH₃), 1.53 – 1.08 (m, 18H, CH₃), 1.27 (s, 9H, *tert*-butyl CH₃), 0.69 (ddd, $J = 24.6, 15.7, 7.0$ Hz, 6H, CH₃), 0.45 (ddd, $J = 21.2, 17.1, 7.1$ Hz, 9H,

CH_3) ppm. ^{31}P NMR (121 MHz, CD_3CN) δ 87.34 (dd, $J = 37.8, 32.6$ Hz), 80.09 (dd, $J = 65.6, 32.4$ Hz), 40.29 (dd, $J = 65.6, 38.0$ Hz) ppm. ^{13}C NMR (126 MHz, CD_3CN) δ 153.48 (s), 152.83 (s), 152.58 (s), 136.06 (s), 135.88 (s), 135.18 (d, $J = 4.2$ Hz), 133.77 (d, $J = 20.9$ Hz), 132.99 (d, $J = 5.1$ Hz), 132.15 (d, $J = 5.2$ Hz), 131.57 (s), 131.47 (s), 129.30 (s), 128.93 (s), 128.84 (s), 128.65 (s), 127.28 (d, $J = 5.6$ Hz), 126.31 (s), 124.39 (s), 124.33 (s), 124.15 (s), 107.54 (s), 102.09 (d, $J = 20.4$ Hz), 94.12 (dd, $J = 24.1, 4.7$ Hz), 38.60 (d, $J = 15.2$ Hz), 35.55 (s), 35.38 (d, $J = 1.9$ Hz), 31.43 (s), 31.32 (s), 31.23 (s), 27.80 (d, $J = 12.8$ Hz), 27.67 (d, $J = 6.0$ Hz), 27.54 (d, $J = 13.9$ Hz), 27.36 (d, $J = 16.7$ Hz), 26.89 (d, $J = 15.5$ Hz), 24.12 (d, $J = 31.7$ Hz), 22.93 (d, $J = 16.8$ Hz), 21.51 (d, $J = 37.5$ Hz), 20.06 (s), 20.02 (s), 19.95 (d, $J = 5.2$ Hz), 19.68 (d, $J = 3.4$ Hz), 18.47 (s), 18.24 (s), 18.21 (s), 18.10 (s), 17.88 (s), 17.87 (s), 17.21 (d, $J = 4.0$ Hz), 16.36 (d, $J = 4.1$ Hz), 15.34 (d, $J = 3.0$ Hz) ppm.

Synthesis of **3b-Pd**

3b-Pd was synthesized analogously to **3a-Pd**.

1H NMR (300 MHz, CD_3CN) δ 7.95 (m, 1H, aryl-*H*), 7.86 (dd, $J = 6.8, 2.1$ Hz, 1H, aryl-*H*), 7.68 – 7.61 (m, 2H, aryl-*H*), 7.58 – 7.52 (m, 3H, aryl-*H*), 7.48 – 7.43 (m, 3H, aryl-*H*), 7.36 (m, 2H, aryl-*H*), 7.31 (app d, $J = 7.5$ Hz, 1H, aryl-*H*), 6.55 (app d, $J = 3.4$ Hz, 1H, central ring-*H*), 6.36 (app m, 1H, central ring-*H*), 4.30 (m, 1H, central ring sp^3 -*H*), 3.84 – 3.49 (m, 4H, CH_2), 3.32 (d, $J = 15.1$ Hz, 1H, CH_2), 3.13 (dd, $J = 14.7, 3.5$ Hz, 1H, CH_2), 2.84 (m, 1H, *CH*), 2.50 (m, 2H, *CH*), 2.35 (m, 1H, *CH*), 2.17 (m, 1H, *CH*), 2.02 (m, 1H, *CH*), 1.69 (dd, $J = 17.3, 7.3$ Hz, 3H, CH_3), 1.45 – 1.41 (m, 3H, CH_3), 1.39 – 1.37 (m, 3H, CH_3), 1.35 – 1.32 (m, 3H, CH_3), 1.31 – 1.24 (m, 6H, CH_3), 1.21 – 1.10 (m, 6H, CH_3), 0.85 (dd, $J = 12.2, 7.1$ Hz, 3H, CH_3), 0.67 (dd, $J = 13.7, 7.1$ Hz, 3H,

CH_3), 0.61 – 0.55 (m, 3H, CH_3), 0.53 – 0.46 (m, 3H, CH_3), 0.39 (dd, $J = 17.4, 7.3$ Hz, 3H, CH_3) ppm. ^{31}P NMR (121 MHz, CD_3CN) δ 86.08 (dd, $J = 37.0, 32.4$ Hz), 78.94 (dd, $J = 63.3, 32.9$ Hz), 38.16 (dd, $J = 63.4, 37.6$ Hz) ppm. ^{13}C NMR (126 MHz, CD_3CN) δ 138.82 (s), 136.97 (s), 136.68 (t, $J = 5.1$ Hz), 135.28 (d, $J = 4.5$ Hz), 134.46 (t, $J = 3.8$ Hz), 132.99 (d, $J = 5.5$ Hz), 132.41 (d, $J = 5.4$ Hz), 131.78 (t, $J = 6.2$ Hz), 131.48 (s), 131.45 (s), 130.51 (d, $J = 8.3$ Hz), 130.49 (s), 129.82 (d, $J = 4.6$ Hz), 129.73 (d, $J = 2.1$ Hz), 129.51 (s), 129.05 (dd, $J = 10.1, 6.7$ Hz), 127.58 (s), 127.58 (s), 127.25 (d, $J = 7.0$ Hz), 127.25 (d, $J = 7.0$ Hz), 125.20 (s), 107.83 (s), 101.32 (d, $J = 19.3$ Hz), 93.64 (dd, $J = 24.6, 5.1$ Hz), 38.44 (d, $J = 21.7$ Hz), 27.87 (s), 27.71 (s), 27.66 (s), 27.52 (d, $J = 6.7$ Hz), 27.42 (s), 27.29 (s), 23.66 (d, $J = 31.5$ Hz), 23.42 (d, $J = 16.6$ Hz), 21.11 (d, $J = 37.8$ Hz), 20.03 (d, $J = 3.2$ Hz), 19.93 (d, $J = 4.8$ Hz), 18.82 (d, $J = 33.8$ Hz), 18.51 (s), 18.44 – 18.32 (m), 18.24 (d, $J = 2.2$ Hz), 17.98 (d, $J = 1.9$ Hz), 17.87 (d, $J = 2.2$ Hz), 17.31 (d, $J = 4.1$ Hz), 16.65 (d, $J = 4.1$ Hz), 15.51 (d, $J = 3.1$ Hz) pm. λ_{max} (CH_3CN , nm), ϵ ($\text{M}^{-1}\text{cm}^{-1}$): 381, 8.66×10^3 ; 331, 1.06×10^4 ; 288, 1.35×10^4 .

Synthesis of 4a-Ni

To a solution of **3a-Ni** (50 mg, 0.041 mmol) in CH_3CN (5 mL) was added sodium acetate (3.4 mg, 0.041 mmol). The mixture was stirred at room temperature for 16 h monitored by ^{31}P NMR spectroscopy. The resulting red-orange solution was filtered and dried under vacuum. The dried residue was taken up in minimal amount of THF to make a concentrated solution, and then hexanes were added to precipitate out product. The precipitate was taken up in diethyl ether. The ether soluble material was dried under vacuum to give the clean product in 65% yield (29 mg, 0.027 mmol). Attempts to obtain crystalline material have been unsuccessful thus far.

^1H NMR (300 MHz, CD_3CN) δ 7.68 (d, $J = 2.0$ Hz, 1H, aryl- H), 7.49 (dt, $J = 4.9, 2.4$ Hz, 2H, aryl- H), 7.37 (s, 1H, aryl- H), 7.34 (s, 1H, aryl- H), 7.28 (app d, $J = 0.9$ Hz, 2H, aryl- H), 7.23 (app d, $J = 8.0$ Hz, 1H, aryl- H), 7.15 (s, 1H, aryl- H), 6.47 (app m, 1H, central aryl- H), 4.56 (s, 1H, central aryl- H), 3.46 – 3.28 (m, 3H, CH_2), 3.15 (ddd, $J = 17.2, 12.4, 2.9$ Hz, 2H, CH_2), 2.76 (t, $J = 12.4$ Hz, 1H, CH_2), 2.39 (m, 1H, CH), 2.21 (m, 2H, CH), 1.86 (m, 3H, CH), 1.40 (s, 9H, *tert*-butyl CH_3), 1.37 – 1.32 (m, 3H, CH_3), 1.32 (s, 9H, *tert*-butyl CH_3), 1.29 (s, 9H, *tert*-butyl CH_3), 1.25 (m, 3H, CH_3), 1.20 – 1.14 (m, 3H, CH_3), 1.09 (m, 6H, CH_3), 1.01 – 0.88 (m, 6H, CH_3), 0.82-0.72 (m, 9H, CH_3), 0.60 – 0.47 (m, 6H, CH_3).

^{31}P NMR (121 MHz, CD_3CN) δ 55.39 (dd, $J = 69.3, 7.6$ Hz), 35.52 (d, $J = 69.3$ Hz), 24.51 (d, $J = 7.5$ Hz) ppm. ^{13}C NMR (126 MHz, CD_3CN) δ 156.65 (s), 152.88 (s), 151.25 (s), 150.88 (s), 142.95 (s), 141.97 (d, $J = 10.6$ Hz), 138.01 (d, $J = 6.8$ Hz), 135.08 (s), 134.38 (s), 131.71 (s), 131.28 (d, $J = 4.2$ Hz), 130.94 (s), 130.35 (d, $J = 8.0$ Hz), 127.06 (s), 125.67 (s), 125.40 (s), 125.02 (s), 123.99 (s), 123.87 (s), 122.20 (d, $J = 8.2$ Hz), 117.56 (s), 88.39 (d, $J = 94.4$ Hz), 70.30 (d, $J = 13.1$ Hz), 68.70 (s), 35.37 (s), 35.15 (s), 34.86 (s), 31.52 (s), 31.46 (s), 31.37 (s), 27.05 (d, $J = 17.1$ Hz), 26.65 (d, $J = 15.7$ Hz), 26.17 (s), 26.02 (d, $J = 7.4$ Hz), 25.97 (d, $J = 5.3$ Hz), 25.43 (d, $J = 16.1$ Hz), 23.36 (s), 23.25 (d, $J = 10.6$ Hz), 23.00 (s), 20.25 (d, $J = 4.6$ Hz), 20.19 (d, $J = 3.2$ Hz), 19.99 (s), 19.92 (d, $J = 6.5$ Hz), 19.59 (s), 19.31 (s), 18.84 (s), 17.92 (s), 17.88 (s), 16.92 (s), 16.57 (d, $J = 2.8$ Hz), 16.10 (s) ppm. Anal. Calcd. for: $\text{C}_{58}\text{H}_{86}\text{F}_3\text{NiO}_3\text{P}_3\text{S}_2$ (%): C, 64.98; H, 8.09. Found: C, 64.87; H, 7.99. λ_{max} (CH_3CN , nm), ϵ ($\text{M}^{-1}\text{cm}^{-1}$): 477, 3.72×10^3 ; 384, 1.13×10^4 ; 325, 6.78×10^3

Synthesis of 4b-Ni

4b-Ni was synthesized analogously to **4a-Ni** in 67% yield. The crystalline product can be obtained through vapor diffusion of hexanes into a THF solution of the material.

^1H NMR (500 MHz, CD_3CN) δ 7.66 (m, 1H, aryl-*H*), 7.51 (app d, $J = 7.7$ Hz, 1H, aryl-*H*), 7.46 – 7.40 (m, 3H, aryl-*H*), 7.35 (app d, $J = 6.9$ Hz, 1H, aryl-*H*), 7.33 – 7.25 (m, 3H, aryl-*H*), 7.22 – 7.13 (m, 2H, aryl-*H*), 7.10 (m, 1H, aryl-*H*), 6.51 (m, 1H, central aryl-*H*), 4.56 (app td, $J = 4.8, 2.0$ Hz, 1H, central aryl-*H*), 3.36 (m, 3H, CH_2), 3.23 – 3.12 (m, 2H, CH_2), 2.78 (app t, $J = 12.3$ Hz, 1H, CH_2), 2.40 (ddd, $J = 14.2, 11.1, 7.1$ Hz, 1H, *CH*), 2.16 (ddt, $J = 19.6, 14.0, 6.9$ Hz, 2H, *CH*), 1.85 (ddd, $J = 15.3, 14.7, 7.1$ Hz, 2H, *CH*), 1.27 (ddd, $J = 23.1, 13.8, 6.7$ Hz, 6H, CH_3), 1.17 (dd, $J = 17.6, 10.5$ Hz, 3H, CH_3), 1.12 – 1.00 (m, 9H, CH_3), 0.93 (dd, $J = 17.2, 6.9$ Hz, 3H, CH_3), 0.81 – 0.69 (m, 9H, CH_3), 0.62 (dd, $J = 14.9, 7.3$ Hz, 3H, CH_3), 0.53 (dd, $J = 14.3, 6.9$ Hz, 3H, CH_3) ppm. ^{31}P NMR (121 MHz, CD_3CN) δ 57.24 (dd, $J = 68.6, 7.5$ Hz), 34.53 (d, $J = 68.6$ Hz), 24.91 (d, $J = 7.2$ Hz) ppm. ^{13}C NMR (126 MHz, CD_3CN) δ 155.73 (s), 142.76 (s), 142.29 (d, $J = 11.9$ Hz), 138.11 (s), 137.98 (d, $J = 7.0$ Hz), 137.03 (d, $J = 4.1$ Hz), 131.68 (d, $J = 3.5$ Hz), 131.40 (d, $J = 4.8$ Hz), 130.44 (s), 130.38 (s), 129.96 (s), 129.36 – 129.25 (m), 129.32 – 129.14 (m), 128.58 (s), 127.87 (s), 127.83 (s), 127.60 (s), 127.28 (s), 126.69 (s), 126.59 (s), 124.79 (d, $J = 7.4$ Hz), 88.51 (d, $J = 87.3$ Hz), 68.97 (d, $J = 13.4$ Hz), 66.74 (s), 26.90 (d, $J = 17.2$ Hz), 26.57 (d, $J = 16.1$ Hz), 26.33 (dd, $J = 13.2, 5.1$ Hz), 25.82 (d, $J = 16.1$ Hz), 25.14 (s), 25.01 (s), 24.69 (s), 23.53 (d, $J = 6.1$ Hz), 22.83 (s), 22.47 (s), 19.96 (d, $J = 6.0$ Hz), 19.74 (d, $J = 7.4$ Hz), 19.40 (d, $J = 6.4$ Hz), 19.17 (dd, $J = 11.3, 4.5$ Hz), 18.01 (s), 17.89 (s), 17.75 (d, $J = 3.1$ Hz), 17.64 (s), 16.62 (s), 16.39 (d, $J = 2.9$ Hz), 15.87 (s).

Synthesis of 4a-Pd

To a solution of **3a-Pd** (66 mg, 0.058 mmol) in CH₃CN (6 mL) was added sodium acetate (5 mg, 0.058 mmol). The mixture turned bright orange yellow over 6 h and was stirred at room temperature for 16 h or monitored by ³¹P NMR spectroscopy. The solvent was removed under vacuum to give yellow-orange residue. The residue was taken up in benzene and hexanes were added to precipitate out the clean product as waxy, oily material. The waxy residue was dried under vacuum to yield the clean product as yellow-orange solid in 61% yield (37 mg, 0.035 mmol). Several recrystallization conditions have been attempted, but no crystalline material has been obtained thus far.

¹H NMR (300 MHz, CD₃CN) δ 7.77 (d, *J* = 2.0 Hz, 1H, aryl-*H*), 7.48 (dd, *J* = 8.1, 2.0 Hz, 1H, aryl-*H*), 7.43 (s, 1H, aryl-*H*), 7.36 – 7.30 (m, 1H, aryl-*H*), 7.24 (s, 1H, aryl-*H*), 7.22 (s, 1H, aryl-*H*), 7.10 (d, *J* = 1.9 Hz, 1H, aryl-*H*), 7.03 (d, *J* = 1.9 Hz, 1H, central aryl-*H*), 5.47 (d, *J* = 1.9 Hz, 1H, central aryl-*H*), 3.46 – 3.17 (m, 1H, CH₂), 3.08 (app dd, *J* = 12.9, 3.4 Hz, 1H, CH₂), 2.78 (m, 1H, CH₂), 2.47 (m, 1H, CH), 2.16 (m, 1H, CH), 1.97 (m, 1H, CH), 1.84 (m, 1H, CH), 1.58 (m, 1H, CH), 1.36 (s, 9H, *tert*butyl- CH₃), 1.33 – 1.29 (m, 3H, CH₃), 1.27 (s, 9H, *tert*butyl- CH₃), 1.23 (s, 9H, *tert*butyl- CH₃), 1.14 (m, 9H, CH₃), 1.05 (m, 3H, CH₃), 1.03 – 0.92 (m, 9H, CH₃), 0.78 – 0.68 (m, 3H, CH₃), 0.66 – 0.62 (m, 3H, CH₃), 0.59 – 0.48 (m, 6H, CH₃) ppm. ³¹P NMR (121 MHz, CD₃CN) δ 62.55 (dd, *J* = 80.0, 7.9 Hz), 32.14 (d, *J* = 80.1 Hz), 27.05 (d, *J* = 7.7 Hz) ppm. ¹³C NMR (126 MHz, CD₃CN) δ 153.30 (s), 151.60 – 151.41 (m), 151.30 (d, *J* = 1.9 Hz), 150.99 (d, *J* = 2.5 Hz), 142.34 (s), 141.48 (d, *J* = 11.0 Hz), 137.65 (d, *J* = 5.2 Hz), 136.37 – 135.94 (m), 133.67 (d, *J* = 3.2 Hz), 130.70 (d, *J* = 8.2 Hz), 129.27 (s), 127.36 (s), 126.09 (s), 125.57 (s), 124.65 (s), 124.47 (s), 122.52 (d, *J* = 8.9 Hz), 120.82 (s), 92.77 (s),

92.01 (d, $J = 12.3$ Hz), 79.71 (s), 35.53 (s), 35.30 (s), 35.03 (s), 31.62 (s), 31.54 (s), 31.52 (s), 27.68 (s), 26.76 (d, $J = 7.8$ Hz), 26.67 (d, $J = 6.0$ Hz), 26.34 (d, $J = 9.8$ Hz), 25.14 (d, $J = 9.9$ Hz), 24.31 (s), 23.47 (s), 23.12 (s), 20.40 (d, $J = 5.2$ Hz), 20.34 (s), 20.27 (d, $J = 8.0$ Hz), 19.88 (d, $J = 7.4$ Hz), 19.56 (s), 19.27 (d, $J = 4.9$ Hz), 19.10 (d, $J = 3.4$ Hz), 19.02 (d, $J = 4.7$ Hz), 18.83 (d, $J = 2.8$ Hz), 18.62 (s), 18.04 (d, $J = 2.3$ Hz), 17.05 (d, $J = 3.0$ Hz), 16.51 (d, $J = 1.9$ Hz) ppm.

Synthesis of 4b-Pd

4a-Pd was synthesized analogously to **4b-Pd**. Recrystallization via vapor diffusion of diethyl ether into a CH_3CN solution of the material afforded the clean product as orange X-ray quality single crystals in 72% yield. ^1H NMR (500 MHz, CD_3CN) δ 7.74 (m, 1H, aryl-*H*), 7.50 (m, 1H, aryl-*H*), 7.47 (m, 1H, aryl-*H*), 7.44 (m, 1H, aryl-*H*), 7.35 (m, 1H, aryl-*H*), 7.32 (app d, $J = 7.9$ Hz, 1H, aryl-*H*), 7.29 (m, 1H, aryl-*H*), 7.22 – 7.18 (m, 2H, aryl-*H*), 7.08 (m, 1H, aryl-*H*), 7.06 (m, 1H, central aryl-*H*), 5.52 (m, 1H, central aryl-*H*), 3.45 (m, 2H, CH_2), 3.38 – 3.27 (m, 2H, CH_2), 3.14 (app dd, $J = 12.9, 3.8$ Hz, 1H, CH_2), 2.83 (m, 1H, CH_2), 2.48 (m, 1H, CH), 2.18 (m, 1H, CH), 1.94 – 1.84 (m, 2H, CH), 1.79 (m, 1H, CH), 1.62 (m, 1H, CH), 1.25 (dd, $J = 11.9, 6.9$ Hz, 3H, CH_3), 1.17 (dd, $J = 11.7, 5.8$ Hz, 3H, CH_3), 1.14 – 1.07 (m, 3H, CH_3), 1.06 – 0.98 (m, 12H, CH_3), 0.79 (dd, $J = 16.6, 8.3$ Hz, 3H, CH_3), 0.72 (dd, $J = 13.4, 6.7$ Hz, 3H, CH_3), 0.67 (dd, $J = 16.8, 7.4$ Hz, 3H, CH_3), 0.61 (dd, $J = 7.0, 3.3$ Hz, 3H, CH_3), 0.58 (dd, $J = 7.0, 1.9$ Hz, 3H, CH_3) ppm. ^{31}P NMR (121 MHz, CD_3CN) δ 64.67 (dd, $J = 77.1, 8.0$ Hz), 31.76 (d, $J = 77.2$ Hz), 27.41 (d, $J = 8.1$ Hz) ppm. ^{13}C NMR (126 MHz, CD_3CN) δ 150.87 (s), 142.40 (s), 141.95 (d, $J = 10.8$ Hz), 139.63 – 139.18 (m), 137.92 (d, $J = 7.5$ Hz), 136.81 (d, $J = 3.5$ Hz), 132.70 (d, $J = 4.5$ Hz), 132.62 (d, $J = 3.5$ Hz), 131.22 (s), 130.96 (d, $J = 8.3$ Hz),

130.50 (s), 130.44 (s), 129.90 (s), 128.83 (s), 128.42 (s), 128.25 (d, $J = 1.8$ Hz), 127.91 (s), 127.66 (d, $J = 2.1$ Hz), 127.47 (s), 125.42 (d, $J = 8.3$ Hz), 121.23 (s), 92.30 (d, $J = 90.8$ Hz), 90.38 (d, $J = 16.6$ Hz), 78.02 (s), 28.22 (s), 26.83 (d, $J = 10.5$ Hz), 26.73 (d, $J = 12.0$ Hz), 26.43 (d, $J = 10.2$ Hz), 25.21 (s), 25.17 (s), 25.13 (s), 23.21 (s), 22.86 (s), 20.59 (d, $J = 8.8$ Hz), 20.17 (d, $J = 10.5$ Hz), 19.98 (d, $J = 2.5$ Hz), 19.91 (s), 19.34 (d, $J = 5.2$ Hz), 19.20 (d, $J = 3.4$ Hz), 19.03 (d, $J = 4.2$ Hz), 18.71 (d, $J = 3.0$ Hz), 18.06 (s), 18.03 (s), 17.11 (d, $J = 3.1$ Hz), 16.49 (d, $J = 2.1$ Hz) ppm. Anal. Calcd. for: $C_{45}H_{62}BF_4P_3Pd$ (%): C, 60.79; H, 7.03. Found: C, 60.59; H, 6.87. λ_{max} (CH_3CN , nm), ϵ ($M^{-1}cm^{-1}$): 418, 4.53×10^3 ; 350, 1.26×10^4

Crystallographic Information

CCDC 920550–920553 contain the supplementary crystallographic data for this chapter. These data can be obtained free of charge from The Cambridge Crystallographic Data Centre via www.ccdc.cam.ac.uk/data_request/cif. The corresponding complexes for the deposition numbers are 920550 (**3a-Ni**), 920551 (**4b-Ni**), 920552 (**4b-Pd**), and 920553 (**2c-Pd**).

Refinement details

In each case, crystals were mounted on a glass fiber or nylon loop using Paratone oil, then placed on the diffractometer under a nitrogen stream. Low temperature (100 K) X-ray data were obtained on a Bruker APEXII CCD based diffractometer (Mo sealed X-ray tube, $K_{\alpha} = 0.71073$ Å). All diffractometer manipulations, including data collection, integration, and scaling, were carried out using the Bruker APEXII software.¹⁹ Absorption corrections were applied using SADABS.²⁰

Space groups were determined on the basis of systematic absences and intensity statistics, and the structures were solved by direct methods using XS⁷ (incorporated into SHELXTL) and refined by full-matrix least squares on F². All non-hydrogen atoms were refined using anisotropic displacement parameters. Hydrogen atoms were placed in idealized positions and refined using a riding model. The structure was refined (weighted least squares refinement on F²) to convergence.

It should be noted that due to the size of these compounds, most crystals included solvent accessible voids, which tended to contain disordered solvent. In addition, due to a tendency to desolvate, the long range order of these crystals and amount of high angle data we were able to record was in some cases not ideal. These disordered solvent molecules were largely responsible for the alerts generated by the checkCIF protocol. For **3a-Ni**, the disordered non-coordinated solvents were removed using the SQUEEZE protocol included in PLATON²¹ (*vide infra*). We are confident this additional electron density is from the solvent molecules in the crystal lattice and not from unaccounted counter ions.

Table 1. Crystal and refinement data for complexes **3a-Ni**, **4b-Ni**, **4b-Pd**, and **2c-Pd**.

	3a-Ni	4b-Ni	4b-Pd	2c-Pd
empirical formula	C ₁₂₈ H ₁₈₈ F ₁₂ Ni ₂ O ₁₃ P ₆ S ₄	C ₁₀₀ H ₁₃₉ F ₆ Ni ₂ O ₈ P ₆ S ₂	C ₅₁ H ₆₈ B F ₄ P ₃ Pd	C ₃₈ H ₅₃ B ₂ F ₈ N ₃ P ₂ Pd
formula wt	2594.26	1950.47	967.17	893.79
T (K)	100	100	100	100
a, Å	15.2622(7)	30.909(6)	9.7632(6)	13.0651(7)
b, Å	20.3413(9)	9.6130(14)	13.8627(9)	19.8103(8)
c, Å	23.5270(10)	33.956(6)	18.8685(11)	15.9572(8)
α, deg	90	90	111.116(3)	90
β, deg	103.125(2)	105.396(6)	96.691(3)	98.120(2)
γ, deg	90	90	92.975(3)	90
V, Å ³	7113.2(5)	9727(3)	2353.9(3)	4088.7(3)
Z	2	4	2	4
cryst syst	Monoclinic	Monoclinic	Triclinic	Monoclinic
space group	P2(1)	P2(1)/n	P-1	P2(1)/c
d _{calcd} , g/cm ³	1.211	1.332	1.365	1.452
θ range, deg	1.70-37.44	1.81-25.27	1.58-28.5	1.57-43.63
μ, mm ⁻¹	0.460	0.595	0.546	0.600
abs cor	Semi-empirical from equivalents	Semi-empirical from equivalents	Semi-empirical from equivalents	Semi-empirical from equivalents
GOF ^c	0.985	1.311	1.070	1.372
R1, ^a wR2 ^b (I > 2σ(I))	0.0618, 0.1647	0.0769, 0.1799	0.0538, 0.1035	0.0437, 0.1033

$${}^a R1 = \sum ||F_o| - |F_c|| / \sum |F_o| \quad {}^b wR2 = \{ \sum [w(F_o^2 - F_c^2)^2] / \sum [w(F_o^2)] \}^{1/2} \quad {}^c GOF = S = \{ \sum [w(F_o^2 - F_c^2)^2] / (n-p) \}^{1/2}$$

Special refinement details for **3a-Ni**

The structure also contains four outer-sphere trifluoromethanesulfonate counter anions that were satisfactorily modeled. Two disordered *tert*-butyl methyl groups were modeled

and split into two positions. Restraints were employed to treat the displacement parameters of one of the triflate molecules to an acceptable size. Benzene and tetrahydrofuran (THF) were used as the crystallization solvents. Accordingly, the compound crystallized with benzene and THF solvent molecules in the lattice. Four additional disordered THF solvent molecules, however, could not be satisfactorily modeled (see Figure S44 for depiction of solvent accessible voids). The SQUEEZE protocol contained with the program PLATON²¹ was used to generate a bulk solvent correction to the observed intensities. The results are appended to the CIF.

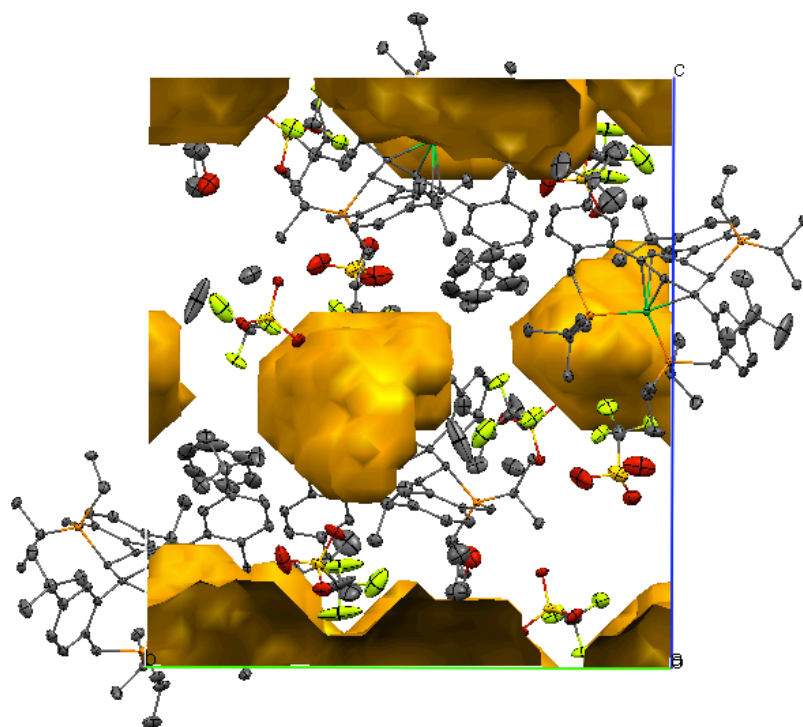


Figure 9. Unit cell packing of **3a-Ni** displaying solvent accessible voids in yellow.

Special refinement details for **4b-Ni**

4b-Ni was crystallized from THF/hexanes mixture. Accordingly, the compound crystallized with two THF solvent molecules in the lattice. The structure also contains

two outer-sphere trifluoromethanesulfonate counterions that were satisfactorily modeled. Restraints were employed to treat the displacement parameters of the methyl of an isopropyl group to an acceptable size. The relatively low level of completeness is due to poor crystal quality. This dataset represents the best of repeated collection attempts using crystals obtained under various crystallization conditions.

Special refinement details for 4b-Pd

Benzene was used as the solvent to crystallize the complex **4b-Pd**. Accordingly, the compound crystallized with one benzene solvent molecule in the lattice. The structure contains an outer-sphere tetrafluoroborate counter anion that was slightly disordered and modeled with occupancy in two positions.

Special refinement details for 2c-Pd

The compound was crystallized from acetonitrile/toluene mixture. Accordingly, the compound crystallized with one acetonitrile in the lattice. The structure also contains two outer-sphere tetrafluoroborate counterion that were satisfactorily modeled.

REFERENCES

- 1 (a) Bergman, R. G. *Nature* **2007**, *446*, 506. (b) Labinger, J. A.; Bercaw, J. E. *Nature* **2002**, *417*, 507. (c) Chen, X.; Engle, K. M.; Wang, D. H.; Yu, J. Q. *Angew. Chem. Int. Ed.* **2009**, *48*, 5094.
- 2 (a) Thompson, M. E.; Baxter, S. M.; Bulls, A. R.; Burger, B. J.; Nolan, M. C.; Santarsiero, B. D.; Schaefer, W. P.; Bercaw, J. E. *J. Am. Chem. Soc.* **1987**, *109*, 203. (b) Cummins, C. C.; Baxter, S. M.; Wolczanski, P. T. *J. Am. Chem. Soc.* **1988**, *110*, 8731. (c) Janowicz, A. H.; Bergman, R. G. *J. Am. Chem. Soc.* **1982**, *104*, 352. (d) Stahl, S. S.; Labinger, J. A.; Bercaw, J. E. *Angew. Chem. Int. Ed.* **1998**, *37*, 2181. (e) Sherry, A. E.; Wayland, B. B. *J. Am. Chem. Soc.* **1990**, *112*, 1259.

- 3 (a) Pape, A. R.; Kaliappan, K. P.; Kündig, P. *Chem. Rev.* **2000**, *100*, 2917. (b) Fretzen, A.; Ripa, A.; Liu, R. G.; Bernardinelli, G.; Kundig, E. P. *Chem.-Eur. J.* **1998**, *4*, 251. (c) Rose-Munch, F.; Gagliardini, V.; Renard, C.; Rose, E. *Coord. Chem. Rev.* **1998**, *178*, 249. (d) Chung, Y. K.; Honig, E. D.; Robinson, W. T.; Sweigart, D. A.; Connelly, N. G.; Ittel, S. D. *Organometallics* **1983**, *2*, 1479. (e) Djukic, J. P.; Rosemunch, F.; Rose, E.; Simon, F.; Dromzee, Y. *Organometallics* **1995**, *14*, 2027. (f) Fretzen, A.; Kundig, E. P. *Helv. Chim. Acta.* **1997**, *80*, 2023. (g) Pike, R. D.; Ryan, W. J.; Carpenter, G. B.; Sweigart, D. A. *J. Am. Chem. Soc.* **1989**, *111*, 8535. (h) Pike, R. D.; Sweigart, D. A. *Synlett.* **1990**, 565. (i) Schmalz, H. G.; Schellhaas, K. *Angew. Chem. Int. Ed. Eng.* **1996**, *35*, 2146. (j) Semmelhack, M. F.; Clark, G. R.; Garcia, J. L.; Harrison, J. J.; Thebtaranonth, Y.; Wulff, W.; Yamashita, A. *Tetrahedron* **1981**, *37*, 3957. (k) Semmelhack, M. F.; Hall, H. T.; Farina, R.; Yoshifuji, M.; Clark, G.; Bargar, T.; Hirotsu, K.; Clardy, J. *J. Am. Chem. Soc.* **1979**, *101*, 3535.
- 4 Keane, J. M.; Harman, W. D. *Organometallics* **2005**, *24*, 1786.
- 5 (a) Maimone, T. J.; Milner, P. J.; Kinzel, T.; Zhang, Y.; Takase, M. K.; Buchwald, S. L. *J. Am. Chem. Soc.* **2011**, *133*, 18106. (b) Milner, P. J.; Maimone, T. J.; Su, M.; Chen, J.; Müller, P.; Buchwald, S. L. *J. Am. Chem. Soc.* **2012**, *134*, 19922. (c) Allgeier, A. M.; Shaw, B. J.; Hwang, T. L.; Milne, J. E.; Tedrow, J. S.; Wilde, C. N. *Organometallics* **2012**, *31*, 519.
- 6 Nielsen, D. K.; Doyle, A. G. *Angew. Chem. Int. Ed.* **2011**, *50*, 6056.
- 7 (a) Lin, S. B.; Day, M. W.; Agapie, T. *J. Am. Chem. Soc.* **2011**, *133*, 3828. (b) Kelley, P.; Lin, S. B.; Edouard, G.; Day, M. W.; Agapie, T. *J. Am. Chem. Soc.* **2012**, *134*, 5480. (c) Chao, S. T.; Lara, N. C.; Lin, S. B.; Day, M. W.; Agapie, T. *Angew. Chem. Int. Ed.* **2011**, *50*, 7529. (d) Velian, A.; Lin, S. B.; Miller, A. J. M.; Day, M. W.; Agapie, T. *J. Am. Chem. Soc.* **2010**, *132*, 6296.
- 8 (a) Smith, R. C.; Protasiewicz, J. D. *Organometallics* **2004**, *23*, 4215. (b) Smith, R. C.; Bodner, C. R.; Earl, M. J.; Sears, N. C.; Hill, N. E.; Bishop, L. M.; Sizemore, N.; Hehemann, D. T.; Bohn, J. J.; Protasiewicz, J. D. *J. Organomet. Chem.* **2005**, *690*, 477. (c) Ma, L. Q.; Woloszynek, R. A.; Chen, W. Z.; Ren, T.; Protasiewicz, J. D. *Organometallics* **2006**, *25*, 3301.

- 9 (a) Ding, K. Y.; Miller, D. L.; Young, V. G.; Lu, C. C. *Inorg. Chem.* **2011**, *50*, 2545. (b) Marlier, E. E.; Tereniak, S. J.; Ding, K.; Milliken, J. E.; Lu, C. C. *Inorg. Chem.* **2011**, *50*, 12219. (c) Tereniak, S. J.; Marlier, E. E.; Lu, C. C. *Dalton Trans.* **2012**, *41*, 7862. (d) Kaganovsky, L.; Cho, K. B.; Gelman, D. *Organometallics* **2008**, *27*, 5139. (e) Birkholz, M. N.; Freixa, Z.; van Leeuwen, P. W. N. M. *Chem. Soc. Rev.* **2009**, *38*, 1099. (f) Kamer, P. C. J.; van Leeuwen, P. W. N.; Reek, J. N. H. *Acc. Chem. Res.* **2001**, *34*, 895. (g) Bessel, C. A.; Aggarwal, P.; Marschlok, A. C.; Takeuchi, K. J. *Chem. Rev.* **2001**, *101*, 1031.
- 10 (a) Brunkan, N. M.; Brestensky, D. M.; Jones, W. D. *J. Am. Chem. Soc.* **2004**, *126*, 3627. (b) Jimenez-Tenorio, M.; Puerta, M. C.; Salcedo, I.; Valerga, P.; Costa, S. I.; Silva, L. C.; Gomes, P. T. *Organometallics* **2004**, *23*, 3139. (c) Pawlas, J.; Nakao, Y.; Kawatsura, M.; Hartwig, J. F. *J. Am. Chem. Soc.* **2002**, *124*, 3669.
- 11 (a) Christmann, U.; Vilar, R.; White, A. J. P.; Williams, D. J. *Chem. Commun.* **2004**, 1294. (b) Christmann, U.; Pantazis, D. A.; Benet-Buchholz, J.; McGrady, J. E.; Maseras, F.; Vilar, R. *J. Am. Chem. Soc.* **2006**, *128*, 6376. (c) Yin, J. J.; Rainka, M. P.; Zhang, X. X.; Buchwald, S. L. *J. Am. Chem. Soc.* **2002**, *124*, 1162. (d) Yamashita, M.; Takamiya, I.; Jin, K.; Nozaki, K. *J. Organomet. Chem.* **2006**, *691*, 3189. (e) Liang, L. C.; Chien, P. S.; Huang, Y. L. *J. Am. Chem. Soc.* **2006**, *128*, 15562.
- 12 (a) Hatnean, J. A.; Beck, R.; Borrelli, J. D.; Johnson, S. A. *Organometallics* **2010**, *29*, 6077. (b) Chen, Y. F.; Sui-Seng, C.; Zargarian, D. *Angew. Chem. Int. Ed.* **2005**, *44*, 7721. (c) Marshall, W. J.; Grushin, V. V. *Organometallics* **2003**, *22*, 555.
- 13 (a) Chung, Y. K.; Choi, H. S.; Sweigart, D. A.; Connelly, N. G. *J. Am. Chem. Soc.* **1982**, *104*, 4245. (b) Ittel, S. D.; Whitney, J. F.; Chung, Y. K.; Williard, P. G.; Sweigart, D. A. *Organometallics* **1988**, *7*, 1323.
- 14 Bach, I.; Porschke, K. R.; Goddard, R.; Kopsike, C.; Kruger, C.; Rufinska, A.; Seevogel, K. *Organometallics* **1996**, *15*, 4959.
- 15 (a) Podgorsek, A.; Stavber, S.; Zupan, M.; Iskra, J. *Eur. J. Org. Chem.* **2006**, 483. (b) Mallory, F. B.; Butler, K. E.; Berube, A.; Luzik, E. D.; Mallory, C. W.; Brondyke, E. J.; Hiremath, R.; Ngo, P.; Carroll, P. J. *Tetrahedron* **2001**, *57*, 3715.

- 16 Fulmer, G. R.; Miller, A. J. M.; Sherden, N. H.; Gottlieb, H. E.; Nudelman, A.; Stoltz, B. M.; Bercaw, J. E.; Goldberg, K. I. *Organometallics* **2010**, *29*, 2176.
- 17 Kao, M. T.; Chen, J. H.; Chu, Y. Y.; Tseng, K. P.; Hsu, C. H.; Wong, K. T.; Chang, C. W.; Hsu, C. P.; Liu, Y. H. *Org. Lett.* **2011**, *13*, 1714.
- 18 Kowalik, J.; Tolbert, L. M. *J. Org. Chem.* **2001**, *66*, 3229.
- 19 APEX2, Version 2 User Manual, M86-E01078, Bruker Analytical X-ray Systems, Madison, WI, June 2006.
- 20 Sheldrick, G. M. "SADABS (Version 2008/1): Program for Absorption Correction for Data from Area Detector Frames", University of Göttingen, 2008.
- 21 Spek, A. L. "PLATON – A Multipurpose Crystallographic Tool, Utrecht University", Utrecht, the Netherlands, 2006.

CHAPTER 3

TRINUCLEAR NICKEL COMPLEXES WITH METAL-ARENE INTERACTIONS SUPPORTED BY
TRIS(PHOSPHINOARYL)BENZENE FRAMEWORK

Published in part as:

Suseno, S.; Horak, K. T.; Day, M. W.; Agapie, T. *Organometallics* **2013**, *32*, 6883-6886

ABSTRACT

A triphosphine ligand with backbone designed to facilitate metal-arene interactions were employed to support multinuclear Ni complexes. Di- and trinuclear metal complexes supported by a triphosphine ligand containing a triarylbenzene linker display diverse metal-arene binding modes. Multinuclear Ni halide complexes were isolated with strongly interacting metal centers bound to opposite faces of the coordinated arene. Upon reaction of the trinickel diiodide complex, **5**, with disodium tetracarbonylferrate, a cofacial triangulo nickel(0) complex, **7**, was isolated. All multinuclear complexes feature strong metal-arene interactions, demonstrating the use of an arene as a versatile ligand design element for small clusters.

INTRODUCTION

Multinickel complexes have been employed for a variety of transformations.¹ Di- and trinickel complexes have been reported to activate, cleave, and electrochemically reduce CO₂.^{1a-c,1g} C–C cross-coupling chemistry has been reported at dinuclear sites as well.^{1f} To further develop the reactivity of multinuclear Ni complexes, the development of new coordination motifs is of interest. A wide variety of multidentate ligands have been utilized to support dinuclear transition metal chemistry.² Ligand design strategies for the controlled synthesis of trinuclear complexes are less developed. Several approaches have been reported recently for targeting trinuclear complexes of Mn, Fe, Co, Cu, and Zn.³

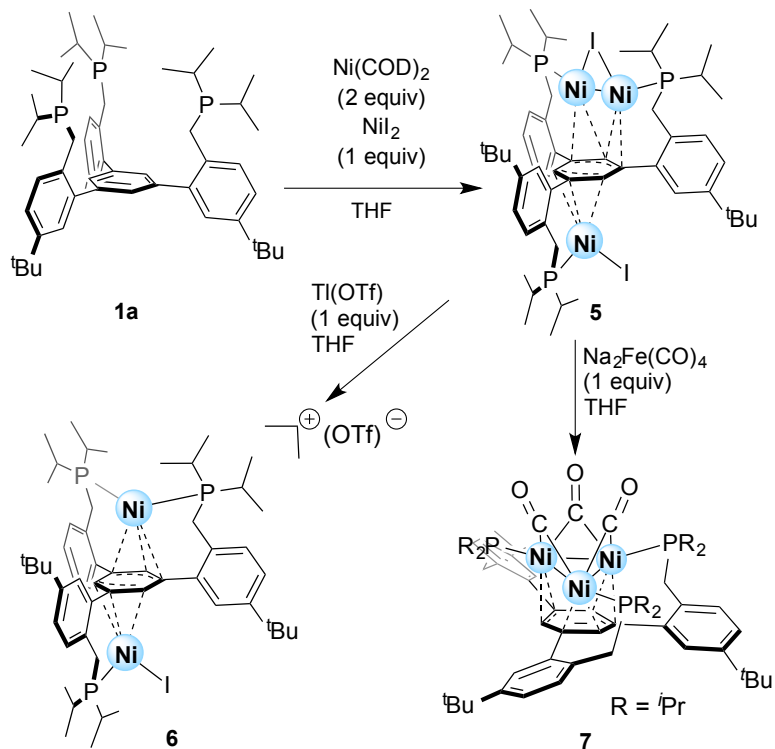
We have employed multidentate phosphines linked by aryl-benzene bridges to support mono- and dinuclear complexes stabilized by strong metal-arene interactions.^{1f,4} The central arene in these systems serves both as a spacer to facilitate the coordination of multiple metals by the phosphines and as a site of metal coordination with a variety of possible binding modes. The rigid aryl-aryl linkages facilitate coordination of the metals in positions prone to interaction with the central arene and also enforce a relatively large distance between donors, depending on ring substitution, favoring coordination of multiple metals. Further exploring the potential of phosphinoaryl-benzene frameworks to support discrete metal clusters with unusual bonding motifs, herein we describe the synthesis and characterization of trinuclear Ni complexes displaying metal-metal bonds and strong metal-arene interactions.

RESULTS AND DISCUSSIONS

Comproportionation reactions between Ni⁰ and Ni^{II} precursors have offered facile access to dinuclear Ni₂^I complexes.^{1f} A similar strategy was employed toward

multinuclear complexes. Treatment of a tris(phosphinoaryl)benzene species, **1a**, with two equivalents of $\text{Ni}(\text{COD})_2$ (COD = cyclooctadiene) followed by one equivalent of NiI_2 afforded the trinickel species **5** (Scheme 1).

Scheme 1. Synthesis of di- and trinickel complexes supported by tris(phosphinoaryl)benzene framework (**1a**)



A single crystal X-ray diffraction (XRD) study of complex **5** reveals a trimetallic complex with one phosphine arm coordinated per Ni center (Figure 1). Two metal centers (Ni1, Ni2) are bridged by an iodide and coordinated cofacially relative to the central arene. The third Ni (Ni3) is located on the opposite face relative to the central arene ring and coordinated by a terminal iodide. Complex **5** exhibits a short Ni1–Ni2 distance (2.3907(2) Å) similar to previously reported bonding $\text{Ni}^{\text{I}}\text{-Ni}^{\text{I}}$ motifs^{1f,1i,4a,5} or metal-metal distances in $[\text{Ni}_3]^{2+}$ species.⁶ Additionally, strong metal-arene interactions to the central ring are observed, with Ni–C distances ranging between 1.95–2.11 Å.^{5a}

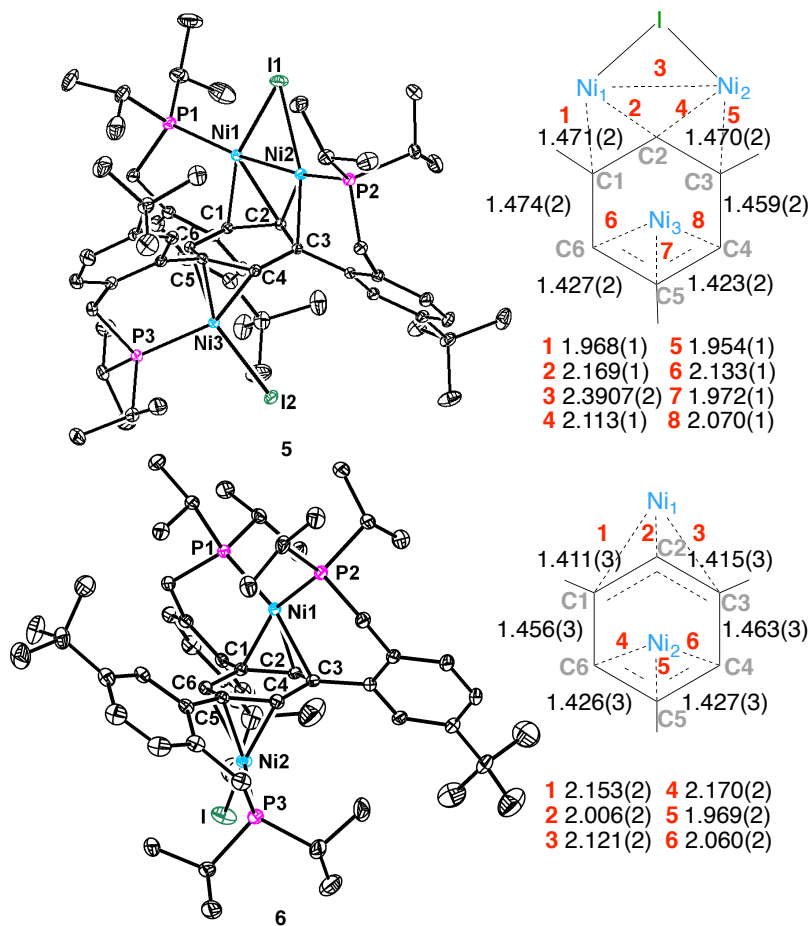


Figure 1. Solid-state structures with thermal ellipsoids at the 50% probability level (left) and selected C–C and Ni–C bond distances (Å, right) of **5** (top) and **6** (bottom). Hydrogen atoms and anions are omitted for clarity

The solution ^1H nuclear magnetic resonance (NMR) spectrum of **5** shows peaks only in the diamagnetic region with significantly upfield shifted proton signals that correspond to the central ring at 4.61 and 3.35 ppm in 2:1 ratio, indicative of strong metal-arene interactions as shown by the crystal structure. The ^{31}P NMR spectrum of **5** in C_6D_6 at room temperature displays two phosphorus signals: a triplet at 11.66 ppm and a broad multiplet at 67.71 ppm in 1:2 ratio. The upfield peak is assigned to the mononickel site, while the second peak corresponds to the dinuclear site. The presence

of two rather than three peaks for the phosphines (^{31}P NMR) and the hydrogen atoms of the central arene (^1H NMR) suggests that although the solid-state structure shows C_1 symmetry, the solution structure is fluxional. An exchange process consistent with the observed spectra involves shifting of the iodide and phosphine coordinated to Ni3 across a reflection plane perpendicular to the central ring and containing C2 and C5.

Previous studies of a dinuclear Ni complex supported by a related triphosphine demonstrated the reversible interconversion of isomers with the two metal centers coordinated to the same face vs. opposite sides of the central arene.^{4a} Halide abstraction induced formation of the cofacial isomer with a $\text{Ni}^{\text{I}}-\text{Ni}^{\text{I}}$ bond and a bridging halide. Analogously, complex **5** was treated with $\text{Tl}(\text{OTf})$ ($\text{OTf} = \text{trifluoromethanesulfonate}$) in an attempt to generate a cationic triangulo trinickel cluster capped by a μ_3 -iodide. However, a dinuclear complex **6** (Scheme 1) was isolated as the major product, as revealed by XRD (Figure 1). Formation of **6** likely results from loss of an equivalent of Ni^0 following halide abstraction, consistent with the black precipitate observed during reaction.

Attempts to regenerate **5** by addition of a third Ni center with $\text{Ni}(\text{COD})_2$ in the presence of a halide do not lead to the trinuclear complex, suggesting that the formation of **6** is irreversible. The solid-state structure of **6** shows the two metal centers on opposite faces of the central arene. Ni1 is coordinated by two phosphines, and Ni2 by one phosphine and a terminal iodide (Figure 1). As with complex **5**, both metal centers interact strongly with the π system of the central ring, indicated by the short $\text{Ni}-\text{C}_{\text{arene}}$ distances of 1.97-2.17 Å. The ^1H NMR spectrum shows broad peaks in the diamagnetic region. Three upshifted signals for the central ring protons in a 1:1:1 ratio (4.5 – 6 ppm) are observed, consistent with the short $\text{Ni}-\text{C}_{\text{arene}}$ distances. Consistent with the low

symmetry suggested by the ^1H NMR spectrum, the ^{31}P NMR spectrum displays three peaks in a 1:1:1 ratio. The NMR data are consistent with the solid-state structure of **6** having C_1 symmetry. The fluxional process exchanging the sides of the molecule as described for **5** is slower for **6**, although the broad peaks observed at room temperature approach to coalescence.

Complexes **5** and **6** represent unusual cases of electronic interactions between Ni centers and arenes. Previous examples of dinickel complexes with metal arene interactions are of three types. Complexes with cofacial Ni^{I} centers display the metals in close proximity (2.3-2.6 Å) consistent with a $\text{Ni}^{\text{I}}-\text{Ni}^{\text{I}}$ bonding interaction.^{1f,4a,5b,7} The metal-arene interactions in these complexes are typically supported by pendant donors, although a tetraphenylborate was reported to coordinate the Ni_2^{I} moiety without additional ligands.^{7a} A second type of Ni_2 -arene complex involves two Ni^0 centers ligated to opposite sides of the arene.^{5a,8} A third class includes dinickel complexes with metals coordinated on opposite faces of the arene, but in higher oxidation states.^{4a,7b,9} A common metal-arene binding mode in these complexes is $\mu-\eta^3:\eta^3$, with structural distortions of the ring away from planarity and elongation of the C-C bonds between the two η^3 metal coordination sites.^{7b,9a-c} This binding mode and the diamagnetism of these complexes has been interpreted as a formal reduction of the ring by Ni^{I} to result in a diallyl moiety and two Ni^{II} centers. For a related $\mu-\eta^1:\eta^3$ binding mode, the two unpaired electrons of the Ni^{I} centers couple via a backbonding interaction with an empty arene δ^* orbital different from the diallyl case, as supported by computation and the shortened C-C bonds adjacent to the η^3 -coordinated moiety.^{4a} Trinuclear complexes

of Ni supported by interactions with an arene have not been structurally characterized to the authors' knowledge.¹⁰

Compounds **5** and **6** both show distortion of the coordinated arene suggestive of a diallyl structure, with the elongated C–C bonds linking the allyl moieties (C1–C6 and C3–C4 ca. 1.46 Å). One allyl moiety coordinates to a monophosphine-mononickel site, and the second binds either a diphosphine-mononickel (**6**) or a diphosphine-dinickel site (**5**). Compound **6**, binding the arene $\mu\text{-}\eta^3\text{:}\eta^3$, belongs to the third class of compounds described above. Compound **5**, binding the arene $\mu_3\text{-}\eta^3\text{:}\eta^3$, displays two metals instead of one coordinated to one of the allyl moieties. There is a single other complex that has been structurally characterized with a $\mu_3\text{-}\eta^3\text{:}\eta^3$ -arene coordinated to three ruthenium centers.¹¹ In the limiting case of a doubly reduced arene, the mononuclear site corresponds to a Ni^{II} and the binuclear site to a Ni^I–Ni^I moiety. The Ni^I₂ motif with bridging allyl ligands has been structurally characterized.¹² The strong interactions between the metal centers and the arene are not only supported by the short distances in the solid-state, but also by NMR spectroscopy. ³¹P–³¹P coupling through five bonds is observed in both **5** and **6**, indicating electronic communication across metals coordinated to opposite faces of the arene.

While halide abstraction results in the loss of Ni⁰, a cofacial trinickel complex (**7**) can be isolated from the reaction of complex **5** with Na₂Fe(CO)₄ (Scheme 1). The hexanes soluble fraction from this reaction shows one singlet in the ³¹P NMR spectrum at 61.90 ppm. The ¹H NMR spectrum displays the central arene proton signal at 5.77 ppm, again indicative of strong metal-arene interactions and also suggesting a high symmetry structure. The solution infrared (IR) spectrum of **7** shows intense bands at

1846 and 1796 cm^{-1} , consistent with μ_2 -CO ligation. In agreement, the XRD study of **7** reveals a pseudo- C_3 -symmetric structure, displaying a triangulo-trinickel core with each metal center coordinated by a phosphine donor, the arene moiety, and bridging μ_2 -CO ligands (Figure 2).

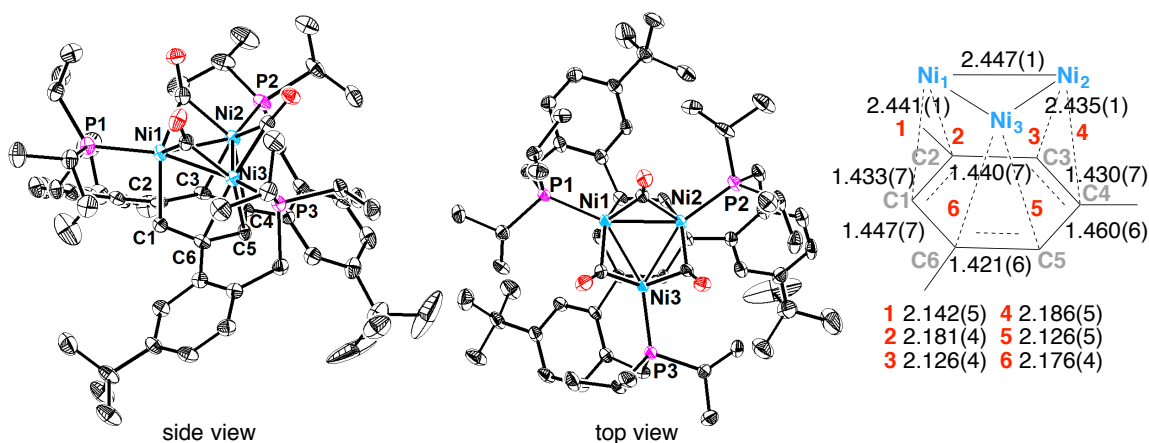


Figure 2. Solid-state structure of **7** with thermal ellipsoids at the 50% probability level (*left*: side view; *center*: top view) and selected C–C and Ni–C bond distances (Å, *right*). Hydrogen atoms are omitted for clarity.

The electron rich Ni^0_3 core is stabilized by back-bonding to CO and arene. The solid-state structure of **7** shows different metal-arene interactions than **5**. In contrast to the $\mu_3\text{-}\eta^3\text{:}\eta^3$ arene binding mode of **5**, complex **7** displays $\mu_3\text{-}\eta^2\text{:}\eta^2\text{:}\eta^2$ metal coordination to localized olefin moieties of the central arene. The bridging CO ligands likely provide additional stabilization to the Ni_3 core that is not accessible from **5** by iodide abstraction, albeit in a different oxidation state. To generate **7**, $\text{Na}_2[\text{Fe}(\text{CO})_4]$ acts as both a reducing agent and CO source. A more direct route to **7** employing a Ni^0 precursor was attempted. Treatment of **1a** with $\text{Ni}(\text{COD})_2$ and appropriate amounts of CO only resulted in the formation of a trinickel nonacarbonyl complex, **8**, with each phosphine arm coordinating a $\text{Ni}(\text{CO})_3$ unit rather than the arene-supported trinuclear

cluster with Ni–Ni contacts (Scheme 2). The preliminary crystal structure of **8** is depicted in Figure 3 (only a partial data set was collected).

Scheme 2. Synthesis of trinickel nonacarbonyl complex supported by a trisphosphine ligand

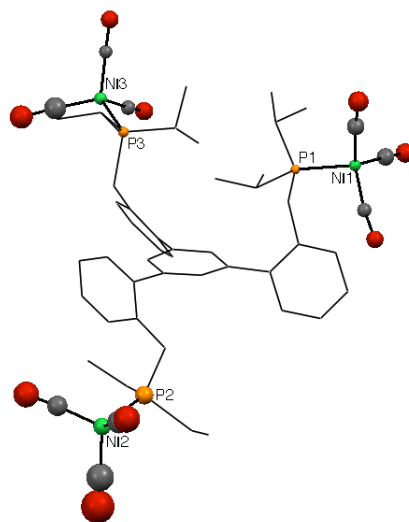
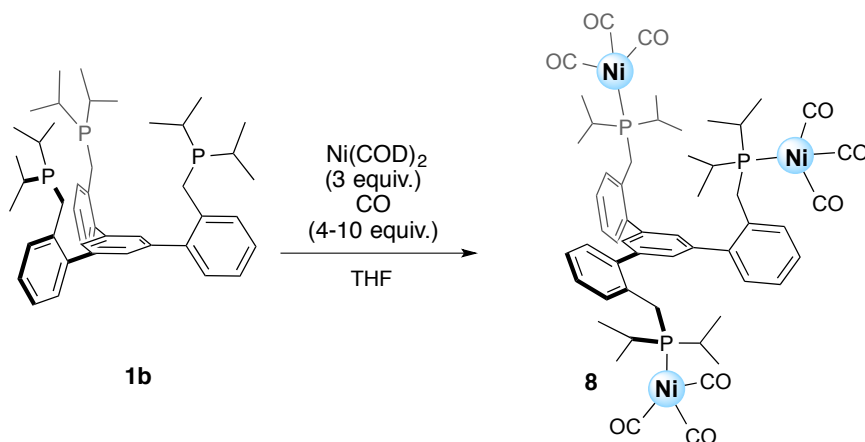


Figure 3. Preliminary solid-state structure of trinickel nonacarbonyl complex, **8**, supported by ligand **1b**, based on a partial data set.

Compound **7** represents the first structurally characterized example of arene-supported triangulo-nickel complex. A Ni₃ cluster supported by the cyclooctatetraenyl dication has been reported.¹⁰ Higher oxidation state Ni₃ moieties are typically supported by cyclopentadienyl or κ²-bridging ligands.¹³ A notable difference compared to the

majority of reported Ni₃ species is the lack of a μ_3 -capping ligand besides the arene. Typically, the Ni₃ core is coordinated by two μ_3 -ligands such as alkyne,¹⁴ CO,^{13a} alkylidyne,¹⁵ benzyne,¹⁶ halide,^{6c} chalcogenide,^{6d} or hydride moieties. Beyond nickel, trimetallic complexes supported by μ_3 -arene donors are known for Os,¹⁷ Co,¹⁸ Rh,¹⁹ Ru,¹¹ and Pd.²⁰ Complex **7** exhibits average Ni–Ni distances of 2.44 Å by XRD studies (Figure 2) that are similar to the previously reported Ni⁰–Ni⁰ motif (2.47–2.50 Å) in a Ni₄(CO)₆(PMe₃)₄ cluster.²¹ The Ni–Ni distances of **7** are also similar to those of the Ni₃(dppm)₃ (dppm = Ph₂PCH₂PPh₂) clusters that are more oxidized.^{6c,22} The observed variation of average Ni–Ni distances may be explained by the difference in Ni oxidation states where our complexes consist of all Ni⁰ centers and the presence of more π -acidic ligands like CO. Treatment of **7** with excess CO₂ resulted in no reaction. This is not surprising considering the number of π -acidic CO's bound around the Ni centers.

CONCLUSIONS

In summary, bi- and trinuclear Ni complexes have been synthesized by employing phosphine ligand architectures that facilitate metal-arene interactions. Two complexes with metal centers coordinated transfacially show structural features consistent with a diallyl motif for the bridging arene. ³¹P–³¹P NMR coupling across five bonds spanning the bridging arene are indicative of the strong interactions with the metals. Cofacial trinuclear Ni₃ complexes have been isolated as well, and exhibit μ_3 - $\eta^2:\eta^2:\eta^2$ arene binding, a novel coordination mode for nickel. The present complexes demonstrate the utility of a coordinating arene as a versatile multidentate ligand design element for the synthesis of new types of metal clusters.

EXPERIMENTAL SECTION

General considerations

Unless otherwise specified, all air- and moisture-sensitive compounds were manipulated using glovebox or using standard Schlenk line techniques with an N₂ atmosphere. Anhydrous tetrahydrofuran (THF) was purchased from Aldrich in 18 L Pure-Pac™ containers. Anhydrous acetonitrile, benzene, dichloromethane, diethyl ether, and THF were purified by sparging with nitrogen for 15 minutes and then passing under nitrogen pressure through a column of activated A2 alumina (Zapp's). Acetonitrile-*d*₃ and chloroform-*d*₁ were purchased from Cambridge Isotopes, dried over calcium hydride, and vacuum transferred prior to use. Benzene-*d*₆ and THF-*d*₈ were also purchased from Cambridge Isotope Laboratories, Inc., dried over sodium/benzophenone ketyl, and vacuum transferred prior to use. Unless indicated otherwise, all commercial chemicals were used as received. Ni(COD)₂ and NiI₂ were purchased from Strem. Compound **1a** and Na₂Fe(CO)₄ were prepared according to previously published protocol.^{4b,23} ¹H, ¹³C, and ³¹P NMR spectra were recorded on Varian Mercury 300 or Varian INOVA-500 spectrometers at room temperature unless indicated otherwise. Chemical shifts for ¹H and ¹³C NMR data are reported relative to residual solvent peaks.²⁴ ³¹P NMR chemical shifts are reported with respect to the deuterated solvent used to lock the instrument. Elemental analyses were performed by Robertson MicroLit Laboratories, Ledgewood, NJ.

Synthesis of complex 5

A suspension of Ni(COD)₂ (191 mg, 0.693 mmol) in dry THF (10 mL) was added to **1a** (300 mg, 0.347 mmol). The solution immediately turned red-orange. The reaction mixture was stirred for 10 mins then a suspension of NiI₂ (109 mg, 0.347 mmol) in THF

(5 mL) was added. The reaction mixture was allowed to stir at r.t. for 4 h. A color change from red-orange to dark brown was observed over the course of reaction time. The reaction mixture was filtered, and the filtrate was dried *in vacuo*. The dry residue was triturated with hexanes, diethyl ether, and benzene. The benzene fraction gives the clean product in 60% yield. Recrystallization via vapor diffusion of *n*-hexanes into benzene yields brown-black crystals. ^1H NMR (300 MHz, C_6D_6) δ 8.81 (s, 2H, aryl-*H*), 7.71 (s, 1H, aryl-*H*), 7.32 (d, $J = 7.8$ Hz, 2H, aryl-*H*), 7.20 (s, 1H, aryl-*H*), 6.99 (d, $J = 7.9$ Hz, 2H, aryl-*H*), 6.85 (d, $J = 8.0$ Hz, 1H, aryl-*H*), 4.61 (s, 2H, central ring-*H*), 3.35 (s, 1H, central ring-*H*), 2.72 (s, 4H, CH_2), 2.47 (app d, 2H, CH_2), 1.90 (s, 2H, CH), 1.69 (s, 18H, *tert*-butyl CH_3), 1.52 (m, 4H, CH), 1.36 (s, 9H, *tert* butyl- CH_3), 1.11 (b, 12H, CH_3), 0.82 (m, 6H, CH_3), 0.70 (m, 12H, CH_3), 0.54 (app dd, 6H, CH_3) ppm; ^{31}P NMR (121 MHz, C_6D_6) δ 67.97 (br s, 2P), 11.66 (t, 1P, $J = 17.1$ Hz) ppm; ^{13}C NMR (126 MHz, C_6D_6) δ 149.94 (s), 142.90 (s), 139.62 (d, $J = 7.1$ Hz), 133.55 (s), 132.25 (d, $J = 5.5$ Hz), 131.46 (s), 130.50 (s), 129.15 (s), 128.19 (s), 125.94 (s), 123.11 (s), 122.86 (s), 95.29 (d, $J = 5.0$ Hz), 69.33 (s), 63.08 (s), 34.84 (s), 34.39 (s), 33.53 (s), 32.15 (s), 31.41 (s), 27.48 (d, $J = 12.3$ Hz), 25.60 (s), 24.71 (d, $J = 13.1$ Hz), 19.24 (d, $J = 20.5$ Hz), 18.34 (d, $J = 22.3$ Hz), 17.04 (s) ppm. Anal. Calcd. for: $\text{C}_{57}\text{H}_{87}\text{I}_2\text{Ni}_3\text{P}_3$ (%): C, 52.86; H, 6.77. Found: C, 53.07; H, 6.91.

Synthesis of complex 6

In an inert atmosphere glovebox, a solution of $\text{Tl}(\text{OTf})$ (13.6 mg, 0.0386 mmol) in THF (1 mL) was added to a solution of **5** (50 mg, 0.0386 mmol) in THF (5 mL). The mixture was stirred at room temperature and checked for progress by ^{31}P NMR. Formation of thallium iodide as light yellow precipitate was observed immediately, and Ni^0 as black

precipitate was observed after 12 h. The reaction mixture was filtered, and the solvent was removed off the filtrate *in vacuo*. The residue was triturated with hexanes, diethyl ether, and benzene. The benzene fraction gives the clean product in 50% yield. Recrystallization via vapor diffusion of *n*-hexanes into benzene yielded the product as brown-black crystals. Complex **6** was observed to decompose overtime in solution and as solid to yield previously characterized mono nickel complex^{4b} and other decomposition products. ¹H NMR (500 MHz, THF-*d*₈, -30°C) δ 8.69 (s, 1H, aryl-*H*), 8.51 (s, 1H, aryl-*H*), 7.87 (s, 1H, aryl-*H*), 7.53 (s, 2H, aryl-*H*), 7.48 (s, 3H, aryl-*H*), 7.30 (s, 1H, aryl-*H*), 6.05 (s, 1H, central aryl-*H*), 5.69 (d, *J* = 10.0 Hz, 1H, central aryl-*H*), 4.67 (s, 1H, central aryl-*H*), 3.51 – 3.32 (m, 4H, CH₂), 3.25 (app d, *J* = 13.9 Hz, 2H, CH₂), 2.77 (app t, *J* = 16.4 Hz, 1H, CH), 2.44 (app d, *J* = 29.1 Hz, 2H, CH), 2.05 (br m, 1H, CH₂), 1.86 (br m, 2H, CH), 1.67 (br m, 3H, CH₃), 1.54 (s, 9H, *tert*-butyl CH₃), 1.44 (s, 18H, *tert*-butyl CH₃), 1.25 (app m, 12H, CH₃), 0.89 (app m, 6H, CH₃), 0.73 (app m, 3H, CH₃), 0.57 (app m, 3H, CH₃), 0.52 – 0.39 (m, 6H, CH₃), 0.35 (app m, 3H, CH₃) ppm. ³¹P NMR (121 MHz, C₆D₆) δ 54.03 (d, *J* = 91.4 Hz), 47.13 (d, *J* = 97.3 Hz), 26.90 (t, *J* = 91.9 Hz) ppm. ¹³C NMR (126 MHz, THF-*d*₈) δ 151.46 (s), 150.86 (s), 135.08 (s), 133.90 (s), 133.67 (s), 131.71 (s), 130.83 (s), 128.52 (d, *J* = 12.7 Hz), 128.28 (s), 128.09 (s), 127.24 (s), 125.80 (s), 98.84 (s), 85.44 (s), 35.50 (s), 35.15 (s), 31.66 (s), 31.52 (s), 30.43 (s), 20.74 (s), 20.54 (s), 19.21 (s), 18.34 (s), 17.69 – 16.97 (m), 16.70 (s) ppm. Anal. Calcd. for: C₅₈H₇₈F₃INi₂O₃P₃S (**6**) (%): C, 55.35; H, 6.97. Anal. Calcd. for: C₆₂H₉₄F₃INi₂O₄P₃S (**6**·**THF**) (%): C, 56.00; H, 7.13. Found: C, 56.40; H, 7.24.

Synthesis of complex 7

In a scintillation vial equipped with a stirbar, a solution of $\text{Na}_2\text{Fe}(\text{CO})_4$ (26 mg, 0.12 mmol) in THF (2 mL) was added to a THF (10 mL) solution of **5** (150 mg, 0.12 mmol). The mixture was stirred at room temperature for 4 h or monitored by ^{31}P NMR spectroscopy. A slight color change was observed from yellow-brown to orange-brown. The mixture was filtered through celite. The filtrate was collected and dried under vacuum. The residue was triturated with hexanes to collect the product. Precipitation of clean product was afforded by cooling a concentrated hexanes solution to -35°C for a few days (47% yield). ^1H NMR (300 MHz, C_6D_6) δ 8.05 (d, $J = 1.4$ Hz, 3H, aryl-*H*), 7.05 (dd, $J = 7.9, 1.4$ Hz, 3H, aryl-*H*), 6.98 (d, $J = 8.0$ Hz, 3H, aryl-*H*), 5.77 (s, 3H, central aryl-*H*), 3.07 (br s, 3H, CH_2), 2.93 (br s, 3H, CH_2), 2.57 (br, 3H, CH), 2.10 (br, 3H, CH), 1.38 – 1.21 (m, 18H, CH_3), 1.13 (s, 27H, *tert*-butyl CH_3), 0.97 (s, 18H, CH_3) ppm. ^{31}P NMR (121 MHz, C_6D_6) δ 61.90 ppm. ^{13}C NMR (126 MHz, C_6D_6) δ 256.34 (s), 148.64 (s), 139.63 (s), 132.98 (s), 130.65 (s), 126.17 (s), 121.91 (s), 76.80 (s), 65.21 (s), 34.08 (s), 31.07 (s), 26.61 (s), 25.44 (s), 21.58 (s), 18.68 (s), 17.25 (s), 16.52 (s), 15.56 (s) ppm. IR (CaF_2 window, THF, cm^{-1}) ν_{CO} : 1847, 1795. Anal. Calcd. for: $\text{C}_{60}\text{H}_{87}\text{Ni}_3\text{O}_3\text{P}_3$ (%): C, 64.04; H, 7.79. Found: C, 64.09; H, 7.63.

Synthesis of trinickel nonacarbonyl complex 8 supported by ligand 1b

$\text{Ni}(\text{COD})_2$ (143 mg, 0.520 mmol, 3 equiv) was added to a solution of **1b** (150 mg, 0.173 mmol, 1 equiv) in THF (15 mL). The solution was degassed and CO gas (0.865 mmol, 5 equiv) was delivered into the headspace using a volumetric gas bulb. The color of the solution changed from red-orange to almost colorless over 3 h. The mixture was left to react for 18 h at room temperature or monitored by ^{31}P NMR spectroscopy. The

solvent removed off the reaction mixture *in vacuo*. The residue was triturated with pentane, and the pentane fraction was collected and dried to give the clean product as a foamy solid (71% yield). Recrystallization of the product via layering of acetonitrile over a concentrated toluene solution at -35 °C yielded crystals. ^1H NMR (300 MHz, C_6D_6) δ 7.59 (d, 3H), 7.48 (s, 3H), 7.41 (s, 3H), 7.31 (d, 3H), 3.07 (d, 6H), 1.62 (m, 6H), 1.24 (s, 27H), 0.82 (m, 36H) ppm. ^{31}P NMR (300 MHz, C_6D_6) δ 54.2 (s) ppm. IR (CaF_2 window, THF, cm^{-1}): 2061.3, 1994.7.

Crystallographic Information

CCDC 833183, 961094, and 961095 contain the supplementary crystallographic data for this chapter. These data can be obtained free of charge from The Cambridge Crystallographic Data Centre via www.ccdc.cam.ac.uk/data_request/cif. The corresponding complexes for the CCDC deposition numbers are 833183 (**5**), 961094 (**6**), and 961095 (**7**).

Refinement details

In each case, crystals were mounted on a glass fiber or nylon loop using Paratone oil, then placed on the diffractometer under a nitrogen stream. Low temperature (100 K) X-ray data were obtained on a Bruker APEXII CCD based diffractometer (Mo sealed X-ray tube, $K\alpha = 0.71073 \text{ \AA}$). All diffractometer manipulations, including data collection, integration, and scaling were carried out using the Bruker APEXII software.²⁵ Absorption corrections were applied using SADABS.²⁶ Space groups were determined on the basis of systematic absences and intensity statistics, and the structures were solved by direct methods using XS (incorporated into SHELXTL) and refined by full-matrix least squares on F^2 . All non-hydrogen atoms were refined using anisotropic

displacement parameters. Hydrogen atoms were placed in idealized positions and refined using a riding model. The structure was refined (weighted least squares refinement on F^2) to convergence.

Table 1. Crystal and refinement data for complexes **5-7**.

Complex	5	6	7
empirical formula	C ₅₇ H ₈₆ I ₂ Ni ₃ P ₃	C _{76.21282} H _{107.54914} F ₃ INi ₂ O	C ₆₁ H ₈₇ N Ni ₃ O ₄ P ₃
formula wt	1294.10	1498.01	1167.36
T (K)	100	100	100
a, Å	13.2841(6)	15.7297(7)	18.977(8)
b, Å	31.8372(15)	19.8722(7)	13.886(5)
c, Å	14.5613(7)	25.1292(11)	24.819(12)
α , deg	90	90	90
β , deg	109.132(2)	102.033(3)	107.965(13)
γ , deg	90	90	90
V, Å ³	5818.2(5)	7682.4(6)	6221(5)
Z	4	4	4
Crystal system	Monoclinic	Monoclinic	Monoclinic
Space group	P2(1)/n	P2(1)/n	P2(1)/n
d _{calcd} , g/cm ³	1.477	1.295	1.246
θ range, deg	1.74-36.40	2.816-72.974	1.70-25.03
μ , mm ⁻¹	2.139	1.032	1.019
Abs. correction	Semi-empirical from equivalents	Semi-empirical from equivalents	Semi-empirical from equivalents
GOF ^c	0.985	1.029	1.084
R1, ^a wR2 ^b (I > 2 σ (I))	0.0274, 0.0462	0.0552, 0.1434	0.0514, 0.1360

$${}^a R1 = \frac{\sum ||F_o| - |F_c||}{\sum |F_o|} \quad {}^b wR2 = \left\{ \frac{\sum [w(F_o^2 - F_c^2)^2]}{\sum [w(F_o^2)]} \right\}^{1/2} \quad {}^c GOF = \frac{S}{n-p} = \left\{ \frac{\sum [w(F_o^2 - F_c^2)^2]}{(n-p)} \right\}^{1/2}$$

Special refinement details for **5**

All esds (except the esd in the dihedral angle between two l.s. planes) are estimated using the full covariance matrix. The cell esds are taken into account

individually in the estimation of esds in distances, angles, and torsion angles; correlations between esds in cell parameters are only used when they are defined by crystal symmetry. An approximate (isotropic) treatment of cell esds is used for estimating esds involving l.s. planes.

Special refinement details for 6

6 was crystallized from benzene/hexanes mixture. Accordingly, the compound crystallized with five benzene solvent molecules in the lattice. The structure also contains one outer-sphere trifluoromethanesulfonate counterion that was satisfactorily modeled.

Special refinement details for 7

Acetonitrile/toluene layering was used as the solvent to crystallize complex **4**. Accordingly, the compound crystallized with one acetonitrile solvent molecule in the lattice.

Special refinement details for 8

The compound was crystallized from benzene/hexane mixture. Only a partial data set was collected.

REFERENCES

- (a) Delaet, D. L.; Delrosario, R.; Fanwick, P. E.; Kubiak, C. P. *J. Am. Chem. Soc.* **1987**, *109*, 754. (b) Lemke, F. R.; Delaet, D. L.; Gao, J. L.; Kubiak, C. P. *J. Am. Chem. Soc.* **1988**, *110*, 6904. (c) Simon-Manso, E.; Kubiak, C. P. *Organometallics* **2005**, *24*, 96. (d) Ratliff, K. S.; Lentz, R. E.; Kubiak, C. P. *Organometallics* **1992**, *11*, 1986. (e) Morgenstern, D. A.; Wittrig, R. E.; Fanwick, P. E.; Kubiak, C. P. *J. Am. Chem. Soc.* **1993**, *115*, 6470. (f) Velian, A.; Lin, S. B.; Miller, A. J. M.; Day, M. W.; Agapie, T. *J. Am. Chem. Soc.* **2010**, *132*, 6296. (g) Lee, C. H.; Laitar, D. S.; Mueller, P.; Sadighi, J. P. *J. Am. Chem. Soc.* **2007**, *129*, 13802. (h) Vicic, D. A.; Anderson, T. J.; Cowan, J. A.; Schultz, A. J. *J. Am. Chem. Soc.* **2004**, *126*, 8132. (i) Keen, A. L.; Johnson, S. A. *J. Am.*

- Chem. Soc.* **2006**, *128*, 1806. (j) Tanabe, M.; Yumoto, R.; Osakada, K. *Chem. Commun.* **2012**, *48*, 2125. (k) Laskowski, C. A.; Hillhouse, G. L. *Chem. Sci.* **2011**, *2*, 321. (l) Torres-Nieto, J.; Brennessel, W. W.; Jones, W. D.; Garcia, J. J. *J. Am. Chem. Soc.* **2009**, *131*, 4120. (m) Shimada, S.; Rao, M. L. N.; Hayashi, T.; Tanaka, M. *Angew. Chem. Int. Ed.* **2001**, *40*, 213.
- 2 Gavrilova, A. L.; Bosnich, B. *Chem. Rev.* **2004**, *104*, 349.
- 3 (a) Brown, E. C.; Johnson, B.; Palavicini, S.; Kucera, B. E.; Casella, L.; Tolman, W. B. *Dalton Trans.* **2007**, 3035. (b) Maiti, D.; Woertink, J. S.; Ghiladi, R. A.; Solomon, E. I.; Karlin, K. D. *Inorg. Chem.* **2009**, *48*, 8342. (c) Chen, P. P. Y.; Yang, R. B. G.; Lee, J. C. M.; Chan, S. I. *Proc. Natl. Acad. Sci. USA* **2007**, *104*, 14570. (d) Cao, R.; Muñàller, P.; Lippard, S. J. *J. Am. Chem. Soc.* **2010**, *132*, 17366. (e) Gonzalez-Alvarez, A.; Alfonso, I.; Cano, J.; Diaz, P.; Gotor, V.; Gotor-Fernandez, V.; Garcia-Espana, E.; Garcia-Granda, S.; Jimenez, H. R.; Lloret, F. *Angew. Chem. Int. Ed.* **2009**, *48*, 6055. (f) Suh, M. P.; Han, M. Y.; Lee, J. H.; Min, K. S.; Hyeon, C. *J. Am. Chem. Soc.* **1998**, *120*, 3819. (g) Zhao, Q. L.; Betley, T. A. *Angew. Chem. Int. Ed.* **2011**, *50*, 709. (h) Tsui, E. Y.; Kanady, J. S.; Day, M. W.; Agapie, T. *Chem. Commun.* **2011**, *47*, 4189. (i) Hatnean, J. A.; Raturi, R.; Lefebvre, J.; Leznoff, D. B.; Lawes, G.; Johnson, S. A. *J. Am. Chem. Soc.* **2006**, *128*, 14992. (j) Guillet, G. L.; Sloane, F. T.; Dumont, M. F.; Abboud, K. A.; Murray, L. J. *Dalton Trans.* **2012**, *41*, 7866. (k) Liu, R. L.; von Malotki, C.; Arnold, L.; Koshino, N.; Higashimura, H.; Baumgarten, M.; Mullen, K. *J. Am. Chem. Soc.* **2011**, *133*, 10372. (l) Tsui, E. Y.; Day, M. W.; Agapie, T. *Angew. Chem. Int. Ed.* **2011**, *50*, 1668. (m) Lionetti, D.; Day, M. W.; Agapie, T. *Chem. Sci.* **2013**, *4*, 785.
- 4 (a) Chao, S. T.; Lara, N. C.; Lin, S. B.; Day, M. W.; Agapie, T. *Angew. Chem. Int. Ed.* **2011**, *50*, 7529. (b) Suseno, S.; Agapie, T. *Organometallics* **2013**, *32*, 3161. (c) Lin, S. B.; Day, M. W.; Agapie, T. *J. Am. Chem. Soc.* **2011**, *133*, 3828. (d) Kelley, P.; Lin, S. B.; Edouard, G.; Day, M. W.; Agapie, T. *J. Am. Chem. Soc.* **2012**, *134*, 5480. (e) Herbert, D. H.; Lara, N. C.; Agapie, T. *Chem.-Eur. J.* **2013**, DOI: 10.1002/chem.201302539. (f) Lin, S. B.; Herbert, D. H.; Velian, A.; Day, M. W.; Agapie, T. *J. Am. Chem. Soc.* **2013**, DOI: 10.1021/ja406696k.
- 5 (a) Beck, R.; Johnson, S. A. *Organometallics* **2013**, *32*, 2944. (b) Ito, M.; Matsumoto, T.; Tatsumi, K. *Inorg. Chem.* **2009**, *48*, 2215.

- 6 (a) Ratliff, K. S.; Broecker, G. K.; Fanwick, P. E.; Kubiak, C. P. *Angew. Chem. Int. Ed. Eng.* **1990**, *29*, 395. (b) Simon-Manso, E.; Kubiak, C. P. *Angew. Chem. Int. Ed.* **2005**, *44*, 1125. (c) Morgenstern, D. A.; Ferrence, G. M.; Washington, J.; Henderson, J. I.; Rosenhein, L.; Heise, J. D.; Fanwick, P. E.; Kubiak, C. P.; Kubiak, P. *J. Am. Chem. Soc.* **1996**, *118*, 2198. (d) Ferrence, G. M.; Fanwick, P. E.; Kubiak, C. P. *Chem. Commun.* **1996**, 1575.
- 7 (a) Chen, Y. F.; Sui-Seng, C.; Zargarian, D. *Angew. Chem. Int. Ed.* **2005**, *44*, 7721. (b) Jones, C.; Schulten, C.; Fohlmeister, L.; Stasch, A.; Murray, K. S.; Moubaraki, B.; Kohl, S.; Ertem, M. Z.; Gagliardi, L.; Cramer, C. J. *Chem.-Eur. J.* **2011**, *17*, 1294.
- 8 (a) Johnson, S. A.; Taylor, E. T.; Cruise, S. J. *Organometallics* **2009**, *28*, 3842. (b) Johnson, S. A.; Mroz, N. M.; Valdizon, R.; Murray, S. *Organometallics* **2011**, *30*, 441. (c) Bach, I.; Porschke, K. R.; Goddard, R.; Kopiske, C.; Kruger, C.; Rufinska, A.; Seevogel, K. *Organometallics* **1996**, *15*, 4959.
- 9 (a) Schneider, J. J.; Spickermann, D.; Blaser, D.; Boese, R.; Rademacher, P.; Labahn, T.; Magull, J.; Janiak, C.; Seidel, N.; Jacob, K. *Eur. J. Inorg. Chem.* **2001**, 1371. (b) Bai, G. C.; Wei, P. R.; Stephan, D. W. *Organometallics* **2005**, *24*, 5901. (c) Dong, Q. S.; Zhao, Y. X.; Su, Y. T.; Su, J. H.; Wu, B. A.; Yang, X. J. *Inorg. Chem.* **2012**, *51*, 13162. (d) Priego, J. L.; Doerrer, L. H.; Rees, L. H.; Green, M. L. H. *Chem. Commun.* **2000**, 779.
- 10 Davidson, J. L.; Green, M.; Stone, F. G. A.; Welch, A. J. *J. Chem. Soc. Dalton.* **1979**, 506.
- 11 Inagaki, A.; Takaya, Y.; Takemori, T.; Suzuki, H.; Tanaka, M.; Haga, M. A. *J. Am. Chem. Soc.* **1997**, *119*, 625. The author was able to find only one structurally characterized complex with a $\mu_3:\eta^2:\eta^2:\eta^3$ arene coordinated to three transition metals via CSD search.
- 12 Hruszkewycz, D. P.; Wu, J. G.; Green, J. C.; Hazari, N.; Schmeier, T. J. *Organometallics* **2012**, *31*, 470.
- 13 (a) Maj, J. J.; Rae, A. D.; Dahl, L. F. *J. Am. Chem. Soc.* **1982**, *104*, 3054. (b) Paquette, M. S.; Dahl, L. F. *J. Am. Chem. Soc.* **1980**, *102*, 6621.
- 14 Thomas, M. G.; Muetterties, E. L.; Day, R. O.; Day, V. W. *J. Am. Chem. Soc.* **1976**, *98*, 4645.

- 15 North, T. E.; Thoden, J. B.; Spencer, B.; Bjarnason, A.; Dahl, L. F. *Organometallics* **1992**, *11*, 4326.
- 16 Buchalski, P.; Jadach, P.; Pietrzykowski, A.; Suwinska, K.; Jerzykiewicz, L.; Sadlo, J. *Organometallics* **2008**, *27*, 3618.
- 17 (a) Gallop, M. A.; Gomezsal, M. P.; Housecroft, C. E.; Johnson, B. F. G.; Lewis, J.; Owen, S. M.; Raithby, P. R.; Wright, A. H. *J. Am. Chem. Soc.* **1992**, *114*, 2502. (b) Ingham, S. L.; Johnson, B. F. G.; Nairn, J. G. M. *J. Chem. Soc. Chem. Commun.* **1995**, 189.
- 18 (a) Wadepohl, H.; Buchner, K.; Pritzkow, H. *Angew. Chem. Int. Ed. Eng.* **1987**, *26*, 1259. (b) Wadepohl, H.; Calhorda, M. J.; Herrmann, M.; Jost, C.; Lopes, P. E. M.; Pritzkow, H. *Organometallics* **1996**, *15*, 5622.
- 19 Muller, J.; Gaede, P. E.; Qiao, K. *Angew. Chem. Int. Ed. Eng.* **1993**, *32*, 1697.
- 20 Murahashi, T.; Fujimoto, M.; Kawabata, Y.; Inoue, R.; Ogoshi, S.; Kurosawa, H. *Angew. Chem. Int. Ed.* **2007**, *46*, 5440.
- 21 Bochmann, M.; Hawkins, I.; Yellowlees, L. J.; Hursthouse, M. B.; Short, R. L. *Polyhedron* **1989**, *8*, 1351.
- 22 Johnson, M. J. A.; Gantzel, P. K.; Kubiak, C. P. *Organometallics* **2002**, *21*, 3831.
- 23 *Inorganic Syntheses, Reagents for Transition Metal Complex and Organometallic Syntheses*, 1990; Vol. 28.
- 24 Fulmer, G. R.; Miller, A. J. M.; Sherden, N. H.; Gottlieb, H. E.; Nudelman, A.; Stoltz, B. M.; Bercaw, J. E.; Goldberg, K. I. *Organometallics* **2010**, *29*, 2176.
- 25 APEX2, Version 2 User Manual, M86-E01078, Bruker Analytical X-ray Systems, Madison, WI, June 2006.
- 26 Sheldrick, G. M. "SADABS (Version 2008/1): Program for Absorption Correction for Data from Area Detector Frames", University of Göttingen, 2008.

CHAPTER 4

SYNTHESIS AND CHARACTERIZATION OF A SERIES OF MIXED TRANSITION METAL
MANGANESE-OXIDO CUBANES AND THEIR OXYGEN ATOM TRANSFER REACTIVITY

ABSTRACT

Discrete oxide clusters displaying two types of transition metals were targeted for systematic metal composition-property studies relevant to mixed transition metal oxides employed in electrocatalysis. A series of heterometallic trimanganese tetraoxido clusters capped with a redox-active metal, $[\text{MMn}_3\text{O}_4]$ ($\text{M} = \text{Fe}, \text{Co}, \text{Ni}, \text{Cu}$), was synthesized starting from a $[\text{CaMn}_3\text{O}_4]$ precursor. Anomalous diffraction data show that metal M is incorporated cleanly at a single position in the cluster. Two redox events were observed between -2.0 and $+0.8$ V (vs. Fc/Fc^+) for $[\text{FeMn}_3\text{O}_4]$ and $[\text{CoMn}_3\text{O}_4]$ vs. one redox event for $[\text{NiMn}_3\text{O}_4]$ and $[\text{CuMn}_3\text{O}_4]$. Spectroscopic and crystallographic studies of $[\text{FeMn}_3\text{O}_4]$, $[\text{CoMn}_3\text{O}_4]$, and $[\text{NiMn}_3\text{O}_4]$ indicate that redox chemistry occurs at Mn for $[\text{FeMn}_3\text{O}_4]$ and $[\text{NiMn}_3\text{O}_4]$, in contrast to $[\text{CoMn}_3\text{O}_4]$ where Co also participates in the electron transfer event. These are the first studies of structurally related heterometallic oxide clusters that address the redox relation between the two types metals. Additional studies on oxygen atom transfer reactivities of $[\text{MMn}_3\text{O}_4]$ and $[\text{MMn}_3\text{O}_2]$ series were performed to investigate the effect of the heterometal M in the reaction rates.

INTRODUCTION

Mixed metal oxides have received significant attention over the last decade for their role as electrocatalysts for the oxygen evolution reaction (OER)¹ and the oxygen reduction reaction (ORR)^{1c} that are central to the development of solar electrolytic water splitting devices,² and fuel cells.³ Heterometallic oxides are also employed for lithium-ion/-air batteries.³⁻⁴ In these systems the effects of the interaction between the heterometallic components are not well understood. The rational synthesis of well-defined oxide-bridged mixed transition metal complexes is desirable to allow for the systematic study of the effects of heterometals and the structure-function relationship of the materials. The synthesis of mixed metal oxide clusters is challenging due to the need to control the relative ratio of the two types of metals and their locations, and to prevent cluster overgrowth by oligomerization. There have been very few reports of these types of complexes that were not isolated as self-assembled materials from recrystallization of the reaction mixtures.⁵ The rational syntheses of multinuclear mixed transition metal complexes displaying metal–metal interactions and [MFe₃S₄] clusters have been reported.⁶ Heterobimetallic complexes bridged by a hydroxy group have also been prepared from the activation of O₂,⁷ however, reports on higher nuclearity metal oxido complexes are rare.

With a structurally characterized series of mixed metal oxide clusters at hand, reactivity studies including oxygen atom transfer reactions are relevant to investigate the effects of variation of the heterometals M. In synthetic small molecule and biomimetic metal oxo complexes, the addition of redox-inactive Lewis acidic metal ions has been shown to tune the reactivities of these systems for different processes. For example, the addition of these Lewis acidic metal cations was shown to cause a significant change in

the redox potentials of the metal oxo moieties. Fukuzumi, Nam, and co-workers have shown for a non-heme $\text{Fe}^{\text{IV}}=\text{O}$ complex **A** (Figure 1), a shift of 0.84 V in the reduction potential was observed upon the addition of $\text{Sc}(\text{OTf})_3$, and remarkably the electron transfer rates were found to be linearly correlated to the Lewis acidity of the metal ions added.⁸

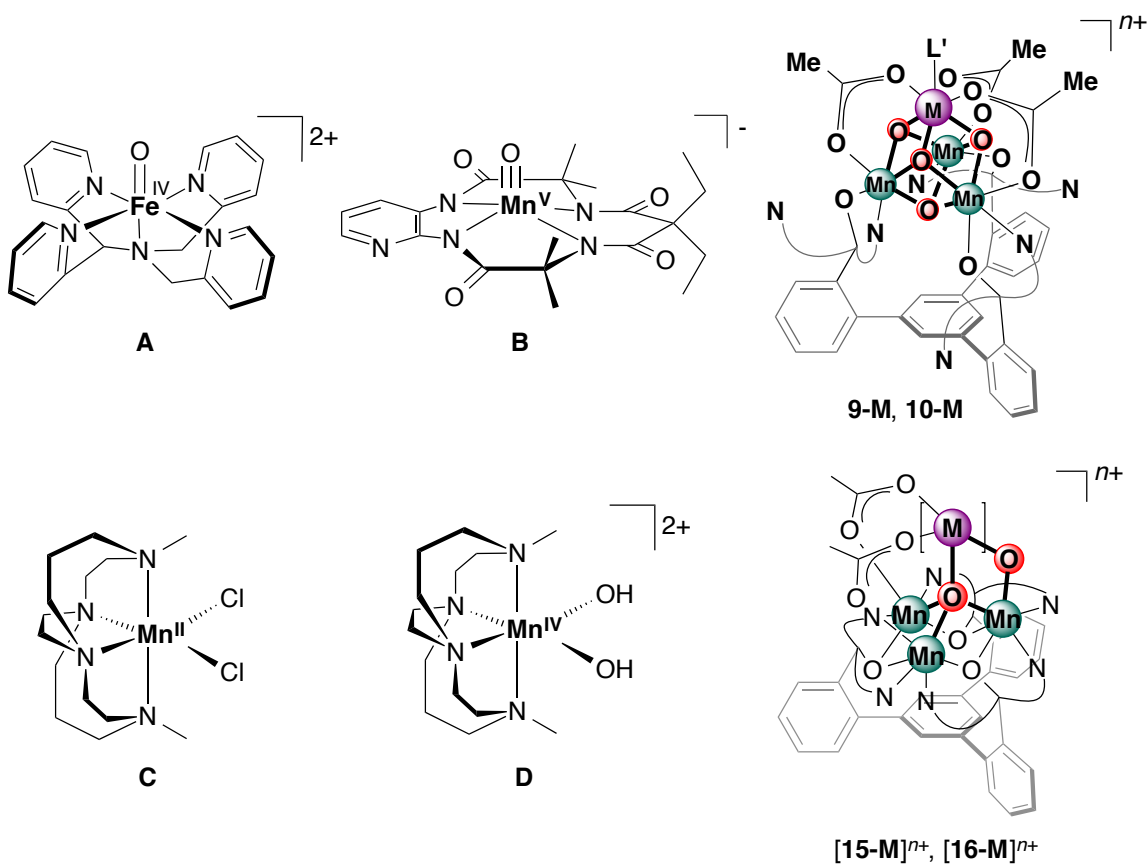


Figure 1. Examples of compounds that perform oxygen atom transfers with rates that are affected by the addition of Lewis acidic metals.⁸⁻⁹

Redox-inactive metal ions have also been shown to affect transformations of metal-oxo compounds such as oxygen atom transfer reaction. Fukuzumi, Nam, and co-workers observed with the same metal complex **A** that the addition of $\text{Sc}(\text{OTf})_3$ can effect a switch of mechanism from direct oxygen atom transfer to metal-ion coupled

electron transfer in the sulfoxation of thioanisoles.^{9a} Collins and co-workers have also reported that the addition of redox-inactive metal cations M (M = Na, Li, Ba, Mg, Zn, and Sc) to the Mn^{IV}-oxo complex **B** affects the oxygen atom transfer rate.^{9b} Yin and co-workers have also studied the oxygen transfer reactions of Mn complexes **C** and **D** upon reaction with iodosobenzene (PhIO) in the presence of metal cations to generate sulfoxide or triphenylphosphine oxide from the corresponding sulfide and triphenylphosphine.^{9c} The oxygen transfer reaction rate displayed by complexes **B**, **C**, and **D** in the presence of redox-inactive metal ions are found to be linearly correlated to the metal ions' pK_a as a measure of Lewis acidity.¹⁰

While the oxygen atom transfer capabilities of these reported complexes have been examined, they lack the structural characterization of the final complex formed prior to transformation of substrate. Two series of clusters, [MMn₃O₄] (**9-M** and **10-M**) and [MMn₃O₂] ([**15-M**]ⁿ⁺ and [**16-M**]ⁿ⁺), have been previously reported by the Agapie group that can be prepared with precise control over the M : Mn : oxido ratios.¹¹ One great advantage of these series is that they have been structurally characterized by X-ray diffraction, thus, the exact positions of each metal centers and oxidos are also known. The isostructural nature of these clusters will allow for the systematic analysis on their reactivities.

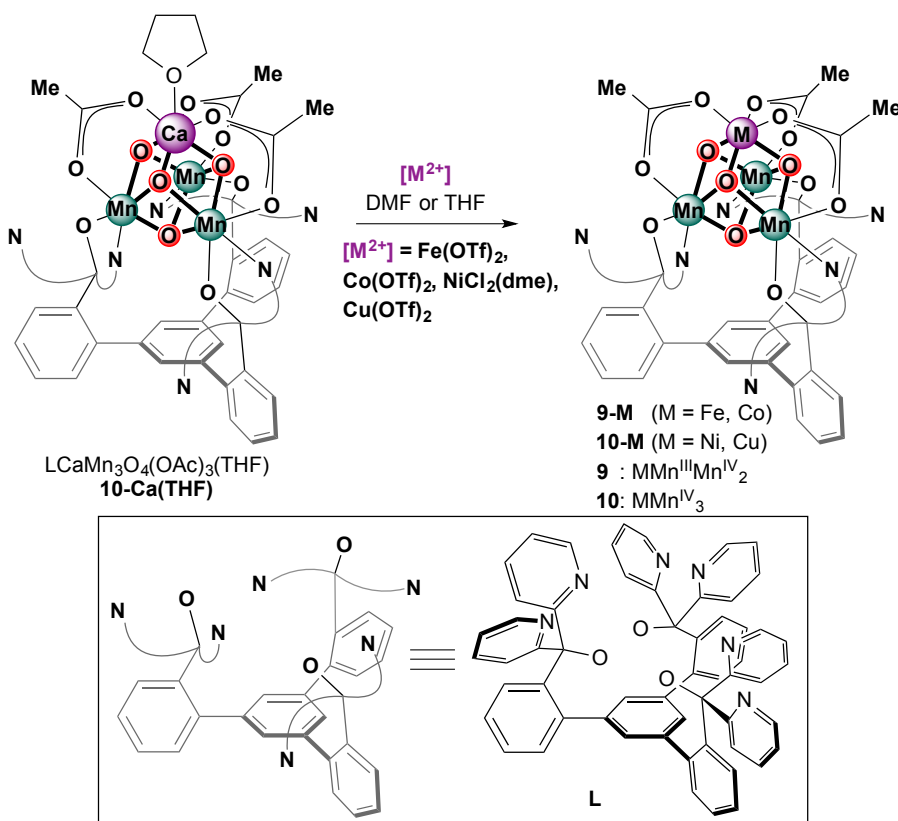
This chapter describes the controlled syntheses and characterization of novel, oxido-bridged mixed transition metal manganese cubane clusters [MMn₃O₄] (M = Fe³⁺, Co³⁺, Ni²⁺, Cu²⁺). Oxygen atom transfer capabilities of the [MMn₃O₄] and [MMn₃O₂] series are also investigated as an extension of previous studies as well as to further understand the role of the Lewis acidic heterometal on the transformation.

RESULTS AND DISCUSSIONS

3.1 Synthesis of $[MMn_3O_4]$ clusters ($M = Fe, Co, Ni, Cu$)

Our group has previously reported structural models of the cubane subsite of the oxygen-evolving complex (OEC) of Photosystem II (PSII).^{11a} Synthetic access to a series of heterometallic complexes of Mn with redox-inactive metals has provided insight into the effect of Ca^{2+} in OEC, in terms of a correlation between Lewis acidity and the reduction potential of the cluster.^{11a,11d} In this study, we targeted analogs of **10-Ca(THF)** with redox-active metal ions in place of Ca^{2+} (Scheme 1).

Scheme 1. Syntheses of mixed transition metal-oxide cubanes



We have previously reported **9-Mn**,^{11a} and herein we describe the syntheses of **9-Fe**, **9-Co**, **10-Ni**, and **10-Cu**. Treatment of a **10-Ca(THF)** suspension with M^{2+} precursors (e.g., $\text{Fe}(\text{OTf})_2$, $\text{Co}(\text{OTf})_2$, $\text{NiCl}_2(\text{dme})$, and $\text{Cu}(\text{OTf})_2$; $\text{OTf} =$

trifluoromethanesulfonate, dme = dimethoxyethane) in dimethylformamide (DMF) or tetrahydrofuran (THF) yielded the corresponding **9-M** and **10-M** analogs (Scheme 1).

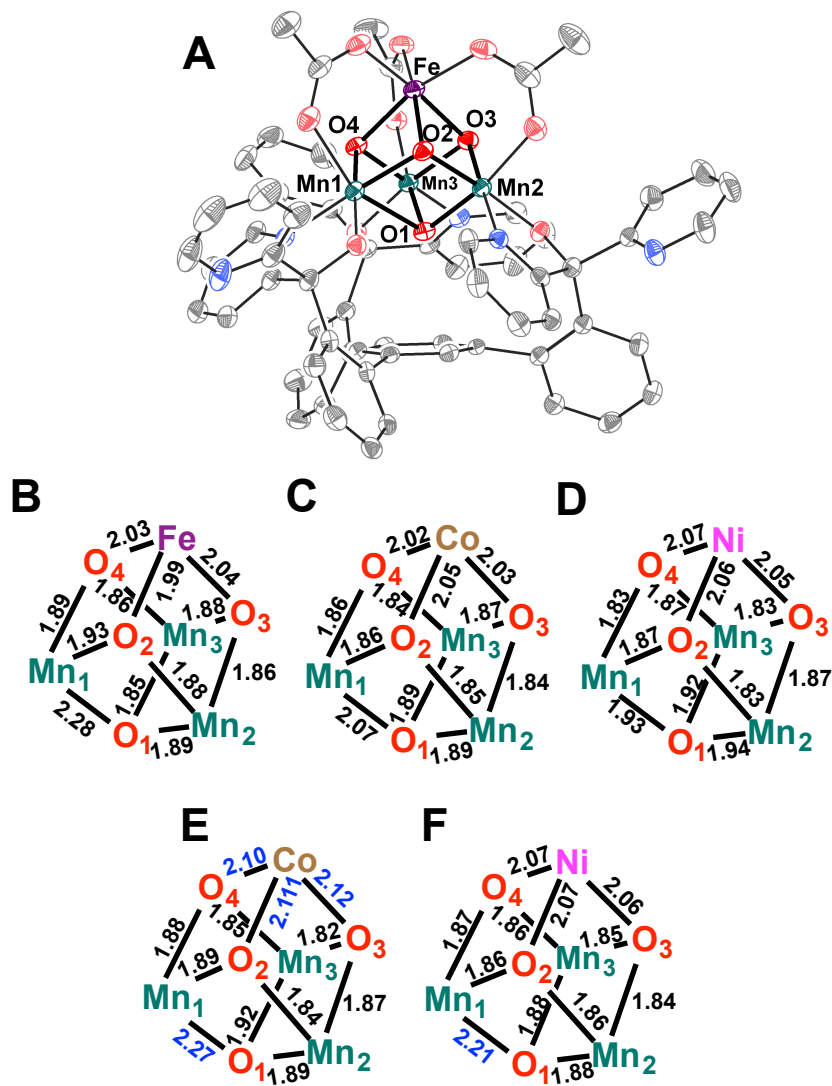


Figure 2. (A) Complete solid-state structure of **9-Fe**. Relevant metal-oxo distances for (B) **9-Fe**, (C) **9-Co**, (D) **10-Ni**, (E) **[11-Co][CoCp₂]**, (F) **[13-Ni][CoCp₂]** in Å. In (E) and (F), the largest bond distance changes are highlighted in blue.

Electrospray ionization mass spectrometry (ESI-MS) of each reaction mixture showed peaks at m/z 1256.6 $[\text{LFeMn}_3\text{O}_4(\text{OAc})_2]^+$ and 1316.8 $[\text{LFeMn}_3\text{O}_4(\text{OAc})_3]^+$ for **9-Fe**, 1319.6 $[\text{LCoMn}_3\text{O}_4(\text{OAc})_2]^+$ and 1354.5 $[\text{LCoMn}_3\text{O}_4(\text{OAc})_3]^+$ for **9-Co**, 1259.8

[LNiMn₃O₄(OAc)₂]⁺ for **9-Ni**, and 1264.7 [LCuMn₃O₄(OAc)₂]⁺ for **9-Cu**. Single crystals suitable for X-ray diffraction (XRD) study were obtained from vapor diffusion of diethyl ether into a benzene solution of **9-Fe**. The XRD study of **9-Fe** showed that the Mn–oxido distances of Mn₁ (1.893(3), 1.927(3), and 2.281(3) Å) vs. those of Mn₂ and Mn₃ (1.846(3)–1.884(3) Å) are consistent with the Mn^{III}Mn^{IV}₂ assignment for the three Mn centers (Figure 2). The *pseudo*-octahedral high-spin d⁴ Mn^{III} center is axially elongated to accommodate the single unpaired electron in a σ-antibonding orbital. The Fe center of **9-Fe** was assigned as Fe^{III} by balancing the charge of the overall neutral complex and by Mössbauer spectroscopy with an isomer shift, δ, of 0.45 mm/s and quadrupole splitting parameter, |ΔE_Q|, of 0.659 mm s⁻¹ (Figure 3).¹²

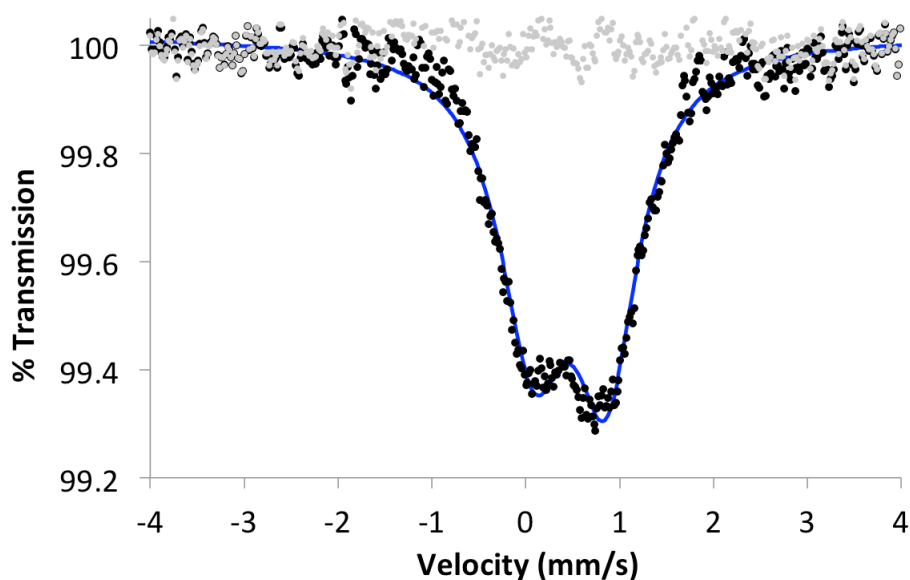


Figure 3. Zero-field ⁵⁷Fe Mössbauer spectrum for **9-Fe** collected by Jonathan Rittle (80 K, data: black, spectral fit: blue, residual: grey).

An XRD study of **9-Co** crystallized by vapor diffusion of diethyl ether into a benzene solution showed that the Mn–oxido distances of Mn₁ (1.857(5), 1.863(5), and 2.071(5) Å) vs. those of Mn₂ and Mn₃ (1.842(5)–1.893(4) Å) are also consistent with the

Mn^{III}Mn^{IV}₂ assignment for the Mn centers (Figure 2) with a Co^{III} center by charge balance. XRD studies for **10-Ni** show that all Mn centers are Mn^{IV} based on the Mn–oxido distances (1.8283(2)–1.9394(2) Å).^{11d} Despite multiple recrystallization attempts of **10-Cu** under various conditions, the complex has always crystallized in space group R-3, convoluting the analysis of metal–oxido distances to determine the metals' oxidation states. The oxidation state assignments above are consistent with reduction of the initial Mn^{IV}₃ moiety (in **10-Ca**) by transmetallating with Fe^{II} and Co^{II} to generate M^{III}Mn^{III}Mn^{IV}₂, where the M^{III} oxidation state is easily accessible.

4.2 Dispersive Difference Diffraction Analysis (DDFS)

As it is difficult to distinguish between Mn, Fe, Co, Ni, and Cu by XRD alone, we exploited the possibility to differentiate between elements by their X-ray absorption properties. As **9-Co** and **9-Fe** crystallized in centrosymmetric space groups, dispersive difference diffraction analysis was performed to confirm that the apical metal in **10-Ca(THF)** was exclusively substituted by the respective d-block metal (Figure 4). To determine the exact position of the absorption edge, X-ray absorption spectra (XAS) around the tabulated values for the Mn K-edge (1.8961 Å), and the Co (1.6083 Å) or Fe K-edge (1.7433 Å) were collected on single crystals of **9-Co** and **9-Fe**, respectively. Three datasets were collected on each crystal, a reference set for refinement (0.95369 Å), and two at the inflection point of the Mn (1.89225 Å, 1.89138 Å, λ_{Mn}) and Fe (1.74007 Å, λ_{Fe}) or Co (1.60554 Å, λ_{Co}) K-edge XAS, respectively. The structures were solved with SHELXS in the reference datasets and refined with SHELXL,¹³ with all heavy atom types assigned to Mn. Dispersive difference densities were calculated with FFT (CCP4) as follows: $F(\text{Fe})=F(\lambda_{\text{Mn}})-F(\lambda_{\text{Fe}})$, $F(\text{Co})=F(\lambda_{\text{Mn}})-F(\lambda_{\text{Co}})$ and $F(\text{Mn})=F(\lambda_{\text{Fe}})-$

$F(\lambda_{\text{Mn}})$ or $F(\text{Mn})=F(\lambda_{\text{Co}})-F(\lambda_{\text{Mn}})$. These data confirm selective substitution of Ca^{2+} with Fe and Co ions. This selectivity is notable, given the chemical lability of the Mn^{III} ions that are present in the cluster. The present “site-differentiated” synthesis of $[\text{MMn}_3\text{O}_4]$ is reminiscent of previous reports of mixed metal $[\text{MFe}_3\text{S}_4]$ clusters.^{6d,6e}

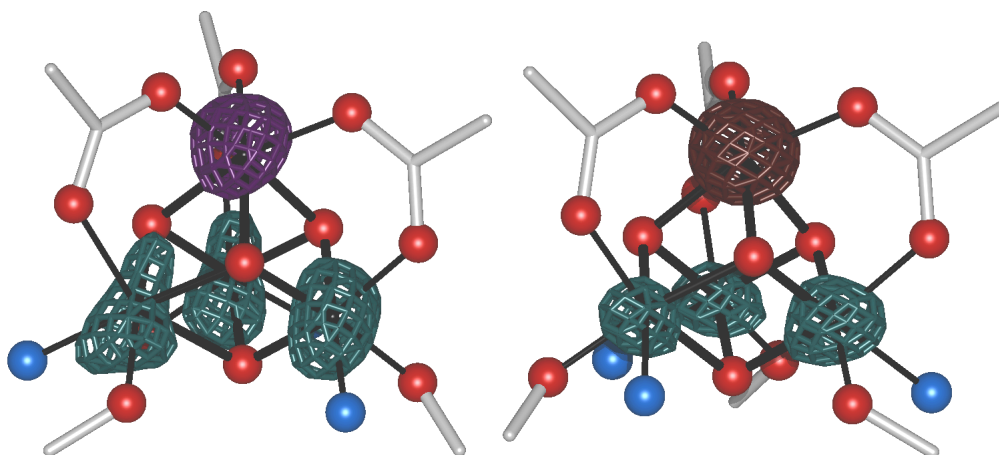


Figure 4. Dispersive difference maps for (left) **9-Fe** and (right) **9-Co** (purple: Fe, green: Mn, brown: Co, red: oxygen, blue: nitrogen, white: carbon). DDFS data collected by Jens Kaiser.

4.3 X-ray absorption spectroscopy studies (XANES and EXAFS) on **9-M** and **10-M**

X-ray absorption near edge structure (XANES) studies on **9-M** and **10-M** (Figure 5) were performed to evaluate the oxidation state assignments in the clusters. The Mn XANES spectra for **10-Ni** and **10-Cu** display a clear shift to higher energy in comparison to **9-Fe** and **9-Co**, indicating a higher average Mn oxidation state for **10-Cu** and **10-Ni**. These shifts support the assignment of Mn^{IV}_3 for **10-Ni** and **10-Cu**, and $\text{Mn}^{\text{III}}\text{Mn}^{\text{IV}}_2$ for **9-Fe** and **9-Co**.

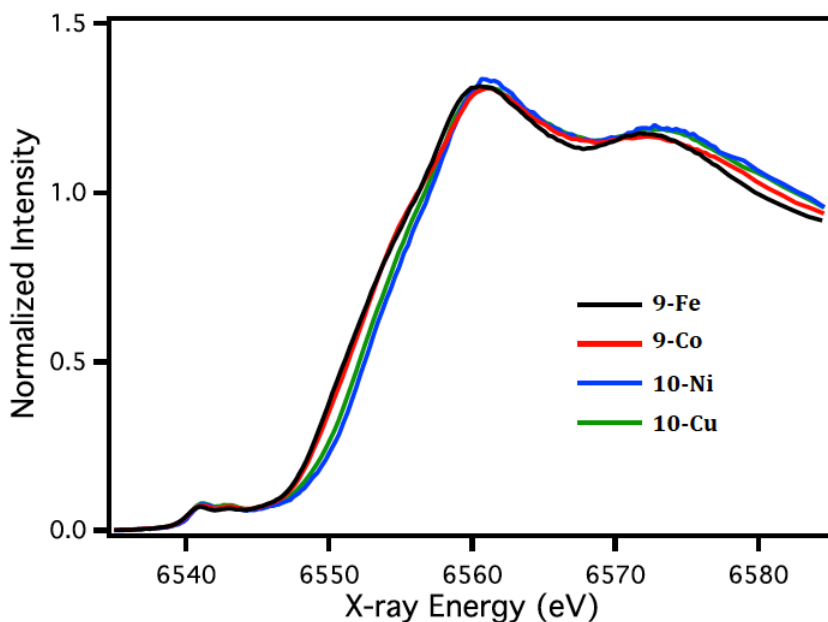


Figure 5. Normalized Mn K-edge XANES spectra from **9-Fe/Co** and **10-Ni/Cu**. XANES data collected by Rosalie Tran and Junko Yano.

4.4 Cyclic voltammetry studies on **9-M** and **10-M**

In addition to the previously reported compounds, the effect of changing the apical metal center to various redox-active metals was studied via cyclic voltammetry. Cyclic voltammograms (CVs) of **9-** and **10-M** in *N,N*-dimethylacetamide (DMA) showed quasireversible redox couples (Figure 6) assigned as the $\text{MMn}^{\text{IV}}_3\text{O}_4/\text{MMn}^{\text{III}}\text{Mn}^{\text{IV}}_2\text{O}_4$ couple at +290 (**9-Fe**), +260 (**9-Co**), -600 (**10-Ni**), and -590 (**10-Cu**) mV, respectively, vs. the ferrocene/ferrocenium couple (Fc/Fc^+). The redox potentials of **9-Fe** and **9-Co** for the $\text{MMn}^{\text{III}}\text{Mn}^{\text{IV}}_2\text{O}_4/\text{MMn}^{\text{IV}}_3\text{O}_4$ couple are similar to that of $\text{LMn}_4\text{O}_4(\text{OAc})_3$ (**9-Mn**) ($E_{1/2} = +290$ mV).^{11a} Despite the M^{3+} charge on the apical metal, the CVs of **9-Fe** and **9-Co** display different redox features from $[\text{LScMn}_3\text{O}_4(\text{OAc})_3][\text{OTf}]$ (**10-Sc(OTf)**) that show the $\text{MMn}^{\text{IV}}_3\text{O}_4/\text{MMn}^{\text{III}}\text{Mn}^{\text{IV}}_2\text{O}_4$ (quasi-reversible) and the $\text{MMn}^{\text{III}}_2\text{Mn}^{\text{IV}}\text{O}_4/\text{MMn}^{\text{III}}\text{Mn}^{\text{IV}}_2\text{O}_4$ (irreversible) couples ($\text{M} =$

Sc).^{11b,11d} The reduction potentials of **10-Ni** and **10-Cu** are closer to **10-Zn** ($E_{1/2} = -630$ mV),^{11d} although Zn^{2+} is a dicationic redox-*inactive* metal. As discussed previously, the variation in redox potentials cannot be attributed to purely electrostatic effects, but correlates to the Lewis acidity of the apical metal.^{11c,11d,14}

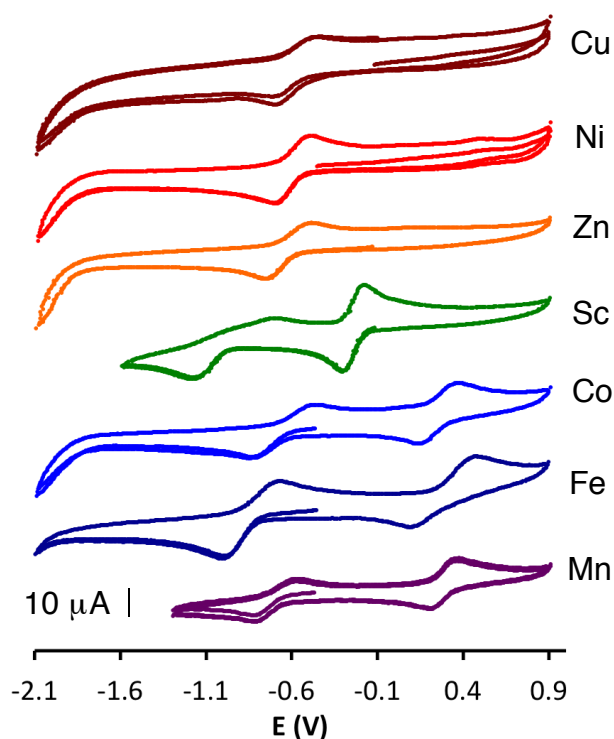


Figure 6. Cyclic voltammograms of $[\text{LMMn}_3\text{O}_4(\text{OAc})_3]^n$ ($\mathbf{M} = \text{Mn, Co, Fe, Sc, Zn, Ni, Cu}$) in 0.1 M NBu_4PF_6 in DMA with scan rate 100 mV/s. Potentials are referenced Fc/Fc^+ . CVs for $\mathbf{M} = \text{Mn, Sc, Zn}$ were previously reported.^{11a,11b,11d}

The $E_{1/2}$ values of $[\text{MMn}_3\text{O}_4]$ ($\text{MMn}^{\text{III}}\text{Mn}^{\text{IV}}_2\text{O}_4 / \text{MMn}^{\text{IV}}_3\text{O}_4$ couple) were plotted against the $\text{p}K_a$'s of the metal aqua ions measured in water,¹⁵ used here as a measure of the Lewis acidity of \mathbf{M} . The plot corresponding to the series of complexes in this chapter is incorporated into the $E_{1/2}$ vs. $\text{p}K_a$ plot that was previously reported by Emily Y. Tsui and Po-Heng Lin to obtain a more complete correlation between all structurally related $[\text{MMn}_3\text{O}_4]$ clusters that have been synthesized (Figure 7).¹⁶

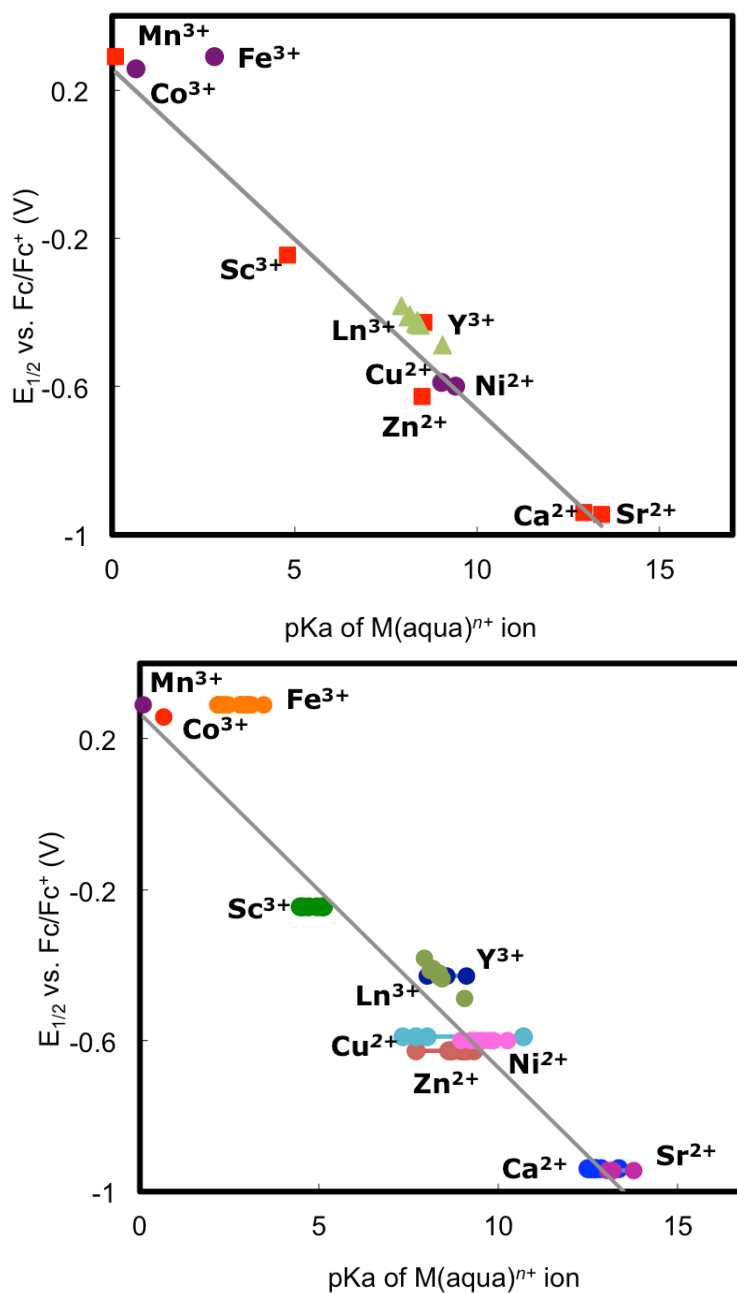


Figure 7. (*Top*) Reduction potentials of $[\text{MMn}_3\text{O}_4]$ complexes vs. midpoint of $\text{p}K_a$ range of the corresponding $\text{M}(\text{aqua})^{n+}$ ion as a measure of Lewis acidity. Potentials are referenced to ferrocene/ferrocenium. M is redox inactive metal (red squares)^{11d}, lanthanide (green triangles),^{16b} or redox-active metal (purple circles, this work). (*Bottom*) Reduction potentials of $[\text{MMn}_3\text{O}_4]$ complexes vs. $\text{p}K_a$ range of the corresponding $\text{M}(\text{aqua})^{n+}$ ion as a measure of Lewis acidity.

As shown in Figure 7, the linear correlation of the plot is retained even with the addition of the data obtained from **9-Fe**, **9-Co**, **10-Ni**, and **10-Cu**. This study supports the current proposal that the positive shift in reduction potential is dependent on the Lewis acidity of the incorporated heterometal M, where the increased electron-withdrawing effect upon the μ_3 -oxido ligands helps stabilize the more reduced Mn centers.

An important difference between the CVs of the clusters capped with redox-active metals is the presence of two redox events for **9-Fe/Co/Mn** vs. only one for **10-Ni/Cu** within the *ca.* 3 V range of the DMA solvent window (Figure 6). This behavior may be relevant to the performance of mixed-metal oxides used for ORR and/or OER catalysts and especially Li-ion batteries, where the presence of other transition metals (Fe, Co, Ni and Cu) strongly influences the response of LiMn_2O_4 spinel as cathodes in lithium cells.¹⁷ Access to two redox events rather than one within a certain potential window is valuable for multielectron reactivity and energy storage. The presence of a more electronegative metal centers (e.g., Mn, Co, Fe) not only shifts the reduction potentials of the cluster toward more positive potentials, but also decreases the separation of the redox events.

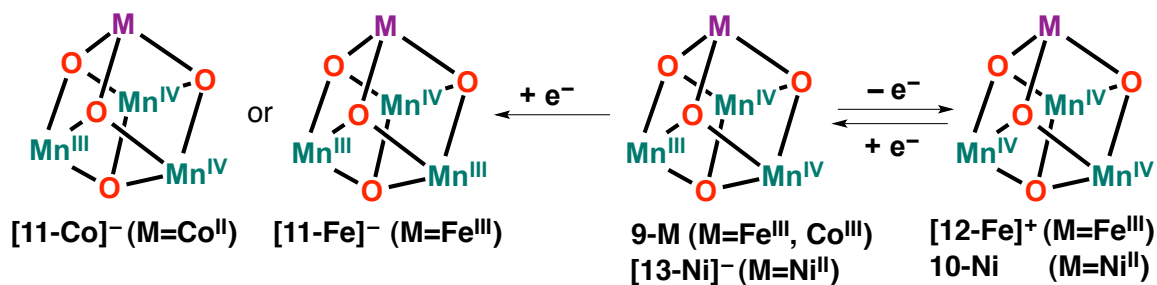
4.5 Electron transfer studies by, XAS, XRD, and EPR

In contrast to redox-*inactive* metal substitution, with redox-*active* metals present in the apical position, assignment of the site of electron transfer requires further elucidation. The electron transfer events are evaluated by multiple spectroscopic techniques that include XAS and electron paramagnetic resonance (EPR). XAS studies on all the $[\text{MMn}_3\text{O}_4]$ series (M = Ca, Sr, Sc, Gd, Mn, Fe, Co, Ni, Cu) synthesized by Sandy Suseno, Emily Y. Tsui, Jacob S. Kanady, and Po-Heng Lin were performed by

Rosalie Tran, Ruchira Chatterjee, and Junko Yano. The edge energies were evaluated by calculating the inflection point energy (IPE), which takes the zero-crossing of the second derivative of the absorption spectrum at the steeply rising edge. All available and calculated Mn and M (M = Ca, Sr, Sc, Gd, Mn, Fe, Co, Ni, Cu) edge energies of analyzed clusters are summarized in Table 1 with their current assignment of metal oxidation states. All EPR studies were performed by Luo Lu and R. David Britt.

Chemical reduction and/or oxidation of **9-Fe**, **9-Co**, and **10-Ni** were attempted. **9-M** (M = Fe, Co) was treated with one equivalent of cobaltocene (CoCp_2) or tris(4-bromophenyl)ammoniumyl hexachloroantimonate (“Magic Blue”) targeting $[\mathbf{11-M}]^-$ or $[\mathbf{12-M}]^+$, respectively (Scheme 2). A XRD study on the crystals of $[\mathbf{11-Fe}]^-$ has been performed previously. While the resulting data confirmed the formation of the reduced cluster, the data set was not optimal (twinned crystals) such that bond distance analysis on the refined structure could not be done accurately. On the other hand, no structural data has been obtained to date for the oxidation of **9-Fe** to generate $[\mathbf{12-Fe}]^+$. The corresponding ESI-MS data displayed a peak at m/z 1506.0 for $[\mathbf{11-Fe}][\text{CoCp}_2]$ and 1316.7 for $[\mathbf{12-Fe}]^+$, indicative of product formation and retention of the structural cubane moiety upon electron transfer.

Scheme 2. Redox conversions of **9-M** and **10-M**



Mn XANES studies of $[\mathbf{11-Fe}]^-$ show a shift to lower energy compared to $\mathbf{9-Fe}$, consistent with reduction at Mn (Figure 8). A much smaller shift was observed upon $\mathbf{9-Fe}$ to $[\mathbf{12-Fe}]^+$ transition (Figure 8). While this suggests a decreased charge density at the Mn site in some extent, a small shift as compared to that from $[\mathbf{11-Fe}]^-$ to $\mathbf{9-Fe}$ may be due to the increased charge delocalization in $[\mathbf{12-Fe}]^+$ and/or the geometry change of the complex. The rising edge positions of the Fe XANES spectra remain the same in $[\mathbf{11-Fe}]^-$, $\mathbf{9-Fe}$, and $[\mathbf{12-Fe}]^+$ (Figure 9). On the other hand, the Mn and Fe EXAFS data (Figure 10-11) are consistent with slight geometric fluctuations due to the changes in M–O and M–Mn bond distances within the cubane moiety. Mössbauer spectra of $[\mathbf{11-Fe}]^-$ and $[\mathbf{12-Fe}]^+$ displayed isomer shift values at 0.42 and 0.51 mm/s, respectively (Figure 12-13), indicative of a Fe^{III} center in both cases.

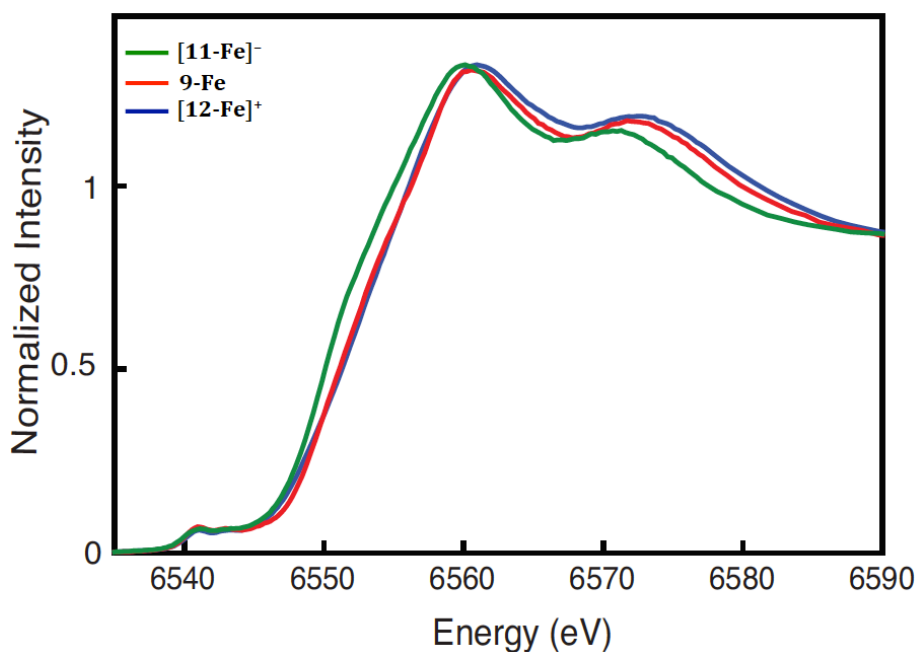


Figure 8. Normalized Mn K-edge XANES spectra for $[\mathbf{11-Fe}][\text{CoCp}_2]$, $\mathbf{9-Fe}$, and $[\mathbf{12-Fe}][\text{SbCl}_6]$. XANES data collected by Rosalie Tran and Junko Yano.

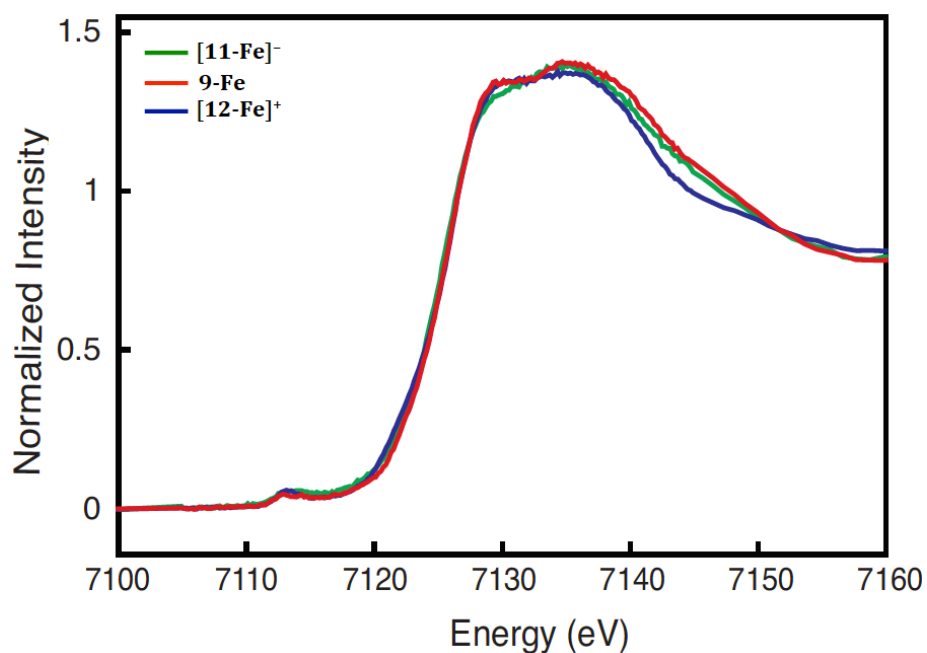


Figure 9. Normalized Fe K-edge XANES spectra for $[11\text{-Fe}]^-$, 9-Fe , and $[12\text{-Fe}]^+$. XANES data collected by Rosalie Tran and Junko Yano.

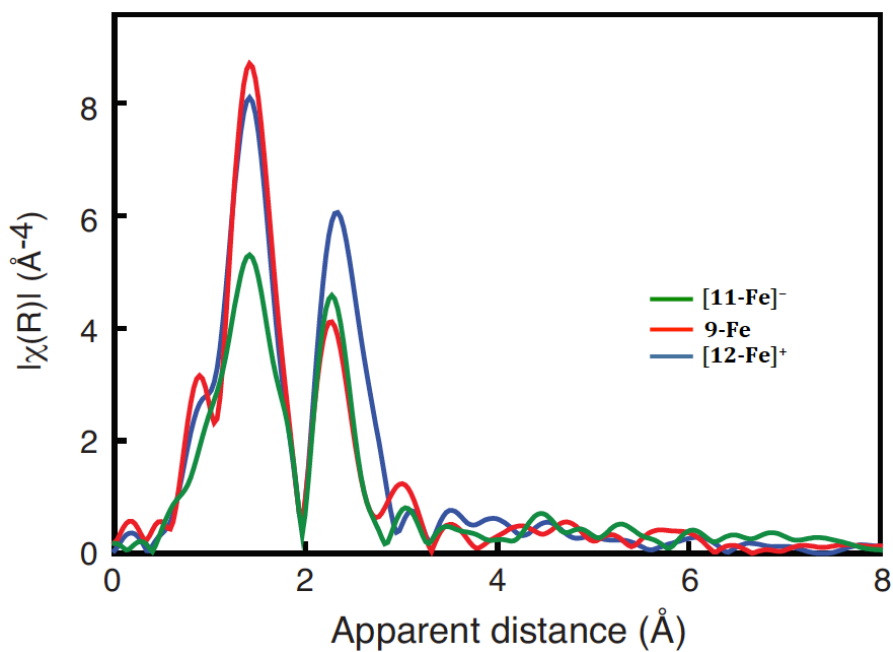


Figure 10. Normalized Mn EXAFS spectra for $[11\text{-Fe}]^-$, 9-Fe , and $[12\text{-Fe}]^+$. EXAFS data collected by Rosalie Tran and Junko Yano.

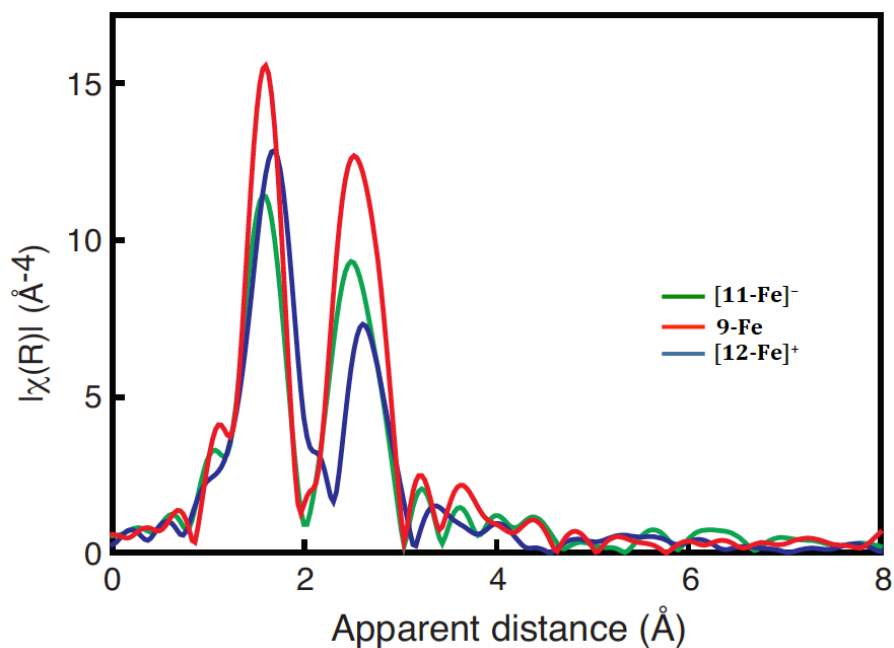


Figure 11. Normalized Fe EXAFS spectra for $[11\text{-Fe}][\text{CoCp}_2]$ and $[12\text{-Fe}][\text{SbCl}_6]$. EXAFS data collected by Rosalie Tran and Junko Yano.

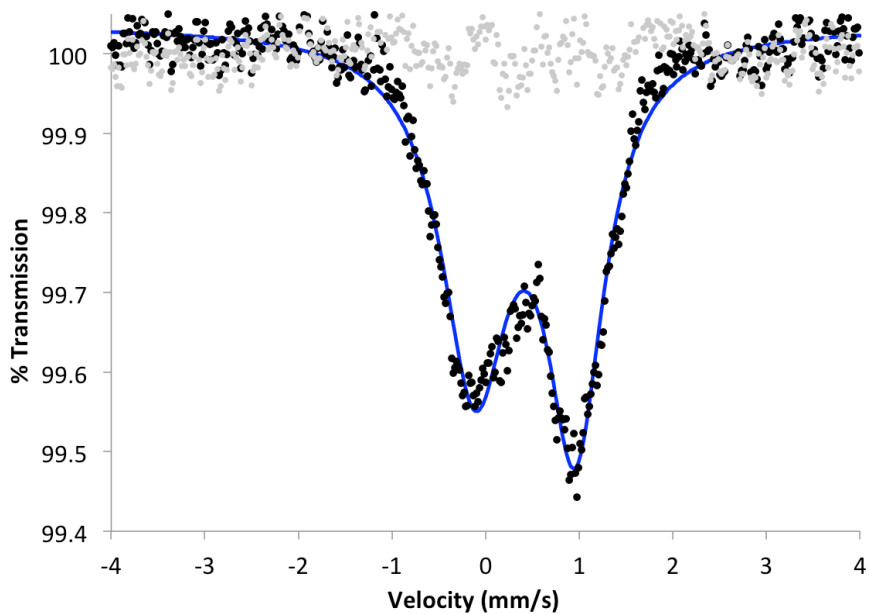


Figure 12. Zero-field ^{57}Fe Mössbauer spectrum for $[11\text{-Fe}][\text{CoCp}_2]$ collected by Jonathan Rittle (80 K, data: black dots, spectral fit: blue line, residual: grey dots); $\delta = 0.418 \text{ mm s}^{-1}$, $|\Delta E_Q| = 1.076 \text{ mm s}^{-1}$.

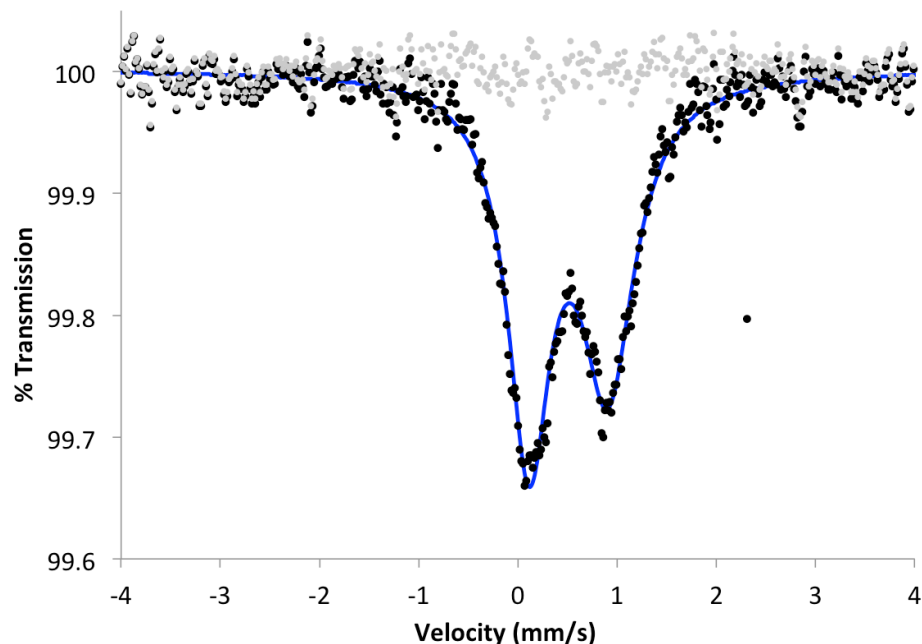


Figure 13. Zero-field ^{57}Fe Mössbauer spectrum for $[\mathbf{12}\text{-Fe}][\text{SbCl}_6]$ collected by Jonathan Rittle (80 K, data: black dots, spectral fit: blue line, residual: grey dots); $\delta = 0.509 \text{ mm s}^{-1}$, $|\Delta E_Q| = 0.796 \text{ mm s}^{-1}$.

Treatment of **9-Co** with an equivalent of CoCp_2 yielded the one-electron reduced $[\mathbf{11}\text{-Co}][\text{CoCp}_2]$ complex. The formation of $[\mathbf{11}\text{-Co}]^-$ was confirmed by XRD study of the crystalline material grown from vapour diffusion of diethyl ether into a concentrated solution in dichloromethane. The bond metrics shown in Figure 2e show that there is only one elongated Mn–O bond distance, indicative of a Mn^{III} oxidation state. The average Co–O bond in $[\mathbf{11}\text{-Co}]^-$ is 2.11 \AA vs. 2.03 \AA for **9-Co**, with $\sim 0.8 \text{ \AA}$ difference. On the other hand, attempts to obtain single crystals suitable for XRD studies for $[\mathbf{12}\text{-Co}]^+$ have been unsuccessful.

The crystal structure of $[\mathbf{11}\text{-Co}]^-$ suggests that the reduction occurs on the Co^{III} to generate a Co^{II} center instead of on one of the basal Mn^{IV} sites, despite the higher oxidation state. In contrast, despite the lack of a XRD study, the one-electron oxidation of **9-Co** is proposed to occur on the Mn^{III} center instead of on the Co^{III} . This rationale

is supported by the XAS studies on **9-Co**, [**11-Co**]⁻, and [**12-Co**]⁺. The Co XANES data (Figure 14) displays the ~ 1 eV shifts in the Co edge energies for [**11-Co**]⁻, **9-Co**, and [**12-Co**]⁺ (7720.30, 7721.48, and 7722.59 eV respectively). This result is in contrast to the [FeMn₃O₄] series, where electron transfer occurs on the Mn center(s). Figure 14 also displays the XANES comparison to compound **14-Co**, a [Co^{III}Mn^{III}₃O₃]-cluster product from O-atom transfer (discussed later in the chapter). The Co XANES data for [**12-Co**]⁺ and **14-Co** shows overlapping edge energy, indicative that for both systems the cobalt center is Co^{III}. The three different edge energies observed in the Co XANES results suggest that **9-Co** may have an intermediate cobalt oxidation state between Co^{II} and Co^{III}. The Mn XANES spectra (Figure 15) display edge energy differences between **9-Co** and [**11-Co**]⁻, while **9-Co** and [**12-Co**]⁺ unexpectedly have similar edge energies. The Co EXAFS data of **9-Co**, [**11-Co**]⁻, and [**12-Co**]⁺ are distinct from one another, consistent with the hypothesis that Co participates in the redox reactions (Figure 16). The Mn EXAFS data are also different between each cluster, especially in the Mn–Co distance (Figure 17).

If the one-electron reduction of **9-Co** exclusively occurs on Co, then only the Co XANES edge energy of [**11-Co**]⁻ is expected to be lower than that of **9-Co**. This is not the case, since the Mn XANES edge energy is also lower for the reduced cluster (6551.56 eV vs. 6552.93 eV). On the other hand, one-electron oxidation of **9-Co** only resulted in increased Co XANES edge energy while the Mn edge energy remains the same. Overall, the XAS studies on the series suggest that Co also participates in redox reactions, although the formal oxidation states assignments for each metal across the three different [CoMn₃O₄]ⁿ⁺ states are not yet elucidated.

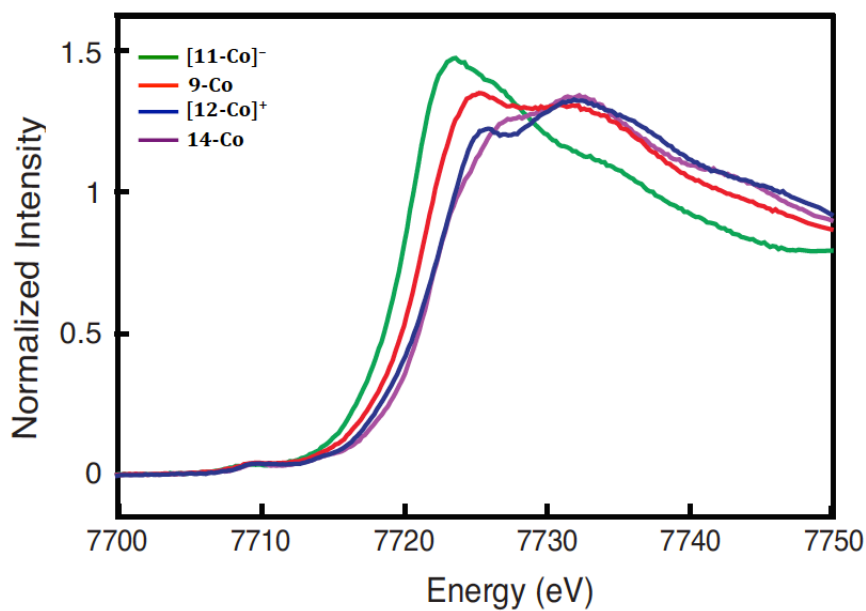


Figure 14. Normalized Co K-edge XANES spectra for [11-Co][Cr(C₆H₆)₂], 9-Co, [12-Co][SbCl₆] and 14-Co. XANES data collected by Ruchira Chatterjee and Junko Yano.

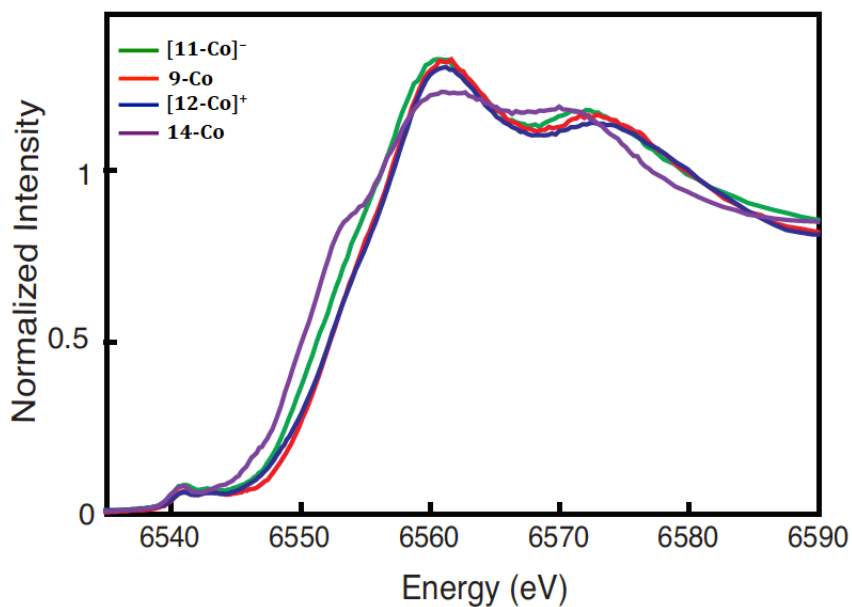


Figure 15. Normalized Mn K-edge XANES spectra for [11-Co][Cr(C₆H₆)₂], 9-Co, [12-Co][SbCl₆] and 14-Co. XANES data collected by Ruchira Chatterjee and Junko Yano.

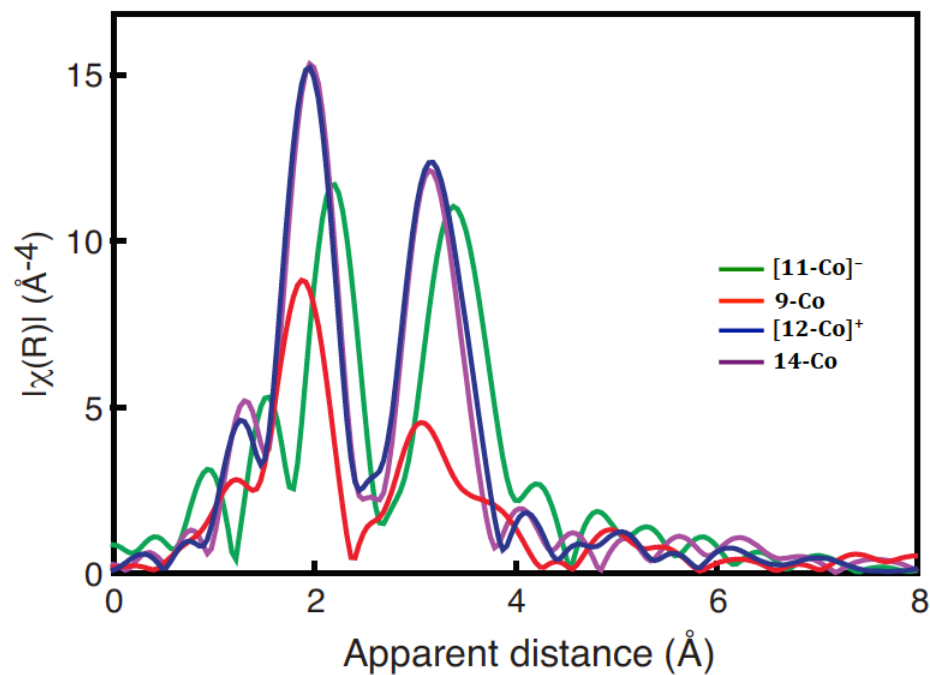


Figure 16. Co EXAFS spectra for $[11\text{-Co}][\text{Cr}(\text{C}_6\text{H}_6)_2]$, 9-Co, $[12\text{-Co}][\text{SbCl}_6]$ and 14-Co. EXAFS data collected by Ruchira Chatterjee and Junko Yano.

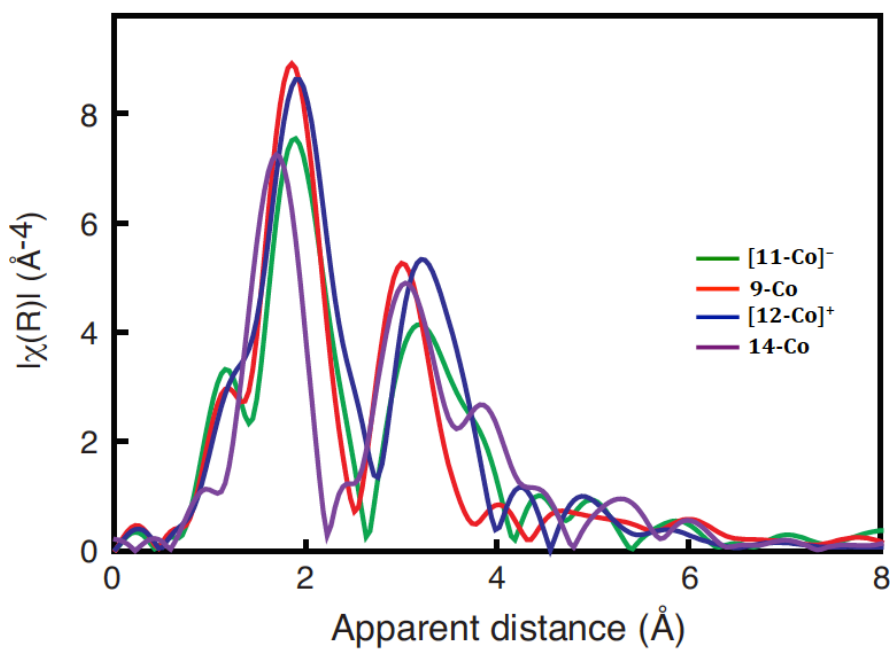


Figure 17. Mn EXAFS spectra for $[11\text{-Co}][\text{Cr}(\text{C}_6\text{H}_6)_2]$, 9-Co, $[12\text{-Co}][\text{SbCl}_6]$ and 14-Co. EXAFS data collected by Ruchira Chatterjee and Junko Yano.

10-Ni was also reduced by CoCp_2 to generate $[\mathbf{13-Ni}][\text{CoCp}_2]$. An XRD study of $[\mathbf{13-Ni}][\text{CoCp}_2]$ shows that one of the Mn centers has elongated Mn–O bond distance (2.21 Å) compared to the others, indicative of a Mn^{III} oxidation state (Figure 2f). On the other hand, the Ni–O bond distances remain relatively the same to **10-Ni** (~2.06 Å). This suggests that for the case of **10-Ni**, one electron reduction occurs on Mn, not Ni. The Ni XANES data of **10-Ni** and $[\mathbf{13-Ni}]^-$ (Figure 18) show that the two complexes' edge energy are relatively similar, consistent with the assignment of Ni^{II} for both cases. With one Mn^{III} center difference in $[\mathbf{13-Ni}]^-$ vs. all Mn^{IV} in **10-Ni**, the Ni EXAFS data (Figure 20) are similar to one another with a slight difference in the Ni–Mn interaction, in agreement with our expectation. On the other hand, the Mn XANES data (Figure 19) display ~ 1 eV energy difference between **10-Ni** and $[\mathbf{13-Ni}]^-$ (6553.38 vs. 6552.39 eV respectively) with $[\mathbf{13-Ni}]^-$ having lower edge energy, consistent with reduction on the Mn instead of Ni. The Mn EXAFS (Figure 21) shows a shoulder on the peak assigned as the Mn–Ni interaction at longer apparent distance, consistent with the slightly longer Ni– Mn^{III} distance observed in the solid-state structure.

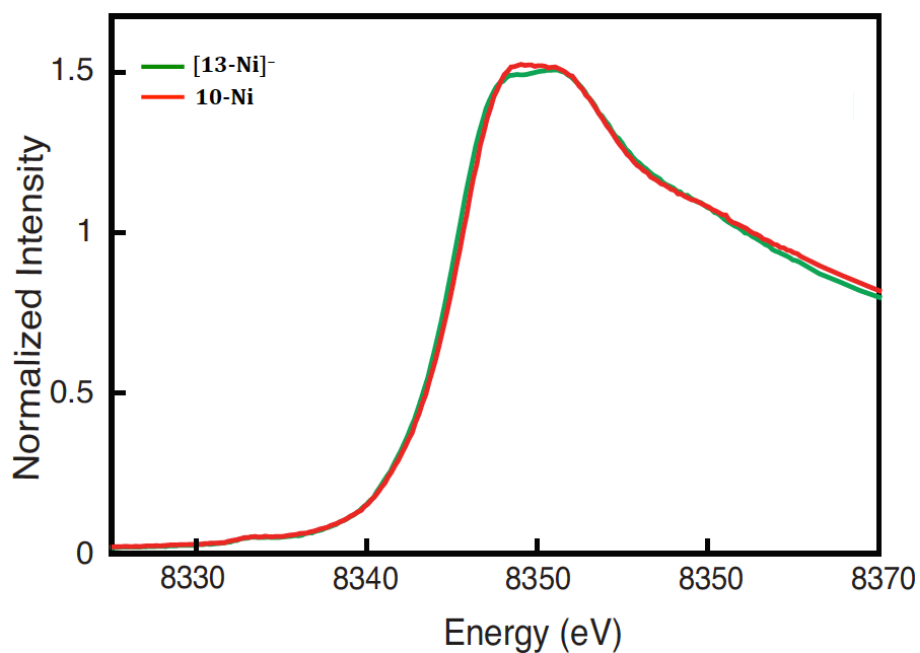


Figure 18. Normalized Ni K-edge XANES spectra for [13-Ni][CoCp₂] and 10-Ni. XANES data collected by Ruchira Chatterjee and Junko Yano.

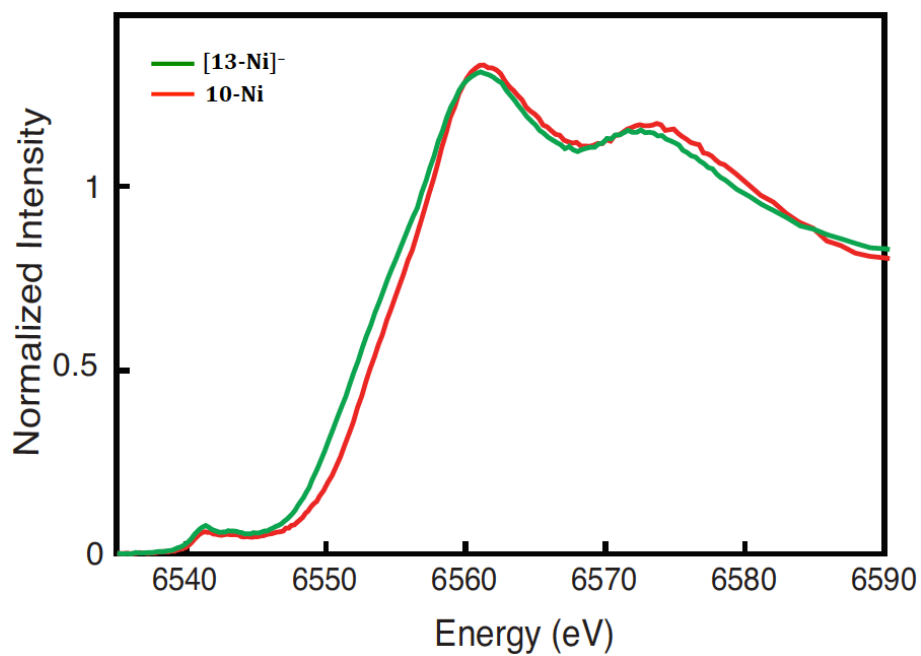


Figure 19. Normalized Mn K-edge XANES spectra for [13-Ni][CoCp₂] and 10-Ni. XANES data collected by Ruchira Chatterjee and Junko Yano.

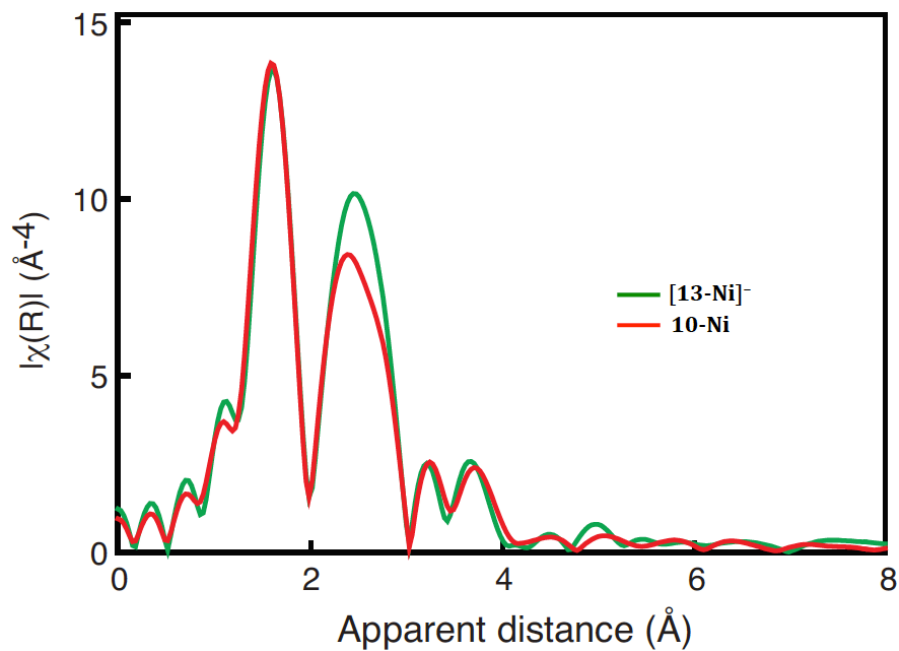


Figure 20. Ni EXAFS spectra for $[\text{13-Ni}][\text{CoCp}_2]$ and 10-Ni . EXAFS data collected by Ruchira Chatterjee and Junko Yano.

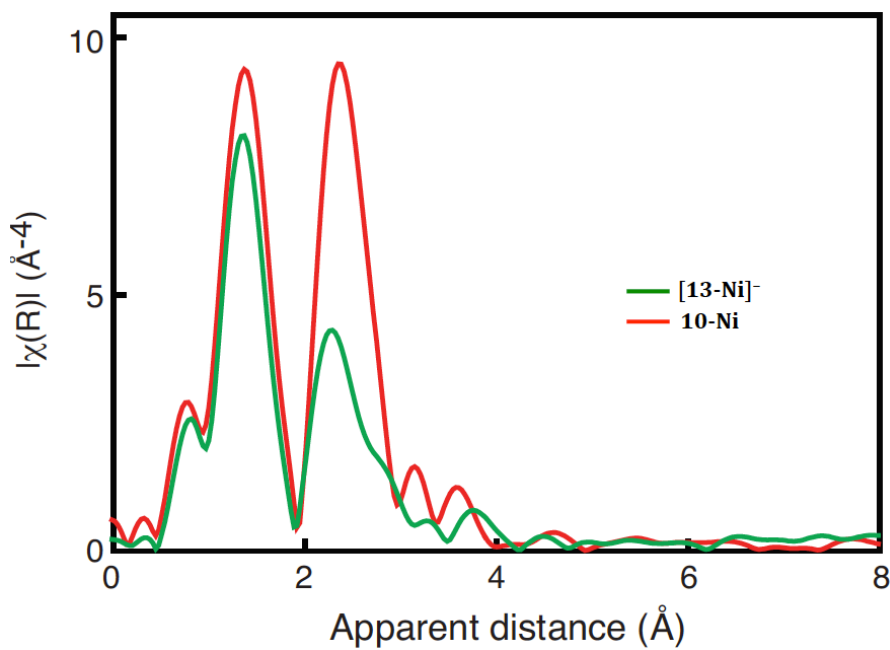


Figure 21. Mn EXAFS spectra for $[\text{13-Ni}][\text{CoCp}_2]$ and 10-Ni . EXAFS data collected by Ruchira Chatterjee and Junko Yano.

Reduction of **10-Cu** did not afford complexes isolable in analytically pure states. Redox studies indicate that both oxidation and reduction events occur at the basal Mn centers and not the apical metal M for M = Fe, Ni. For M = Co, reduction occurs on Co while oxidation occurs on one of the basal Mn (Scheme 2).

Table 1. Summary of all XANES edge energies and tentative oxidation state assignments of $[\text{MMn}_3\text{O}_4]$ synthesized by author, Emily Y. Tsui, Jacob S. Kanady, and Po-Heng Lin

Entry	Compounds	Oxidation state	Mn Edge Energy (eV)	M Edge Energy (eV)
1	10-Ca	$\text{Ca}^{\text{II}}\text{Mn}^{\text{IV}}_3$	6553.82	4046.24
2	[13-Ca]⁻	$\text{Ca}^{\text{II}}\text{Mn}^{\text{III}}\text{Mn}^{\text{IV}}_2$	6552.93	4047.44
3	10-Sr	$\text{Sr}^{\text{II}}\text{Mn}^{\text{IV}}_3$	6553.53	n/a
4	10-Ni	$\text{Ni}^{\text{II}}\text{Mn}^{\text{IV}}_3$	6553.38	8345.38
5	[13-Ni]⁻	$\text{Ni}^{\text{II}}\text{Mn}^{\text{III}}\text{Mn}^{\text{IV}}_2$	6552.39	8344.91
6	10-Cu	$\text{Cu}^{\text{II}}\text{Mn}^{\text{IV}}_3$	6552.78	8989.73
7	[10-Gd]⁺	$\text{Gd}^{\text{III}}\text{Mn}^{\text{IV}}_3$	6553.49	n/a
8	13-Gd	$\text{Gd}^{\text{III}}\text{Mn}^{\text{III}}\text{Mn}^{\text{IV}}_2$	6553.28	n/a
9	[10-Sc]⁺	$\text{Sc}^{\text{III}}\text{Mn}^{\text{IV}}_3$	6553.47	n/a
10	13-Sc	$\text{Sc}^{\text{III}}\text{Mn}^{\text{III}}\text{Mn}^{\text{IV}}_2$	6551.93	n/a
11	[11-Fe]⁻	$\text{Fe}^{\text{III}}\text{Mn}^{\text{III}}_2\text{Mn}^{\text{IV}}$	6550.14	7125.31
12	9-Fe	$\text{Fe}^{\text{III}}\text{Mn}^{\text{III}}\text{Mn}^{\text{IV}}_2$	6550.87	7125.71
13	[12-Fe]⁺	$\text{Fe}^{\text{III}}\text{Mn}^{\text{IV}}_3$	6552.80	7125.93
14	[11-Co]⁻	$\text{Co}^{\text{II}}\text{Mn}^{\text{III}}\text{Mn}^{\text{IV}}_2$	6551.56	7720.30
15	9-Co	$\text{Co}^{\text{III}}\text{Mn}^{\text{III}}\text{Mn}^{\text{IV}}_2$	6552.93	7721.48
16	[12-Co]⁺	$\text{Co}^{\text{III}}\text{Mn}^{\text{IV}}_3$	6552.84	7722.59
17	14-Co	$\text{Co}^{\text{III}}\text{Mn}^{\text{III}}_3$	6550.39	7721.94
18	[11-Mn]⁻	$\text{Mn}^{\text{III}}_3\text{Mn}^{\text{IV}}$	6550.00	n/a
19	9-Mn	$\text{Mn}^{\text{III}}_2\text{Mn}^{\text{IV}}_2$	6551.84	n/a
20	[12-Mn]⁺	$\text{Mn}^{\text{III}}\text{Mn}^{\text{IV}}_3$	6552.48	n/a

Preliminary temperature dependence X-band EPR studies have been performed on the $[\text{FeMn}_3\text{O}_4]$ and $[\text{CoMn}_3\text{O}_4]$ series (Figure 22-27) by Britt and co-workers. These

EPR data have *not* been simulated yet, but the detailed analyses are currently ongoing. The EPR spectra of **9-Fe** (Figure 22) display peaks at 1250 G and 1891 G with strong intensity, indicative of a half-spin system and in agreement with the $\text{Fe}^{\text{III}}\text{Mn}^{\text{III}}\text{Mn}^{\text{IV}}_2$ assignment. The EPR spectra for $[\mathbf{11}\text{-Fe}]^-$ (Figure 23) displays low signal intensity, indicative of integer spin system and consistent with the oxidation states assignment of $\text{Fe}^{\text{III}}\text{Mn}^{\text{III}}_2\text{Mn}^{\text{IV}}$. On the other hand, the EPR spectra for $[\mathbf{12}\text{-Fe}]^+$ (Figure 24) shows strong intensity despite the magic blue impurity at $g \sim 2$ in higher temperature (40 K). High intensity spectra indicates half-spin system, which disagrees with the current oxidation state assignment of $[\mathbf{12}\text{-Fe}]^+$ ($\text{Fe}^{\text{III}}\text{Mn}^{\text{IV}}_3$) that should be an integer spin system.

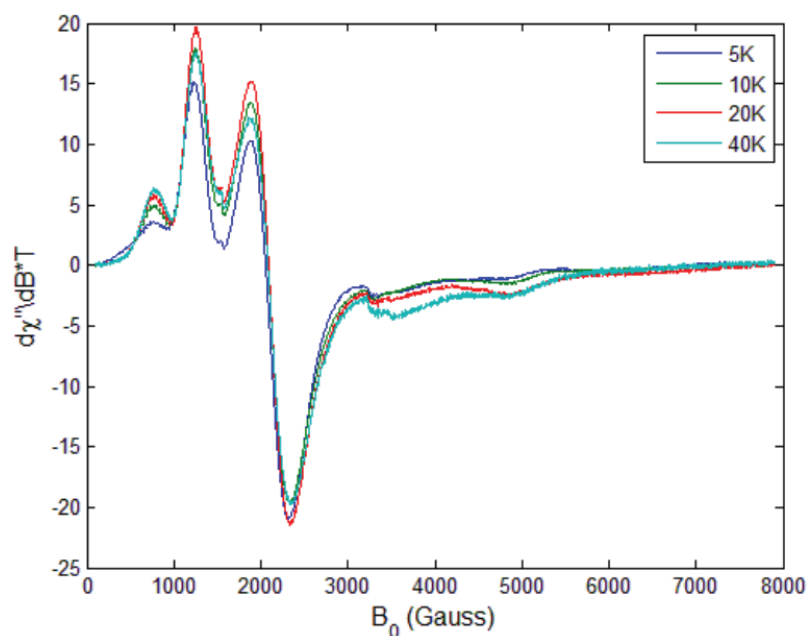


Figure 22. Temperature-dependent CW X-Band EPR spectra of the frozen solutions of **9-Fe** dissolved in CH_2Cl_2 . Experimental parameters: microwave frequency = 9.37–9.42 GHz; power = 0.1589 mW; modulation amplitude = 10 G; modulation frequency = 100 kHz.

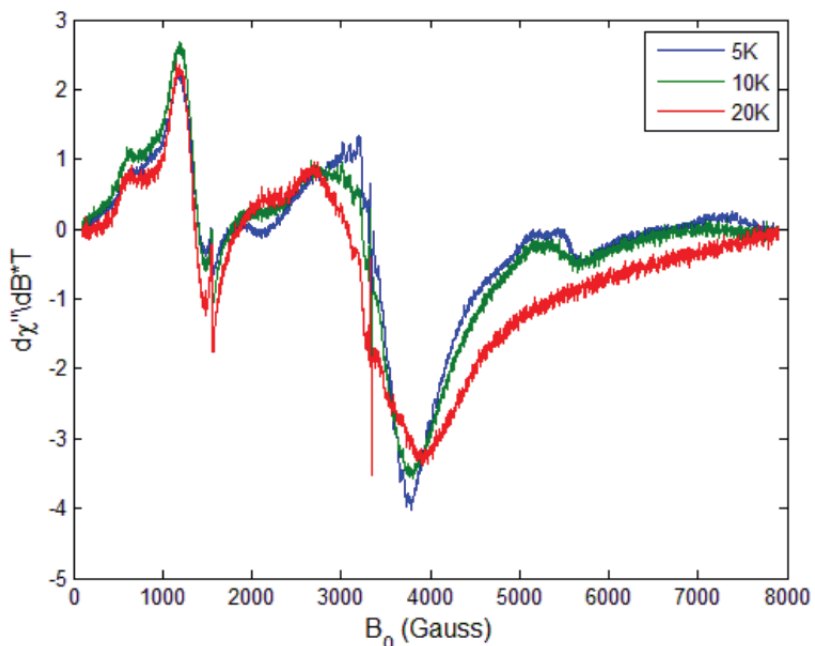


Figure 23. Temperature-dependent CW X-Band EPR spectra of the frozen solutions of $[11\text{-Fe}]^-$ dissolved in CH_2Cl_2 . Experimental parameters: microwave frequency = 9.37–9.42 GHz; power = 0.03991 mW; modulation amplitude = 10 G; modulation frequency = 100 kHz.

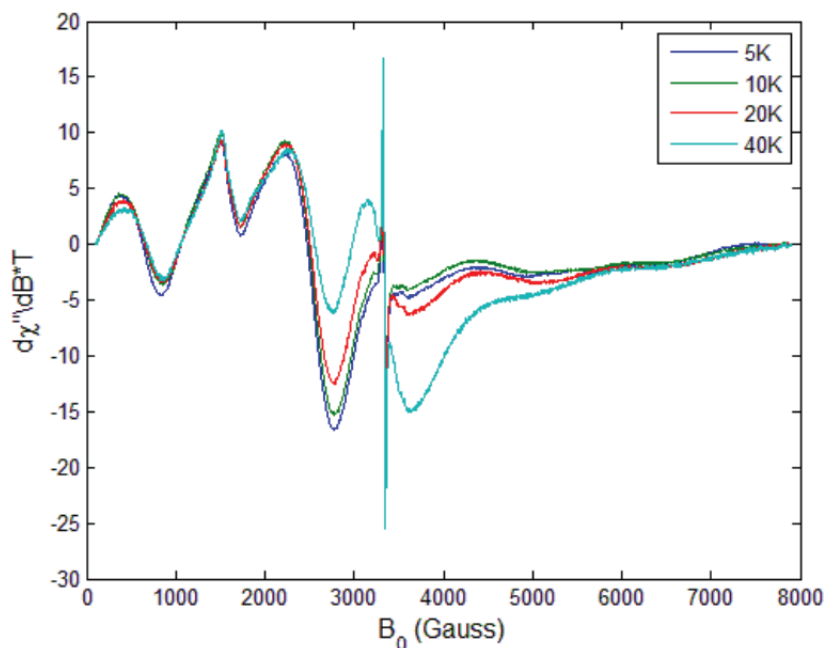


Figure 24. Temperature-dependent CW X-Band EPR spectra of the frozen solutions of $[12\text{-Fe}]^+$ dissolved in CH_2Cl_2 . Experimental parameters: microwave frequency = 9.37–9.42 GHz; power = 0.1589 mW; modulation amplitude = 10 G; modulation frequency = 100 kHz.

The X-band EPR data on **9-Co** show low intensity signals, indicative of an integer spin system (Figure 25). This result is in agreement with the current oxidation states assignment of **9-Co** ($\text{Co}^{\text{III}}\text{Mn}^{\text{III}}\text{Mn}^{\text{IV}}_2$). Figure 26 represents the EPR spectra acquired for $[\mathbf{11-Co}]^-$, displaying high intensity signals. The EPR spectra of $[\mathbf{11-Co}]^-$ suggest a half-spin system, which agrees with the oxidation states assignment of $\text{Co}^{\text{II}}\text{Mn}^{\text{III}}\text{Mn}^{\text{IV}}_2$. The EPR spectra of $[\mathbf{12-Co}]^+$ (Figure 27) shows small signals except for the large $g \sim 2$ signal that may come from the radical (magic blue) impurity. Small EPR signals are indicative of an integer-spin system, but this is not consistent with the oxidation states assignment of $\text{Co}^{\text{III}}\text{Mn}^{\text{IV}}_3$ for $[\mathbf{12-Co}]^+$.

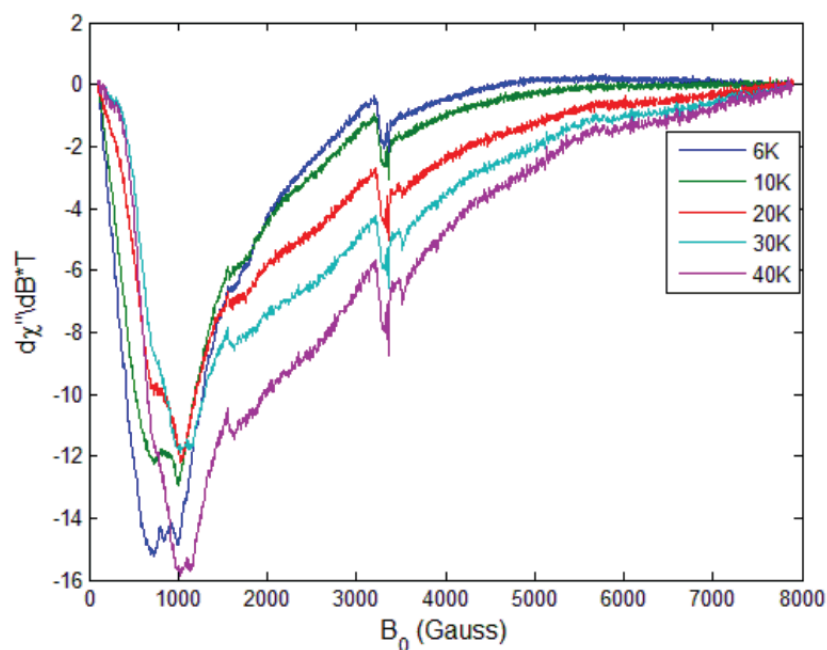


Figure 25. Temperature-dependent CW X-Band EPR spectra of the frozen solutions of **9-Co** dissolved in CH_2Cl_2 . Experimental parameters: microwave frequency = 9.37–9.42 GHz; power = 0.6325 mW; modulation amplitude = 10 G; modulation frequency = 100 kHz.

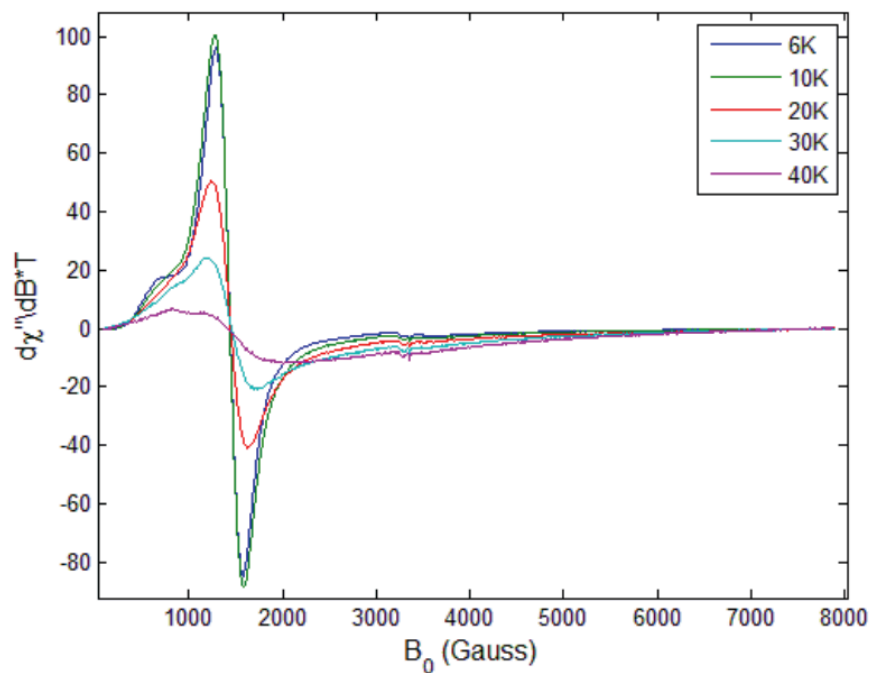


Figure 26. Temperature-dependent CW X-Band EPR spectra of the frozen solutions of $[11\text{-Co}]^-$ dissolved in CH_2Cl_2 . Experimental parameters: microwave frequency = 9.37–9.42 GHz; power = 0.6325 mW; modulation amplitude = 10 G; modulation frequency = 100 kHz.

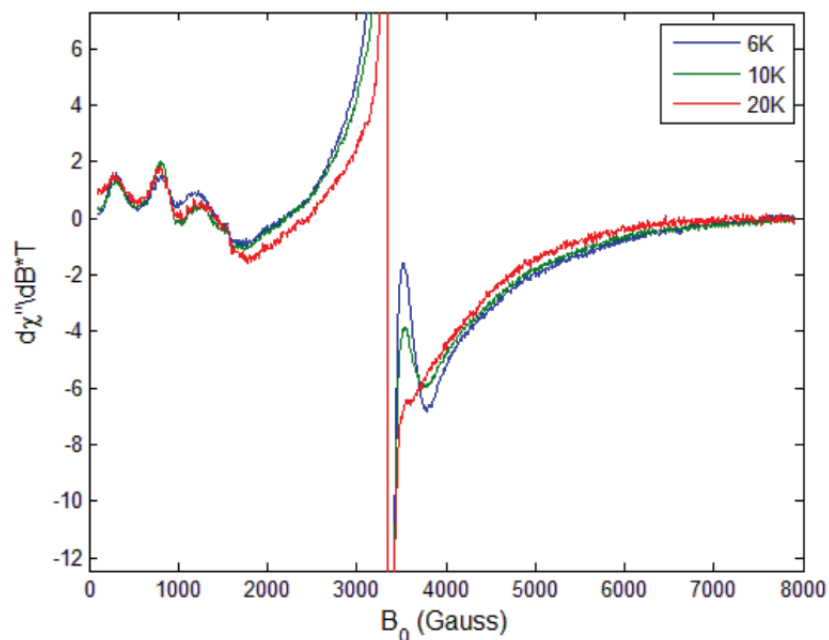


Figure 27. Temperature-dependent CW X-Band EPR spectra of the frozen solutions of $[12\text{-Co}]^+$ dissolved in CH_2Cl_2 . Experimental parameters: microwave frequency = 9.37–9.42 GHz; power = 1.262 mW; modulation amplitude = 10 G; modulation frequency = 100 kHz.

In summary, all EPR data except for those of $[\mathbf{12-Fe}]^+$ and $[\mathbf{12-Co}]^+$ agrees with the tentative oxidation state assignments on the metal centers. The inconsistent data for $[\mathbf{12-Fe}]^+$ and $[\mathbf{12-Co}]^+$ may result from the decomposition of the species, the formation of the wrong cluster by magic blue oxidation, or the oxidation/interaction of the ligand to the metal. Despite the results from the perpendicular mode EPR spectroscopy, the preliminary parallel mode EPR spectra of $[\mathbf{12-Fe}]^+$ display strong EPR signal, while those of $[\mathbf{12-Co}]^+$ have no EPR signal (spectra not shown). Strong parallel mode EPR signal is generally indicative of integer spin system while no signal is correlated to half-spin system. Therefore, by parallel EPR spectroscopy, the spectra for $[\mathbf{12-Fe}]^+$ and $[\mathbf{12-Co}]^+$ agree with the tentative oxidation state assignments on the metal centers. Since the parallel mode EPR results on $[\mathbf{12-Fe}]^+$ and $[\mathbf{12-Co}]^+$ are not consistent with the perpendicular mode EPR, further analyses are still required.

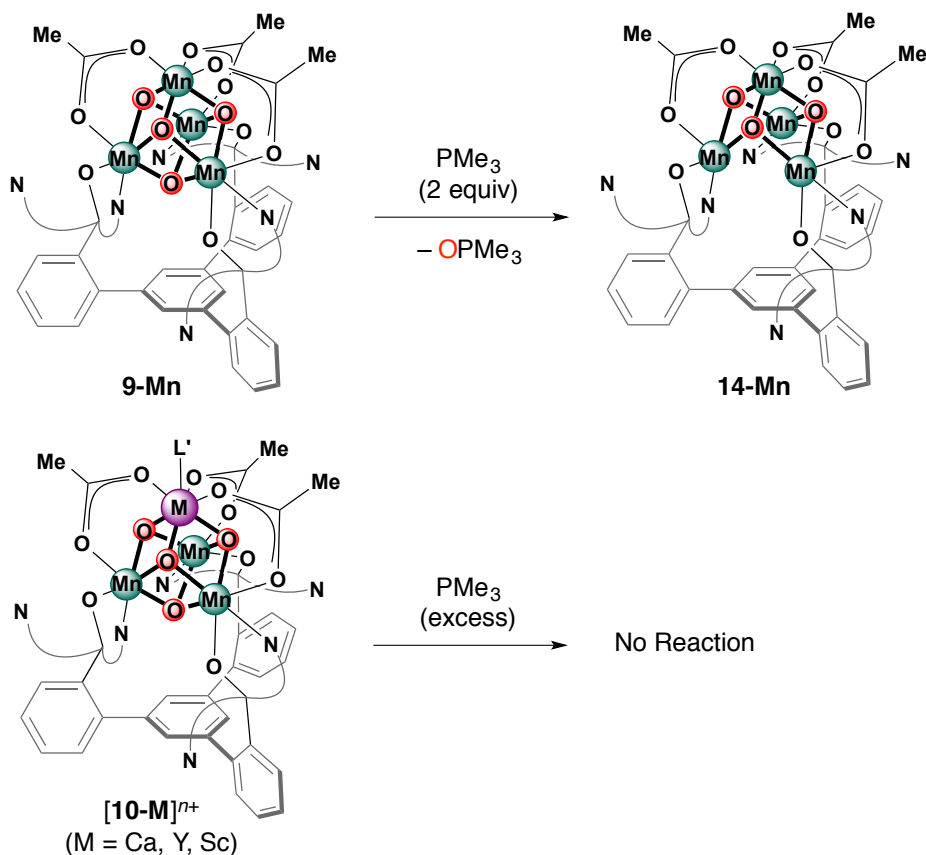
4.6 Oxygen atom transfer reactivity of $[\mathbf{MMn}_3\mathbf{O}_4]$ ($M = Sc, Y, Co$)

The oxygen atom transfer reactivities of $[\mathbf{MMn}_3\mathbf{O}_4]$ ($M = Ca, Y, Sc, Co, Mn$) and $[\mathbf{MMn}_3\mathbf{O}_2]$ ($M = Ca, Y$) were also investigated as an extension to the results obtained by Emily Y. Tsui and Jacob S. Kanady.^{11b} We would like to determine whether the reactivity is dictated thermodynamically based on the Lewis acidity of the heterometal M. If the reactivity is indeed dependent on the oxidizing power of the cluster complex, then the O atom transfer propensity of this series is expected to be correlated to the reduction potentials of the clusters reported.^{11d}

To test this hypothesis, some of the structurally characterized clusters were treated with phosphine reagents as the oxygen atom acceptor (Scheme 2). The reduction potentials of the clusters, $Mn^{IV}_2Mn^{III}_2/Mn^{IV}Mn^{III}_2$ for **9-Mn** and $MMn^{IV}_3/MMn^{III}Mn^{IV}_2$

for $[10-M]^{n+}$, are tabulated in Table 2. Based on the reduction potentials of the series in Table 2, $[10-Sc]^+$ is the most oxidizing with the more positive reduction potential, thus, therefore, it is initially expected to be more reactive than the other three compounds toward oxygen atom transfer.

Scheme 2. (*Top*) Oxygen atom transfer to trimethylphosphine by **9-Mn** to yield trimethylphosphine oxide and **15-Mn** (done by Jacob S. Kanady). (*Bottom*) **10-Ca**, $[10-Y]^+$, and $[10-Sc]^+$ show no oxygen atom transfer reactivity over days upon treatment with trimethylphosphine (done by Emily Y. Tsui).^{11b}



Experimentally, the tetramanganese tetraoxido cluster **9-Mn** was reported to react quickly with two equivalents of trimethyl phosphine (PMe_3) within 15 minutes to yield the tetramanganese trioxido complex **14-Mn** and trimethyl phosphine oxide^{11b} (Scheme 2). On the other hand, complexes **10-Ca**, $[10-Y]^+$, and $[10-Sc]^+$ did not react

with PMe_3 over days where the formation of decomposition products was observed by Emily Y. Tsui. This result contradicts our initial hypothesis that the oxygen atom transfer capability of these clusters is directly related to the strength of the apical Lewis acid M or correlated to the reduction potentials of the complexes.

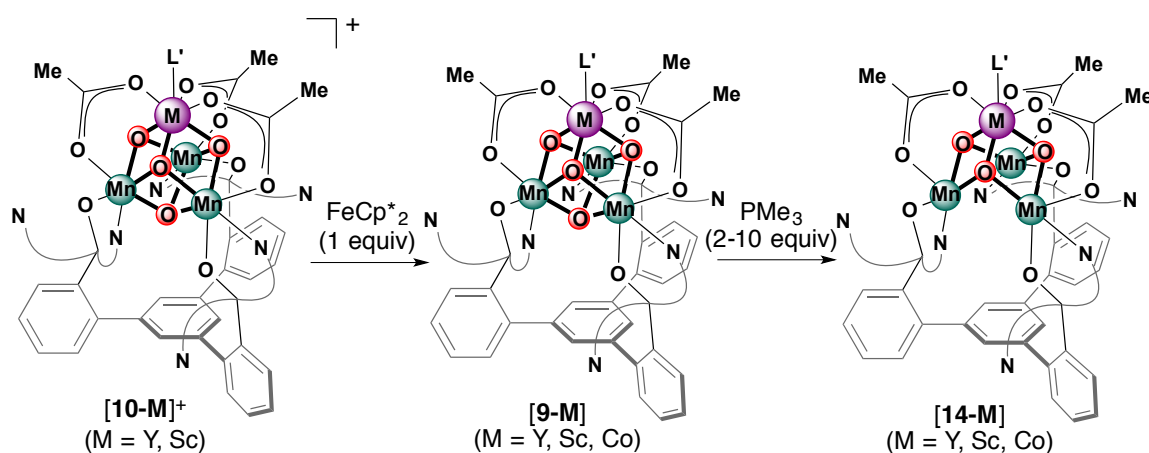
Table 2. One-electron reduction potentials of $[\text{MMn}_3\text{O}_4]$ vs. Fc/Fc^+

Compound	Potential (V) vs. Fc/Fc^+	Redox couple
9-Mn	-0.70	$\text{Mn}^{\text{IV}}_2\text{Mn}^{\text{III}}_2/\text{Mn}^{\text{IV}}\text{Mn}^{\text{III}}_3$
10-Ca	-0.94	$\text{MMn}^{\text{IV}}_3/\text{MMn}^{\text{IV}}_2\text{Mn}^{\text{III}}$
[10-Y]⁺	-0.43	$\text{MMn}^{\text{IV}}_3/\text{MMn}^{\text{IV}}_2\text{Mn}^{\text{III}}$
[10-Sc]⁺	-0.24	$\text{MMn}^{\text{IV}}_3/\text{MMn}^{\text{IV}}_2\text{Mn}^{\text{III}}$

The contrasting of reactivity for oxygen atom transfer within the $[\text{MMn}_3\text{O}_4]$ series can be rationalized by the lower ligand (acetate) lability of the Mn^{IV} centers in $[\mathbf{10-M}]^+$ vs. one Mn^{III} in $[\mathbf{9-Mn}]$. This proposed rationale is supported by computational studies performed by Goddard and co-workers where the Mn^{III} site of **9-Mn** is more labile due to electrons occupying the M-O σ -antibonding orbital that leads to weaker metal-ligand bonds.^{11b} The difference in Mn oxidation states between **9-M** and $[\mathbf{10-M}]^{n+}$ affects the kinetic instead of the thermodynamic of the oxygen atom reactivity. With this proposed rationale, one alternative to study the Lewis acid effect on oxygen atom transfer reactivity is by reducing $[\mathbf{10-M}]^{n+}$ ($\text{M} = \text{Y}, \text{Sc}$) by one-electron to generate one Mn^{III} site in the corresponding **9-M** product (Scheme 3). The oxygen atom transfer capability of **9-Co** is also investigated to determine whether this proposal also holds for the redox-active heterometallic Mn oxido clusters. With this approach, the oxygen atom reactivity across the $[\mathbf{9-M}]$ series can be studied systematically to determine the Lewis acid effect.

One-electron reduction of $[\mathbf{10-M}]^{n+}$ can be achieved using a reductant such as CoCp_2 or decamethylferrocene (FeCp^*_2). In the case of $\mathbf{10-Ca(THF)}$, Jacob S. Kanady has previously shown that CoCp_2 can reduce the cluster by one electron, however the product $[\mathbf{9-Ca}][\text{CoCp}_2]$ was highly unstable and difficult to isolate cleanly. Due to this reason, the oxygen atom transfer studies were performed on $\mathbf{9-Sc}$ and $\mathbf{9-Y}$. Treatment of $[\mathbf{10-Sc}]^+$ with an equivalent of FeCp^*_2 yields the neutral complex, $\mathbf{9-Sc}$, quantitatively. Similarly, one equivalent of FeCp^*_2 was added to $[\mathbf{10-Y}]^+$ to generate $\mathbf{9-Y}$. It is worth noting that $\mathbf{9-Y}$ is unstable in solution and as a solid at room temperature. The reduction of $[\mathbf{10-Sc}]^+$ and $[\mathbf{10-Y}]^+$ was first performed by Emily Y. Tsui.

Scheme 3. One-electron reduction of $[\mathbf{10-M}]^+$ by decamethylferrocene



The addition of 10 equiv. of PMe_3 to $\mathbf{9-Sc}$ eventually yields the trioxo $\mathbf{14-Sc}$ over 1.5 weeks at r.t., but the oxygen atom transfer reaction can be accelerated to 30 h by heating the reaction mixture in benzene to 50 °C, as monitored by ^1H NMR spectroscopy (Figure 28). A control reaction was performed by heating a solution of $\mathbf{9-Sc}$ at 50 °C over 30 h where $\mathbf{14-Sc}$ was generated as a decomposition product albeit in negligible amount ($< \sim 10\%$) compared to the reaction in the presence of excess PMe_3 .

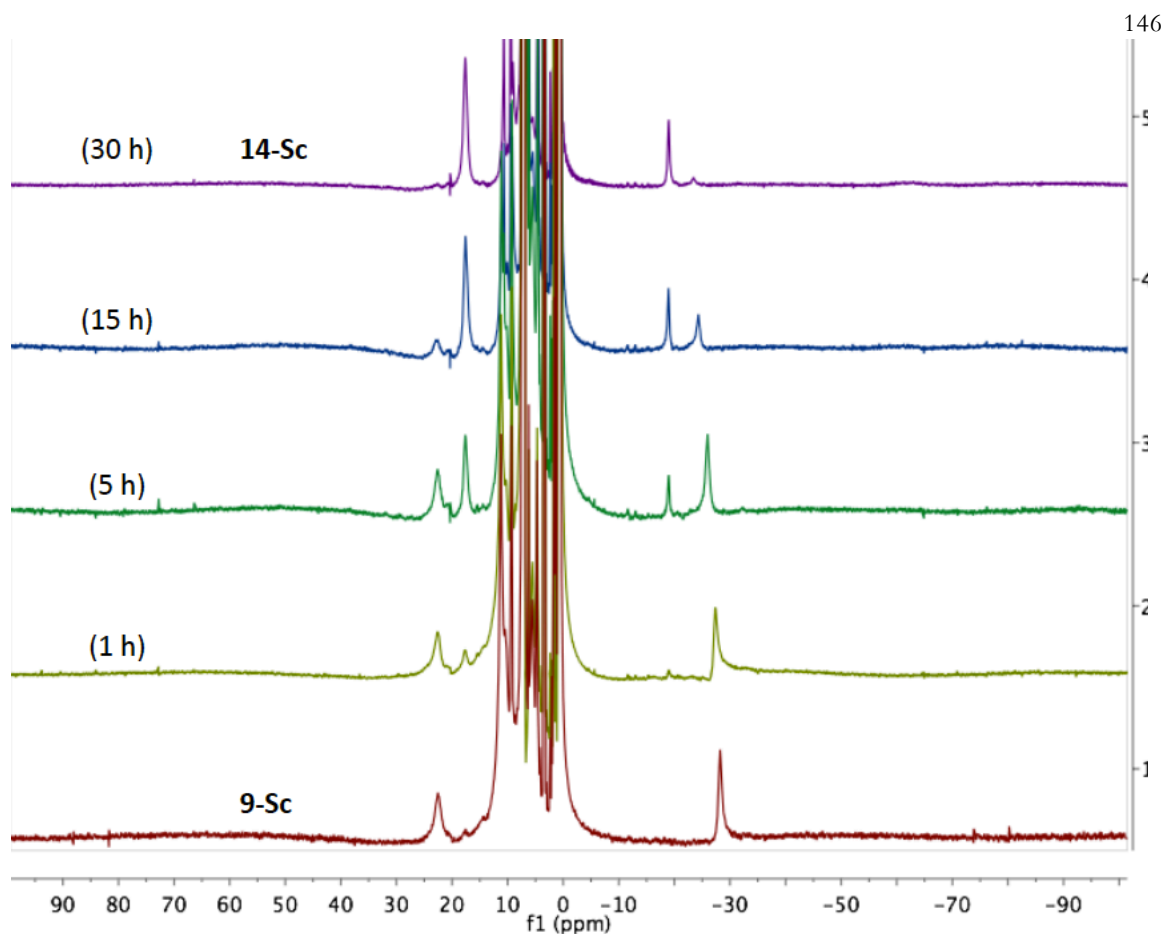


Figure 28. ¹H NMR spectra (in C₆D₆) of the reaction of **9-Sc** with 10 equiv. PMe₃ at 50 °C over 30 h to make **14-Sc**

The trimethyl phosphine oxide (O=PMe₃) side product is proposed to be bound to the generated **14-Sc** in the reaction mixture because the no phosphorus signal from O=PMe₃ could be detected by ³¹P NMR spectroscopy throughout the reaction. The formation of O=PMe₃ was verified later via gas chromatography mass-spectrometry (GC-MS) after removing the excess PMe₃ *in vacuo* and by diethyl ether wash followed by methanolysis. A XRD study was performed on the single crystals of **14-Sc** (Figure 29). The oxidation states of the Mn in **14-Sc** are assigned as all Mn^{III} to balance the charge, while the average Mn–O(acetate) bond distance is 2.14 Å, consistent with axial elongation of a Mn^{III} center.

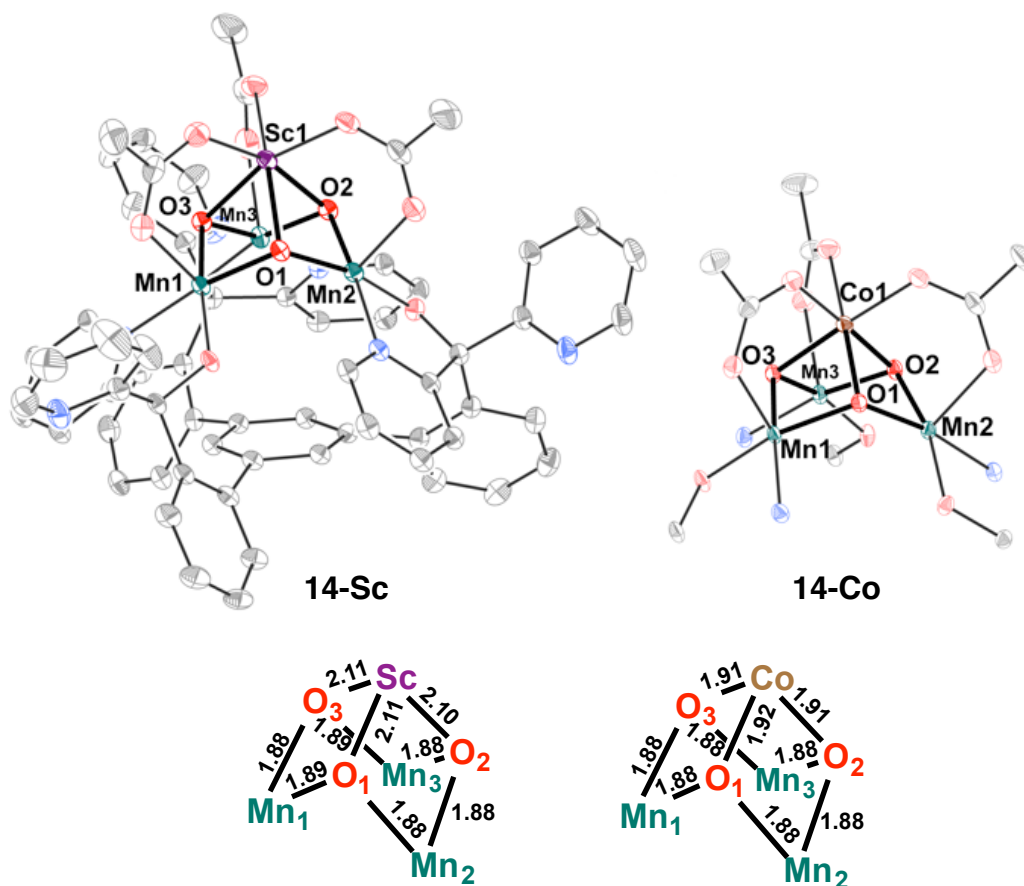


Figure 29. (Top) Solid-state structures of **14-Sc** (full) and **14-Co** (truncated). Hydrogen atoms are omitted for clarity. (Bottom) relevant M–O and Mn–O bond distances in Å.

On the other hand, the reaction of 10 equiv. of PMe_3 to **9-Y** was sluggish and incomplete even after 2 weeks at room temperature (performed by Emily Y. Tsui). Heating the mixture to 50 °C seemed to accelerate the reaction time to 12 h, however, it was found that a solution of **9-Y** under heating alone decomposed to make the same product(s) at a similar rate as the reaction run in the presence of excess PMe_3 . Nevertheless, the products formed from the reaction of **9-Y** with PMe_3 have not been structurally characterized by XRD studies. The products were evaluated by ESI–MS, displaying signals at m/z : 1128.9 $[\text{LYMn}_2\text{O}(\text{OAc})_2]^+$, 1188.7 $[\text{LYMn}_2\text{O}(\text{OAc})_2]^+$, and 1318.5 $[\text{LYMn}_3\text{O}_2(\text{OAc})_3]^+$. None of these signals indicates the formation of **14-Y**, but

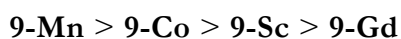
suggests the generation of lower oxido content than 3 and possibly also the loss of Mn center. It is possible that perhaps PMe_3 first extracted an oxygen atom from **9-Y**, and the product reacted or decomposed to make multiple different species in solution. On the other hand, it is worth noting that **9-Y** is not stable in solution or as a solid even at room temperature, therefore evaluation the oxygen atom transfer reactivity of **9-Y** is potentially more convoluted than **9-Sc** or **9-Mn**.

Due to the instability of **9-Y** at room temperature, an alternative of using **9-Gd** instead of **9-Y** is expected to be a more effective approach since Gd^{3+} and Y^{3+} have relatively similar Lewis acidity. Treatment of **9-Gd** with 10 equiv. PMe_3 and heating the reaction mixture to 50 °C result in the formation of a stable product over 50 hours, although the final product has not yet been structurally characterized and identified as **14-Gd**. A control reaction of heating **9-Gd** to 50 °C over days show no decomposition of the cluster, in contrast to complex **9-Y** that was shown to be unstable even at r.t. To determine the consumption of PMe_3 , **9-Gd** was treated with 3 equiv. PMe_3 , and the reaction was analogously run at 50 °C. The consumption of PMe_3 was monitored by ^{31}P NMR against an internal PPh_3 standard (2 equiv.). A total of one equivalent of PMe_3 was consumed throughout the reaction time of 67 h. This result suggests that the presence of excess (10 equiv.) PMe_3 in the reaction mixture did not cause **9-Gd** to fall apart to form more reduced cluster species with < 3 oxido contents where consumption of > 1 equiv. PMe_3 would be observed.

Treatment of **9-Co** with 2 equiv. PMe_3 yields **14-Co** in less than 2 h at r.t. The formation of **14-Co** is confirmed by a XRD study (Figure 29). The average Mn–oxo and Mn–O(acetate) distances are 1.88 and 2.10 Å respectively, consistent with all Mn^{III} centers. Co^{3+} has similar $\text{p}K_{\text{a}}$ value to Mn^{3+} (0.66 vs. 0.1 respectively), and **9-Co** also has

similar reduction potential compared to **9-Mn** (Figure 6-7). The qualitative rate of O atom transfer by **9-Co** in the same time scale to that of **9-Mn** is consistent with our expectation, therefore, the oxygen atom transfer capability of **9-Co** is similar to that of **9-Mn**. This result is still in agreement with the rationale that a more labile Mn^{III} center is required for oxygen atom transfer to be facilitated. The slightly slower reaction for **9-Co** may be because Co³⁺ is a weaker Lewis acid with slightly higher pK_a value in comparison to Mn³⁺. The reaction of **9-Co** with 3 equiv. PMe₃ at elevated temperature (65 °C) was attempted as well to compare the relative rate to that of **9-Sc**. The reaction was complete within 45 min but there was a substantial amount of Mn scrambling into the Co position within the cluster (~20 %) as detected by ¹H NMR spectroscopy. Metal scrambling was not observed when the reaction was carried out at room temperature.

Based on the data that for the oxygen atom transfer capabilities of **9-M** (M = Mn, Co, Sc, Gd), the reactivity correlates with the Lewis acidity of the clusters. Qualitative analyses of the relative rate of oxygen transfer capabilities of **9-M** using PMe₃ as the acceptor result in the trend as follows from fastest to slowest:



The oxygen atom transfer studies of **9-M** that have been performed are summarized in Table 3 in the next section alongside with the results from [MMn₃O₂] reactivities.

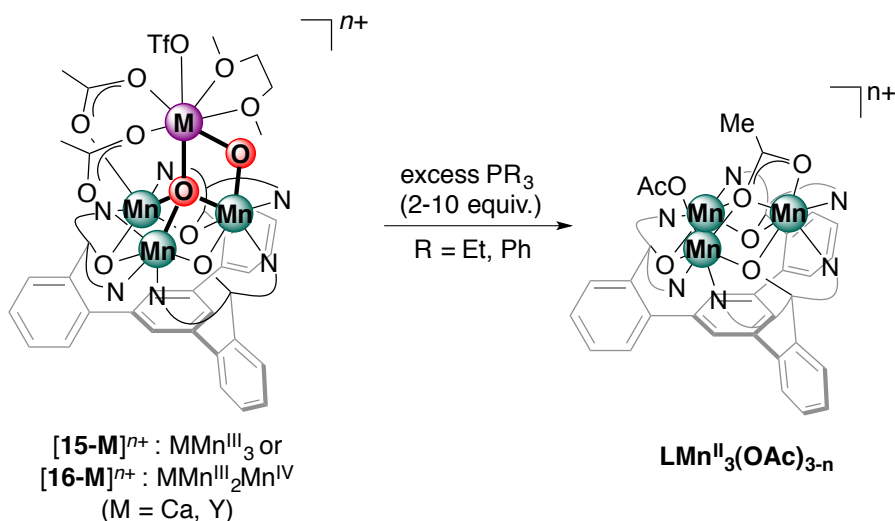
4.7 Oxygen atom transfer reactivity of [MMn₃O₂] (M = Ca, Y)

In addition to studying the oxygen atom transfer propensity in the [MMn₃O₄] series, the reactivity of the heterometallic trimanganese dioxido [MMn₃O₃] series with phosphines^{11c} was also investigated. Previously Emily Y. Tsui reported the reactivity studies for some of the dioxido complexes [**15-M**]ⁿ⁺ (M = Ca, Y) and the corresponding

one-electron oxidized $[\mathbf{16-M}]^{n+}$ ($M = \text{Ca}$) (Scheme 4). This section of the chapter extends the studies on the dioxido clusters previously performed by Emily Y. Tsui towards completing the comparison for O atom reactivity amongst the different Mn oxido clusters under analogous conditions.

The complexes $[\mathbf{15-M}]^{n+}$ and $[\mathbf{16-M}]^{n+}$ where $M = \text{Ca}$ or Y are chosen due to the large Lewis acidities range of the redox-inactive metals and the potential electronic effect of the cluster with one e^- difference towards oxygen atom transfer reactivity. Another variance between the complexes within each $[\mathbf{15-M}]^{n+}$ or $[\mathbf{16-M}]^{n+}$ series to also be considered is the overall complex charge where Y is tricationic vs. Ca is dicationic, which may affect the electrophilicity of the complexes towards the phosphine reagent(s).

Scheme 4. Reactions of heterometallic trimanganese dioxido complexes with triethyl- or triphenylphosphine



$[\mathbf{15-Ca}]^+$ reacted much more slowly in the presence 10 equiv. PEt_3 (36 h) vs. $[\mathbf{15-Y}]^{2+}$ (30 min) to make the trimanganese (II) complex (Scheme 4, Table 3), presumably by the loss of $\text{M}(\text{OTf})_n$ and triethylphosphine oxide ($\text{O}=\text{PEt}_3$). Similar to the case for

the tetraoxido clusters, the formation of $\text{O}=\text{PEt}_3$ was only confirmed after removal of the excess PEt_3 and methanolysis of the reaction mixture by GC–MS. Possible explanation for this observation includes the difference in the reduction potential in $[\mathbf{15-M}]^{n+}$ for the $\text{MMn}^{\text{III}}/\text{MMn}^{\text{III}}_2\text{Mn}^{\text{II}}$ couple, although this is for one-electron rather than two-electron process; the reduction potential of $[\mathbf{15-Y}]^{2+}$ is 0.3 V more positive than that of $[\mathbf{15-Ca}]^+$ as an effect of the more Lewis acidic M. Another rationale for the reaction rate variation is that $[\mathbf{15-Y}]^{2+}$ is an overall dicationic complex, thus, more electrophilic towards PEt_3 compared to $[\mathbf{15-Ca}]^+$.

Using the one-electron oxidized clusters $[\mathbf{16-M}]^{n+}$ will allow for direct comparison of the oxygen atom transfer reactivities to the less electrophilic $[\mathbf{15-M}]^{n+}$. The reaction of $[\mathbf{16-Ca}]^{2+}$ with 10 equiv. of PEt_3 yields the trimanganese (II) complex within 3 h. To slow down the rate, using 10 equiv. of the less nucleophilic PPh_3 required 20 h of reaction time.

On the other hand, the $[\mathbf{16-Y}]^{3+}$ complex required to complete the comparison to the $[\mathbf{15-M}]^{n+}$ series has not been successfully characterized to confirm its identity and geometry. An attempt to synthesize $[\mathbf{16-Y}]^{3+}$ includes the oxidation of $[\mathbf{15-Y}]^{2+}$ by one electron (performed by Emily Y. Tsui) using tris(4-bromophenyl)ammoniumyl hexachloroantimonate (“Magic Blue” reagent). This approach resulted in the chlorination of the complex and the loss of yttrium. Another approach was the transmetallation of $[\mathbf{16-Ca}]^{2+}$ with $\text{Y}(\text{OTf})_3$. Attempts to obtain single crystals of the product suitable for XRD study were done in multiple different solvents and conditions, albeit only resulting in oily precipitate. While there was no structural evidence of the starting material $[\mathbf{16-Y}]^{3+}$, the hexamanganese bis-yttrium tetraoxido

dimer $[(16-Y)_2]^{5+}$ has been structurally characterized previously by Emily Y. Tsui as the side product of the reaction to make $[15-Y]^{2+}$ (Figure 30).

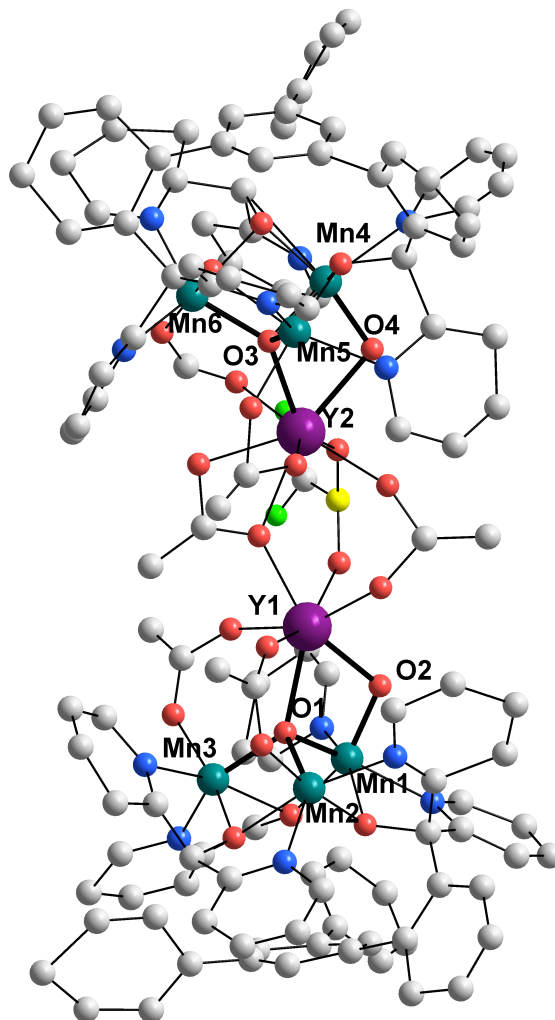
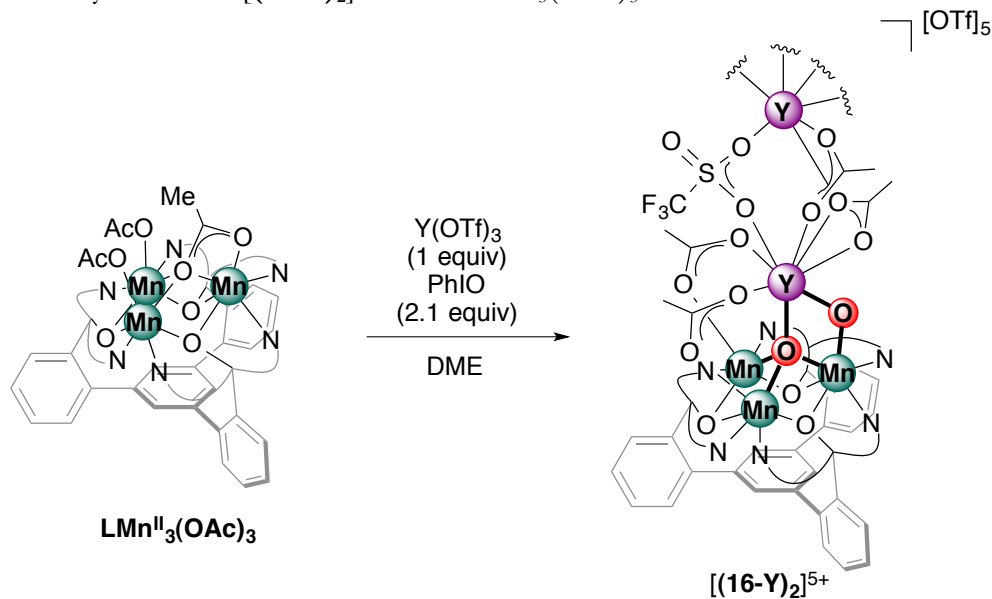


Figure 30. Preliminary solid-state structure of $[(16-Y)_2]^{5+}$. Solvents and 5 molecules of outer sphere triflates are omitted for clarity.

$[(16-Y)_2]^{5+}$ is a dimeric complex of $[16-Y]^{3+}$ where instead of dimethoxyethane (DME) ligand on top as what is normally found in the $[16-M]^{n+}$ series, a monomer is bridged by two acetates and a triflate to the other monomer (Figure 30). There are 5 outer sphere triflate counter anions found in the crystal lattice, thus, the Mn centers are assigned as $Mn^{III}_2Mn^{IV}$, equivalent to the targeted Mn oxidation states in $[16-Y]^{3+}$.

Therefore, the dimer $[(16-Y)_2]^{5+}$ was used as a synthetic analog to the monomer $[16-Y]^{3+}$ for the oxygen atom transfer studies. Additionally, $[(16-Y)_2]^{5+}$ can be directly synthesized in relatively good yield from the trimanganese(II) complex by treatment with one equivalent of $Y(OTf)_3$ and 2.1 equivalent PhIO (Scheme 5).

Scheme 5. Synthesis of $[(16-Y)_2]^{5+}$ from $LMn^{II}_3(OAc)_3$



Treatment of $[(16-Y)_2]^{5+}$ dimer with 20 equiv. of PEt_3 (or 10 equiv. PEt_3 per *monomer*) yields the $LMn^{II}_3(OAc)_3$ back in less than 15 min, monitored by 1H NMR spectroscopy and as indicated by the color change from purple-pink to pale yellow solution. This rate is significantly faster than that of $[16-Ca]^{2+}$ with 3 h of reaction time. Accordingly, to slow down the reaction rate, 20 equiv. of PPh_3 was added to $[(16-Y)_2]^{5+}$. The reaction was complete within 30 min monitored by 1H NMR spectroscopy while the reaction of $[16-Ca]^{2+}$ with 10 equiv. of PPh_3 took 20 h. In this case, the enhanced Lewis acidity of Y^{3+} greatly affected the oxygen atom transfer capability by rate acceleration as compared to Ca^{2+} in the $[16-M]^{n+}$ series. Additionally, the overall more cationic $[(16-Y)_2]^{5+}$ complex than $[16-Ca]^{2+}$ is expected to also effect the rate enhancement.

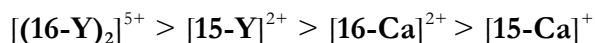
Table 3. Summary of oxygen atom transfer reactions of **9-M**, **[15-M]ⁿ⁺**, and **[16-M]ⁿ⁺**

Entry	Compounds	Lewis acid	pK _a	Reagent (equiv)	Time _{rxn}	T (°C)
1	9-Mn	Mn ³⁺	0.1	2 PMe ₃	15 min	r.t.
2	9-Co	Co ³⁺	0.66	2 PMe ₃	1-2 h	r.t.
3	[10-Sc]⁺	Sc ³⁺	4.8	10 PMe ₃	18 h ^a	r.t.
4	9-Sc	Sc ³⁺	4.8	10 PMe ₃	1.5 weeks	r.t.
5	9-Sc	Sc ³⁺	4.8	10 PMe ₃	30 h	50
6	[10-Gd]⁺	Gd ³⁺	8.4	10 PMe ₃	24 h ^a	r.t.
7	9-Gd	Gd ³⁺	8.4	10 PMe ₃	> 2 weeks	r.t.
8	9-Gd	Gd ³⁺	8.4	10 PMe ₃	50 h	50
9	10-Ca	Ca ²⁺	12.9	10 PMe ₃	N. R.	r.t.
10	[15-Y]²⁺	Y ³⁺	8.6	10 PEt ₃	30 min	r.t.
11	[15-Y]²⁺	Y ³⁺	8.6	10 PPh ₃	1 h	r.t.
12	[(16-Y)₂]⁵⁺	Y ³⁺	8.6	10 PEt ₃	< 15 min	r.t.
13	[(16-Y)₂]⁵⁺	Y ³⁺	8.6	10 PPh ₃	< 30 min	r.t.
14	[15-Ca]⁺	Ca ²⁺	12.9	10 PEt ₃	36 h	r.t.
15	[15-Ca]⁺	Ca ²⁺	12.9	10 PPh ₃	> 2 week	r.t.
16	[16-Ca]²⁺	Ca ²⁺	12.9	10 PEt ₃	3 h	r.t.
17	[16-Ca]²⁺	Ca ²⁺	12.9	10 PPh ₃	20 h	r.t.

^a Decomposition products were observed instead of the corresponding [MMn₃O₃]

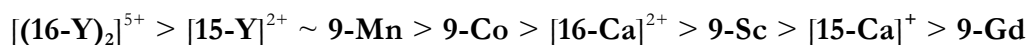
Comparing the **[15-M]ⁿ⁺** vs. **[16-M]ⁿ⁺** series, **[16-M]ⁿ⁺** complexes underwent faster O-atom transfer reactions than the analogous **[15-M]ⁿ⁺**. This is consistent with the hypothesis that compounds **[16-M]ⁿ⁺** are more electrophilic than compounds **[15-M]ⁿ⁺**, thus, more active towards oxygen-atom transfer. Based on the reactivity studies on **[15-**

$\mathbf{Ca}]^+$, $[\mathbf{15-Y}]^{2+}$, $[\mathbf{16-Ca}]^{2+}$, and $[(\mathbf{16-Y})_2]^{5+}$, a qualitative trend was observed from the fastest to slowest as shown below, and these studies are summarized in Table 3.



It is worthy to note that in the presence of excess phosphine reagents, the oxygen atom transfer reactivity of the dioxido complexes is not limited to *one* oxygen atom since $\text{LMn}^{\text{II}}_3(\text{OAc})_n$ was always observed as the end product. It is probable that after the first oxygen atom transfer possibly on the more accessible μ_2 -oxo, the cluster becomes more sterically open, and the second O atom transfer event on the μ_4 -oxo becomes kinetically favorable. While there is no experimental evidence yet to test this hypothesis, a possible future experiment to be performed is to add excess phosphines to the corresponding $[\text{MMn}_3\text{O}]$ or the “mono-oxo” complexes and compare the oxygen atom transfer capability on the μ_4 -oxo to determine if the reaction occurs at a similar rate. Current studies are also ongoing to repeat some reactions using the same equivalents of phosphine reagents on the $[\text{MMn}_2\text{O}_2]$ series for more direct comparisons.

From Table 3, a general trend across all compounds studied for oxygen atom transfer reactivity can be generated. From the fastest to slowest reaction, the trend is as follows:



Additional experiments of running some of the $[\text{MMn}_3\text{O}_4]$ compounds using PEt_3 will be performed to determine if the resulting oxygen atom transfer rates will be different between using PMe_3 vs. PEt_3 .

CONCLUSIONS

In summary, starting from **10-Ca(THF)**, a series of hetero metallic MMn_3 -oxido cubanes has been rationally synthesized, and systematic composition-property studies were performed. Fe^{II} and Co^{II} reduce the Mn^{IV}_3 moiety. Clusters displaying Sc^{III} , Mn^{III} , Fe^{III} , and Co^{III} ions show two redox events, in contrast to the Ni^{II} , Cu^{II} , and Zn^{II} species that show a single redox event. Spectroscopic investigations suggest that all redox events occur at the Mn centers for the series of $[\text{MMn}_3\text{O}_4]$, except for when $\text{M} = \text{Co}$ where reduction occurs on the Co^{III} center instead of Mn. Efforts to further the understanding of these systems by density functional theory are currently ongoing by Goddard and co-workers. Nevertheless, the identity of the apical metal has a significant effect on the cluster properties. This systematic study of discrete and well-defined MMn_3O_4 clusters highlights the intrinsic effect of the heterometallic combination on redox chemistry, with potential implications for mixed-metal heterogeneous oxides employed in redox catalysis and batteries.

Additional experiments on oxygen atom transfer reactivities of $[\text{MMn}_3\text{O}_4]$ and $[\text{MMn}_3\text{O}_2]$ as an extension on previous studies were also performed. The results from the reactivity studies are consistent with the proposed stronger Lewis acidity effect on enhanced reaction rate. In general, the $[\text{MMn}_3\text{O}_2]$ compounds underwent faster O atom transfer than $[\text{MMn}_3\text{O}_4]$ due to the kinetic barrier of the acetate lability on the tetraoxido clusters. For the $[\text{MMn}_3\text{O}_2]$ series, the overall cationic charge of the cluster also affects its electrophilicity, and consequently results in enhanced reaction rate. Current studies are focused on finalizing the comparison between the $[\text{MMn}_3\text{O}_4]$ and the $[\text{MMn}_3\text{O}_2]$ series for oxygen atom transfer reactivities. Another focus of is on the application of these $[\text{MMn}_3\text{O}_4]$ clusters ($\text{M} = \text{Co}, \text{Ni}$) as homogeneous precursors for heterogeneous OER electrocatalysts as a tool for further understanding the structure-function relationship of heterometallic oxides in catalysis described in the next chapter.

EXPERIMENTAL SECTION

General Considerations

Unless otherwise specified, all compounds were manipulated using a glovebox or standard Schlenk line techniques with an N₂ atmosphere. Anhydrous tetrahydrofuran (THF) was purchased from Aldrich in 18 L Pure-PacTM containers. Anhydrous benzene, dichloromethane, diethyl ether, and THF were purified by sparging with nitrogen for 15 minutes and then passing under nitrogen pressure through a column of activated A2 alumina (Zapp's). Methylene chloride-*d*₂ was purchased from Cambridge Isotopes, dried over calcium hydride, and vacuum transferred prior to use. Benzene-*d*₆ was also purchased from Cambridge Isotope Laboratories, Inc., dried over sodium/benzophenone ketyl, and vacuum transferred prior to use. Unless indicated otherwise, all commercial chemicals were used as received. Fe(OTf)₂, NiCl₂(dme), Cu(OTf)₂, and cobaltocene were purchased from Strem. Co(OTf)₂, tris(4-bromophenyl)ammoniumyl hexachloroantimonate, **H₃L**, **LMn₃(OAc)₃**, **LCaMn₃O₄(OAc)₃(THF)**, **[10-Sc]⁺**, **[10-Y]⁺**, and **[15-Y]²⁺** were prepared according to previously published protocols.^{11a-c,18} ¹H NMR spectra were recorded on Varian Mercury 300 at room temperature. Elemental analyses were performed by Robertson Microlit Laboratories, Ledgewood, NJ.

Synthesis of 9-Fe

To a suspension of **LCaMn₃O₄(OAc)₃(THF)** (250 mg, 0.182 mmol) in THF (20 mL) was added a suspension of Fe(OTf)₂ (71 mg, 0.20 mmol, 1.1 equiv) in THF (0.5 mL). The resulting suspension was stirred at r.t. for 16-18 h. The reaction mixture was observed to be slightly more homogeneous after 6 h into the reaction but was still a suspension. The suspension was filtered through Celite, and the residue was washed 3

times with THF. The filtrate and the THF wash were collected and dried under vacuum. The dry residue was recrystallized to give the clean product in 50% yield (120 mg) as crystalline brown blocks from either vapor diffusion of diethyl ether into a concentrated DCM solution or vapor diffusion of hexane into a concentrated benzene solution of the material. ^1H NMR (CD_2Cl_2 , 300 MHz): δ 17.2 (v br), 10.6 (v br overlapped), 10.2 (v br overlapped), 8.8 (v br), 7.6 (v br), 3.7 (br), 3.0 (br), 2.0 (br overlapped), 1.8 (br overlapped), -19.5 (v br) ppm. UV-Vis [λ_{max} (CH_2Cl_2 , nm), ϵ ($\text{M}^{-1}\text{cm}^{-1}$): 380 (shoulder), 6.3×10^3 ; 521, 1.3×10^3 . Anal. Calcd. for: $\text{C}_{63}\text{H}_{48}\text{FeMn}_3\text{N}_6\text{O}_{13}$ (**9-Fe**) (%): C, 57.42; H, 3.67; N, 6.38. Anal. Calcd. for: $\text{C}_{65}\text{H}_{52}\text{Cl}_4\text{FeMn}_3\text{N}_6\text{O}_{13}$ (**9-Fe · 2CH₂Cl₂**) (%): C, 52.48; H, 3.52; N, 5.65. Found: C, 52.83; H, 3.18; N, 5.64.

Synthesis of **9-Co**

To a suspension of **LCaMn₃O₄(OAc)₃(THF)** (150 mg, 0.109 mmol) in DMF (10 mL) was added a solution of $\text{Co}(\text{OTf})_2$ (43 mg, 0.120 mmol, 1.1 equiv) in DMF (0.5 mL). The reaction mixture was stirred at room temperature for 2 h. To the reaction mixture was added 30 mL diethyl ether. The resulting suspension was allowed to sit at r.t. for 5-8 h to precipitate out product. The suspension was then filtered through Celite, and the precipitate was washed with diethyl ether three times. The precipitate was eluted with dichloromethane and dried under vacuum to give the clean product in 70% yield (100 mg). The product can be recrystallized to give small blocks of brown crystals from vapor diffusion of diethyl ether into a concentrated solution of the product in methylene chloride. ^1H NMR (CD_2Cl_2 , 300 MHz): δ 19.4 (v br overlapped), 16.1 (v br overlapped), 11.4 (br), 9.3 (br), 7.9 (v br), 4.8 (v br), 3.0 (v br), 1.2, -24.9 (v br) ppm. UV-Vis [λ_{max} (CH_2Cl_2 , nm), ϵ ($\text{M}^{-1}\text{cm}^{-1}$): 371 (shoulder), 4.6×10^3 ; 478, 1.3×10^3 . Anal.

Calcd. for: $C_{63}H_{48}CoMn_3N_6O_{13}$ (**9-Co**) (%): C, 57.29; H, 3.66; N, 6.36. Found: C, 57.01; H, 3.29; N, 6.17.

Synthesis of 10-Ni

An analogous procedure to the synthesis of **9-Co** was carried out to make **10-Ni**. $NiCl_2(dme)$ was used instead of $Co(OTf)_2$. The yield for the reaction was 90% (69 mg). 1H NMR (CD_2Cl_2 , 300 MHz): δ 20.1 (v br), 11.5 (v br overlapped), 10.9 (v br overlapped), 8.9 (v br), 7.4, 7.2 (v br overlapped), 5.6 (v br overlapped), 4.8 (v br overlapped), 4.4 (v br overlapped), 3.06, 2.97, 0.6 (v br), -18.5 (v br) ppm. UV-Vis [λ_{max} (CH_2Cl_2 , nm), ϵ ($M^{-1}cm^{-1}$)]: 321 (shoulder), 2.1×10^4 ; 554, 1.9×10^3 . Anal. Calcd. for: $C_{63}H_{48}NiMn_3N_6O_{13}$ (**10-Ni**) (%): C, 57.30; H, 3.66; N, 6.36. Anal. Calcd. for: $C_{70}H_{64}Cl_6Mn_3N_6NiO_{14}$ (**10-Ni** · **3CH₂Cl₂** · **Et₂O**) (%): C, 52.48; H, 3.52; N, 5.65. Found: C, 52.83; H, 3.18; N, 5.64.

Synthesis of 10-Cu

To a suspension of $LCaMn_3O_4(OAc)_3(THF)$ (40 mg, 0.0291 mmol) in THF (4 mL) was added a suspension of $Cu(OTf)_2$ (11.6 mg, 0.032 mmol, 1.1 equiv) in THF (0.5 mL). The resulting suspension was stirred overnight at r.t. for 16-18 h. The suspension was filtered through Celite, and the residue was washed 3 times with THF. The precipitate was eluted with DCM and collected. Volatiles were removed from both THF and DCM fractions under vacuum separately and mostly clean product was observed as checked by 1H NMR in CD_2Cl_2 . The residue can be recrystallized from CH_2Cl_2/Et_2O to give the clean product in 40% yield via vapor diffusion of diethyl ether into a concentrated THF or DCM. 1H NMR (CD_2Cl_2 , 300 MHz): δ 18.8 (v br), 11.4 (br), 10.7 (v br), 8.8 (br), 7.1 (br), 5.6 (v br overlapped), 5.1 (br overlapped), 4.4 (br overlapped), 2.9 (br), 0.5 (v br), -

16.7 (br), -74.3 (v br) ppm. UV-Vis [λ_{\max} (CH₂Cl₂, nm), ϵ (M⁻¹cm⁻¹): 328 (shoulder), 1.9×10^4 ; 555, 0.8×10^3 . Anal. Calcd. for: C₆₃H₄₈CuMn₃N₆O₁₃ (**10-Cu**) (%): C, 57.09; H, 3.65; N, 6.34. Anal. Calcd. for: C₈₀H₉₀Cl₂CuMn₃N₆O₁₇ (**9-Cu** · CH₂Cl₂ · 4Et₂O) (%): C, 56.29; H, 5.31; N, 4.92. Found: C, 56.42; H, 4.98; N, 5.19.

Synthesis of [11-Fe][CoCp₂]

To a stirring solution of **9-Fe** (15 mg, 0.0114 mmol) in CH₂Cl₂ (2 mL) in a scintillation vial was added a solution of cobaltocene (2.2 mg, 0.0114 mmol, 1 equiv). The reaction mixture was stirred for 5 min, and the solvent was removed under vacuum to yield the clean product by ¹H NMR. The reduced product is not stable at room temperature over a few hours, which prevented the elemental analysis data from being acquired. ¹H NMR (CD₂Cl₂, 300 MHz): δ 17.3 (v br), 12.6 (v br), 9.4 (br overlapped), 8.8 (br overlapped), 7.5 (d), 7.4(br) , 6.4 (br), 5.8 (v br overlapped), 1.3 (br), 0.9 (br overlapped), -6.8 (v br) ppm.

Synthesis of [12-Fe][SbCl₆]

To a stirring solution of **9-Fe** (15 mg, 0.0114 mmol) in CH₂Cl₂ (2 mL) in a scintillation vial was added a solution of tris(4-bromophenyl)ammoniumyl hexachloroantimonate (9.6 mg, 0.0114 mmol, 1 equiv). The reaction mixture was stirred for 5 min, and the solvent was removed under vacuum to give the clean product by ¹H NMR. The oxidized product is not stable at room temperature over a few hours, which prevented the elemental analysis data from being acquired. ¹H NMR (CD₂Cl₂, 300 MHz): δ 26.7 (v br), 11.3 (v br), 9.2 (v br overlapped), 7.1 (v br overlapped), 4.2 (br), 3.5 (br), 1.26 (br), 0.9 (br), -18.9 (v br) ppm.

Synthesis of [11-Co][CoCp₂] and [11-Co][Cr(C₆H₆)₂]

[11-Co][CoCp₂]: An analogous procedure to the synthesis of [11-Fe][CoCp₂] was carried out to make [11-Co][CoCp₂]. **9-Co** was used as the starting material instead of **9-Fe**.

[11-Co][Cr(C₆H₆)₂] was used to prepare XAS samples. An analogous procedure to the synthesis of [11-Fe][CoCp₂] was carried out to make [11-Co][Cr(C₆H₆)₂]. **9-Co** and Cr(C₆H₆)₂ were used as the reagents instead of **9-Fe** and CoCp₂.

For both complexes, the products are not stable at room temperature over a few hours, which prevented the elemental analysis data from being acquired. The ¹H NMR spectra are the same for both [11-Co]⁻ complexes. ¹H NMR (CD₂Cl₂, 300 MHz): δ 26.53 (br), 21.52 (v br), 10.69 (br overlapped), 10.58 (br overlapped), 8.55 (br), 7.82 (br), 7.11 (v br), 5.89 (br), 5.11 (br), 4.42 (v br), -23.35 (br), -102.87 (v br) ppm.

Synthesis of [12-Co][SbCl₆]

An analogous procedure to the synthesis of [12-Co][SbCl₆] was carried out to make [12-Fe][SbCl₆]. **9-Co** was used as the starting material instead of **9-Fe**. The oxidized product is not stable at room temperature over a few hours, which prevented the elemental analysis data from being acquired. ¹H NMR (CD₂Cl₂, 300 MHz): δ 11.87 (v br overlapped), 11.55 (v br overlapped), 9.32 (br), 7.36 (br), 6.93 (v br), 4.31 (v br overlapped), 4.02 (br overlapped), -20.28 (br) ppm.

Synthesis of [13-Ni][CoCp₂]

To a stirring solution of **10-Ni** (9 mg, 0.00681 mmol) in CH₂Cl₂ (2 mL) in a scintillation vial was added a solution of cobaltocene (1.4 mg, 0.0075 mmol, 1 equiv). The reaction mixture was stirred for 5 min, and the solvent was removed under vacuum to yield the product as shown by the ¹H NMR spectrum. The product was recrystallized from a

CH₂Cl₂/Et₂O solution mixture at -35 °C overnight. The reduced product is not stable at room temperature over a few hours, which prevented the elemental analysis data from being acquired. ¹H NMR (CD₂Cl₂, 300 MHz): δ 30.4 (v br), 11.1 (v br overlapped), 8.8 (br), 7.7 (br), 1.1 (v br), 0.4 (v br), -26.2 (v br) ppm.

Synthesis of 14-Sc

Synthesis of **9-Sc** was previously reported by Emily Y. Tsui in her thesis.

In an inert atmosphere glovebox, **9-Sc** (13.5 mg, 0.0103 mmol, 1 equiv) was initially dissolved in C₆D₆ in a J. Young NMR tube. To the wall of the J. Young tube was added PMe₃ (11 μL, 0.103 mmol, 10 equiv) quickly via a Hamilton syringe. The J. Young tube was sealed and brought outside the glovebox. The reaction mixture was heated to 50 °C using an oil bath. The reaction was monitored over time by ¹H NMR spectroscopy and was complete after 30 h. The solvent and excess unreacted PMe₃ were removed under vacuum. The residue was washed with Et₂O to remove trace PMe₃ (no O=PMe₃ was detected in the Et₂O wash). The residue was resuspended in benzene and then filtered. Crystals were obtained via vapor diffusion of Et₂O into a concentrated benzene solution to give the clean product in 77% yield. ¹H NMR (C₆D₆, 300 MHz): δ 17.62 (v br), 10.69 (v br), 9.44 (br overlapped), 9.05 (v br overlapped), 4.57 (br), 3.53 (br), 2.34 (br), 1.84 (br), 1.63 (br), 1.35 (m overlapped), -18.98 (v br) ppm. Anal. Calcd. for: C₆₃H₄₈Mn₃N₆O₁₂Sc (**14-Sc**) (%): C, 58.62; H, 3.75; N, 6.51. Found: C, 57.88; H, 3.70; N, 6.65.

Synthesis of 14-Co

In an inert atmosphere glovebox, **9-Co** (20 mg, 0.0151 mmol, 1 equiv) was completely dissolved in CD₂Cl₂ in a J. Young tube. To the solution was added PMe₃ (3.2 μL, 0.03

mmol, 2 equiv) quickly using a Hamilton syringe. The J. Young tube was capped. The reaction was allowed to run at rt and monitored by ^1H NMR spectroscopy. After 2 h, the reaction was complete. Volatiles were removed under vacuum. The dried residue was washed with Et_2O to remove any left over PMe_3 and trimethylphosphine oxide. The product was recrystallized in $\text{C}_6\text{H}_6/\text{Et}_2\text{O}$ to give crystalline solids in 81% yield. ^1H NMR (CD_2Cl_2 , 300 MHz): δ 23.65 (br), 16.10 (br), 11.00 (br), 9.77 (br overlapped), 7.7 (br), 7.12 (v br), 6.20 (v br), 4.64 (br), 3.70 (br), 1.83 (br), -19.39 (br), -60.84 (v br) ppm. Anal. Calcd. for: $\text{C}_{63}\text{H}_{48}\text{CoMn}_3\text{N}_6\text{O}_{12}$ (**14-Co**) (%): C, 57.99; H, 3.71; N, 6.44. Found: C, 57.94; H, 3.59; N, 6.25.

Synthesis of $[(16\text{-Y})_2]^{5+}$

To a suspension of $\text{LMn}_3(\text{OAc})_3$ (150 mg, 0.125 mmol, 1 equiv) in DME was added $\text{Y}(\text{OTf})_3$ (67 mg, 0.125 mmol, 1 equiv). The mixture was stirred for 5 min then PhIO was added (58 mg, 0.263 mmol, 2.1 equiv). The mixture was stirred for 1 h then filtered. The purple filtrate was collected and the solvent was removed under vacuum. The DME fraction was recrystallized in $\text{CH}_3\text{CN}/\text{Et}_2\text{O}$ to give clean product as precipitate in 71% yield. ^1H NMR (CD_2Cl_2 , 300 MHz): δ 77.49 (v br), 67.83 (m overlapped), 52.93 (m br overlapped), 41.12 (v br), 38.51 (v br), 35.34 (v br), 25.17 (m br overlapped), 17.40 (br overlapped), 8.3 (m br overlapped), -21.81 (m br overlapped), -24.47 (d br overlapped), -28.05 (m br overlapped), -33.46 (m br overlapped) ppm. Anal. Calcd. for: $\text{C}_{132}\text{H}_{96}\text{F}_{18}\text{Mn}_6\text{N}_{12}\text{O}_{40}\text{S}_6\text{Y}_2$ $[(16\text{-Y})_2]^{5+}$ (%): C, 44.89; H, 2.74; N, 4.76. Found: C, 44.89; H, 2.94; N, 4.57.

Mössbauer Spectroscopy

Spectra were recorded on a spectrometer from SEE Co. operating in the constant acceleration mode in a transmission geometry. Spectra were recorded with the

temperature of the sample maintained at 80 K. The sample was kept in an SVT-400 Dewar from Janis, at zero field. Application of a magnetic field of 54 mT parallel to the γ -beam did not cause detectable changes in the spectra recorded at 80 K. The quoted isomer shifts are relative to the centroid of the spectrum of a metallic foil of α -Fe at room temperature. Samples were prepared by grinding polycrystalline material into a fine powder and then mounting in a cup fitted with a screw cap as a boron nitride pellet. Data analysis was performed using the program WMOSS (www.wmoss.org) and quadrupole doublets were fit to Lorentzian lineshapes.

Dispersive Difference Fourier Synthesis (DDFS)

As it is very hard to distinguish Mn and Fe with conventional crystallography, we resorted to the fact that they are easily identified by their absorptive properties. Therefore, multi wavelength diffraction data were collected at the Stanford Synchrotron Radiation Laboratory, beamline 14-1 on a MAR325 CCD detector. Due to the centrosymmetric nature of the crystals, it was impossible to take advantage of the violation of Friedel's law. Instead, we resorted to utilize the dispersive differences near the absorption edges of Mn and Fe. In order to maximize the signal, variable resolution X-ray absorption spectra (with a maximum resolution of 1 eV around the edge) were recorded around the Mn and Fe edges using the BluIce interface. The optimal energies for data collection were determined as the inflection points of the respective X-ray absorption spectra ($\lambda_{\text{Mn1}}=1.89225 \text{ \AA}$, $\lambda_{\text{Mn2}}=1.89138 \text{ \AA}$, $\lambda_{\text{Fe}}=1.74007 \text{ \AA}$, $\lambda_{\text{Mn1}}=1.60554 \text{ \AA}$). Due to the experimental geometry, the low energy edge data could only be collected to a maximum resolution of about 2.1 \AA (comparable to a 2θ of 43° on a Cu K_α source). Therefore, a high energy dataset (13 keV, the maximum at BL 14-1) was collected as a

reference dataset. The high resolution datasets were used to solve the structures (SHELXS)¹³ with all metal atoms assigned to Mn. A final round of refinement was performed with PHENIX¹⁹ to ensure coordinate compatibility with the macromolecular crystallography programs used in subsequent steps. The phases obtained this way were used to calculate dispersive difference Fourier maps with amplitudes derived as the differences $\lambda_{\text{Fe}} - \lambda_{\text{Mn1}}$ for the Manganese positions, $\lambda_{\text{Mn1}} - \lambda_{\text{Fe}}$ for the Iron positions in **9-Fe**, and $\lambda_{\text{Co}} - \lambda_{\text{Mn2}}$ and $\lambda_{\text{Mn2}} - \lambda_{\text{Co}}$ for the Manganese and Cobalt positions in **9-Co**, respectively. Structure factor differences were calculated with SFTOOLS (CCP4),²⁰ and the Fourier maps were produced with FFT (CCP4).²¹

X-ray Absorption Spectroscopy (XAS) Data Collection

Mn XAS measurements were performed at the Stanford Synchrotron Radiation Laboratory (SSRL) on Beamline 7-3 at an electron energy of 3.0 GeV and an average current of 500 mA. The intensity of the incident X-ray beam was monitored using a N₂-filled ion chamber (I₀) in front of the sample. A Si(220) double-crystal monochromator was used to detune to 50% of the maximum flux to attenuate higher harmonics. The data was collected as fluorescence excitation spectra with a Ge 30-element detector (Canberra). The monochromator energy was calibrated using the pre-edge peak of KMnO₄ (6543.3 eV). The calibration standard was placed between two N₂-filled ionization chambers (I₁ and I₂) after the sample. To minimize radiation damage, samples were maintained at a temperature of 10 K in a liquid He flow cryostat.

To prepare the XAS solid samples, 5-10 mg of the individual complexes were finely ground with a mortar and pestle in a glovebox, and diluted with boron nitride (1% w/w). The mixture was packed anaerobically into 0.5 mm thick aluminum sample

holders and sealed with Mylar tape. XAS solution samples were prepared by loading the solution into a 0.8mm thick Lucite frame backed with Mylar tape. To ensure that no X-ray induced radiation damage occurred, the Mn K-edge was closely monitored for any reduction of manganese as seen by a shift in the K-edge inflection point energy.

Data Reduction and Analysis for XANES

Data reduction of the XANES spectra was performed using SamView (SixPACK software, Dr. Samuel M. Webb, SSRL). The pre-edge and post-edge backgrounds were subtracted from the XAS spectra using Athena (IFEFFIT software²²), and the resulting spectra were normalized with respect to the edge height. The background removal in k -space was performed using a cubic spline function. For the energy (eV) to wave vector (k , \AA^{-1}) axis conversion, E_0 was defined as 6561.3 eV. The energy position of the main edge was defined as the inflection point energy (IPE), which was determined from the zero-crossing of the second derivative of the XANES spectrum. The third-order polynomial second derivative function was taken with a 3 eV differentiation interval on each side of a data point. The estimated error in the IPE was ± 0.1 eV for individual samples.

Cyclic Voltammetry Electrochemical Measurements

Reported cyclic voltammetry studies were recorded with a Pine Instrument Company AFCBP1 bipotentiostat using the AfterMath software package. CVs were recorded on *ca.* 1 mM solutions of the relevant complexes in the glovebox at 20 °C with an auxiliary Pt-coil electrode, a Ag/Ag⁺ reference electrode (0.01 M AgNO₃, 0.1 M ⁿBu₄NPF₆ in CH₃CN), and a 3.0 mm glassy carbon electrode disk (Bioanalytical Systems, Inc.). The electrolyte solution was 0.1 M ⁿBu₄NPF₆ in DMA. Reported potentials were referenced internally to ferrocene/ferrocenium, and are an average of at least two separate CV

experiments. The measured reduction potentials typically varied by less than 15 mV between experiments.

Crystallographic Information. CCDC 980707-980711 (for **9-Fe**, **9-Co**, **10-Ni**, **10-Cu**, and **[13-Ni]⁻**, respectively) and 1035171, 1035166, and 1035222 (for **[11-Co]⁻**, **14-Co**, and **14-Sc**, respectively) contain the supporting crystallographic data for this paper. These data can be obtained free of charge from The Cambridge Crystallographic Data Centre via www.ccdc.cam.ac.uk/data_request/cif.

Refinement details

In each case, crystals were mounted on a glass fiber or nylon loop using Paratone oil, then placed on the diffractometer under a nitrogen stream. Low temperature (100 K) X-ray data were obtained on a Bruker APEXII CCD based diffractometer (Mo sealed X-ray tube, $K_{\alpha} = 0.71073 \text{ \AA}$). All diffractometer manipulations, including data collection, integration, and scaling, were carried out using the Bruker APEXII software.²³ Absorption corrections were applied using SADABS.²⁴ Space groups were determined on the basis of systematic absences and intensity statistics and the structures were solved by direct methods using XS²⁵ (incorporated into SHELXTL)¹³ and refined by full-matrix least squares on F^2 . All non-hydrogen atoms were refined using anisotropic displacement parameters. Hydrogen atoms were placed in idealized positions and refined using a riding model. The structure was refined (weighted least squares refinement on F^2) to convergence.

It should be noted that due to the size of these compounds, most crystals included solvent accessible voids, which tended to contain disordered solvent. In addition, due to a tendency to desolvate, the long range order of these crystals and amount of high angle data we were able to record was in some cases not ideal. These

disordered solvent molecules were largely responsible for the alerts generated by the checkCIF protocol. For **10-Ni** and **10-Cu**, the disordered non-coordinated solvents were removed using the SQUEEZE protocol included in PLATON²⁵ (*vide infra*). We are confident this additional electron density is from the solvent molecules in the crystal lattice and not from unaccounted counter ions.

Table 4. Crystal and refinement data for complexes **9-Fe**, **9-Co**, **10-Ni**, and **10-Cu**

	9-Fe	9-Co	10-Ni	10-Cu
empirical formula	C ₇₉ H ₈₀ Fe Mn ₃	C ₇₅ H ₆₀ Co Mn ₃	C ₁₀₂ H ₈₇ Mn ₃ N ₆	C ₆₉ H ₆₀ Cu Mn ₃
formula wt	1606.16	1477.04	1828.31	1457.59
T (K)	100	100	100	100
a, Å	13.7266(6)	13.491(3)	17.0877(9)	17.433(3)
b, Å	18.0723(7)	15.301(3)	17.3276(10)	17.433(3)
c, Å	28.1288(11)	16.931(3)	19.8214(11)	16.931(3)
α, deg	90	70.61(3)	64.244(3)	37.666(8)
β, deg	92.111(2)	81.49(3)	66.307(3)	90
γ, deg	90	81.77(3)	66.418(3)	90
V, Å ³	6973.2(5)	3243.9(11)	4656.0(4)	120
Z	4	2	2	6
Cryst. system	Monoclinic	Triclinic	Triclinic	Rhombohedral
space group	P2(1)/c	P-1	P-1	R-3
d _{calcd} , g/cm ³	1.530	1.512	1.304	1.465
θ range, deg	1.84 - 29.52	1.28 - 24.57	2.03 - 31.07	1.45 - 33.73
μ, mm ⁻¹	0.813	0.895	0.661	0.951
abs cor	Semi-empirical from equivalents	Semi-empirical from equivalents	Semi-empirical from equivalents	Semi-empirical from equivalents
GOF ^c	1.037	0.998	0.831	1.399
R1, ^a wR2 ^b (I > 2σ(I))	0.0637, 0.1422	0.0742, 0.1691	0.0541, 0.1418	0.1163, 0.3387

$${}^a R1 = \frac{\sum ||F_o| - |F_c||}{\sum |F_o|} \quad {}^b wR2 = \left\{ \frac{\sum [w(F_o^2 - F_c^2)^2]}{\sum [w(F_o^2)^2]} \right\}^{1/2} \quad {}^c GOF = S = \left\{ \frac{\sum [w(F_o^2 - F_c^2)^2]}{(n-p)} \right\}^{1/2}$$

Table 5. Crystal and refinement data for complexes [11-Co][CoCp₂], [13-Ni][CoCp₂], [14-Co], and [14-Sc]

	[11-Co]-	[13-Ni]-	[14-Co]	[14-Sc]
empirical formula	C _{77.84} H _{68.25} Cl _{7.44}	C _{79.81} H _{73.61} Cl _{5.79}	C ₇₇ H ₇₇ Co Mn ₃	C ₈₂ H ₇₄ Mn ₃ N ₆
formula wt	1846.60	1828.38	1534.19	1579.44
T (K)	100	100	100	100
a, Å	13.8147(14)	13.5317(6)	12.2466(5)	12.2754(13)
b, Å	23.617(2)	15.0164(8)	15.4777(7)	15.4073(17)
c, Å	23.691(2)	40.901(2)	20.5356(9)	20.687(2)
α, deg	82.029(3)	90	85.617(3)	85.434(6)
β, deg	92.111(2)	99.190(2)	73.279(2)	72.878(6)
γ, deg	89.636(3)	90	76.096(2)	76.278(6)
V, Å ³	83.542(3)	8204.3(7)	3618.6(3)	3632.1(7)
Z	4	4	2	2
Cryst. system	Triclinic	Monoclinic	Triclinic	Triclinic
Space group	P-1	P2(1)/n	P-1	P-1
d _{calcd} , g/cm ³	1.613	1.480	1.431	1.444
θ range, deg	1.484 – 23.257	1.53 – 26.12	1.035 – 30.562	1.698 – 30.666
μ, mm ⁻¹	1.242	1.126	0.808	0.670
abs cor	Semi-empirical from equivalents	Semi-empirical from equivalents	Semi-empirical from equivalents	Semi-empirical from equivalents
GOF ^c	1.079	1.176	1.047	1.080
R1, ^a wR2 ^b (I > 2σ(I))	0.1662, 0.2067	0.1118, 0.2480	0.0812, 0.1901	0.0608, 0.1283

$${}^a R1 = \frac{\sum ||F_o| - |F_c||}{\sum |F_o|} \quad {}^b wR2 = \left\{ \frac{\sum [w(F_o^2 - F_c^2)^2]}{\sum [w(F_o^2)^2]} \right\}^{1/2} \quad {}^c GOF = S = \left\{ \frac{\sum [w(F_o^2 - F_c^2)^2]}{(n-p)} \right\}^{1/2}$$

Special refinement details for 9-Fe

9-Fe was crystallized from CH₂Cl₂/Et₂O or THF/Et₂O mixtures. Accordingly, the compound crystallized with either CH₂Cl₂ or THF solvent molecules in the lattice. The structure obtained from the recrystallization from THF/Et₂O mixtures gave non R-3 space group, and is therefore, included in this report for **9-Fe**. Four THF solvents molecules were satisfactorily modeled.

Special refinement details for 9-Co

Benzene was used as one of the crystallization solvents for **9-Co**. The structure contains two benzene solvent molecules that were satisfactorily modeled with restraints employed to treat the C–C distances and the displacement parameters of one of the benzene solvent molecules to an acceptable size. The relatively low level of completeness is due to poor crystal quality. This dataset represents the best of repeated collection attempts using crystals obtained under various crystallization conditions.

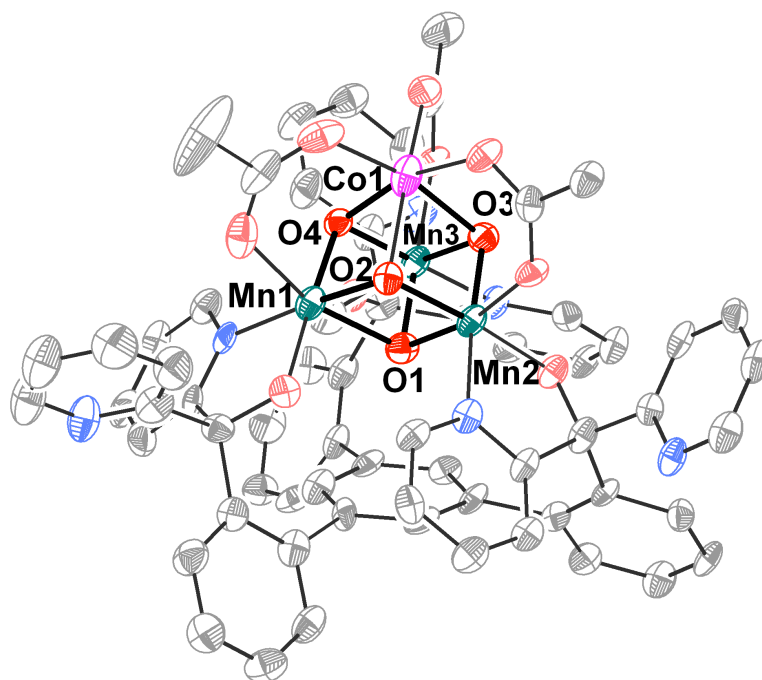


Figure 31. Solid-state structure of **9-Co** as 50% thermal ellipsoids. Hydrogen atoms and solvents are omitted for clarity.

Special refinement details for 10-Ni

10-Ni were crystallized from either $\text{CH}_2\text{Cl}_2/\text{Et}_2\text{O}$ or benzene/ Et_2O mixtures. Accordingly, the compound crystallized with either CH_2Cl_2 or benzene solvent molecules in the lattice. The structure that was obtained from the recrystallization from benzene/ Et_2O mixtures gave a non R-3 space group, and therefore, included in this

report for **10-Ni**. The structure contains a number of benzene solvent molecules, seven of them satisfactorily modeled with some restraints. There were some additional disordered diethyl ether solvent molecules, however, that could not be satisfactorily modeled. The SQUEEZE protocol contained with the program PLATON²⁵ was used to generate a bulk solvent correction to the observed intensities. The results are appended to the CIF.

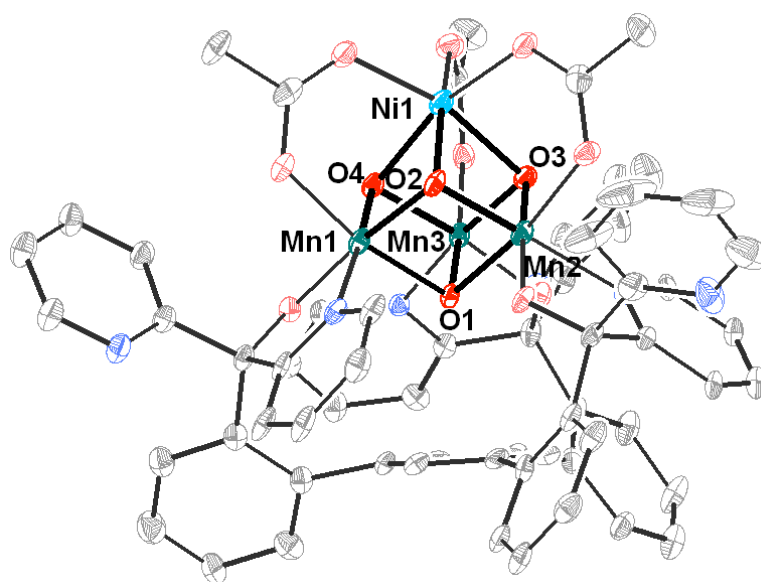


Figure 32. Solid-state structure of **10-Ni** as 50% thermal ellipsoids. Hydrogen atoms and solvents are omitted for clarity

Special refinement details for **10-Cu**

10-Cu were crystallized from either $\text{CH}_2\text{Cl}_2/\text{Et}_2\text{O}$ or benzene/ Et_2O mixtures. Accordingly, the compound crystallized with either CH_2Cl_2 , Et_2O , or benzene solvent molecules in the lattice. The structure that was obtained from the recrystallization from benzene/ Et_2O mixtures still gave an R-3 space group, which is reported in this manuscript for **10-Cu**. One disordered diethyl ether was modeled and split into 3 positions. One additional benzene solvent molecule that is sitting on a special position,

however, could not be satisfactorily modeled. The SQUEEZE protocol contained with the program PLATON²⁵ was used to generate a bulk solvent correction to the observed intensities. The results are appended to the CIF.

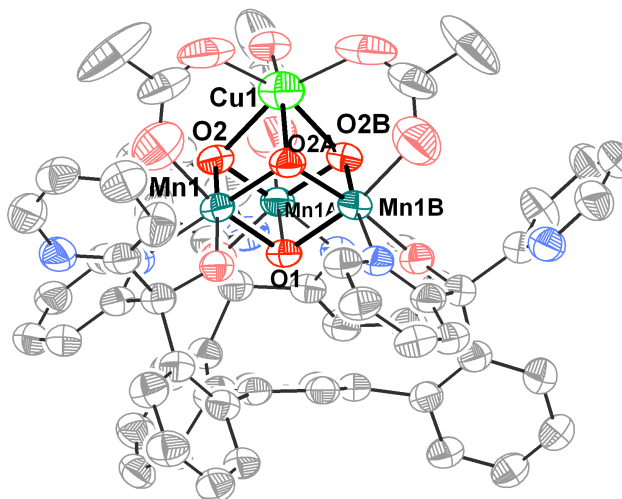


Figure 33. Solid-state structure of **10-Cu** as 50% thermal ellipsoids. Hydrogen atoms and solvents are omitted for clarity.

Special refinement details for [11-Co][CoCp₂]

[11-Co][CoCp₂] was crystallized from CH₂Cl₂/Et₂O mixture. Two molecules of the complex crystallized in the asymmetric unit. The compound co-crystallized with nine dichloromethane solvent molecules and one diethyl ether solvent molecule in the lattice that were modeled successfully. Some constraints were employed to treat the displacement parameters of the atoms on some solvent molecules to an acceptable size. The structure also contains two outer-sphere cobaltocenium counterions that were satisfactorily modeled, consistent with the formation of the one-electron reduced complex. The atom O14 of the second complex molecule in the asymmetric was successfully modeled as disordered at two positions. This dataset represents the best of

repeated collection attempts using crystals obtained under various crystallization conditions.

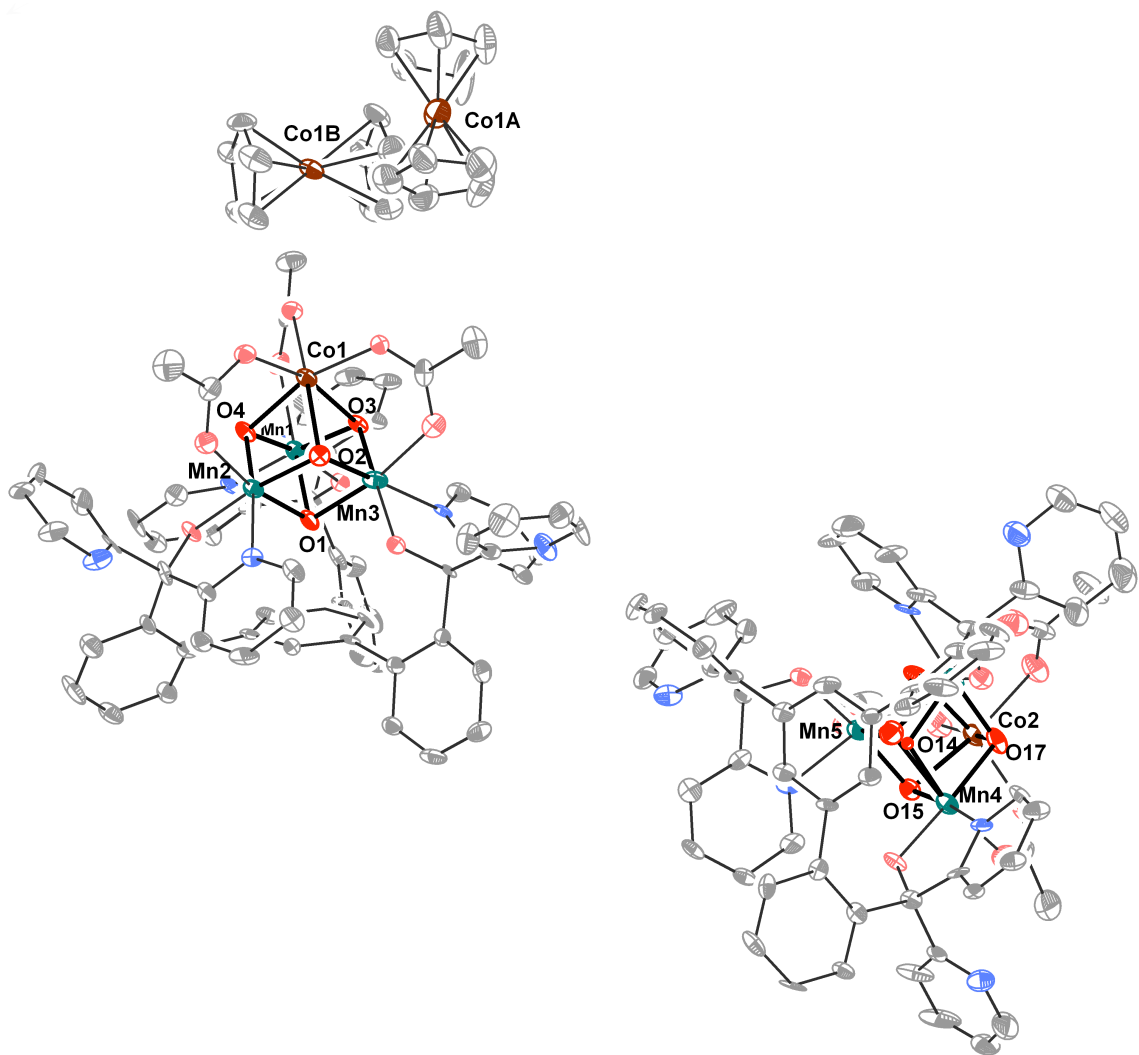


Figure 34. Solid-state structure of $[11\text{-Co}][\text{CoCp}_2]$ as 50% thermal ellipsoids. Hydrogen atoms and solvents are omitted for clarity.

Special refinement details for $[13\text{-Ni}][\text{CoCp}_2]$

$[13\text{-Ni}][\text{CoCp}_2]$ was crystallized from $\text{CH}_2\text{Cl}_2/\text{Et}_2\text{O}$ mixture at $-35\text{ }^\circ\text{C}$. Accordingly, the compound crystallized with four dichloromethane and two diethyl ether solvent molecules in the lattice that were modeled successfully. Some constraints were

employed to treat the displacement parameters of the atoms on some solvent molecules to an acceptable size. The structure also contains one outer-sphere cobaltocenium counterion that was satisfactorily modeled over two positions. The atom O1 was successfully modeled as disordered at two positions. The relatively low level of completeness is due to poor crystal quality. This dataset represents the best of repeated collection attempts using crystals obtained under various crystallization conditions.

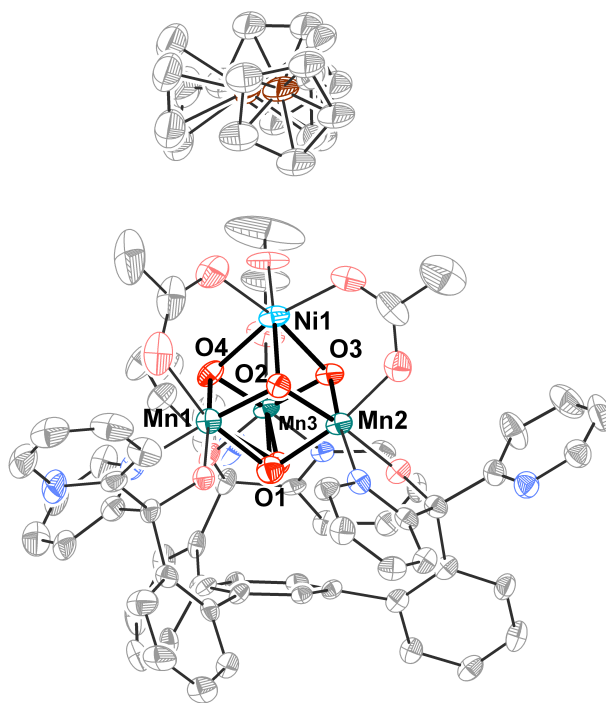


Figure 35. Solid-state structure of $[13\text{-Ni}][\text{CoCp}_2]$ as 50% thermal ellipsoids. Hydrogen atoms and solvents are omitted for clarity.

Special refinement details for 14-Sc

14-Sc was crystallized from $\text{C}_6\text{H}_6/\text{Et}_2\text{O}$ mixture. The compound crystallized with two benzene and two diethyl ether solvent molecules in the lattice that were modeled successfully. Some constraints were employed to treat the displacement parameters of the atoms on some solvent molecules to an acceptable size. One of the benzenes

solvents was disordered at two positions. The atom O4 was modeled with 15% occupancy (85% occupancy of **14-Sc**). The 15% occupancy of O4 may have come from co-crystallized starting material or uptake of oxygen atom from the air upon crystal handling/mounting.

Special refinement details for **14-Co**

14-Sc was crystallized from C₆H₆/Et₂O mixture. The compound crystallized with one benzene and two diethyl ether solvent molecules in the lattice that were modeled successfully. Some constraints were employed to treat the displacement parameters of the atoms on some solvent molecules to an acceptable size.

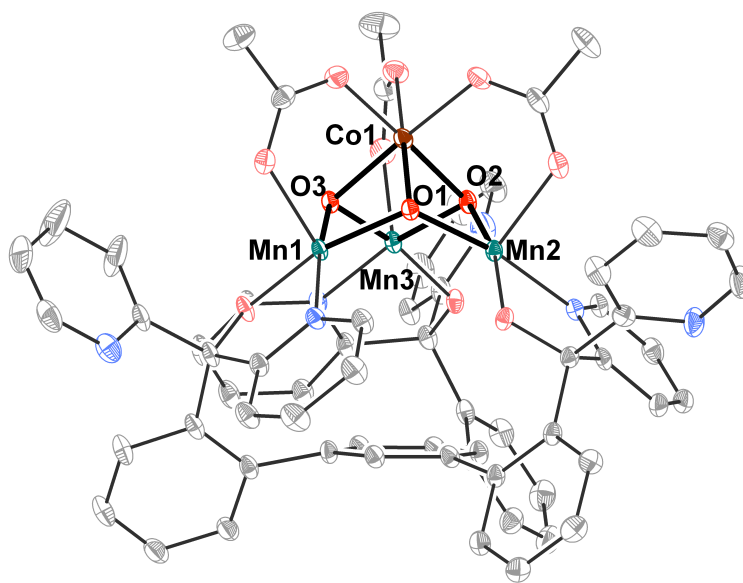


Figure 36. Solid-state structure of **14-Sc** as 50% thermal ellipsoids. Hydrogen atoms and solvents are omitted for clarity.

REFERENCES

- 1 (a) Smith, R. D. L.; Prevot, M. S.; Fagan, R. D.; Zhang, Z. P.; Sedach, P. A.; Siu, M. K. J.; Trudel, S.; Berlinguette, C. P. *Science* **2013**, *340*, 60. (b) Smith, R. D. L.; Prevot, M. S.; Fagan, R. D.; Trudel, S.; Berlinguette, C. P. *J. Am. Chem. Soc.* **2013**, *135*, 11580. (c) Liang, Y. Y.; Wang, H. L.; Zhou, J. G.; Li, Y. G.; Wang, J.; Regier, T.; Dai, H. J. *J. Am. Chem. Soc.* **2012**, *134*, 3517.
- 2 (a) Gray, H. B. *Nature Chem.* **2009**, *1*, 112. (b) Lewis, N. S.; Nocera, D. G. *Proc. Natl. Acad. Sci. U.S.A.* **2006**, *103*, 15729. (c) Kanan, M. W.; Nocera, D. G. *Science* **2008**, *321*, 1072.
- 3 Suntivich, J.; Gasteiger, H. A.; Yabuuchi, N.; Nakanishi, H.; Goodenough, J. B.; Shao-Horn, Y. *Nature Chem.* **2011**, *3*, 647.
- 4 (a) Goodenough, J. B.; Kim, Y. *Chem. Mater.* **2010**, *22*, 587. (b) Hassoun, J.; Lee, K. S.; Sun, Y. K.; Scrosati, B. *J. Am. Chem. Soc.* **2011**, *133*, 3139. (c) Wang, Z.-L.; Xu, D.; Xu, J.-J.; Zhang, X.-B. *Chem. Soc. Rev.* **2014**, DOI: 10.1039/C3CS60248F.
- 5 (a) Feng, P. L.; Beedle, C. C.; Wernsdorfer, W.; Koo, C.; Nakano, M.; Hill, S.; Hendrickson, D. N. *Inorg. Chem.* **2007**, *46*, 8126. (b) Langley, S. K.; Chilton, N. F.; Moubaraki, B.; Murray, K. S. *Dalton Trans.* **2012**, *41*, 1033. (c) Saalfrank, R. W.; Prakash, R.; Maid, H.; Hampel, F.; Heinemann, F. W.; Trautwein, A. X.; Bottger, L. H. *Chem-Eur. J.* **2006**, *12*, 2428.
- 6 (a) Tereniak, S. J.; Carlson, R. K.; Clouston, L. J.; Young, V. G.; Bill, E.; Maurice, R.; Chen, Y. S.; Kim, H. J.; Gagliardi, L.; Lu, C. C. *J. Am. Chem. Soc.* **2014**, *136*, 1842. (b) Powers, T. M.; Gu, N. N. X.; Pout, A. R.; Baldwin, A. M.; Sanchez, R. H.; Alfonso, D. M.; Chen, Y. S.; Zheng, S. L.; Betley, T. A. *J. Am. Chem. Soc.* **2013**, *135*, 14448. (c) Krogman, J. P.; Foxman, B. M.; Thomas, C. M. *J. Am. Chem. Soc.* **2011**, *133*, 14582. (d) Stack, T. D. P.; Holm, R. H. *J. Am. Chem. Soc.* **1988**, *110*, 2484. (e) Zhou, J.; Raebiger, J. W.; Crawford, C. A.; Holm, R. H. *J. Am. Chem. Soc.* **1997**, *119*, 6242.
- 7 Sano, Y.; Weitz, A. C.; Ziller, J. W.; Hendrich, M. P.; Borovik, A. S. *Inorg. Chem.* **2013**, *52*, 10229.
- 8 Morimoto, Y.; Kotani, H.; Park, J.; Lee, Y. M.; Nam, W.; Fukuzumi, S. *J. Am. Chem. Soc.* **2011**, *133*, 403.

- 9 (a) Park, J.; Morimoto, Y.; Lee, Y. M.; Nam, W.; Fukuzumi, S. *J. Am. Chem. Soc.* **2011**, *133*, 5236. (b) Miller, C. G.; Gordon-Wylie, S. W.; Horwitz, C. P.; Strazisar, S. A.; Peraino, D. K.; Clark, G. R.; Weintraub, S. T.; Collins, T. J. *J. Am. Chem. Soc.* **1998**, *120*, 11540. (c) Dong, L.; Wang, Y. J.; Lv, Y. Z.; Chen, Z. Q.; Mei, F. M.; Xiong, H.; Yin, G. C. *Inorg. Chem.* **2013**, *52*, 5418.
- 10 Lionetti, D.; Suseno, S. *Manuscript in preparation* **2014**.
- 11 (a) Kanady, J. S.; Tsui, E. Y.; Day, M. W.; Agapie, T. *Science* **2011**, *333*, 733. (b) Kanady, J. S.; Mendoza-Cortes, J. L.; Tsui, E. Y.; Nielsen, R. J.; Goddard, W. A.; Agapie, T. *J. Am. Chem. Soc.* **2013**, *135*, 1073. (c) Tsui, E. Y.; Tran, R.; Yano, J.; Agapie, T. *Nature Chem.* **2013**, *5*, 293. (d) Tsui, E.; Agapie, T. *Proc. Natl. Acad. Sci. U.S.A.* **2013**, *110*, 10084.
- 12 (a) Fultz, B. In *Characterization of Materials*; Kaufmann, E., Ed.; John Wiley: New York, 2011. (b) Juarezgarcia, C.; Hendrich, M. P.; Holman, T. R.; Que, L.; Munck, E. *J. Am. Chem. Soc.* **1991**, *113*, 518. (c) Menage, S.; Brennan, B. A.; Juarezgarcia, C.; Munck, E.; Que, L. *J. Am. Chem. Soc.* **1990**, *112*, 6423.
- 13 Sheldrick, G. M. *Acta Crystallogr. A* **2008**, *D65(2)*, 148.
- 14 Herbert, D. E.; Lionetti, D.; Rittle, J.; Agapie, T. *J. Am. Chem. Soc.* **2013**, *135*, 19075.
- 15 Perrin, D. D. *Ionisation Constants of Inorganic Acids and Bases in Aqueous Solution*; Pergamon Press: New York, 1982.
- 16 (a) Tsui, E. Y.; Agapie, T. *Proc. Natl. Acad. Sci. U.S.A.* **2013**, *110*, 10084. (b) Lin, P.-H.; Takase, M. K.; Agapie, T. *Inorg. Chem.*, *Manuscript submitted*.
- 17 (a) Malyovanyi, S. M.; Andriiko, A. A.; Monko, A. P. *J. Solid State Electrochem.* **2003**, *8*, 7. (b) Caballero, A.; Cruz, M.; Hernan, L.; Melero, M.; Morales, J.; Castellon, E. R. *J. Electrochem. Soc.* **2005**, *152*, A552. (c) Arora, P.; Popov, B. N.; White, R. E. *J. Electrochem. Soc.* **1998**, *145*, 807.
- 18 (a) Kamienska-Piotrowicz, E.; Stangret, J.; Szymanska-Cybulska, J. *Spectrochim. Acta. A* **2007**, *66*, 1. (b) Bell, F. A.; Ledwith, A.; Sherring, D. C. *J. Chem. Soc. C-Org.* **1969**, 2719. (c) Tsui, E. Y.; Day, M. W.; Agapie, T. *Angew. Chem. Int. Ed.* **2011**, *50*, 1668. (d) Tsui, E. Y.; Kanady, J. S.; Day, M. W.; Agapie, T. *Chem. Commun.* **2011**, *47*, 4189.
- 19 Adams, P. D.; Afonine, P. V.; Bunkoczi, G.; Chen, V. B.; Davis, I. W.; Echols, N.; Headd, J. J.; Hung, L. W.; Kapral, G. J.; Grosse-Kunstleve, R. W.; McCoy, A. J.;

- Moriarty, N. W.; Oeffner, R.; Read, R. J.; Richardson, D. C.; Richardson, J. S.; Terwilliger, T. C.; Zwart, P. H. *Acta Crystallogr. D* **2010**, *66*, 213.
- 20 Hazes, B. *Unpublished results*.
- 21 Ten Eyck, L. F. *Acta Crystallogr.* **1973**, *A29*, 183.
- 22 (a) Ravel, B.; Newville, M. *Synchrotron Radiation* **2005**, *12*, 537. (b) Newville, M. *Synchrotron Radiation* **2001**, *8*, 322.
- 23 APEX2, Version 2 User Manual, M86-E01078, Bruker Analytical X-ray Systems, Madison, WI, June 2006.
- 24 Sheldrick, G. M.; 2008/1 ed.; University of Göttingen, Germany: 2008.
- 25 Spek, A. L. “PLATON – A Multipurpose Crystallographic Tool, Utrecht University”, Utrecht, the Netherlands, 2006.

CHAPTER 5

MOLECULAR MIXED-METAL MANGANESE OXIDO CUBANES AS PRECURSORS TO HETEROGENEOUS OXYGEN EVOLUTION CATALYSTS

ABSTRACT

Well-defined mixed-metal $[\text{CoMn}_3\text{O}_4]$ and $[\text{NiMn}_3\text{O}_4]$ cubane complexes were synthesized and used as precursors for heterogeneous oxygen evolution reaction (OER) electrocatalysts. The discrete clusters were dropcasted onto glassy carbon (GC) and indium-tin oxide (ITO) electrodes, and the OER activities of the resulting films were evaluated. The catalytic surfaces were analysed by various techniques to gain insight into the structure-function relationships of the electrocatalysts' heterometallic composition. Depending on preparation conditions, the Co-Mn-oxide was found to change metal composition during catalysis, while the Ni-Mn-oxide maintained the NiMn_3 ratio. These studies demonstrate the use of discrete heterometallic-oxide clusters as precursors for heterogeneous water oxidation catalysts of novel composition and the distinct behaviour of two sets of ternary oxides.

INTRODUCTION

Metal oxides have been extensively studied over the last decade as electrocatalysts for the oxidation of water to O₂ in the oxygen evolution reaction (OER, Eq. 1).¹ Typically, metal oxide films are obtained through anodic electrodeposition or adsorption/deposition of certain metals onto the electrode surface (Fe, Co, Ni, Ir, Ru, Mn).²



The detailed mechanism for the formation of the O–O bond is still under debate although several mechanistic pathways have been proposed.^{1a,3} A general mechanism for the OER on metal oxides involves water coordination to the surface active site followed by a proton transfer to the solvent and an electron transfer to the electrode to form a surface M–OH species. Subsequently, a metal-oxo species is generated via proton-coupled oxidation or disproportionation of two M–OH species to lose H₂O. The metal-oxo species is envisioned to react bimolecularly or to be attacked by water or hydroxide to generate O₂. Despite the lack of full mechanistic insight into this transformation, all proposals suggest the importance of the M–OH intermediates, and subsequently, the M–O bond in the OER electrocatalytic activity. Bockris has demonstrated that the OER activity linearly correlates to the standard enthalpy of formation of the corresponding M(OH)₃ for late first-row transition metal perovskites.⁴ Tseung and co-worker also proposed that O₂ evolution follows a metal oxide redox transitions where they demonstrated the linear correlation between the minimum potential required for OER and their lower oxide/higher oxide redox potentials.⁵ On the other hand, the “volcano plot” proposed by Trasatti relates the OER activity to the M–O bond strength by

correlating the overpotential of certain metal oxides at a fixed current density to the enthalpy of a lower-to-higher oxide transition.⁶ With these mechanistic proposals for homometallic oxides, mixed-metal oxides with weaker M–O bonds are expected to display enhanced OER activities.

The OER activity of mixed metal oxides, especially in spinels, has been examined to determine the heterometallic effect relative to each homometallic oxides.^{4,7} The enhanced activity has been proposed to be correlated to the changes in the enthalpy of the metal-oxide oxidation state transition⁸ and work function upon metal atom substitution.^{7a} Some of the mixed metal oxides that have shown enhanced OER activity are Ni–Fe,⁹ Ni–Co,¹⁰ Ni–Cu,¹¹ Co–Mo,¹² Fe–Mo,¹³ Cu–Co,¹⁴ and Co–Cr–Fe.¹⁵

The preparation of mixed metal oxide material with controlled metal-to-metal stoichiometry has been more challenging as binary metal oxide films typically have bulk- and surface-metal compositions that differ from the stoichiometry of the precursor solutions.^{9c,16} Recently, Berlinguette et al. have introduced a photochemical metal-organic deposition method as a facile technique for preparing amorphous phases of mixed metal oxides with controlled stoichiometry and high OER electrocatalytic activity.¹⁷ While many metal-oxides have been reported for OER, composition-function relationships of heterometallic oxides have been less-extensively studied.^{7a,9c,16a,18}

Herein, we employ discrete synthetic cluster precursors for the synthesis of ternary metal oxides active for electrolytic water oxidation. The effect of the preparation method and type of precursor on the composition and electrocatalytic performance of the heterogeneous oxide is evaluated. Maintaining of the ratio of two metals during electrolysis is dependent on the nature of the components.

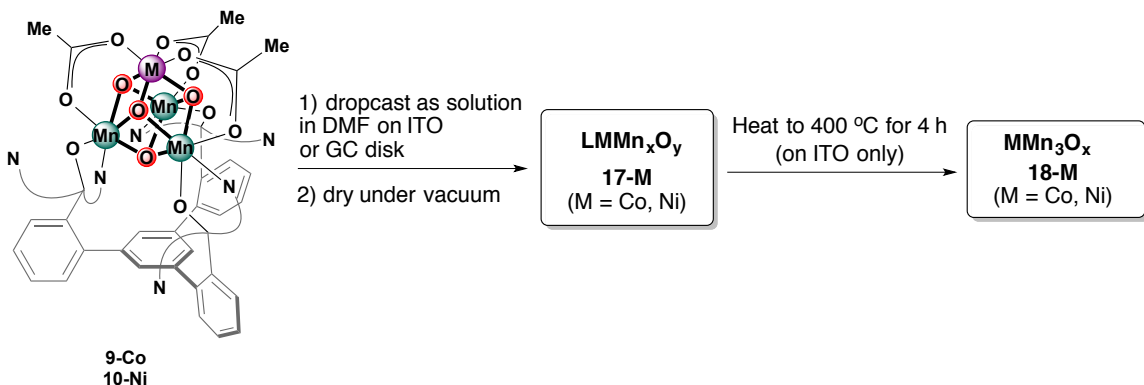
The syntheses of redox-active heterometallic manganese oxido cubane clusters $[\text{MMn}_3\text{O}_4]$ (**9-M** and **10-M**; $\text{M} = \text{Fe}^{3+}, \text{Co}^{3+}, \text{Ni}^{2+}, \text{Cu}^{2+}$) were reported in the last chapter, and they are structurally analogous to the previously investigated complexes (where $\text{M} = \text{Ca}^{2+}, \text{Sr}^{2+}, \text{Zn}^{2+}, \text{Y}^{3+}, \text{Sc}^{3+}, \text{Mn}^{3+}$).¹⁹ These clusters can serve as precursors to make binary metal oxide materials to potentially control the M:Mn ratio of 1:3. This study provides examples of the observed structural changes of the metal composites after electrolysis vs. the initial precursor complexes, stressing the importance of extensive characterization pre- and post-electrolysis for heterogeneous materials.

RESULTS AND DISCUSSIONS

The syntheses of redox-active heterometallic manganese oxido cubane clusters $[\text{MMn}_3\text{O}_4]$ (**9-M** and **10-M**; $\text{M} = \text{Fe}^{3+}, \text{Co}^{3+}, \text{Ni}^{2+}, \text{Cu}^{2+}$) were reported in the last chapter. These are structurally analogous to the previously investigated complexes (where $\text{M} = \text{Ca}^{2+}, \text{Sr}^{2+}, \text{Zn}^{2+}, \text{Y}^{3+}, \text{Sc}^{3+}, \text{Mn}^{3+}$).¹⁹ These clusters serve as precursors to ternary metal oxides of controlled M:Mn ratio of 1:3. The catalytically active metal oxide films were prepared by dropcasting a solution of **9-Co** and **10-Ni** in dimethylformamide (DMF) onto the surface of indium tin oxide (ITO) on glass substrates or glassy carbon (GC) disk electrodes (Scheme 1). The solvent was removed *in vacuo* to yield a thick layer of film, **17-M**, that was subsequently used as a precursor to the catalyst (Scheme 1). During electrolysis in basic media (pH 13 or 14) and release of gas, the top layer of the dropcasted film **17-M** was observed to fall into solution, producing the catalytically active thin layer ($< 200 \mu\text{m}$) on the electrode. Another protocol used to prepare a different material, **18-M**, involves heating the dried film **17-M** on ITO at 400°C for 4 h to thermally remove the organic ligands (L and acetates) from the metal-oxido core

(Scheme 1), as investigated by thermogravimetric analysis (Figure 8). The samples will be referred to as **17-M** for the dropcasted only samples and **18-M** (M = Co, Ni) for the dropcasted and thermally treated samples.

Scheme 1. Synthetic route for the preparation of LMMn_xO_y (**17-M**) and MMn_3O_x (**18-M**). Heating of **17-M** at 400 °C yields **18-M** where all the organic ligand was calcined.



The electrochemical behaviors of **17-M** and **18-M** were studied in basic aqueous media, and the steady-state current densities (j) as a function of the overpotential (η) were recorded to probe the kinetics of the reaction. Cyclic voltammetry (CV), rotating disk voltammetry (RDV), chronopotentiometry (CP), and chronoamperometry (CA) studies were performed to investigate the activity of the resulting surface material before and after 2 h electrolysis ($t_{\text{CP}} = 0$ and 2 h) by evaluating the overpotential required to achieve current densities of 10 mA cm^{-2} ($\eta_{j=10 \text{ mA cm}^{-2}}$) as the metric relevant for solar fuel synthesis^{7a} and 1 mA cm^{-2} ($\eta_{j=1 \text{ mA cm}^{-2}}$). Figure 1a-c represents the cyclic voltammetry and stability studies on **17-Co** and **17-Ni** in 1 M KOH under RDV conditions. Figure 2a-b represents the cyclic voltammetry studies of **18-Co** and **18-Ni** in 0.1 M KOH under non-RDV conditions. The current density of each catalyst on ITO was measured as a function of the overpotential (Tafel plot) in 0.1 M KOH (Figure 1d). The corresponding Tafel slopes, $\eta_{j=1 \text{ mA cm}^{-2}}$, and $\eta_{j=10 \text{ mA cm}^{-2}}$ values are listed in Table 1. It

is worthy to note that **9-Mn** and **9-Fe** were dropcasted on ITO electrodes to make **17-Mn** and **17-Fe**, but these materials did not display any catalytic OER activity. In this chapter, we will focus on **17-Co**, **17-Ni**, **18-Co**, and **18-Ni**.

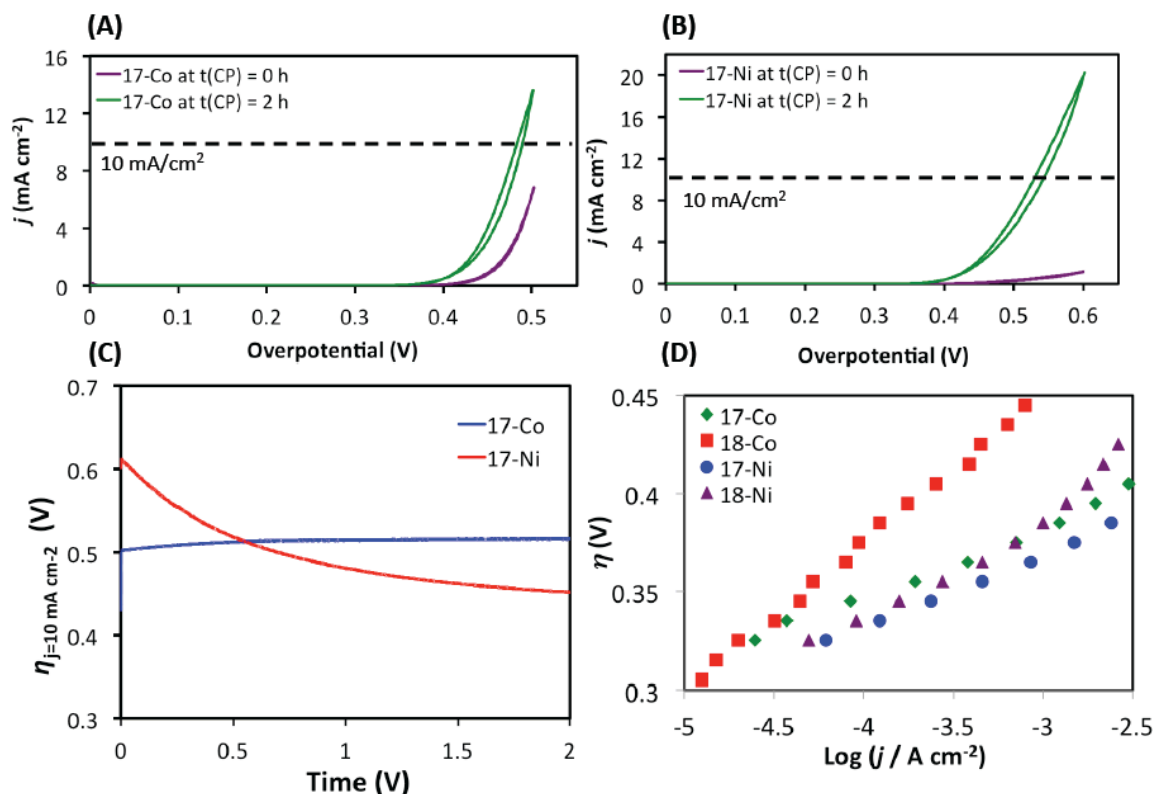


Figure 1. CV of **17-Co** (A) and **17-Ni** (B) layers on glassy carbon disks before and after 2 h CP in 1 M NaOH solution; (C) stability test of **17-Co** and **17-Ni** over 2 h of CP held at 10 mA cm⁻²; (D) Tafel plots of the metal oxides on ITO: **17-Co** (green diamond), **18-Co** (red squares), **17-Ni** (blue circles), and **18-Ni** (purple triangles). Electrochemical studies displayed in (a-c) were performed using rotating disk voltammetry (RDV).

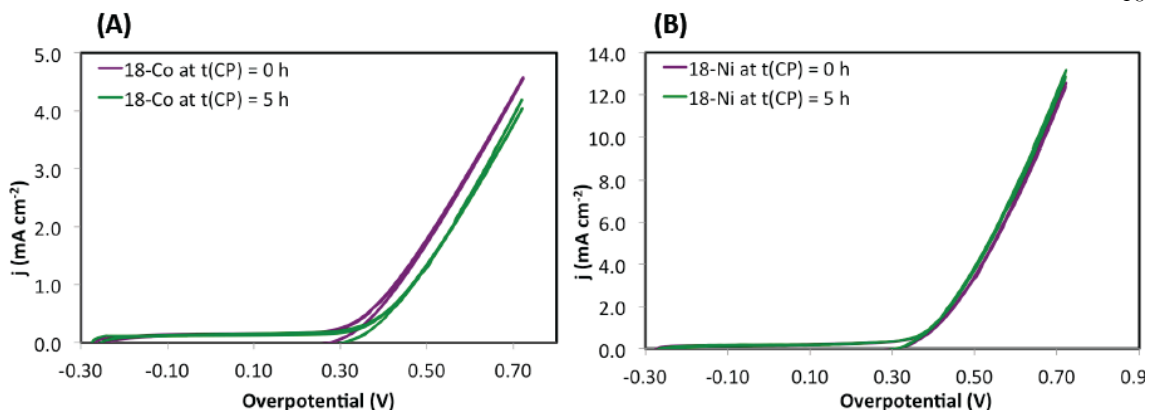


Figure 2. CV of (a) **18-Co** and (b) **18-Ni** before and after 5 h CP in 0.1 M KOH solution. CV studies were performed using the Solartron potentiostat.

Table 1. Tafel slopes and overpotential parameters for **17-Co**, **17-Ni**, **18-Co**, and **18-Ni**

Catalyst	Tafel slope (mV dec ⁻¹) ^a	$\eta_{j=1 \text{ mA cm}^{-2}}$ (V) ^a	$\eta_{j=10 \text{ mA cm}^{-2}}$ (V) ^b
17-Co	42 ± 5	0.39 ± 0.02	0.47 ± 0.01
18-Co	69 ± 9	0.43 ± 0.2	–
17-Ni	40 ± 4	0.37 ± 0.01	0.42 ± 0.01
18-Ni	58 ± 1	0.36 ± 0.01	–

^aTafel slope and $\eta_{j=1 \text{ mA cm}^{-2}}$ parameters are derived from CP experiments on materials **17-Co/Ni** and **18-Co/Ni** dropcasted on ITO coated glass. Electrochemical experiments were performed in 0.1 M KOH (pH 13)

^b**17-Co** and **17-Ni** were dropcasted on GC disk for various electrochemical experiments using a rotating disk voltammetry (RDV) according to a reported procedure⁹ⁱ

The elemental compositions of the **17-M** and **18-M** were determined by X-ray photoelectron spectroscopy (XPS), energy dispersive X-ray spectroscopy (EDS), and inductively coupled plasma mass spectrometry (ICP–MS). The results from the three techniques are summarized in Table 2. Prior to electrolysis, the dropcasted films **17-Co** and **17-Ni** are expected to have the same M to Mn ratio of ~1:3 as **9-Co** and **10-Ni**, in agreement with the observed data by XPS and EDS (only XPS data are shown in Table 1 for this series). The elemental composition analyses of the resulting metal oxide films

after electrolysis (1-5 h of CP) show retention of the $\sim 1 : 3$ M to Mn ratio for all **17-Ni**, **18-Co**, and **18-Ni**, but resulted in lower average Co:Mn ratio of 1 to 1.2 for **17-Co** (Table 2). Both **17-Co** and **17-Ni** films after electrolysis and **18-Co** and **18-Ni** films do not display any N 1s peak by XPS, indicating the loss of ligand L upon electrolysis/heat treatment respectively. This is supported by the thermogravimetric analysis of **1-Co** (Figure 8 in experimental section) where the loss of $\sim 77\%$ mass was observed upon heating at 400 °C for 4 h, consistent with calculated mass loss of all ligands (acetates and L) at $\sim 78\%$. ICP-MS studies were performed only on the resulting materials after electrolysis of **17-M** on the GC disks to avoid signal saturation by ITO.

Table 2. Normalized relative metal stoichiometry of catalyst films by XPS, EDS, and ICP-MS

Catalyst	XPS						EDS			ICP-MS		
	<i>Before electrolysis</i>			<i>After electrolysis</i>			<i>After electrolysis</i>					
	Co	Ni	Mn	Co	Ni	Mn	Co	Ni	Mn	Co	Ni	Mn
17-Co	1	-	3.4 ± 0.2	1	-	1.2 ± 0.3	1	-	1.3 ± 0.7	1	-	1.1 ± 0.2
18-Co	1	-	3.9 ± 0.4	1	-	3.9 ± 1.0	1	-	3.1 ± 0.4			
17-Ni	-	1	2.8 ± 0.1	-	1	3.4 ± 0.3	-	1	2.9 ± 0.8	-	1	2.1 ± 0.3
18-Ni	-	1	3.4 ± 0.2	-	1	3.6 ± 1.1	-	1	2.8 ± 0.3			

^aICP-MS analyses were only performed on **17-Co** and **17-Ni** after electrolysis on GC disks to prevent signal saturation from ITO

Scanning electron microscopy (SEM) was used to characterize the surface morphologies for all metal oxide films **17-M** and **18-M** (Figure 3). The initial surface of the dropcasted material (in this case **9-Co**) is shown in Figure 3a as a thick amorphous layer on the ITO electrode. Upon water electrolysis (CP at 5 mA cm^{-2}) with this material for 5 h, the resulting film consists of a very thin electroactive metal oxide layer represented by Figure 3c. Figures 3b, d show the resulting thermally treated electroactive layer of **18-Co** and **18-Ni**, respectively, before and after electrolysis, where

no obvious change on the surface morphology was observed. Figures 3e, f display the crystalline-looking final thin layer film of **17-Ni** after electrolysis from the top view and the cross-section respectively. In addition to SEM, elemental mapping of the surfaces was also performed. The elemental maps of **18-Ni** and **17-Co** on ITO electrode are displayed in Figure 4. The elemental map reveals the uniformly scattered presence of Ni and Mn in the heterogeneous material. This observation is in contrast to the Co-containing materials where Co was detected throughout the surface while the presence of Mn was more localized on the “island” (Figure 4).

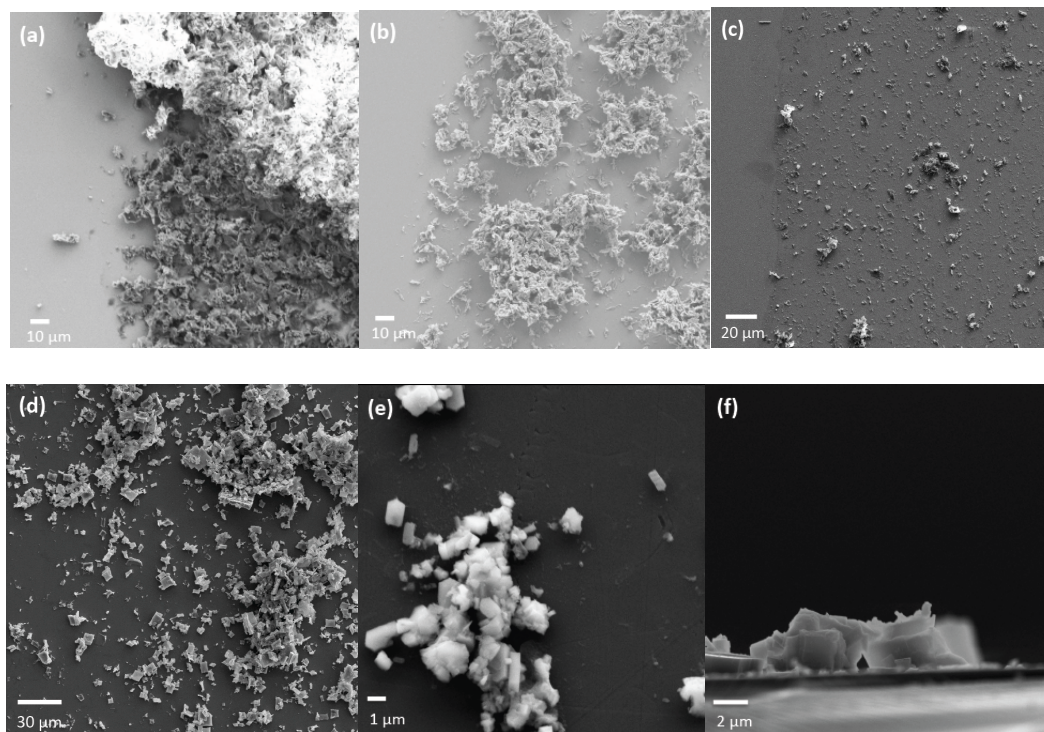


Figure 3. SEM images of ITO electrode surfaces with: (a) **9-Co** initially dropcasted pre-electrolysis; (b) **18-Co** pre- and post-electrolysis; (c) **17-Co** post-electrolysis; (d) **18-Ni** pre- and post-electrolysis; (e) **17-Ni** post-electrolysis; (f) cross section side-view of electrode with **17-Ni** post-electrolysis.

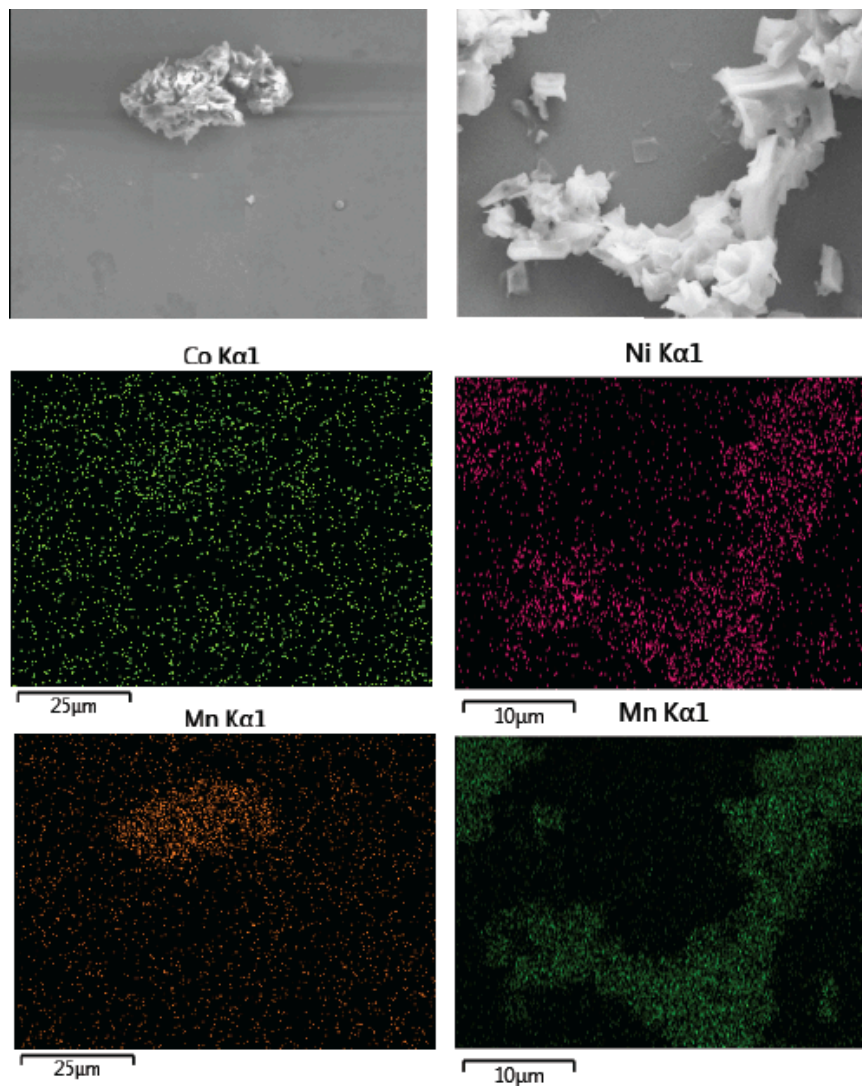


Figure 4. SEM images and elemental mappings of **17-Co** (left) and **18-Ni** (right) on ITO after 5 h CP, displaying the SEM image with the corresponding Mn and Co/Ni K α 1 compositional maps.

Powder X-ray diffraction studies of these surfaces show no other patterns from those resulting from the background ITO electrode (Figure 5), which is indicative that they are either amorphous or possibly too thin with $\sim 2 \mu\text{m}$ thickness (Figure 3f) for detection.

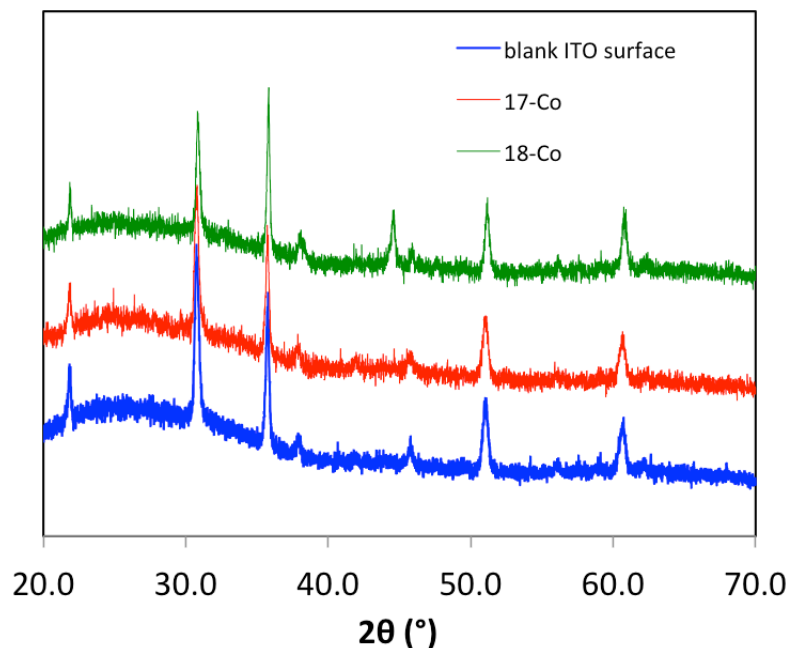


Figure 5. Representative powder X-ray diffraction patterns for ITO, **17-Co**, and **18-Co**.

CV and CP studies of **17-Co** show relatively similar activity at $t_{CP} = 0$ h vs. 2 h (Figure 1a, c). On the other hand, the electrochemical studies on **17-Ni** film indicated that the initial film has low electrocatalytic activity for OER, but possibly structurally rearranged upon electrolysis to generate a more active material with improved overpotential to produce 10 mA cm^{-2} current density (Figure 1b, c). The **18-Co** and **18-Ni** films display similar electrocatalytic activity throughout electrolysis period (Figure 2). The observed overpotentials ($0.36 - 0.43 \text{ V}$) to reach 1 mA cm^{-2} current density for **17** and **18** (Figure 1d, Table 1) as a measure of electrocatalytic activity are comparable to a number of other homo- and heterometallic oxide electrocatalysts (Table 3).^{2a-c,2f,9h,9i}

In addition, RDV studies of **17-Co** and **17-Ni** on GC electrodes in the same solution resulted in $\eta_{j=10 \text{ mA cm}^{-2}}$ values that are similar to other reported metal oxide films.⁹ⁱ These results indicate that the synthetic cubane complexes **9-Co** and **10-Ni** can serve as precursors to generate OER electrocatalysts with applied oxidative potentials.

The amount of O₂ produced by each material throughout 2-h constant current electrolyses at 1 mA cm⁻² was quantified using a fluorescent oxygen sensor and suggests nearly 100% Faradaic efficiency for the electrocatalytic process (Figure 6).

Table 3. Comparison of **17-Co** and **17-Ni** (boxed in blue) before and after 2 h CP to selected electrodeposited metal oxide OER electrocatalysts⁹ⁱ

Entry	Catalyst	ECSA/cm ²	$\eta_{t=2h}/V$	ϵ
1	CoO _x -(a)	1.9 ± 0.6	0.42 ± 0.04	0.94 ± 0.08
2	CoO _x -(b) (“CoPi”)	5.1 ± 1.7	0.44 ± 0.02	1.00 ± 0.10
3	IrO _x	21 ± 10	1.05 ± 0.20	0.92 ± 0.07
4	NiO _x	1.8 ± 0.5	0.41 ± 0.05	0.93 ± 0.08
5	NiCoO _x	5.2 ± 2.1	0.35 ± 0.01	0.92 ± 0.08
6	NiFeO _x	1.1 ± 0.5	0.38 ± 0.02	1.00 ± 0.04
7	GC background	1.9 ± 0.9	1.29 ± 0.02	0.76 ± 0.07
8	17-Co	2.0 ± 0.5	0.47 ± 0.01	0.97 ± 0.04
9	17-Ni	1.8 ± 0.5	0.42 ± 0.01	1.00 ± 0.05

ECSA = electrochemically active surface area ($C_{\text{DoubleLayer}}/C_{\text{Specific}}$); $\eta_{t=2h}$ = overpotential at t = 2 h, ϵ = Faradaic efficiency

The results from the electrochemical studies warrant further investigation on the final metal compositions of these electrocatalysts. In Table 2, **17-Co** was observed to undergo the largest variation in M to Mn stoichiometry before vs. after 1-5 h electrolysis. While the reported value in Table 2 is an average of all analyzed spots on the non-uniform electrode surface, there were multiple areas on the electrode evaluated by XPS and EDS that display Co : Mn ratio of 1 to ~0.1; the Co 2p_{3/2} peak was primarily the only metal signal observed in the spectrum. This result suggests that most of the Mn centers dissolved in the solution during electrocatalytic oxidation of hydroxide ions probably by reduction to labile Mn^{II} ions during O₂ generation. Upon

prolonged electrolysis of **17-Co**, XPS and EDS data suggest that the potentially produced Co^{II} ions were electrodeposited back onto the electrode,^{9c,20} in contrast to Mn^{II} , to generate predominantly the homometallic cobalt oxide (CoO_x) film that further carries out the catalytic transformation.

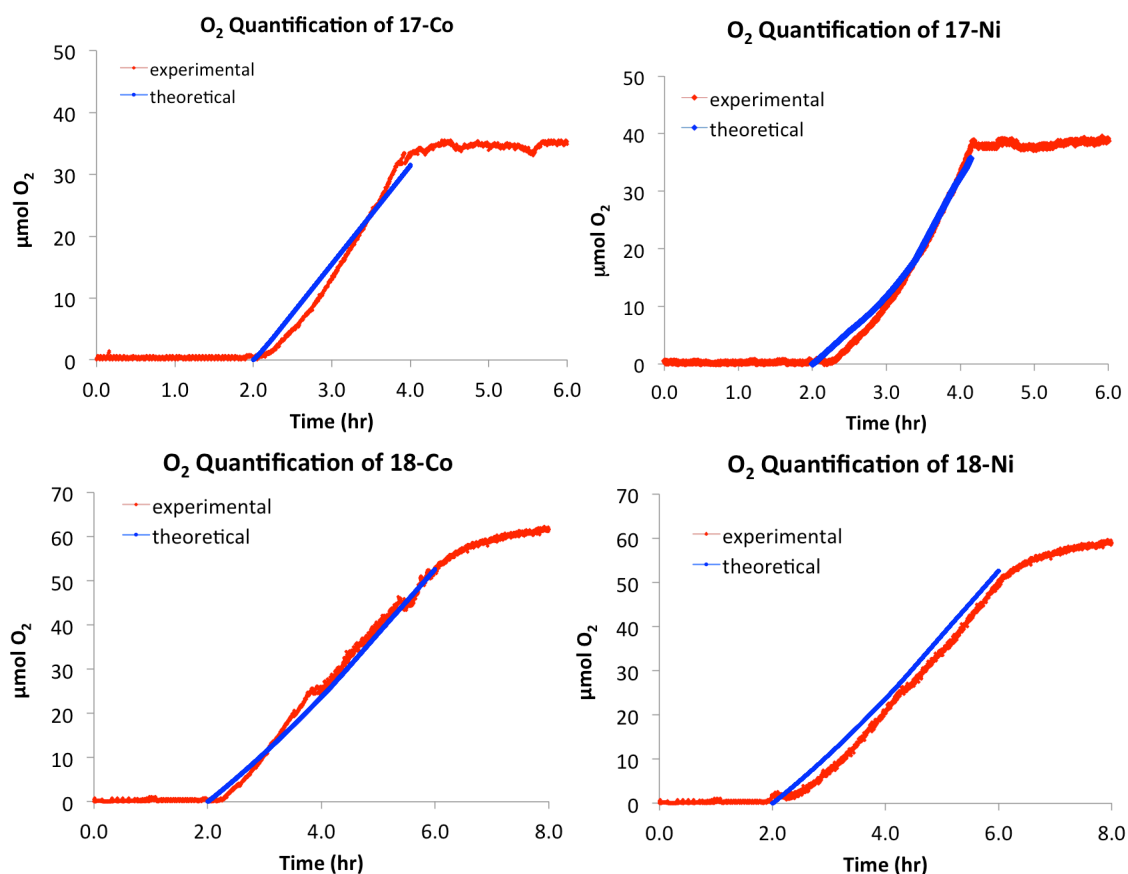


Figure 6. Results of the oxygen sensing experiments. Amount of oxygen detected by the fluorescence sensor is indicated by the red line while the theoretical yield at 100% Faradaic efficiency is depicted with the blue line.

The elemental analyses data for **17-Ni**, **18-Co**, and **18-Ni** display retention of the metal stoichiometry even after prolonged electrolysis periods, providing evidence that the cluster cores may have stayed intact in those films. Additionally, elemental mapping of the surfaces of **17-Ni**, **18-Co**, and **18-Ni** (Figure 4 and Figure 20 in experimental)

after electrolysis show no apparent phase separation of M and Mn, suggesting the retention of both metals in the electrocatalysts. On the other hand, the elemental map of **17-Co** *after* electrolysis shows variable distribution of Co and Mn on the larger island piece vs. the rest of the surface (Figure 4), consistent with the non-uniform electrodeposition of Co back onto the electrode throughout electrolysis. Further studies are still required to determine whether structural rearrangements may have occurred or the thermodynamic electrodeposition of the dissociated M^{II} salts back onto the electrode favors similar 1:3 M to Mn metal stoichiometry.

Based on the elemental composition studies, **9-Co** and **10-Ni** can indeed serve as useful precursors to catalytically active materials for OER with control over M:Mn ratio for **17-Ni**, **18-Co**, and **18-Ni**. This demonstration suggests that the structure and composition of mixed-metal catalysts can be tuned by the selection of heterometallic molecular precursors. The variation in composition of **17-Co** highlights the importance of thoroughly evaluating the compositions of metal oxide materials pre- and post-catalysis, especially for those heterometallic oxides that were not prepared via electrodeposition method.

The Ni-Mn OER catalysts maintain the metal ratio despite being prepared under different conditions. However, the variation in catalytic properties of **17-Ni** suggests that structural changes may occur during catalysis. X-ray absorption spectroscopic (XAS) studies, in particular near-edge structure (XANES) and extended X-ray absorption fine-structure (EXAFS), were performed for **17-Ni** and **18-Ni** at $t_{CP} = 0, 1,$ and 5 h to determine whether the metal oxides underwent structural changes/rearrangements during electrocatalysis (Figure 7).

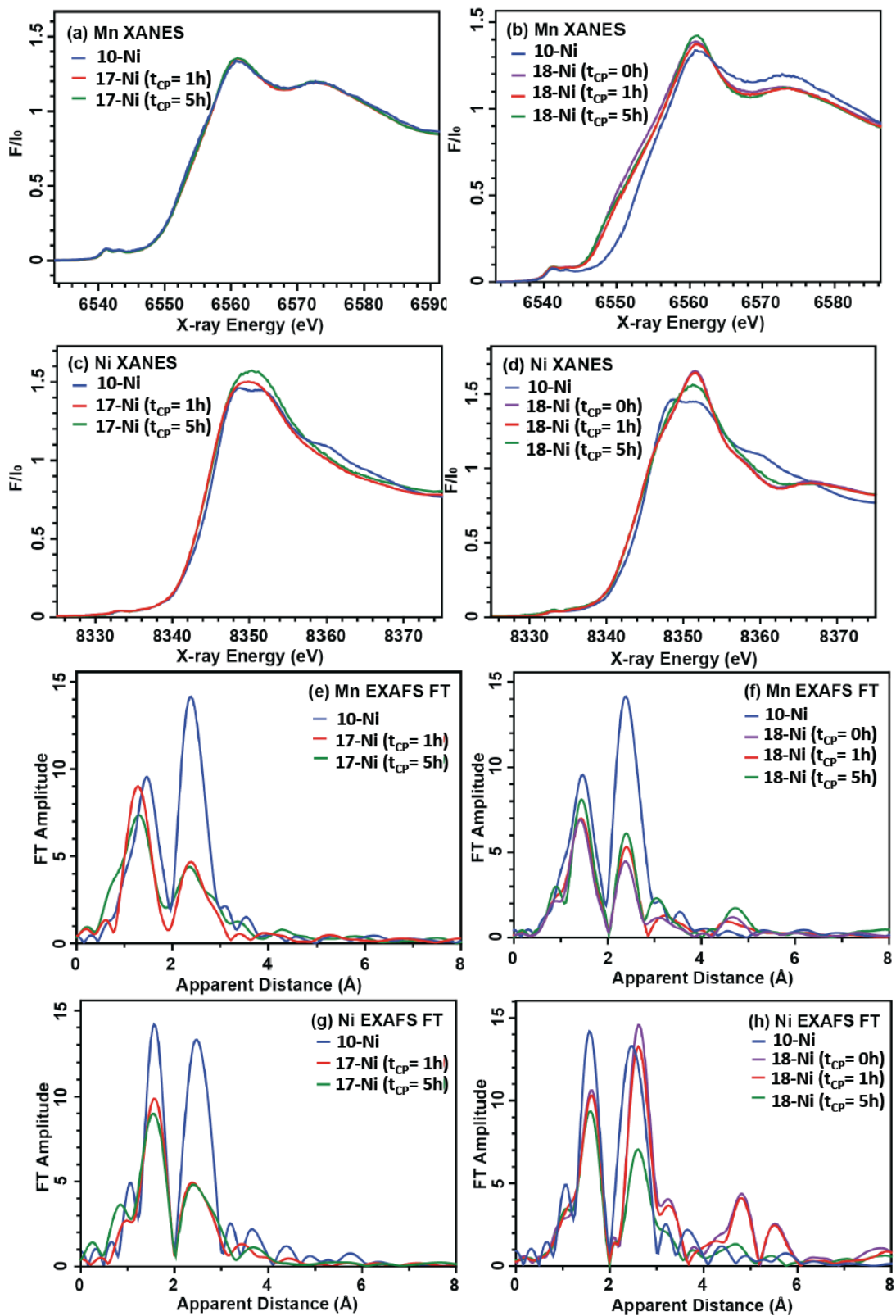


Figure 7. Preliminary XAS data for 17-Ni and 18-Ni vs. 10-Ni at $t_{CP} = 0, 1, 5$ h.

All XAS data are preliminary and still require final fitting and analysis. The Mn XANES of **17-Ni** look more similar to that of **10-Ni** (Figure 7a), suggesting the retention of the cubane moiety during electrolysis. On the other hand, the Mn XANES data collected on all the **18-Ni** films at different t_{CP} are different from the dropcasted complex **10-Ni**, potentially from the heat treatment (Figure 7b). The Mn XANES spectra of **18-Ni** more resemble the spectra of birnessites (Mn oxides) by displaying generally broad, featureless pre-edge shapes.^{2d,16a} The Ni XANES and EXAFS of **17-Ni** and **18-Ni** display different edge energies and shapes from **10-Ni** (Figure 7c, d), suggesting the nickel's participation as redox active centers during electrocatalysis by both films. The **18-Ni** film is sensitive to electrolysis progression as observed by the Mn EXAFS spectra at t_{CP} = 0–5 h (Figure 7f), suggesting that the Mn centers may play a role during OER electrocatalysis. The final fitting of the XAS spectra and the direct comparison of the **18-Ni** Mn XANES spectra to the Mn oxide birnessites are still ongoing efforts.

CONCLUSIONS

Well-defined, synthetic **9-Co** and **10-Ni** cubane complexes were dropcasted on ITO or glassy carbon disk electrodes and used as precursors for OER electrocatalysts with known 1:3 M to Mn ratio. Upon heat treatment at 400 °C and/or electrolysis, the OER activities of **17-M** and **18-M** (M = Co, Ni) were evaluated to be similar to many other reported homo- and heterometallic oxide electrocatalysts, although **17-Ni** requires structural rearrangements to yield the desired active species. The **17-Co** film underwent structural changes to a CoO_x-like material upon prolonged electrolysis, losing the majority of Mn into the solution. The **17-Ni** film may have rearranged structurally, as suggested by the Ni XANES, yet still retained its cubane structural moiety by Mn XANES and the Ni : Mn ratio of 1 to 3 in the final material. The distinct behavior of

the heterogeneous OER electrocatalysts described here indicate that the composition and structural changes post-electrolysis of heterometallic catalysts is critical in understanding the behavior of these catalysts. XAS studies provided structural insights that the resulting **17-Ni** film after electrolysis is indeed different from the initial **10-Ni** synthetic precursor. In contrast, the thermally generated **18-Ni** resembles the structure of Mn oxide birnessites according to XAS studies, reminiscent of the Ca-Mn oxides reported by Dau and coworkers that display structural motifs related to the biological Oxygen Evolving Complex in Photosystem II. If this is true, then this structural relation suggests a catalytic function of the MMn_3O_4 cubane moiety found in these systems. The use of molecular heteromultimetallic oxido cubane precursors has been demonstrated as a facile method to access OER electrocatalysts of novel compositions that allows for systematic study of the effect of structure on catalytic activity.

EXPERIMENTAL SECTION

General considerations

Unless otherwise specified, all compounds were manipulated under air. Dichloromethane (DCM) and *N, N*-dimethylformamide (DMF) were purchased from J.T. Baker and EMD Millipore respectively. High purity sodium hydroxide (NaOH) and potassium hydroxide (KOH) were purchased from Sigma Aldrich. All water was used was Milli-Q water purified by a Millipore water purification system (18.2 M Ω cm resistivity). Indium tin oxide (ITO) coated glass slides (with surface resistivity 8-12 Ω /sq) were purchased from Sigma Aldrich. The complex **10-Co** was synthesized according to literature procedure.^{19a} Syntheses of complexes **9-Co** and **10-Ni** are discussed in the previous chapter.

Preparation of 17-Co and 17-Ni

In a scintillation vial, 3 mg of **9-Co** or **10-Ni** was fully dissolved in DCM (0.3 mL). DMF (0.3 mL) was added into the solution. The DCM was allowed to evaporate in air, then the DMF solution of **9-Co** or **10-Ni** was dropcasted using a Hamilton syringe onto 5 separate cleaned ITO coated glass substrate (with a 0.5 cm \times 0.5 cm window or geometric surface area of 0.25 cm²) or glassy carbon disks equally in 60 μ L portions. The dropcasted solution on the electrodes was then dried under vacuum over 1 h to yield a thick film on the ITO. These resulting films, **17-Co** and **17-Ni**, were used as precursors to the catalytically species after electrolysis.

Preparation of 18-Co and 18-Ni

The dried films, **17-Co** and **17-Ni**, on ITO coated glass substrate were then heated at 400 $^{\circ}$ C in the thermolyne muffle furnace for \geq 4 h to remove the organic ligand and generate a non-uniform, thin, black metal oxide film on the ITO. Removal of organic

ligands from **9-Co** was confirmed by thermogravimetric analysis (TGA) (Figure 8), and the analogous event is assumed to occur for **10-Ni**. These resulting films, **18-Co** and **18-Ni**, are used as is for further electrochemical experiments.

Note: preparation of **18-Co/Ni** on the GC disks was not conducted due to the possibility of compromising the GC electrode quality under high heat (400 °C) for a prolonged period of time.

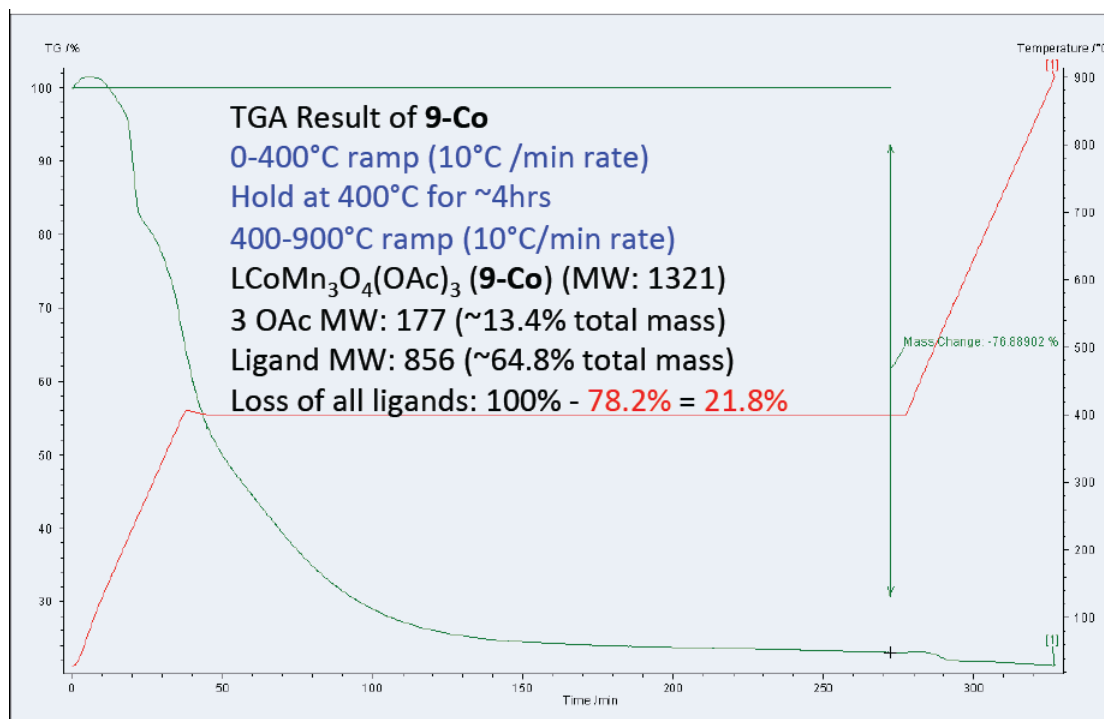


Figure 8. Thermogravimetric analysis of **9-Co**, displaying loss of ~77% mass upon heating at 400 °C for 4 h, consistent with calculated mass loss of all ligands (acetates and L) at ~78%.

Electrochemistry

Electrochemical measurements of **9-Co** and **10-Ni** were conducted with a Solartron 1287/1260 potentiostat/galvanostat with a built-in electrochemical impedance spectroscopy (EIS) analyzer. The working electrode was ITO on glass substrate, and catalysts were deposited as described above. The auxiliary electrode was a Pt mesh electrode, and the reference electrode was a BASi or CH Instruments Ag/AgCl

reference electrode. All potentials reported in this manuscript were converted to RHE reference scale.

Cyclic Voltammetry

Electrocatalyst films with geometric surface area of 0.25 cm² on ITO were used as the working electrode with Pt mesh as the auxiliary electrode and Ag/AgCl reference electrode. A two-compartment cell was used for cyclic voltammetry experiments filled with 0.1 M KOH (pH 13) solution. Cyclic voltammograms were collected at 100 mV/s.

Tafel Plot

Current-potential data were obtained by performing chronoamperometry in 0.1 M KOH electrolyte at a variety of applied potentials in a two-compartment cell. The geometric surface area of the catalyst was 0.25 cm² prepared as mentioned above for **17-M** and **18-M**. Steady-state currents were measured at a variety of applied potentials while the solution was stirred, starting at 1.75 V and proceeding in 10 mV steps to 1.5 V vs. RHE. The current reached a steady state at a certain potential within 1-2 minutes. The measurements were made three times and averaged with the variation in steady-state current <5%.

Oxygen Evolution Faradaic Efficiency Measurements

The experiment was performed in a custom built two-compartment gas-tight electrochemical cell with a 14/20 port on each compartment and a Schlenk connection with a Teflon valve on the working compartment. The cell volume was 154 mL. A NeoFox oxygen sensing system by Ocean Optics with FOXY fluorescence probe was used in O₂ detection. The oxygen concentration was monitored throughout the measurement, and was tabulated via measured values from a fluorescence detector. These values were calibrated using the standard concentration of oxygen in air as 20.9%

partial pressure of O₂ atmosphere. The cell was initially evacuated under vacuum. 54 mL of degassed 0.1 M KOH electrolyte solution was transferred into the cell under positive N₂ pressure, and the headspace used as a 0.0% O₂ atmosphere. The calculated volume of the headspace was 96 mL. An Ag/AgCl electrode was the reference electrode placed in one compartment, while the counter electrode was a Pt mesh positioned in a separate, fritted compartment.

All catalysts used were prepared by subjecting the film through chronopotentiometry experiments for 5 h prior to oxygen evolution measurements. The ITO electrode with the catalyst film was clipped inside the electrochemical cell prior to evacuating the cell under vacuum mentioned above.

To ensure no leakage occurred, the partial pressure of O₂ was measured for 2 h in the absence of an applied potential. The chronopotentiometry experiment was run at a steady current of 1 mA cm⁻² for 2-4 h with stirring of the solution. Upon terminating the electrolysis, the O₂ signal was recorded for an additional 2 h. At the conclusion of the experiment, the volume of the solution and the volume of the headspace in the working compartment were measured again (54 mL and 96 mL, respectively). The blue curves in Figure 6 were calculated by dividing the charge passed in the electrolysis by 4F (theoretical yield) and the red curve was calculated by converting the measured partial pressure of O₂ into μmols, correcting for the O₂ in solution using Henry's Law (experimental yield).

Rotating Disk Voltammetry

All activity, stability, and surface area measurements on the glassy carbon (GC) disk electrodes were conducted with a Bio-Logic VMP3 multichannel potentiostat/galvanostat with a built-in EIS analyzer. The working electrodes were 5

mm diameter disk electrodes, and catalysts were deposited as described above. The working electrodes were mounted in a Pine Instrument Company E6-series ChangeDisk rotating disk electrode assembly in an MSR rotator. The auxiliary electrodes were carbon rods (99.999%, Alfa Aesar), and the reference electrode was a commercial saturated calomel electrode (SCE) (CH-Instruments) that was externally referenced to a solution of ferrocene monocarboxylic acid (Sigma-Aldrich) in a 0.2 M phosphate buffer at pH 7 (0.284 V vs. SCE).²¹ Data were recorded using the Bio-Logic EC-Lab and EC-Lab Express software packages. Electrochemical experiments were carried out according to a previously-described protocol for the evaluation of heterogeneous electrocatalysts for the OER.⁹ⁱ A comparison of the OER performance of **17-Co** and **17-Ni** against selected electrodeposited electrocatalysts under identical conditions (Table 3).

Structural Characterizations

Powder X-Ray Diffraction (XRD)

Powder XRD patterns were obtained with a PANalytical X'Pert Pro rotating anode X-ray diffractometer (185 mm) using Cu K α radiation ($\lambda = 1.5405 \text{ \AA}$). Data was collected at a scan rate of $1^\circ/\text{min}$. A pattern was collected for an ITO-coated glass substrate and for the electrocatalysts prepared (Figure 5). The ITO peaks were observed as the only signals arising from all XRD pattern of the electrocatalysts. Given that the final deposited catalyst sample is $\sim 100 \text{ nm}$ thick, the presence of peaks from the relatively thin ITO layer and the absence of any non-ITO associated peaks indicate that the catalyst material is probably too thin or amorphous.

Scanning Electron Microscopy (SEM)

Scanning-electron micrograph (SEM) was obtained using a high-resolution analytical scanning electron microscope (ZEISS 1550VP) at an accelerating voltage of 10 kV with a working distance of 8 mm and an in-lens secondary electron detector.

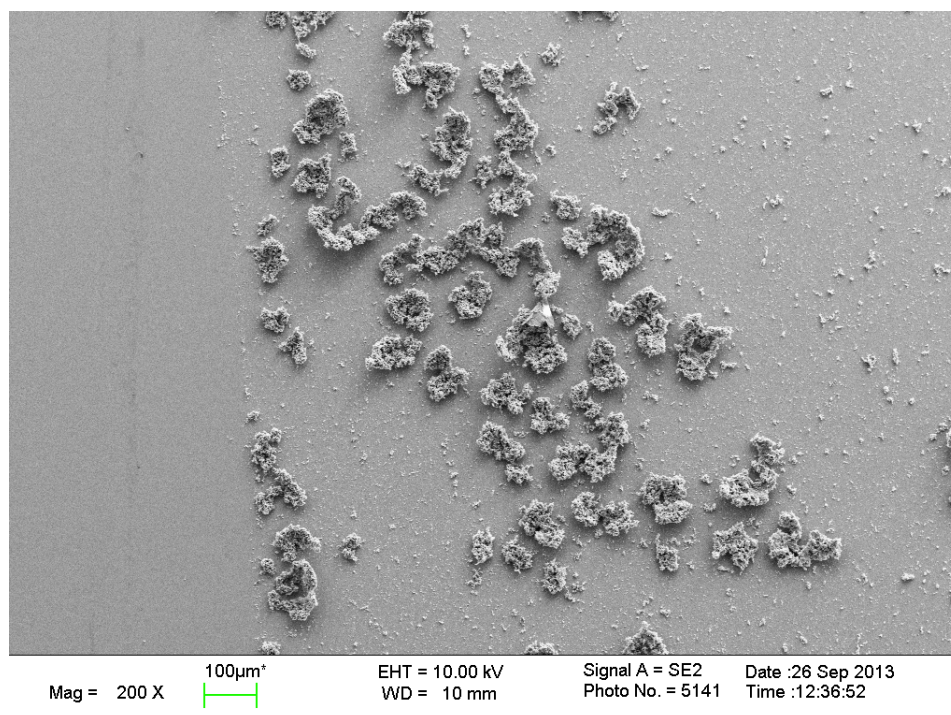


Figure 9. SEM image of **18-Co** before electrolysis at 200 \times low magnification, displaying the non-uniform surface on the ITO.

X-ray Absorption Spectroscopy (XAS) Data Collection

Mn XAS measurements were performed at the Stanford Synchrotron Radiation Laboratory (SSRL) on Beamline 7-3 at an electron energy of 3.0 GeV and an average current of 500 mA. The intensity of the incident X-ray beam was monitored using a N₂-filled ion chamber (I_0) in front of the sample. A Si(220) double-crystal monochromator was used to detune to 50% of the maximum flux to attenuate higher harmonics. The data was collected as fluorescence excitation spectra with a Ge 30-element detector (Canberra). The monochromator energy was calibrated using the pre-

edge peak of KMnO_4 (6543.3 eV). The calibration standard was placed between two N_2 -filled ionization chambers (I_1 and I_2) after the sample. To minimize radiation damage, samples were maintained at a temperature of 10 K in a liquid He flow cryostat. The ITO electrodes containing **17-Ni** and **18-Ni** at $t_{\text{CP}} = 0, 1, 5$ hr after chronopotentiometry were used as prepared.

Data Reduction and Analysis for XANES

Data reduction of the XANES spectra was performed using SamView (SixPACK software, Dr. Samuel M. Webb, SSRL). The pre-edge and post-edge backgrounds were subtracted from the XAS spectra using Athena (IFEFFIT software²²), and the resulting spectra were normalized with respect to the edge height. The background removal in k -space was performed using a cubic spline function. For the energy (eV) to wave vector (k , \AA^{-1}) axis conversion, E_0 was defined as 6561.3 eV. The energy position of the main edge was defined as the inflection point energy (IPE), which was determined from the zero-crossing of the second derivative of the XANES spectrum. The third-order polynomial second derivative function was taken with a 3 eV differentiation interval on each side of a data point. The estimated error in the IPE was ± 0.1 eV for individual samples.

Elemental Composition Analyses

X-ray Photoelectron Spectroscopy (XPS)

X-ray photoelectron spectroscopy (XPS) data were collected using a Surface Science Instruments M-Probe ESCA controlled by Hawk Data Collection software (Service Physics, Bend OR; V7.04.04). The monochromatic X-ray source was the Al K α line at 1486.6 eV, directed at 35° to the sample surface (55° off normal). Emitted photoelectrons were collected at an angle of 35° with respect to the sample surface

(55° off normal) by a hemispherical analyzer. The angle between the electron collection lens and X-ray source is 71°. Low-resolution survey spectra were acquired between binding energies of 1-1100 eV. Higher-resolution detailed scans, with a resolution of ~0.8 eV, were collected on individual XPS lines of interest. The sample chamber was maintained at $< 2 \times 10^{-9}$ Torr. Analysis of the spectra was done using the Hawk Data Analysis software (V7.04.04) and the CasaXPS Version 2.3.15 software package.

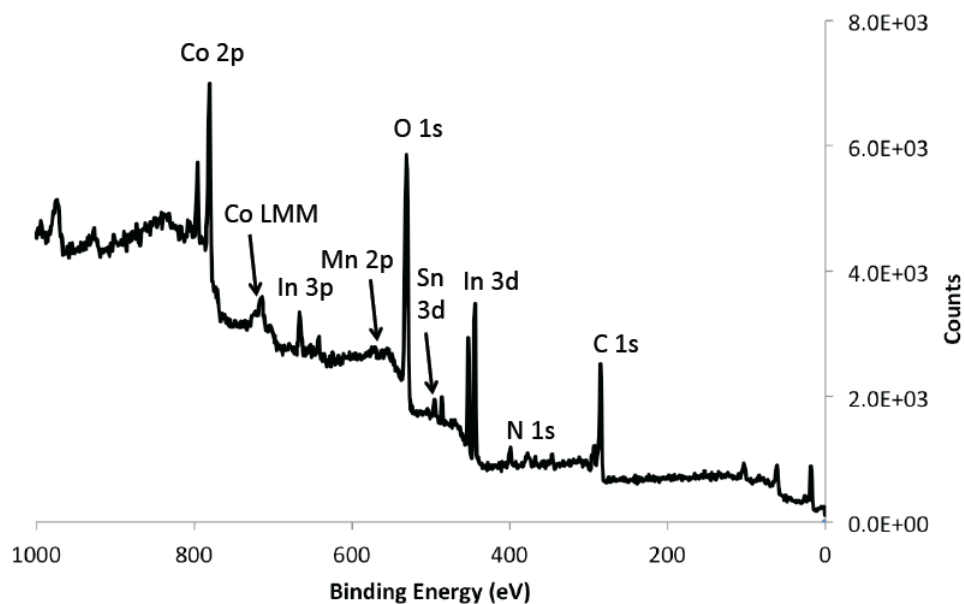


Figure 10. A representative example of a XPS spectrum of **17-Co** on ITO after 5 h electrolysis, displaying 1 : 0.07 Co to Mn ratio.

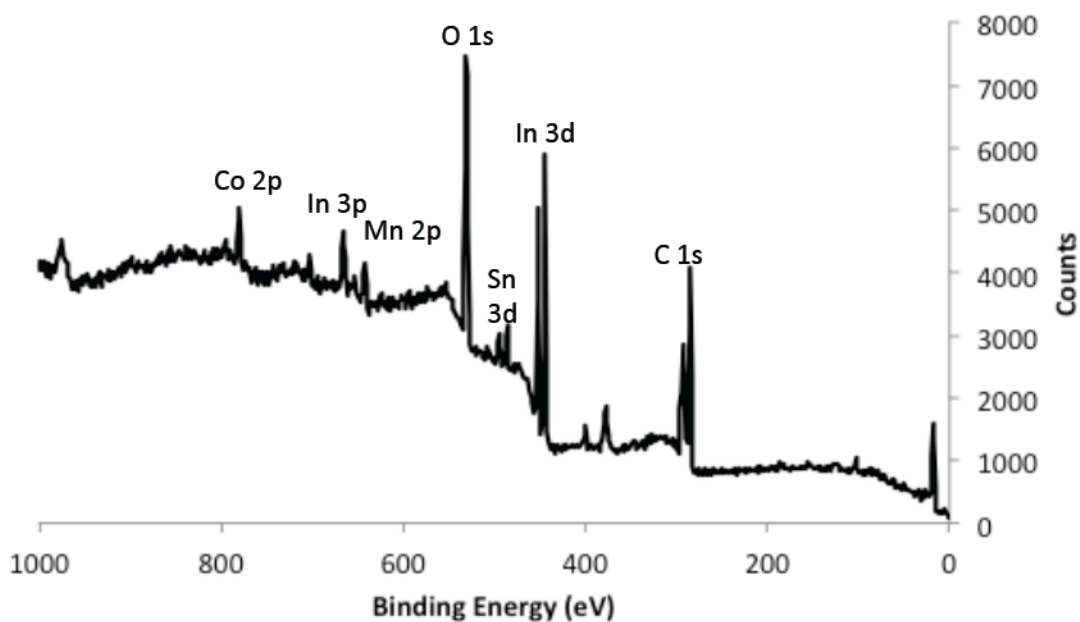


Figure 11. A representative example of a XPS spectrum of **17-Co** on ITO after 5 h electrolysis, displaying 1 : 1.3 Co to Mn ratio.

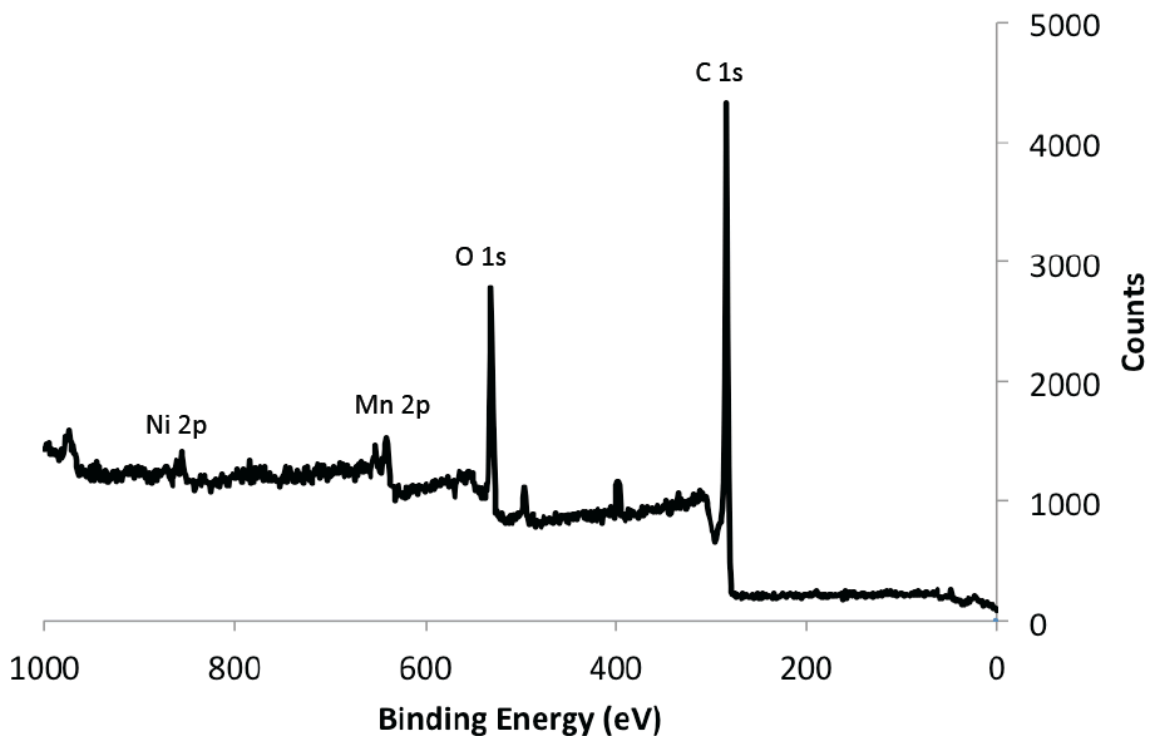


Figure 12. A representative example of a XPS spectrum of **17-Ni** on GC disk after 5 h electrolysis, displaying 1 : 2.0 Ni to Mn ratio.

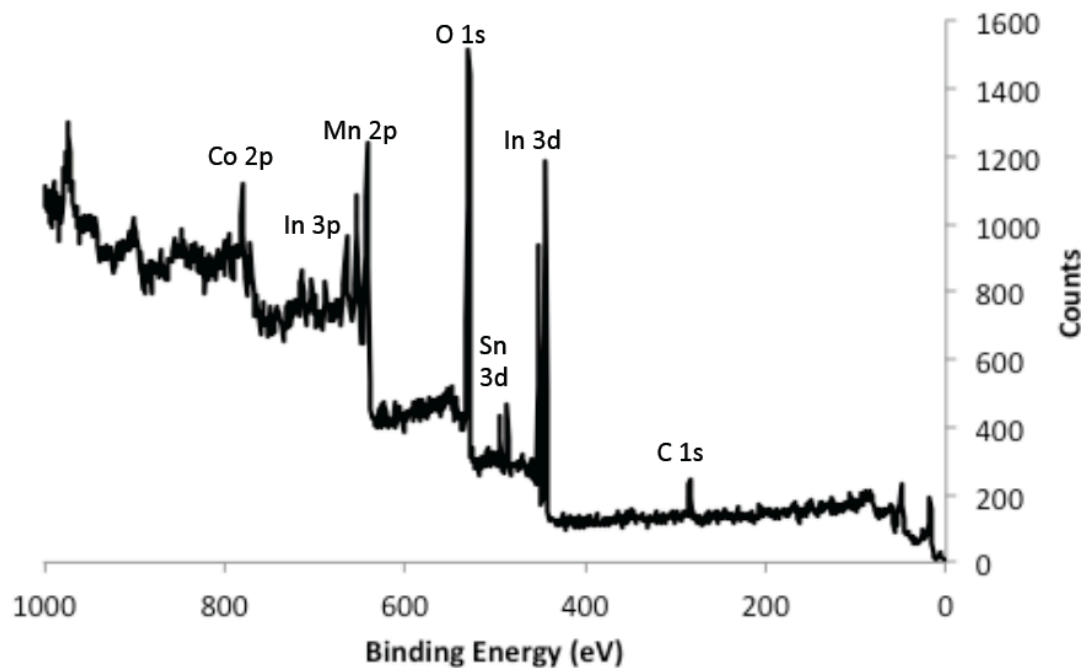


Figure 13. A representative example of a XPS spectrum of **18-Co** on ITO after 5 h electrolysis, displaying 1 : 3.2 Co to Mn ratio.

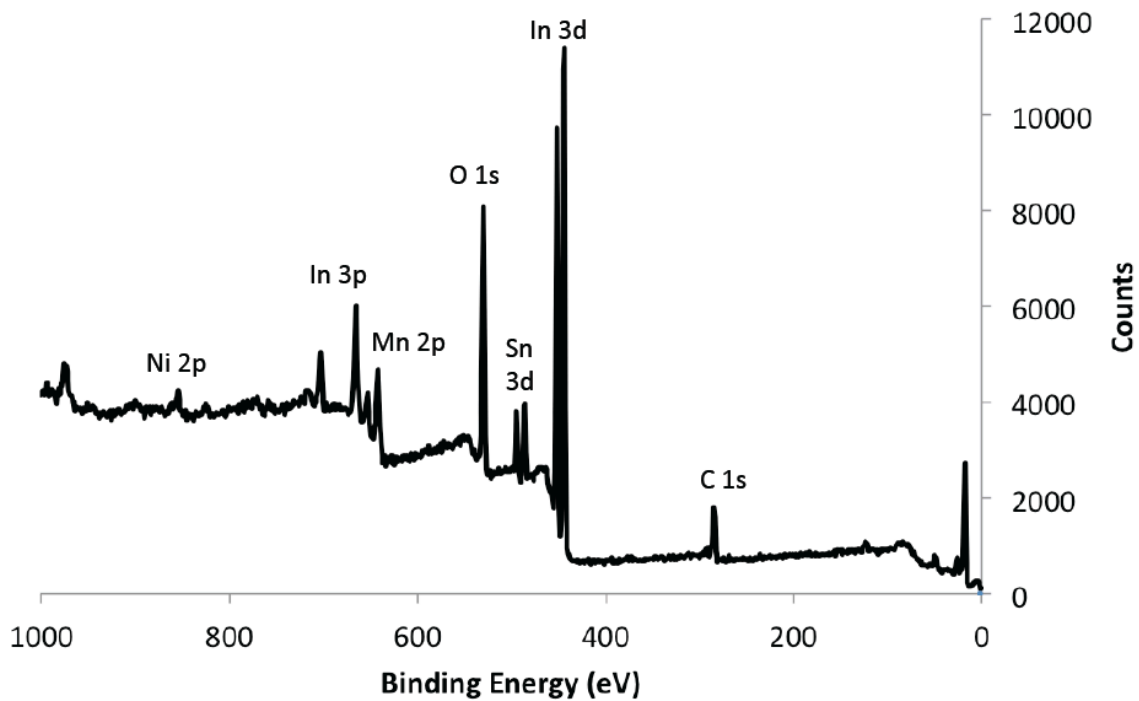


Figure 14. A representative example of a XPS spectrum of **18-Ni** on ITO after 5 h electrolysis, displaying 1 : 3.5 Ni to Mn ratio.

Energy dispersive X-ray spectroscopy (EDS) and elemental mapping

An Oxford X-Max SDD energy-dispersive X-ray spectrometer (EDS) equipped in the SEM instrument was used at a working distance of 12 mm using an accelerating voltage of 20 kV.

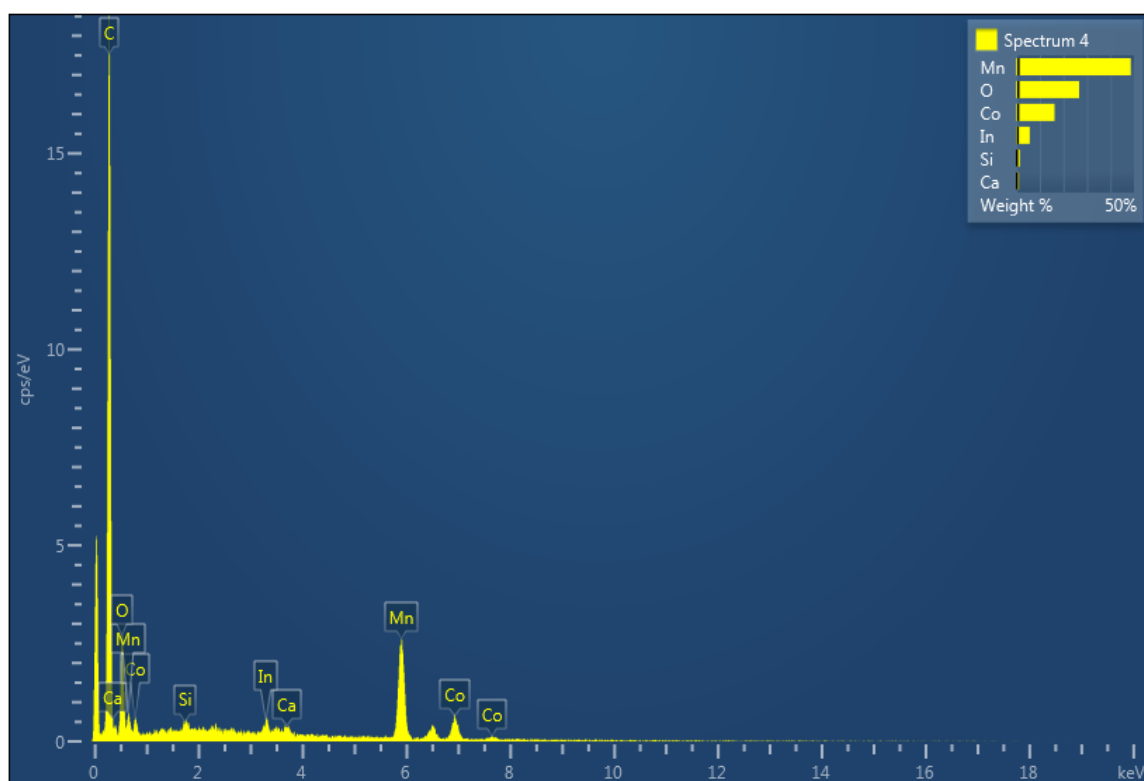


Figure 15. EDS spectrum of **17-Co** before electrolysis.

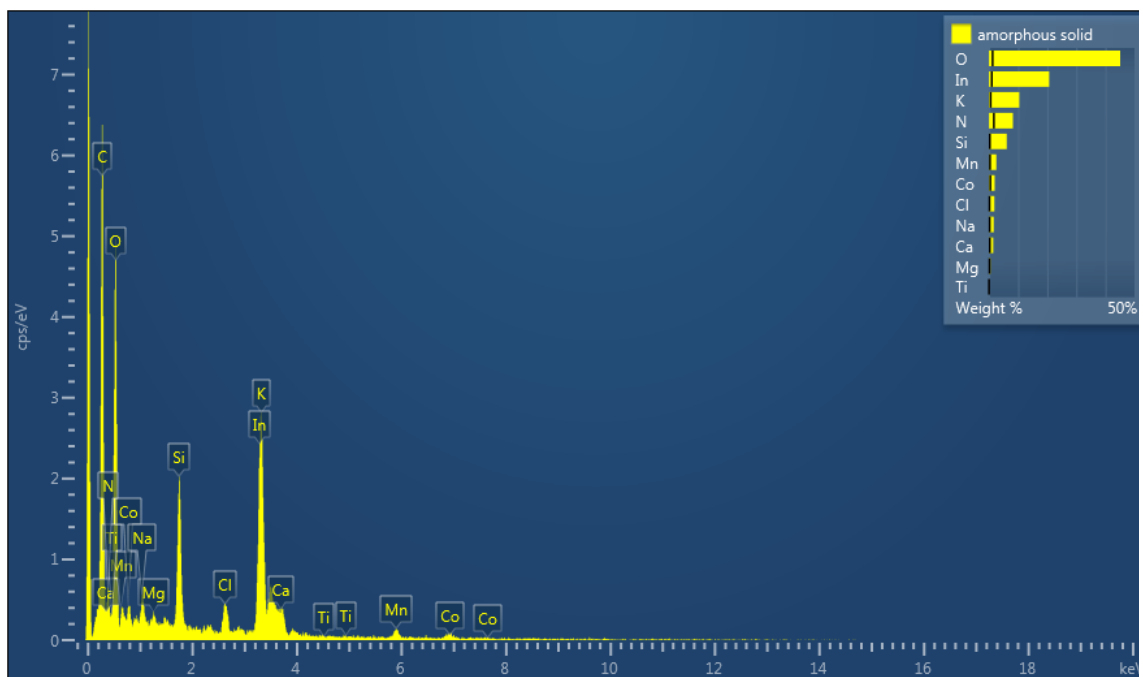


Figure 16. EDS spectrum of 17-Co after electrolysis.

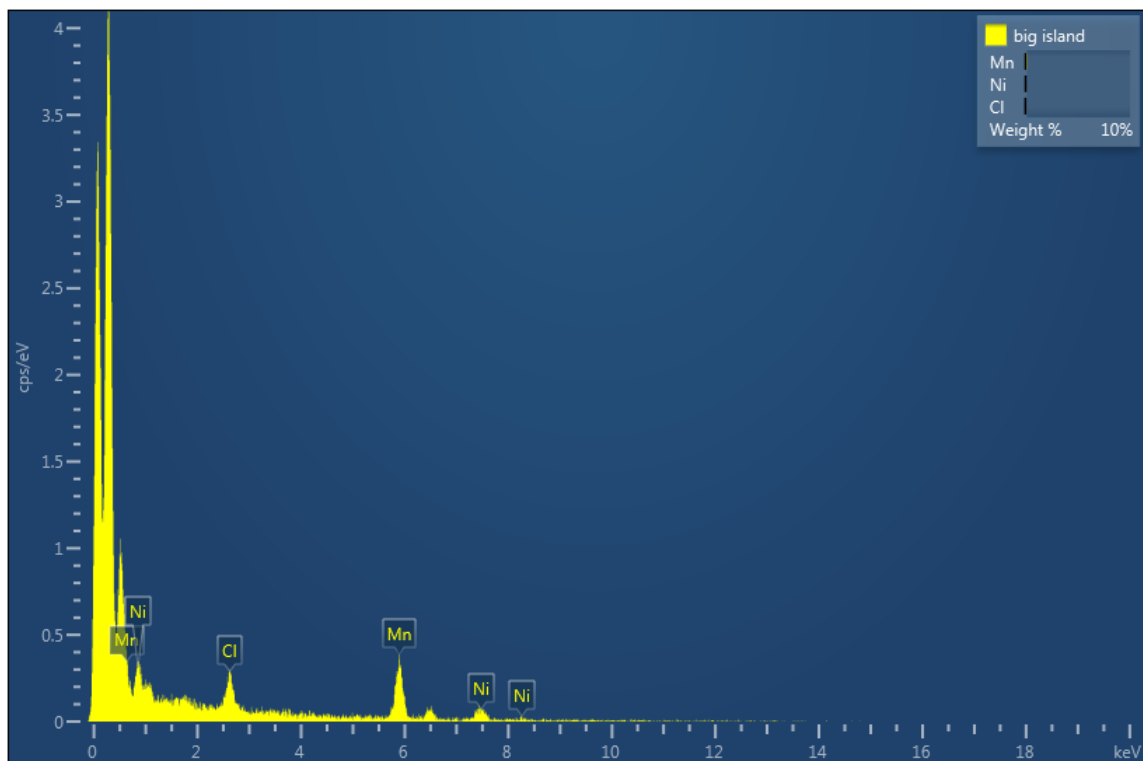


Figure 17. EDS spectrum of 17-Ni after electrolysis.

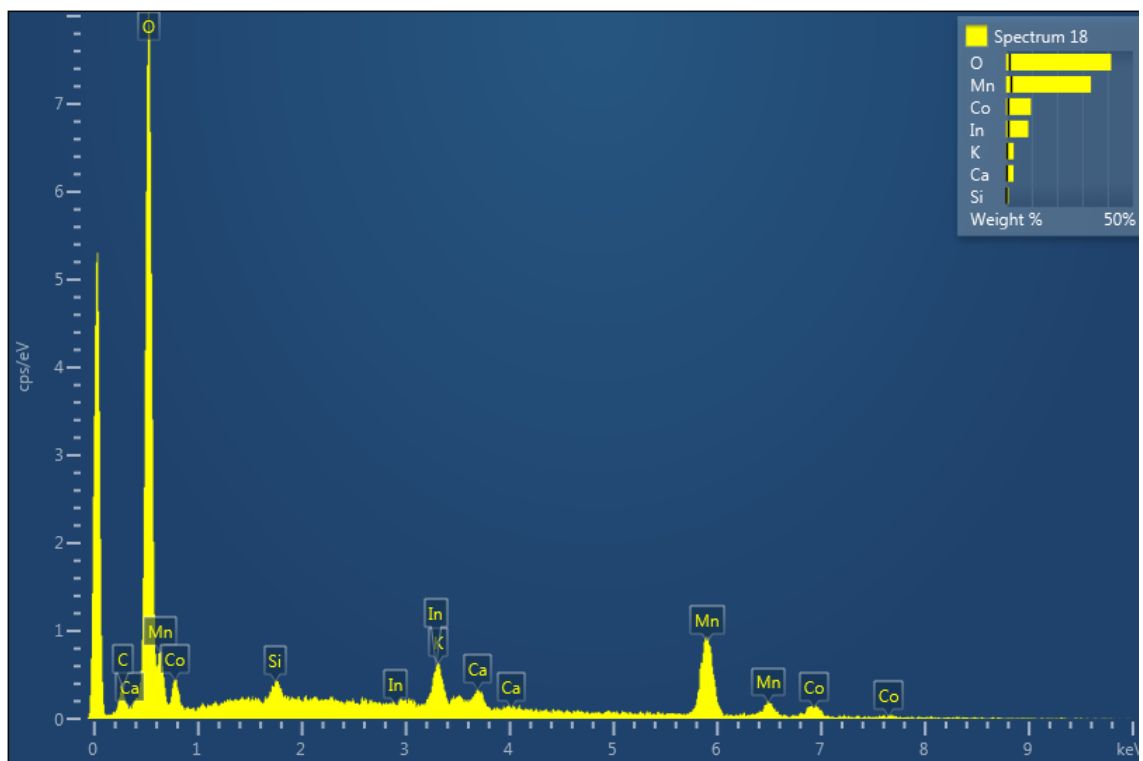


Figure 18. EDS spectrum of 18-Co *after* electrolysis.

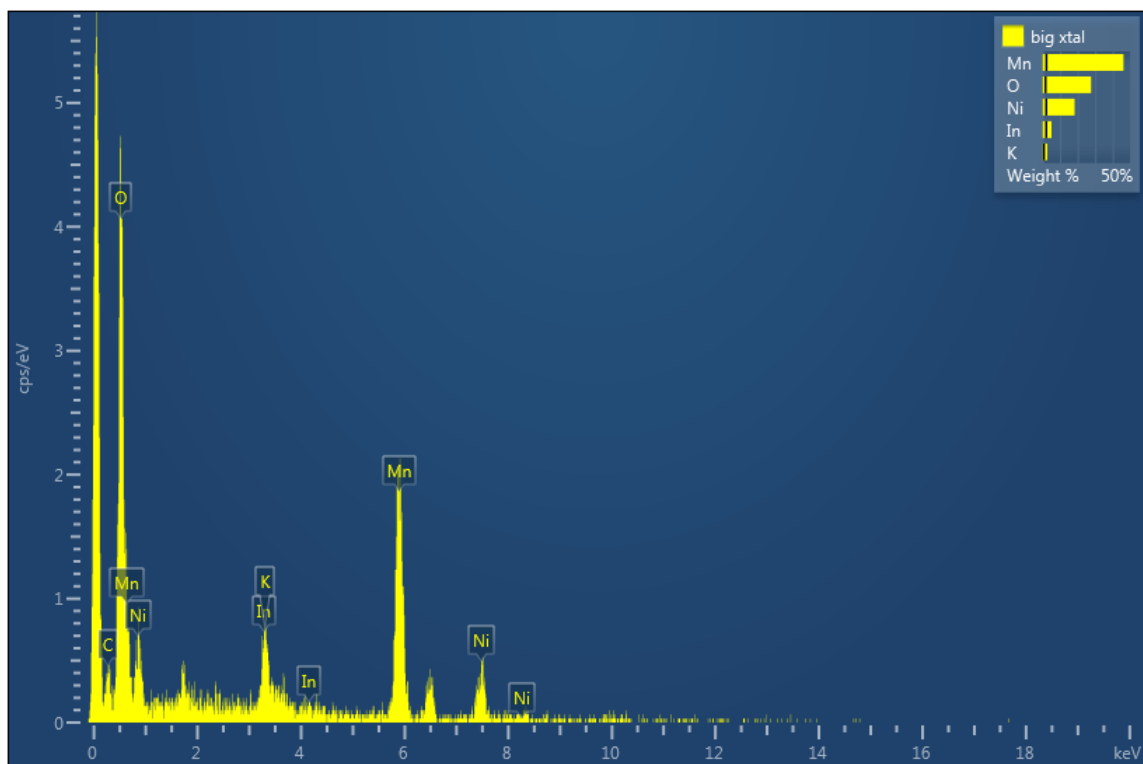


Figure 19. EDS spectrum of 18-Ni *after* electrolysis.

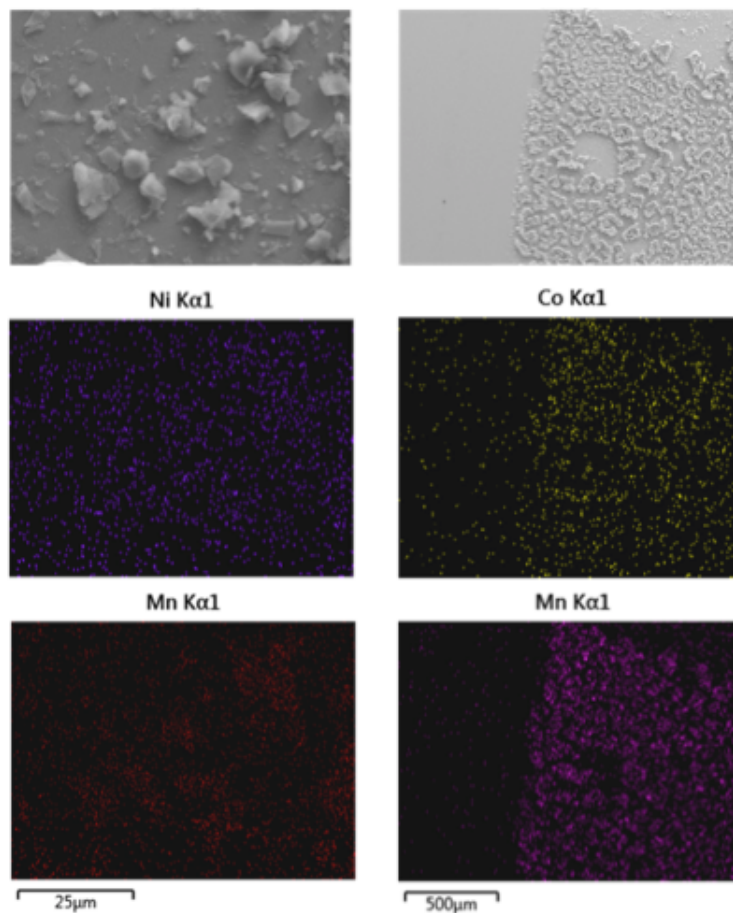


Figure 20. SEM images and elemental mappings of **2-Ni** (left) and **3-Co** (right) on ITO after electrolysis, displaying the SEM image with the corresponding Mn and Ni/Co Kα1 compositional maps.

Inductively Coupled Mass Spectrometry (ICP-MS)

Inductively coupled plasma mass spectrometry (ICP-MS) data were collected using a Hewlett-Packard 4500 ICP-MS System with a Babbington nebulizer and a Scott-type spray chamber maintained at 5 °C. The plasma was operated at 1250 W. All samples were diluted to concentrations between 10-20 ppb and analyzed against a standard curve of known concentrations of specific metals.

REFERENCES

- 1 (a) Cook, T. R.; Dogutan, D. K.; Reece, S. Y.; Surendranath, Y.; Teets, T. S.; Nocera, D. G. *Chem. Rev.* **2010**, *110*, 6474. (b) Walter, M. G.; Warren, E. L.; McKone, J. R.; Boettcher, S. W.; Mi, Q. X.; Santori, E. A.; Lewis, N. S. *Chem. Rev.* **2010**, *110*, 6446.
- 2 (a) Kanan, M. W.; Nocera, D. G. *Science* **2008**, *321*, 1072. (b) Gorlin, Y.; Jaramillo, T. F. *J. Am. Chem. Soc.* **2010**, *132*, 13612. (c) Dinca, M.; Surendranath, Y.; Nocera, D. G. *Proc. Natl. Acad. Sci. U.S.A.* **2010**, *107*, 10337. (d) Zaharieva, I.; Chernev, P.; Risch, M.; Klingan, K.; Kohlhoff, M.; Fischer, A.; Dau, H. *Energy Environ. Sci.* **2012**, *5*, 7081. (e) Schley, N. D.; Blakemore, J. D.; Subbaiyan, N. K.; Incarvito, C. D.; D'Souza, F.; Crabtree, R. H.; Brudvig, G. W. *J. Am. Chem. Soc.* **2011**, *133*, 10473. (f) Suntivich, J.; May, K. J.; Gasteiger, H. A.; Goodenough, J. B.; Shao-Horn, Y. *Science* **2011**, *334*, 1383. (g) Subbaraman, R.; Tripkovic, D.; Chang, K. C.; Strmcnik, D.; Paulikas, A. P.; Hirunsit, P.; Chan, M.; Greeley, J.; Stamenkovic, V.; Markovic, N. M. *Nature Mater.* **2012**, *11*, 550. (h) Jiao, F.; Frei, H. *Energy Environ. Sci.* **2010**, *3*, 1018. (i) Yang, J. H.; Walczak, K.; Anzenberg, E.; Toma, F. M.; Yuan, G. B.; Beeman, J.; Schwartzberg, A.; Lin, Y. J.; Hettick, M.; Javey, A.; Ager, J. W.; Yano, J.; Frei, H.; Sharp, I. D. *J. Am. Chem. Soc.* **2014**, *136*, 6191. (j) Rumberger, E. M. W.; Ahn, H. S.; Bell, A. T.; Tilley, T. D. *Dalton Trans.* **2013**, *42*, 12238.
- 3 (a) Rossmeisl, J.; Logadottir, A.; Norskov, J. K. *Chem. Phys.* **2005**, *319*, 178. (b) Conway, B. E.; Tilak, B. V. *Advances in Catalysis*; Academic Press: New York, 1992; Vol. 38.
- 4 (a) Bockris, J. O.; Otagawa, T. *J. Phys. Chem.* **1983**, *87*, 2960. (b) Bockris, J. O.; Otagawa, T. *J. Electrochem. Soc.* **1984**, *131*, 290.
- 5 Rasiyah, P.; Tseung, A. C. C. *J. Electrochem. Soc.* **1984**, *131*, 803.
- 6 Trasatti, S. *J. Electroanal. Chem.* **1980**, *111*, 125.
- 7 (a) Matsumoto, Y.; Sato, E. *Mater. Chem. Phys.* **1986**, *14*, 397. (b) Hoare, J. P. *Encyclopedia of Electrochemistry of the Elements*; Marcel Dekker: New York, 1982; Vol. 2.
- 8 Trasatti, S. *Electrochim. Acta.* **1984**, *29*, 1503.
- 9 (a) Corrigan, D. A. *J. Electrochem. Soc.* **1987**, *134*, 377. (b) Corrigan, D. A.; Bendert, R. M. *J. Electrochem. Soc.* **1989**, *136*, 723. (c) Merrill, M. D.; Dougherty, R. C. *J. Phys. Chem. C* **2008**, *112*, 3655. (d) Trotochaud, L.; Young, S. L.; Ranney, J. K.; Boettcher,

- S. W. *J. Am. Chem. Soc.* **2014**, *136*, 6744. (e) Landon, J.; Demeter, E.; Inoglu, N.; Keturakis, C.; Wachs, I. E.; Vasic, R.; Frenkel, A. I.; Kitchin, J. R. *ACS Catal.* **2012**, *2*, 1793. (f) Gong, M.; Li, Y. G.; Wang, H. L.; Liang, Y. Y.; Wu, J. Z.; Zhou, J. G.; Wang, J.; Regier, T.; Wei, F.; Dai, H. J. *J. Am. Chem. Soc.* **2013**, *135*, 8452. (g) Louie, M. W.; Bell, A. T. *J. Am. Chem. Soc.* **2013**, *135*, 12329. (h) Trotochaud, L.; Ranney, J. K.; Williams, K. N.; Boettcher, S. W. *J. Am. Chem. Soc.* **2012**, *134*, 17253. (i) McCrory, C. C. L.; Jung, S. H.; Peters, J. C.; Jaramillo, T. F. *J. Am. Chem. Soc.* **2013**, *135*, 16977.
- 10 (a) Jasem, S. M.; Tseung, A. C. C. *J. Electrochem. Soc.* **1979**, *126*, 1353. (b) Ho, J. C. K.; Piron, D. L. *J. Appl. Electrochem.* **1996**, *26*, 515.
- 11 (a) Kibria, A. K. M. F.; Tarafdar, S. A. *Int. J. Hydrogen Energy* **2002**, *27*, 879. (b) Li, X. H.; Walsh, F. C.; Pletcher, D. *Phys. Chem. Chem. Phys.* **2011**, *13*, 1162.
- 12 Singh, R. N.; Madhua; Awasthi, R.; Sinha, A. S. K. *Electrochim. Acta.* **2009**, *54*, 3020.
- 13 Singh, R. N.; Madhu; Awasthi, R.; Tiwari, S. K. *Int. J. Hydrogen Energy* **2009**, *34*, 4693.
- 14 Singh, R. N.; Pandey, J. P.; Singh, N. K.; Lal, B.; Chartier, P.; Koenig, J. F. *Electrochim. Acta.* **2000**, *45*, 1911.
- 15 Singh, R. N.; Singh, N. K.; Singh, J. P. *Electrochim. Acta.* **2002**, *47*, 3873.
- 16 (a) Wiechen, M.; Zaharieva, I.; Dau, H.; Kurz, P. *Chem. Sci.* **2012**, *3*, 2330. (b) Haber, J. A.; Xiang, C. X.; Guevarra, D.; Jung, S. H.; Jin, J.; Gregoire, J. M. *ChemElectroChem.* **2014**, *1*, 524. (c) Cattarin, S.; Frateur, I.; Guerriero, P.; Musiani, M. *Electrochim. Acta.* **2000**, *45*, 2279.
- 17 (a) Smith, R. D. L.; Prevot, M. S.; Fagan, R. D.; Zhang, Z. P.; Sedach, P. A.; Siu, M. K. J.; Trudel, S.; Berlinguette, C. P. *Science* **2013**, *340*, 60. (b) Smith, R. D. L.; Prevot, M. S.; Fagan, R. D.; Trudel, S.; Berlinguette, C. P. *J. Am. Chem. Soc.* **2013**, *135*, 11580. (c) Zhang, C. J.; Trudel, S.; Berlinguette, C. P. *Eur. J. Inorg. Chem.* **2014**, 660.
- 18 (a) Gorlin, Y.; Chung, C. J.; Benck, J. D.; Nordlund, D.; Seitz, L.; Weng, T. C.; Sokaras, D.; Clemens, B. M.; Jaramillo, T. F. *J. Am. Chem. Soc.* **2014**, *136*, 4920. (b) Gorlin, Y.; Lassalle-Kaiser, B.; Benck, J. D.; Gul, S.; Webb, S. M.; Yachandra, V. K.; Yano, J.; Jaramillo, T. F. *J. Am. Chem. Soc.* **2013**, *135*, 8525.
- 19 (a) Kanady, J. S.; Tsui, E. Y.; Day, M. W.; Agapie, T. *Science* **2011**, *333*, 733. (b) Tsui, E. Y.; Agapie, T. *Proc. Natl. Acad. Sci. U.S.A.* **2013**, *110*, 10084.
- 20 Lutterman, D. A.; Surendranath, Y.; Nocera, D. G. *J. Am. Chem. Soc.* **2009**, *131*, 3838.

21 Liaudet, E.; Battaglini, F.; Calvo, E. J. *J. Electroanal. Chem.* **1990**, *293*, 55.

22 (a) Ravel, B.; Newville, M. *Synchrotron Radiation* **2005**, *12*, 537. (b) Newville, M. *Synchrotron Radiation* **2001**, *8*, 322.

APPENDIX A

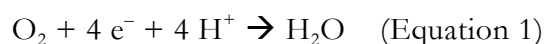
SYNTHESIS OF HETEROMETALLIC $[MMn_3X]$ CLUSTERS ($X = N, O, F, S$) FOR O_2
ACTIVATION

ABSTRACT

A number of heteromultimetallic [MMn₃X] clusters (X = O, S, F) have been synthesized and structurally characterized. Complexes such as [ZnMn₃O] and [CoMn₃O] have been made, and the bis-oxime ligand, PRABO, has been shown to exchange with two of the acetates on the [ZnMn₃O] cluster. The PRABO-substituted, reduced [ZnMn₃O] cluster with an acetate bound only underwent an outer-sphere, one-electron oxidation of the cluster by the addition of O₂. The synthesis of [Mn₃S] complex has also been achieved, however, efforts to install a fourth metal using M(OAc)₂ to the cluster have been unsuccessful, possibly due to the formation of the thermodynamically favored decomposition trimanganese-acetate product and the steric around the Mn^{II} center caused by the μ₃-S ligand. A [Mn₄F] complex was synthesized by using XeF₂ as a fluorinating agent and **LMn₃(OAc)₃**. Efforts to build and structurally characterize other heterometallic [MMn₃X] clusters are still ongoing, targeting O₂ binding and reduction.

INTRODUCTION

Metalloenzymes that catalyze multi-electron redox reactions are essential to biological functions such as respiration,¹ photosynthesis,² and nitrogen fixation.³ These metalloenzymes consist of multimetallic active sites that perform the useful transformations. One example is the Cytochrome *c* oxidase (CcO) that consists of a heterobimetallic active site, namely an iron heme and a copper center ligated by three histidine donors. The main function of the CcO during the final stage of respiration is to catalytically reduce dioxygen by four electrons and four protons to generate water (Eq. 1) without producing other reactive oxygen species.¹



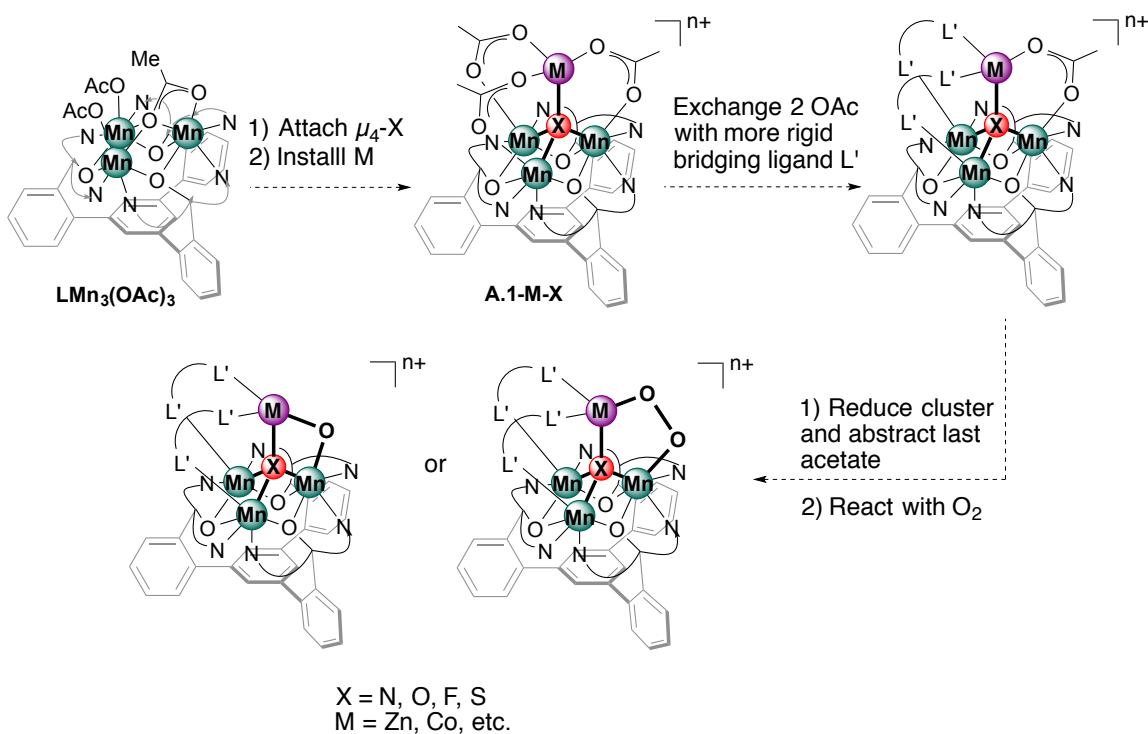
Not only the detailed mechanism of selective oxygen reduction by the bimetallic site of CcO is still under debate,⁴ mimicking this transformation itself by synthetic complexes is of interest for fuel cell application by developing cheap catalysts that can efficiently activate dioxygen at the anode. For multi-electron transformation, transition metal complexes with discrete multinuclear cores may act as functional mimics of the metalloenzymes in the biological systems. Instead of performing 4 e⁻ reduction by a single metal center, the load may possibly be alleviated or shared by having multiple metal centers as the source of electrons. Hence, we would like to target multimetallic complexes that can perform O₂ activation.

The Agapie group has reported previously the syntheses and characterization of a series of multimetallic clusters in the form of [MMn₃O₂] and [MFe₃O(OH)].⁵ In these cases, the μ₄-oxo bridging ligand of the clusters acts a spacer for the metal centers. On the other hand, it can be envisioned that the other μ₂-oxo/hydroxo is the intermediate

product(s) of O_2 reduction if dioxygen were to bind to the clusters and be reduced.

In this chapter, we explore building a series of $[MMn_3X]$ clusters for O_2 reduction where M is either redox-active or -inactive metal, and X is the interstitial μ_4 -bridging ligand (Scheme 1). The bridging ligand X can be varied from O, N, F, and S to study its role in tuning the steric as well as the electronic of the multimetallic cluster overall towards reactivity with O_2 . We envision that O_2 can bridge between M and Mn while the other Mn centers can donate electrons to reduce dioxygen. Additionally, due to the lack of structural characterization of the CcO models after the reaction with O_2 , it would be beneficial if we can monitor and study this transformation structurally and systematically using different M and X.

Scheme 1. Proposed route toward O_2 activation by $[MMn_3X]$ complexes

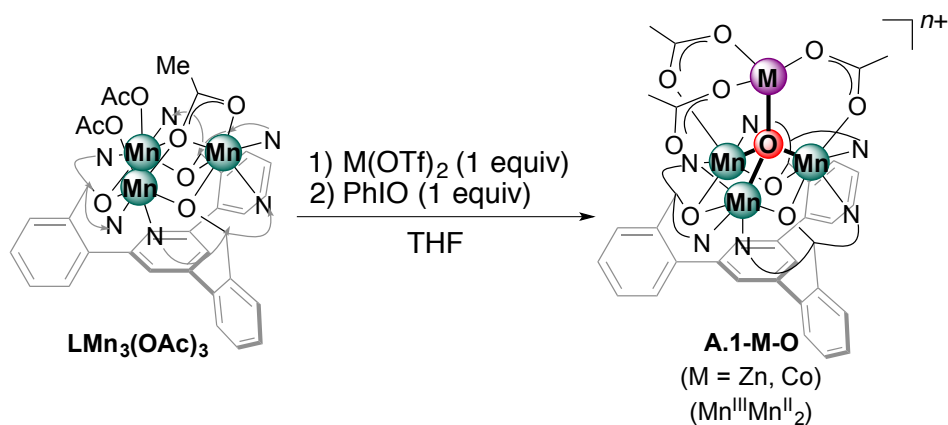


RESULTS AND DISCUSSION

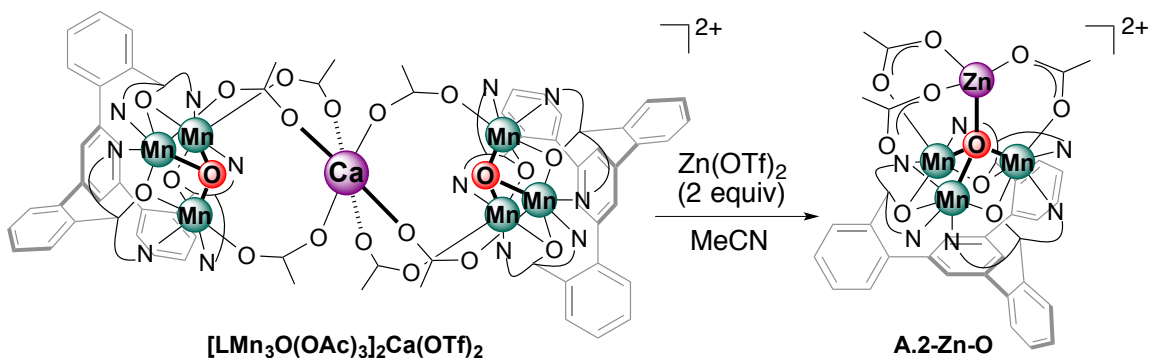
A.1 Synthesis of $[MMn_3O(OAc)_3]$

The zinc-trimanganese mono-oxo, **A.1-Zn-O**, was prepared previously by Emily Y. Tsui by treatment of the trimanganese(II) with one equivalent of $Zn(OTf)_2$ and one equivalent of iodosobenzene (Scheme 2). The product isolated by this route is the reduced $[ZnMn_3O]$ species where the Mn oxidation states are $Mn^{III}Mn^{II}_2$.

Scheme 2. Direct synthesis of the reduced $[MMn_3O]$



Scheme 3. Synthesis of **A.2-Zn-O** via transmetallation



Attempts to reproduce the synthesis of **A.1-Zn-O** were done, but purification was challenging although the desired species was the major product formed in the reaction mixture as evidenced by 1H NMR spectroscopy. Instead, an alternative route to synthesize $[ZnMn_3O]$ was performed by transmetallation of the previously reported

$[\text{LMn}_3\text{O}(\text{OAc})_3]_2\text{Ca}(\text{OTf})_2$ by $\text{Zn}(\text{OTf})_2$ (Scheme 3). The isolated product is the oxidized $[\text{ZnMn}_3\text{O}]$ complex, **A.2-Zn-O** where the Mn oxidation states are $\text{Mn}^{\text{III}}_2\text{Mn}^{\text{II}}$. The one electron oxidized **A.2-Zn-O** can be converted to **A.1-Zn-O** by simply adding one equivalent of decamethylferrocene (FeCp^*_2).

On the other hand, synthesis of **A.1-Co-O** can be afforded by the route described in Scheme 2. Single crystals suitable for X-ray diffraction study (XRD) were grown from the vapor diffusion of diethyl ether into a concentrated dimethoxyethane solution of **A.1-Co-O**. XRD study confirmed the structural identity of the product (Figure 1). The metals' oxidation states of **A.1-Co-O** were assigned as $\text{Co}^{\text{II}}\text{Mn}^{\text{III}}\text{Mn}^{\text{II}}_2$. The Mn–oxido bond distances are 2.147, 2.220, and 1.842 Å, consistent with the $\text{Mn}^{\text{III}}\text{Mn}^{\text{II}}_2$ assignment. The Co–oxido bond distance is 1.855 Å.

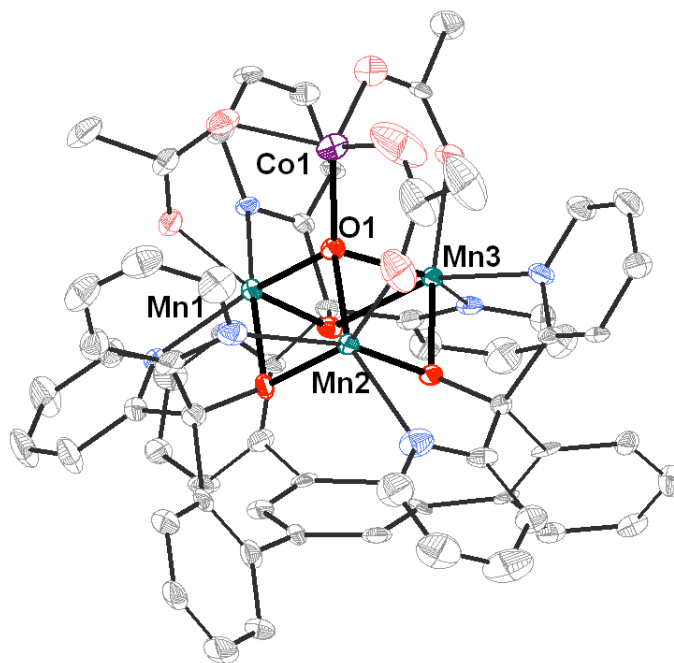


Figure 1. Solid-state structure of **A.1-Co-O**. Hydrogen atoms and outer sphere anions are omitted for clarity.

Attempts to synthesize other $[\text{MMn}_3\text{O}]$ complexes with $M = \text{Y}$ or Sc as larger apical heteroatom were done. Transmetallation of $[\text{LMn}_3\text{O}(\text{OAc})_3]_2\text{Ca}(\text{OTf})_2$ with either $\text{Sc}(\text{OTf})_3$ or $\text{Y}(\text{OTf})_3$ yielded the same green-colored product that has not been structurally characterized. This green color for a mono-oxo series is generally associated with the presence of water in the mixture, which in this case may have come from the starting $\text{Sc}(\text{OTf})_3$ or $\text{Y}(\text{OTf})_3$. Efforts to synthesize $[\text{MMn}_3\text{O}]$ cluster with larger radius M are still ongoing.

*A.2 Cyclic voltammetry studies on **A.2-Zn-O** and **A.1-Co-O***

Cyclic voltammetry (CV) studies were performed on **A.2-Zn-O** and **A.1-Co-O** to determine their redox properties. The CV of **A.2-Zn-O** (Figure 2) consists of irreversible two reduction events with at -0.31 and -1.26 V (vs. Fc/Fc^+) that are currently assigned to the reduction of $[\text{ZnMn}^{\text{II}}\text{Mn}^{\text{III}}_2/\text{ZnMn}^{\text{II}}_2\text{Mn}^{\text{III}}]$ and of $[\text{ZnMn}^{\text{II}}_2\text{Mn}^{\text{III}}/\text{ZnMn}^{\text{II}}_3]$, respectively. This observation of irreversible redox events is surprising because the one electron reduced species, **A.1-Zn-O**, can be stably isolated by chemical reduction of **A.2-Zn-O** using an equivalent of FeCp^*_2 . Given this experimental result, it was initially expected that the CV would display the first reduction event as reversible or quasi-reversible. With no XRD studies performed on **A.2-Zn-O** to date, a possible explanation of this phenomenon is that the structural rearrangement upon reduction is large enough to result in this irreversible redox event.

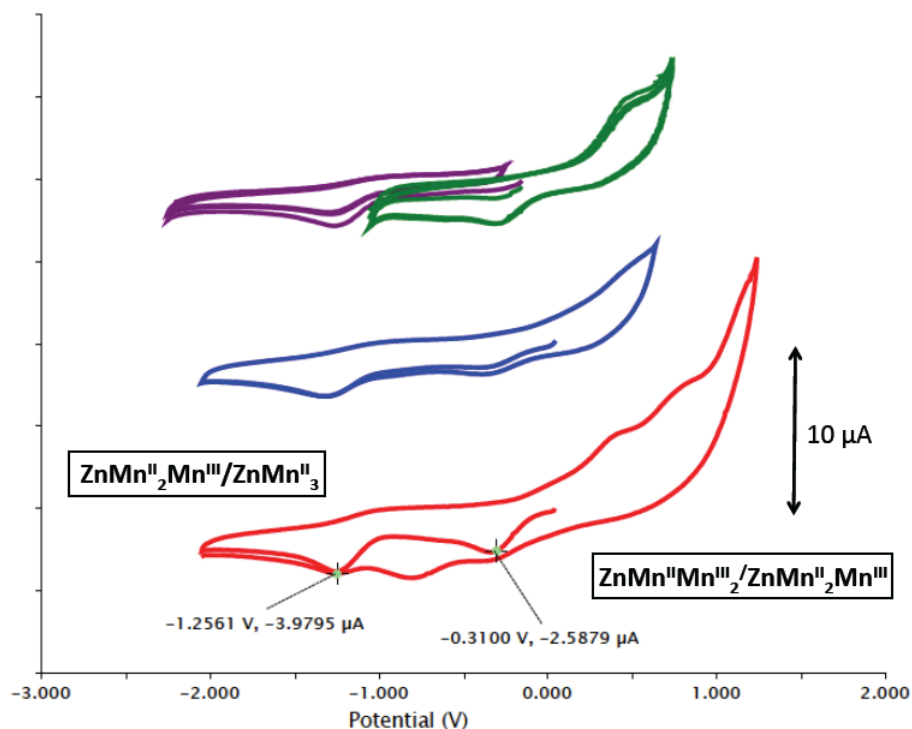


Figure 2. Cyclic voltammetry of **A.2-Zn-O** (vs. Fc/Fc^+): 1 mM complex in CH_2Cl_2 (0.1 M $n\text{-Bu}_4\text{PF}_6$), 100 mV/s scan rate, glassy carbon working electrode, Pt wire counter electrode. (*Bottom*) Full CV scan within the solvent window; (*middle*) CV window to isolate two redox events; (*top*) separation of each redox events.

The CV of **A.1-Co-O** is displayed in Figure 3. Unlike the case for **A.2-Zn-O**, the CV of **A.1-Co-O** shows one quasi-reversible reduction event and one irreversible oxidation event. Both redox events can be isolated as shown in the top of Figure 3. The reduction event is currently assigned as the $[\text{Co}^{\text{II}}\text{Mn}^{\text{II}}_2\text{Mn}^{\text{III}}/\text{Co}^{\text{II}}\text{Mn}^{\text{II}}_3]$ couple while the oxidation event is assigned as the $[\text{Co}^{\text{II}}\text{Mn}^{\text{II}}\text{Mn}^{\text{III}}_2/\text{Co}^{\text{II}}\text{Mn}^{\text{II}}_2\text{Mn}^{\text{III}}]$ couple. Since Co is another redox-active metal center in addition to Mn, it is also possible that the oxidation may also occur on the Co^{II} center to generate Co^{III} (as a $\text{Co}^{\text{II}}\text{Mn}^{\text{II}}\text{Mn}^{\text{III}}_2/\text{Co}^{\text{III}}\text{Mn}^{\text{II}}\text{Mn}^{\text{III}}_2$ couple), although there is no structural evidence yet to indicate whether this is indeed the case.

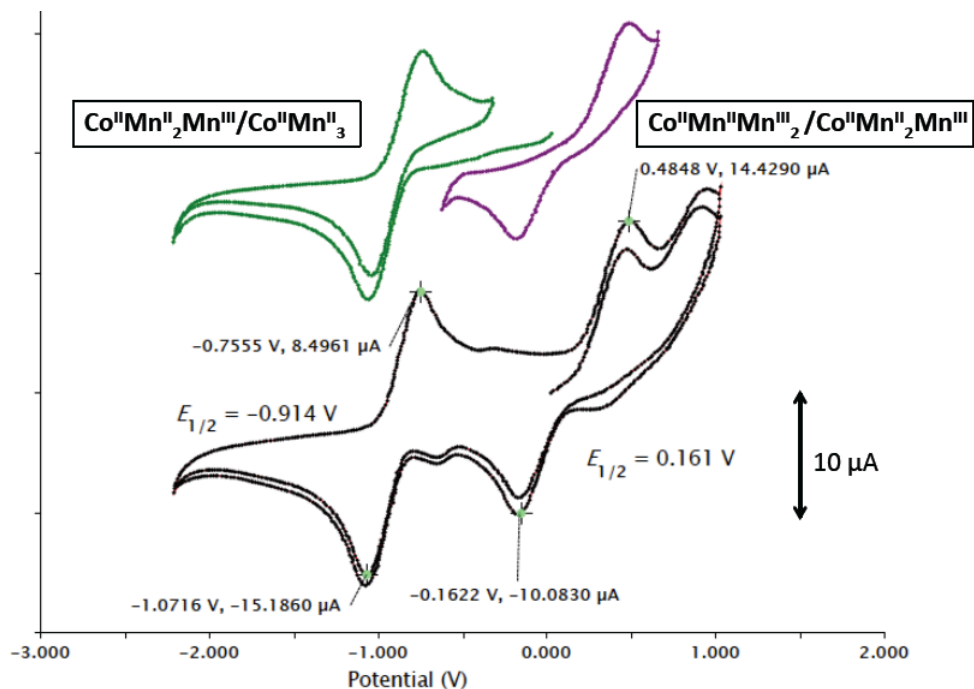


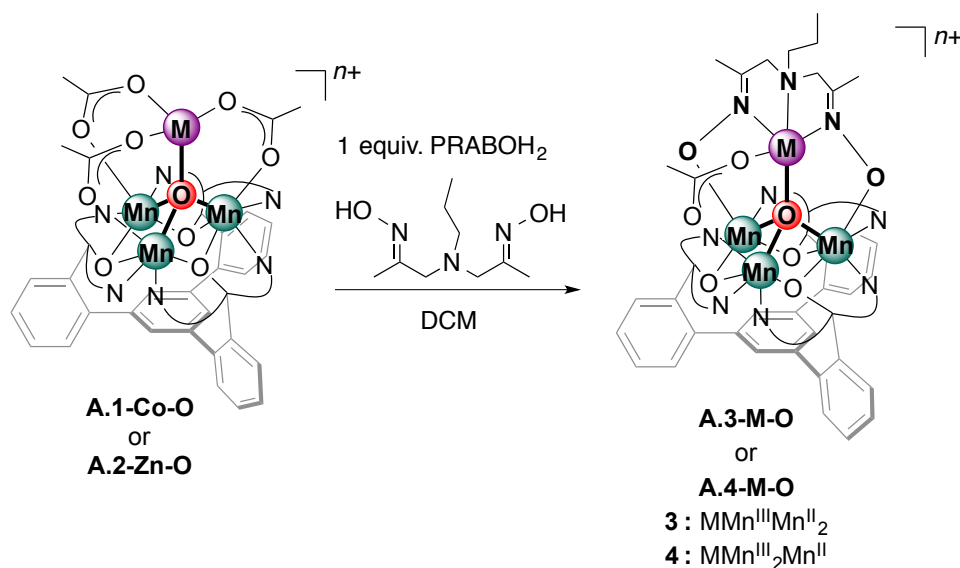
Figure 3. Cyclic voltammetry of **A.1-Co-O** (vs. Fc/Fc^+): 1 mM complex in CH_2Cl_2 (0.1 M $n\text{-Bu}_4\text{PF}_6$), 100 mV/s scan rate, glassy carbon working electrode, Pt wire counter electrode. (*Bottom*) Full CV scan within the solvent window; (*top*) separation of each redox events.

A.3 Exchange of the $[\text{MMn}_3\text{O}]$ acetates with bis-oxime ligands and reactivity with O_2 and NO

With **A.2-Zn-O** and **A.1-Co-O** complexes at hand, installing a more rigid bridging ligand by replacing two acetates was attempted. Due to the successful ligand exchange on the analogous $[\text{ZnFe}_3\text{O}]$ complex using *N,N*-propyl-*N,N*-bis(1-propan-2-onyl oxime)-amine (PRABOH₂) by Davide Lionetti, the same bis-oxime ligand, PRABOH₂, was used to replace two acetates on **A.2-Zn-O** and generate **A.4-Zn-O** (Scheme 4). The ligand exchange reaction was monitored by ¹H NMR spectroscopy (Figure 4). The ¹H NMR spectrum of **A.4-Zn-O** consists of ≥ 24 proton signals, which are significantly more proton signals than the ≥ 7 proton signals from **A.2-Zn-O**. This suggests desymmetrization of the cluster complex, as expected from the exchange of

two acetates from a C_3 -symmetric **A.2-Zn-O** by one PRABO. A XRD study on the single crystal of **A.4-Zn-O** confirmed the structural identity and geometry of the PRABO substituted $[ZnMn_3O]$ cluster (Figure 5).

Scheme 4. Acetates exchange by $PRABOH_2$



One electron reduction of **A.4-Zn-O** by one equivalent of $FeCp^*_2$ yielded the tentatively assigned **A.3-Zn-O** as monitored by 1H NMR spectroscopy (Figure 4). **A.3-Zn-O** has not yet been structurally characterized by XRD. Regardless, assuming the tentatively assigned **A.3-Zn-O** product as the one electron reduced version of **A.4-Zn-O**, 1 atm of O_2 was added to the headspace of a J. Young tube NMR containing a solution of **A.3-Zn-O**. The solution was observed to immediately turn darker brown upon O_2 addition and mixing. However, the 1H NMR spectrum of the reaction mixture after 24 h shows only the formation of **A.4-Zn-O**. This result suggests that **A.3-Zn-O** only performs an outer sphere electron transfer/autoxidation in the presence of O_2 (Scheme 5). No formation of an O_2 adduct or the corresponding dioxido product (Scheme 1) was observed. Reactivity with nitric oxide (NO^\bullet) was also tested, albeit with

similar outcome of just an outer sphere electron transfer/one electron oxidation of **A.3-Zn-O** back to **A.4-Zn-O**.

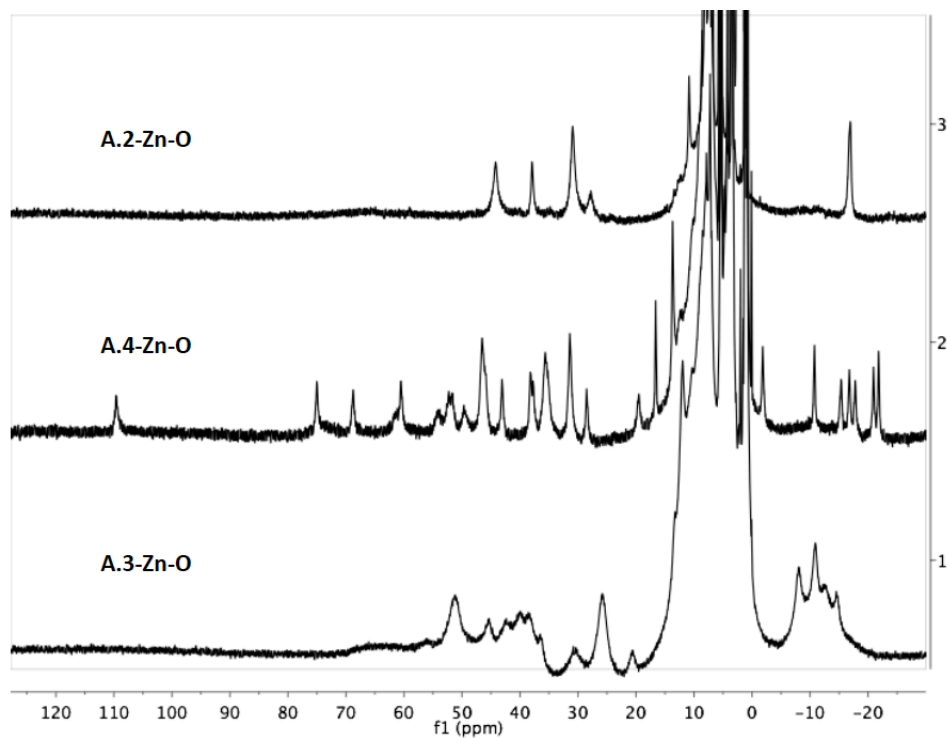


Figure 4. ^1H NMR spectra of **A.2-Zn-O**, **A.4-Zn-O**, and **A.3-Zn-O** in CD_2Cl_2

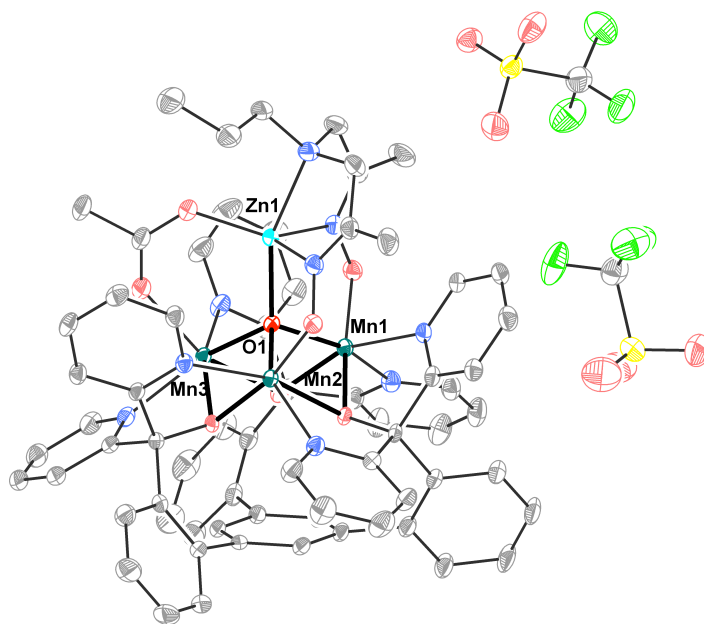
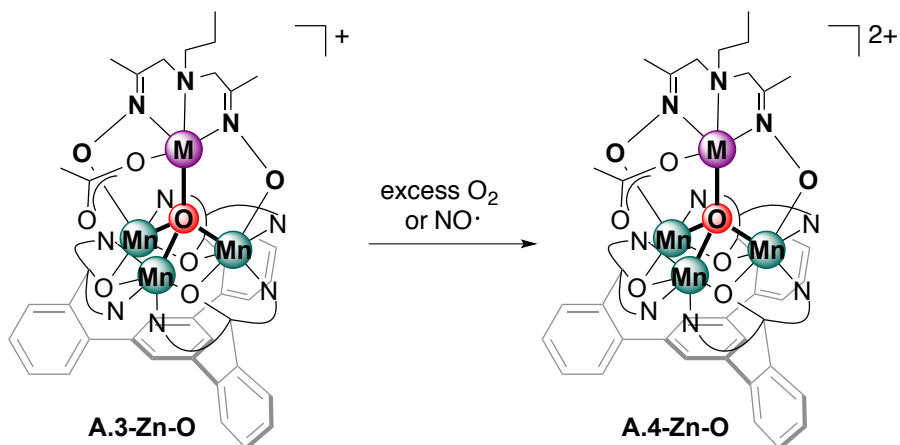


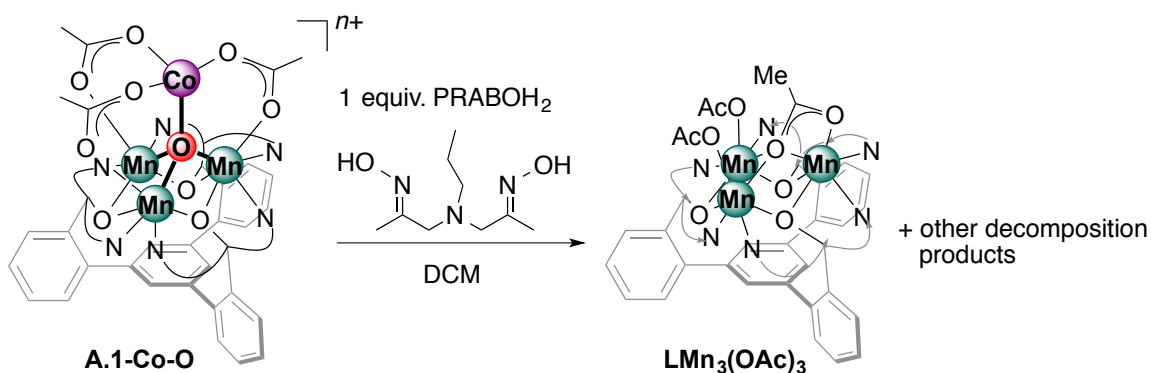
Figure 5. Solid-state structure of **A.4-Zn-O**. Hydrogen atoms and solvents are omitted for clarity

Scheme 5. Reactivity of **A.3-Zn-O** with O_2 and $NO\cdot$



This outer sphere electron transfer reactivity may be due to the presence of the last acetate that could potentially block O_2 from binding/bridging the Zn and Mn. Another possible cause is the propyl group of PRABO that seems to be protruding above the Zn center in the solid-state structure (Figure 5). Viewing the crystal structure of **A.4-Zn-O** in space-filling model, the propyl group seems to add significant steric profile around the Zn center, which may also lead to the non-observed O_2 or $NO\cdot$ binding. Control reactions that involved addition of O_2 and $NO\cdot$ to **A.1-Zn-O** were conducted, but no reaction was observed. Without exchanging two of the acetates with PRABO, **A.1-Zn-O** did not react with O_2 or $NO\cdot$ to yield the oxidized **A.2-Zn-O**.

Scheme 6. Reaction of **A.1-Co-O** with $PRABOH_2$



Installation of PRABO to **A.1-Co-O** was attempted using an analogous protocol to generate **A.4-Zn-O**. In contrast to the [ZnMn₃O] cluster, the addition of PRABOH₂ to a solution of **A.1-Co-O** in DCM generated LMn^{II}₃(OAc)₃ along with other decomposition product (Scheme 6). The formation of LMn^{II}₃(OAc)₃ was also confirmed by ESI-MS. In this case, PRABOH₂ only behaves as a reductant that can also abstract Co metal to replenish the starting trimanganese(II) starting complex.

Due to the possibility of PRABO's propyl group sterically hindering O₂ or other small molecules to bind to the metal centers, other variations of bis-oxime ligands without amine functionality were attempted, such as ethylene bis(oxime) (EBOH₂) and glycerol-bis(oxime) (GBOH₂) (Figure 6); these bis-oxime ligands were synthesized analogously to PRABOH₂ and following literature procedure.⁶ The addition of EBOH₂ to **A.2-Zn-O** or **A.1-Co-O** resulted in a color change from purple to pale tan and the formation of insoluble tan precipitates. The insoluble precipitates may be metal salts from the cluster decomposition, and possibly the deprotonated EBO ligand is capable in abstracting metal centers from the initial cluster. This phenomenon may arise from the smaller size of EBO compared to PRABO with an extra N_{amine} atom. The reaction of an equivalent of GBOH₂ with **A.2-Zn-O** also eventually gave multiple decomposition products, including insoluble metal salts, similar to what was observed with EBOH₂, despite the ESI-MS displaying a signal that corresponds to the desired ligand exchange product. These results imply that the N_{amine} atom in PRABOH₂ is essential for binding to the apical metal and stabilizing the capping of the ligand during acetate exchange. Efforts to design different ligands for acetate exchange are still ongoing.

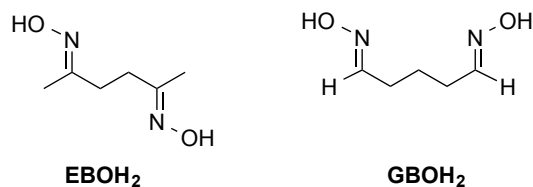


Figure 6. Other non-amine, bis-oxime ligands used to exchange acetates in [MMn₃O].

An alternative route is to abstract one of the three acetates *prior* to ligand exchange. This attempt was conducted by the addition of one equivalent of trimethylsilyl trifluoromethanesulfonate (Me₃Si(OTf)) to **A.1-Co-O** in DCM solution. Within 10 min as monitored by ¹H NMR spectroscopy, the production of the one electron oxidized **A.2-Co-O** and the bis(trimethylsilane) (Me₃Si–SiMe₃) along with other intractable mixture of products.

A.4 Synthesis of [MMn₃S(OAc)₃]

Aside from the [MMn₃O] series, the [MMn₃S] complexes are also of interest due to the larger size of sulfide and the difference in electronics between S²⁻ and O²⁻, and how these differences affect the structure and reactivity of the clusters. A slightly different approach is taken to build the [MMn₃S], where first an acetate in **LMn₃(OAc)₃** is exchanged with a triflate to make **LMn₃(OAc)₂(OTf)** and the μ₃-sulfide is installed by treatment with bis(trimethylsilyl)sulfide (S(SiMe₃)₂) without the addition of the 4th metal (Scheme 7). The driving force of the reaction upon the addition of S(SiMe₃)₂ to **LMn₃(OAc)₂(OTf)** is the formation of (Me₃Si)(OAc) as the thermodynamic product. Excess S(SiMe₃)₂ was added instead of 1 equiv only to accelerate the reaction time.

The structure of **A.5-S** was confirmed by a XRD study of the single crystal (Figure 7). Complex **A.5-S** is distinct from the other [Mn₃O] complexes obtained thus far in which all Mn centers are 5-coordinate Mn^{II}. The average Mn–S bond distance is

2.46 Å, ~ 0.2 Å longer compared to the Mn^{II}–O bond in the **LMn₃OCl₃** complex.⁷

The elongation in Mn–S bond vs. Mn–O is caused by the much larger radius of the sulfide ligand compared to the oxo and the all Mn^{II} centers. Ultimately, having the larger μ_3 -sulfide ligand causes the Mn centers to be 5-coordinate because the angle of the N_{pyr}–Mn–S (104.6°) may not allow for the sixth ligand to coordinate to Mn due to steric congestion around the metal center.

Scheme 7. Synthesis of trimanganese sulfide **A.5-S**

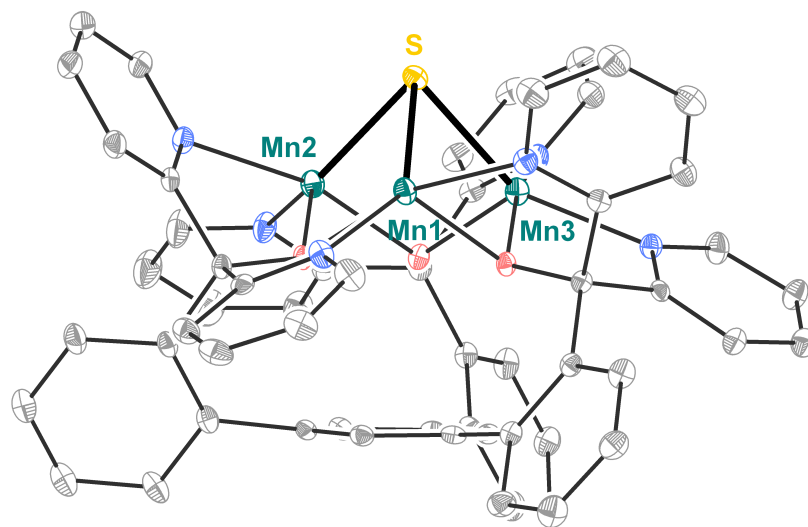
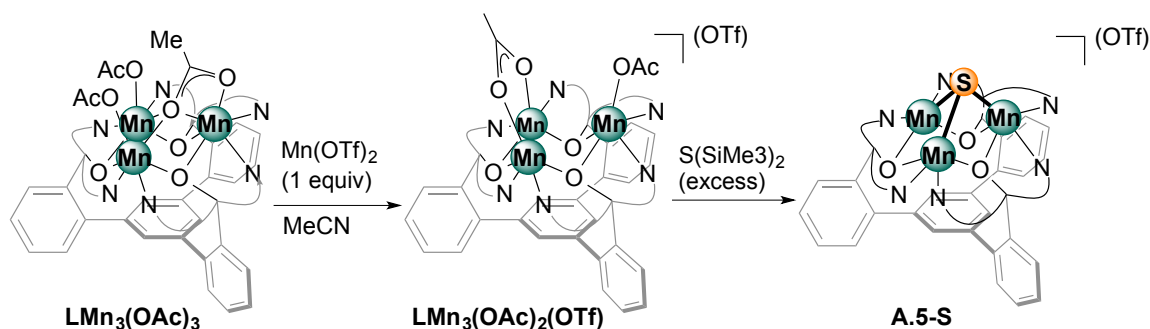


Figure 7. Solid-state structure of **A.5-S**. Hydrogen atoms and one outer sphere triflate anion are omitted for clarity.

With **A.5-S** at hand, attempts to install a fourth metal were done. $\text{M}(\text{OAc})_n$ salts were used for the purpose of having bridging acetates from M to Mn and exchange with

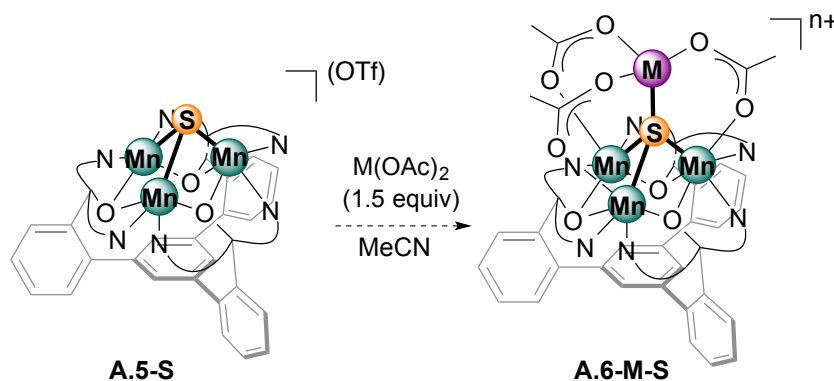
the outer sphere triflate from **A.5-S** to lose $M(\text{OTf})_2$ as the side product (Scheme 8).

$\text{Zn}(\text{OAc})_2$ (1.5 equiv) was added to **A.5-S**, where the reaction mixture turned from bright yellow to pale almost colorless solution. The ESI-MS data of the reaction mixture shows signals with distinct Zn isotopic envelope at m/z : 1236.9 $[\text{LZMn}_3\text{S}(\text{OAc})_2]^+$ and others that correspond to the desired product with with additional Na or H_2O . Despite the promising result, recrystallization from the vapor diffusion of Et_2O into a concentrated MeCN solution of potentially **A.6-Zn-S** only gave crystals that were structurally characterized as a different variant of the trimanganese complex with no fourth metal incorporation. The XRD data collection was incomplete but based on the connectivity, and the preliminary structure was identified as $\text{LMn}_3(\mu_3-1,1,3-\text{OAc})(\text{CH}_3\text{CN})(\text{L}'')$, where L'' can be either Cl or S. The single crystals of obtained from this mixture did not seem to represent the majority of the product.

Other attempts to install a different fourth metal from Zn have also been conducted with $\text{Mn}(\text{OAc})_2$ and $\text{Ca}(\text{O}_2\text{CCF}_3)_2$, and both reactions yielded crystals that were identified as $\text{LMn}_3(\mu_3-1,1,3-\text{OAc})(\text{CH}_3\text{CN})(\text{L}'')$. It is possible that the desired complex **A.6-Zn-S** was the kinetically formed product that was unstable and could only crystallize by losing the fourth metal. As mentioned previously, looking at the crystal structure of **A.5-S**, there seems to be no space for a 6th ligand to bind to Mn due to steric reasons. Perhaps the acetates that were envisioned to bridge between Mn and M could not bind to Mn, and consequently were unable stabilize the cluster. An approach that should be attempted is oxidation of one or two Mn^{II} centers to make Mn^{III} . $\text{Mn}^{\text{III}}-\text{S}$ distance is expected to be shorter than $\text{Mn}^{\text{II}}-\text{S}$ distance, which may alleviate the steric

around the Mn^{III} centers to allow for acetate binding. Efforts to install a fourth metal to generate a $[\text{MMn}_3\text{S}]$ cluster are still ongoing.

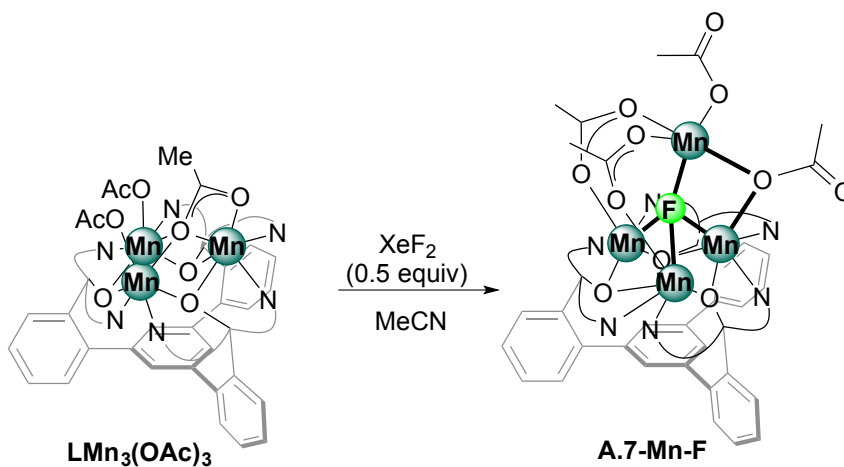
Scheme 8. Proposed route to install a fourth metal to make **A.6-M-S**



A.4 Synthesis of $[\text{MMn}_3\text{F(OAc)}_3]$

Installing a fluoride as the μ_4 -interstitial ligand bridging four metals will be an insightful comparison to the oxo and sulfide counterparts. Fluoride as a ligand, with a very small radius and its electronegativity, will affect the binding of the metals as well as the covalency of the M-F bonds compared to other interstitial ligands.

Scheme 9. Installing a fluoride on $\text{LMn}_3(\text{OAc})_3$ using XeF_2 as fluorinating agent



A similar approach was taken to install a fluoride instead of sulfide. Instead of $\text{S}(\text{SiMe}_3)_2$ as a sulfide donor, xenon difluoride (XeF_2) was used instead as a fluorinating

agent. The first synthesis is to install a $\mu_3\text{-F}$ to $\text{LMn}_3(\text{OAc})_3$. Assuming that each fluorine in XeF_2 can act as a fluorinating agent, $\text{LMn}_3(\text{OAc})_3$ was treated with 0.5 equiv of XeF_2 (Scheme 9). The ESI-MS result of the reaction displayed peaks with m/z : 1093 $[\text{LMn}_4\text{F}]^+$ and 1271 $[\text{LMn}_4\text{F}(\text{OAc})_3]^+$.

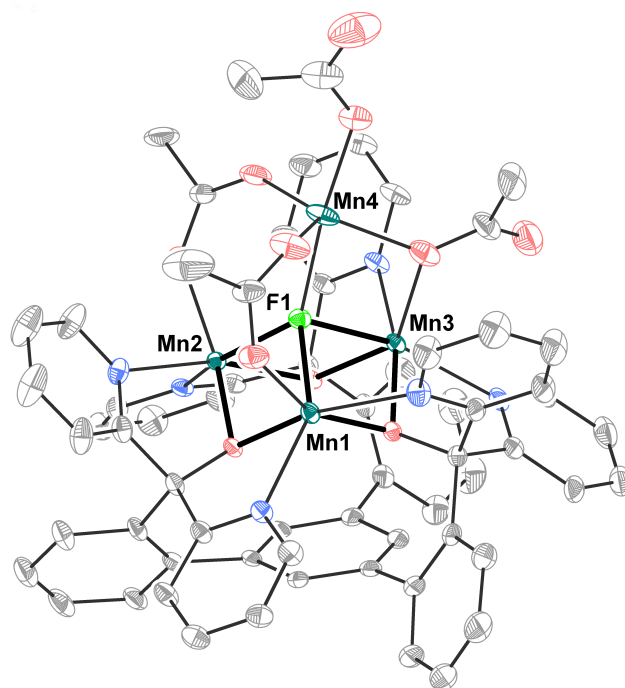


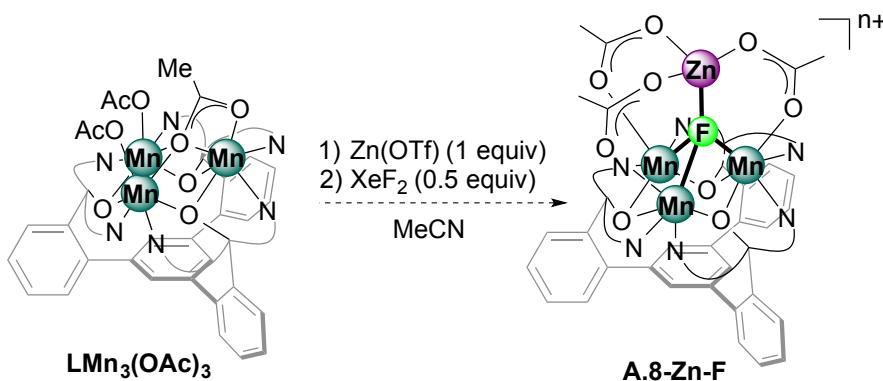
Figure 8. Solid-state structure of **A.7-Mn-F**. Hydrogens atoms and solvents are omitted for clarity.

One of the products' structural identity was confirmed by XRD study on the single crystals obtained from the DCM fraction of the reaction (Figure 8). It is worthy to note that the isolated crystals of **A.7-Mn-F** did not make up most of the materials in the mixture. This is expected because in order to make a tetramanganese product from a trimanganese starting material, some of the clusters must disproportionate and lose at least one Mn to provide the fourth metal in **A.7-Mn-F**. Some blue precipitate was also observed to be present at the end of the reaction, which may be some Mn salts as the side products. The XRD study shows that there was no outer sphere anion found in the

crystal lattice, which suggests that all the Mn centers are Mn^{II}. The Mn–F bond distances are 2.23 Å (Mn1–F), 2.21 Å (Mn2–F), 2.32 Å (Mn3–F), and 2.11 Å (Mn4–F); these bond distances are all within the range for Mn^{II}.⁸

A different route to install a μ_4 -F and a fourth metal (M = Zn) was attempted, as depicted in Scheme 10. Treatment of **LMn₃(OAc)₃** with 1 equiv of Zn(OTf)₂ and 0.5 equiv XeF₂. The ESI-MS data of this reaction showed promise of the formation of the [ZnMn₃F] cluster due to the m/z signal at 1276.7 [LZnMn₃F(OAc)₃]⁺ with the Zn isotopic envelope. No structural characterization by XRD has been done because no single crystal has been obtained to date. The recrystallization efforts and work on this synthesis are still ongoing.

Scheme 10. Synthetic route to generate [ZnMn₃F] complex



CONCLUSIONS AND FUTURE DIRECTIONS

The synthesis of [MMn₃X] (X = O, S, F, N) are being targeted to study the effect of the X ligand on the overall electronic and reactivity of the clusters, especially toward O₂ reduction. The syntheses of [ZnMn₃O] and [CoMn₃O] have been accomplished, and the bis-oxime ligand, PRABO, has been shown to exchange with two of the acetates on the [ZnMn₃O] cluster. For the PRABO-substituted, reduced [ZnMn₃O] cluster, **A.3-Zn-O**, the addition of O₂ only resulted in the one electron

oxidation of the compound back to **A.4-Zn-O** with no observed O₂ binding. Future direction of the [MMn₃O] subproject includes the abstraction of the last acetate followed by O₂ reactivity studies. The synthesis of [Mn₃S] complex has been achieved, however, efforts to install a fourth metal using M(OAc)₂ to the cluster have been unsuccessful, possibly due to the formation of the thermodynamically favored decomposition trimanganese-acetate product and the steric around the Mn^{II} center caused by the μ₃-S ligand. Some of the future experiments to append the fourth metal to the [Mn₃S] cluster include the oxidation of some of the Mn^{II} centers to Mn^{III} to alleviate the steric around the Mn and allow for a 6th bridging ligand to bind and stabilize the heterometal. To obtain [MMn₃F] clusters, XeF₂ has proved to be an appropriate reagent to install a μ₄-F, as evidenced by the crystallographically characterized formation of **A.7-Mn-F**, albeit as a minor product of the reaction. Efforts to build and structurally characterize heterometallic [MMn₃F] clusters are still ongoing.

EXPERIMENTAL SECTION

General Considerations

Unless otherwise specified, all compounds were manipulated using a glovebox or standard Schlenk line techniques with an N₂ atmosphere. Anhydrous tetrahydrofuran (THF) was purchased from Aldrich in 18 L Pure-PacTM containers. Anhydrous benzene, dichloromethane, diethyl ether, and THF were purified by sparging with nitrogen for 15 minutes and then passing under nitrogen pressure through a column of activated A2 alumina (Zapp's). Methylene chloride-*d*₂ and acetonitrile-*d*₃ were purchased from Cambridge Isotopes, dried over calcium hydride, and vacuum transferred prior to use. Unless indicated otherwise, all commercial chemicals were used as received. Zn(OTf)₂ was purchased from Strem. Co(OTf)₂,⁹ H₃L,¹⁰ LMn₃(OAc)₃,¹¹ [LMn₃O(OAc)₃]₂Ca(OTf)₂,¹² and PRABOH₂¹³ were prepared according to previously

published protocols. ^1H NMR spectra were recorded on Varian Mercury 300 at room temperature. Elemental analyses were performed by Robertson Microlit Laboratories, Ledgewood, NJ.

Synthesis of A.2-Zn-O

To a solution of $[\text{LMn}_3\text{O}(\text{OAc})_3]_2\text{Ca}(\text{OTf})_2$ (50 mg, 0.018 mmol, 2 equiv) in CH_3CN (5 mL) was added $\text{Zn}(\text{OTf})_2$ (13.2 mg, 0.036 mmol, 2 equiv). The mixture was stirred and the color changed to brown purple. After 1 h, the mixture was dried under vacuum. The residue was resuspended in DCM and then filtered through Celite. The DCM filtrate was collected and dried. The clean product was afforded in 64% yield through recrystallization of the DCM fraction via vapor diffusion of Et_2O into a concentration DCM solution of the residue. ^1H NMR (CD_2Cl_2 , 300 MHz): δ 44.20 (br), 37.942 (br), 30.90 (br), 27.78 (v br), 10.86 (br), 8.62–6.85 (m overlapped), –16.98 (br) ppm.

Synthesis of A.1-Co-O

To a stirring suspension of $\text{LMn}_3(\text{OAc})_3$ (100 mg, 0.084 mmol, 1 equiv) in THF (10 mL) was added a suspension of $\text{Co}(\text{OTf})_2$ (30 mg, 0.084 mmol, 1 equiv) in THF (1 mL). The mixture was stirred for 10 min, then PhIO (18.4 mg, 0.084 mmol, 1 equiv) was added as solid. Within 30 min, the mixture appeared brown and homogeneous. Reaction mixture was stirred for a total of 45 min. The mixture was stirred through a Celite pad. The THF filtrate was dried under vacuum. The dried residue was washed with benzene to remove iodobenzene side product, then the residue was resuspended in DCM and filtered through Celite. Solvent was removed from the filtrate *in vacuo*. The clean product can be afforded in 85% yield through recrystallization in DCM/ Et_2O . ^1H NMR (CD_2Cl_2 , 300 MHz): δ 182.74 (v br), 136.74 (v br), 45.99 (br), 39.23 (br), 36.45 (v br),

29.97 (br overlapped), 29.42 (br overlapped), 11.31 (br), 8.55 (m overlapped), -7.05 (br), -8.47 (br), -50.89 (v br) ppm.

Synthesis of A.4-Zn-O

To a solution of **A.2-Zn-O** (50 mg, 0.032 mmol, 1 equiv) in DCM (5 mL) was added a suspension of PRABOH₂ (6.4 mg, 0.032 mmol, 1 equiv) in DCM (0.5 mL). The mixture changed color from purple to brown-purple. The reaction mixture was stirred for 30 min and then the volatiles were removed *in vacuo*. The residue was resuspended in DCM, and the product was precipitated out in DCM/Et₂O mixture to yield oily brown purple precipitate and some white precipitate. The supernatant was discarded, and the precipitates were washed with Et₂O twice. The dried precipitates were resuspended in DCM, leaving the white precipitate insoluble in the mixture. The mixture was filtered through Celite, and the DCM filtrate was dried under vacuum. Recrystallization of the product was afforded by slow vapor diffusion of Et₂O into a concentrated DME solution. The clean product was isolated as crystals in 51% yield. ¹H NMR (CD₂Cl₂, 300 MHz): δ 109.56 (v br), 75.02 (br), 68.73 (br), 61.60 (v br overlapped), 60.49 (br overlapped), 54.09 (v br overlapped), 52.25 (m overlapped), 45.94 (v br), 46.51 (br overlapped), 43.09 (br), 38.29 (br d), 35.63 (v br), 31.40 (br), 28.50 (br), 19.44 (v br), 16.60 (br), 13.62 (br), 7.87 (m overlapped), 4.22 (br overlapped), -1.92 (br), -10.74 (br), -15.42 (br), -16.84 (br), -17.76 (br), -21.01 (br), -21.87 (br) ppm.

Synthesis of A.3-Zn-O

To a stirring solution of **A.4-Zn-O** (15 mg, 0.009 mmol, 1 equiv) in CD₂Cl₂ (1 mL) was added a solution of CoCp₂ (1.7 mg, 0.009 mmol, 1 equiv) in CD₂Cl₂ (0.5 mL). The solution immediately changed color from purple to light olive brown. The reaction was

complete within 15 min as monitored by ^1H NMR spectroscopy. The reaction mixture was dried under vacuum. The dried residue was washed 3 times with Et_2O to remove excess unreacted CoCp_2 . The isolated solid was clean (quantitative yield) and carried forward for reactivity with O_2 . ^1H NMR (CD_2Cl_2 , 300 MHz): δ 51.15 (v br), 45.29 (v br), 40.0 (m v br overlapped), 30.56 (v br), 25.82 (v br), 20.64 (v br), 7.35 (m br overlapped), -8.15 (v br overlapped), -10.92 (v br overlapped), -12.73 (v br overlapped), -14.53 (v br overlapped) ppm.

Synthesis of $\text{LMn}_3(\text{OAc})_2(\text{OTf})$

To a stirring suspension of $\text{LMn}_3(\text{OAc})_3$ (410 mg, 0.342 mmol, 1 equiv) in THF (20 mL) was added a suspension of $\text{Mn}(\text{OTf})_2 \cdot 2\text{CH}_3\text{CN}$ (67.6 mg, 0.171 mmol, 0.5 equiv) in THF (1 mL). The heterogeneous mixture was stirred for 18 h. The mixture remained heterogeneous throughout the reaction but the suspension color turned paler yellow. The suspension was filtered through Celite, and the filtrate was discarded. The insoluble solid was resuspended in DCM and filtered through Celite. The DCM fraction was dried under vacuum to yield the clean product in 97% yield. ^1H NMR (CD_2Cl_2 , 300 MHz): δ 61.33 (v br), 37.74 (v br), 10.66 (v br overlapped), 3.68 (s), 1.82 (s), -11.21 (v br) ppm.

Synthesis of A.5-S

To a suspension of $\text{LMn}_3(\text{OAc})_2(\text{OTf})$ (428 mg, 0.332 mmol, 1 equiv) in MeCN (15 mL) was added $\text{S}(\text{SiMe}_3)_2$ (0.350 mL, 1.66 mmol, 5 equiv). The initially insoluble suspension became homogeneous yellow over a few hours. The reaction mixture was stirred overnight for 18 h. Mixture was dried under vacuum, and the residue was washed with Et_2O to remove excess $\text{S}(\text{SiMe}_3)_2$. The solid was then resuspended in DCM and filtered through Celite. The DCM fraction was dried under vacuum. Recrystallization in

a mixture of MeCN/Et₂O afforded the clean product in 54% yield. ¹H NMR (CD₂Cl₂, 300 MHz): δ 41.14 (v br), 28.22 (d v br), 11.09 (b overlapped), 8.07 (v br overlapped), 6.35 (v br overlapped), 3.43 (d), -8.65 (br overlapped), -10.16 (br overlapped) ppm.

Synthesis of **A.7-Mn-F**

To a suspension of **LMn₃(OAc)₃** (40 mg, 0.033 mmol, 1 equiv) in MeCN (3 mL) was added a suspension of XeF₂ (2.8 mg, 0.0167 mmol, 0.5 equiv) in MeCN (1 mL). The mixture turned into slightly darker suspension and stirred for 1 h where the suspension appeared slightly green. The reaction mixture was then dried under vacuum. The residue was resuspended in MeCN where there was some blue insoluble solid left behind. The insoluble blue solid was resuspended in DCM. Both MeCN fraction and DCM fraction were subjected to crystallization in MeCN/Et₂O mixture and DCM/Et₂O mixture, respectively. The recrystallization of the DCM fraction via vapor diffusion of Et₂O into a DCM solution gave mostly blue green precipitate and a few light brown crystal blades. These pale brown crystals are **A.7-Mn-F**, which did not make up the majority of the material (low yield that was not quantified). ¹H NMR (CD₂Cl₂, 300 MHz): δ 61.61 (v br), 40.15 (v br), 8.44 (m br overlapped), -6.25 (v br overlapped), -10.45 (v br overlapped) ppm.

Crystallographic Information. None of the structures have been deposited to CCDC. **A.4-Zn-O** structure has been finalized and ready for CCDC deposition. The rest of the structures still need final refinements for disordered solvents, therefore, the GOF, R1, and wR2 values in Table A.1 are not finalized.

Refinement details

In each case, crystals were mounted on a glass fiber or nylon loop using Paratone oil, then placed on the diffractometer under a nitrogen stream. Low temperature (100 K) X-ray data were obtained on a Bruker APEXII CCD based diffractometer (Mo sealed X-ray tube, $K_{\alpha} = 0.71073 \text{ \AA}$). All diffractometer manipulations, including data collection, integration, and scaling, were carried out using the Bruker APEXII software.¹⁴ Absorption corrections were applied using SADABS.¹⁵ Space groups were determined on the basis of systematic absences and intensity statistics and the structures were solved by direct methods using XS¹⁶ (incorporated into SHELXTL)¹⁷ and refined by full-matrix least squares on F^2 . All non-hydrogen atoms were refined using anisotropic displacement parameters. Hydrogen atoms were placed in idealized positions and refined using a riding model. The structure was refined (weighted least squares refinement on F^2) to convergence.

Table A.1. Crystal and refinement data for complexes **A.1-Co-O**, **A.4-Zn-O**, **A.5-S**, and **A.7-Mn-F**.

	A.1-Co-O	A.4-Zn-O	A.5-S	A.7-Mn-F
empirical formula	C ₆₅ H ₄₈ Cl ₂ Co F ₆ Mn ₃ N ₆ O ₁₆ S ₂	C ₇₈ H ₇₉ F ₆ Mn ₃ N ₉ O ₁₆ S ₂ Zn	C ₆₆ H ₅₅ F ₃ Mn ₃ N ₈ O ₇ S ₂	C ₆₇ H ₈₇ Cl ₂ F Mn ₄ N ₆ O ₁₄
formula wt	1641.86	1806.81	1358.12	1510.08
T (K)	100	100	100	100
a, Å	12.3384(9)	19.565(2)	12.6255(11)	12.7888(10)
b, Å	18.7465(13)	16.6999(17)	32.947(3)	15.4002(12)
c, Å	29.537(2)	26.046(3)	14.6040(12)	19.5456(14)
α, deg	84.440(2)	90	90	86.594(2)
β, deg	82.889(2)	111.270(2)	98.5075(16)	78.660(3)
γ, deg	74.371(2)	90	90	69.316(2)
V, Å ³	6514.3(8)	7930.3(14)	6008.0(9)	3530.9(5)
Z	4	4	4	2
Cryst. system	Triclinic	Monoclinic	Monoclinic	Triclinic
space group	P-1	P 21/c	P 1 21/c 1	P-1
d _{calcd} , g/cm ³	1.674	1.513	1.501	1.420
θ range, deg	1.723– 27.578	1.117 – 30.567	2.470 - 34.445	1.413 - 39.476
μ, mm ⁻¹	1.057	0.905	0.763	0.843
abs correction	Semi-empirical from equivalents	Semi-empirical from equivalents	Semi-empirical from equivalents	Semi-empirical from equivalents
GOF ^c	1.014	1.290	0.897	0.987
R1, ^a wR2 ^b (I > 2σ(I))	0.1798, 0.3158	0.0753, 0.1688	0.1107, 0.1154	0.1318, 0.2771

$${}^a R1 = \sum ||F_o| - |F_c|| / \sum |F_o|. \quad {}^b wR2 = (\sum [w(F_o^2 - F_c^2)^2] / \sum [w(F_o^2)^2])^{1/2}. \quad {}^c GOF = S = [\sum [w(F_o^2 - F_c^2)^2] / (n-p)]^{1/2}$$

Special refinement details for **A.1-Co-O**

A.1-Co-O was recrystallized from CH₂Cl₂/Et₂O mixture. There may be some co-crystallized solvents that have not yet been modeled successfully. The structure also contains two outer-sphere trifluoromethanesulfonate counterions that were satisfactorily modeled.

Special refinement details for A.4-Zn-O

A.4-Zn-O was crystallized from DME/Et₂O mixtures. The compound crystallized with two Et₂O solvent molecules in the lattice. The Et₂O solvents and two outer sphere triflates molecules were all satisfactorily modeled.

Special refinement details for A.5-S

A.5-S was crystallized from MeCN/Et₂O mixture. Accordingly, the compound crystallized with two MeCN and one Et₂O solvent molecules in the lattice that were successfully modeled. The structure also contains one outer-sphere trifluoromethanesulfonate counterion that was satisfactorily modeled.

Special refinement details for A.7-Mn-F

A.7-Mn-F was crystallized from DCM/Et₂O mixture. The compound crystallized with two Et₂O and one DCM solvent molecules. One DCM and one Et₂O solvent molecules were modeled successfully. There is a possibility that an acetate also cocrystallized in the lattice, but this outer sphere anion has yet to be modeled.

REFERENCES

- 1 (a) Babcock, G. T.; Wikstrom, M. *Nature* **1992**, *356*, 301. (b) FergusonMiller, S.; Babcock, G. T. *Chem. Rev.* **1996**, *96*, 2889. (c) Ludwig, B.; Bender, E.; Arnold, S.; Huttemann, M.; Lee, I.; Kadenbach, B. *Chembiochem* **2001**, *2*, 392.
- 2 (a) Wydrzynski, T. J.; Satoh, K. *Photosystem II: The Light-Driven Water: Plastoquinone Oxidoreductase*; Springer: Dordrecht, the Netherlands, 2005; Vol. 22. (b) McEvoy, J. P.; Brudvig, G. W. *Chem. Rev.* **2006**, *106*, 4455. (c) Brudvig, G. W. *Philos. Trans. Royal Soc. B* **2008**, *363*, 1211.
- 3 (a) Howard, J. B.; Rees, D. C. *Chem. Rev.* **1996**, *96*, 2965. (b) Hoffman, B. M.; Lukoyanov, D.; Yang, Z. Y.; Dean, D. R.; Seefeldt, L. C. *Chem. Rev.* **2014**, *114*, 4041.
- 4 Collman, J. P.; Decreau, R. A. *Chem. Commun.* **2008**, 5065.

- 5 (a) Tsui, E. Y.; Tran, R.; Yano, J.; Agapie, T. *Nature Chem.* **2013**, *5*, 293. (b) Herbert, D. E.; Lionetti, D.; Rittle, J.; Agapie, T. *J. Am. Chem. Soc.* **2013**, *135*, 19075.
- 6 Trofimov, B. A.; Zaitsev, A. B.; Schmidt, E. Y.; Vasil'tsov, A. M.; Mikhaleva, A. I.; Ushakov, I. A.; Vashchenko, A. V.; Zorina, N. V. *Tetrahedron Lett.* **2004**, *45*, 3789.
- 7 Han, Z. 2014.
- 8 Kanady, J. S.; Tran, R.; Stull, J. A.; Lu, L.; Stich, T. A.; Day, M. W.; Yano, J.; Britt, R. D.; Agapie, T. *Chem. Sci.* **2013**, *4*, 3986.
- 9 Kamienska-Piotrowicz, E.; Stangret, J.; Szymanska-Cybulska, J. *Spectrochim. Acta. A* **2007**, *66*, 1.
- 10 Tsui, E. Y.; Day, M. W.; Agapie, T. *Angew. Chem. Int. Ed.* **2011**, *50*, 1668.
- 11 Tsui, E. Y.; Kanady, J. S.; Day, M. W.; Agapie, T. *Chem. Commun.* **2011**, *47*, 4189.
- 12 Kanady, J. S.; Tsui, E. Y.; Day, M. W.; Agapie, T. *Science* **2011**, *333*, 733.
- 13 Goldcamp, M. J.; Edison, S. E.; Squires, L. N.; Rosa, D. T.; Vowels, N. K.; Coker, N. L.; Bauer, J. A. K.; Baldwin, M. J. *Inorg. Chem.* **2003**, *42*, 717.
- 14 APEX2, Version 2 User Manual, M86-E01078, Bruker Analytical X-ray Systems, Madison, WI, June 2006.
- 15 Sheldrick, G. M.; 2008/1 ed.; University of Göttingen, Germany: 2008.
- 16 Spek, A. L. "PLATON – A Multipurpose Crystallographic Tool, Utrecht University", Utrecht, the Netherlands, 2006.
- 17 Sheldrick, G. M. *Acta Crystallogr. A* **2008**, *D65(2)*, 148.

APPENDIX B

SYNTHESIS OF [CO₃O]-CLUSTERS AS PRELIMINARY ROUTES TO BUILD [CO₄O₄] CUBANE

ABSTRACT

Multiple synthetic routes have been approached to build a $[\text{Co}_4\text{O}_4]$ -cubane complex relevant to heterogeneous water oxidation catalysis. Taking ligand L to build the tricobalt core $[\text{LCo}_3(\text{O}_2\text{CR})_3]$ and treatment with iodosobenzene, peroxides, and other strong oxidants that can also serve as an oxygen atom source in the presence of one equivalent of Co^{2+} salt yields different tricobalt mono-oxo complexes with no fourth cobalt incorporation. Different attempts to assemble the cubane are discussed. This work is ongoing.

INTRODUCTION

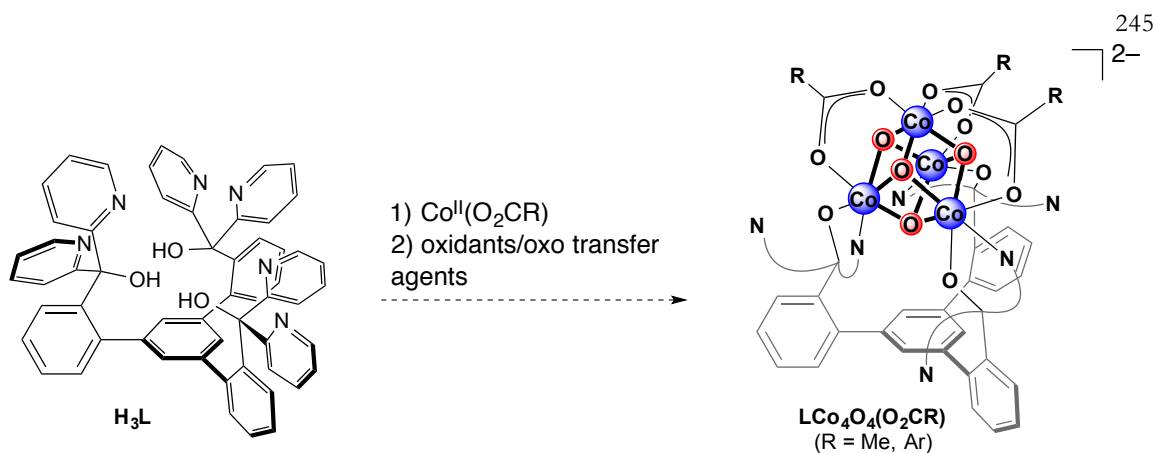
With the currently growing global energy demand, a new technology to obtain solar fuels derived from renewable sources is desirable. Therefore, the development of efficient water oxidation catalysts made from earth-abundant metals for the oxygen-evolving half reaction (eq. 1) has been a popular area of research.



A structural component now recognized as critical for oxygen evolution reaction electrocatalysis is the transition-metal-oxo cubical core such as the $[\text{Mn}_4\text{O}_4]^{7+}$ core.¹ Other cubical cores reported to catalyze water oxidation include $[\text{Mn}_3\text{O}_4]$,² $\text{MMn}_{2/3}\text{O}_4$,³ NiO_x ,⁴ $[\text{Co}_4\text{O}_4]$,⁵ $[\text{Co}_3\text{O}_4]$,⁶ and non-crystalline solid of $\text{CoO}_x(\text{CoPi})$.⁷ These cubical cores resemble the natural photosynthetic enzyme Photosystem II (PSII), composed of a CaMn_3O_4 cluster bridged by an oxo to the fourth Mn atom. While nature uses Mn in the PSII oxygen evolving complex (OEC), there are a number of examples where Co-based systems replicate the catalytic performance of Mn-based materials.⁸

A ligand framework consisting of a 1,3,5-triarylbenzene core with pendant six pyridines and three alcohol groups (**H₃L**, Scheme 1)⁹ has been successfully utilized to support a heterometallic cluster $\text{LMn}_3\text{CaO}_4(\text{OAc})_3$ ¹⁰ to serve as a synthetic model of $[\text{CaMn}_3\text{O}_4]$ subsite of the PSII oxygen evolving complex. This project targets the synthesis of a Co_4O_4 -cluster supported by **L** by either building the cluster from the bottom-up approach (Scheme 1) or by ligand exchange of previously synthesized cobalt-oxo cubane.¹¹ Electrochemical, spectroscopic, and OER catalytic reactivity studies will follow the synthesis of $[\text{LCo}_4\text{O}_4(\text{O}_2\text{CR})_3]^{n+}$.

Scheme 1. Targeting a synthetic $[\text{Co}_4\text{O}_4]$ cubane supported by **L**

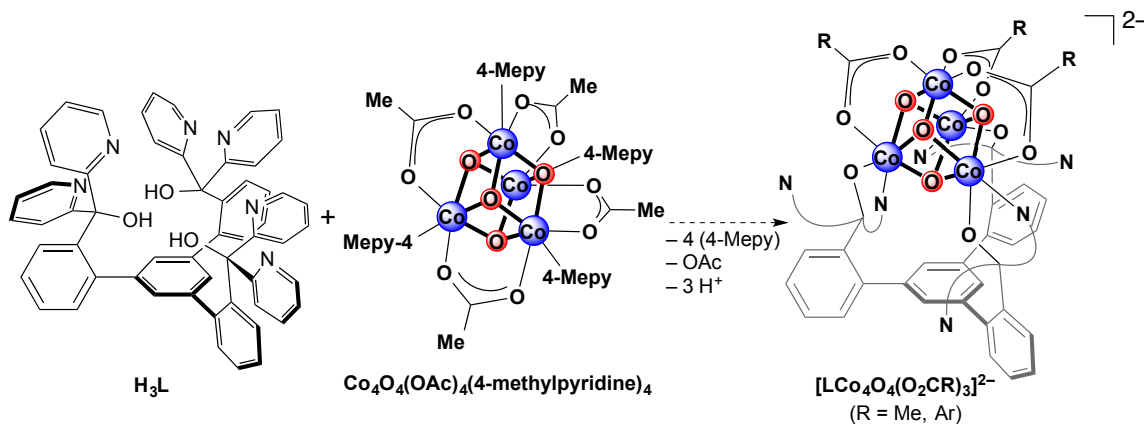


RESULTS AND DISCUSSIONS

B.1 Ligand exchange on the preformed $[\text{Co}_4\text{O}_4]$ -cubane with **L**

The ligand **H₃L** was synthesized following literature procedure.⁹ The first rational approach to obtain the desired **H₃L**-supported Co_4O_4 cubane was to add the ligand to a preformed cubane complex, $\text{Co}_4\text{O}_4(\text{OAc})_4(4\text{-methylpyridine})_4$ (OAc = acetate), previously reported by Das and coworkers.¹¹ (Scheme 2). Upon leaving the reaction mixture to stir for a few days at room temperature in tetrahydrofuran (THF), no reaction was observed. The addition of triethylamine to this mixture as a proton scavenger through the course of the reaction did not improve the reactivity either. Increasing the temperature of the reaction mixture also yields no reaction with the recovery of the starting reagents. Using the lithium salt of the ligand (**Li₃L**) by first deprotonation using LiHMDS (HMDS = hexamethyldisilazide) and then adding to the preformed cobalt cubane also yielded no reaction. The preformed cubane did not undergo ligand exchange with **L**, likely due to the non-labile acetates and pyridines bound to the Co^{III} centers.

Scheme 2. First approach to obtain the target complex by the addition to $\mathbf{H}_3\mathbf{L}$ to $\text{Co}_4\text{O}_4(\text{OAc})_4(4\text{-methylpyridine})_4$

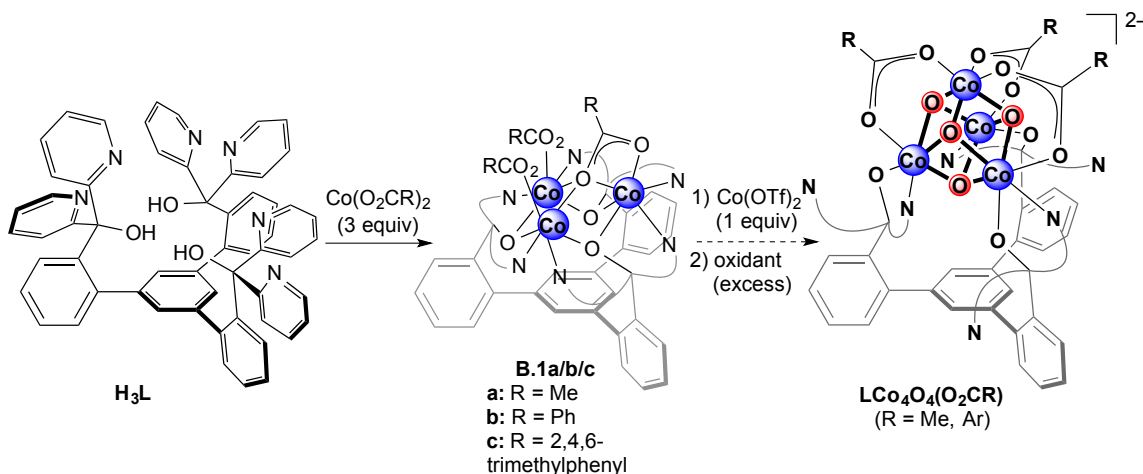


To further test this hypothesis, an equivalent of trimethylsilylchloride (Me_3SiCl) was added to the preformed cobalt-oxo cubane to see whether a chloride can replace an acetate. This route may allow the alkoxide arm of $\mathbf{Li}_3\mathbf{L}$ to replace the chloride and produce lithium chloride as the entropically favored side-product. Once one alkoxide arm is bound to a cobalt center, it should allow for more facile ligand substitutions by the other two alkoxide groups of \mathbf{L} . Treatment of the preformed cobalt-oxo cubane with Me_3SiCl produced a mixture of species that are different from the starting material, as monitored by ^1H NMR spectroscopy, but the proton signal corresponding to trimethylsilyl acetate (Me_3SiOAc) was observed. Assuming that the mixture may contain mono-, di-, tri-, and tetra-substituted chloride cobalt-cubane, the product was added to $\mathbf{Li}_3\mathbf{L}$. Monitoring the reaction via proton NMR over two days shows no reaction where all starting materials were recovered. From these observations, the route to obtain the desired $[\text{LCo}^{\text{III}}_4\text{O}_4(\text{O}_2\text{CR})_3]^{2-}$ will require building the cluster starting from the \mathbf{L} itself instead of using a preformed cobalt-oxo cubane complex.

B. 2 Building a $[Co_4O_4]$ -cluster supported by **L**

Analogous to the published procedure to synthesize the $LMn_3CaO_4(OAc)_3$ cubane,^{10,12} a similar approach has been taken to build the target complex $[LCo^{III}_4O_4(O_2CR)_3]^{2-}$. The proposed route is to first synthesize a tricobalt-triscarboxylate moiety (**B.1**) followed by the addition of an equivalent of cobalt (II) precursor and excess oxidizing agent to yield the desired cobalt-oxo cubane (Scheme 3). The syntheses of the tricobalt-triscarboxylate complexes **B.1a-c** were adapted from a published protocol¹² but without the addition of an external base (Scheme 3). Three different cobalt (II) carboxylates ($Co(O_2CR)_2$), namely cobalt (II) acetate, cobalt (II) benzoate, and cobalt (II) 2,4,6-trimethylbenzoate, were used as the Co^{II} salts to prepare **B.1a-c**, respectively, by adding three equivalents of $Co(O_2CR)_2$ to **H₃L** in dichloromethane. Complexes **B.1a-c** can be recrystallized from the vapor diffusion of Et_2O into a concentrated CH_2Cl_2 solution.

Scheme 3. Synthesis of tricobalt-tricarboxylate complexes (**B.1a-c**) and proposed synthetic step to make the target complex $[LCo^{III}_4O_4(O_2CR)_3]^{2-}$



Varying the sizes of the carboxylate group may provide information on how the steric bulk of the substituents affects the structural moiety of the product. This effect was seen through the comparison of proton NMR spectra of complex **B.1a,b** to that of **B.1c**. While the acetate and benzoate version, **B.1a** and **B.1b** respectively, share similar broad, distinct peaks in the paramagnetic region of the ^1H NMR spectra (Figure 1), the spectrum corresponding to complex **B.1c** shows significantly broader chemical shift features with less distinctive peaks.

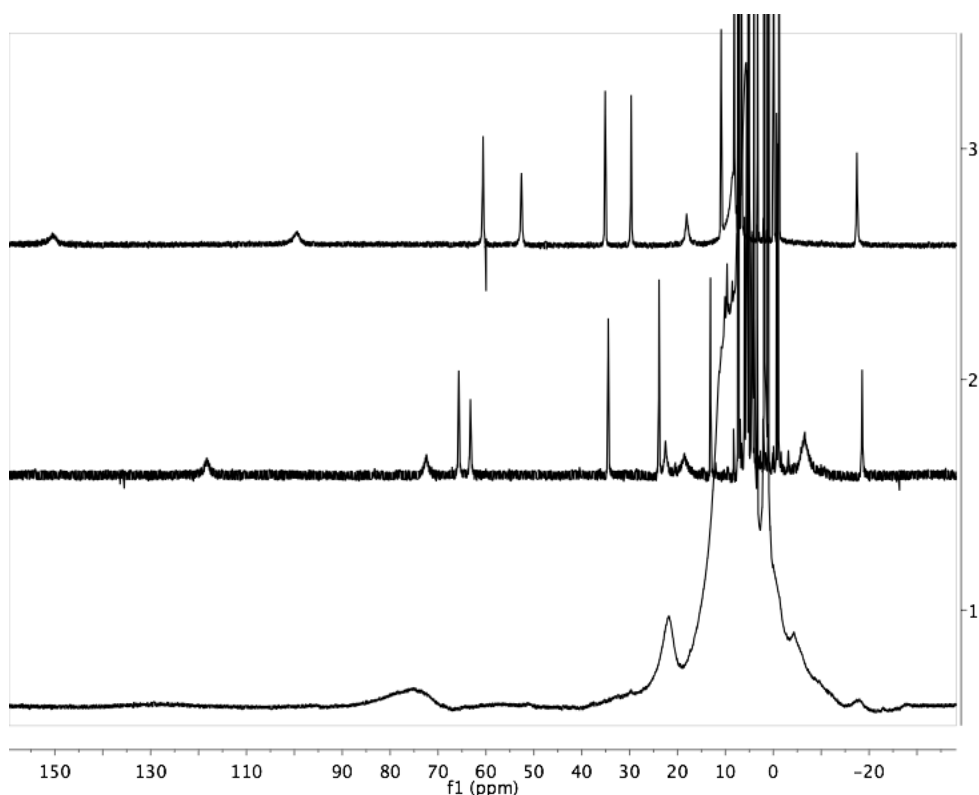


Figure 1. ^1H NMR spectra (300 MHz, CDCl_3) of complexes **B.1a** (top), **B.1b** (middle), and **B.1c** (bottom).

The more bulky mesityl substituent on the carboxylate group may prevent the complex to have three bound carboxylate groups on the three Co centers, and instead have one or two carboxylate groups bound to the Co center(s) while the rest may be the

outer sphere counterion(s). Structural characterization by XRD on compound **B.1c** has yet to be obtained, however, a crystal structure of a **B.1** variant with carboxylates ligand, each bearing a biphenyl moiety, supports the previously discussed hypothesis; this solid-state structure was reported by David E. Herbert. The ESI-MS analysis on **B.1c** results in a spectrum displaying peaks with m/z of 1358.3 $[\text{LCo}_3(\text{O}_2\text{CR})_2]^+$ and 1195.2 $[\text{LCo}_3(\text{O}_2\text{CR})]^+$ (R = mesityl) consistent with a triscobalt complex with two and one carboxylate(s) respectively. This ESI-MS result is analogous with those obtained from crystalline material of **B.1a** and **B.1b** that have been previously reported.¹²

The first attempt to build a $[\text{Co}_4\text{O}_4]$ -cluster involved treatment of complex **B.1a** with an equivalent of $\text{Co}(\text{OTf})_2$ (OTf = trifluoromethanesulfonate) in tetrahydrofuran (THF) followed by the addition of an equivalent of oxidant such as iodosobenzene (PhIO) or potassium superoxide (KO_2). This reaction generated a mixture of species by ^1H NMR spectroscopy. One of the species from the DCM fraction formed single crystals and was structurally identified as the tricobalt(II) complex with two of the acetates exchanged with the triflates, or $\text{LCo}_3(\text{OAc})(\text{OTf})_2$ (**B.2a**), by a XRD study first reported by David E. Herbert. In this case, **B.2a** precipitated out upon its formation in THF, thus, preventing it from oxidation by the oxidants in a heterogeneous mixture. The synthesis of **B.2a** can be directly achieved by the addition of $\text{Co}(\text{OTf})_2$ to **B.1a** in THF or DCM (Scheme 4), indicative of facile acetates exchange in the presence of triflates when the Co centers are Co^{II} . This reaction showed a slight color change from red-purple to violet solution and could be monitored by ^1H NMR spectroscopy (Figure 2). The same ligand-exchange event seems to apply as well to **B.1c** when in solution with an equivalent of $\text{Co}(\text{OTf})_2$. Although single crystals of this product (**B.2c**) have not

been successfully grown for XRD studies, the ^1H NMR spectrum displays a similar trend in comparison to **B.2a** (Figure 2).

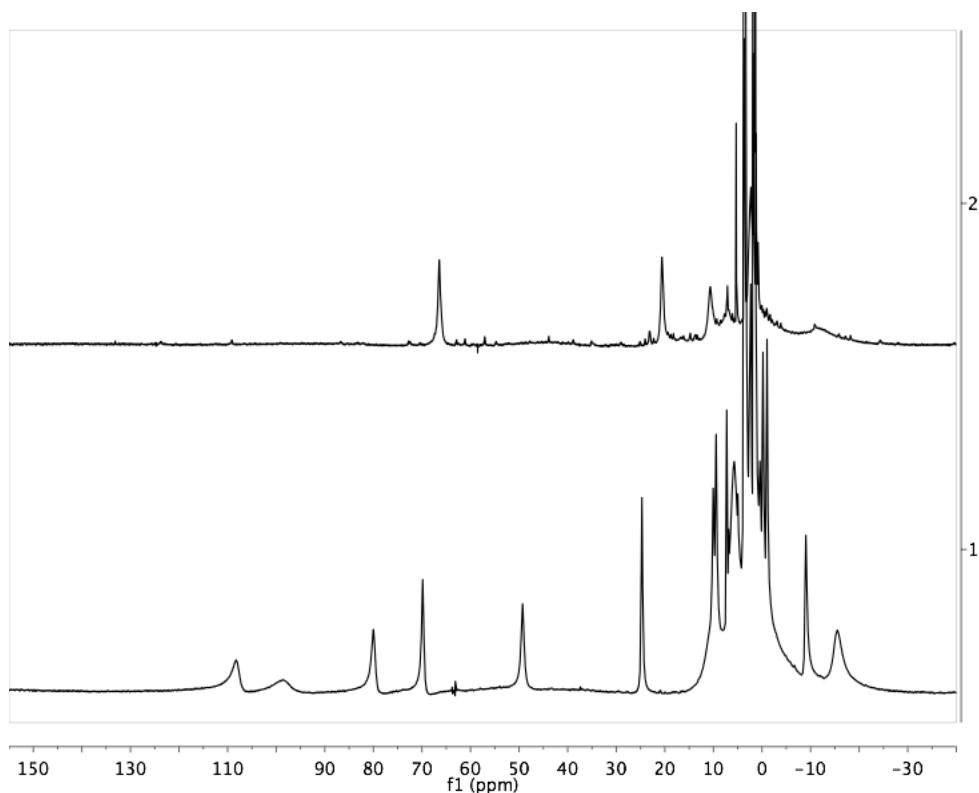
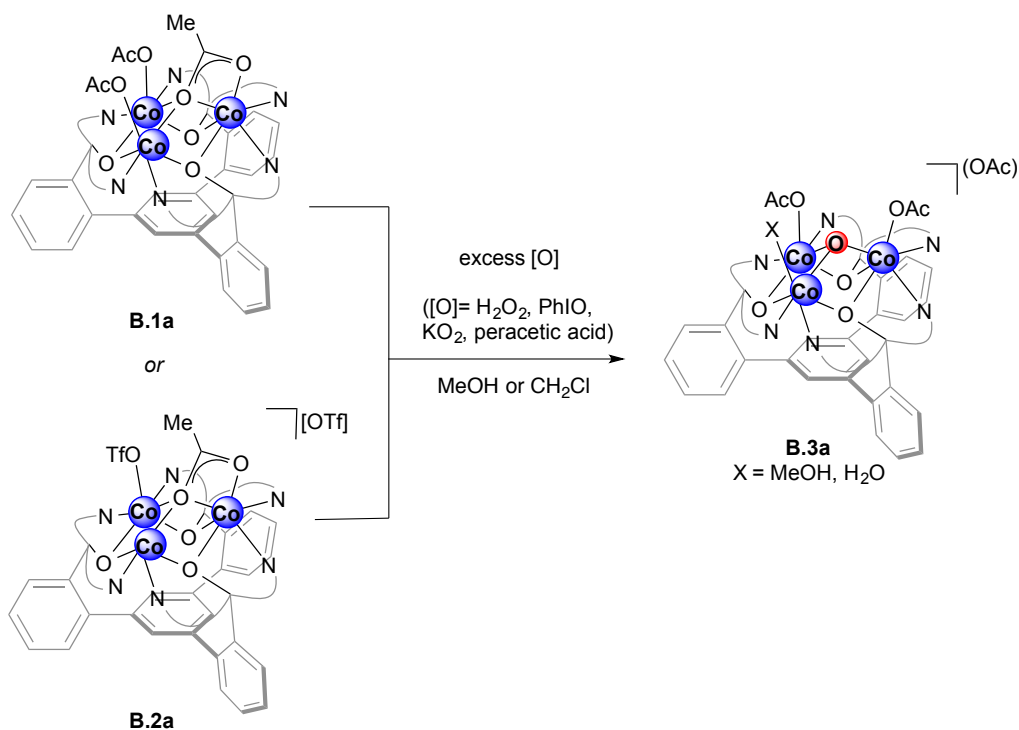


Figure 2. ^1H NMR spectra of **B.2a** and **B.2c**.

Several attempts to oxidize the mixtures of complex **B.1** and $\text{Co}(\text{OTf})_2$ have been done in DCM for **B.1a** and THF for **B.1c**, where **B.2a** and **B.2c** are soluble respectively. A strongly coordinating solvent such as methanol (MeOH), which may also bind to the cobalt in this case, has also been used. The reaction of **B.1a** with $\text{Co}(\text{OTf})_2$ in the presence of two or more equivalents of PhIO in MeOH resulted in the isolation of a species that corresponds to a mono-oxo species, $[\text{LCo}_3\text{O}(\text{OAc})_2\text{X}](\text{OAc})$ or **B.3a** (Scheme 4, X= MeOH, H_2O) in $\sim 20\%$ yield by recrystallization. Complex **B.3a** could also be isolated from the reaction of **B.1a** with excess hydrogen peroxide, potassium superoxide (KO_2), oxone, dimethyldioxirane, or peracetic acid in MeOH (Scheme 4),

albeit still in low yield (~10%). Running the reaction in a strongly coordinating solvent like MeOH seems to affect the OTf/OAc ligand-exchange equilibrium, as evidenced by the ^1H NMR spectra of **B.3a** that look distinct in CD_3OD vs. CDCl_3 (Figure 3) since methanol can also bind to cobalt as a ligand.

Scheme 4. Reaction of **B.1a** or **B.2a** with oxidants “[O]” to yield the mono-oxo species **B.3a**



The solid-state structure of **B.3a** was confirmed via a XRD study of the single crystals of **B.3a** obtained from the recrystallization via vapor diffusion of diethyl ether into a methanol solution (Figure 4). Comparison of the Co–O(oxo), Co–O(hydroxy), Co–N(pyridine), Co–OAc, and Co–OH₂ bond distances to the literature reports was done to assign the Co centers’ oxidation states.¹¹⁻¹³ Summary of the relevant bond distances within the structure of **B.3a** is summarized in Table 1. Based on the Co–O bond distances, complex **B.3a** was isolated as a mono-oxo species with mixed valent

$\text{Co}^{\text{III}}\text{Co}^{\text{II}}_2$ centers. This result was unexpected because only one Co out of three was oxidized by one e^- in the presence of excess oxidant. It is worthy to note that using $\text{Co}(\text{NO}_3)_2(\text{H}_2\text{O})_6$ as the cobalt precursor instead of $\text{Co}(\text{OAc})_2$ yielded **B.3a**(NO_3) (not pictured) where all the acetates in **B.3a** are nitrates instead.

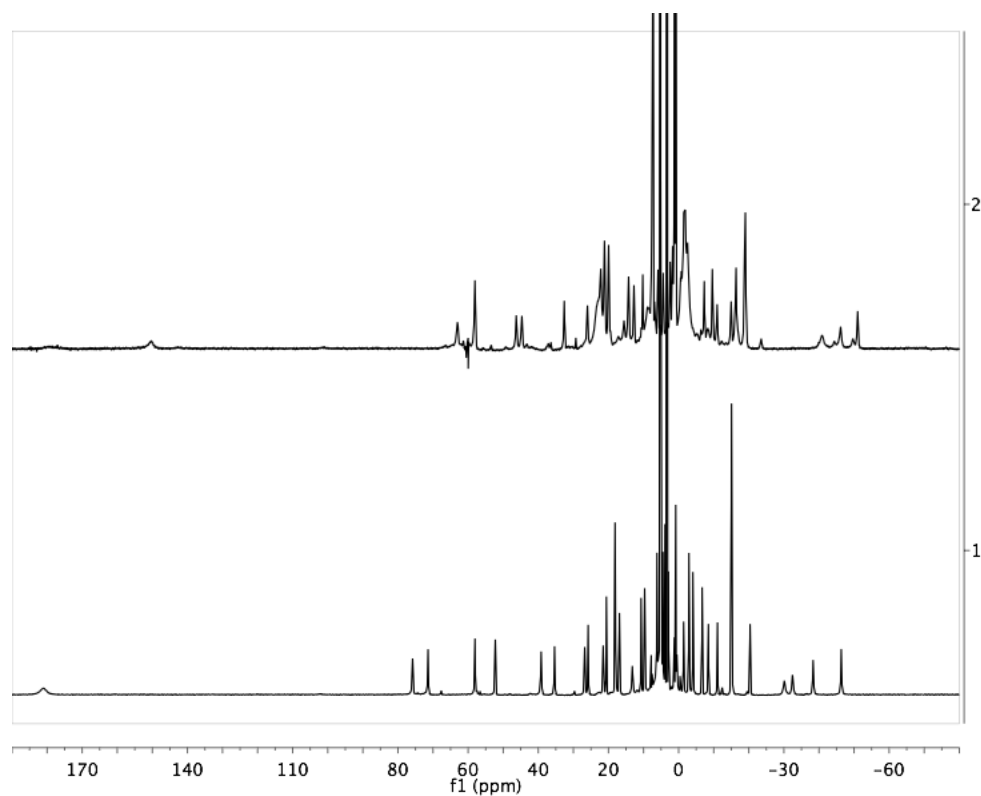


Figure 3. ^1H NMR spectra of **B.3a** in CDCl_3 (top) and CD_3OD (bottom).

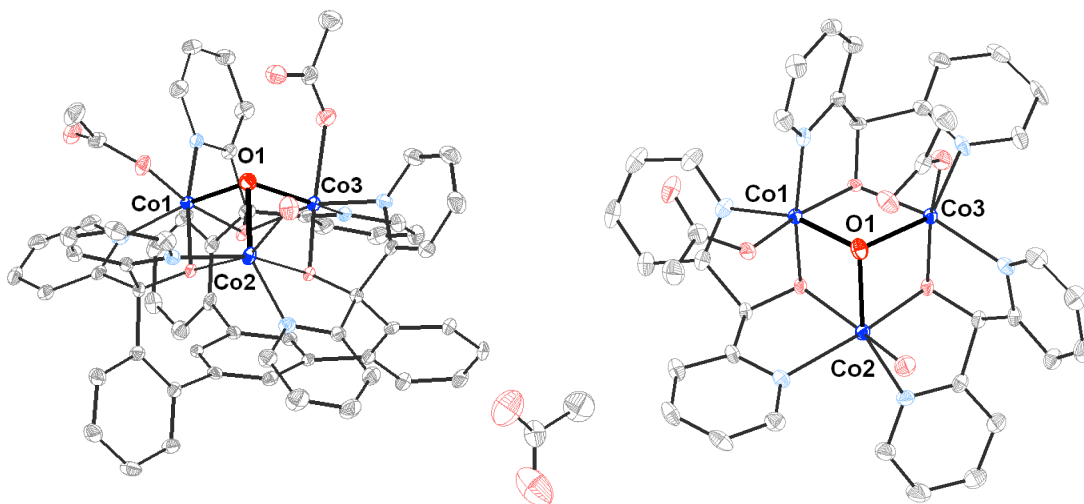


Figure 4. Crystal structure of complex **B.3a**. (*Left*) side view; (*right*) top view with the triarylbenzene core of **L** truncated. Hydrogen atoms and solvents are omitted for clarity.

Table 1. Summary of relevant bond distances of the solid-state structure of **B.3a**

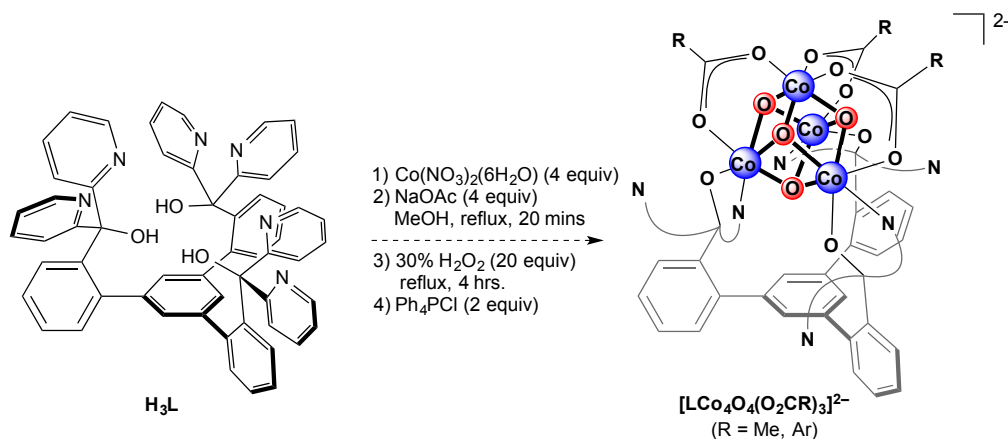
Bond	Distances (Å)
Co1–O1	1.912
Co2–O1	2.184
Co3–O1	2.020
Co1–OAc	1.935
Co2–OH ₂	2.088
Co3–OAc	2.159

For most of the oxidation reactions discussed above, similar protocols have been carried out with **B.1c** as the starting material instead of **B.1a** (Scheme 4). One advantage of having a bulkier carboxylate as opposed to an acetate is the full solubility of **B.1c** in THF. Reactions of **B.1a** that were performed in dichloromethane were instead run in THF in the case for using **B.1c** as the starting metal complex. Without any XRD study, the resulting proton NMR spectra are still inconclusive in terms of

determining the structural identity of the products. Thus far, no single crystal suitable for a XRD study has been obtained for any of the reactions involving **B.1c** as the starting material.

Another approach has been attempted to build the target cluster by following Das and coworkers' general self-assembly approach for the synthesis of **Co₄O₄(OAc)₄(4-methylpyridine)₄** (Scheme 5).¹¹ Addition of Co(NO₃)₂•6H₂O (4 equiv) and sodium acetate (4 equiv) under refluxing conditions in MeOH for 20 min resulted in a purple red solution similar in color to that of **B.1a**. To the mixture was added excess hydrogen peroxide, in which the solution turned green then brown, followed by refluxing the mixture for an additional 4 h or overnight. Tetraphenylphosphonium chloride (Ph₄PCl) was added to the mixture to aid in crystallization/precipitation of the product. Unfortunately this approach was not successful in building the desired L-supported cobalt-oxo cubane and instead formed a complex structurally analogous to **B.3a** (with nitrate ligands and counterion instead of acetates) as indicated by ¹H NMR spectroscopy and XRD data. Again, methanol might play an important role in the ligand exchange process, possibly preferentially binding to the cobalt in solution as opposed to the acetates that are hypothesized to affect structural rigidity and integrity during the cubane cluster formation. Another aspect to consider was that the tricobalt-triscarboxylate complex (**B.1**) could have been made first *in situ* judging by the mixture color, and was the stable product such that the fourth cobalt was not incorporated prior to oxidation. Other attempts include changing the carboxylates of cobalt to benzoates, 2,4,6-trimethylbenzoates, and 4-*tert*-butylbenzoates, and all variation yielded the [Co₃O] species by ¹H NMR spectroscopy.

Scheme 5. Self-assembly approach using Chakrabarty's method to obtain $[\text{Co}_4\text{O}_4]$ cluster



At this stage, the mechanism by which **B.3a** is preferentially formed and how the target $[\text{Co}_4\text{O}_4]$ could be attained is still unclear. Unlike the $[\text{CaMn}_3\text{O}_4]$ cubane (**10-Ca**) synthesized by Jacob S. Kanady,¹⁰ perhaps for the case of cobalt, ligand rearrangements are more difficult. This may not be too surprising if the presence of a substitutionally inert Co^{III} center prevents facile ligand rearrangements/reorganization from generating a cubane structure like the case of the Mn complexes.

The experimental challenge to obtain the target cubane in this system is that the tricobalt species **B.1** could not be oxidized past a single oxo-transfer and a one-electron oxidized $\text{Co}^{\text{III}}\text{Co}^{\text{II}}_2$ system. It is worth noting that the more highly oxidized species, if synthesized in the reaction mixture, have not been successfully isolated or structurally characterized.

To gain more insights on the currently isolated and crystallographically characterized species, cyclic voltammetry (CV) studies were done to determine the oxidation potential of complexes **B.1a**, **B.2a**, and **B.3a** (Figure 5). The oxidation potentials found for complex **B.1a** are at +0.67 V, +0.95 V, and +1.27 V (vs. Fc/Fc^+);

the oxidation potentials for complex **B.2a** are at +0.58 V, +0.80 V, and +1.20 V (vs. Fc/Fc⁺), while those for complex **B.3a** are at +0.61 V, +0.92 V, and +1.25 V (vs. Fc/Fc⁺). All observed redox events are non-reversible, which is expected since the complexes should undergo structural rearrangements or ligand exchange upon oxidation.

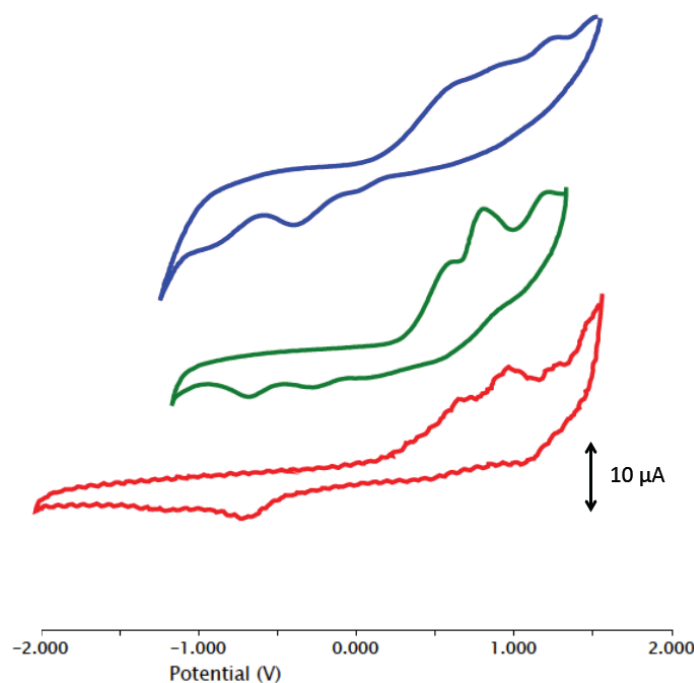


Figure 5. CV (vs. Fc/Fc⁺) of complexes 1 mM solution of **B.1a** (red, done by Jacob S. Kanady), **B.2a** (green), and **B.3a** (blue) at 100 mV/s on glassy carbon electrode in CH₂Cl₂ containing 0.1M Bu₄NClO₄.

The oxidation potentials for all three complexes are similar to one another (within ~100 mV), however, these potentials are much more positive compared to Das' cobalt-oxo cubane system with the oxidation potential from 4Co^{III} to 3Co^{III}Co^{IV} at approximately +0.23 V (vs. Fc/Fc⁺). The relatively high oxidation potentials may be one of the reasons why further oxidation of these complexes is challenging. To test this

hypothesis, using a stronger oxidizing reagent may be able to oxidize more than one Co center of **B.1a**.

Some of these oxidizing agents that were used include ceric ammonium nitrate (CAN) and oxone. Treatment of **B.1a** with excess CAN resulted in an intractable mixture of paramagnetic species indicated by ^1H NMR spectroscopy. The reaction of **B.1a** with excess CAN in the presence of one equivalent of $\text{Co}(\text{OTf})_2$ and 4 equivalents of tetrabutylammonium hydroxide (TBAOH) as an oxo-source yields a different paramagnetic NMR spectrum of multiple species, albeit with no major product observed. Using a different oxidizing agent, treatment of **B.1a** with an equivalent of $\text{Co}(\text{OTf})_2$ and excess oxone yielded a mixture of species by ^1H NMR spectroscopy as well. All these attempts to oxidize the **B.1a** with stronger oxidizing agents seem to yield intractable mixtures, yet efforts to obtain single crystals suitable for XRD studies have been unsuccessful. This alternative route is no longer pursued due to the difficulty in obtaining pure products.

With the lack of success in building higher nuclearity tetracobalt cluster, a different approach was conducted by first synthesizing a tricobalt complex with bound triflates as opposed to carboxylates in **B.1a**. It is envisioned that a tricobalt species with the less strongly bound triflates will more readily react with an oxo-transfer oxidants in the presence of one equivalent $\text{Co}(\text{OTf})_2$ and undergo ligand rearrangements such that subsequent addition of carboxylates may generate the target cubane. The protocol used for this reaction is treatment of the deprotonated ligand **Li₃L** with three equivalents of $\text{Co}(\text{OTf})_2$ in THF (Scheme 6).

Scheme 6. Synthesis of **B.4**

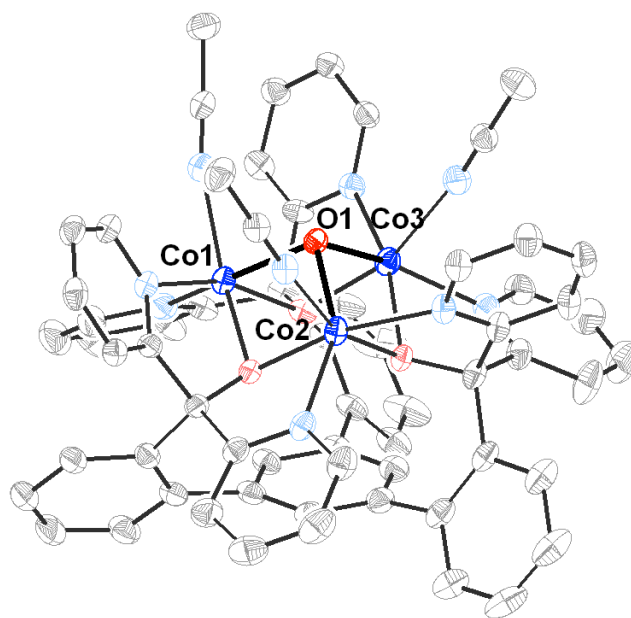
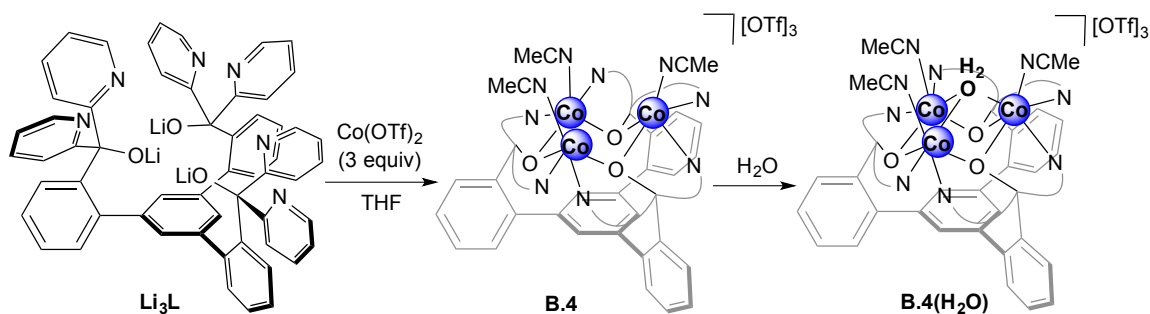


Figure 6. Solid-state structure of **B.4(H₂O**). Hydrogen atoms and outer-sphere anions are omitted for clarity.

The product that recrystallized via vapor diffusion of diethyl ether into MeCN under air yielded **B.4(H₂O**). A XRD of the single crystals of **B.4(H₂O**) shows that three terminal acetonitrile and one μ_3 -H₂O ligands are bound to the cobalt centers while the triflate anions remain outer sphere (Figure 6). The μ_3 -H₂O ligand presumably originated from the moisture in air. No crystalline material of **B.4** without the μ_3 -H₂O ligand was obtained anaerobically in the glovebox after multiple attempts. The ¹H NMR

spectra of complex **B.4** and crystalline **B.4(H₂O)** in CD₃CN are identical. Therefore, although no XRD data on **B.4** without the water ligand has been obtained yet, **B.4(H₂O)** is actually **B.4** that cocrystallized with a H₂O bound.

The crystal structure of **B.4(H₂O)** (Figure 6) shows a “ μ_3 -oxygen” ligand that bridges to all three Co centers. The Co–(μ_3 -O) bond distances are relatively similar to one another: 2.058, 2.069, and 2.077 Å, consistent with all Co^{II} centers. The red color of the crystals also suggests the presence of low valent, Co^{II}₃ species. Balancing the charges within the complex and the three outer sphere triflate counterions, the “ μ_3 -O” moiety is assigned as μ_3 -H₂O instead of an oxo or hydroxo. This oxidation state assignment is also based the absence of strong oxidizing agent during the reaction, and oxygen was found unable to oxidize **B.1** Co^{II}₂ complexes. To further support that the “ μ_3 -O” ligand is water instead of hydroxo, an equivalent of aqueous tetrabutylammonium hydroxide (TBAOH) was added to the solution of **B.4**. By ¹H NMR spectroscopy, the resulting NMR spectrum of the product from the TBAOH reaction did not match the NMR spectrum of **B.4(H₂O)**. Further studies using **B.4** as a starting tricobalt precursor are still ongoing.

B.3 Attempts to build [Co₃N] cluster

Another goal of this project is to build a series of tricobalt-triscarboxylate moiety capped by different μ_3 -functional group (e.g., oxo, hydroxo, imido, oxo-M (M = Zn, Ca, Sr, Na)). To date attempts to synthesize an imido-capped tricobalt complex have been unsuccessful. The addition of an equivalent of tetrabutylammonium azide (TBAN₃) to complex **B.1d** where the carboxylate group is *para-tert*-butylbenzoate (instead of acetate in **B.1a**) in THF yields a mixture of species, which upon

recrystallization gave cleanly the starting tricobalt complex. Raising the temperature of the same reaction and exposure to UV-irradiation did not assist in installing an azide group to replace a carboxylate ligand bound to a Co center, nonetheless forming a capping imide to three Co centers.

A different reaction attempted was the addition of excess ammonia to **B.1** followed by treatment of an excess oxidant (CAN). The ammonia reaction was left overnight at room temperature to give an orange suspension with white cloudy precipitate. Upon removal of the solvent under vacuum, the dried residue was a pink solid. The proton NMR spectrum of the reaction displayed an intractable mixture of species. It is unclear at this point whether a tricobalt-imido complex can be synthesized.

CONCLUSIONS AND FUTURE DIRECTIONS

Numerous approaches have been taken to obtain the desired **L**-supported $[\text{Co}_4\text{O}_4]$ cluster, however the successful assembly of the target complex has not been achieved yet. Due to the recurring formation of **B.3a** despite the different approaches and oxidants used, optimizing the yield for the production of the tricobalt mono-oxo complex (**B.3**) for use as a starting material will be done. Cyclic voltammetry studies show that the oxidation potentials of the **B.1a**, **B.2a**, and **B.3a** complexes are relatively high, thus, consistent with the difficulty to oxidize these species past $\text{Co}^{\text{III}}\text{Co}^{\text{II}}_2$. The synthesis of a tricobalt complex without any carboxylate ligand can be achieved by treating the deprotonated ligand, **Li₃L**, with $\text{Co}(\text{OTf})_2$ to generate **B.4**. Studies on using **B.4** as starting tricobalt species to build the target $[\text{Co}_4\text{O}_4]$ cluster are still ongoing. Similar to the mono-oxo tricobalt species, a μ_3 -imido-capped tricobalt species is also targeted by treating **B.1** with azide or ammonia and an oxidant. Characterization of this

product is still in progress. Ultimately, if **H₃L** is proven incapable of supporting a [Co₄O₄] cluster, a different ligand framework must be synthesized to counter this problem. A proposed ligand design that might solve this challenge is by having one pyridine group instead of two attached to each of the aryl arm.

EXPERIMENTAL SECTION

All reactions were performed aerobically. Unless indicated otherwise, all chemicals were used as received. Methylene chloride- d_2 and chloroform- d_1 were purchased from Cambridge Isotopes. For glovebox use, the NMR solvents were dried over calcium hydride, and vacuum transferred prior to use. 1,3,5-tris(2-di(2'-pyridyl)hydroxymethylphenyl) benzene (**H₃L**) was prepared using previously published procedures.⁹ Iodosobenzene (PhIO),¹⁴ Co(OTf)₂,¹⁵ and cobalt(II)(2,4,6-trimethylbenzoate)₂¹⁶ were prepared according to literature procedures. ¹H NMR spectra were recorded on Varian Mercury 300 at room temperature.

Synthesis of B.1a-c

Representative procedure is given for **B.1a**. Syntheses of **B.1b** and **B.1c** were carried out in an identical manner except using a different cobalt(II) source, namely Co^{II}(O₂C₇H₅)₂ (Co^{II}(benzoate)₂) and Co^{II}(O₂C₁₀H₁₁)₂ (Co^{II}(2,4,6-trimethylbenzoate)₂), respectively.

B.1a: To a solution of **H₃L** (1 g, 1.16 mmol) in CH₂Cl₂ (20 mL) was added Co(OAc)₂ · 4H₂O (870 mg, 3.50 mmol). The resulting suspension was stirred at room temperature for 15 h to give a homogeneous, red-purple solution. Solvent was removed *in vacuo* to give a purple residue. The residue was washed with diethyl ether (Et₂O) to remove the carboxylic acid side product. Recrystallization via vapor diffusion of Et₂O into CH₂Cl₂ afforded clean product in 85% yield. ¹H NMR (300 MHz, CDCl₃) δ 150.5 (v br), 99.3 (v br), 60.5 (br), 52.6 (v br), 35.1 (br), 29.7 (br), 18.06 (v br), 10.9 (br), 8.5 (v br), 8.12 (br), 6.61 (br), -0.06 (br), -1.19 (br), -17.5 (br) ppm.¹²

B.1b: ^1H NMR (300 MHz, CDCl_3) δ 118.4 (v br), 72.5 (v br), 65.7 (br), 63.2 (br), 34.5 (br), 23.9 (br), 22.5 (v br), 13.1 (br), 7.33 (br), 6.0 (br), 5.6 (br), 4.5 (v br), -0.68 (br), -1.03 (br), -6.6 (v br), -18.54 (br) ppm.

B.1c: ^1H NMR (300 MHz, CDCl_3) δ 75.6 (v br), 21.9 (v br), 5.7 (v br), 4.0 (br), 3.4 (br), 2.0 (br), 1.2 (br) ppm.

Synthesis of **B.2a** and **B.2c**

Representative procedure is given for **B.2a**. Synthesis of **B.2c** was carried out in an identical manner except using **B.1c** as starting material and THF as solvent.

B.2a: To a red-purple solution of **B.1a** (38 mg, 0.031 mmol) in CH_2Cl_2 (3 mL) was added $\text{Co}(\text{OTf})_2$ (11.2 mg, 0.031 mmol) to make a suspension. The suspension quickly became homogeneous and turned color to violet. Solvent was removed *in vacuo* to give a purple residue. Recrystallization via vapor diffusion of Et_2O into CH_2Cl_2 afforded fuchsia crystals. ^1H NMR (300 MHz, CD_2Cl_2) δ 66.6 (br), 45.8 (v br), 20.7 (br), 10.7 (br), 7.2 (v br), 3.7 (br), 2.8 (v br), 2.4 (v br), 1.8 (br), 1.3 (br), 0.86 (br), -11.4 (v br) ppm. ^{19}F NMR (282 MHz, CD_2Cl_2) δ -65.74 ppm.

B.2c: ^1H NMR (300 MHz, CDCl_3) δ 108.2 (v br), 98.7 (v br), 80.0 (v br), 69.8 (v br), 49.3 (v br), 24.7 (v br), 10.1 (v br), 9.5 (br), 5.8 (v br), 3.6 (br), 2.5 (br), 2.2 (br), 1.74 (br), 1.4 (br), 0.43 (v br), 0.19 (v br), -1.0 (v br), -9.0 (v br), -15.5 (v br) ppm. ^{19}F NMR (282 MHz, CDCl_3) δ -76.99 ppm.

Synthesis of **B.3a**

To a red-purple solution of **B.1a** (20 mg, 0.017 mmol) in MeOH (3 mL) was added PhIO (7.3 mg, 0.033 mmol). The resulting suspension turned homogeneous within 1 h and the color changed to green-brown. Solvent was removed *in vacuo* to give a green-

brown residue that was recrystallized from MeOH/Et₂O to give dark green-brown crystals as the clean product in 20% yield. ¹H NMR (300 MHz, CD₃OD) δ 180.0 (v br), 75.8 (br), 71.4 (br), 58.0 (br), 52.3 (br), 39.2 (br), 35.4 (br), 26.8 (br), 25.8 (br), 21.5 (br), 20.6 (br), 18.1 (br), 17.9 (br), 16.9 (br), 13.2 (br), 10.7 (br), 9.7 (br), 6.2 (br), 4.5 (br), 3.9 (br), 2.9 (br), 1.23 (br), 1.21 (br), 0.84 (br), 0.82 (br), 0.80 (br), -1.4 (br), -2.9 (br), -4.1 (br), -6.7 (br), -8.5 (br), -11.1 (br), -15.1 (br), -20.4 (br), -30.1 (br), -32.4 (br), -38.3 (br) ppm. ¹⁹F NMR (282 MHz, CD₂Cl₂) δ -78.39 ppm.

¹H NMR (300 MHz, CDCl₃) δ 179.3 (v br), 150.4 (v br), 63.0 (br), 58.1 (br), 46.3 (br), 44.7 (br), 32.6 (br), 26.0 (br), 23.1 (v br), 22.2 (br), 21.1 (br), 20.0 (br), 15.6 (v br), 14.3 (br), 12.7 (br), 10.2 (br), 8.8 (v br), 7.7 (br), 6.9 (v br), 5.9 (br), 4.4 (br), 2.4 (br), 1.7 (br), 1.2 (br), 1.04 (br), 0.80 (br), -0.58 (br), -0.78 (v br), -1.5 (v br), -1.9 (v br), -2.5 (v br), -7.3 (br), -9.6 (br), -11.0 (br), -15.0 (br), -16.4 (br), -19.0 (br), -40.9 (v br), -46.2 (v br), -51.0 (br) ppm. ¹⁹F NMR (282 MHz, CD₂Cl₂) δ -78.39 ppm.

Synthesis of B.4

In the glovebox under inert atmosphere, to a solution of **H₃L** (50 mg, 0.0582 mmol) in THF (3 mL) was added a solution of LiHMDS (29.2 mg, 0.175 mmol) in THF (2 mL). The solution turned darker yellow, and the reaction mixture was allowed to stir at room temperature for 15 mins. Co(OTf)₂ (62.5 mg, 0.175 mmol) was then added as a solid to the mixture. The solution initially turned slightly more orange. The resulting suspension was stirred at r.t. overnight, upon which pink solid precipitate was observed. The suspension was filtered and washed with THF. The THF filtrate and wash were collected. The pink solid precipitate was eluted with MeCN as red solution. Both the THF filtrate and MeCN elute were dried under vacuum. Recrystallization of both

fractions was done in a mixture of MeCN/Et₂O to yield the clean product as solid precipitate in 77% yield. Single crystal of **B.4(H₂O)** was obtained from recrystallization of **B.4** via vapor diffusion of diethyl ether into MeCN at room temperature outside the box to yield red crystals. ¹H NMR (300 MHz, CD₃CN) δ 192.5 (v br), 83.1 (br), 42.3 (br), 31.5 (br), 23.2 (br), 23.5 (br), 2.35 (v br), 1.66 (v br), -6.27 (br), -12.72 (br), -14.27 (br), -37.7 (br), -38.3 (br) ppm. ¹⁹F NMR (282 MHz, CD₃CN) δ -78.17 ppm.

Crystallographic Information. None of the structures have been deposited to CCDC. All structures still need final refinements for disordered solvents, therefore, the GOF, R1, and wR2 values in Table B.1 are not finalized.

Refinement details

In each case, crystals were mounted on a glass fiber or nylon loop using Paratone oil, then placed on the diffractometer under a nitrogen stream. Low temperature (100 K) X-ray data were obtained on a Bruker APEXII CCD based diffractometer (Mo sealed X-ray tube, K_α = 0.71073 Å). All diffractometer manipulations, including data collection, integration, and scaling, were carried out using the Bruker APEXII software.¹⁷ Absorption corrections were applied using SADABS.¹⁸ Space groups were determined on the basis of systematic absences and intensity statistics, and the structures were solved by direct methods using XS¹⁹ (incorporated into SHELXTL)²⁰ and refined by full-matrix least squares on F². All non-hydrogen atoms were refined using anisotropic displacement parameters. Hydrogen atoms were placed in idealized positions and refined using a riding model. The structure was refined (weighted least squares refinement on F²) to convergence.

Table B.1. Crystal and refinement data for complexes **B.3a**, **B.3a(NO₃)**, and **B.4(H₂O)**

	B.3a	B.3a(NO₃)	B.4(H₂O)
empirical formula	C ₆₃ H ₄₉ Co ₃ N ₆ O ₁₁	C ₆₀ H ₄₉ Co ₃ N ₉ O ₁₄	C ₆₅ H ₄₈ Co ₃ F ₆ N ₉ O ₁₃ S ₂
formula wt	1242.87	1296.87	1518.03
T (K)	100	100	100
a, Å	12.4026(6)	10.8607(11)	15.8676(12)
b, Å	15.8398(7)	12.4985(12)	15.8676(12)
c, Å	16.4646(7)	22.363(2)	14.4829(12)
α, deg	90	94.201(2)	90
β, deg	107.2230(10)	102.659(2)	90
γ, deg	90	115.080(2)	120
V, Å ³	3089.5(2)	2634.7(4)	3158.0(5)
Z	2	2	2
Cryst. system	Monoclinic	Triclinic	Trigonal
space group	P 1 21 1	P-1	P -3
d _{calcd} , g/cm ³	1.336	1.635	1.596
θ range, deg	9.677– 26.372	1.832 – 32.652	1.406- 36.359
μ, mm ⁻¹	0.858	1.016	0.936
abs correction	Semi-empirical from equivalents	Semi-empirical from equivalents	Semi-empirical from equivalents
GOF ^c	1.009	0.905	1.067
R1, ^a wR2 ^b (I > 2σ(I))	0.0959, 0.2372	0.0531, 0.1133	0.0835, 0.2216

$$^a R_1 = \sum ||F_o| - |F_c|| / \sum |F_o|. \quad ^b wR_2 = [\sum [w(F_o^2 - F_c^2)^2] / \sum [w(F_o^2)]^{1/2}.$$

Special refinement details for **B.3a**

B.3a was recrystallized from MeOH/Et₂O mixture. There may be some co-crystallized MeOH solvents that have not yet been modeled successfully. The structure also contains one outer-sphere acetate counterion that was satisfactorily modeled.

Special refinement details for **B.3a(NO₃)**

B.3a(NO₃) was synthesized using Co(NO₃)₂(H₂O)₆ as a cobalt precursor, therefore the compound cocrystallized with a nitrate outer-sphere anion. The outer-sphere nitrate was satisfactorily modeled.

Special refinement details for B.4(H₂O)

B.4(H₂O) was crystallized from MeCN/Et₂O mixtures in air. The compound crystallized with three MeCN solvent molecules in the lattice. The MeCN solvents and three outer sphere triflates molecules were all satisfactorily modeled.

REFERENCES

- 1 Brimblecombe, R.; Swiegers, G. F.; Dismukes, G. C.; Spiccia, L. *Angew. Chem. Int. Ed.* **2008**, *47*, 7335.
- 2 Jiao, F.; Frei, H. *Chem. Commun.* **2010**, *46*, 2920.
- 3 (a) Wiechen, M.; Zaharieva, I.; Dau, H.; Kurz, P. *Chem Sci* **2012**, *3*, 2330. (b) Zaharieva, I.; Chernev, P.; Risch, M.; Klingan, K.; Kohlhoff, M.; Fischer, A.; Dau, H. *Energy Environ. Sci.* **2012**, *5*, 7081.
- 4 (a) Dinca, M.; Surendranath, Y.; Nocera, D. G. *Proc. Natl. Acad. Sci. U.S.A.* **2010**, *107*, 10337. (b) Risch, M.; Klingan, K.; Heidkamp, J.; Ehrenberg, D.; Chernev, P.; Zaharieva, I.; Dau, H. *Chem. Commun.* **2011**, *47*, 11912.
- 5 McCool, N. S.; Robinson, D. M.; Sheats, J. E.; Dismukes, G. C. *J. Am. Chem. Soc.* **2011**, *133*, 11446.
- 6 Jiao, F.; Frei, H. *Angew. Chem. Int. Ed.* **2009**, *48*, 1841.
- 7 (a) Kanan, M. W.; Nocera, D. G. *Science* **2008**, *321*, 1072. (b) Kanan, M. W.; Yano, J.; Surendranath, Y.; Dinca, M.; Yachandra, V. K.; Nocera, D. G. *J. Am. Chem. Soc.* **2010**, *132*, 13692.
- 8 (a) Umena, Y.; Kawakami, K.; Shen, J. R.; Kamiya, N. *Nature* **2011**, *473*, 55. (b) Yin, Q. S.; Tan, J. M.; Besson, C.; Geletii, Y. V.; Musaev, D. G.; Kuznetsov, A. E.; Luo, Z.; Hardcastle, K. I.; Hill, C. L. *Science* **2010**, *328*, 342.
- 9 Tsui, E. Y.; Day, M. W.; Agapie, T. *Angew. Chem. Int. Ed.* **2011**, *50*, 1668.
- 10 Kanady, J. S.; Tsui, E. Y.; Day, M. W.; Agapie, T. *Science* **2011**, *333*, 733.
- 11 Chakrabarty, R.; Bora, S. J.; Das, B. K. *Inorg. Chem.* **2007**, *46*, 9450.
- 12 Tsui, E. Y.; Kanady, J. S.; Day, M. W.; Agapie, T. *Chem. Commun.* **2011**, *47*, 4189.

- 13 (a) Sumner, C. E. *Inorg. Chem.* **1988**, 27, 1320. (b) Gao, S.; Zhang, Z.; Huo, L.; Zhao, H.; Zhao, J. *Acta Cryst. E* **2004**, E60, m1422. (c) Sarkar, B.; Roy, A.; Ng, S. W.; Tiekink, E. R. T. *Acta Crystallogr. E* **2010**, 66, M365.
- 14 Saltzman, H.; Sharefkin, J. G. *Organic Synthesis Collective* **1973**, 5, 658.
- 15 Kamienska-Piotrowicz, E.; Stangret, J.; Szymanska-Cybulska, J. *Spectrochim. Acta A* **2007**, 66, 1.
- 16 Wemple, M. W.; Tsai, H. L.; Wang, S. Y.; Claude, J. P.; Streib, W. E.; Huffman, J. C.; Hendrickson, D. N.; Christou, G. *Inorg. Chem.* **1996**, 35, 6437.
- 17 APEX2, Version 2 User Manual, M86-E01078, Bruker Analytical X-ray Systems, Madison, WI, June 2006.
- 18 Sheldrick, G. M.; 2008/1 ed.; University of Göttingen, Germany: 2008.
- 19 Spek, A. L. "PLATON – A Multipurpose Crystallographic Tool, Utrecht University", Utrecht, the Netherlands, 2006.
- 20 Sheldrick, G. M. *Acta Crystallogr. A* **2008**, D65(2), 148.

APPENDIX C

MODELING [FeFe] HYDROGENASE: INCORPORATION OF SYNTHETIC DI-IRON COMPLEX
TO BIONGINEERED AND SYNTHETIC [4Fe4S]-CLUSTERS

ABSTRACT

This report includes the approach to model the H-cluster framework of [FeFe]-hydrogenase by incorporating a synthetic diiron complex onto a protein-supported or a synthetic ligand-supported [Fe₄S₄]-cluster. The mutant ferredoxin with a [Fe₄S₄]-cluster has been characterized by multiple spectroscopic techniques. The multi-nucleating tricarbene or triphosphine ligands have been synthesized and characterized. To date, the reconstruction of a functional H-cluster mimic has not yet been reached, but this project is no longer pursued due to the difficulty of obtaining crystallographic evidence and ambiguity of the EPR results to prove the formation of the full model complex.

INTRODUCTION

The accumulation of carbon dioxide and other greenhouse gases in the atmosphere has triggered the need for clean, sustainable energy production.¹ Hydrogen has been proposed as a renewable fuel due to its clean, carbon-neutral combustion characteristics in fuel cell technology.^{1b,2} The production of H₂ from protons (eq. 1) requires an electrocatalyst to proceed at diffusion-controlled rates without a large overpotential. Currently, the most efficient catalyst is a platinum electrocatalyst, which is expensive and not sustainable.³ On the other hand, Nature catalyzes the reaction at the thermodynamic equilibrium potential via the hydrogenase enzymes. Understanding and expanding the underlying chemistry of hydrogenase is crucial toward the design of new electrocatalytic systems for H₂ production.

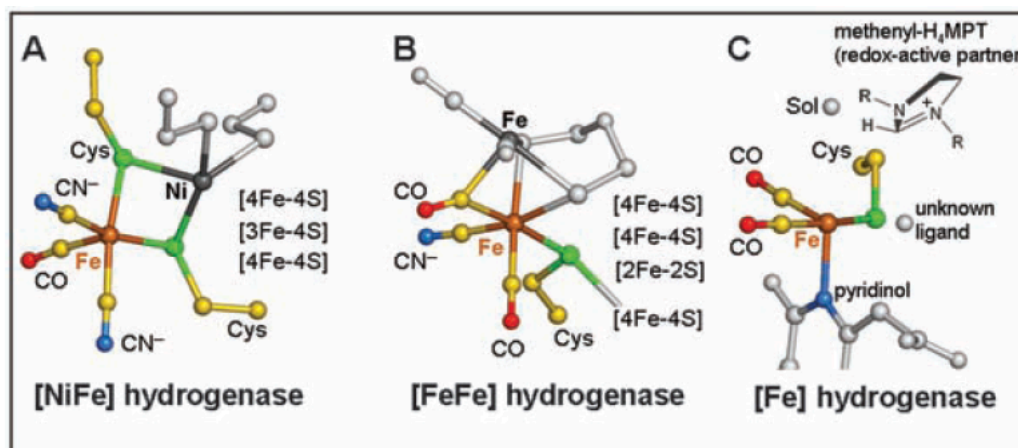


Figure 1. The active sites of the hydrogenases: (a) [NiFe]–hydrogenase, (b) [FeFe]–hydrogenase, and (c) [Fe]–only hydrogenase. Figure taken from reference 4.

There are three classes of hydrogenase discovered to date: [NiFe]–hydrogenase, [FeFe]–hydrogenase, and [Fe]–only hydrogenase. These hydrogenases' active site are displayed in Figure 1.⁴ The most prominent hydrogenases are the [NiFe]– and [FeFe]–

hydrogenases. They consist of bimetallic active sites and are bound to a $[\text{Fe}_4\text{S}_4]$ -cluster.^{4a,4c} For this appendix chapter, the focus will be on the $[\text{FeFe}]$ -hydrogenase.

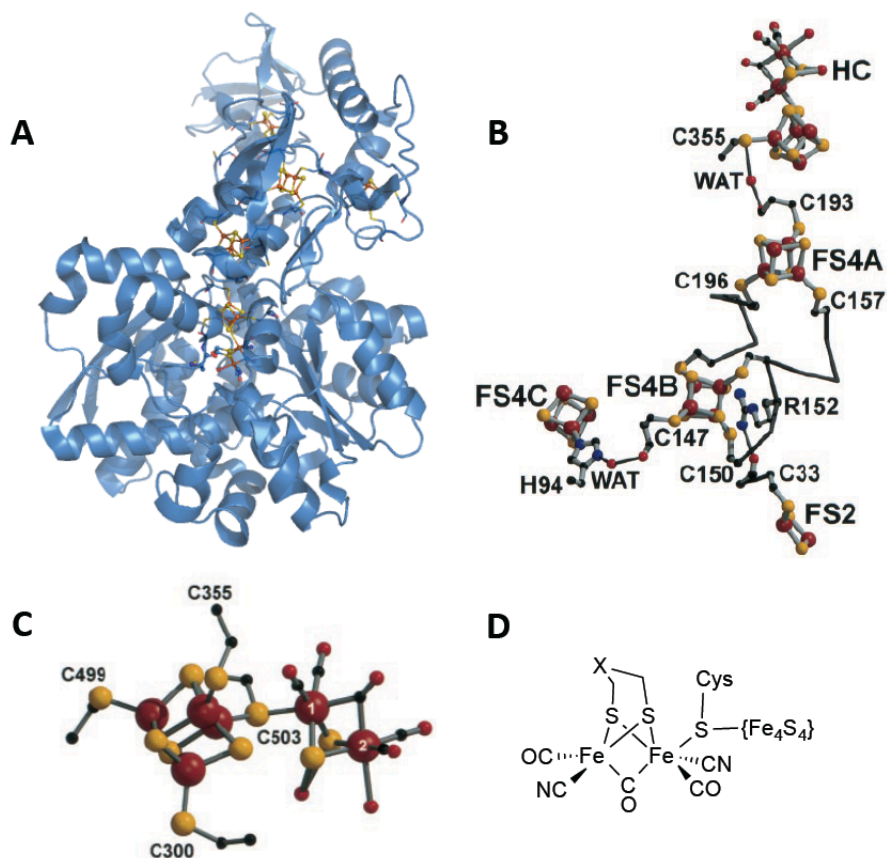


Figure 2. (A) Crystal structure of the $[\text{FeFe}]$ -hydrogenase; (B) an array of iron sulfur clusters leading to the H-cluster; (C) crystal structure of the H-cluster; (D) schematic of the H-cluster. Figures c and d are obtained from reference 5c.

The H-cluster of $[\text{FeFe}]$ -hydrogenase is composed of an $[\text{Fe}_4\text{S}_4]$ -core linked by a cysteinyl residue to a diiron active site (Figure 2c-d). Many synthetic diiron dithiolate-based systems have been synthesized but they show poor electron transfer kinetics.^{2,5} Since the $[\text{Fe}_4\text{S}_4]$ -cluster is implicated to play an important role in the electron transfer,⁶ the goal of the research project is to model the H-cluster with an $[\text{Fe}_4\text{S}_4]$ -cluster attached to the diiron unit synthetically or through protein bioengineering (Figure 3). The electron transfer mechanism from the cubane to the diiron-subsite will be

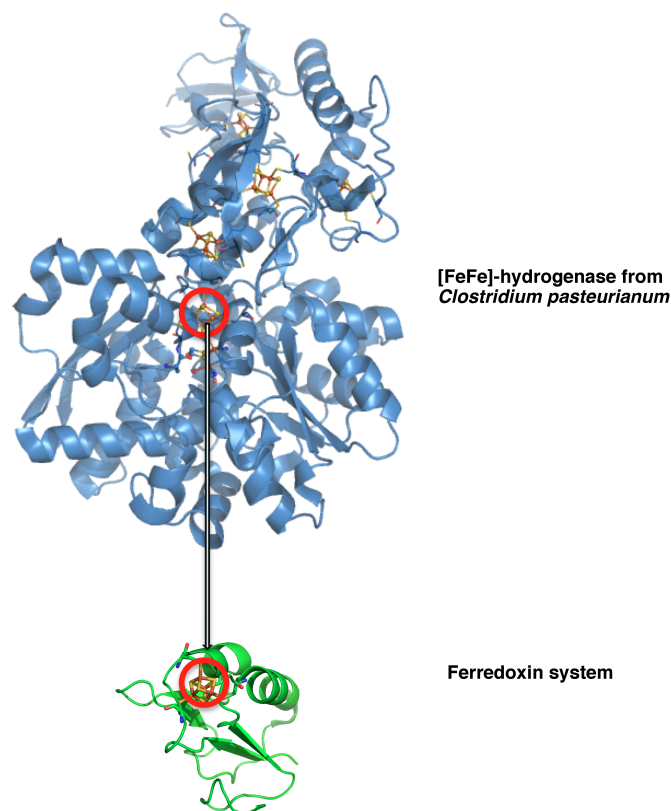


Figure 4. Comparison of the [FeFe]-hydrogenase from *C. pasteurianum* to the ferredoxin from *B. thermoproteolyticus*.

A synthetic [Fe₄S₄]-cubane supported by phosphine or *N*-heterocyclic carbene trinucleating ligand such as **1a** or **C.1** (Figure 3 bottom) is desirable to facilitate the tuning of the cluster's electronic properties by the ligand. Variation of the R' group of **C.1** from electron-withdrawing groups such as trifluoromethyl to electron-donating groups such as 4-*N,N*-dimethylamino and the R group of **1a** with different alkyl substituents may allow for tuning of the cluster's redox potentials.

While many of the iron-sulfur clusters previously synthesized have core charges of [Fe₄S₄]¹⁺, [Fe₄S₄]²⁺, and [Fe₄S₄]³⁺, the system with the **1a** and **C.3** ligands may allow for the study of the electronic properties of a [Fe₄S₄]⁰ state of the cluster (all-ferrous state).⁷ Holm and co-workers have shown that the *N*-heterocyclic carbene (NHC)

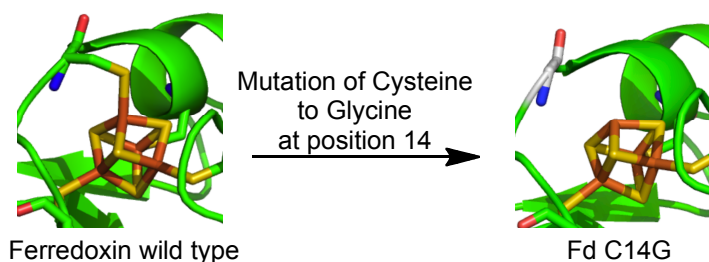
ligand, 1,3-diisopropyl-4,5-dimethylimidazol-2-ylidene, can stabilize a fully reduced iron-sulfur cluster.⁷ Based on Holm's methods to construct a synthetic iron-sulfur cluster supported by an NHC framework, reactions of **1a** or **C.1** with related iron-sulfur precursors were run to assemble a triscarbene- or trisphosphine-supported [Fe₄S₄]-cluster. The resulting electron-rich core cluster is expected to affect electron transfer to the incorporated diiron subsite and can be studied extensively via cyclic voltammetry.

RESULTS AND DISCUSSIONS

C.1 Ferredoxin protein engineering: expression and purification of FdC14G

A single point mutation to the Fd gene on the cysteine residue at position 14 to glycine was performed to make the mutant protein FdC14G (Scheme 1). The Cys to Gly mutation was done to free a coordination site on the Fe closest to the protein surface.

Scheme 1. Single point mutation to BtFd to make mutant FdC14G



The gene sequence for Fd protein was obtained from the organism *Bacillus thermoproteolyticus*. A site-directed mutagenesis was made to the wild-type ferredoxin on the cysteine residue at position 14 to a glycine (Scheme 1). The mutated ferredoxin construct (FdC14G) was cloned into the pET28b vector that contains an N-terminal His₆-tag and a TEV protease cleavage site for purification purposes. Protein expression using a fermentor was carried out in *E. coli* Tuner (DE3)pLysS with Terrific Broth as the media and induced by 1-2 mM IPTG. FdC14G was observed to not bind very well

to the Ni-NTA superflow resin, so low-imidazole buffer was used to wash the non-specifically binding protein off the column. High-imidazole buffer eluted the desired protein along with a significant amount of other impurities. Cleavage of the His₆-tag by TEV protease was performed and followed by a second run through the Ni-NTA superflow column. The flowthrough from the second nickel column showed slightly enhanced purity (by SDS-PAGE with AgNO₃ staining). Further purification was done by running the protein through the DEAE anionic exchange column and eluting with high-salt buffer. The protein was eluted from the DEAE column with purity higher than 95% determined by UV-Vis spectroscopy (a ratio of A₄₀₀/A₂₈₀ of 0.72).

This procedure gives low yield of FdC14G (~1 mg/L) in contrast to the high yield of the wild type ferredoxin protein (>15mg/L). The low yield of the mutant protein expression may be due to the mutation causing the protein to misfold and degrade back to amino acid units by the organism. Another attempt to improve the protein expression yield has been done using a different *E. coli* line, BL21(DE3); however, no significant improvement of the yield has been observed.

C.2 Characterizations of FdC14G as expressed and isolated

A number of spectroscopic techniques were used to characterize FdC14G. These characterization experiments include UV-Visible spectroscopy, electron paramagnetic resonance (EPR) spectroscopy, and infrared (IR) spectroscopy. The iron content of FdC14G was also determined via the iron quantification assay.

Iron Quantification of the FdC14G as Isolated

The quantification of iron content in FdC14G was performed according to literature protocol.⁸ The iron quantification assay on FdC14G further suggested that the mutant protein was purified as a [Fe₃S₄]-species where the resulting ratio of iron to

protein concentration was calculated to be 3.2 to 1. The loss of the fourth iron in the metal cluster indicates the need to reconstitute an iron to the cluster toward obtaining the enzyme's active species.

Characterization by UV-Visible Spectroscopy

The UV-Vis spectroscopy data revealed that the mutant FdC14G was isolated as an oxidized $[\text{Fe}_3\text{S}_4]$ -cluster protein with $\epsilon_{400} = 17 \text{ mM}^{-1}\text{cm}^{-1}$ as opposed to $[\text{Fe}_4\text{S}_4]$ -cluster like the wild-type ferredoxin with known $\epsilon_{410} = 16 \text{ mM}^{-1}\text{cm}^{-1}$ (Figure 5).⁹ The observed UV-Vis spectrum of the reduced FdC14G also differs from that of the wild-type ferredoxin (Figure 6). These UV-Vis data serve as additional evidence that the FdC14G protein was not isolated as a $[\text{Fe}_4\text{S}_4]$ -cluster protein.

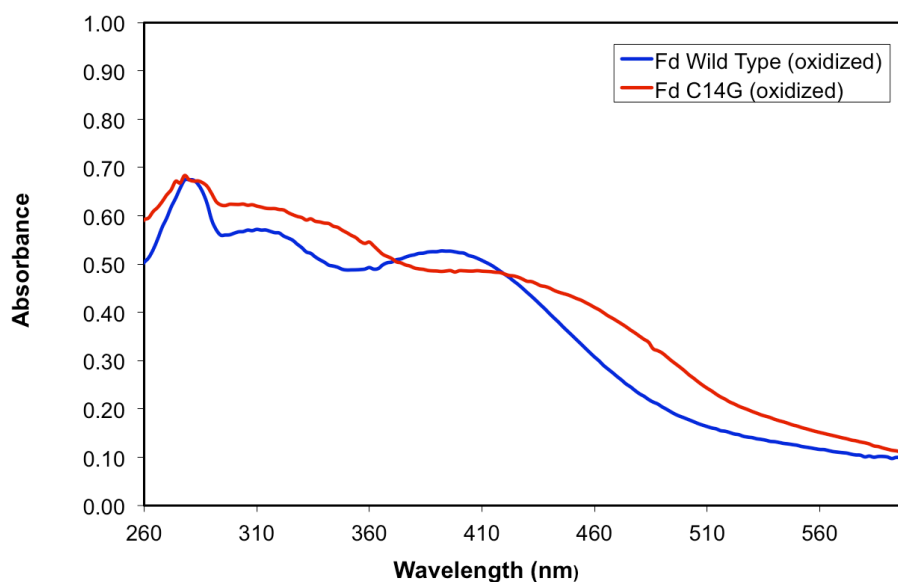


Figure 5. UV-Vis spectra of the oxidized wild-type Fd vs. oxidized FdC14G.

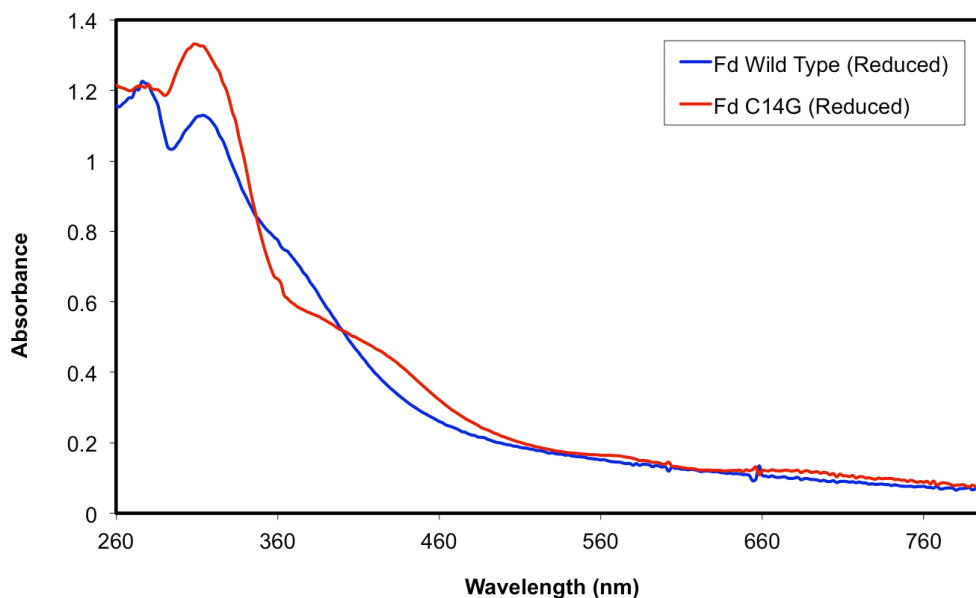


Figure 6. UV-Vis spectra comparing the reduced wild-type Fd vs. reduced FdC14G.

EPR Analysis of FdC14G after as expressed and purified

To support the resulting UV-Vis spectra and iron quantification assay, EPR experiments were performed on FdC14G to determine whether the isolated protein contains a mixture of the $[\text{Fe}_3\text{S}_4]$ - and $[\text{Fe}_4\text{S}_4]$ -species or purely the $[\text{Fe}_3\text{S}_4]$ -species. The EPR of the oxidized FdC14G species shown in Figure 7 agrees with the characteristic EPR spectrum of the oxidized $[\text{Fe}_3\text{S}_4]$ -cluster (with 3Fe^{3+} ; $S = 5/2$); the reduced FdC14G- $[\text{Fe}_3\text{S}_4]$ was EPR silent, consistent with the oxidation states 2Fe^{3+} , 1Fe^{2+} where $S =$ integral number and is magnetically coupled.⁸⁻¹⁰

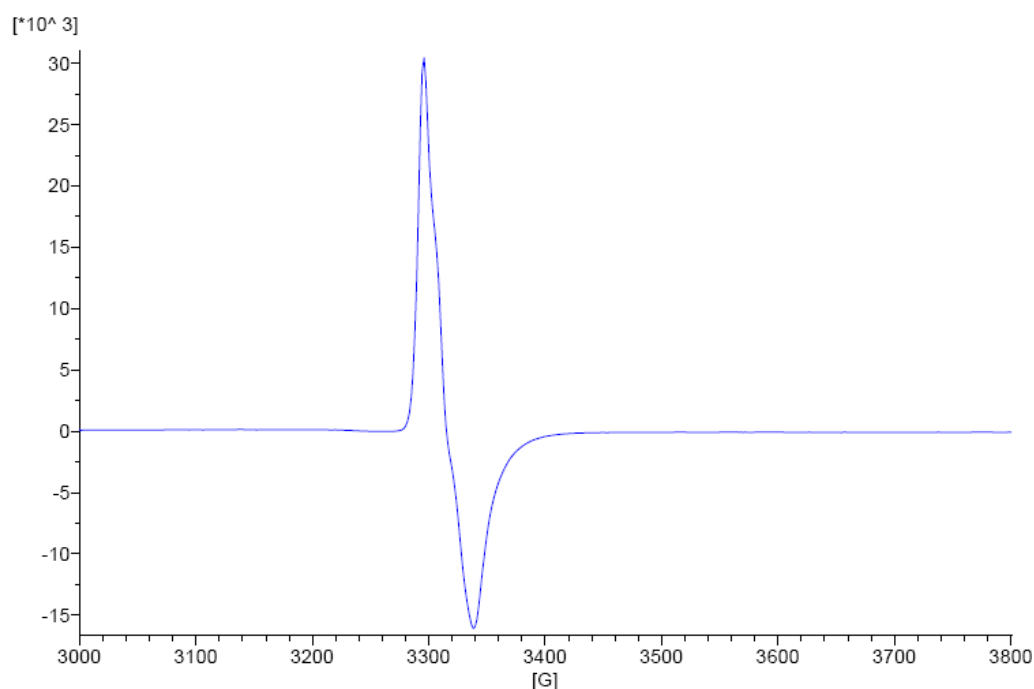


Figure 7. EPR spectrum of oxidized **[Fe₃S₄]-FdC14G** (as isolated)

C.3 Reconstitution of [Fe₃S₄]-FdC14G to [Fe₄S₄]-FdC14G and characterization

From the UV-Vis spectroscopy, iron quantification assay, and EPR spectroscopy data, FdC14G was purified as a [Fe₃S₄]-species (**[Fe₃S₄]-FdC14G**) (Scheme 2). To obtain the [Fe₄S₄]-species, FdC14G was reconstituted by the addition of excess Fe^{II}, beta-mercaptanol as a thiol source, and dithionite as a reducing agent (Scheme 2). After allowing the reaction to stir for two hours, the mixture was loaded onto the DEAE anionic exchange column to wash off the excess reagents. The reconstituted mutant protein, **[Fe₄S₄]-FdC14G**, was eluted with a high-salt buffer containing 1 mM beta-mercaptanol.

After collecting the purified [Fe₄S₄]-FdC14G, the reconstituted protein was analyzed by UV-Vis spectroscopy. The UV-Vis spectra comparing **[Fe₃S₄]-FdC14G**, **[Fe₄S₄]-FdC14G**, and the wild-type ferredoxin are shown in Figure 8. The 410 nm region of the spectra in Figure 8 shows that **[Fe₃S₄]-FdC14G** has been mostly

reconstituted to make $[\text{Fe}_4\text{S}_4]\text{-FdC14G}$ by comparison to the UV-Vis spectrum of the wild-type ferredoxin. The spectrum representing the $[\text{Fe}_4\text{S}_4]\text{-FdC14G}$ in Figure 8 was taken after allowing the reconstitution reaction to stir for 2 h. Allowing the reconstitution reaction to run up to 12 h did not increase the concentration of $[\text{Fe}_4\text{S}_4]\text{-FdC14G}$ in the solution as monitored by the absorbance at 410 nm.

Scheme 2. Reconstitution of $[\text{Fe}_3\text{S}_4]\text{-FdC14G}$ to $[\text{Fe}_4\text{S}_4]\text{-FdC14G}$

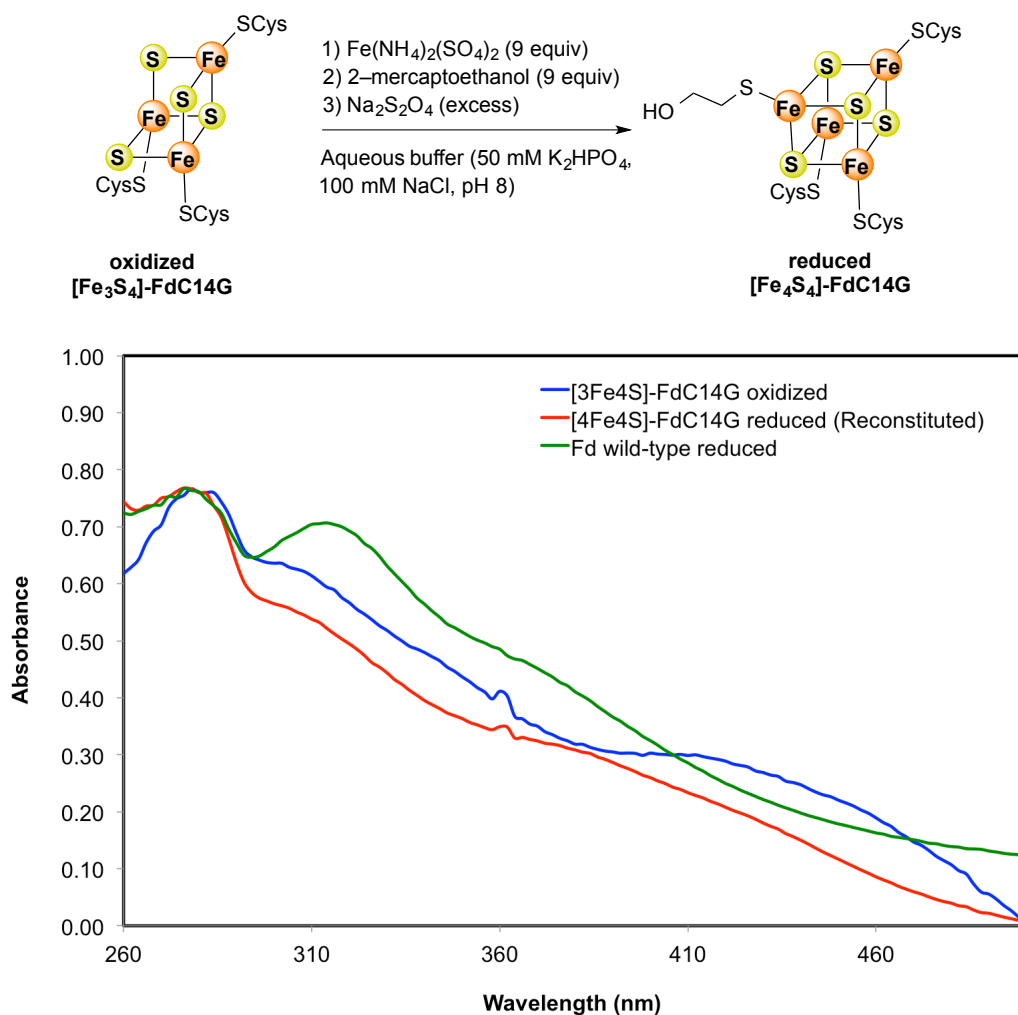


Figure 8. UV-Vis spectra comparing $[\text{Fe}_3\text{S}_4]\text{-FdC14G}$, $[\text{Fe}_4\text{S}_4]\text{-FdC14G}$, and wild-type ferredoxin.

On the other hand, the oxidized **[Fe₄S₄]-FdC14G** is expected to be EPR silent (with 2Fe³⁺, 2Fe²⁺; overall S = 0, magnetically coupled) while the reduced species should have a signature EPR spectrum (with 1Fe³⁺, 3Fe²⁺; S = 1/2 or 3/2).⁹⁻¹⁰ Figure 9 displays the result of the FdC14G reconstitution, which matches the signature EPR spectrum of a [Fe₄S₄]-cluster protein, confirming the reconstitution to generate **[Fe₄S₄]-FdC14G** successful. It is worth noting that EPR spectroscopy would not be sufficient to indicate the full or partial reconstitution of **[Fe₃S₄]-FdC14G** to make **[Fe₄S₄]-FdC14G**.

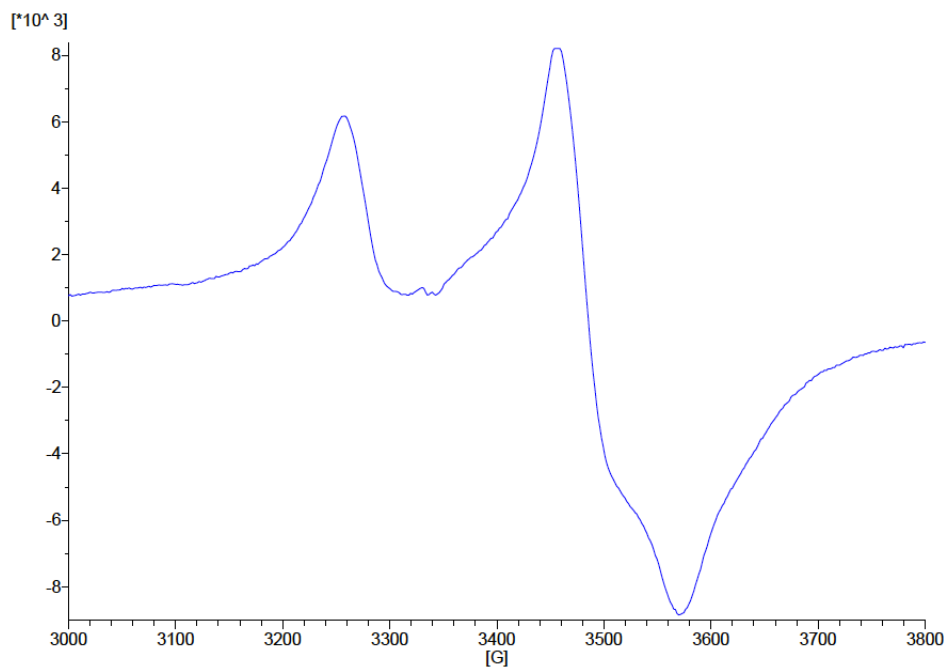


Figure 9. EPR spectrum reduced **[Fe₄S₄]-FdC14G** in 1:1 acetonitrile/water at 12K.

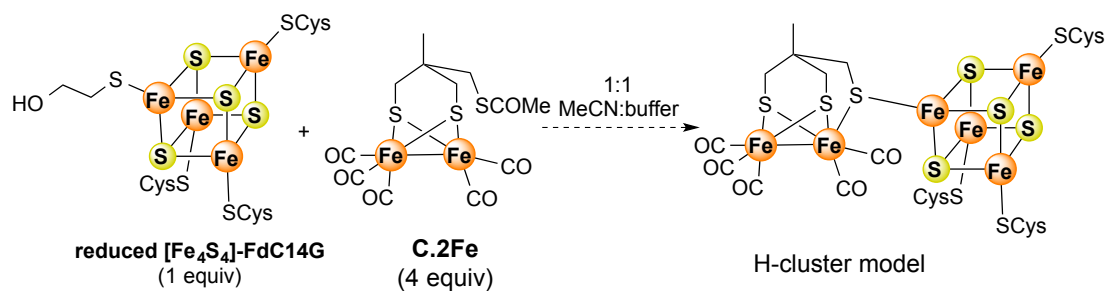
C.4 Diiron complex C.2Fe incorporation to [Fe₄S₄]-FdC14G

Following purification of **[Fe₄S₄]-FdC14G**, the reported synthetic diiron complex **C.2Fe**^{6a} with a thioester arm would be appended to model the H-cluster of [FeFe]-hydrogenase (Scheme 2). The diiron unit, **C.2Fe**, was synthesized according to literature procedure.^{6a} Determining the solubility of **C.2Fe** in various mixtures of

organic and aqueous solvents is crucial for the reaction with the FdC14G. After several trials, the mixture of MeCN to buffer best solubilizes the **C.2Fe** at certain compound concentrations. On the contrary, the protein can only tolerate a certain ratio of buffer to organic solvent without denaturing. The optimized solvent mixture to solubilize both reagents was determined to be 1:1 buffer to MeCN; this solvent mixture was used throughout the reaction between the protein and the diiron complex.

To a solution of **[Fe₄S₄]-FdC14G**, an excess of **C.2Fe** was added to construct the H-cluster framework (Scheme 2). The reaction was allowed to run for 30 minutes and was then loaded onto the anionic exchange column (DEAE). The protein was eluted with a high-salt buffer, while the excess diiron unit remained bound on the surface of the column resin. The eluted protein was characterized by EPR spectroscopy, UV-Vis spectroscopy, and mass spectrometry.

Scheme 2. Proposed route to model the [FeFe]-hydrogenase via protein engineering



EPR spectroscopy analysis of the product from the reaction of C.2Fe with [Fe₄S₄]-FdC14G

The resulting EPR spectrum from the reaction of diiron complex, **C.2Fe**, with **[Fe₄S₄]-FdC14G** is depicted in Figure 10. Comparing Figure 10 to Figure 9, the two EPR spectra have similar line shapes with a subtle difference. The shoulder around $g = 1.89$ in the spectrum from Figure 9 differs from the shoulder visible at $g = 1.8$ in the spectrum from Figure 10. The EPR signal of the product is expected to arise from the

$[\text{Fe}_4\text{S}_4]$ -core since the diiron complex, **C.2Fe**, was observed to be EPR silent.

Therefore, the desired product, H-cluster mimic, could potentially have a similar line shape to **$[\text{Fe}_4\text{S}_4]$ -FdC14G**. Although this slight distinction between the two EPR spectra may be indicative of successful incorporation of **C.2Fe** to **$[\text{Fe}_4\text{S}_4]$ -FdC14G**, other experiments must still be carried out to further prove this hypothesis.

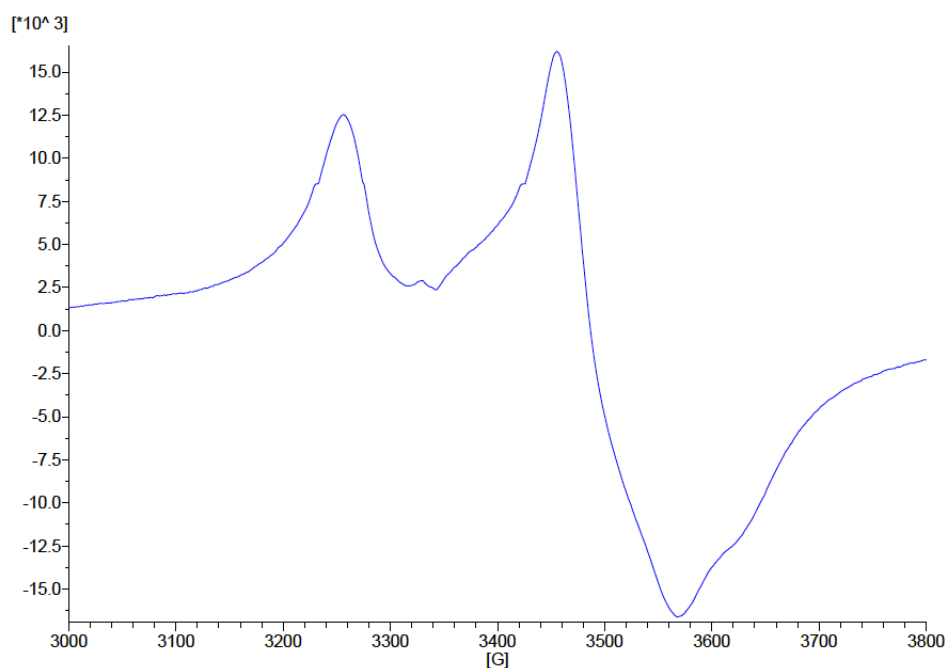


Figure 10. EPR spectrum of the product from the reaction between **C.2Fe** and **$[\text{Fe}_4\text{S}_4]$ -FdC14G** in 1:1 $\text{CH}_3\text{CN}/\text{H}_2\text{O}$ at 12 K.

*Infrared spectroscopy analysis of the product from the reaction of **C.2Fe** with **$[\text{Fe}_4\text{S}_4]$ -FdC14G***

Infrared spectroscopy experiments were performed to characterize the product of the reaction between complex **C.2Fe** and **$[\text{Fe}_4\text{S}_4]$ -FdC14G**. To reduce the signal arising from the OH stretch from aqueous buffer, D_2O was used instead of water in the 1:1 buffer/acetonitrile solution mixture. The resulting IR spectra of **C.2Fe** and the product resulting from the reaction of **C.2Fe** with **$[\text{Fe}_4\text{S}_4]$ -FdC14G** are shown in Figure 11 and 12 respectively.

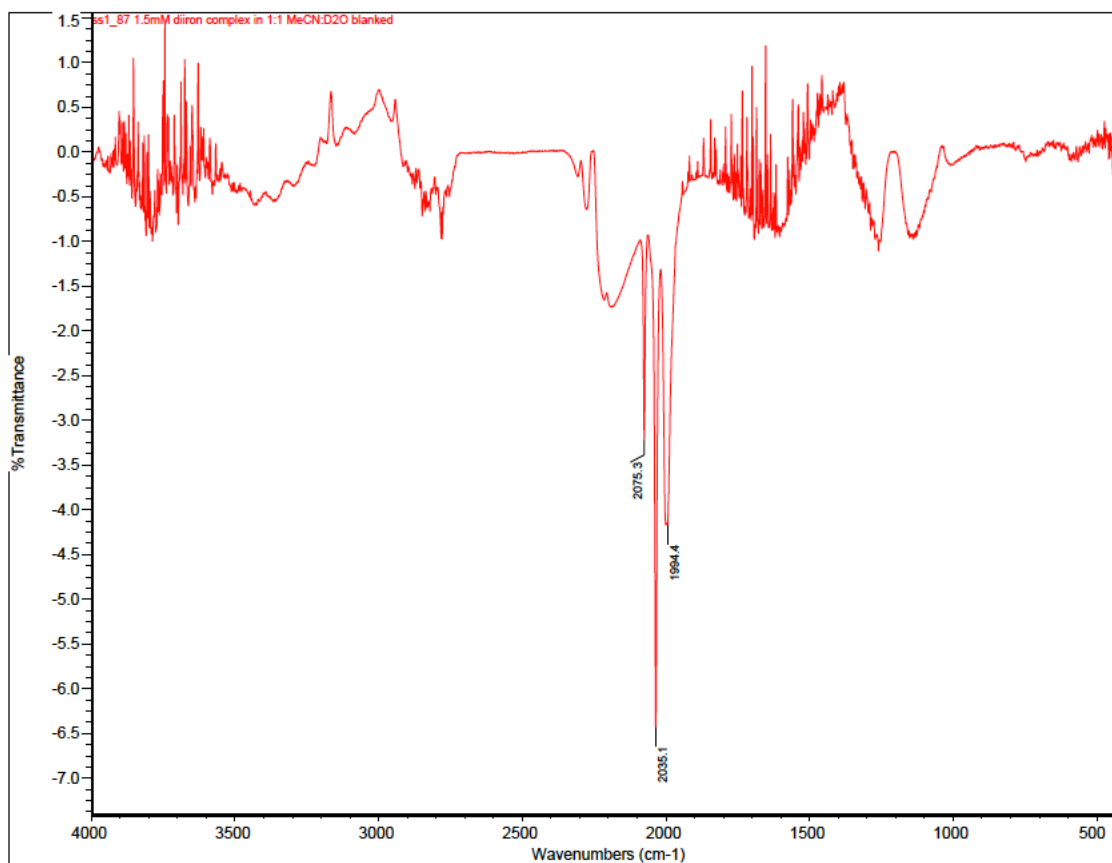


Figure 11. IR spectrum of complex **C.2Fe** in 1:1 D₂O : MeCN solution.

The IR spectrum of complex **C.2Fe** in Figure 11 revealed the three sharp peaks (2075, 2035, and 1994 cm⁻¹) that correspond to the carbonyl stretches bound to the iron centers.^{6a} In Figure 12, the observed sharp stretches are at 2075, 2035, 2000, 1959, 1652, and 1575 cm⁻¹. Some of these stretches are in the same wavenumber as those of complex **C.2Fe** while the rest are different. Characterization of the product via IR spectroscopy may suggest the possibility of having the desired product in the mixture due to the IR stretches in the 1500-2000 cm⁻¹ region that do not correspond to complex **C.2Fe**. On the other hand, the observed stretches at 2075 and 2035 cm⁻¹ also suggest that there is equilibrium between the product and the starting reagents in the solution mixture. Nonetheless, obtaining a good IR spectrum of the product had been

challenging due to the inevitable traces of water impurity that significantly affects the resulting spectra as well as the solubility of the protein mixture.

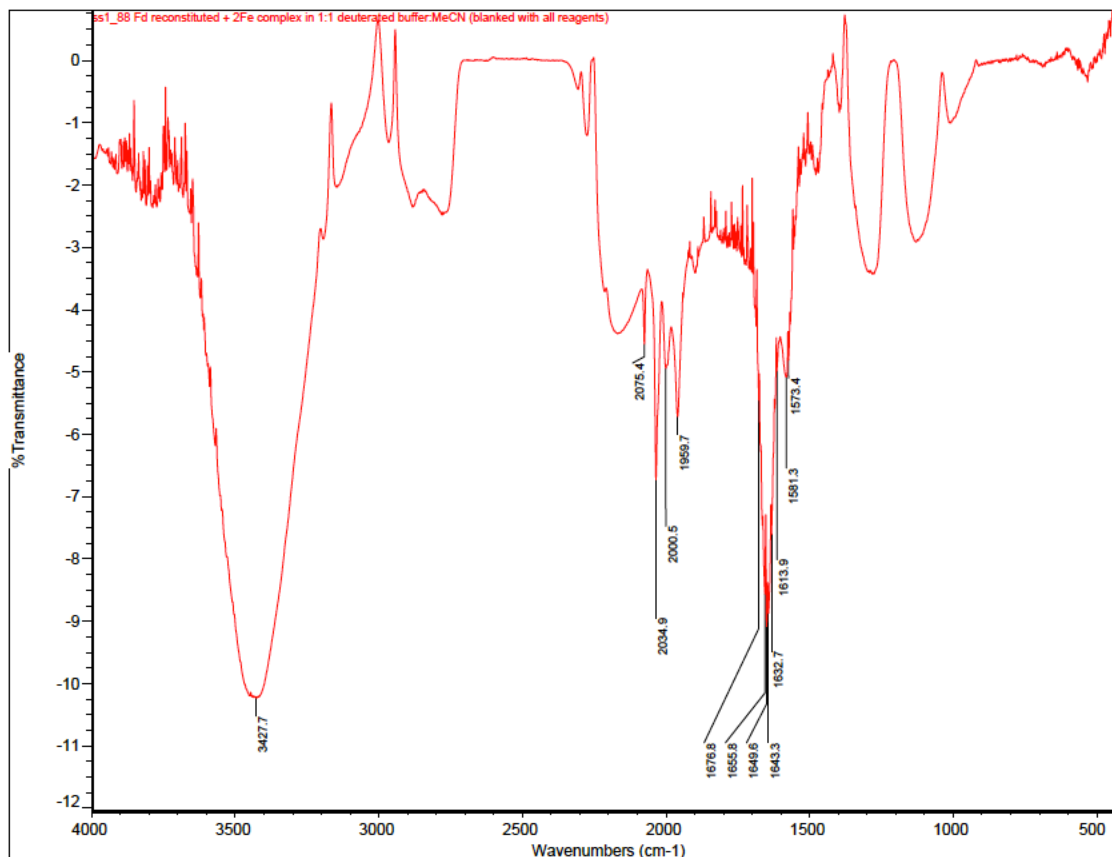


Figure 12. IR spectrum of the reaction mixture of **C.2Fe** and **[Fe₄S₄]-FdC14G**

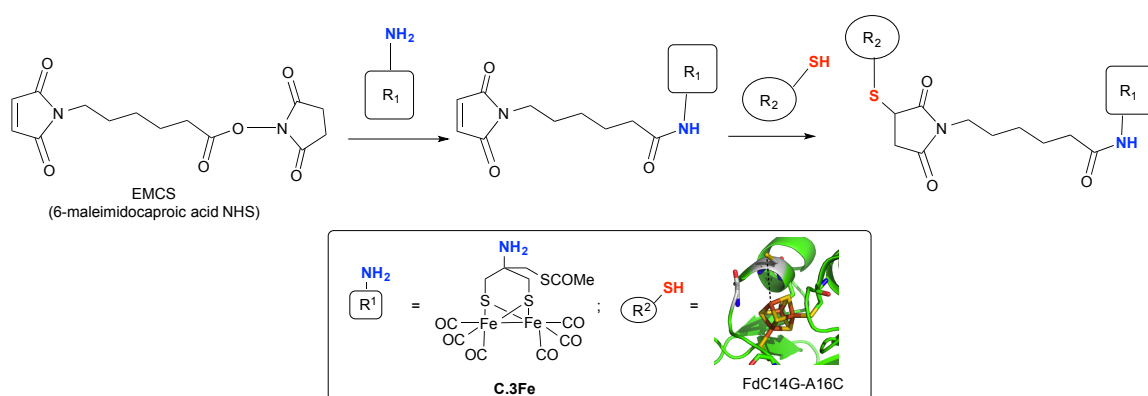
ESI-MS analysis of the product from the reaction of C.2Fe with [Fe₄S₄]-FdC14G

By electrospray mass ionization-mass spectrometry (ESI-MS), the signal corresponding to the mass/charge (m/z) of the desired H-cluster mimic was *not* observed while the signals corresponding to the **[Fe₃S₄]-FdC14G** and **[Fe₄S₄]-FdC14G** were present. The difficulty in isolating and detecting the desired H-cluster mimic could arise from the readily dissociated diiron unit from the protein in solution at equilibrium.

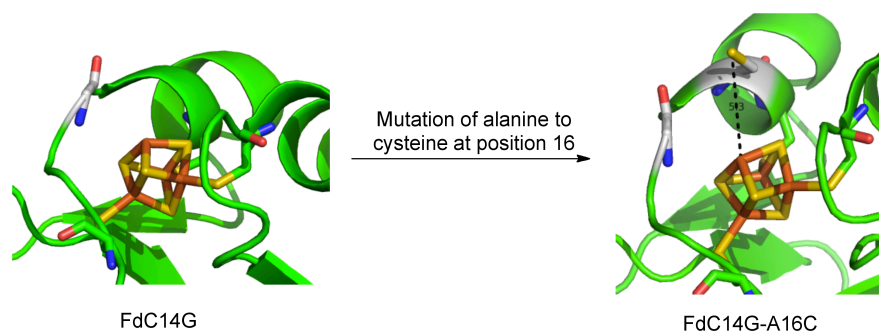
Alternative Approach to Obtain an H-cluster Mimic

Due to the unsuccessful attempts to isolate and characterize the targeted H-cluster mimic, another strategy was attempted. The alternative strategy was to obtain the target H-cluster model by covalently tethering the two complexes together via a crosslinking reagent, EMCS (Scheme 3).

Scheme 3. An alternative approach to binding the diiron unit **C3.Fe** to **[Fe₄S₄]-FdC14G** via a crosslinking reagent



Scheme 4. A point mutation to FdC14G to make FdC14G-A16C



In order to covalently link the protein to the crosslinker, an additional cysteine mutation to the protein was introduced on the protein surface that is approximately 5 Å away from the open Fe site of the **[Fe₄S₄]-cluster** (Scheme 4). The distance of 5 Å was chosen due to the similar length of the EMCS crosslinking reagent. Modeling the

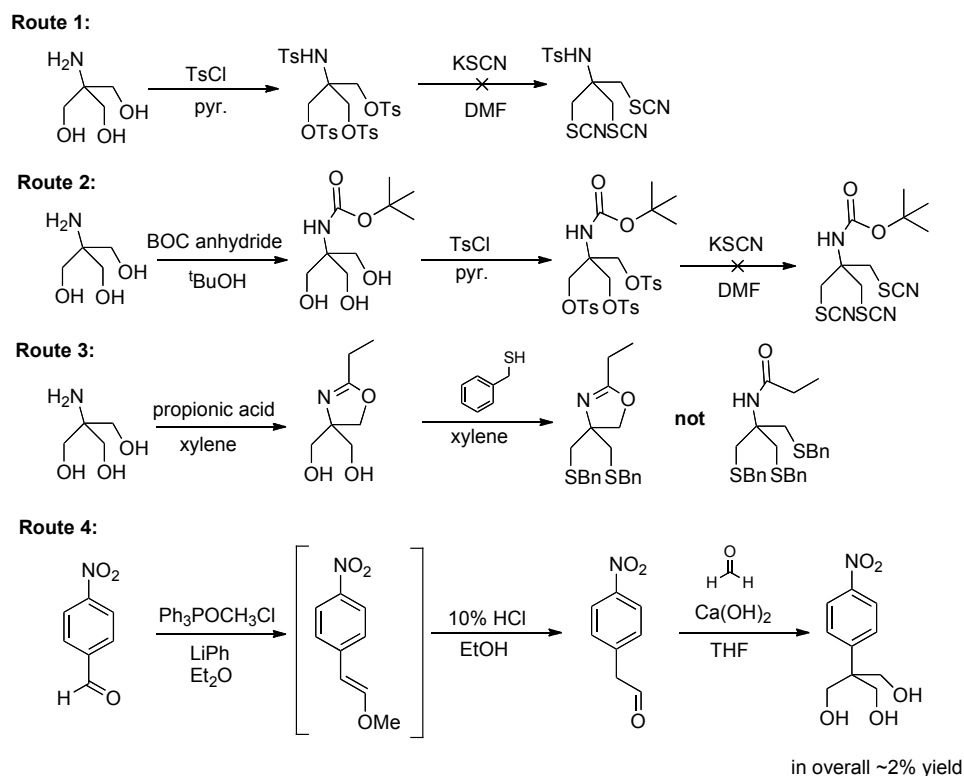
FdC14G using Pymol software and analyzing the residues on the protein surface, a potential residue to be modified was found to be the alanine residue at position 16.

A site-directed mutagenesis on FdC14G to make a mutation from alanine to cysteine residue at position 16 was performed. The resulting gene was used to recombinantly express the mutant protein, FdC14G-A16C, in a similar manner to FdC14G protein expression. Purification of FdC14G-A16C was also carried out according to previous purification methods. The FdC14G-A16C protein has not yet been fully characterized via all the techniques used to characterize FdC14G. The UV-Vis spectrum of FdC14G-A16C indicated that the double-mutant protein was isolated as a $[\text{Fe}_3\text{S}_4]$ -species.

This alternative approach also requires synthesis of a slightly different diiron unit in which the terminal methyl group of **C.2Fe** is changed to an amino functional group to make complex **C3.Fe**. The amino group on **C3.Fe** will then facilitate the nucleophilic attack of the crosslinker, thus, displacing the alkoxide group and making an amide (Scheme 3).

Attempts to Synthesize C3.Fe

Four routes have been attempted to synthesize the ligand of **C3.Fe** (Scheme 4). Routes 1 to 3 did not show any promising results by ^1H NMR spectroscopy. Although route 4 was the most promising approach to obtain **C3.Fe**, the overall yield was approximately 2% over two steps through the challenging purification via column chromatography. Another disadvantage of using route 4 was the costly reagents for the synthesis to be performed at a large scale to obtain a considerable amount of product to carry onto the next step. Therefore, other approaches to obtain **C3.Fe** in sufficient yield still need to be explored.

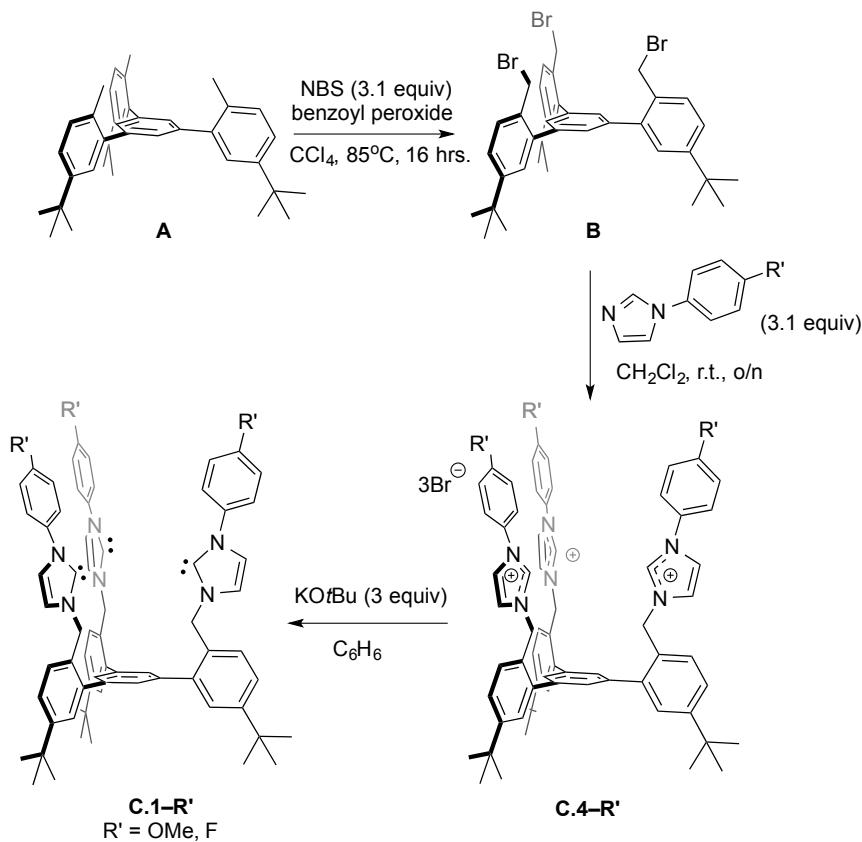
Scheme 4. Previous attempts to synthesize the precursors of **C.3Fe**

C.5 Synthetic model of $[Fe_4S_4]$ supported by multi-nucleating ligands

The triscarbene and trisphosphine ligands, **C.1** and **1a**, were synthesized as outlined in Scheme 5 and as described in Chapter 2, respectively. Continuing from the same precursor **A**, bromination at the benzylic position to yield compound **B** was afforded by the addition of *N*-bromosuccinimide (NBS) and benzoyl peroxide at elevated temperature. Compound **B** served as a precursor for the triscarbene ligands. Synthesis of **B** was accomplished with an overall yield of 20% over three steps.¹¹ Reaction of **B** with functionalized aryl imidazole yielded the imidazolium bromide ligand precursor **C.4-R'** ($R' = \text{OMe}, \text{F}$) in 75% yield, which upon deprotonation with a strong base potassium *tert*-butoxide (KO^tBu) yielded the final triscarbene ligand **C.1-R'**. The R' group of **C.1** was varied from a methoxy group to a fluorine substituent as NMR

spectroscopy handle that could be useful for ligand characterization and preliminary metalation analysis.

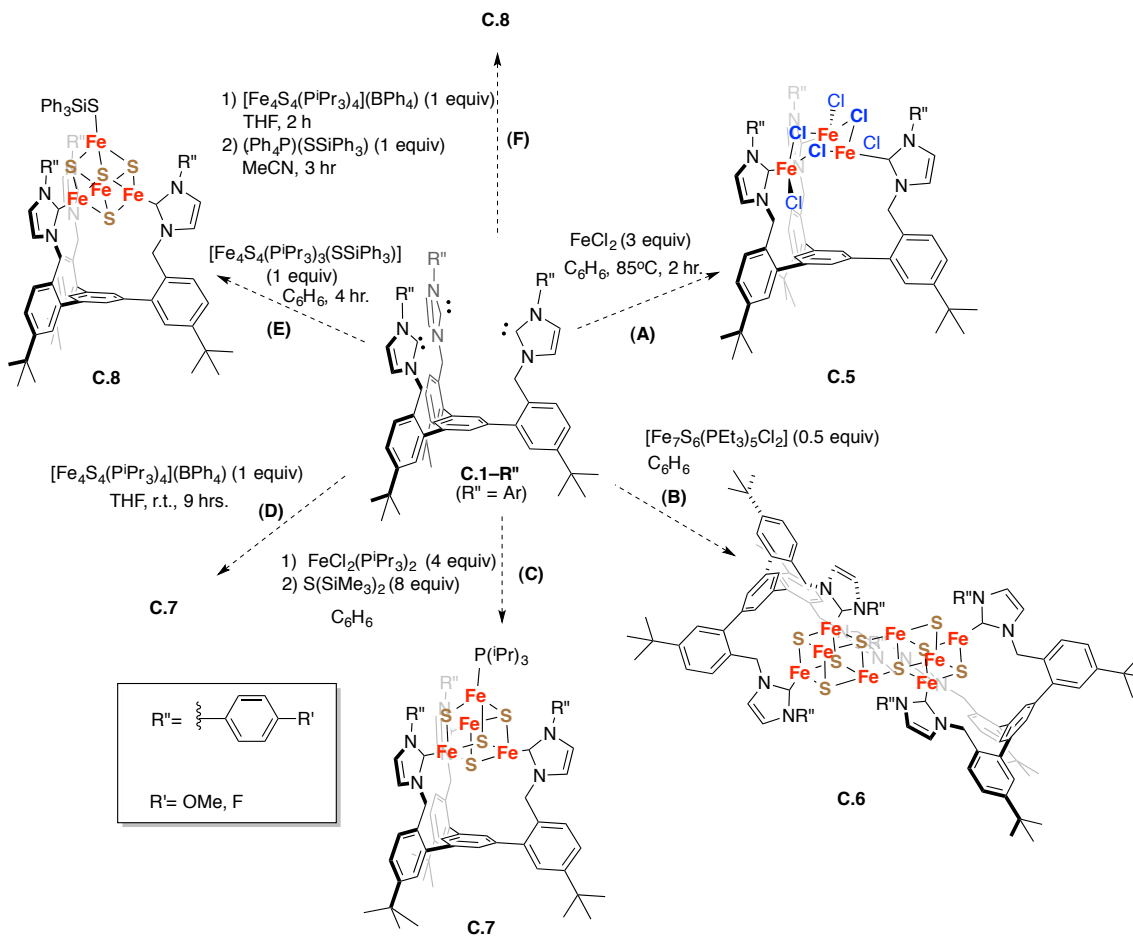
Scheme 5. Syntheses of ligands **C.1–R'**



Reaction of C.1–R' with Different Iron Precursors

N-heterocyclic carbene (NHC) ligands have been shown to coordinate high-spin Fe^{II} centers.¹² Addition of three equivalents of FeCl₂ to **C.4–OMe** in a mixture of benzene and THF under inert atmosphere (reaction A, Scheme 6) at 85°C gave a reddish-brown mixture. Reaction A produced either decomposition products or multiple species shown by numerous peaks observed in the ¹H NMR spectrum.

Scheme 6. Attempted reaction of **C.1** with various iron complexes to reconstruct a [Fe₄S₄]-cluster



The iron precursors used were [Fe₇S₆(PEt₄)₅Cl₂], FeCl₂(PⁱPr₃)₂, [Fe₄S₄(PⁱPr₃)₄](BPh₄), and [Fe₄S₄(PⁱPr₃)₃(SSiPh₃)], and they were synthesized according to literature procedure.^{7,13} The addition of 4 equivalent of FeCl₂(PⁱPr₃)₂ and 8 equivalents of bis(trimethylsilyl) sulfide to **C.1-OMe** in benzene (reaction C, Scheme 6) resulted in the formation of a paramagnetic species and free triisopropylphosphine indicated by ¹H and ³¹P NMR spectroscopy. The release of free triisopropylphosphine in this reaction implies that the carbenes from the ligand have replaced the phosphine bound to the iron. However, the possibility of having mono-, di-, or tri-substitution of the iron-sulfur cluster by the ligand could not be resolved by NMR spectroscopy. Recrystallization of the product from reaction C has yet to produce crystals for structural characterization.

A preliminary reaction of **C.1-OMe** with one equivalent of $[\text{Fe}_4\text{S}_4(\text{P}^i\text{Pr}_3)_4](\text{BPh}_4)$ in THF (reaction D, Scheme 6) yielded a mixture of paramagnetic species and triisopropyl phosphine as indicated by NMR spectroscopy. By the absence of the starting reagents' signals, the NMR spectroscopy data suggest that the reaction went to completion. The recrystallization of product from reaction D was attempted since the NMR spectra were inconclusive regarding the success of the metal-cluster construction.

The reaction between the ligand **C.1-OMe** with the iron precursor $[\text{Fe}_7\text{S}_6(\text{PET}_3)_5\text{Cl}_2]$ (reaction B, Scheme 6) produced a mixture of paramagnetic species and triethylphosphine, as indicated by ^1H and ^{31}P NMR spectroscopy. The electrospray ionization mass spectrometry (ESI-MS) data on the collected black precipitate displayed peaks centered at $m/z = 946.6$, 1051.7 , and 1390.2 . The peak at $1051.7 m/z$ may indicate the presence of $[\text{Fe}_4\text{S}_4]$ -cluster trimer without any coordinated **C.1-OMe**. The peak at $m/z 1390.2$ differs by 5 from 1385, which is the expected mass of $[\text{Fe}_4\text{S}_4]$ -cluster bound to the ligand, **C.1-OMe** bound to $[\text{Fe}_4\text{S}_4]$. The result from the ESI-MS analysis indicates the presence of multiple complexes as the products of reaction B. To date, no structural characterization of these products has been done due to the lack of single crystals for XRD studies.

Since previous reactions with **C.1-OMe** were inconclusive, a fluorine NMR handle was incorporated in **C.1-F** to monitor the reactions. The addition of 0.5 equivalents of $[\text{Fe}_7\text{S}_6(\text{PET}_3)_5\text{Cl}_2]$ to **C.1-F** formed a mixture of paramagnetic species that are silent by ^1H and ^{31}P NMR spectroscopy. The ^{19}F NMR spectrum also proved inconclusive due to the observed weak and broad peaks. The ESI-MS data of the solid precipitate from the recrystallization attempt of reaction B using **C.1-F** ligand showed

peaks centered at m/z : 946.5, 1051.5, and 1382.8. The 1051.5 peak may suggest the presence of a trimer $[\text{Fe}_4\text{S}_4]$ -cluster. The peak at m/z 1382.8 was off by 34 from the desired mass of 1349 of **C.1–F** bound to $[\text{Fe}_4\text{S}_4]$. This difference of mass may be due to an extra sulfur atom or a contamination from the atmosphere that caused the incorporation of oxos or iron oxides. Adding one equivalent of $[\text{Fe}_4\text{S}_4(\text{P}^i\text{Pr}_3)_4](\text{BPh}_4)$ to **C.1–F** (reaction D, Scheme 6) yielded a mixture of paramagnetic species and triisopropylphosphine shown by ^1H and ^{31}P NMR spectra. The ^{19}F NMR spectrum of the reaction mixture displays two weak signals that may indicate the presence of more than one fluorinated species in the mixture. ESI-MS analysis of the filtrate from reaction D with **C.1–F** displayed peaks centered at m/z : 667.6, 1064.0, 1346.8, and 1630.5. The peak at m/z 1346.8 is off by one mass unit from the desired mass of 1349 of **C.1–F** bound to $[\text{Fe}_4\text{S}_4]$.

Due to the paramagnetic character of the resulting product and the inability to obtain single crystals for XRD, EPR spectroscopy and cyclic voltammetry were used to help identify the products of reaction D. The EPR spectra and CVs of the product from reaction D and the iron-precursor reagent, $[\text{Fe}_4\text{S}_4(\text{P}^i\text{Pr}_3)_4](\text{BPh}_4)$, are shown in Figure 13a and 14a. By EPR spectroscopy and cyclic voltammetry (Figure 13b and 14b), the iron-sulfur cluster precursor, $[\text{Fe}_4\text{S}_4(\text{P}^i\text{Pr}_3)_4](\text{BPh}_4)$, was pure. The EPR spectrum of the product from reaction D displays signals at $g = 2.14$, 2.00, and 1.94 while the signals from of the iron-sulfur cluster precursor are observed at $g = 2.15$ and 1.94. The overall lineshape of the EPR spectrum and the signal at $g = 2.00$ from the reaction mixture might indicate the formation of a type of iron-sulfur cluster product, although the spectrum suggests that there is more than one species in the mixture.

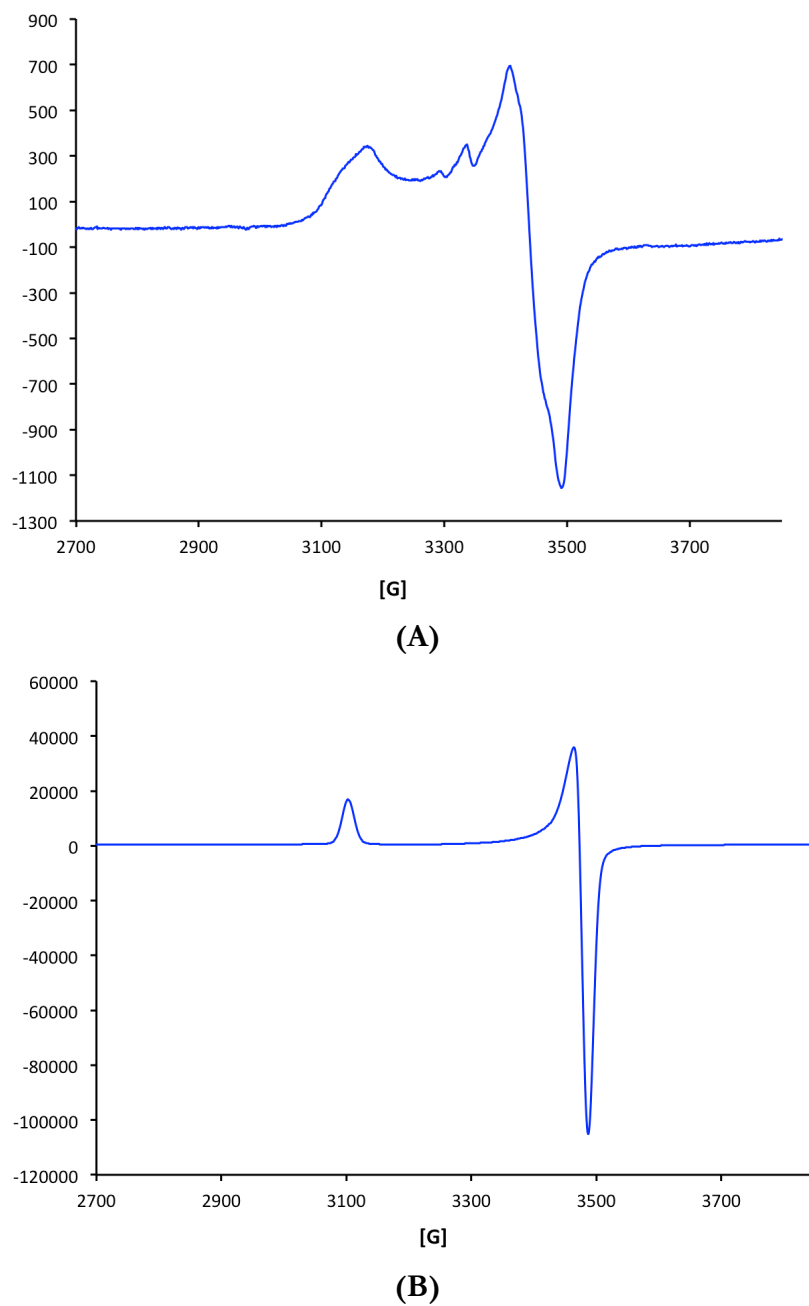


Figure 13. X-band EPR spectra of (a) the product from reaction D and (b) $[\text{Fe}_4\text{S}_4(\text{P}^i\text{Pr}_3)_4](\text{BPh}_4)$ reagent at 12 K in 2-methyltetrahydrofuran.

The cyclic voltammograms of $[\text{Fe}_4\text{S}_4(\text{P}^i\text{Pr}_3)_4](\text{BPh}_4)$ (Figure 14b) exhibits one reduction and one oxidation step at $E_{1/2} = -1.65$ and -0.40 V, respectively, in the three-member $[\text{Fe}_4\text{S}_4(\text{P}^i\text{Pr}_3)_4]^{0/+ / 2+}$. The CV of the product from reaction D (Figure 14a)

displays no reversible peak other than the two peaks around -1.55 and -0.75 V that were observed to couple to one another. Figure 14a may imply the presence of other species with overlapping redox peaks, causing the CV to broaden with no distinct redox event.

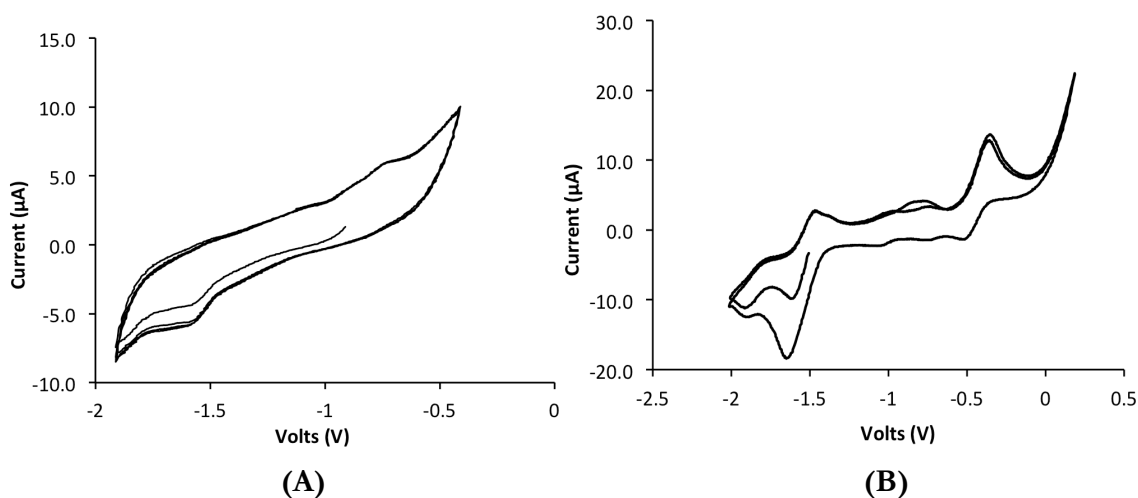


Figure 14. Cyclic voltammograms (100 mV/s, Pt electrode) of (a) the product from reaction D and (b) $[\text{Fe}_4\text{S}_4(\text{P}^i\text{Pr}_3)_4](\text{BPh}_4)$ reagent in 0.1 M $(\text{Bu}_4\text{N})(\text{PF}_6)$ in THF. Number peak potentials are referenced to Fc/Fc^+ .

Another route attempted was the reaction between **C.1–F** and one equivalent of $[\text{Fe}_4\text{S}_4(\text{P}^i\text{Pr}_3)_3(\text{SSiPh}_3)]$ (reaction E, Scheme 6) in benzene. No diamagnetic products were identified by ^1H and ^{31}P NMR spectroscopy. EPR spectroscopy and cyclic voltammetry were used to further characterize the resulting product from reaction E and the iron-sulfur cluster reagent, $[\text{Fe}_4\text{S}_4(\text{P}^i\text{Pr}_3)_3(\text{SSiPh}_3)]$ (Figure 15a and 16a). By EPR spectroscopy and cyclic voltammetry (Figure 15b and 16b), the iron-sulfur cluster precursor, $[\text{Fe}_4\text{S}_4(\text{P}^i\text{Pr}_3)_3(\text{SSiPh}_3)]$, was pure. The EPR spectrum of the product from reaction E displays signals at $g = 2.07$, and $g = 1.94$, while the signals from of $[\text{Fe}_4\text{S}_4(\text{P}^i\text{Pr}_3)_3(\text{SSiPh}_3)]$ are observed at $g = 2.13$ and $g = 1.94$. In the product mixture of reaction E, the EPR signal at $g = 2.13$ that corresponds to the $[\text{Fe}_4\text{S}_4(\text{P}^i\text{Pr}_3)_3(\text{SSiPh}_3)]$

precursor was not observed. This may indicate that reaction E has gone to completion, albeit producing a mixture of paramagnetic species indicated by the broad peak at $g = 2.07$.

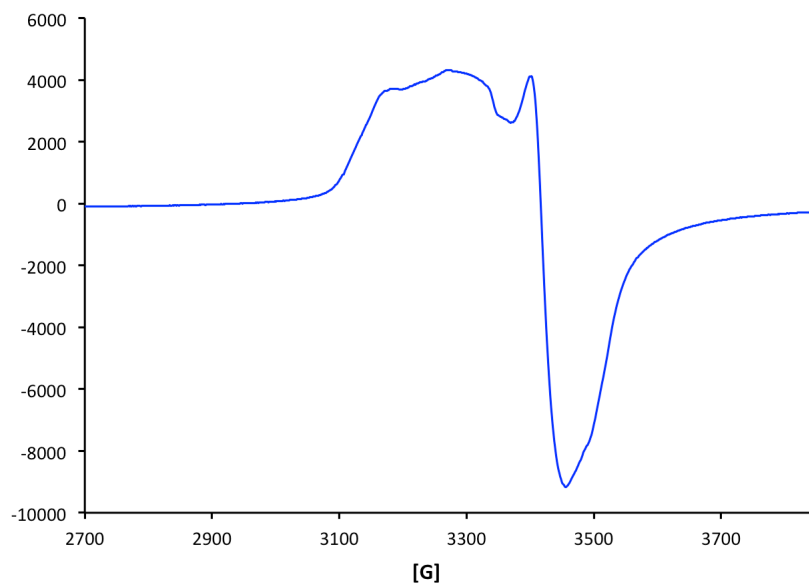
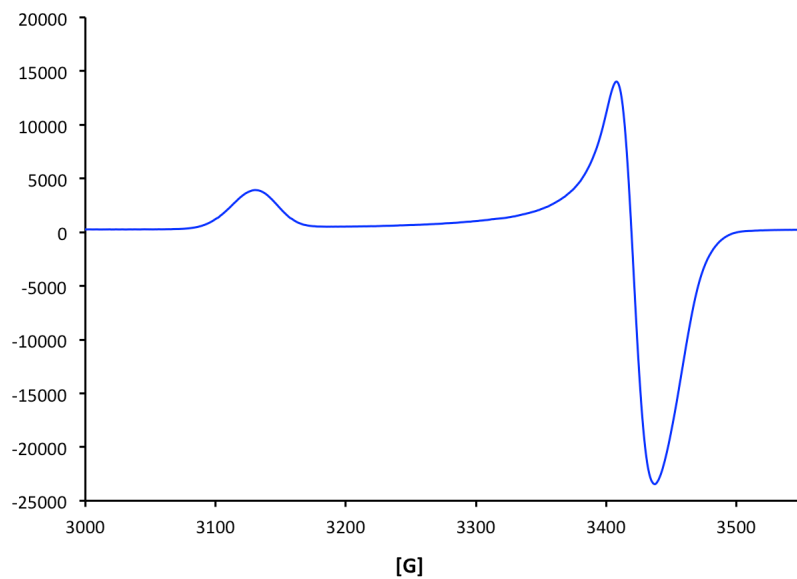
**(A)****(B)**

Figure 15. EPR spectra of (a) the product from reaction E and (b) $[\text{Fe}_4\text{S}_4(\text{P}^i\text{Pr}_3)_3(\text{SSiPh}_3)]$ reagent at 12 K in 2-methyltetrahydrofuran.

In the presence of triisopropylphosphine in the solution, four redox steps develop in the CV of $[\text{Fe}_4\text{S}_4(\text{P}^i\text{Pr}_3)_3(\text{SSiPh}_3)]$ (Figure 16b), although the iron-sulfur precursor looked pure by NMR and EPR spectroscopy. Those at -0.37 and -1.50 V are due to $[\text{Fe}_4\text{S}_4(\text{PPr}^i)_4]^+$ impurity, while the other features are assigned to the species $[\text{Fe}_4\text{S}_4(\text{PPr}^i)_2(\text{SSiPh}_3)_2]^{0/-/2}$ with $E_{1/2} = -0.80$ and -1.83 V. This phenomenon can be explained by equation (2).^{13c} The CV of the product from reaction E (Figure 16a) displays no distinct reversible peak but several peaks around -2.50 , 0.00 and $+0.50$ V were observed. The number of peaks observed in the CV (Figure 16a) implies the presence of other species with overlapping redox peaks, consistent with the production of multiple species.

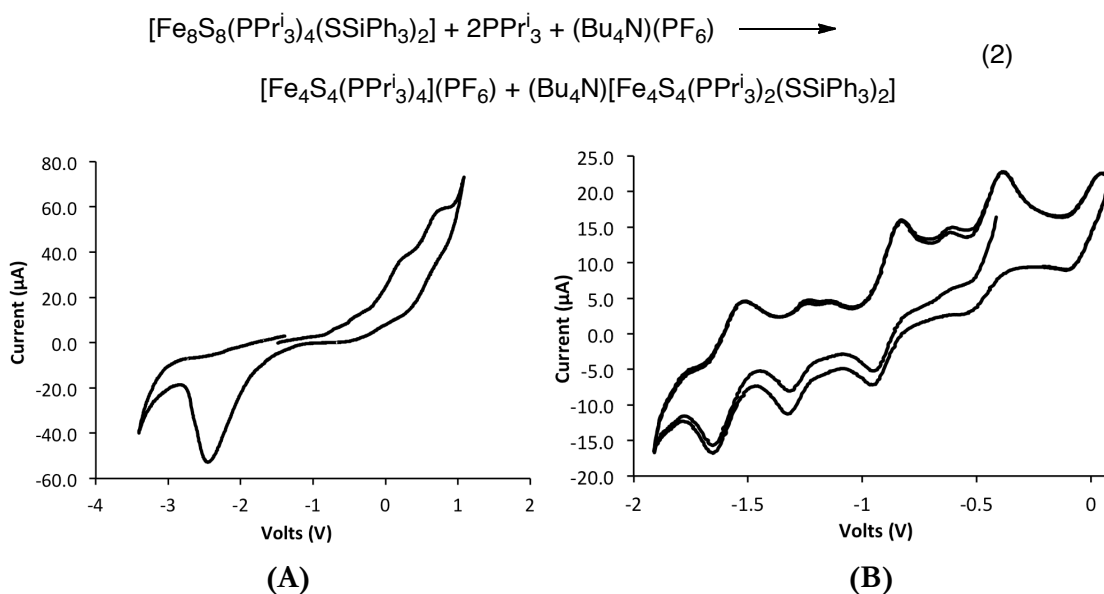


Figure 16. Cyclic voltammograms (Pt electrode, 100 mV/s) of (a) the product from reaction E and (b) $[\text{Fe}_4\text{S}_4(\text{P}^i\text{Pr}_3)_3(\text{SSiPh}_3)]$ reagent in 0.1 M $(\text{Bu}_4\text{N})(\text{PF}_6)$ solution in THF. Number peak potentials are referenced to Fc/Fc^+ .

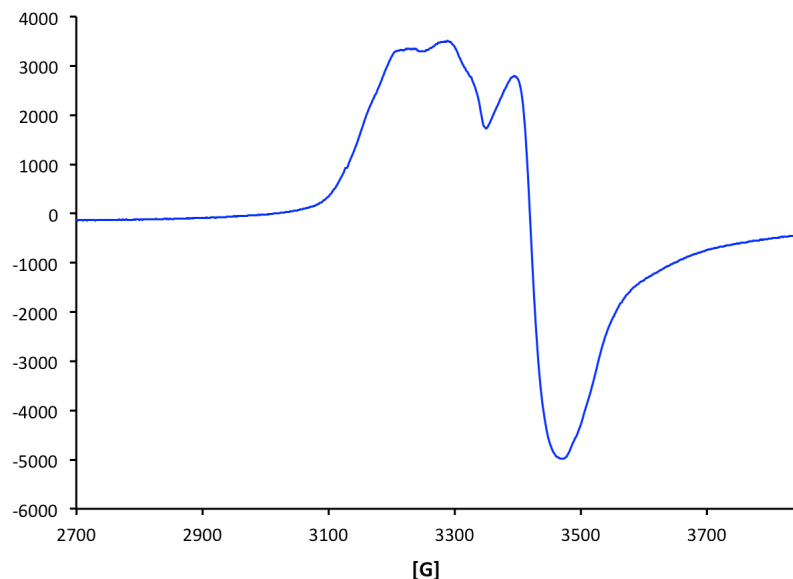


Figure 17. EPR spectrum of the product from reaction F at 12 K in (2-methyl)THF.

The first step in reaction F (Scheme 6) involved the addition of one equivalent of $[\text{Fe}_4\text{S}_4(\text{P}^i\text{Pr}_3)_4](\text{BPh}_4)$ to a solution of **C.1–F** in THF. After allowing the reaction to run for 2 hours, the mixture was filtered, and the solvent was removed *in vacuo*. ^1H and ^{31}P NMR spectroscopy suggested the presence of paramagnetic species in the product of the first step reaction F. To the dried filtrate residue was then added a solution of $(\text{Ph}_4\text{P})(\text{SSiPh}_3)$ (1 equiv) in acetonitrile. The reaction was allowed to run for 3 hours. Reaction F is similar to E except that the reagents were added in a different order. NMR spectroscopy data showed the formation of free triisopropyl phosphine and the presence of a paramagnetic species in the product mixture.

Comparing the EPR spectra of the products from reaction E and F (Figure 15a and 17 respectively), the line shapes of the two spectra were expected to be identical to one another, assuming that the two reactions should ideally yield the same product. The broadness of the peak on the EPR spectra around $g = 2.0$ may indicate the presence of multiple products in the solution. Fractionations of the product mixture were carried

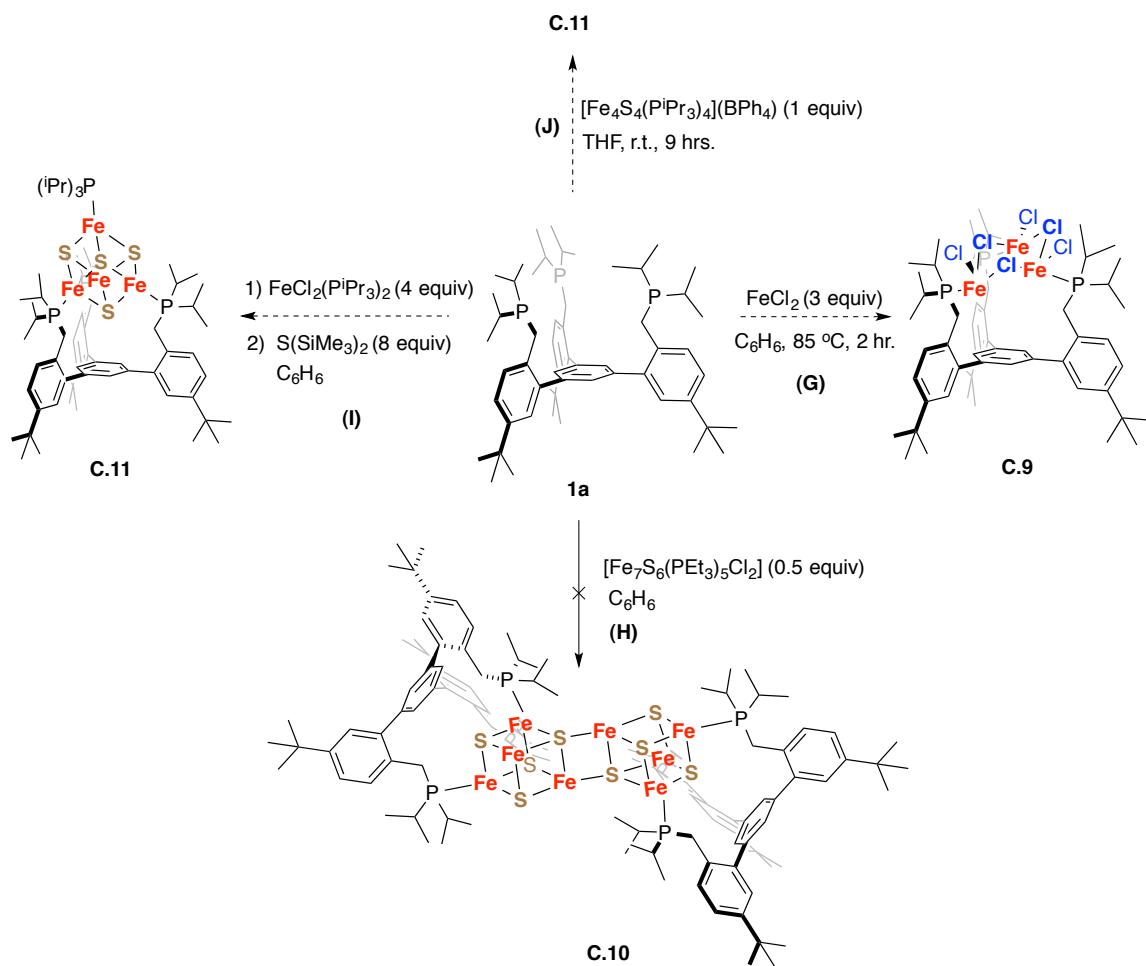
out in order to obtain better EPR spectra with distinct peaks. Unfortunately, the resulting EPR spectra from the fractionation of the products from both reaction E and F displayed different line shapes from one another around the region $g = 2.0$. This EPR data further supports the hypothesis of having a mixture of paramagnetic products as the outcome of these reactions. Since the EPR spectra, NMR spectra, and the CVs of the iron-sulfur cluster precursors, $[\text{Fe}_4\text{S}_4(\text{P}^i\text{Pr}_3)_4](\text{BPh}_4)$ and $[\text{Fe}_4\text{S}_4(\text{P}^i\text{Pr}_3)_3(\text{SSiPh}_3)]$, confirmed the purity of the starting materials and were consistent with the literature values, the one proposed hypothesis on the multiple products formation may be due to oligomerization by having the ligand bridge between two clusters.

Aside from using *N*-heterocyclic carbenes as ligands for the $[\text{Fe}_4\text{S}_4]$ -cluster, a triphosphine ligand **1a** was also used. Similar reactions to those shown in Scheme 6 were carried out with **1a** in place of **C.1**. The reaction of **1a** with three equivalents of FeCl_2 at 85°C for three days (reaction G, Scheme 7) did not go to completion as indicated by the peak corresponding to free ligand in the ^1H and ^{31}P NMR spectrum. Unlike the case with the **C.1** ligand, the addition of 0.5 equivalents of $[\text{Fe}_7\text{S}_6(\text{PEt}_3)_5]$ to **1a** (reaction H, Scheme 7) resulted in no reaction, as indicated by ^1H NMR spectroscopy. This outcome was not surprising due to the similarity of free PEt_3 and the phosphine moiety on the **1a** ligand.

Another attempt to construct the metal-sulfur cluster was by adding four and eight equivalents of $\text{FeCl}_2(\text{P}^i\text{Pr}_3)_2$ and $\text{S}(\text{SiMe}_3)_2$, respectively, to **1a** in benzene (reaction I, Scheme 7). Reaction I may be a promising route to achieve **1a**-supported iron-sulfur cluster due to the observed free triisopropylphosphine peaks in both the ^1H and ^{31}P NMR spectra. However, allowing reaction I to continue for 18 h at 60°C did not

indicate further product formation (or more triisopropylphosphine) by NMR spectroscopy. Possible rapid exchange between the ligand and free triisopropylphosphine may be occurring in reaction I, thus, the reaction does not go to completion even when run at higher temperatures for a longer period of time. In the future, a higher boiling solvent may be used instead of benzene so the reaction can be run at higher temperature under vacuum to pump off the triisopropylphosphine produced through the course of the reaction.

Scheme 7. Reactions of **1a** with various iron complexes in an attempt to reconstruct a $[\text{Fe}_4\text{S}_4]$ -cluster



The addition of an equivalent of $[\text{Fe}_4\text{S}_4(\text{P}^i\text{Pr}_3)_4](\text{BPh}_4)$ to **1a** in THF (reaction J, Scheme 7) led to no reaction even after raising the temperature of the reaction to 50°C over 14 h, shown by the presence of broad peaks corresponding to the free **1a** ligand and starting iron-sulfur salt by ^{31}P NMR spectroscopy. However, the broad peaks could be proposed as a fast exchange between **1a** and triisopropylphosphine such that no peak corresponding to free P^iPr_3 at the ^{31}P NMR spectrum was detected. After raising the temperature of the reaction even further to 80°C , ^{31}P NMR spectroscopy showed the formation of triisopropylphosphine while the peak corresponding to the starting material $[\text{Fe}_4\text{S}_4(\text{P}^i\text{Pr}_3)_4](\text{BPh}_4)$ was no longer observed. The remaining **1a** peak in the NMR spectrum indicates that the $[\text{Fe}_4\text{S}_4(\text{P}^i\text{Pr}_3)_4](\text{BPh}_4)$ starting material might have decomposed at 80°C before fully reacting with the ligand. Although reaction J does not seem promising, it can be repeated by using a higher boiling point solvent and running under vacuum to drive the equilibrium toward product formation.

For all the reactions performed with **C.1** and **1a**, crystallizations attempts have been unsuccessful, although recrystallizations of the product from each reaction were set up using vapor-diffusion technique and a variety of solvent combination. Efforts to further this project are no longer ongoing.

CONCLUSIONS

FdC14G, a mutant ferredoxin from the organism *Bacillus thermoproteolyticus*, has been recombinantly expressed, albeit in low yield, and characterized as an $[\text{Fe}_3\text{S}_4]$ -cluster ferredoxin. The mutant protein can be reconstituted to make the $[\text{Fe}_4\text{S}_4]$ -species under reducing conditions. Isolation and characterization efforts to incorporate the diiron unit **C.2Fe** to the protein still remain challenging. The approach to tether the diiron unit to

the protein can be pursued possibly through the use of a different functional group to bind to the crosslinker.

The sterically hindered tricarbene and triphosphine ligands based were synthesized. Preliminary experiments to make the ligand-supported iron-sulfur cluster have been inconclusive due to unsuccessful attempts in recrystallization and the lack of observable signals of the paramagnetic species by NMR spectroscopy. Reactions that seem promising will be optimized and repeated on a larger scale. Consequently, recrystallization attempts of the products from the metallation experiments will still be performed under various conditions to get X-ray quality crystals.

A challenge in the effort of constructing the **C.1**- or **1a**-supported $[\text{Fe}_4\text{S}_4]$ cluster has been in growing X-ray quality crystals, which might be due to the freely rotating aryl-aryl bonds of the benzene core. One possible solution to solve this problem is through 2,4,6-methyl substitution of the central aryl ring that should help lock the triaryl substituents in the *syn*-atropisomer. Another alternative is to run the reactions in more dilute solution upon thawing to avoid oligomerization as a proposed cause of the multiple paramagnetic species observed. Preliminary EPR experiments at 12 K can be used to characterize the product from these reactions.

Due to the difficulty in obtaining structural characterizations in all of these compounds and reaction mixtures, this project is no longer pursued.

EXPERIMENTAL SECTION

Materials and Methods

Unless otherwise specified, all synthetic compounds were manipulated using a glovebox or standard Schlenk line techniques with an N₂ atmosphere. Anhydrous tetrahydrofuran (THF) was purchased from Aldrich in 18 L Pure-Pac™ containers. Anhydrous benzene, dichloromethane, diethyl ether, and THF were purified by sparging with nitrogen for 15 minutes and then passing under nitrogen pressure through a column of activated A2 alumina (Zapp's). Chloroform-*d*₁ and D₂O were purchased from Cambridge Isotopes. 1-methoxyphenylimidazole¹⁴ was synthesized according to literature procedure. Unless indicated otherwise, all commercial chemicals were used as received. ¹H NMR spectra were recorded on a Varian 300 MHz instrument with shifts reported relative to the residual solvent peak.

Gene Sequence

The wild type ferredoxin was generated from bacterial gene (*Bacillus thermoproteolyticus*) with the sequence:

```
5'-CCGAAATACACCATTTGTGGATAAAGAGACGTGCATTGCATGCGGCGCAT
GCGGCGCGGCGGCCCCAGATATTTACGACTATGACGAGGACGGTATCGCC
TATGTGACGCTGGATGACAATCAGGGTATTGTTCGAAGTTCCGGATATCCTG
ATCGATGATATGATGGACGCGTTTGAAGGCTGCCCCACCGACAGCATCAAA
GTTGCCGATGAACCATTCGATGGTGATCCGAACAAGTTTGAATAA-3'
```

The gene coding for FdC14G was obtained by performing a single point mutation to the parent sequence via Quikchange mutagenesis to the mutant sequence:

```
5'-CCGAAATACACCATTTGTGGATAAAGAGACGTGCATTGCAGGCGGCGCAT
```

GCGGCGCGGCGGCCCCAGATATTTACGACTATGACGAGGACGGTATCGC
 CTATGTGACGCTGGATGACAATCAGGGTATTGTTCGAAGTTCCGGATATCCT
 GATCGATGATATGATGGACGCGTTTGAAGGCTGCCCGACCGACAGCATCAA
 AGTTGCCGATGAACCATTCGATGGTGATCCGAACAAGTTTGAATAA-3'

The gene coding for Fd C14G A16C was obtained by performing a single point mutation to the Fd C14G sequence via Quikchange mutagenesis to the mutant sequence:

5'-CCGAAATACACCATTGTGGATAAAGAGACGTGCATTGCAGGCGGCT**GGCT**
 GCGGCGCGGCGGCCCCAGATATTTACGACTATGACGAGGACGGTATCGCC
 TATGTGACGCTGGATGACAATCAGGGTATTGTTCGAAGTTCCGGATATCCTG
 ATCGATGATATGATGGACGCGTTTGAAGGCTGCCCGACCGACAGCATCAAA
 GTTGCCGATGAACCATTCGATGGTGATCCGAACAAGTTTGAATAA-3'

The gene coding for the mutant ferredoxin was integrated into the pET28b plasmid.

Protein Expression and Purification

pET28b plasmids containing the gene of interest were transformed into *E. coli* Tuner (DE3)pLysS cells. Small overnight cultures of Tuner cells already transformed with the pET28b-FdC14G and pET28b-FdC14G A16C were utilized to prepare for the large scale protein expression using the fermentor (9L of Terrific Broth containing 30 mg/L of kanamycin and chloramphenicol). The large scale culture was done using a fermentor at 37°C and with air bubbled through the culture. When the A_{600} of the cell culture reached 3, bubbling of O₂ through the culture was started. When the A_{600} of the cell culture reached 4, the culture was cooled to 25°C, and protein expression was induced by IPTG (isopropyl-beta-D-thiogalactopyranoside, 1-2 mM final

concentration). After 18-20 hours, the culture was harvested by centrifugation at 4400 rpm.

Cell pellets were resuspended in lysis buffer (50 mM sodium phosphate, 100 mM NaCl, 10 mM imidazole, 10% glycerol, pH 8) and lysed by a sonicator (15 x 30 sec sonication with 1 minute interval between each sonication). The lysed cells were pelleted via centrifugation for 1.5 hr at 13500 rpm. Supernatant was loaded to batch Ni-NTA superflow column (purchased from 5prime), and the column was washed with five column volumes of washing buffer (50 mM sodium phosphate, 100 mM NaCl, 25 mM imidazole, 10% glycerol, pH 8). Elution of protein was done using 1.5 column volume of elution buffer (50 mM sodium phosphate, 100 mM NaCl, 250 mM imidazole, 10% glycerol, pH 8). The buffer from the elution fraction was exchanged to 50 mM Tris-HCl, 1 mM DTT, pH 8 via dialysis for preparation of the His₆-tag cleavage by TEV protease.

Following buffer exchange, TEV protease was added to the protein solution. The cleavage reaction was allowed to proceed overnight at room temperature. The mixture was then loaded onto the Ni-NTA column followed by washing the column 2x with the lysis buffer. The flowthrough from the nickel column was collected and then loaded onto the DEAE Sepharose column (purchased from GE Healthcare). The DEAE column was initially washed with 5 column volumes of 50 mM sodium phosphate, 100 mM NaCl, pH 8 buffer, followed by a second washing with 5 column volumes of 50 mM sodium phosphate, 175 mM NaCl, pH 8 buffer. The brown-colored FdC14G was eluted by 50 mM sodium phosphate, 350 mM NaCl, pH 8 buffer. Fractions containing the FdC14G were brown-orange in color and checked for purity

by SDS-PAGE with AgNO_3 staining. Protein obtained (1 mg/mL) by this procedure has purity >95%. Quantification of protein was done by UV VIS spectroscopy analysis.

UV-Vis Spectroscopy Characterization of FdC14G

Protein solution was prepared aerobically and anaerobically. To reduce the protein, dithionite reducing agent was added under inert atmosphere (N_2) in a glove box. Concentration of **FdC14G-[Fe₃S₄]** and **FdC14G-[Fe₄S₄]** were analyzed by monitoring the absorption at 400 nm with $\epsilon = 17 \text{ mM}^{-1}\text{cm}^{-1}$ and $\epsilon = 16 \text{ mM}^{-1}\text{cm}^{-1}$ respectively.

Reconstitution of 4th Iron to FdC14G-[Fe₃S₄]

Reconstitution experiments were carried out in 200 μL final volume of mixture of reagents. The 200 μL mixture consists of 100 μM FdC14G, 1 mM sodium dithionite reducing agent, 1 mM $\text{Fe(II)(NH}_4)_2(\text{SO}_4)_2$, and 1 mM b-mercaptanol in 1:1 ratio of MeCN: buffer (50 mM sodium phosphate, 350 mM NaCl, pH 8) as the solvent.

Incorporation of the C.2Fe to FdC14G-[Fe₄S₄]

The reaction mixture has a total volume of 200 μL that consists of 100 μM FdC14G, 1 mM sodium dithionite reducing agent, 1 mM $\text{Fe(II)(NH}_4)_2(\text{SO}_4)_2$, 1 mM diiron complex, and 1 mM b-mercaptanol. The solvent used to prepare the mixture was 1:1 ratio of MeCN : buffer (50 mM sodium phosphate, 350 mM NaCl, pH 8).

Characterization of FdC14G by EPR

All protein samples were from the reconstitution and the incorporation of the **C.2Fe** complex experiments. Once the protein samples were made, they were quickly frozen in liquid nitrogen. EPR samples were taken using the Bruker BioSpin GmbH instrument with parameters 3400 G center field, 800 G sweep width, 9.373 GHz

frequency, 2.036 mW frequency, 100 kHz modulation frequency, and 4.00 G modulation amplitude.

Synthesis of C.2Fe

C.2Fe was synthesized according to a literature protocol.^{6a}

Synthesis of B

To a solution of compound **A** (12.75 g, 24.67 mmol, 1 equiv) in CCl₄ (167 mL) under N₂ was added N-bromosuccinimide (13.61 g, 76.48 mmol, 3.1 equiv) and benzoyl peroxide (564 mg, 2.33 mmol). The mixture was stirred at 85°C for 20 hours. The reaction mixture was allowed to cool then the succinimide was removed by filtration. The filtrate was rotary evaporated and then resuspended in dichloromethane. The resulting crude product in dichloromethane was run through a silica plug and concentrated to give yellow-orange solid. The clean product can be purified via flash chromatography (4:1 hexanes : CH₂Cl₂) in 60% yield after multiple runs (although challenging due to the presence of mono- and dibrominated side products). ¹H NMR (300 MHz, CDCl₃) δ 7.59 (s, 3 H), 7.51 (d, *J* = 9.0 Hz, 3H), 7.42 (s overlapped, 3H), 7.41 (d overlapped, *J* = 9.0 Hz, 3H), 4.62 (s, 6H), 1.35 (s, 27H) ppm.

Synthesis of C.4-R'

Similar procedures were carried out to synthesize **C.4-OMe** and **C.4-F**. Only representative procedure is shown for **C.4-OMe**.

C.4-OMe: To a solution of **B** (610 mg, 0.810 mmol) in dichloromethane (3 mL) was added 1-methoxyphenylimidazole¹⁴ (438 mg, 2.51 mmol). The mixture was stirred for 12 hours at room temperature. The desired product was precipitated out with the addition of *n*-hexane as white solid. The solid was collected through filtration, washed with hexane, and dried under vacuum to afford the clean product in 80% yield. ¹H NMR

(300 MHz, CDCl₃) δ 10.66 (s, 3H), 8.11 (s, 3H), 7.71 (s, 3H), 7.59 (d, J = 9.0 Hz, 6H), 7.51 (s, 3H), 7.45 (d, J = 2.0 Hz, 3H), 7.35 (dd, J = 8.2, 2.0 Hz, 3H), 6.97 (d, J = 9.0 Hz, 6H), 6.80 (d, J = 8.2 Hz, 3H), 6.02 (s, 6H), 3.79 (s, 9H), 1.35 (s, 27H) ppm.

C.4–F: ¹H NMR (300 MHz, CDCl₃) δ 10.71 (s, 3H), 8.12 (s, 4H), 7.81 – 7.66 (m, 9H), 7.51 (s, 3H), 7.47 (d, J = 1.9 Hz, 3H), 7.23 – 7.16 (dd, J = 8.8 Hz, 6H), 6.80 (d, J = 8.2 Hz, 3H), 6.04 (s, 6H), 1.35 (s, 27H) ppm. ¹⁹F NMR (282 MHz, CDCl₃) δ –109.45 (ddd, J = 12.2, 8.1, 4.4 Hz) ppm.

Synthesis C.1–R'

An analogous procedure to **C.1–OMe** was carried out for the synthesis of **C.1–F**. Only the synthesis of **C.1–OMe** is presented as representative protocol.

C.1–OMe: In an inert atmosphere environment, to a suspension of 5b (200 mg, 0.157 mmol) in dry benzene (5 mL) was added potassium *tert*-butoxide (59.4 mg, 0.486 mmol) in dry benzene (5 mL). The reaction mixture turned dark brown after 15 mins and was stirred for 1 hour at room temperature. The mixture was filtered through celite and washed with benzene. Solvent was removed off the filtrate *in vacuo* to give clean product as brown solid in quantitative yield (98%): ¹H NMR (300 MHz, C₆D₆) δ 7.66 (d, J = 8.9 Hz, 6H), 7.62 (s, 6H), 7.36 (d, J = 8.2 Hz, 6H), 7.24 (dd, J = 8.1, 2.0 Hz, 6H), 6.88 (d, J = 1.6 Hz, 3H), 6.72 (d, J = 8.9 Hz, 6H), 6.61 (d, J = 1.5 Hz, 3H), 5.55 (s, 6H), 3.26 (s, 9H), 1.20 (s, 27H) ppm.

C.1–F: ¹H NMR (300 MHz, C₆D₆) δ 7.60 (s, 6H), 7.50 (d, J = 4.8 Hz, 3H), 7.47 (d, J = 4.8 Hz, 3H), 7.29 (d, J = 8.2 Hz, 3H), 7.26 (d, J = 1.9 Hz, 3H), 7.23 (d, J = 1.9 Hz, 3H), 6.73 (dd, J = 11.8, 5.2 Hz, 6H), 6.56 (d, J = 1.7 Hz, 3H), 5.47 (s, 6H), 1.19 (s, 27H) ppm. ¹⁹F NMR (282 MHz, C₆D₆) δ –117.81 (ddd, J = 13.0, 8.4, 4.8 Hz) ppm.

REFERENCES

- 1 (a) Lewis, N. S.; Nocera, D. G. *Proc. Natl. Acad. Sci. U.S.A.* **2006**, *103*, 15729. (b) Tard, C.; Pickett, C. J. *Chem. Rev.* **2009**, *109*, 2245.
- 2 Gloaguen, F.; Rauchfuss, T. B. *Chem. Soc. Rev.* **2009**, *38*, 100.
- 3 Winter, M.; Brodd, R. J. *Chem. Rev.* **2004**, *104*, 4245.
- 4 (a) Volbeda, A.; Charon, M. H.; Piras, C.; Hatchikian, E. C.; Frey, M.; Fontecillacamps, J. C. *Nature* **1995**, *373*, 580. (b) Ogata, H.; Mizoguchi, Y.; Mizuno, N.; Miki, K.; Adachi, S.; Yasuoka, N.; Yagi, T.; Yamauchi, O.; Hirota, S.; Higuchi, Y. *J. Am. Chem. Soc.* **2002**, *124*, 11628. (c) Peters, J. W.; Lanzilotta, W. N.; Lemon, B. J.; Seefeldt, L. C. *Science* **1998**, *282*, 1853. (d) Shima, S.; Pilak, O.; Vogt, S.; Schick, M.; Stagni, M. S.; Meyer-Klaucke, W.; Warkentin, E.; Thauer, R. K.; Ermler, U. *Science* **2008**, *321*, 572.
- 5 Liu, X. M.; Ibrahim, S. K.; Tard, C.; Pickett, C. J. *Coord. Chem. Rev.* **2005**, *249*, 1641.
- 6 (a) Tard, C.; Liu, X. M.; Ibrahim, S. K.; Bruschi, M.; De Gioia, L.; Davies, S. C.; Yang, X.; Wang, L. S.; Sawers, G.; Pickett, C. J. *Nature* **2005**, *433*, 610. (b) Camara, J. M.; Rauchfuss, T. B. *J. Am. Chem. Soc.* **2011**, *133*, 8098.
- 7 Deng, L.; Holm, R. H. *J. Am. Chem. Soc.* **2008**, *130*, 9878.
- 8 Kennedy, M. C.; Kent, T. A.; Emptage, M.; Merkle, H.; Beinert, H.; Munck, E. *J. Biol. Chem.* **1984**, *259*, 4463.
- 9 Shirakawa, T.; Takahashi, Y.; Wada, K.; Hirota, J.; Takao, T.; Ohmori, D.; Fukuyama, K. *Biochemistry* **2005**, *44*, 12402.
- 10 (a) Beinert, H.; Kennedy, M. C.; Stout, C. D. *Chem. Rev.* **1996**, *96*, 2335. (b) Koay, M. S.; Antonkine, M. L.; Gartner, W.; Lubitz, W. *Chem. Biodivers.* **2008**, *5*, 1571. (c) Beinert, H.; Thomson, A. J. *Arch. Biochem. Biophys.* **1983**, *222*, 333.
- 11 Suseno, S.; Agapie, T. *Organometallics* **2013**, *32*, 3161.
- 12 (a) Vogel, C.; Heinemann, F. W.; Sutter, J.; Anthon, C.; Meyer, K. *Angew. Chem. Int. Edit.* **2008**, *47*, 2681. (b) Louie, J.; Grubbs, R. H. *Chem. Commun.* **2000**, 1479.
- 13 (a) Averill, B. A.; Herskovi, T.; Holm, R. H.; Ibers, J. A. *J. Am. Chem. Soc.* **1973**, *95*, 3523. (b) Wong, G. B.; Bobrik, M. A.; Holm, R. H. *Inorg. Chem.* **1978**, *17*, 578. (c) Zhou, H. C.; Holm, R. H. *Inorg. Chem.* **2003**, *42*, 11.
- 14 Flahaut, A.; Roland, S.; Mangeney, P. *J. Organomet. Chem.* **2007**, *692*, 5754.

APPENDIX D

NMR SPECTRA

CHAPTER 2

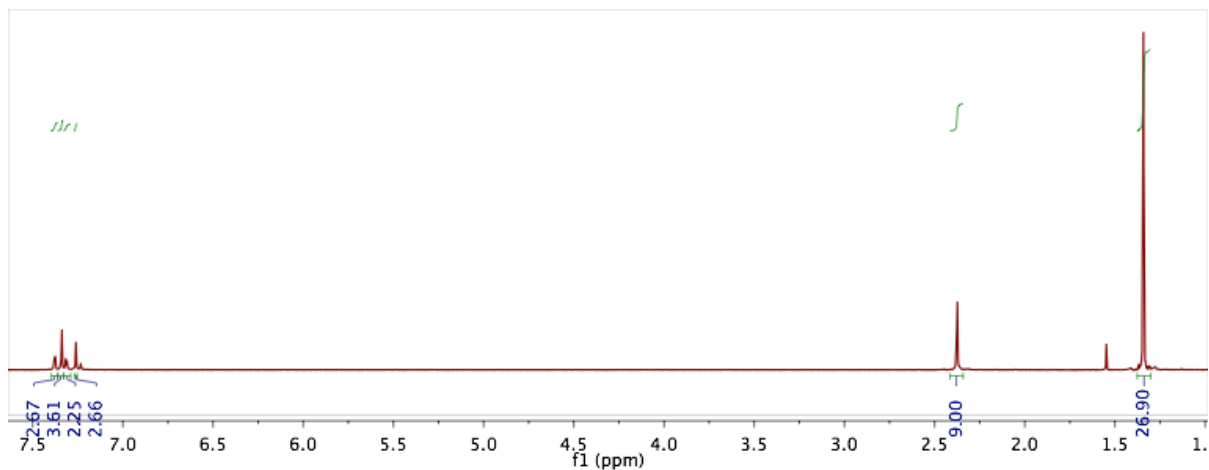


Figure 1. ^1H (left, 300 MHz, CDCl_3) NMR spectrum of **A**

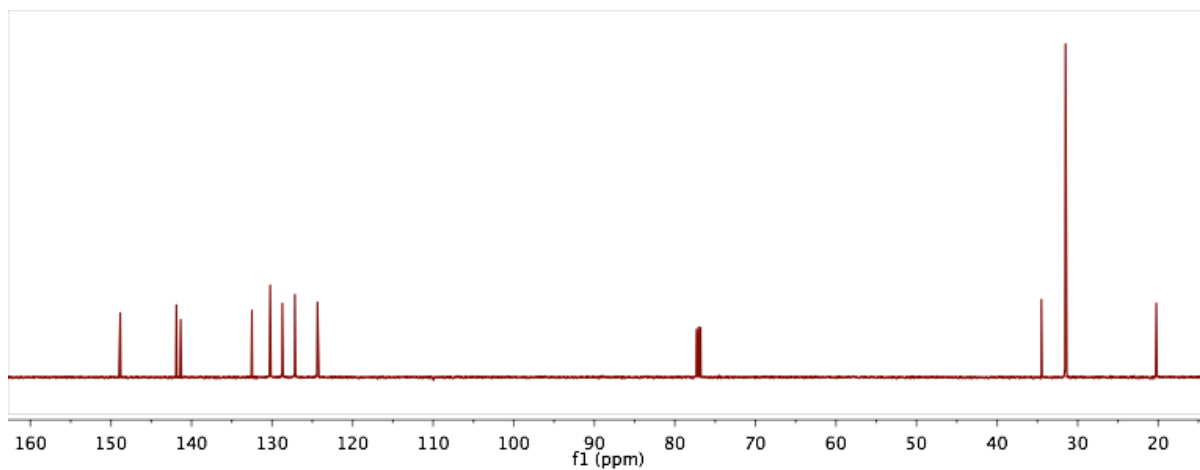


Figure 2. ^{13}C NMR (126 MHz, CDCl_3) spectrum of **A**

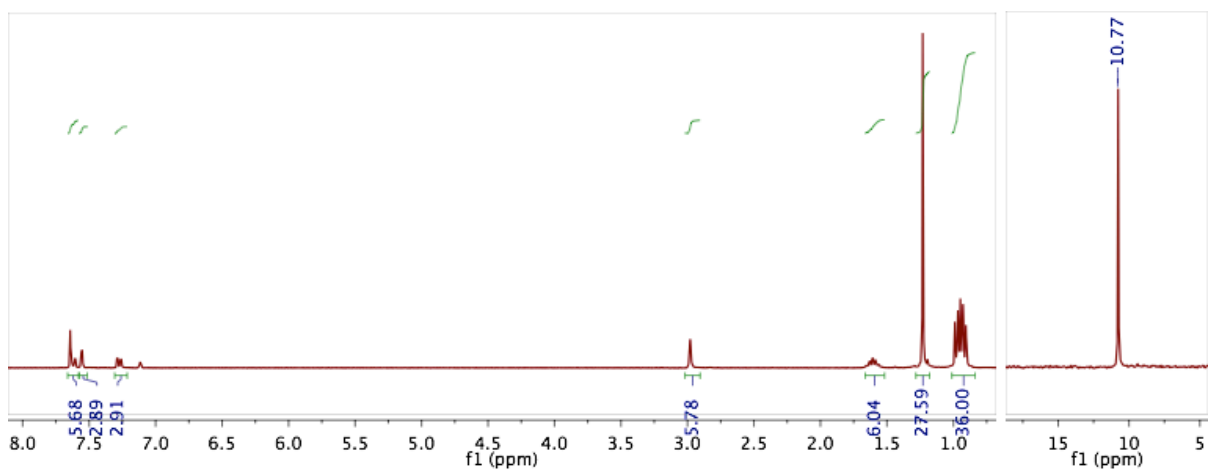


Figure 3. ^1H (left, 300 MHz, C_6D_6) and ^{31}P (right, 121 MHz, C_6D_6) NMR spectra of **1a**

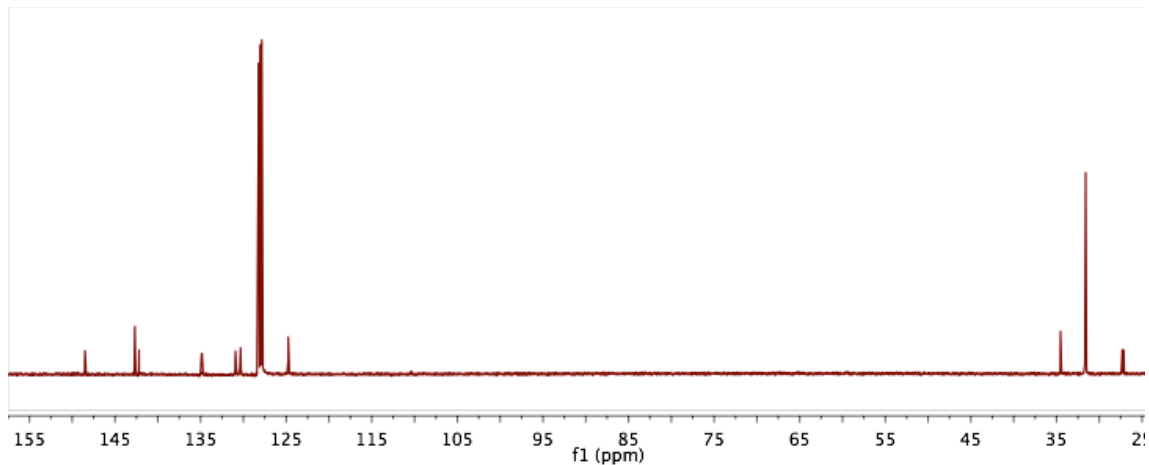


Figure 4. ^{13}C NMR (126 MHz, C_6D_6) spectrum of **1a**

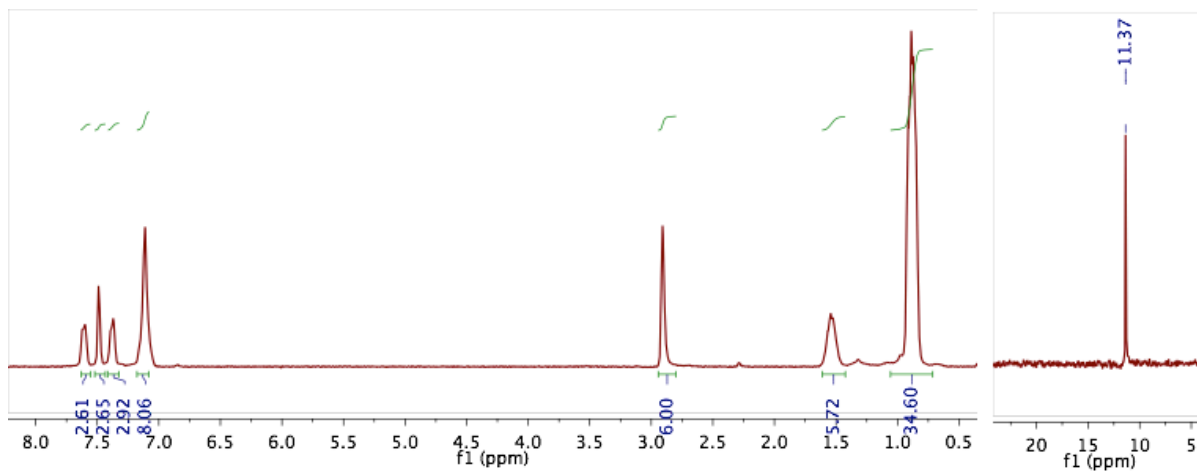


Figure 5. ^1H (left, 300 MHz, C_6D_6) and ^{31}P (right, 121 MHz, C_6D_6) NMR spectra of **1b**

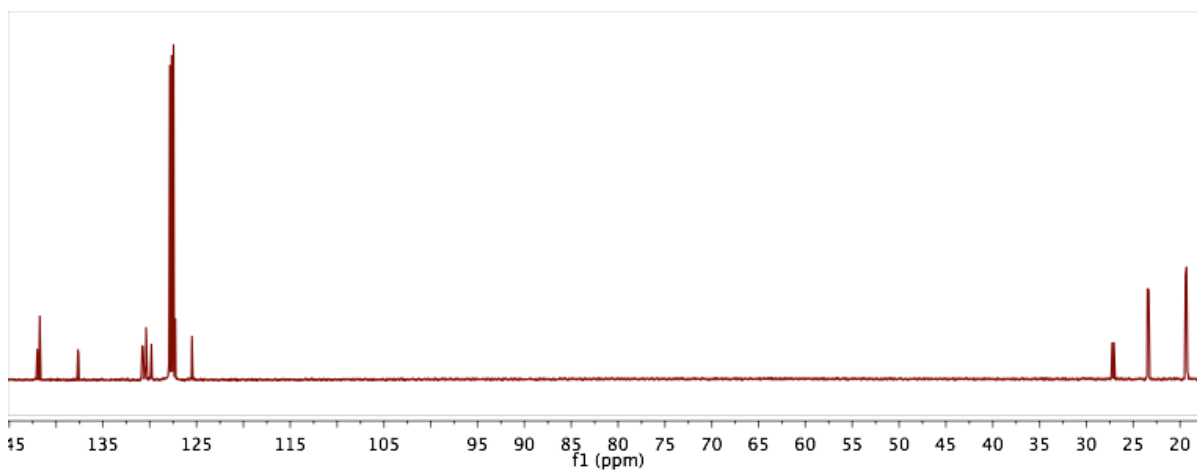


Figure 6. ^{13}C NMR (126 MHz, C_6D_6) spectrum of **1b**

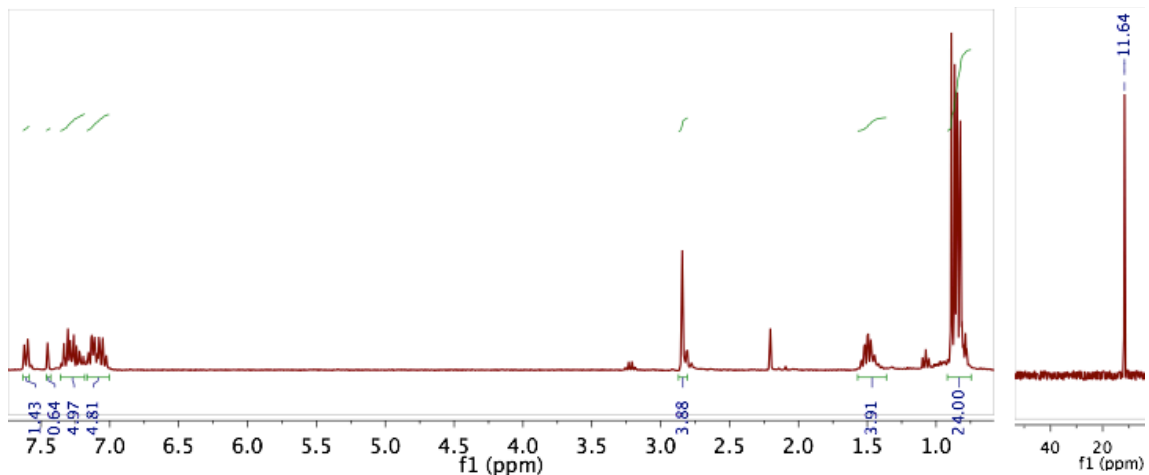


Figure 7. ^1H (left, 300 MHz, C_6D_6) and ^{31}P (right, 121 MHz, C_6D_6) NMR spectra of **1c**

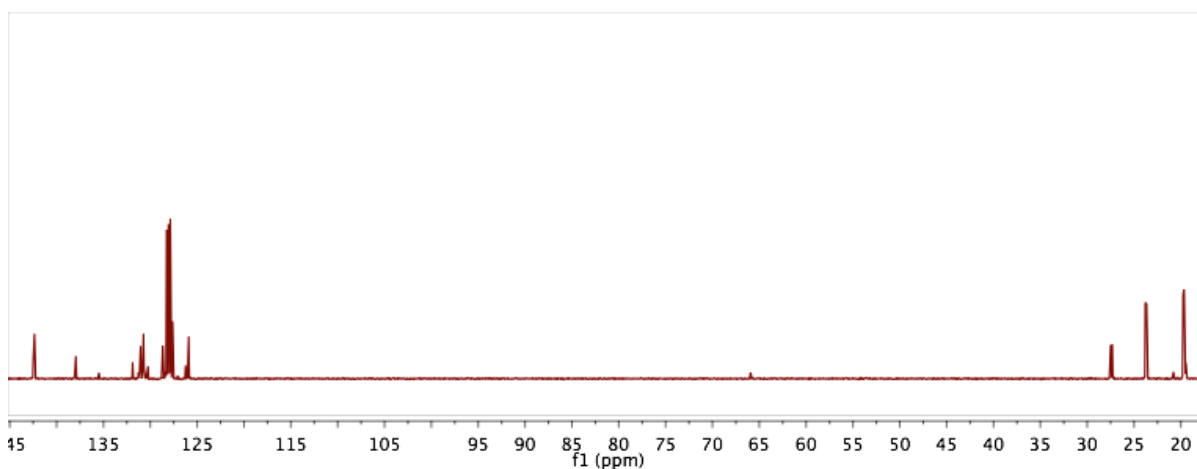


Figure 8. ^{13}C NMR (126 MHz, C_6D_6) spectrum of **1c**

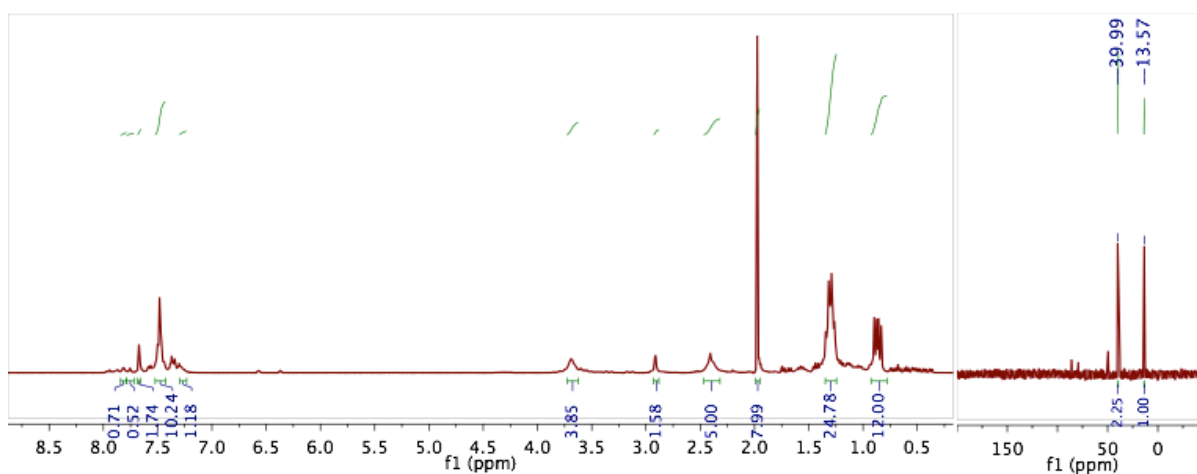


Figure 9. ^1H (left; 300 MHz, CD_3CN) and ^{31}P (right; 121 MHz, CD_3CN) NMR spectra of **2b-Pd**. Note: the smaller impurity peaks correspond to the concurrent formation of **3b-Pd**.

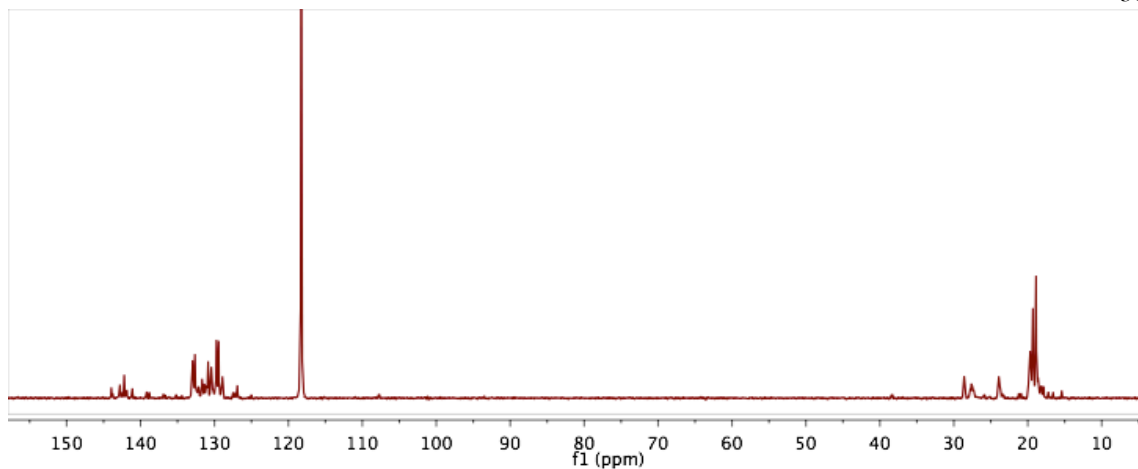


Figure 10. ^{13}C NMR (126 MHz, CD_3CN) spectrum of **2b-Pd**. Note: the smaller impurity peaks correspond to the increasing formation of **3b-Pd** during the reaction.

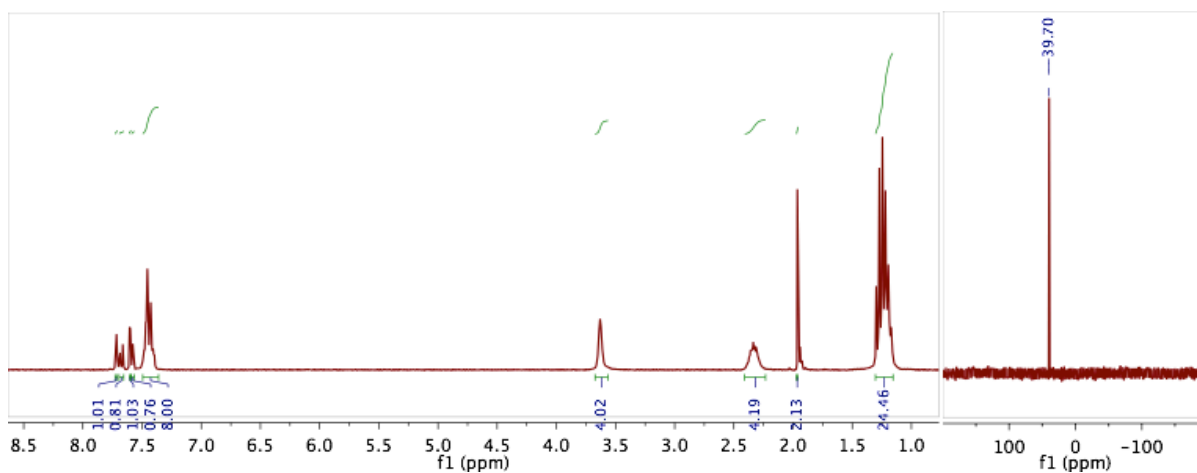


Figure 11. ^1H (left; 300 MHz, CD_3CN) and ^{31}P (right; 121 MHz, CD_3CN) NMR spectra of **2c-Pd**

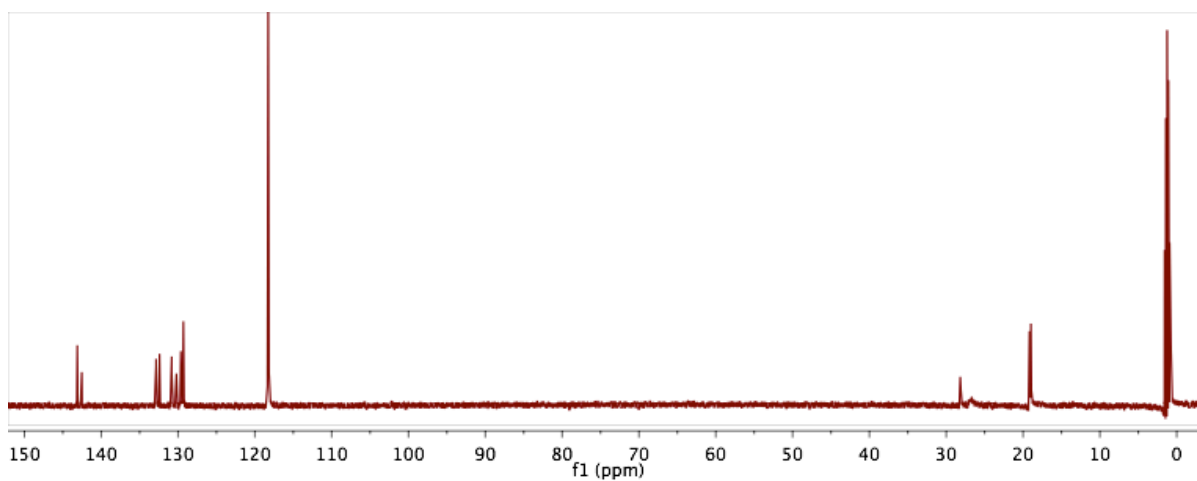


Figure 12. ^{13}C NMR (126 MHz, CD_3CN) spectrum of **2c-Pd**

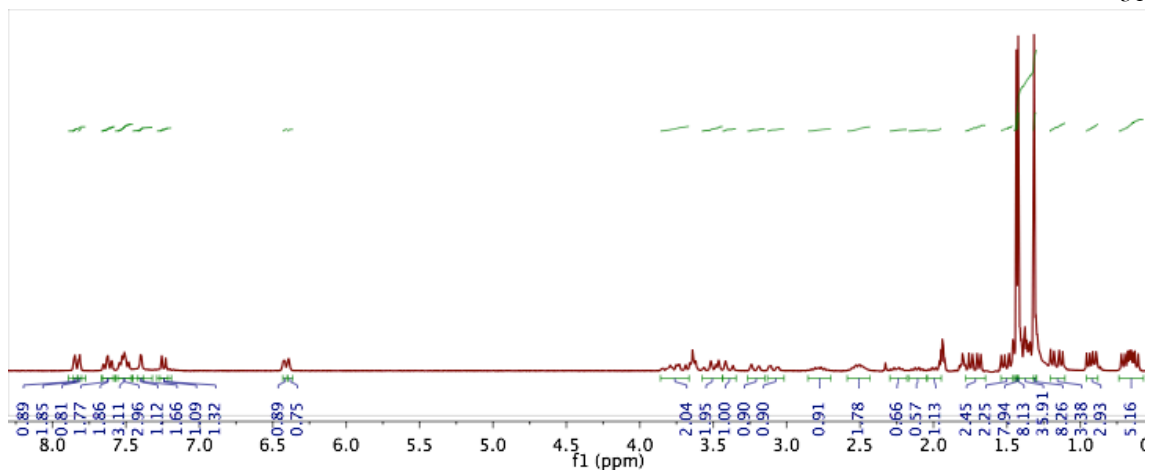


Figure 13. ¹H NMR (300 MHz, CD₃CN) spectrum of 3a-Ni

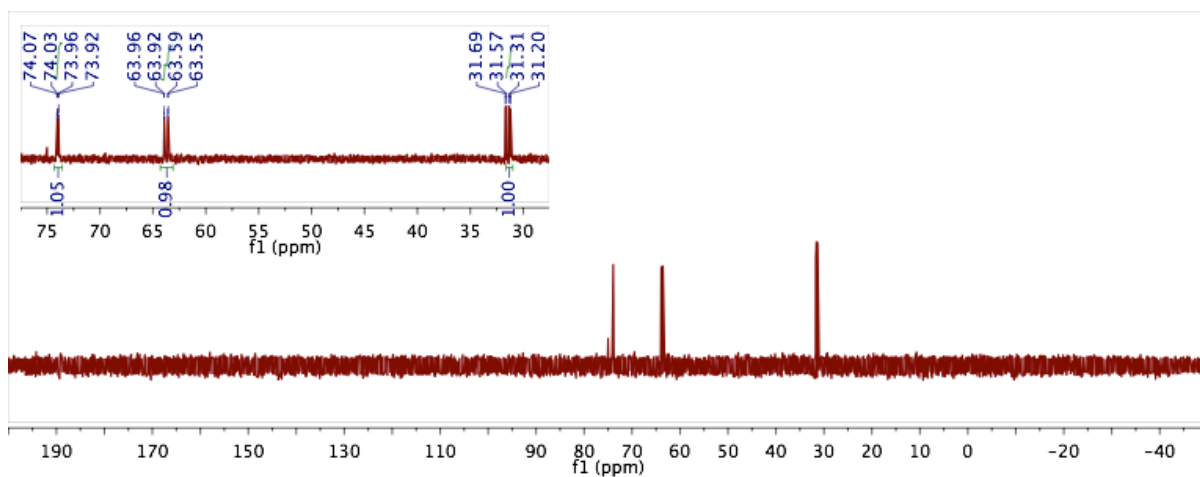


Figure 14. ³¹P NMR (121 MHz, CD₃CN) spectrum of 3a-Ni

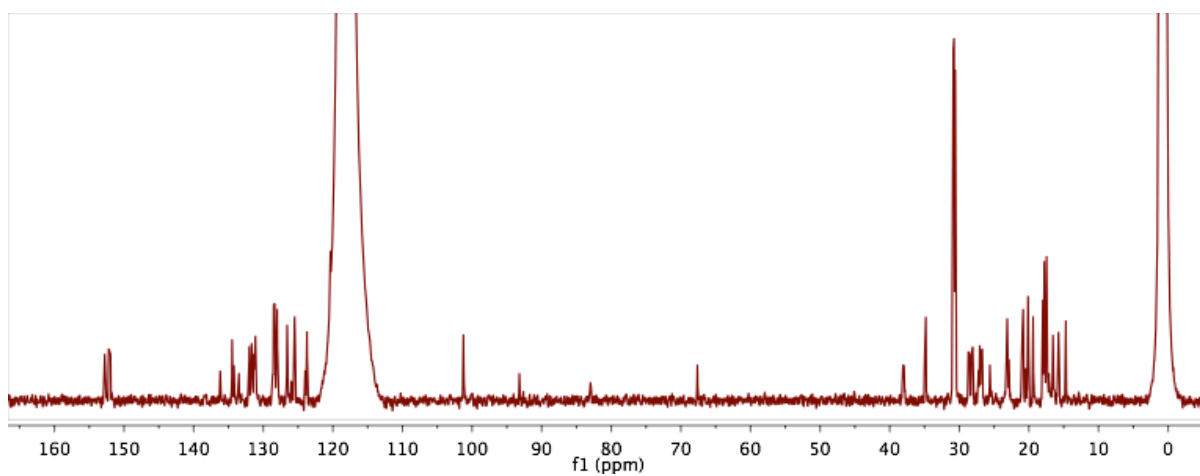


Figure 15. ¹³C NMR (126 MHz, CD₃CN) spectrum of 3a-Ni

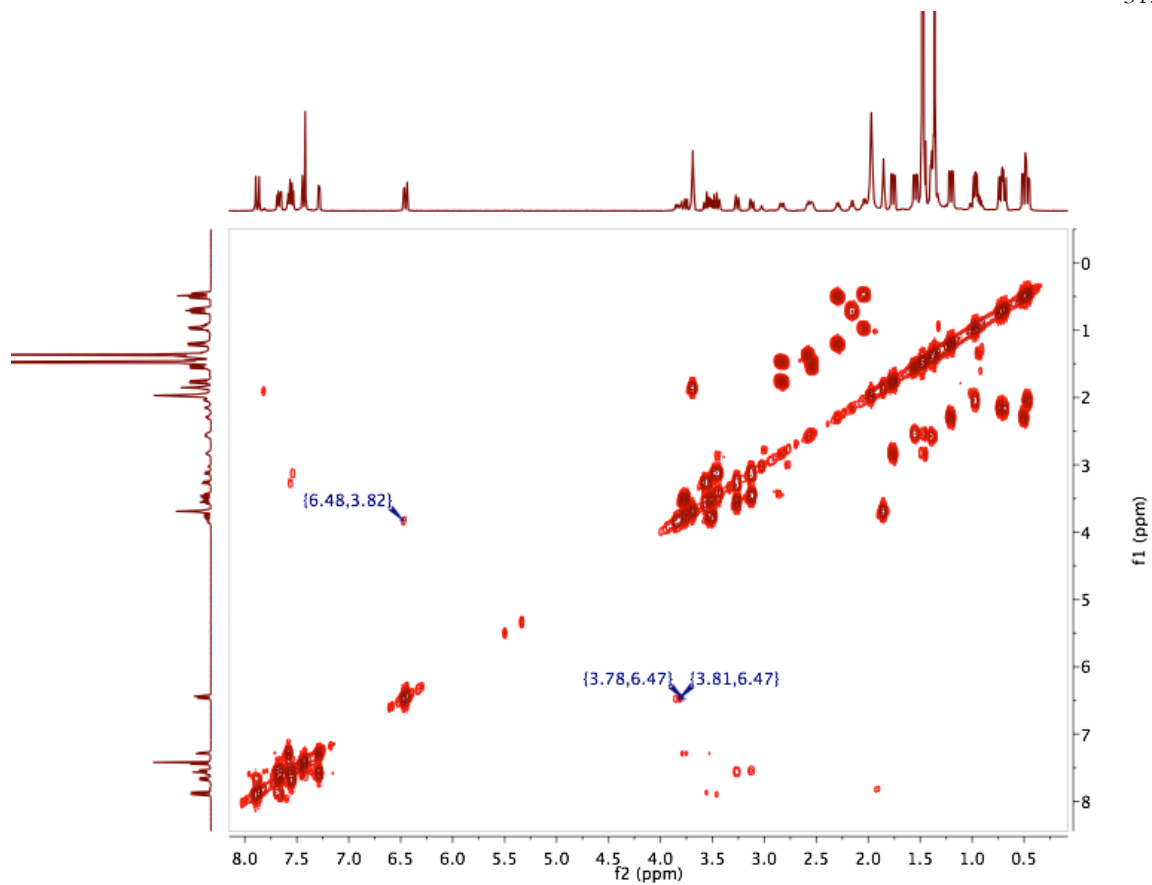


Figure 16. ^1H - ^1H gCOSY(600 MHz, CD_3CN) spectrum of **3a-Ni**. The labeled peaks are the central-ring proton correlations

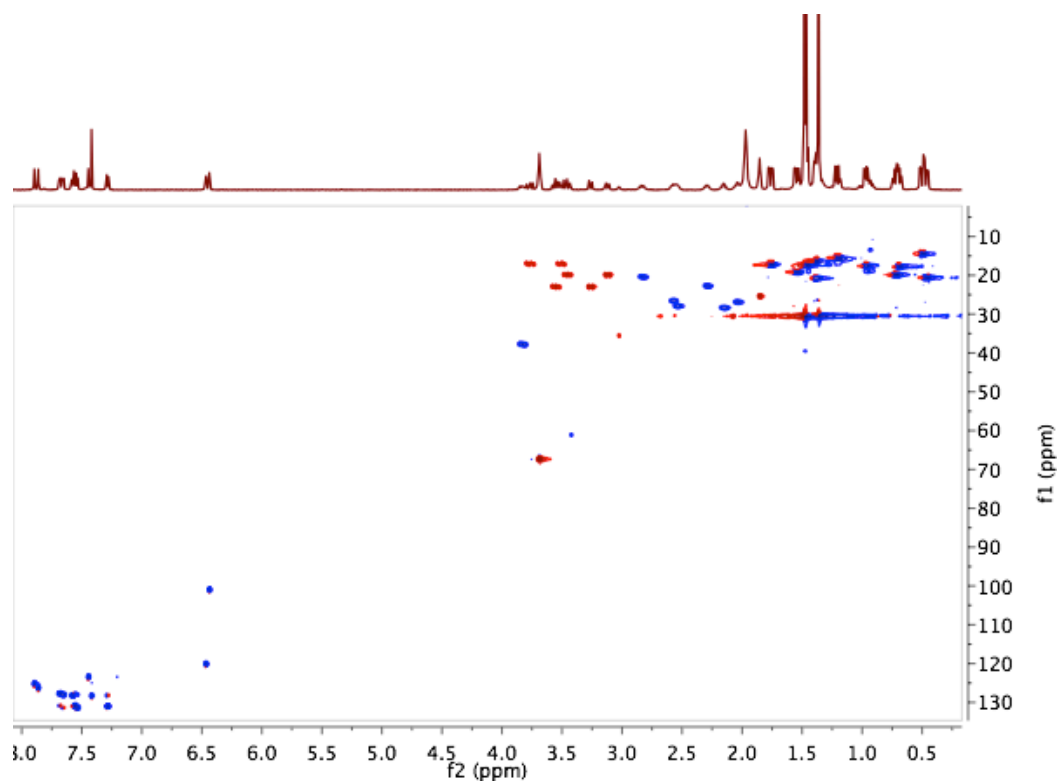


Figure 17. ^1H - ^{13}C gHSQC (600 MHz, CD_3CN) spectrum of **3a-Ni**

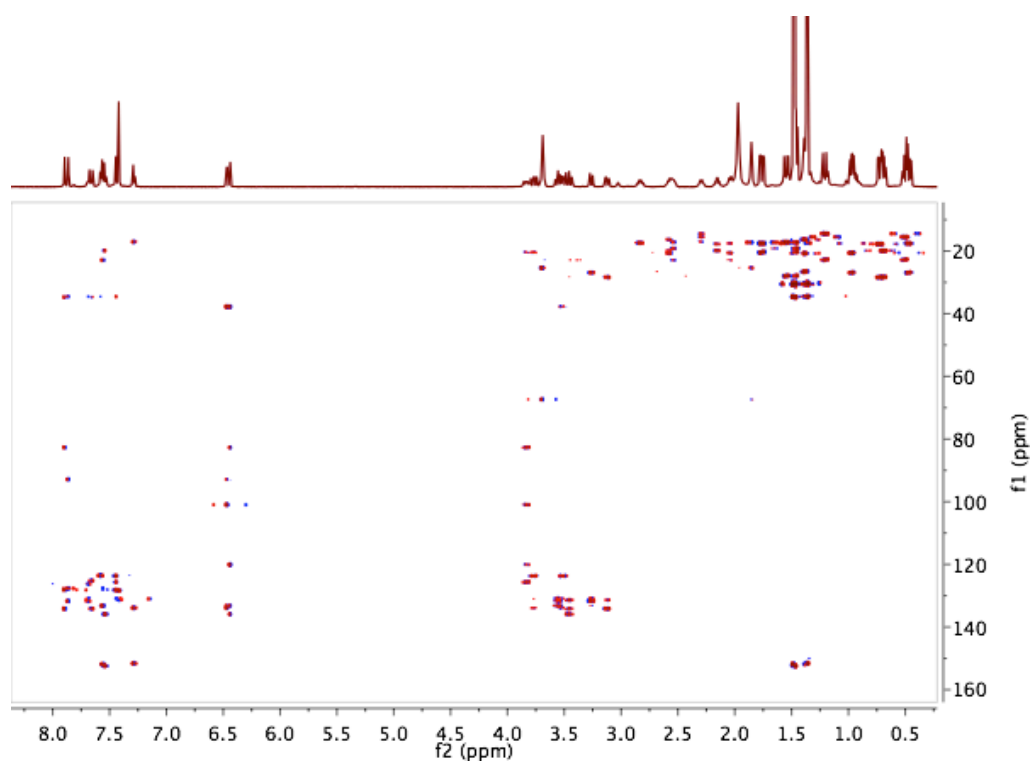


Figure 18. ^1H - ^{13}C gHMBC (600 MHz, CD_3CN) spectrum of **3a-Ni**

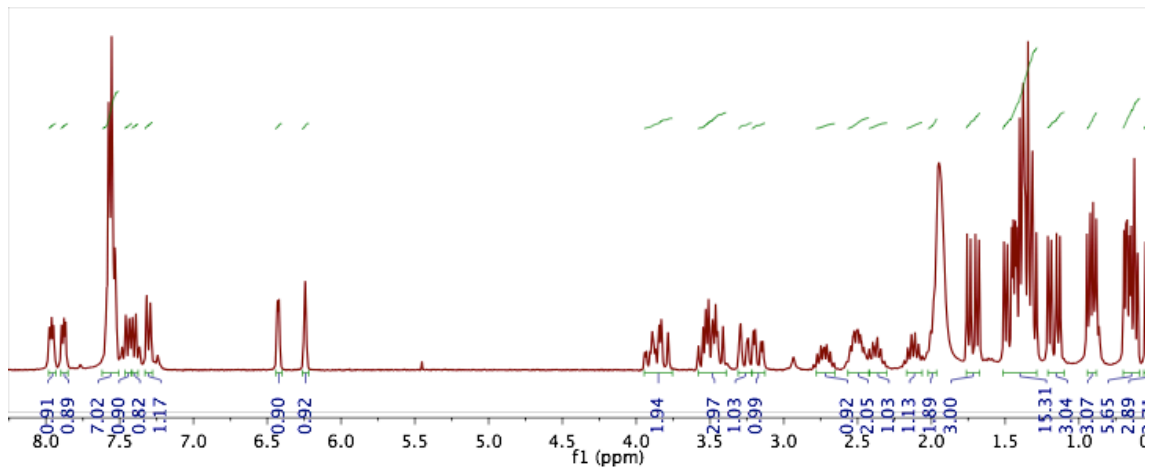


Figure 19. ^1H NMR (300 MHz, CD_3CN) spectrum of **3b-Ni**

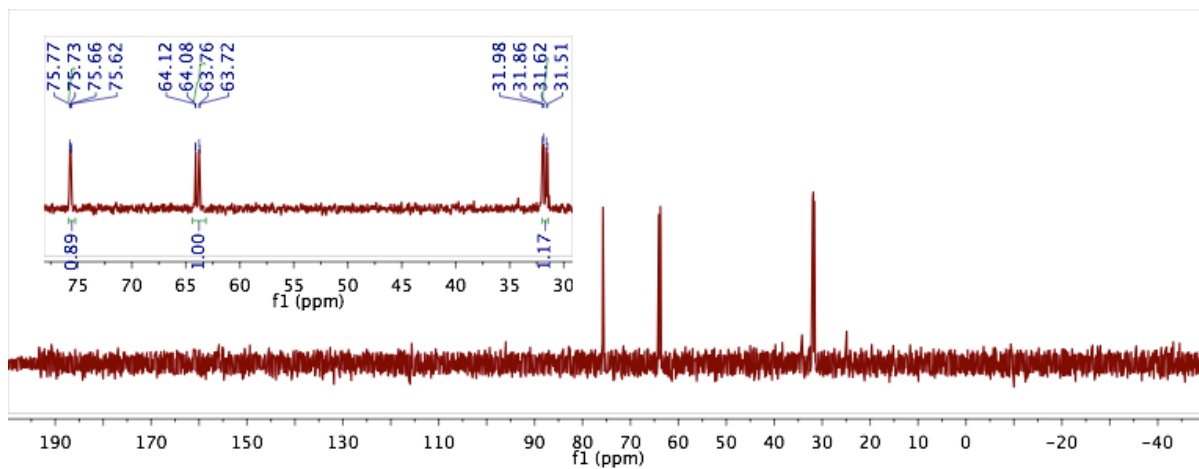


Figure 20. ^{31}P NMR (121 MHz, CD_3CN) spectrum of **3b-Ni**

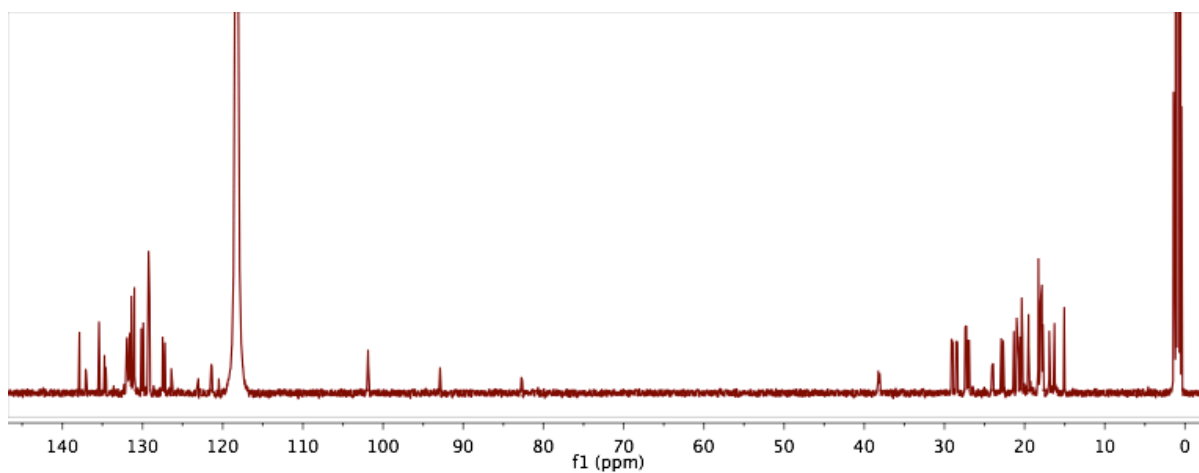


Figure 21. ^{13}C NMR (126 MHz, CD_3CN) spectrum of **3b-Ni**

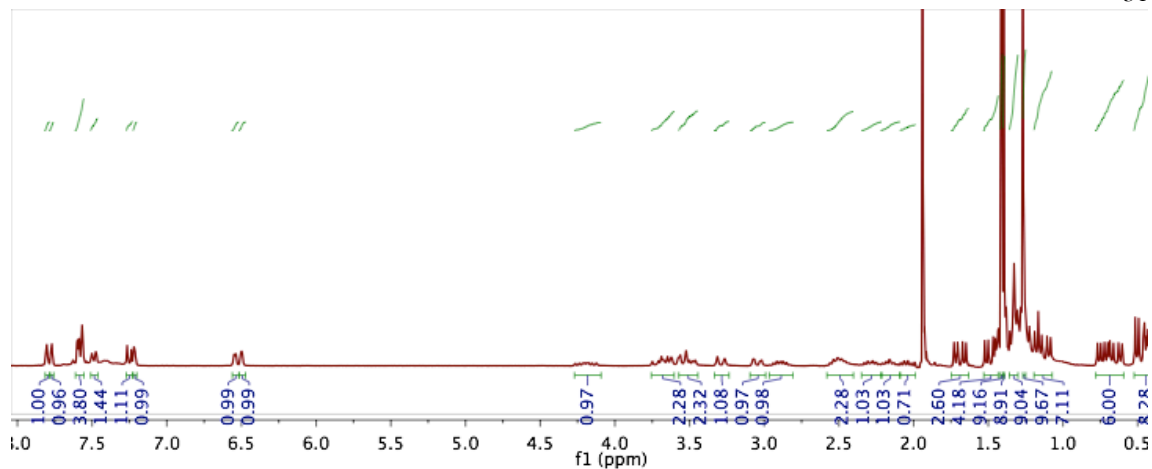


Figure 22. ^1H NMR (300 MHz, CD_3CN) spectrum of **3a-Pd**

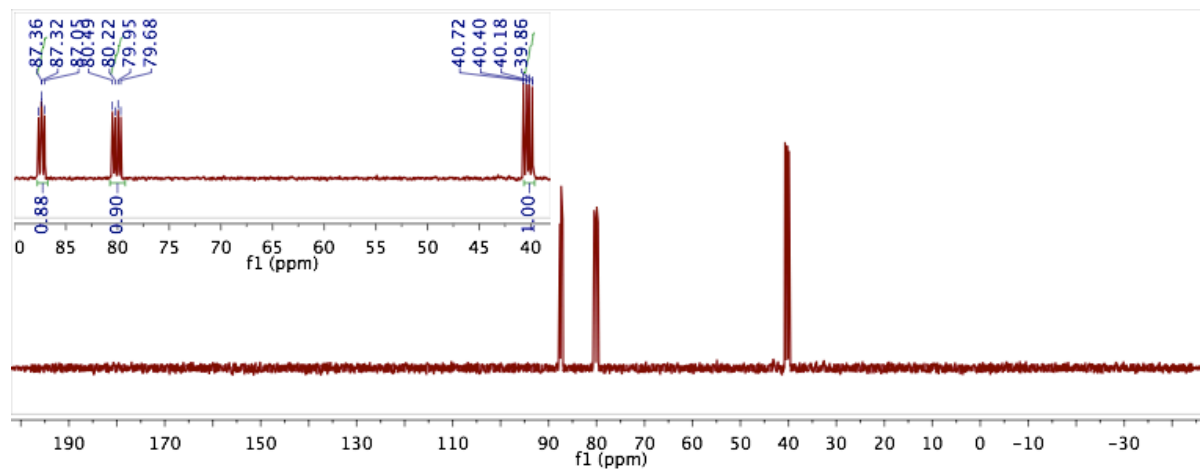


Figure 23. ^{31}P NMR (121 MHz, CD_3CN) spectrum of **3a-Pd**

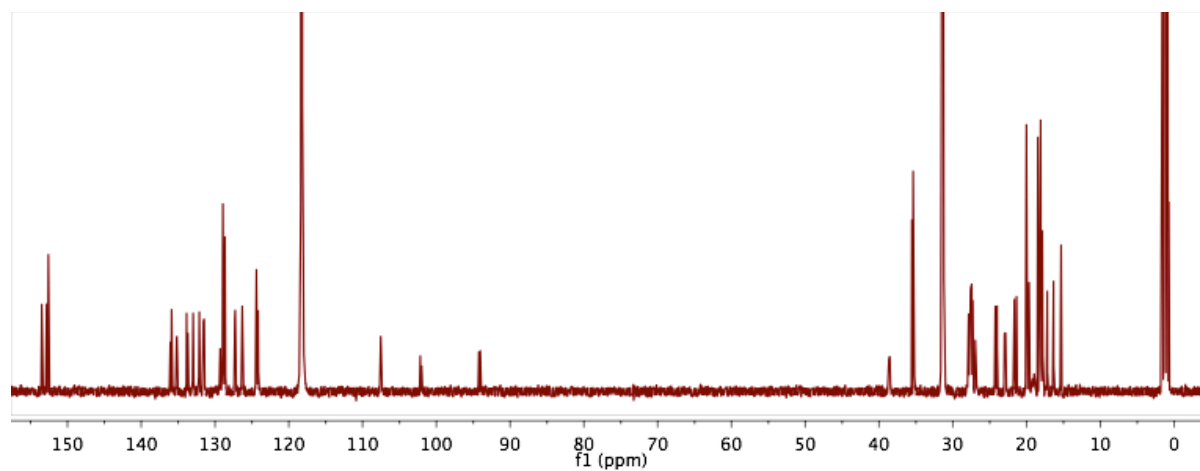


Figure 24. ^{13}C NMR (126 MHz, CD_3CN) spectrum of **3a-Pd**

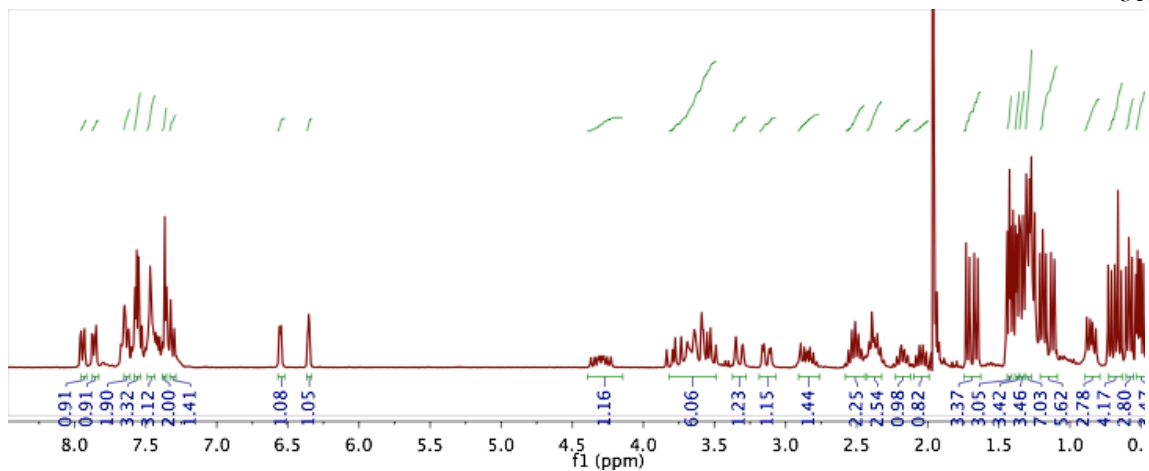


Figure 25. ^1H NMR (300 MHz, CD_3CN) spectrum of **3b-Pd**

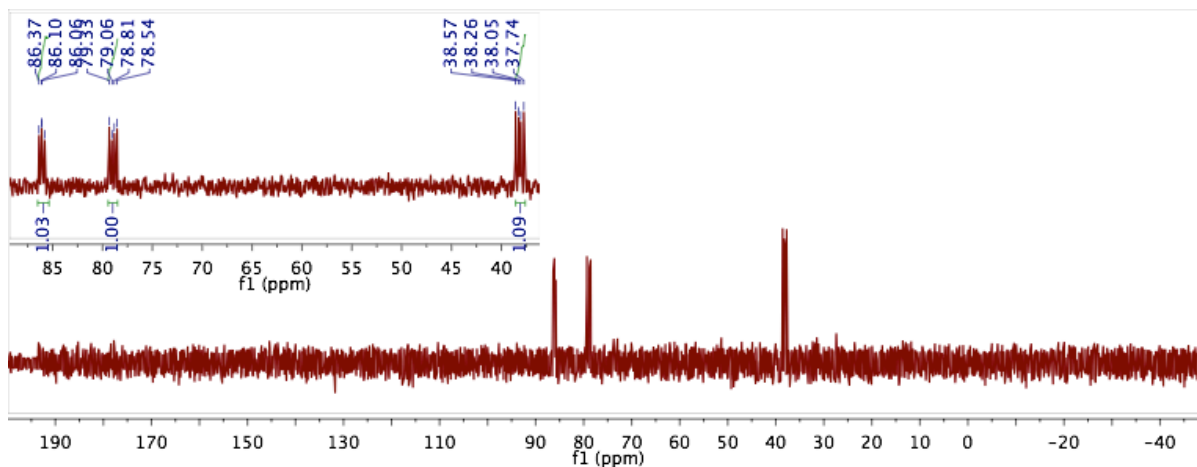


Figure 26. ^{31}P NMR (121 MHz, CD_3CN) spectrum of **3b-Pd**

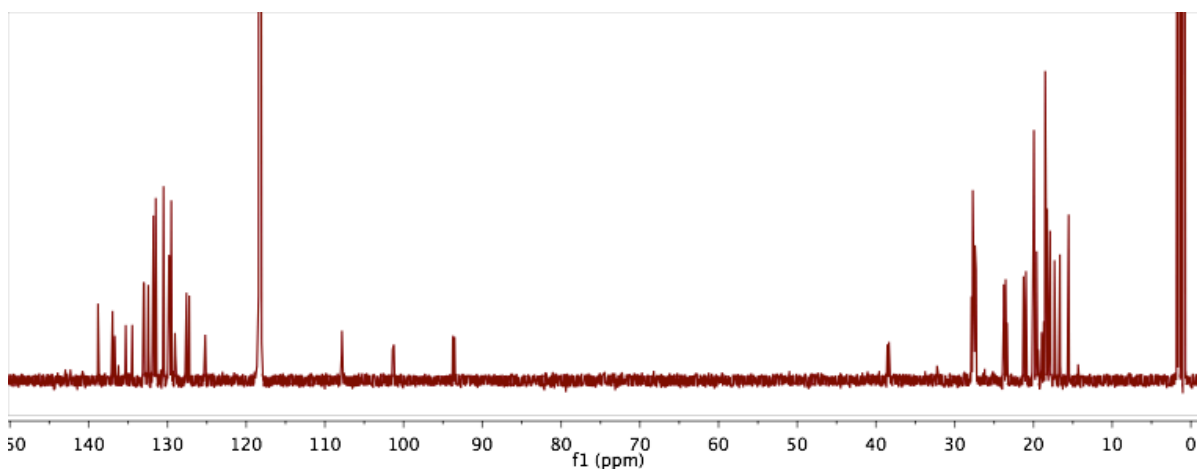


Figure 27. ^{13}C NMR (126 MHz, CD_3CN) of **3b-Pd**

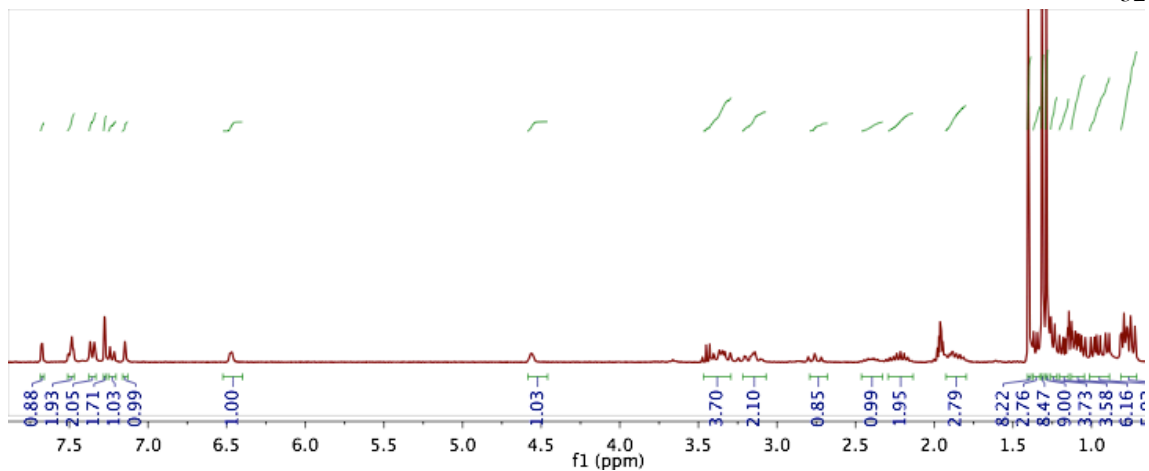


Figure 28. ^1H NMR (300 MHz, CD_3CN) spectrum of **4a-Ni**

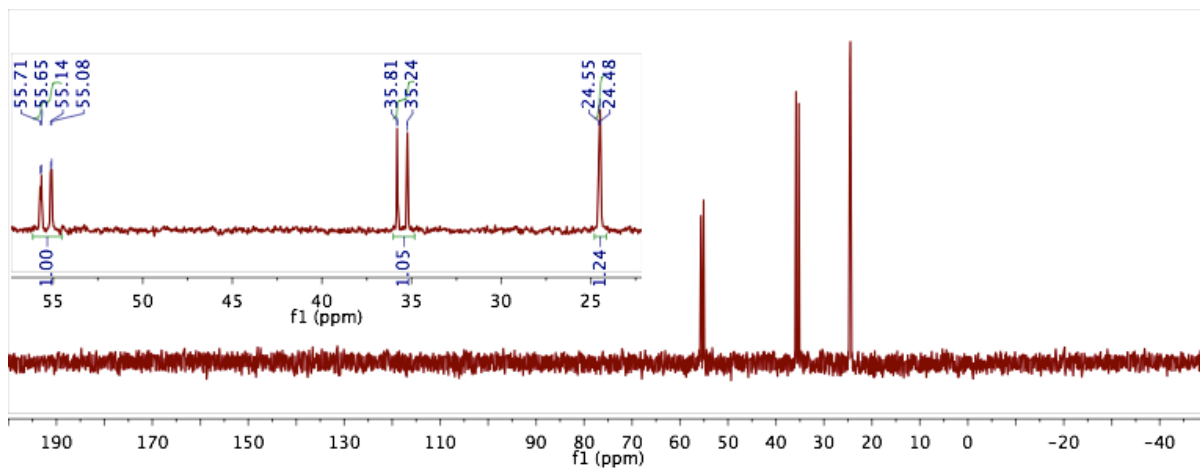


Figure 29. ^{31}P NMR (121 MHz, CD_3CN) spectrum of **4a-Ni**

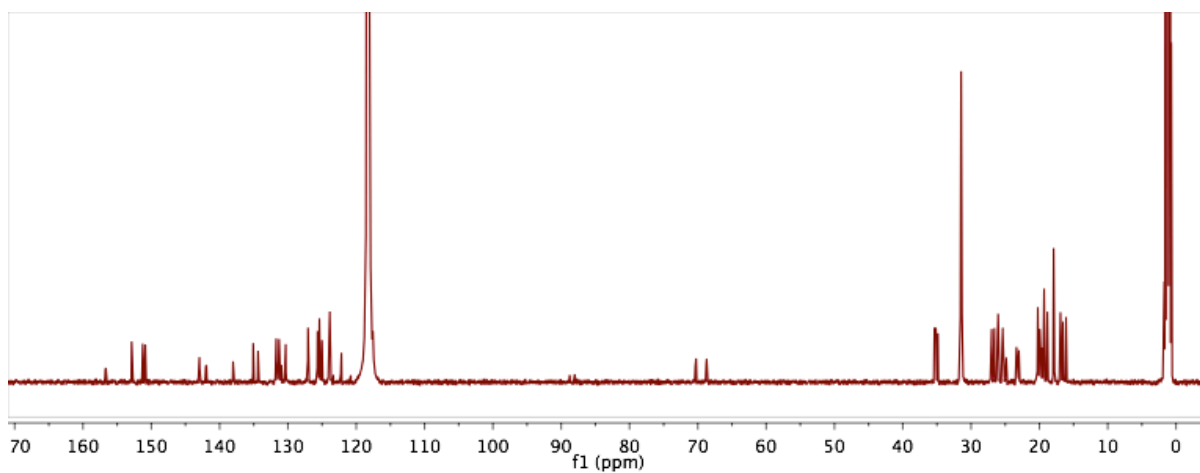


Figure 30. ^{13}C NMR (126 MHz, CD_3CN) spectrum of **4a-Ni**

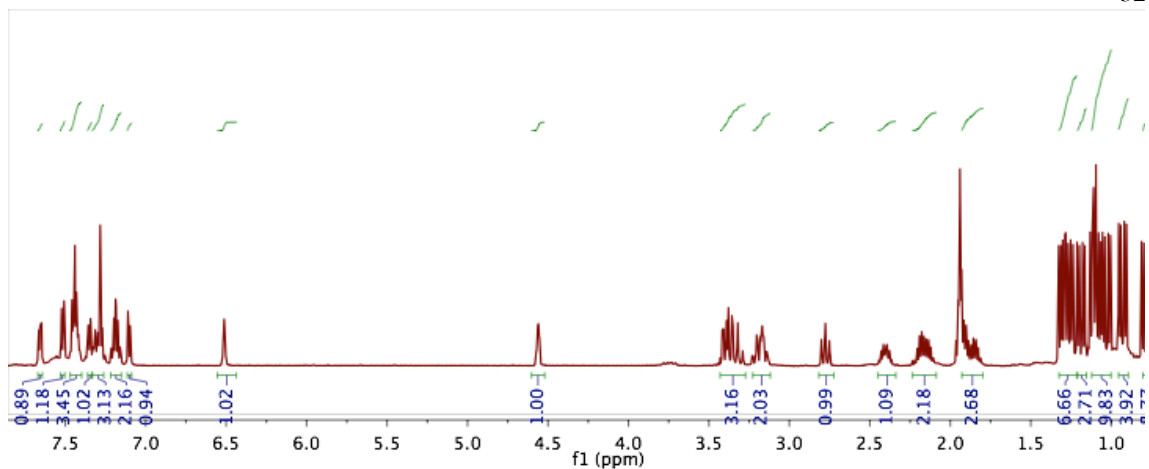


Figure 31. ^1H NMR (300 MHz, CD_3CN) spectrum of **4b-Ni**

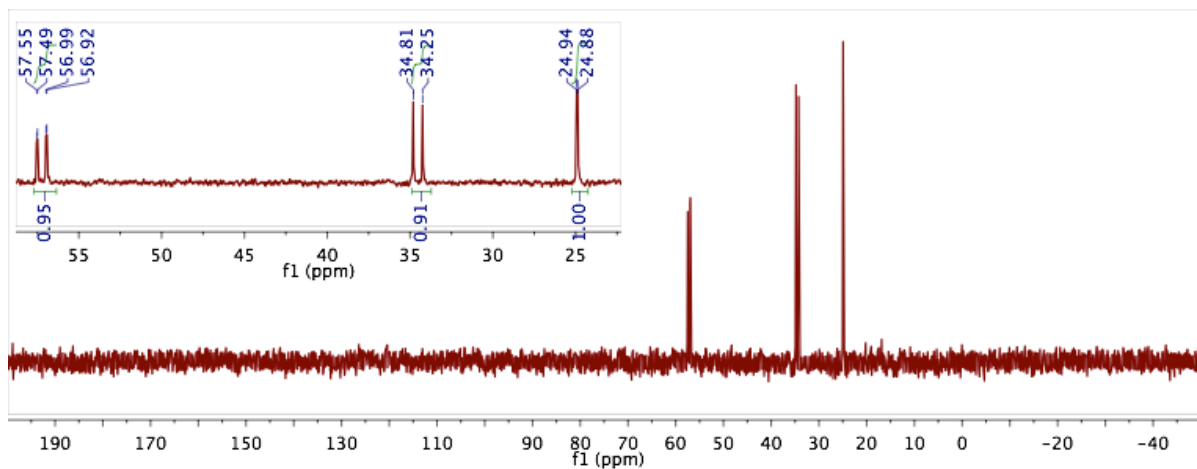


Figure 32. ^{31}P NMR (121 MHz, CD_3CN) spectrum of **4b-Ni**

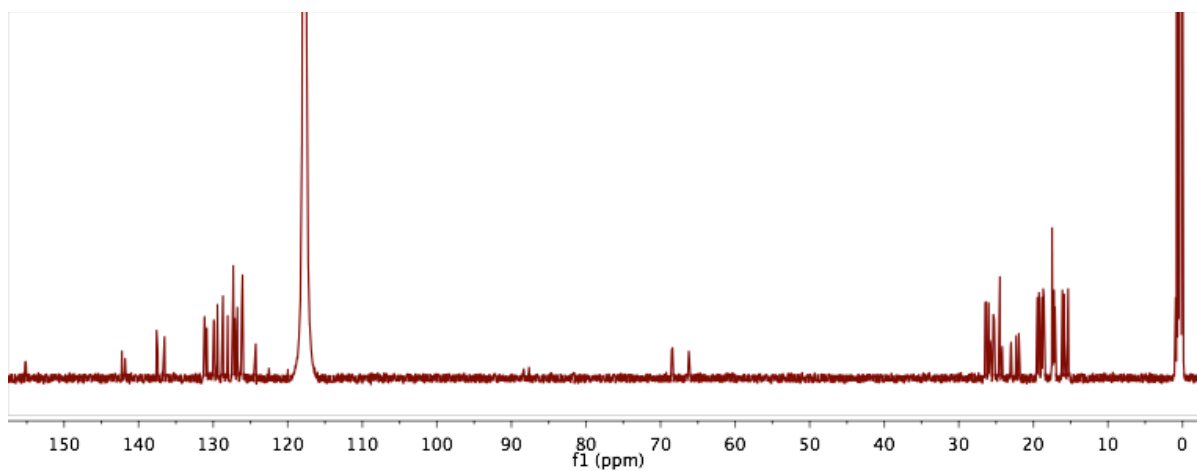


Figure 33. ^{13}C NMR (126 MHz, CD_3CN) spectrum of **4b-Ni**

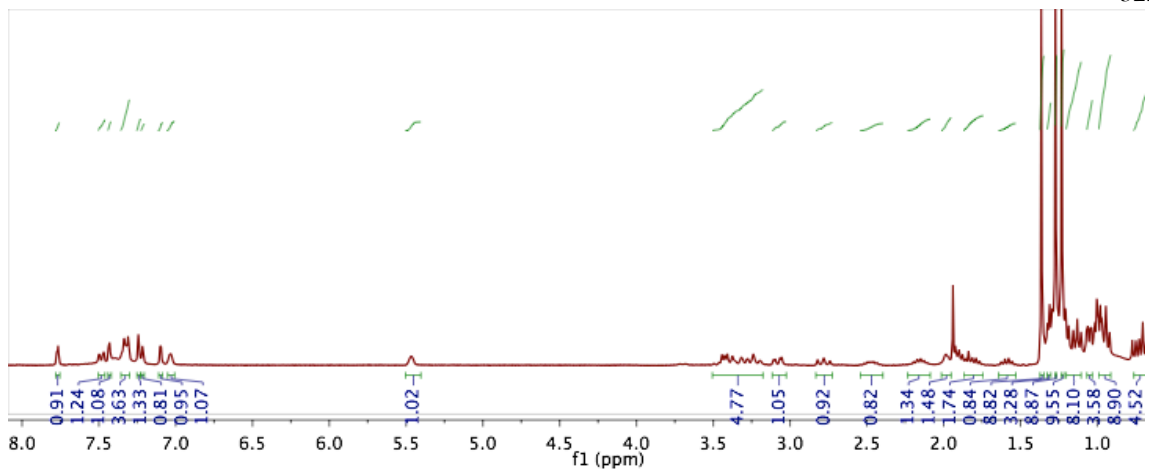


Figure 34. ¹H NMR (300 MHz, CD₃CN) spectrum of 4a-Pd

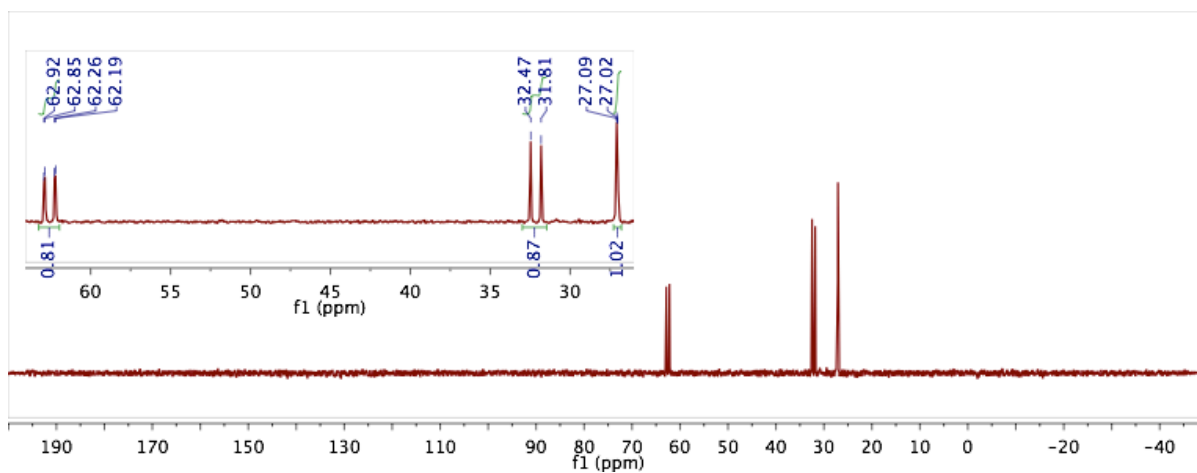


Figure 35. ³¹P NMR (121 MHz, CD₃CN) spectrum of 4a-Pd

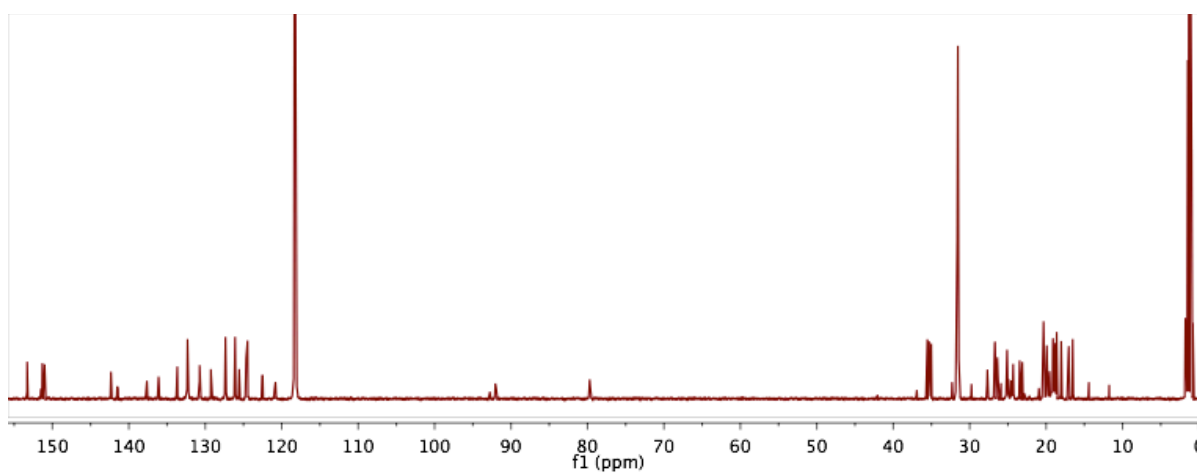


Figure 36. ¹³C NMR (126 MHz, CD₃CN) spectrum of 4a-Pd

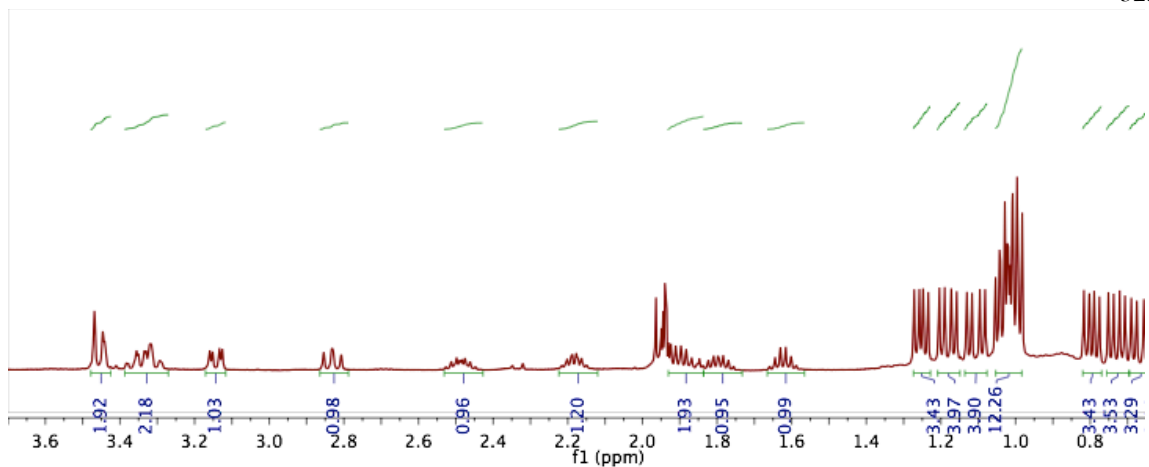


Figure 37. ^1H NMR (500 MHz, CD_3CN) spectrum of **4b-Pd**

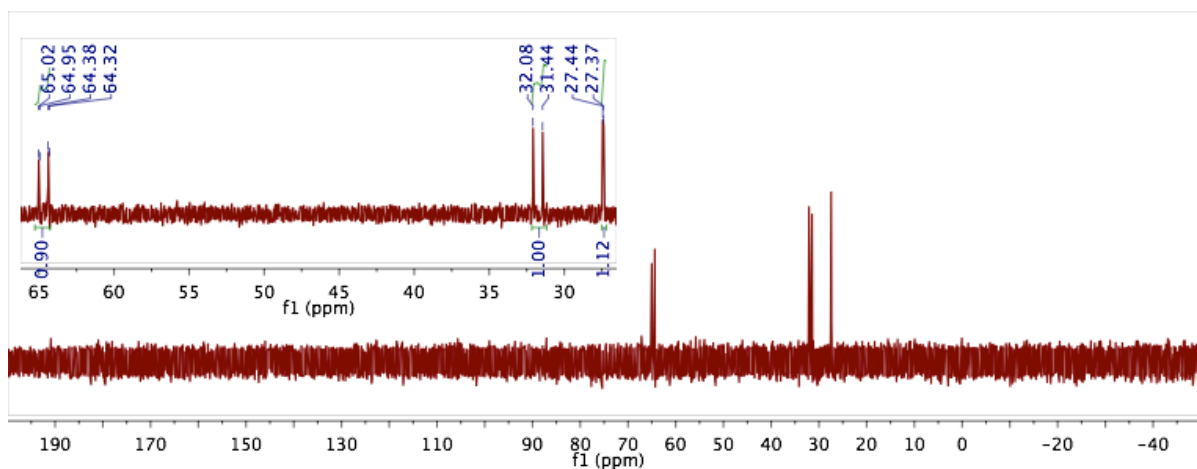


Figure 38. ^{31}P NMR (121 MHz, CD_3CN) spectrum of **4b-Pd**

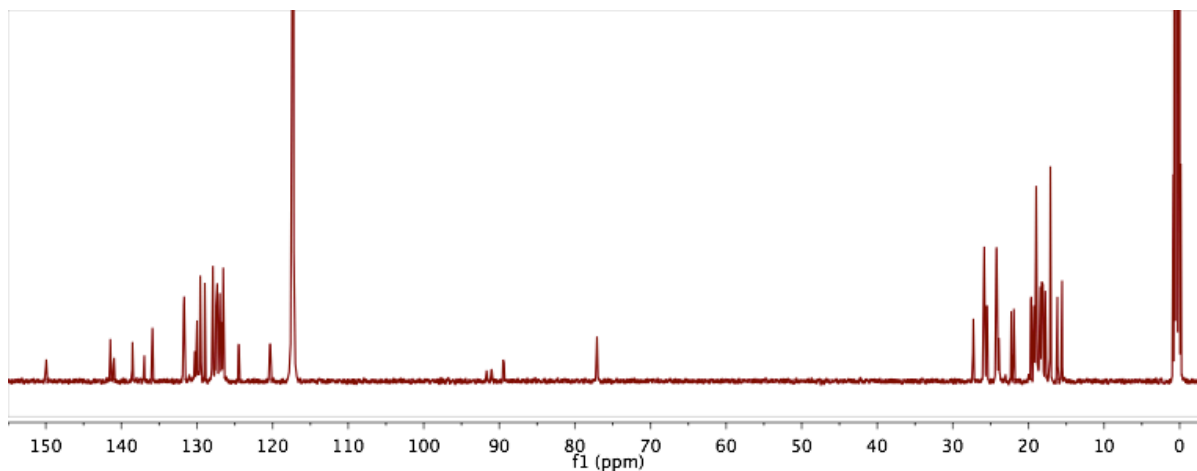


Figure 39. ^{13}C NMR (126 MHz, CD_3CN) spectrum of **4b-Pd**

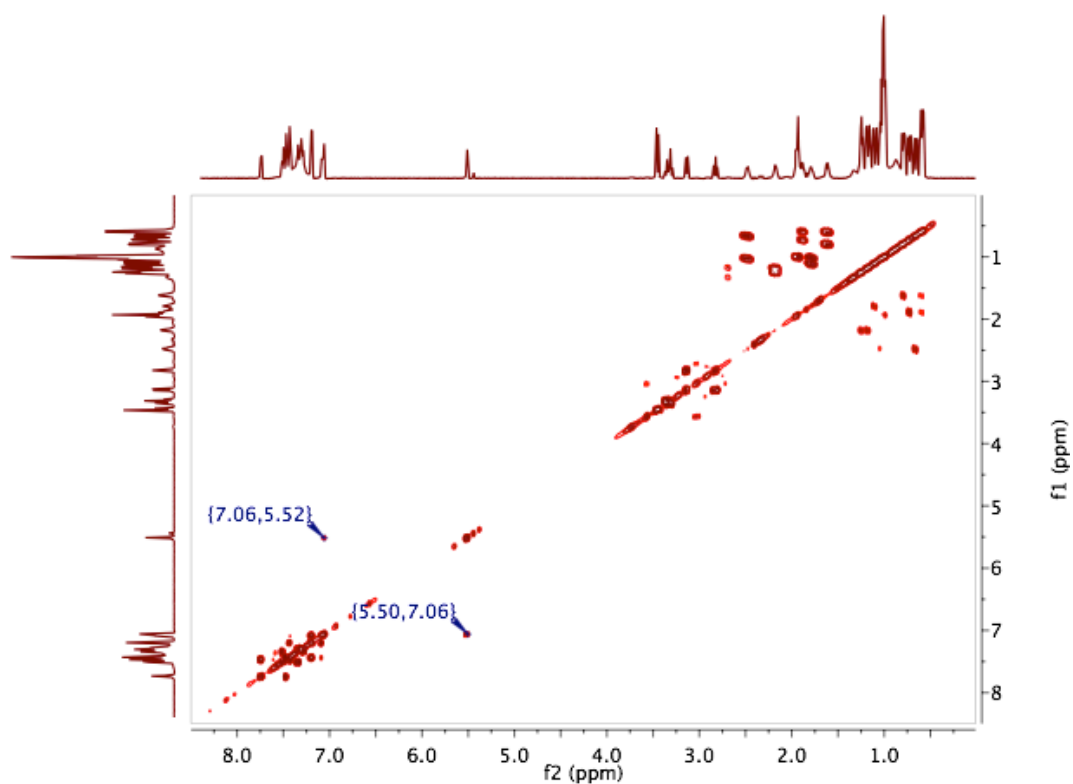


Figure 40. ^1H - ^1H gCOSY(600 MHz, CD_3CN) spectrum of **4b-Pd**. The labeled peaks are the central-aryl ring proton correlations

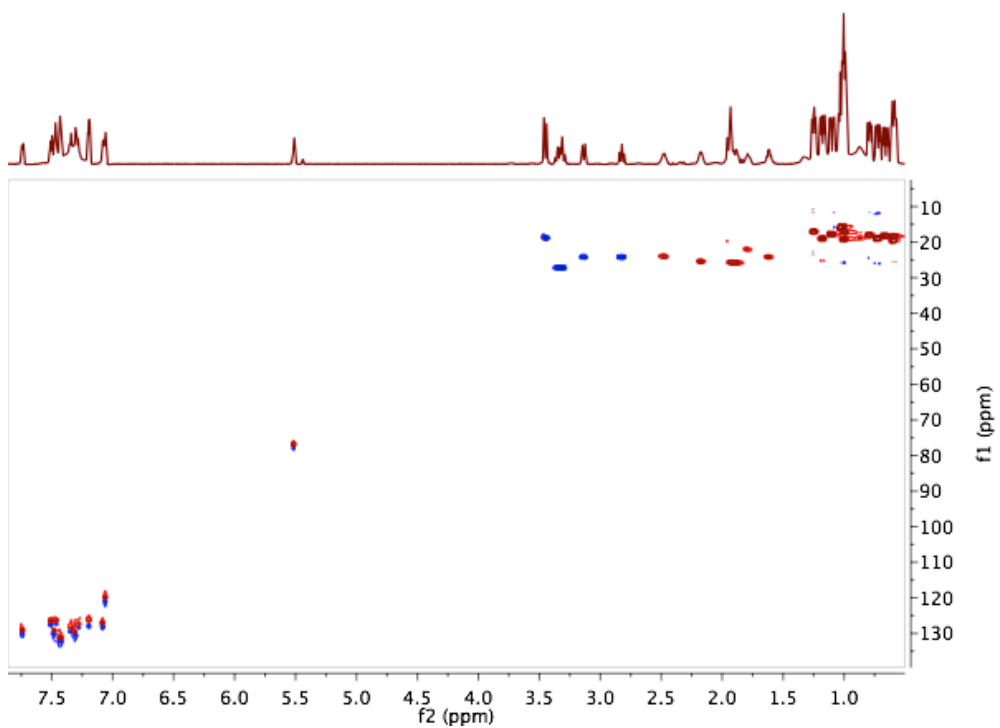


Figure 41. ^1H - ^{13}C gHSQC (600 MHz, CD_3CN) spectrum of **4b-Pd**

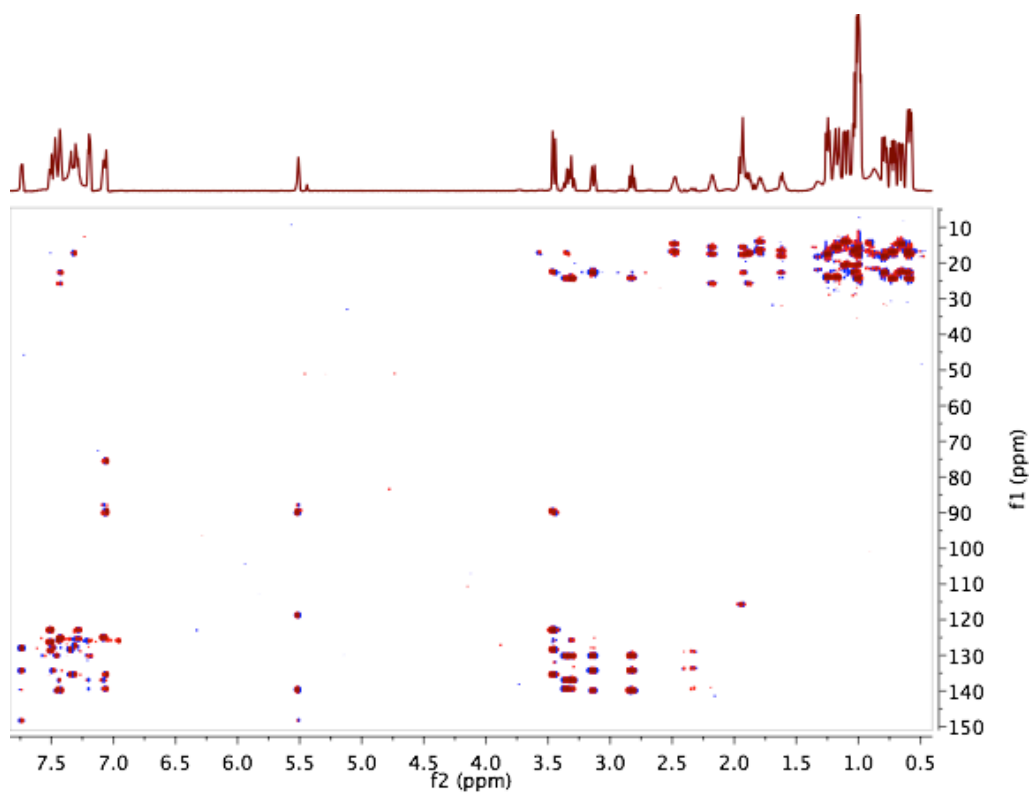
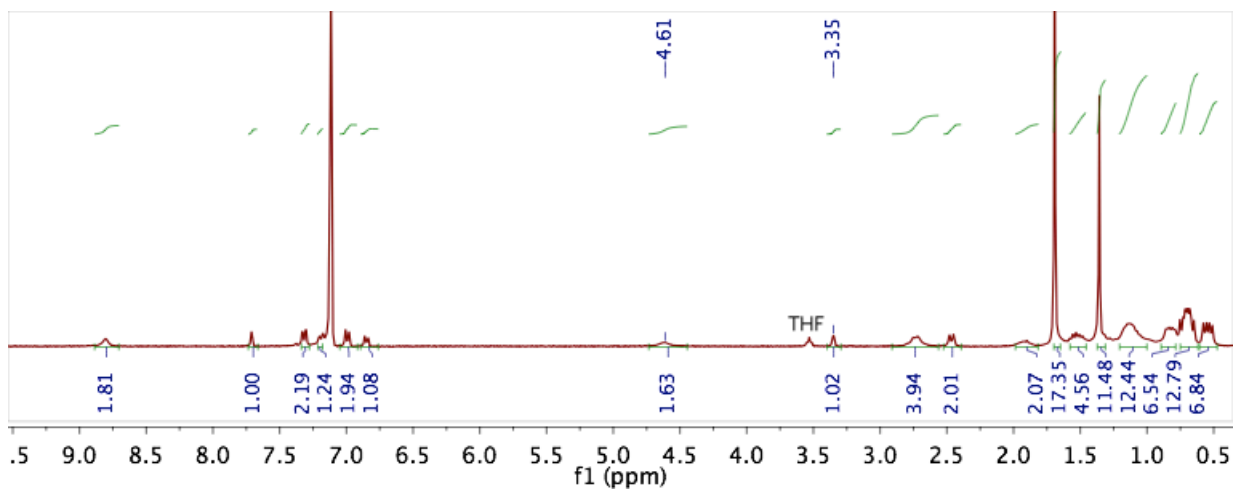
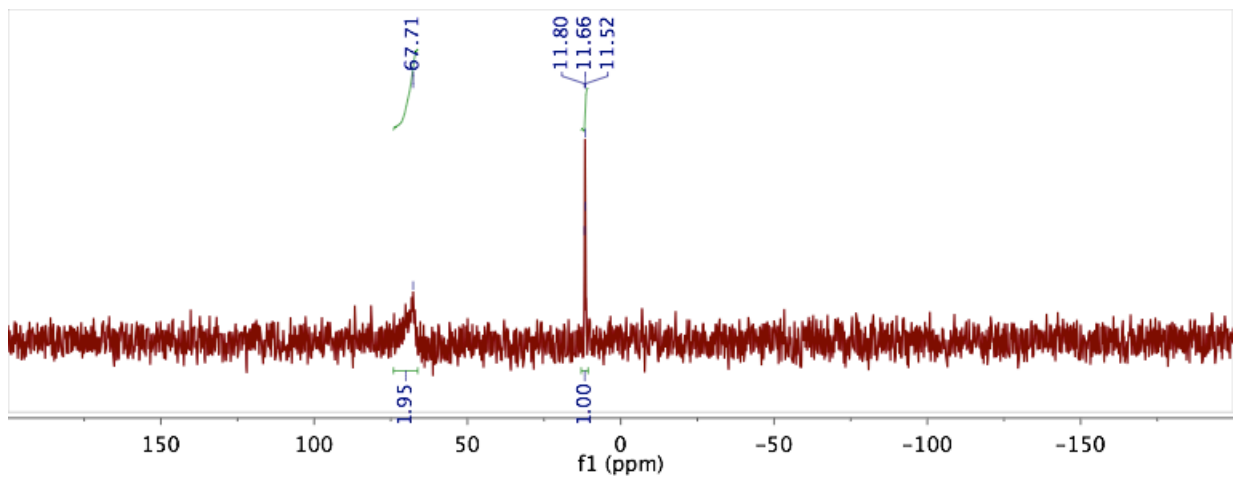
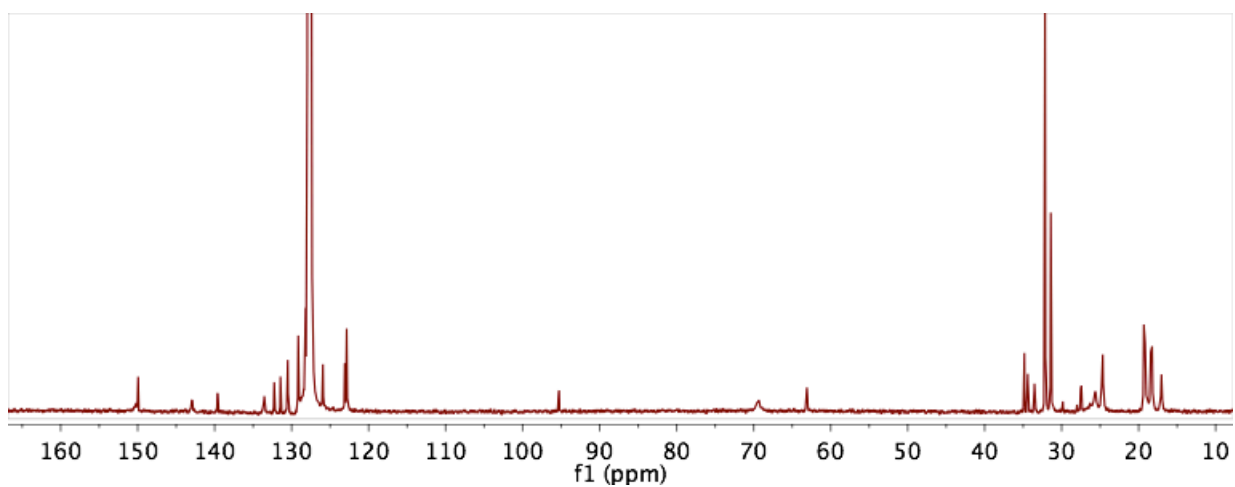


Figure 42. ^1H - ^{13}C gHMBC (600 MHz, CD_3CN) spectrum of **4b-Pd**

CHAPTER 3

Figure 43. ^1H NMR (300 MHz, C_6D_6) spectrum of 5Figure 44. ^{31}P NMR (121 MHz, C_6D_6) spectrum of 5Figure 45. ^{13}C NMR (126 MHz, C_6D_6) spectrum of 5

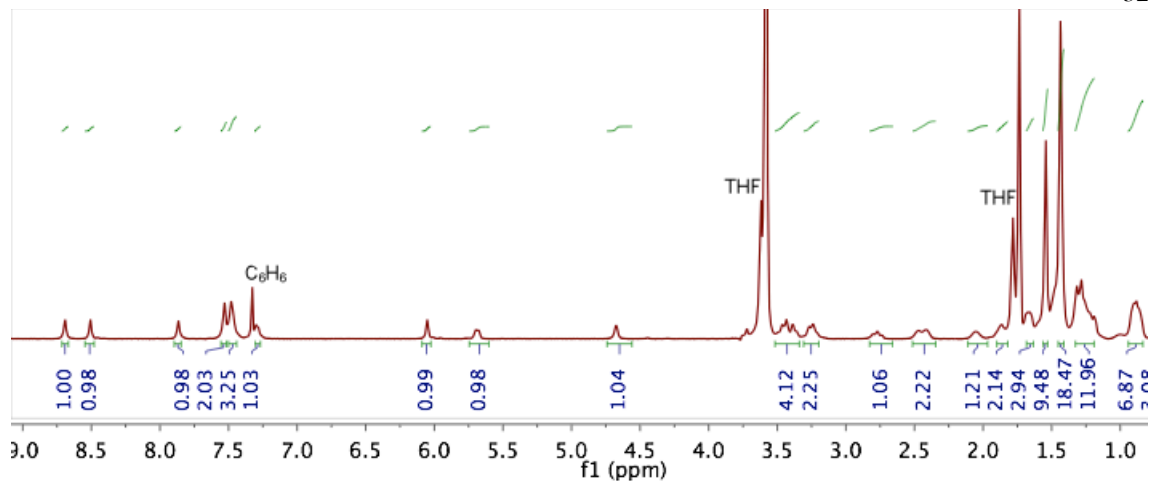


Figure 46. ^1H NMR (500 MHz, THF-d_8 , -30°C) spectrum of **6**

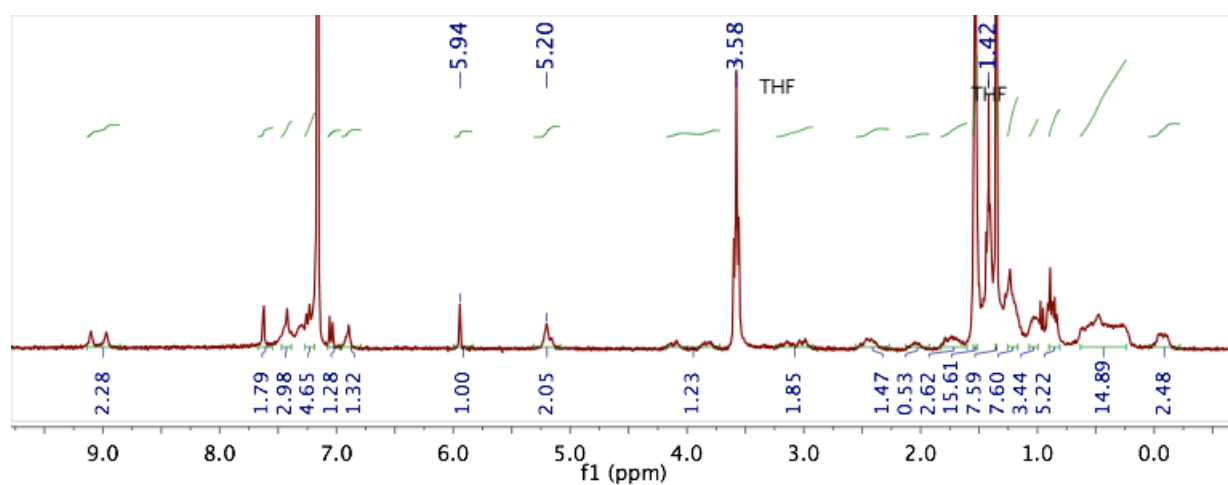


Figure 47. ^1H NMR (300 MHz, C_6D_6) spectrum of **6**

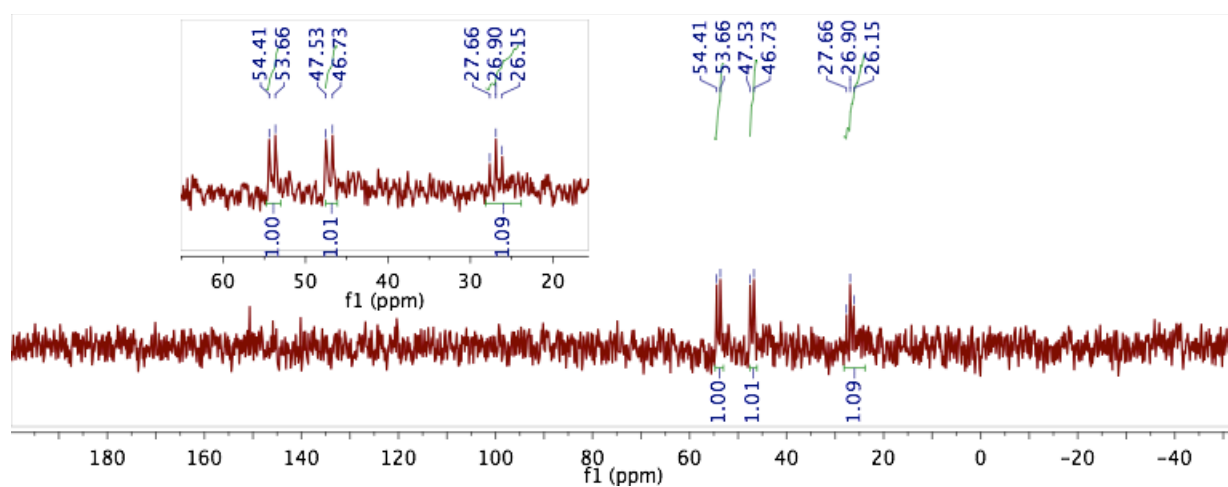


Figure 48. ^{31}P NMR (121 MHz, C_6D_6) spectrum of **6**

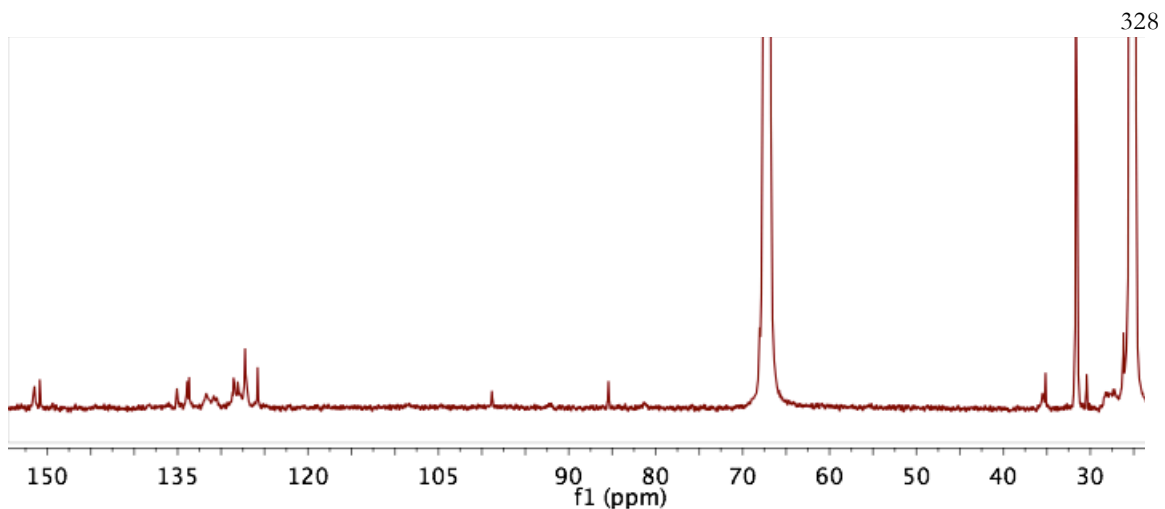


Figure 49. ¹³C NMR (126 MHz, THF-*d*₈) spectrum of 6

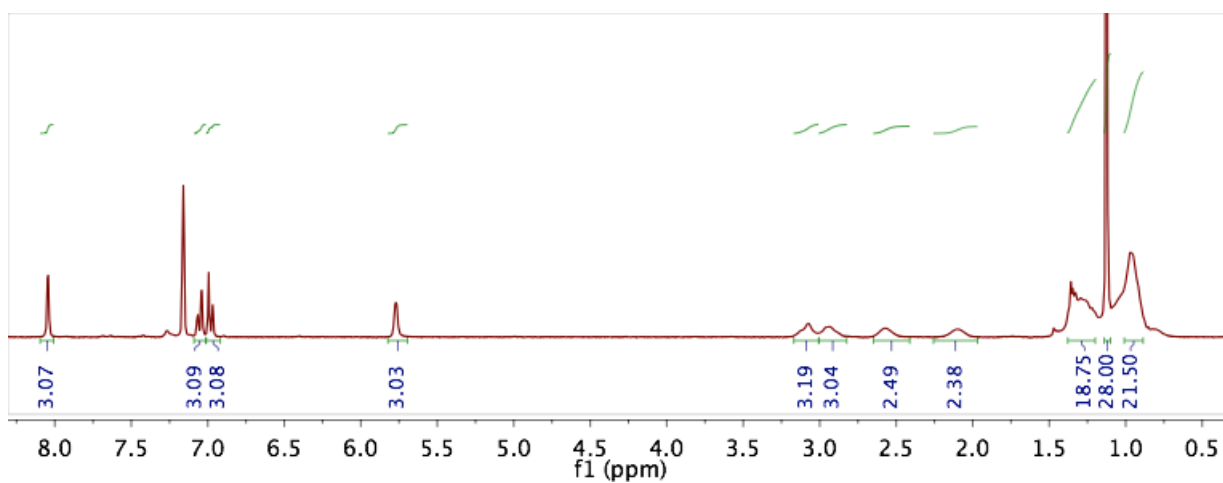


Figure 50. ¹H NMR (300 MHz, C₆D₆) spectrum of 7

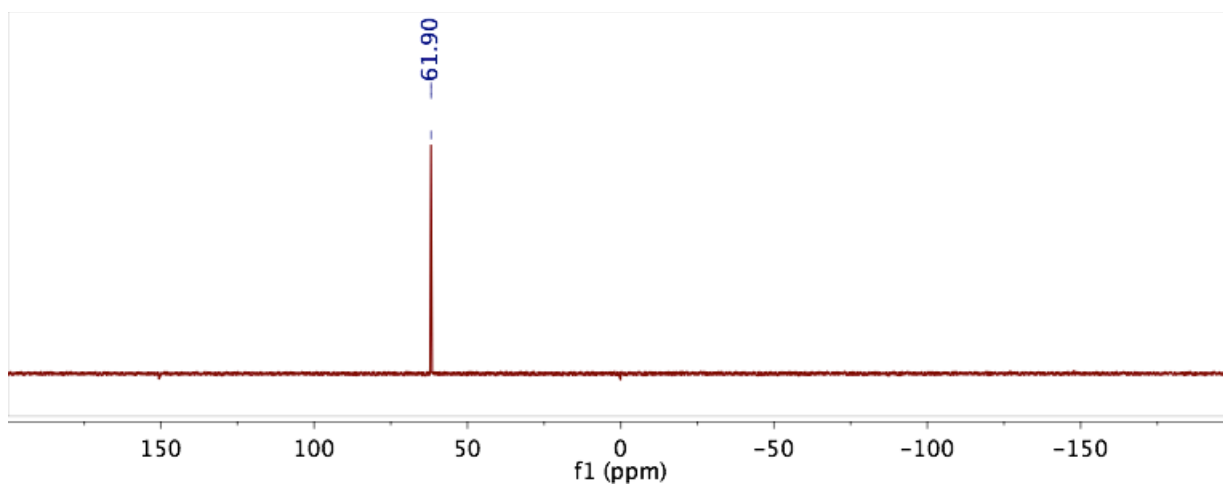


Figure 51. ³¹P NMR (121 MHz, C₆D₆) spectrum of 7

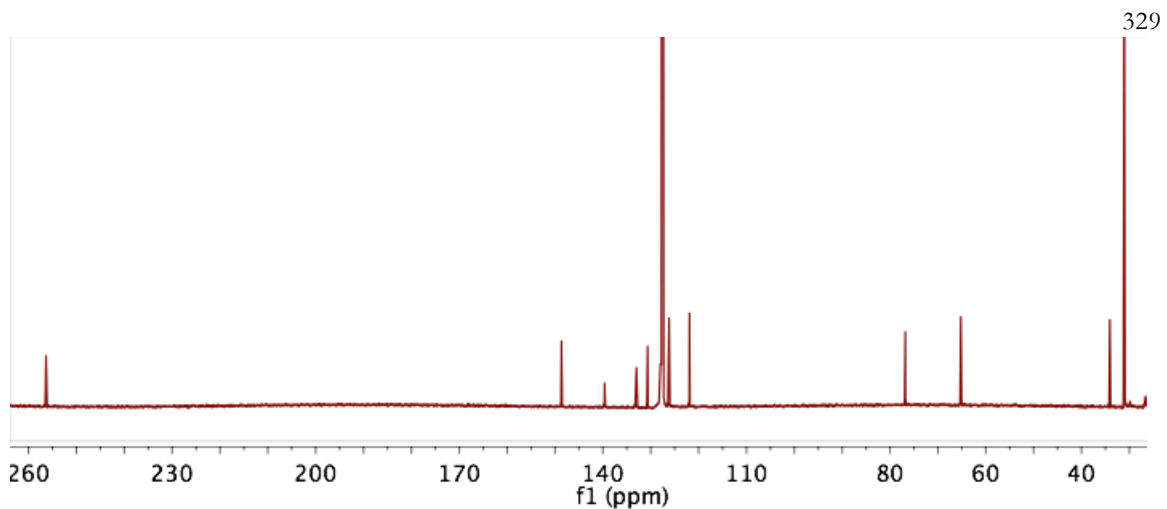


Figure 52. ^{13}C NMR (126 MHz, C_6D_6) spectrum of 7

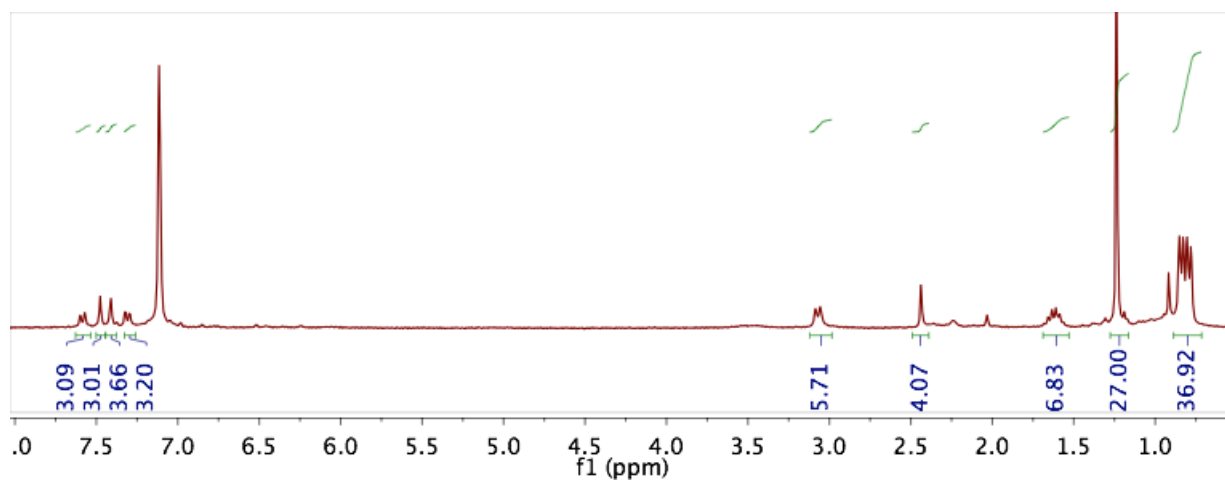


Figure 53. ^1H NMR (300 MHz, C_6D_6) spectrum of 8

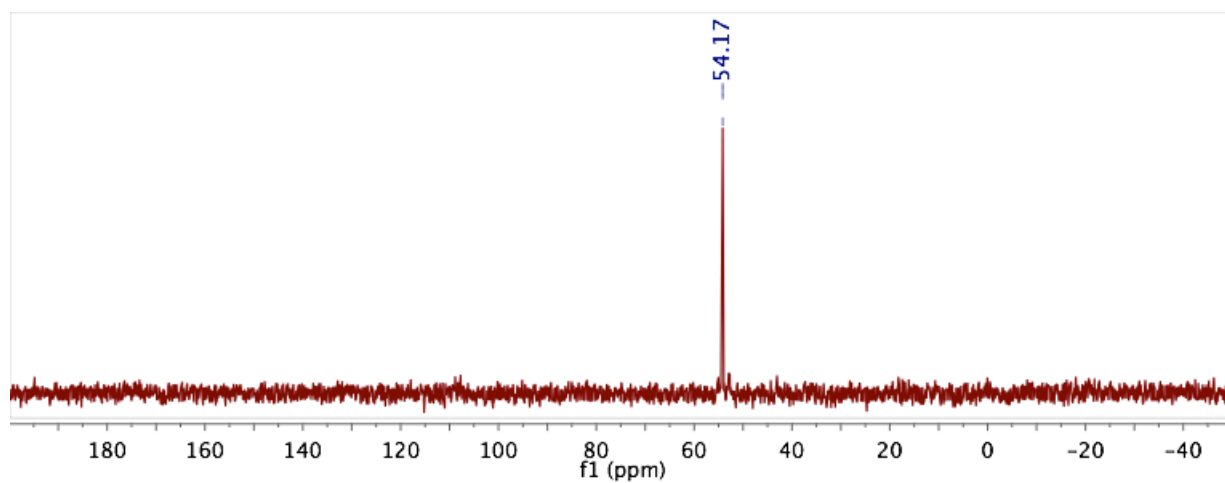


Figure 54. ^{31}P NMR (121 MHz, C_6D_6) spectrum of 8

CHAPTER 4

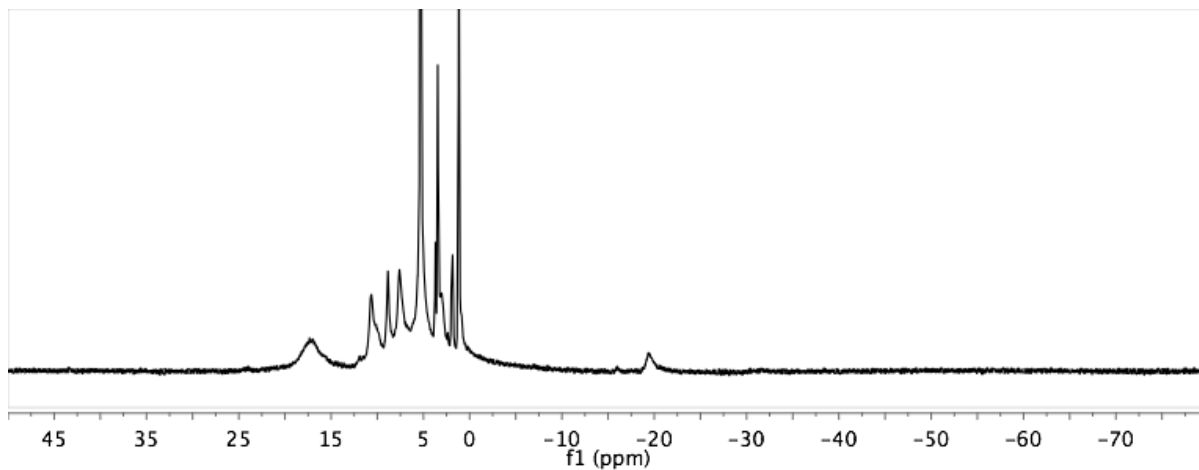


Figure 55. ^1H NMR (300 MHz, CD_2Cl_2) spectrum of **9-Fe**

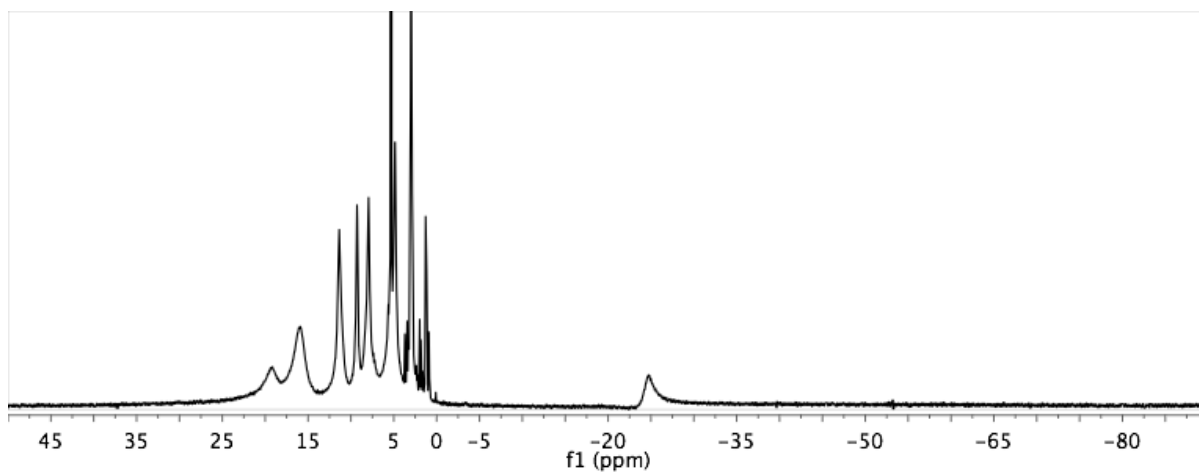


Figure 56. ^1H NMR (300 MHz, CD_2Cl_2) spectrum of **9-Co**

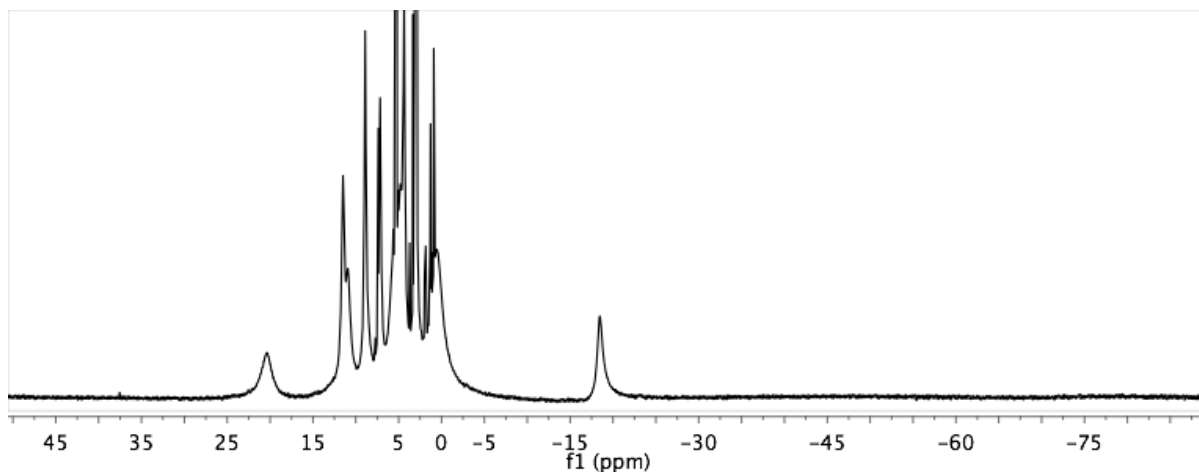


Figure 57. ^1H NMR (300 MHz, CD_2Cl_2) spectrum of **10-Ni**

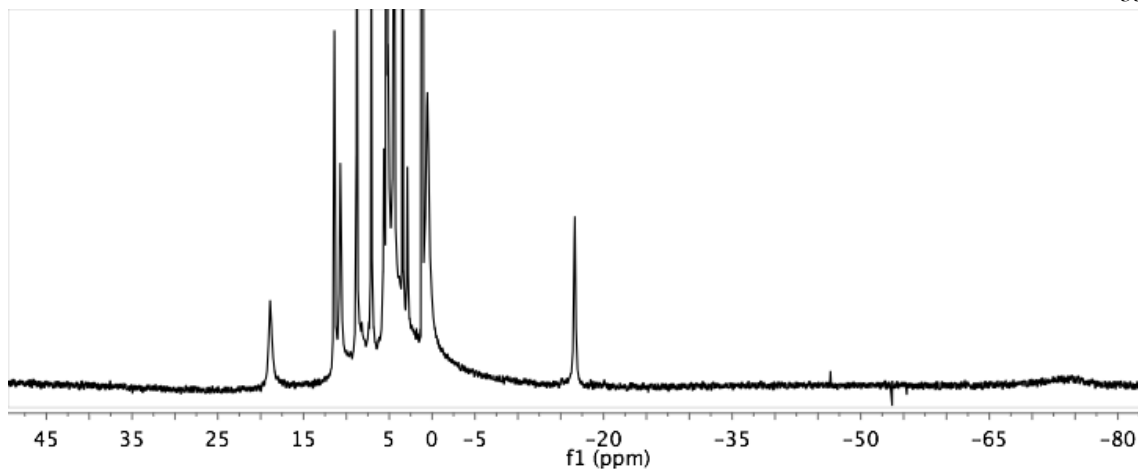


Figure 58. ^1H NMR (300 MHz, CD_2Cl_2) spectrum of **10-Cu**

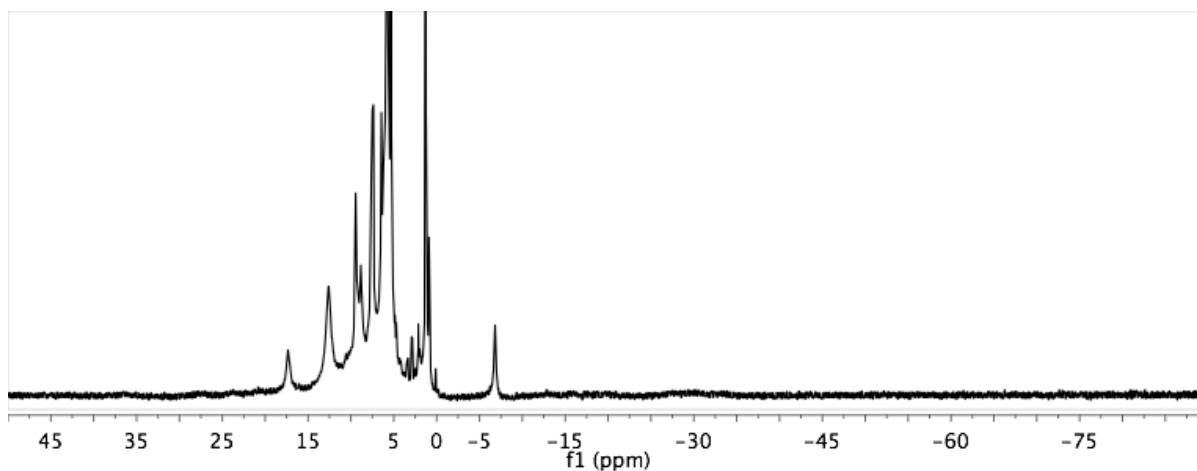


Figure 59. ^1H NMR (300 MHz, CD_2Cl_2) spectrum of **[11-Fe][CoCp₂]**

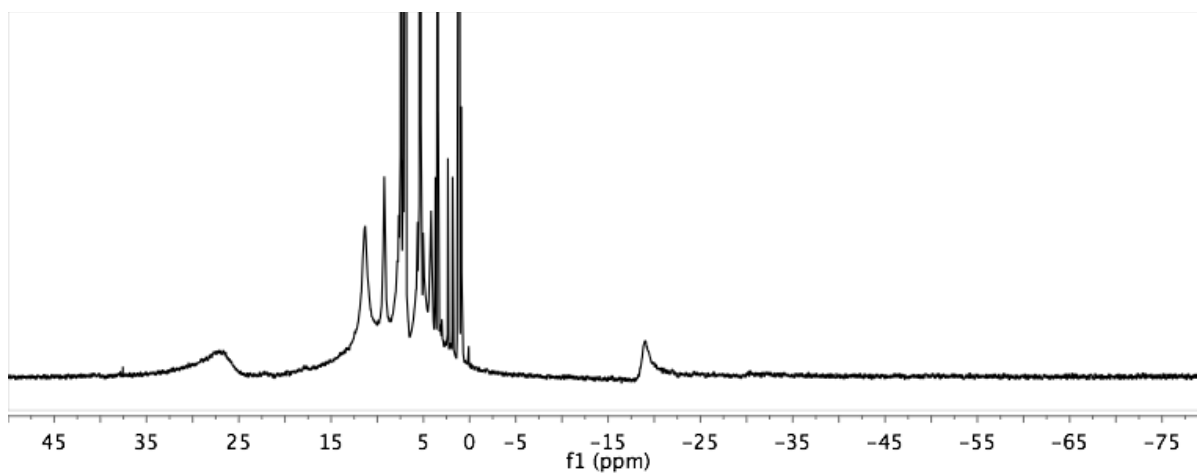


Figure 60. ^1H NMR (300 MHz, CD_2Cl_2) spectrum of **[12-Fe][SbCl₆]**

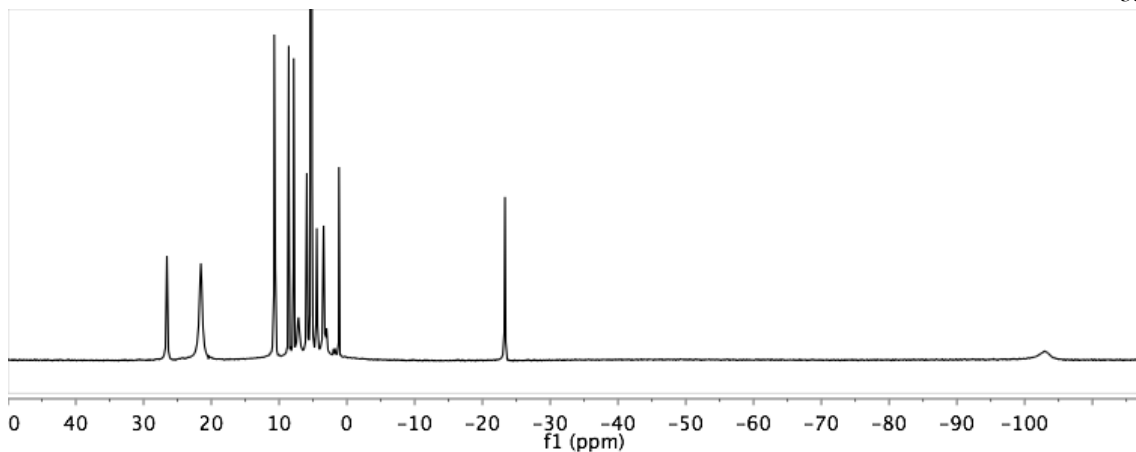


Figure 61. ^1H NMR (300 MHz, CD_2Cl_2) spectrum of $[\mathbf{11-Co}][\text{CoCp}_2]$ or $[\mathbf{11-Co}][\text{Cr}(\text{C}_6\text{H}_6)_2]$

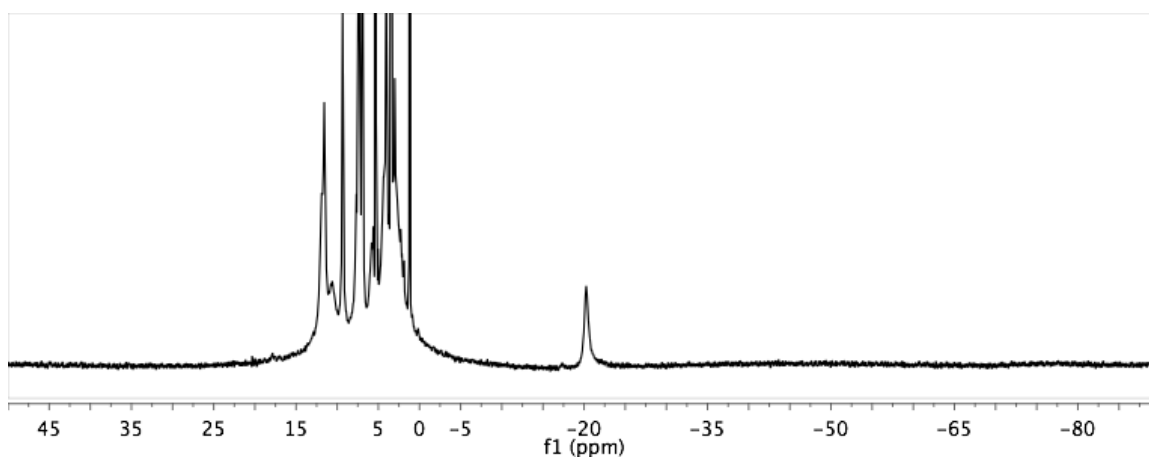


Figure 62. ^1H NMR (300 MHz, CD_2Cl_2) spectrum of $[\mathbf{12-Co}][\text{SbCl}_6]$

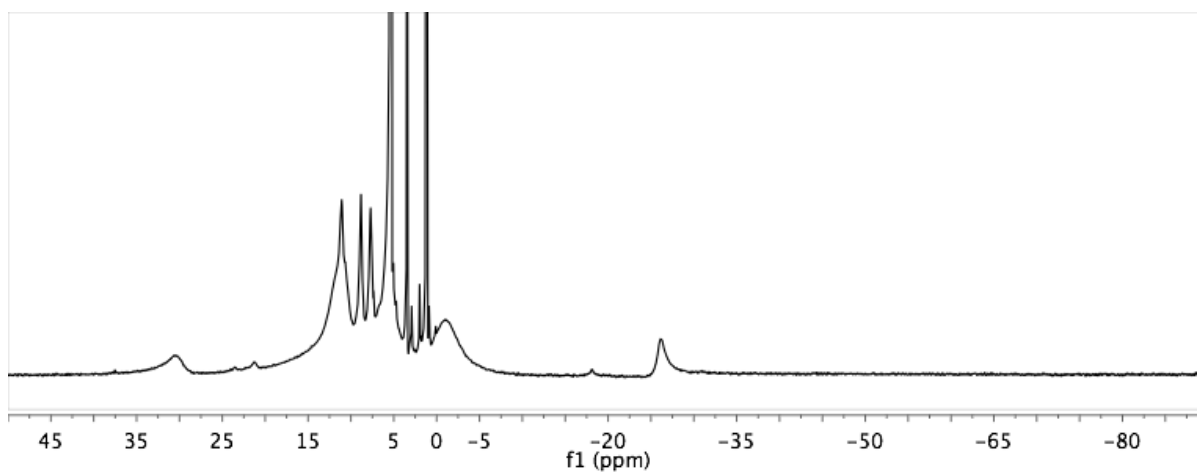


Figure 63. ^1H NMR (300 MHz, CD_2Cl_2) spectrum of $[\mathbf{13-Ni}][\text{CoCp}_2]$

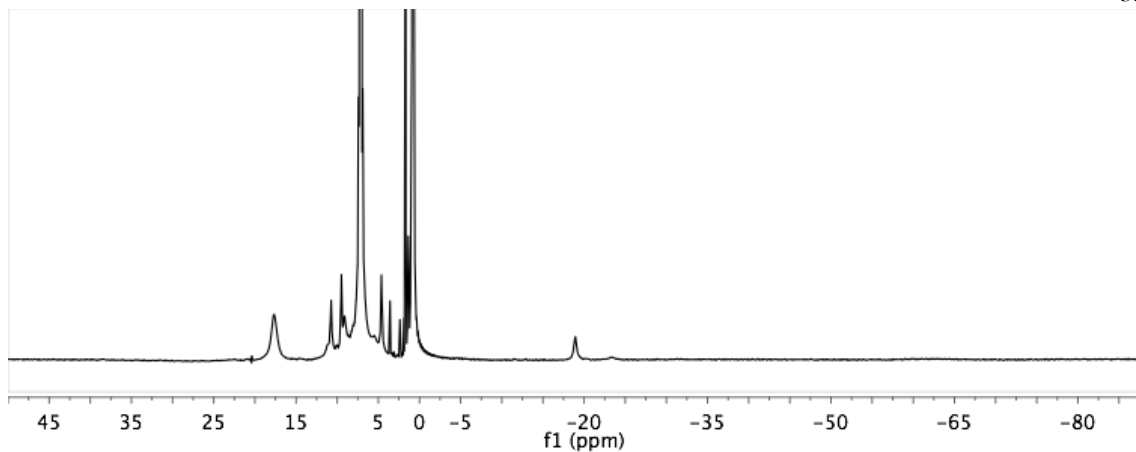


Figure 64. ^1H NMR (300 MHz, C_6D_6) spectrum of **14-Sc**

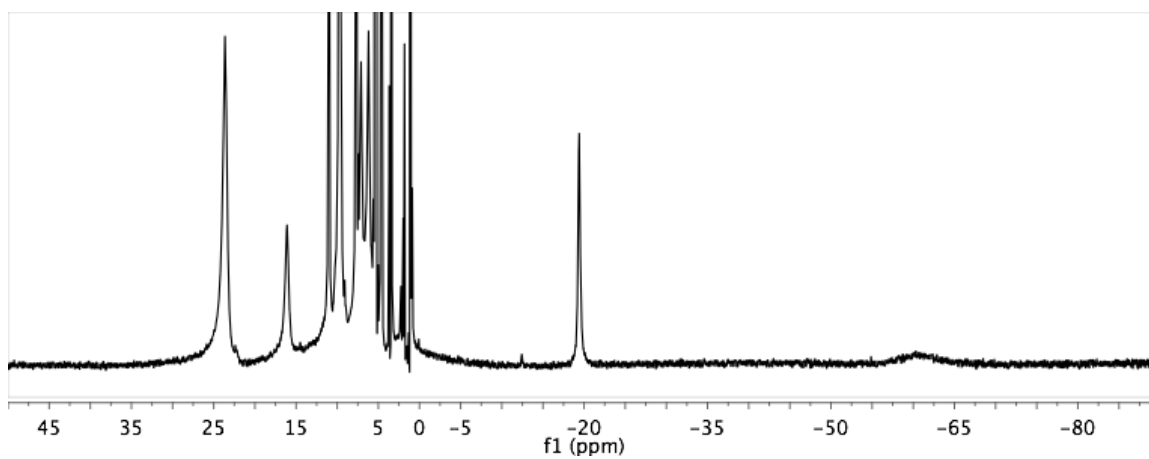


Figure 65. ^1H NMR (300 MHz, CD_2Cl_2) spectrum of **14-Co**

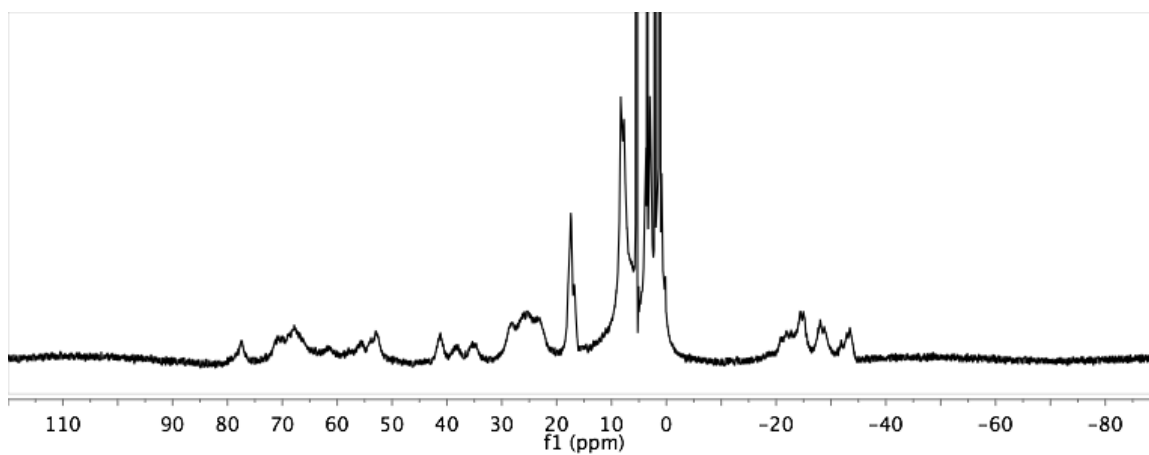


Figure 66. ^1H NMR (300 MHz, CD_2Cl_2) spectrum of $[(\mathbf{16-Y})_2]^{5+}$

APPENDIX A

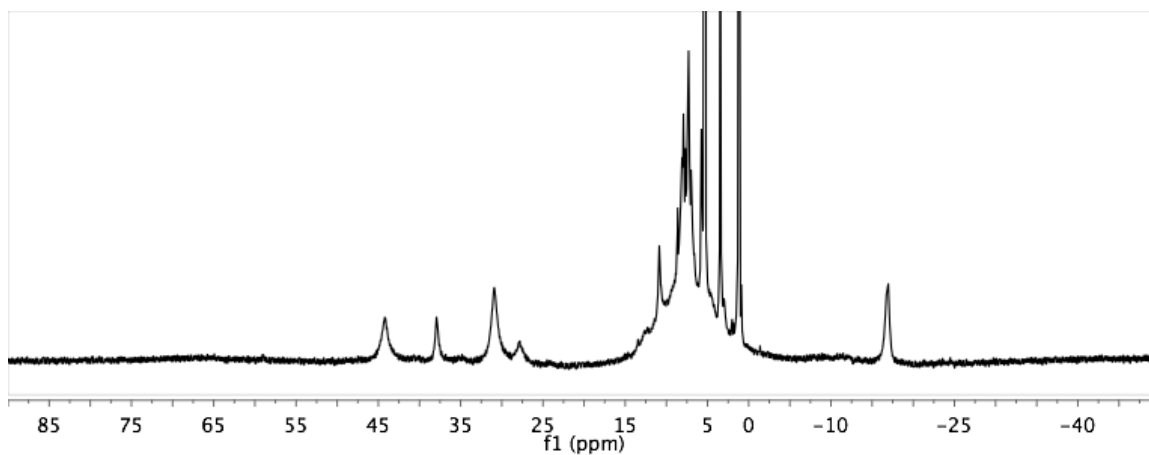


Figure 67. ¹H NMR (300 MHz, CD₂Cl₂) spectrum of A.2-Zn-O

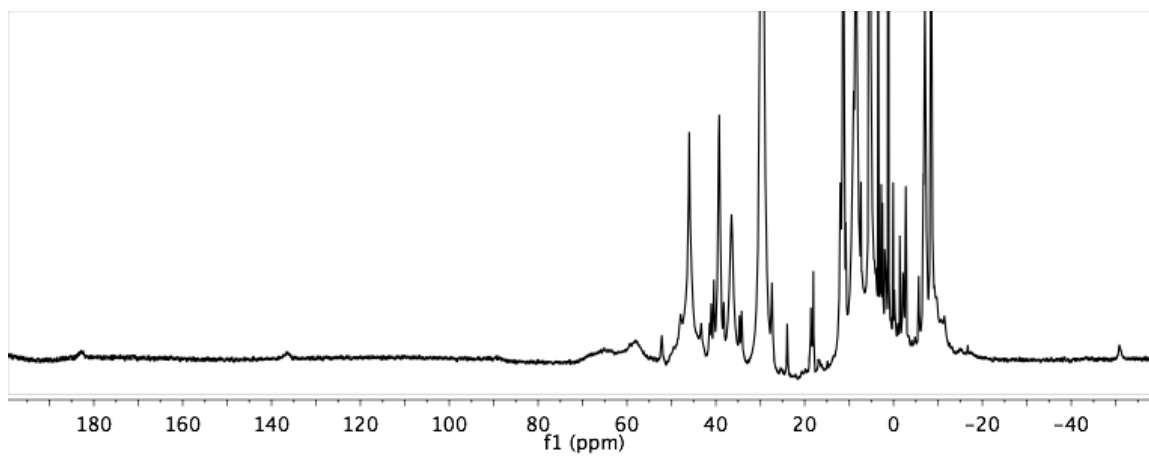


Figure 68. ¹H NMR (300 MHz, CD₂Cl₂) spectrum of A.1-Co-O

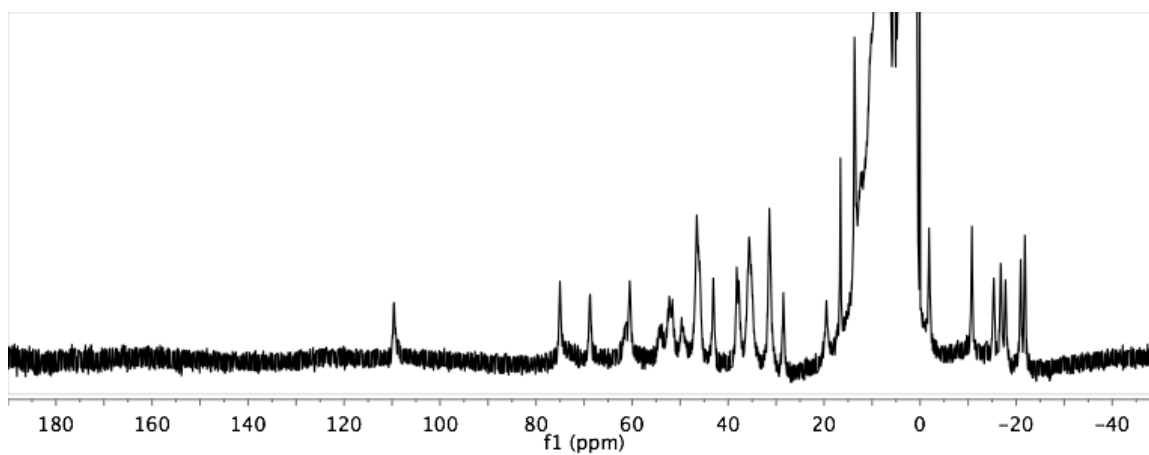


Figure 69. ¹H NMR (300 MHz, CD₂Cl₂) spectrum of A.4-Zn-O

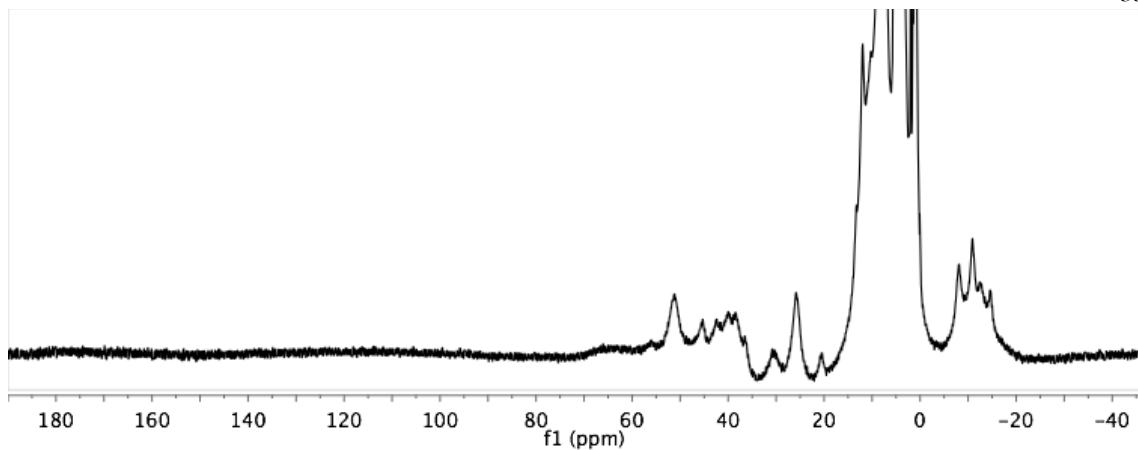


Figure 70. ¹H NMR (300 MHz, CD₂Cl₂) spectrum of **A.3-Zn-O**

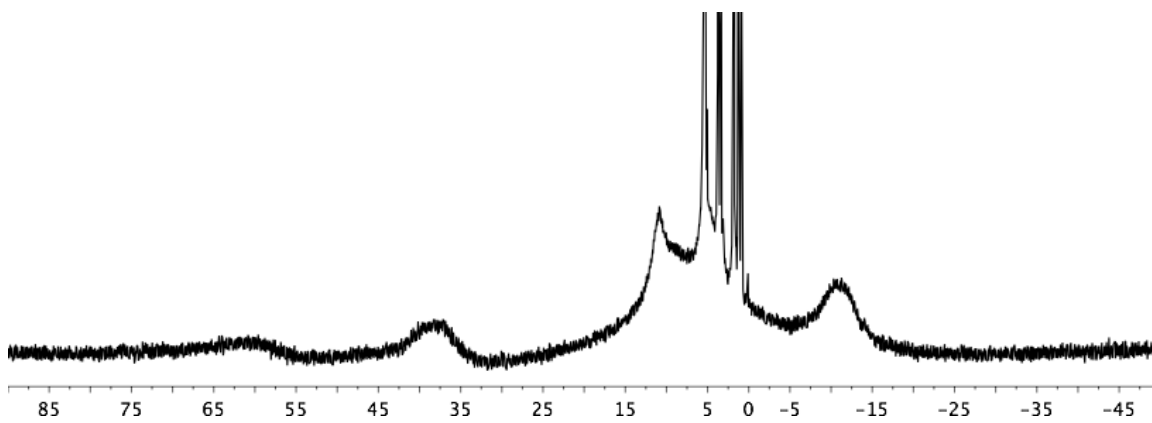


Figure 71. ¹H NMR (300 MHz, CD₂Cl₂) spectrum of **LMn₃(OAc)₂(OTf)**

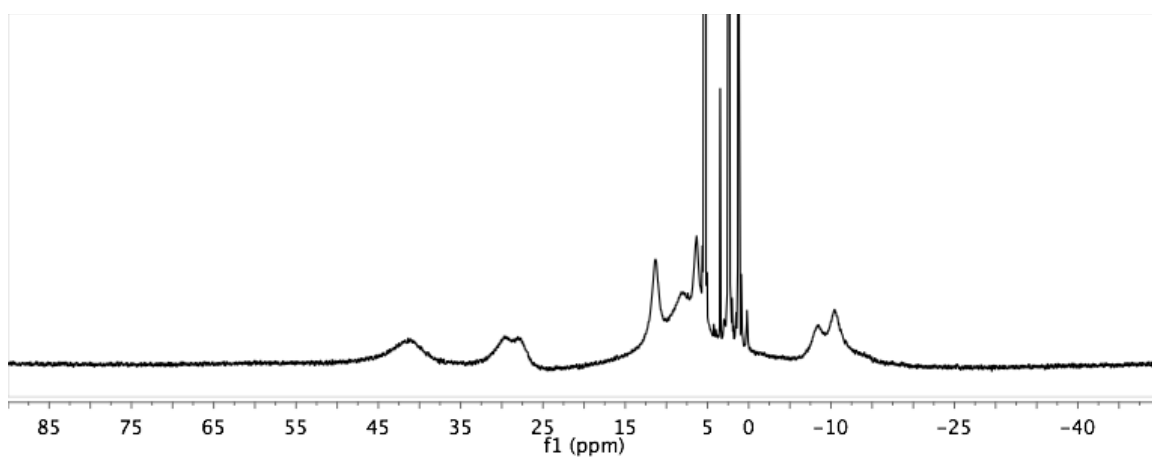


Figure 72. ¹H NMR (300 MHz, CD₂Cl₂) spectrum of **A.5-S**

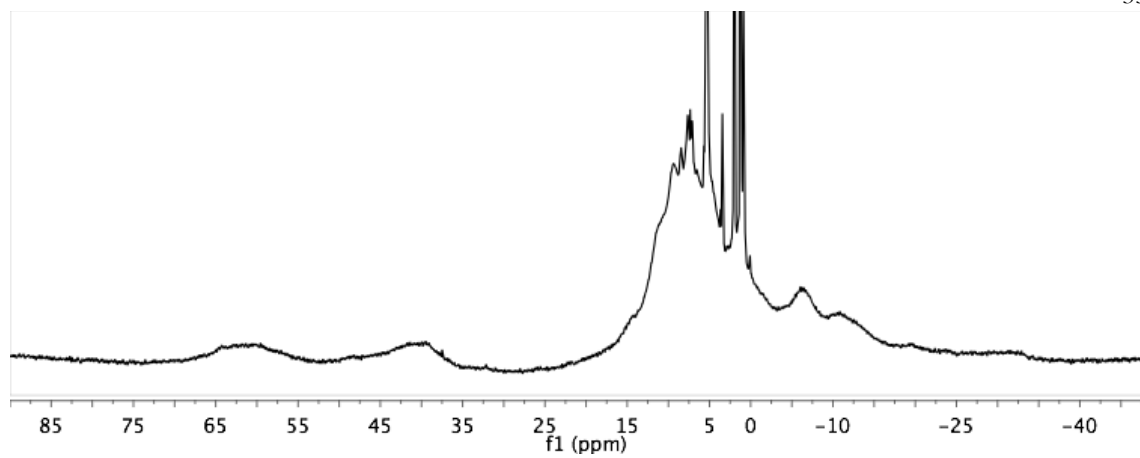


Figure 73. ^1H NMR (300 MHz, CD_2Cl_2) spectrum of **A.7-Mn-F**

APPENDIX B

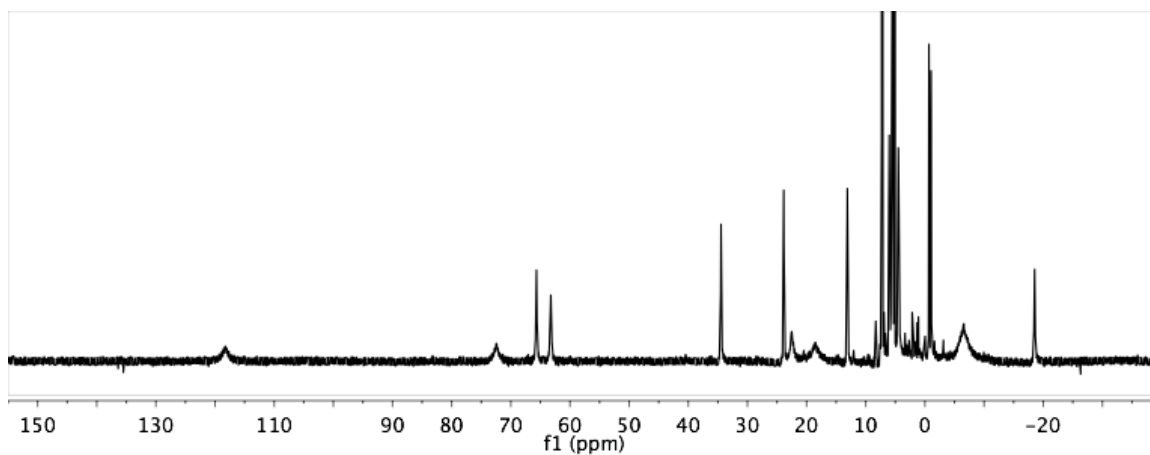


Figure 74. ¹H NMR (300 MHz, CDCl₃) spectrum of **B.1b**

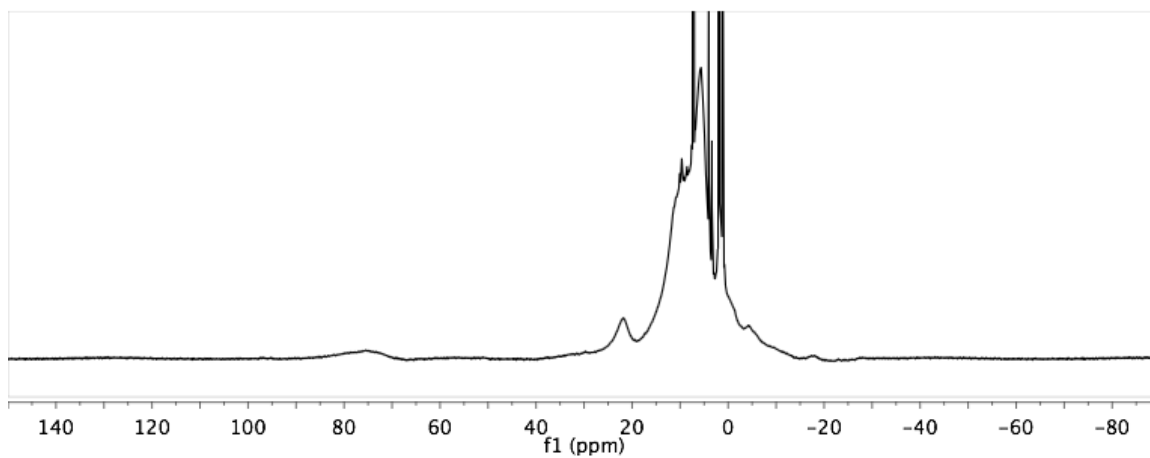


Figure 75. ¹H NMR (300 MHz, CDCl₃) spectrum of **B.1c**

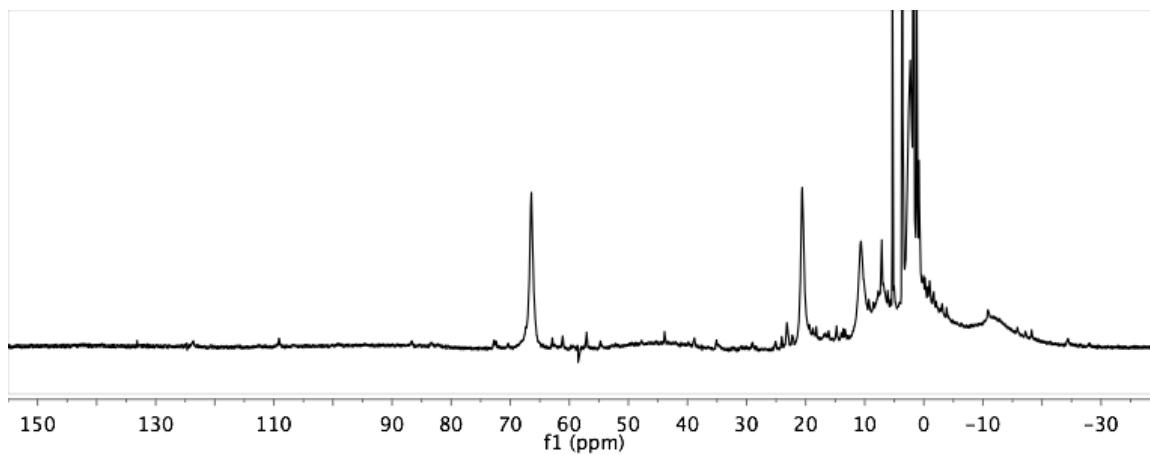


Figure 76. ¹H NMR (300 MHz, CD₂Cl₂) spectrum of **B.2a**

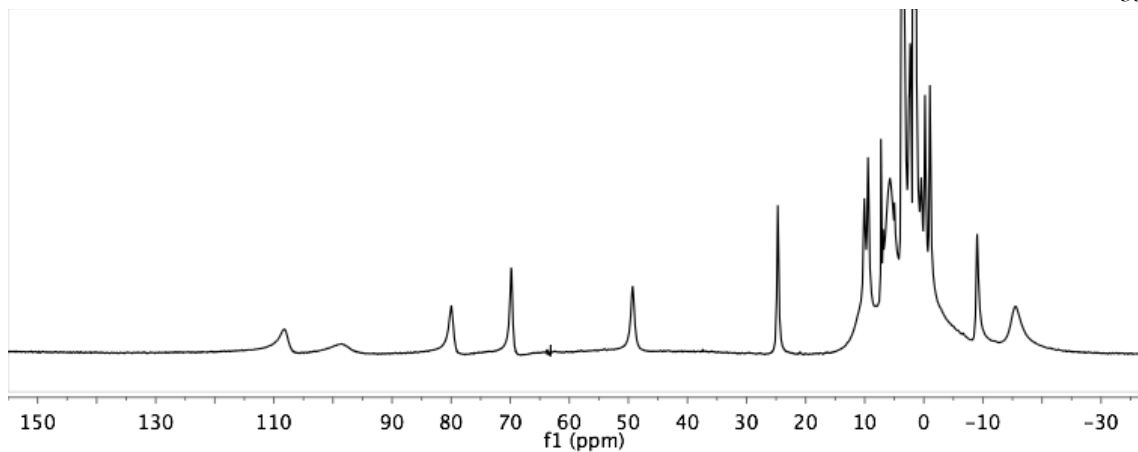


Figure 77. ^1H NMR (300 MHz, CDCl_3) spectrum of **B.2c**

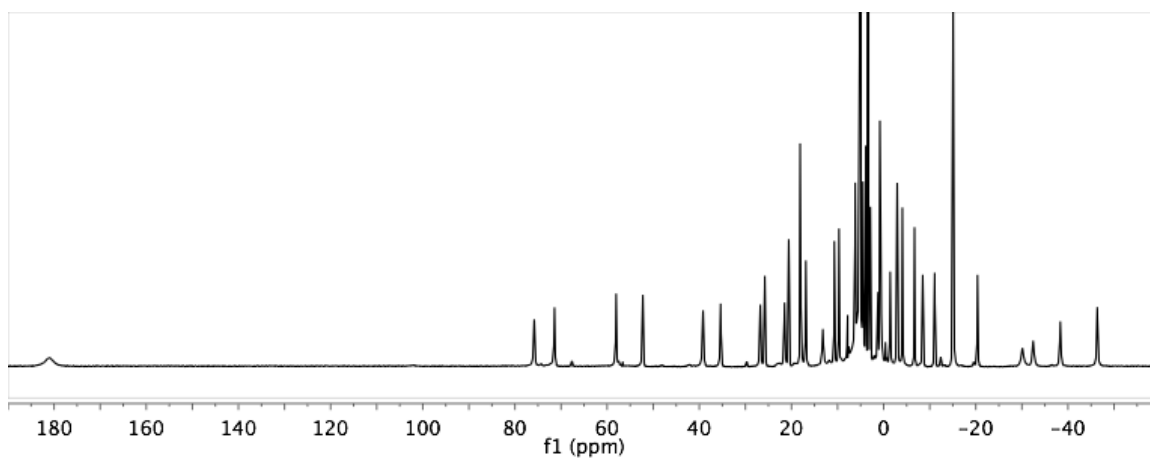


Figure 78. ^1H NMR (300 MHz, CD_3OD) spectrum of **B.3a**

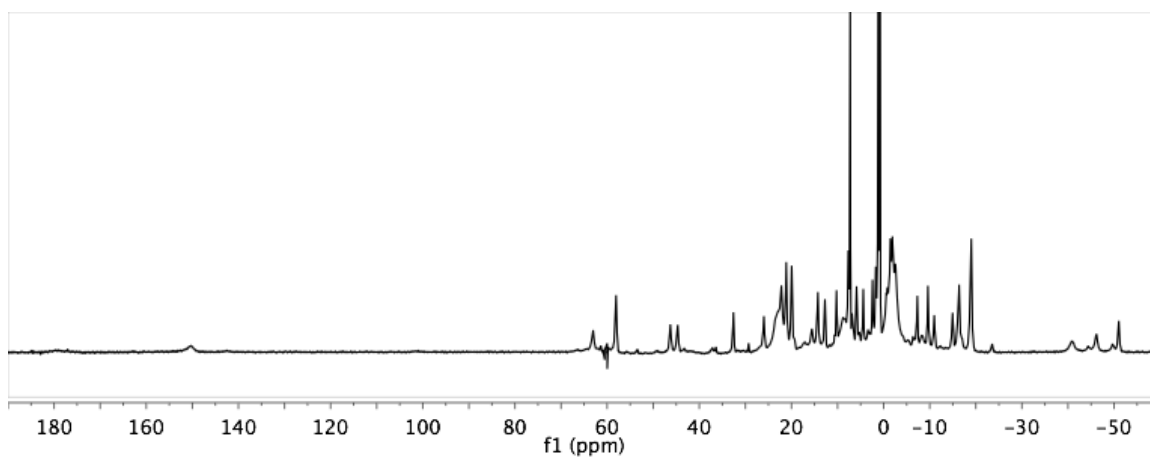


Figure 79. ^1H NMR (300 MHz, CDCl_3) spectrum of **B.3a**

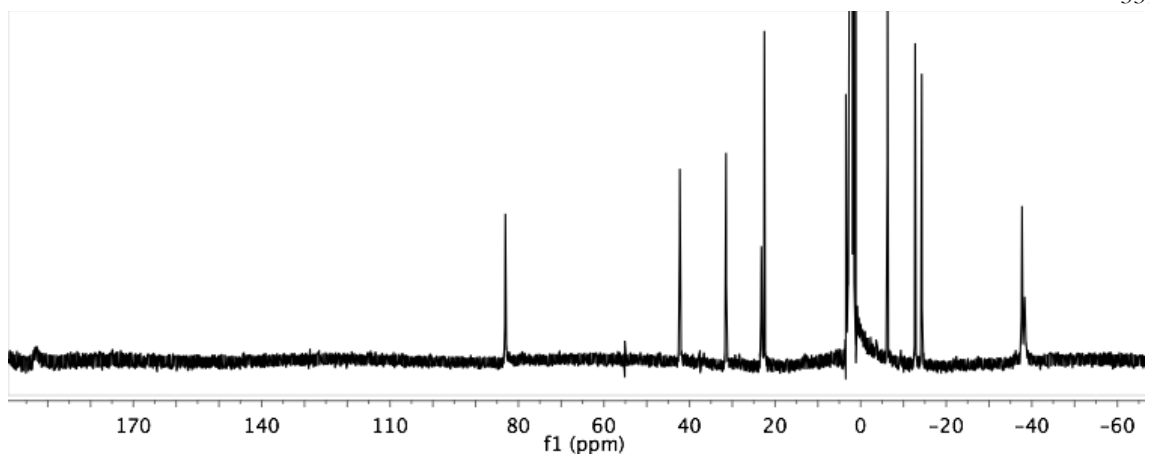


Figure 80. ^1H NMR (300 MHz, CD_3CN) spectrum of **B.4**

APPENDIX C

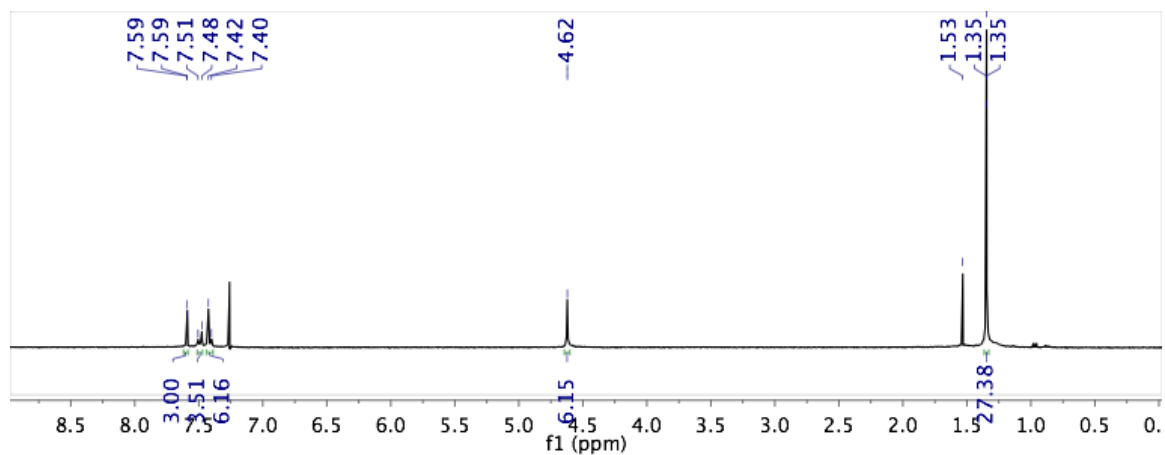


Figure 81. ^1H NMR (300 MHz, CDCl_3) spectrum of **B**

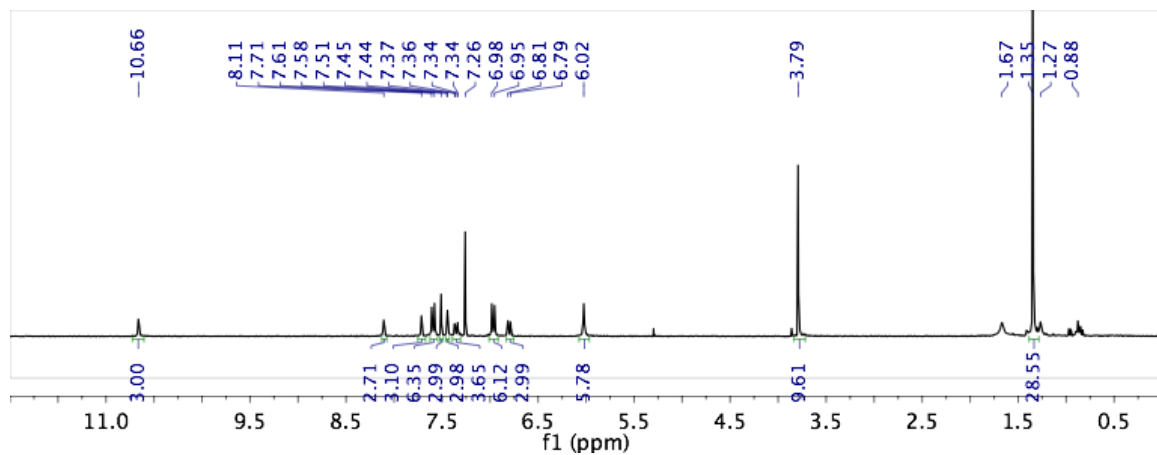


Figure 82. ^1H NMR (300 MHz, CDCl_3) spectrum of **C.4-OMe**

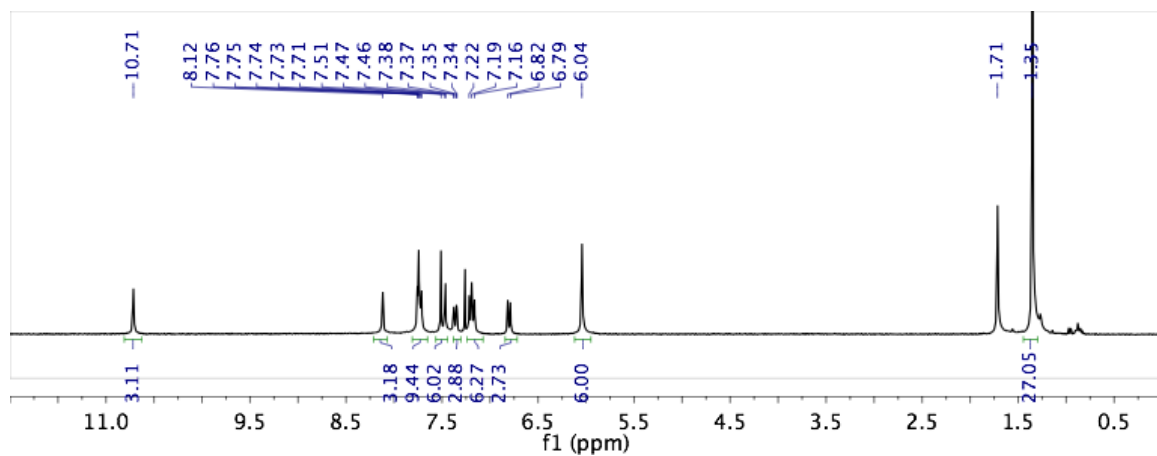


Figure 83. ^1H NMR (300 MHz, CDCl_3) spectrum of **C.4-F**

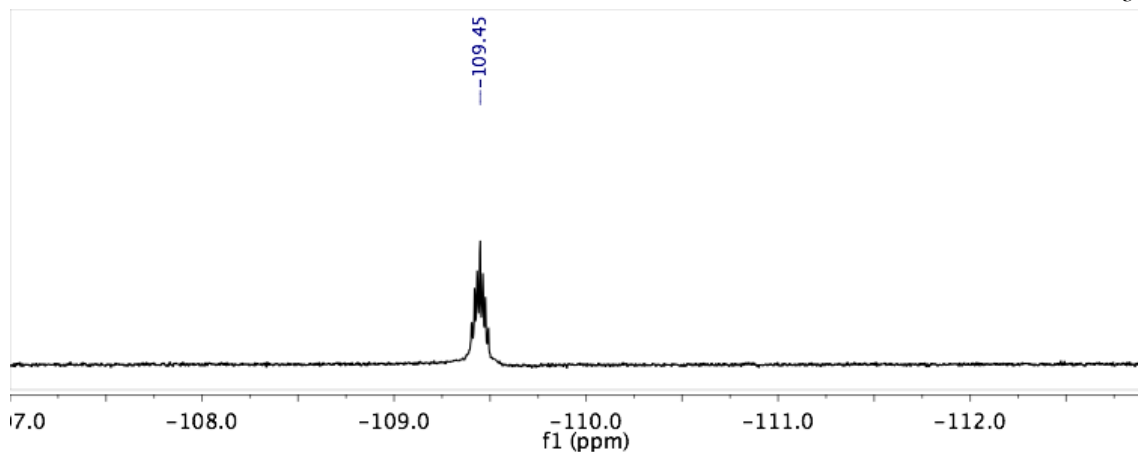


Figure 84. ^{19}F NMR (282 MHz, CDCl_3) spectrum of **C.4-F**

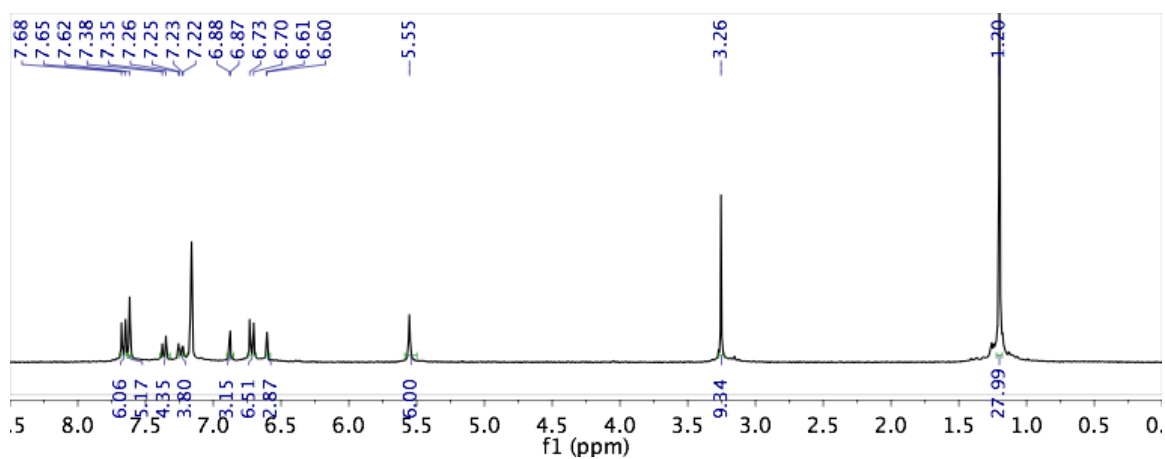


Figure 85. ^1H NMR (300 MHz, C_6D_6) spectrum of **C.1-OMe**

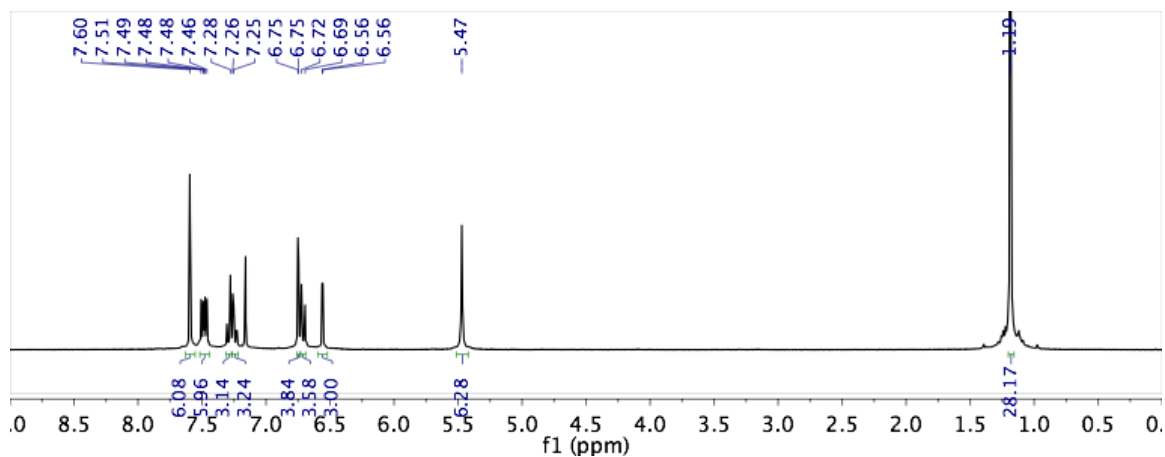


Figure 86. ^1H NMR (300 MHz, C_6D_6) spectrum of **C.1-F**

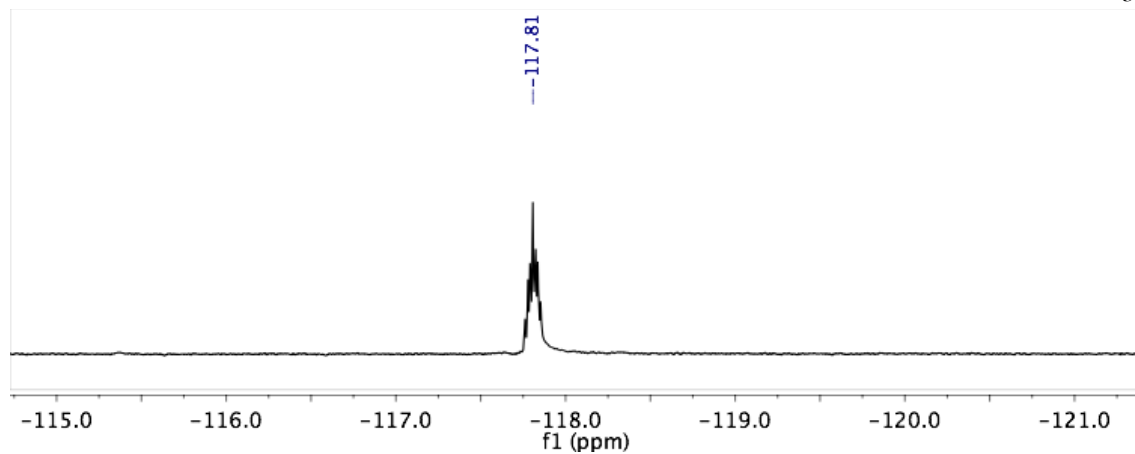


Figure 87. ^{19}F NMR (282 MHz, CDCl_3) spectrum of **C.1-F**